Development of New Concepts for Photoswitchable DNA-Nanostructures

Dissertation
zur Erlangung des Doktorgrades
der Naturwissenschaften

vorgelegt im Fachbereich Biocheme, Chemie und Pharmazie
der Goethe-Universität
in Frankfurt am Main

von
Nikolai Michal Grebenovsky
aus Wiesbaden (Deutschland)

Frankfurt am Main 2019
(D30)

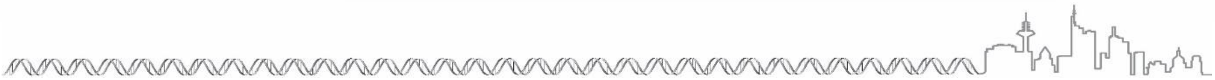

Die vorliegende Arbeit wurde im Institut für Organische Chemie und Chemische Biologie unter der Leitung von Prof. Dr. Alexander Heckel angefertigt und vom Fachbereich Biochemie, Chemie und Pharmazie als Dissertation angenommen.

Dekan: Prof. Dr. Clemens Glaubitz

Erstgutachter: Prof. Dr. Alexander Heckel

Zweitgutachter: Prof. Dr. Mike Heilemann

Datum der Disputation: 17.12.2019

Abstract

The fact that the interaction of oligonucleotides follows strict rules has been utilized to create two- or three-dimensional objects made of DNA. With computer-assisted design of DNA sequences, any arbitrary structure on the nanometer- to micrometer-scale can be generated just by hybridization of the needed strands. As astonishing these structures are, without any modification of the DNA strands involved no function can be assigned to them. Many different ways of functionalizing DNA-nanostructures have been developed with light-responsive nanostructures having a rather subordinated role. Almost all light responsive DNA-nanostructures involve the acyclic azobenzene-linking system *t*Azo based on *D*-threoninol which is known to work best at elevated temperatures to ensure optimal switching. As the structure of DNA-constructs is mainly maintained by hydrogen-bonding, variation of the temperature should be avoided in order to keep the structure intact.

To develop a light-responsive nanostructure model system with low-temperature operating azobenzene *C*-nucleosides, DNA-minicircles have been utilized. Those minicircles bear a lariat-like protrusion with a 10 base long single-stranded overhang, which is responsible for the dimerization with a ring bearing a complementary binding region. DNA-minicircles have been produced in a sequential manner by building and purifying the single stranded minicircle first by splint ligation and prepratative PAGE or RP-HPLC, followed by annealing it to the outer ring and subsequent purification by molecular-weight cut-off. Imaging of DNA-minicircles by atomic force microscopy (AFM) was possible with several methods of sample preparation leading to images of varying quality. With the help of AFM, qualitative analysis of the minicircles was possible. It could be shown, that theoretical and empirical size dimensions of the rings and their interactions were in great accordance. Designing the interaction site of the minicircles proved to be the main task in this project. The amount of *C*-nucleosidic modifications was identified by screening, followed by a screening of their optimal position and binding partners in the counterstrand. Two azobenzene *C*-nucleosides in a 10mer binding region and abasic sites opposing them appeared to give the best compromise between absolute dimerization ratio and photocontrolled change of it, as identified by native PAGE. In the following, the dimerization ratios of minicircles containing azobenzene *C*-nucleosides were compared with minicircles containing *t*Azo and unmodified minicircles. It could be shown, that the *t*Azo-modification leads to an elevated binding affinity compared to the unmodified minicircles, but the change upon irradiation is relatively humble compared to the *C*-nucleosides. For the *C*-nucleosidic modifications dimerization ratios reached a maximum of 40% in favored *trans*-state, but could be almost completely turned-off when switching into *cis*-state. In addition, arylazopyrazole-modified *C*-nucleosides could be switched into *trans*-state by irradiating at 530 nm, which is an improvement compared to standard azobenzene, as it shifts irradiation wavelength closer to the phototherapeutic window.

The utilization of DNA-analogous *C*-nucleosides bring two drawbacks with them: the ribose units include the flexibility of the sugar conformation and it is reasonable to think, that upon isomerization of the azobenzene, part of the steric stress generated is compensated by the sugar reconfiguration, which is lost for duplex

destabilization. In addition, the combination of the ribosidic linker end the end-to-end distance of *trans*-azobenzene causes the chromophore to penetrate deep into the base stack of the opposing strand, causing a serious destabilization even in favored *trans*-state. The goal was to find a linker system, that combines the benefits of the azobenzene *C*-nucleoside without the possibility to change sugar conformation and the strong destabilization in the *trans*-state. For this reason locked azobenzene *C*-nucleosides in analogy to LNA nucleosides have been synthesized. The synthesis of LNA analogous azobenzene *C*-nucleosides (LNAzo) was possible over a 16-step synthesis, with the critical step being the addition of *in situ* lithiated azobenzene to protected sugar aldehyde. Both anomers of LNAzo and mAzo as reference where incorporated into different oligonucleotide test systems by solid phase synthesis for thorough evaluation. It could be shown, that LNAzo β has a similar performance to mAzo in DNA with overall slightly increased T_M- and ΔT_M-values. Performance of LNAzo β was similar to mAzo even if steric stress is reduced by using abasic sites in the counterstrand opposing the azobenzene. Only in a RNA context, the true potential of LNAzo β could be observed. In a DNA/RNA duplex, photocontrol could be improved by almost 50%, in a RNA/RNA duplex even by over 100%. Although the primary goal was the improvement of the azobenzene *C*-nucleoside for a DNA-nanostructure context, LNAzo β proved not to give a sufficient improvement in regard to the cost-value ratio. Never the less, the invention of the locked azobenzene *C*-nucleoside was a huge success for reversible photoregulation of RNA hybridization. With this, a new way to regulate RNA hybridization has been found, which could be used to create RNA therapeutics in an antisense-approach.

As LNAzo β improved duplex stability only in a limited amount in DNA, further improvements on the backbone have been declared futile and focus shifted onto optimization of the chromophore. First, the azobenzene as it is installed on the ribosidic linker decreases duplex stability by forcing its distal aromat deep into opposing base stacking region. It would be an improvement, if in favored *trans*-state the distal aromat would be positioned in the less confined space of either major or minor groove and only upon isomerization would shift into base pairing region. Second, the azobenzene itself is not able to contribute to attractive interactions aside from relatively weak π-interactions to adjacent nucleobases, which could be improved, if it could partake in hydrogen bonding. For those apparent reasons, 2-phenyldiazenyl-modified purines have been selected as targets. They combine the ability to contribute to hydrogen bonding of nucleobases with the photochomicity of azobenzenes. Both 2'-deoxyadenosine- and 2'-deoxyguanosine-analogue photoswitches dA_{Azo} and dG_{Azo} have been synthesized and incorporated into 10mer DNA test systems by solid phase synthesis. It could be shown, that duplex stability could be increased compared to established azobenzene *C*-nucleoside. The improvement was stronger for dA_{Azo} than for dG_{Azo} as in the case for guanosine the amino function on the *C*2-position had to be replaced by the phenyldiazenyl function, reducing its ability to form hydrogen bonds. Unfortunately, photocontrol of duplex stability caused by 2-phenyldiazenyl purines was rather limited. A reason for this could be the positioning of the distal aromat within the duplex, which can be close to the opposing nucleobase (endo-helical) or in greater distance (exo-helical). The exo-helical conformation of the *trans*-isomer can only switch to the exo-*P*-*cis*-conformation, which relocates the distal aromat in the minor groove, without significant impact on duplex stability.

Zusammenfassung

Die Rolle der Desoxyribonukleinsäure (DNA) als Informationsträger für Transkriptionsprodukte wie Peptide, Proteine oder andere Ribonukleinsäuren, quasi als Bauplan für das Leben selbst, korreliert direkt mit ihren präzisen, strukturellen Eigenschaften. Angetrieben durch Entropie tendiert DNA dazu im wässrigen Medium zu dimerisieren. Die Wasserstoffbrücken der Nukleobasen und die aromatischen π-Wechselwirkungen tragen hierzu bei. Um alle Bindungspartner in optimale Distanz für die attraktiven Wechselwirkungen zu bringen, haben Oligonukleotide diskrete Arten entwickelt sich ineinander zu winden, welche als A-, B- und Z-helix bekannt sind.

Die Regulation der Hybridisierung von Oligonukleotiden ist ein Ziel, welches die Wissenschaft seit der Entdeckung der DNA-Struktur 1953 anstrebt. Die Steuerung der Hybridisierung durch äußere Stimuli ist ein attraktives Ziel, da hierdurch Prozesse in Lebenden Organismen gesteuert werden können. Die Wahl eines externen Stimulus ist nicht leicht, da viele Vor- und Nachteile passend für die jeweilige Anwendung abgewogen werden müssen. Kaum ein äußerer Reiz bringt so viele Vorteile mit sich, wie die Steuerung der Oligonukleotidhybridisierung mit Licht. Im Gegensatz zu chemischen Stimuli kontaminiert Licht das zu untersuchende System nicht, durch moderne Technik kann es mit hoher Orts- und Zeitauflösung verwendet werden und ist nicht schädlich für biologische Anwendungen, sofern entsprechende Wellenlängen und Intensitäten verwendet werden.

Um reversible Kontrolle über die Oligonukleotidhybridisierung zu erhalten können lichtschaltbare Moleküle wie Azobenzol in die Oligonukleotide eingebaut werden. Das planare *trans*-Azobenzol kann zwischen die benachbarten Nukleobasen interkalieren, ohne deren Struktur stark zu beeinflussen. Während der lichtinduzierten *trans*-nach-*cis*-Isomerisierung nehmen die beiden Aromaten des Azobenzols eine gewinkelte Konformation an. Dies führt zu einer Erhöhung des sterischen Anspruchs des Chromophors im Duplex, was dazu führt, dass die Nukleobasen aus ihrem optimalen Bindungsabstand gedrängt werden und hierdurch die Stabilität des Duplexes verringert wird. Um diese Eigenschaft des Azobenzols optimal nutzen zu können ist die Frage, wie das Azobenzol im Oligonukleotid befestigt wird, von größter Bedeutung. Der Linker hat die Aufgabe das Azobenzol so zu positionieren, dass es immer in den Basenstapel des Duplex zeigt und auch während der Isomerisierung nicht in die große oder kleine Furche migriert. Zudem muss der Linker so rigide sein, dass er die Energie gewonnen durch Licht und übersetzt durch den Chromophor in eine mechanische Bewegung auf die Nukleobasen überträgt um diese auseinander zu bringen, anstatt sich selber zu verformen.

Im Gegensatz zu azyklischen Linkern wie das *D*-Threoninol haben sich Azobenzol *C*-Nukleoside im Besonderen bewährt. Sie verfügen über die nötige Rigidität, um auch bei Raumtemperatur optimal zu agieren, während azyklische Linker erhöhte Temperaturen brauchen. Azobenzol *C*-Nukleoside ahmen den natürlichen Zustand in einem Oligonukleotid nach, mit dem Unterschied, dass die Nukleobase gegen den Chromophor ausgetauscht ist und wurden bereits vor Beginn der vorliegenden Arbeit genutzt, um die Duplexstabilität in RNA und DNA zu steuern.

Zu diesem Zeitpunkt wurden das Azobenzol und der ribosidische Linker als essenzieller Schritt der Syntheseroute über eine palladiumkatalysierte Heck-Kupplung verbunden. Diese Reaktion erfolgt mit einer hohen Stereoselektivität, hat allerdings zum Nachteil, dass sie nur in sehr limitierten Syntheseansätzen erfolgreich umsetzbar ist. Um genügend Material für die weiteren Syntheseschritte zu akkumulieren, musste die Heck-Kupplung in hohem Aufwand in Kleinstmaßstäben durchgeführt werden, was das Nadelöhr dieser Syntheseroute darstellte.

Im Zuge der vorliegenden Arbeit wurde die Syntheseroute zu Azobenzol *C*-Nukleosiden neu entwickelt. Essenziell hierbei war ein Lithium-Halogen-Austausch an iodierten Azobenzolen bei tiefen Temperaturen und die subsequente Addition eben jener an geschützte Ribonolactone und folgender Dehydroxylierung. Hierbei konnte identifiziert werden, dass die Schutzgruppen am Ribonolacton einen gewissen sterischen Anspruch nicht übersteigen durften, da sonst der nukleophile Angriff des lithiierten Azobenzols gemäß der Bürgi-Dunitz-Trajektorie nicht erfolgen konnte. Auf diese Weise konnten Azobenzol *C*-Nukleoside im Multigrammmaßstab hergestellt werden, wobei eine anomere Verunreinigung einen geringfügigen Nachteil dieser Methode darstellt.

Die Tatsache, dass die Interaktion von Oligonukleotiden derart klar definierten Regeln folgt, wird dazu genutzt zwei- oder dreidimensionale Objekte aus DNA zu schaffen. Mit computergestützer Hilfe im Designprozess entsprechender DNA-Sequenzen und dem technischen Fortschritt der Oligonukleotid-Festphasensynthese, um diese Sequenzen in die Realität umzusetzen, kann mittlerweile jede noch so willkürliche Struktur im Nano- bis Mikrometermaßstab Umgesetzt werden. So beeindruckend diese DNA-Nanostrukturen auch sein mögen, die meisten von ihnen besitzen keine inhärente Funktion. Seit der Entwicklung der ersten DNA-Nanostrukturen durch Nadrian Seeman 1982 hat sich ein großer Teil der Bemühungen in diesem Feld darauf konzentriert, DNA-Nanostrukturen zu funktionalisieren. Im Vergleich zu anderen chemischen oder biochemischen Modifikationen von DNA Nanostrukturen spielen lichtsteuerbare Modifikationen eine eher untergeordnete Rolle.

Für die Entwicklung reversibel lichtsteuerbarer Nanostrukturen kam bis zum Beginn der vorliegenden Arbeit fast ausschließlich der von Prof. Dr. Hiroyuki Asanuma 2001 entwickelte *D*-Threoninol Azobenzol Baustein *t*Azo zum Einsatz. Die simple synthetische Zugänglichkeit dieses Bausteins trägt zu dessen großer Beliebtheit bei, auch wenn dessen Nachteil, die benötigte Temperaturerhöhung für eine optimale Schaltamplitude, die strukturelle Integrität der Nanostrukturen gefährdet. Die Entwicklung photoschaltbarer DNA-Nanostrukturen auf Basis von Azobenzol *C*-Nukleosiden zur Verbesserung der Lichtschaltbarkeit bei niedrigen Temperaturen erschien daher als logischer Schritt in der Entwicklung lichtschaltbarer DNA-Nanostrukturen.

Hierfür wurde ein Nanostruktur-Modellsystem auf Basis von dimerisierenden Ringen ausgewählt, da diese synthetisch leicht zugänglich sind, gut mit Rastermikroskopiemethoden charakterisierbar sind und durch ihren modularen Aufbau sich gut für ein Screening verschiedener Modifikationen eignen. Die DNA-

Ringe wurden sequentiell aufgebaut, indem zuerst der „Innenring“ durch Splint-Ligation enzymatisch hergestellt wurde. Für die Aufreinigung des einzelsträngigen Innenringes wurden präparative denaturierende PAGE oder RP-HPLC als Aufreinigungsmethoden der Wahl ohne Präferenz identifiziert. Der „Außenring“, bestehend aus vier Einzelsträngen, wurde daraufhin durch Hybridisierung mit dem Innenring verbunden. Viele Aufreinigungsmethoden wurden für die assemblierten Konstrukte getestet, wobei sich Größenausschluss durch Spin-Filtration als einzige Methode durchsetzen konnte. Das Abbilden von DNA-Ringen mittels der Rasterkraftmikroskopie (AFM) für eine qualitative Analyse ließ sich durch verschiedene Probenpräparationstechniken umsetzen. Es konnte gezeigt werden, dass theoretische und empirische Dimensionen der Ringe in gutem Einklang zueinander waren. Aufgrund der großen Diskrepanz in der Dimerisierungsrate unmodifizierter Ringe zwischen AFM und nativer PAGE, wurde das AFM lediglich zur qualitativen Analyse verwendet.

Die Entwicklung des Designs der Bindungsstelle der DNA-Ringe stellte eine der zentralen Aufgaben dieses Projektes dar. Zuerst wurde die notwendige Anzahl von Azobenzol *C*-Nukleosiden durch ein Screening auf zwei Modifikationen in einer 10mer bindungsstelle identifiziert, anschließend wurde die optimale Position bestimmt. Da hierbei im Vergleich zum unmodifizierten Wildtyp immer noch eine starke Destabilisierung zu beobachten war, wurden in der gegenüberliegenden Bindungsstelle abasische Linker eingesetzt, um die sterische Abstoßung zu den Azobenzolen zu mindern. Die hierbei erhaltenen photochromen Bindungsstellen lieferten den bestmöglichen Kompromiss zwischen absoluter Dimerisierungsrate und photochemischer Kontrolle eben jener. Im direkten Vergleich der Dimerisierungsraten aller Azobenzol *C*-Nukleosid-Modifikationen mit dem Wildtyp und der *t*Azo-Modifikation auf Basis nativer PAGE konnte gezeigt werden, dass eine maximale Dimerisierungsrate von etwa 40% erreicht werden konnte im *trans*-Zustand, welche sich fast komplett ausschalten ließ im *cis*-Zustand. Zusätzlich konnte durch Verwendung von Arylazopyrazol-modifizierten *C*-Nukleosiden der *trans*-Zustand bathochrom verschoben angeregt werden im Vergleich zu normalem Azobenzol. Dies ist von großem Nutzen für etwaige *in vivo* Anwendungen, da hierdurch die Anwendung der Azobenzolmodifikationen näher in Richtung phototherapeutisches Fenster rückt. Nichts desto trotz konnte durch Temperaturvariation während des PAGE Experiments gezeigt werden, dass noch viel Arbeit auf dem Feld der thermodynamischen und kinetischen Charakterisierung DNA-basierter Nanokonstruktaggregation notwendig ist, um ein System komplett zu verstehen und demensprechend auf die jeweilige Anwendung anzupassen.

Die Untersuchungen der Azobenzol *C*-Nukleoside im Bezug die Dimerisierungseigenschaften in DNA-Ringen hat gezeigt, dass der Einbau von Azobenzolen als *C*-Nukleoside einen intrinsischen sterischen Anspruch an das System stellt, welches der Duplex selbst bei *trans*-Azobenzol mit verringerter Duplexstabilität beantwortet. Obwohl die erreichbare Schaltamplitude der Duplexstabilität in einem nützlichen Rahmen stattfindet, ist die Gesamtstabilität des Duplexes stark herabgesetzt, sobald Azobenzol *C*-Nukleoside eingebaut werden. Um dieses Problem in den Griff zu bekommen wurden verbrückte Azobenzol *C*-Nukleoside auf Basis von *Locked Nucleic Acids* (LNA) entwickelt. LNA Bausteine, welche in der therapeutischen Industrie aufgrund ihrer hohen

Nukleasestabilität in der Entwicklung moderner RNA-Therapeutika eingesetzt werden, haben die Eigenschaft die Hybridisierungsaffinität von Oligonukleotiden zu steigern. Zusätzlich könnte das Verbrücken des Zuckers noch das Problem der konformationellen Freiheit der Ribose-Einheit lösen. Da ribosidische Linker in einem Azobenzol *C*-Nukleosid sowohl in der 2'-endo-, als auch in der 3'-endo-Konformation vorliegen kann, ist es nur plausibel, dass die kinetische Energie des Azobenzols zumindest teilweise in einer Konformationellen Änderung entladen werden kann. Dies wäre im Falle eines verbrückten Zuckers nicht möglich, weswegen die gesamte Energie für die Schwächung der Wasserstoffbrücken genutzt werden kann. Dies könnte noch zusätzlich zur Verbesserung der Duplexstabilität zu einer verbesserten Photokontrolle ebenjener führen. Aufgrund ihres kommerziellen Interesses sind LNA-Bausteine in ihrer Synthese sehr etabliert, was die Synthese und Evaluierung von verbrückten Azobenzol *C*-Nukleosiden als lohnenswertes Ziel greifbar macht.

Die Synthese von verbrückten Azobenzol *C*-Nukleosiden (LNAzo) erfolgte über eine 16-stufige Synthese, wobei der essenzielle Schritt ein nukleophiler Angriff des *in situ* lithiierten azobenzols an einem offenkettigen Zuckeraldehyden war. Diese Reaktion war insofern problematisch, da nach Deprotonierung durch das erste Äquivalent lithiierten Azobenzols sich ein Gleichgewicht zwischen dem offenkettigen 4'-Alkoholat und dem zyklisierten 1'-Alkoholat einstellte. Da ausschließlich das 4'-Alkoholat für eine nukleophile Addition zugänglich war, das Gleichgewicht aber auf Seiten des 1'-Alkoholats lag, war die Reaktion nur in sehr kleinen Maßstäben zu beschreiten, was die Gesamtausbeute von synthetisiertem LNAzo minderte. Hierbei konnten beide Anomere des LNAzo Bausteins hergestellt und voneinander getrennt verarbeitet werden. Beide LNAzo-Anomere wurden daraufhin mit dem *meta*-Azobenzol *C*-Nukleosid (mAzo) als Referenz über Festphasensynthese in Oligonukleotid-Testsysteme eingebaut, um ihre Eigenschaften optimal charakterisieren zu können.

In DNA erscheint das β-Anomer von LNAzo eine leichte Verbesserung gegenüber dem etablierten mAzo zu zeigen, mit leicht erhöhter Stabilität und Photokontrolle. Wenn der sterische Stress durch Einbringung von abasischen Modifikationen im Gegenstrang vermindert wird, veränderten sich diese Beobachtungen nur geringfügig. Da LNA-Bausteine dafür bekannt sind die A-Helixbildung zu fördern, wurden die neuen Bausteine zusätzlich in einem RNA-Kontext evaluiert. In einem DNA/RNA-Duplex konnte die Photokontrolle um fast 50% Erhöht werden, in einem RNA/RNA-Duplex sogar um über 100%. Obgleich das primäre Ziel die Verbesserung der Azobenzol *C*-Nukleoside für die Anwendung in DNA-Nanostrukturen war, war die dadurch erzielte Verbesserung in Hinsicht auf eine Kosten-Nutzen-Relation eher fraglich. Nichtsdestotrotz war die Entwicklung des LNAzo Bausteins ein voller Erfolg für die reversible Photoregulation von RNA-Hybridisierung. Mithilfe des LNAzo Bausteins wurde eine neuartige, potente Methode gefunden RNA-Hybridisierung gezielt zu steuern und könnte Anwendungen im Bereich der Oligonukleotidtherapeutika finden.

Mit der Entwicklung der verbrückten Azobenzol *C*-Nukleoside wurde zudem gezeigt, dass die Modifikation des Rückgrates die Duplexstabilität und Photokontrolle nur bis zu einem gewissen Grad verbessert werden konnte. Da weitere Bestrebungen das Rückgrat zu optimieren als nutzlos erachtet wurden, verlagerte sich das Interesse nun darauf, den Chromophor selbst in seinen

morphologischen und photochemischen Eigenschaften zu verbessern. Zwei Hauptmerkmale des Azobenzols standen hierbei im besonderen Fokus. Zunächst ist das Azobenzol durch seinen starren ribosidischen Linker und seiner End-zu End-Ausdehnung so beschaffen, dass der distale Aromat tief in den gegenüberliegenden Basenstapel hineinragt und somit zur Störung maßgeblich beiträgt. Eine elegante Verbesserung des gegenwärtigen Zustandes wäre, wenn sich im begünstigten Zustand der distale Aromat im offenen Raum der großen oder kleinen Furche aufhalten würde, durch Belichtung dann aber in die Basenpaarungsregion hineinschieben würde. Des Weiteren ist das Azobenzol selbst nicht in der Lage zu den attraktiven Wechselwirkungen im Duplex abgesehen von den relativ schwachen aromatischen π-Wechselwirkungen beizutragen. Eine durchaus nutzbringende Verbesserung wäre zu erwarten, wenn der Chromophor an der Wasserstoffbrückenbildung teilnehmen könnte, da diese einen Hauptanteil attraktiver Wechselwirkungen zwischen zwei komplementären Oligonukleotiden ausmachen.
Aus eben jenen Gründen wurden 2-Phenyldiazenyl-modifizierte Purine als Zielstrukturen ausgewählt. Sie kombinieren die Fähigkeit einer Nukleobase Wasserstoffbrücken ausbilden zu können mit der Photochromizität eines Azobenzols. Im Zuge dieses Projekts wurden die 2‘-Deoxyadenosin- und 2‘-Deoxyguanosin-analogen Photoschalter dA_{Azo} und dG_{Azo} synthetisiert und zusammen mit mAzo als Referenz in DNA-Testsysteme durch Festphasensynthese eingebaut. Es konnte gezeigt werden, dass sich die Duplexstabilität verbessern lies im Vergleich zum etablierten mAzo. Die Stabilitätsverbesserung war dominanter für dA_{Azo} als für dG_{Azo}, was vermutlich daran lag, dass im Zuge der Funktionalisierung der Guanosin-analoge Baustein um einen Bindungsbeitrag reduziert wurde und somit nicht dieselbe Qualität an Bindungsbildung beitragen konnte.

Leider war die Photokontrolle durch die neuartigen Bausteine nicht von derselben Qualität, wie durch den Referenzbaustein mAzo. Ein möglicher Grund hierfür könnte die Positionierung des distalen Aromaten sein. Selbst im *trans*-Zustand kann der distale Aromat der 2-Phenyldiazenylpurine in kleiner (*endohelikal*) oder großer (*exohelikal*) Entfernung von der gegenüberliegenden Nukleobase positioniert sein. Während die endohelikale *trans*-Konformation ihren distalen Aromaten in die Basenpaarungsregion einbringen kann, führt ein Schalten in der exohelikalen Konformation lediglich zu einer Bewegung des distalen Aromaten in der kleinen Furche ohne größere Auswirkung auf die Duplexstabilität.

Nichtsdestotrotz lieferte die generelle Idee eines Photoschalters, welcher Wasserstoffbrücken ausbilden kann, einen nützlichen Ansatz für zukünftige Verbesserungen. Durch die Migration des distalen Aromaten aus dem offenen Raum der kleinen Furche in die räumlich beschränkte Basenpaarungsregion ist vielversprechend, da hier maximaler Effekt auf die Duplexstabilität gewährleistet wäre. Als zusätzliches Kriterium sollte lediglich sichergestellt werden, dass der Photoschalter in zukünftigen Projekten nicht in mehr Konformationen existieren kann, als gewünscht.

Table of content

1. Introduction 1
  1.1 DNA-based nanostructures 1
  1.2 Azobenzene in an oligonucleotide context 6
  1.3 Light-responsive DNA-nanostructures 18
2. DNA-minicircles as model system for light responsive DNA-nanostructures 27
  2.1 Motivation and objective 27
  2.2 Results and discussion 29
    2.2.1 In search of a model system 29
    2.2.2 Synthesis and purification of single stranded DNA-minicircles 32
    2.2.3 Synthesis and purification of double stranded DNA-minicircles 38
    2.2.4 AFM-imaging of DNA-minicircles 44
    2.2.5 Synthesis of azobenzene *C*-nucleosides 51
    2.2.6 Light-dependent dimerization studies 61
  2.3 Summary and outlook 76
3. Locked azobenzene C-nucleosides 79
  3.1 Motivation and objective 79
  3.2 Results and discussion 80
    3.2.1 Identification of suitable *C*-nucleoside modifications 80
    3.2.2 Synthesis of the locked azobenzene *C*-nucleoside LNAzo 84
    3.2.3 Influence of LNAzo in oligonucleotides 89
  3.3 Summary and outlook 96
4. 2-Phenyldiazenyl purines 99
  4.1 Motivation and objective 99
  4.2 Results and discussion 102
    4.2.1 Choosing a suitable photochromic nucleobase-modification 102
    4.2.2 Synthesis of 2-phenyldiazenyl purine nucleotides 105
    4.2.3 Influence of 2-phenyldiazenyl purines in a DNA test system 108
  4.3 Summary and outlook 112
5. Experimental section 115
  5.1 Chemical syntheses 115
    5.1.1 Devices and materials 115
    5.1.2 Chemical syntheses of the DNA-minicircle project 116
    5.1.3 Chemical syntheses of the LNAzo project 138
    5.1.4 Chemical syntheses of the 2-phenyldiazenyl purine project 155

5.2 Oligonucleotide syntheses ... 167
5.3 Spectroscopic studies ... 169
  5.3.1 Spectroscopic studies of the DNA-minicircle project ... 169
  5.3.2 Spectroscopic studies of the LNAzo project ... 174
  5.3.3 Spectroscopic studies of the 2-phenyldiazenyl purine project ... 177
5.4 Polyacrylamide gel electrophoresis ... 185
  5.4.1 Buffer systems and general procedures ... 185
  5.4.2 Standard procedure for poly acryl amide gel electrophoresis and PAGE-imaging ... 186
  5.4.3 Standard Procedure and evaluation of PAGE-irradiation experiments for the DNA-minicircle project ... 186
5.5 CD-spectroscopy ... 197
  5.5.1 CD-spectra of the LNAzo project ... 197
  5.5.2 CD-spectra of the 2-phenyldiazenyl purine project ... 201
5.6 UV/vis absorption-based melting curves ... 203
  5.6.1 Melting curves of the DNA-minicircle project ... 203
  5.6.2 Melting curves of the LNAzo project ... 206
  5.6.3 Melting curves of the 2-phenyldiazenyl purine project ... 212
5.7 Fluorescence-based melting point studies ... 214
5.8 Enzymatic synthesis of DNA-minicircles ... 220
5.9 AFM-Imaging ... 220
6. Appendix ... 221
6.1 NMR-Spectra ... 221
6.2 List of abbreviations ... 277
6.3 References ... 279
6.4 Acknowledgements ... 287
6.5 Declaration ... 289
6.6 Curriculum vitae ... 290
6.7 List of scientific publications ... 291

1. Introduction

1.1 DNA-based nanostructures

The role of desoxyribonucleic acid (DNA) as information carrier for ribonucleic molecules, peptides and proteins, as a building plan for life itself, is strongly correlated with its precise structural features. Since the discovery of its helical nature by Watson, Franklin and Wilkins in 1953, the structural key features have been thoroughly investigated.[1–3] Driven by entropy, DNA tends to dimerize in aqueous solution. The hydrogen bonding of the nucleobases, as well as their aromatic π-bonding contribute to the integrity of the duplex. In order to bring all binding partners into optimal distance for proper hydrogen bonding and π-stacking, oligonucleotides have discreet ways of entwining, which are known as A-, B- Z-helix. The most prominent one for DNA-duplex formation is the right-handed B-helix (Fig. 1). Its key features include a 2 nm diameter with 34.2° turn per base and thereby 10.5 bases per rotation.[4] Additionally, the stiffness of a duplex is manifold higher than in a single stranded oligonucleotide, since its degree of freedom is drastically reduced compared to the single strand.[5]

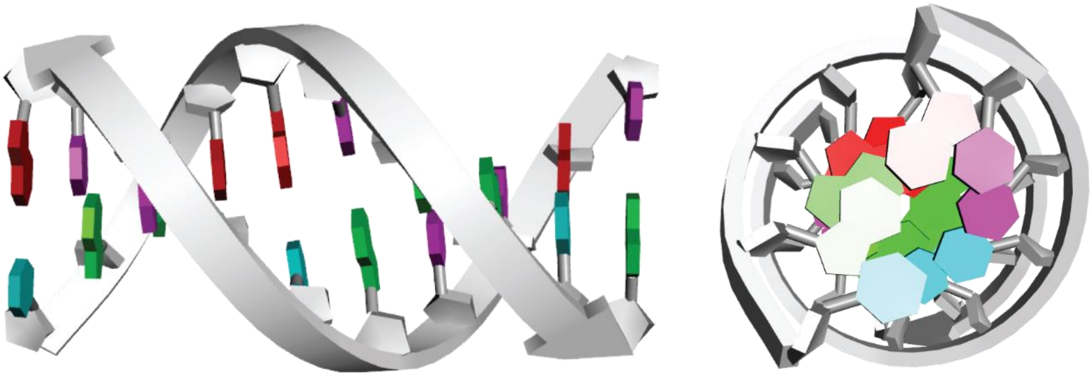

Fig. 1 Schematic display of a 10mer DNA B-helix with the backbone (white) and the nucleobases (colored). Side view left, top view right, created with Discovery Studio Visualizer.

By designing an oligonucleotide sequence to be only partially complementary to its binding partner, regions of altered flexibility are created and more than two oligonucleotides can interact with each other. The first approach following this thought was by Seeman in 1982, where, inspired by DNA junctions during replication in cells and the intriguing art of M. C. Escher, he created DNA junction motifs, which would allow three or more DNA strands to interact and form a higher ordered structure (Fig. 2).[6]

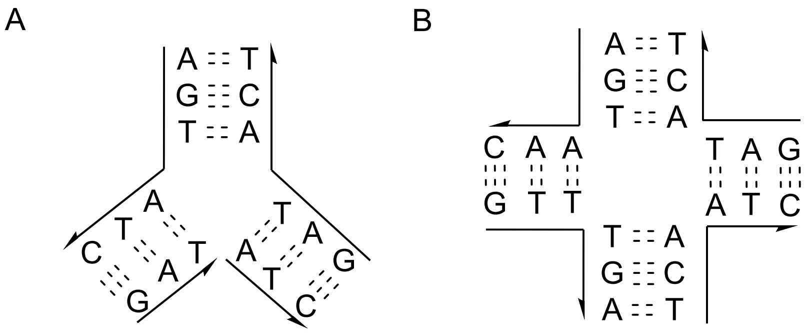

Fig. 2 Schematic display of a three point junction (A), as found during replication[7] and a four point junction (B), as found in Holliday junctions[8] during genetic recombinantion.

If the junction is designed in a way, that a single stranded overhang at the 3'-end is complementary to the 5'-end of the strand in the opposing position of the junction, aggregation of multiple junctions might occur, which could lead to higher ordered structures like lattices, as it was predicted in Seemans work.[6] Utilizing this idea, two-dimensional DNA crystals out of DNA tiles[9] and the first three-dimensional structures like cubes[10] and truncated octahedrons[11] where made. Unfortunately, the idea of using rather short sequences with a high degree of sequencial symmetry limits this approach to simple structures as there are many possible ways of hybridization for the same sequence.[12]

A somewhat different approach is the DNA origami. Origami (折り紙), the japanese art of paper folding, creates a three-dimensional object by folding a two-dimensional plane (the paper) into a shape, mostly mimicking animals or objects of daily use, inspired this unique way of creating higher ordered DNA structures. Staying in this analogy, the paper to be folded is a very long DNA guide strand of natural source, in the most cases viral DNA like M13mp18, which is a 7249 nucleotide long single strand. The folding takes place when, hybridized with the right set of rather short staple strands, double stranded, rigid parts of the guide strand open up to form flexible single strands, which are bent and held into correct positions by different staple strands. A repeated hybridization of mostly synthetic staple strands to the guide strand interconnecting different regions of it lead to a formation of a higher ordered structure of the construct (Fig. 3). This concept was established by Rothemund in 2006 to create arbitrary two-dimensional shapes of around 100 nm scale like stars or smiley-faces.[13]

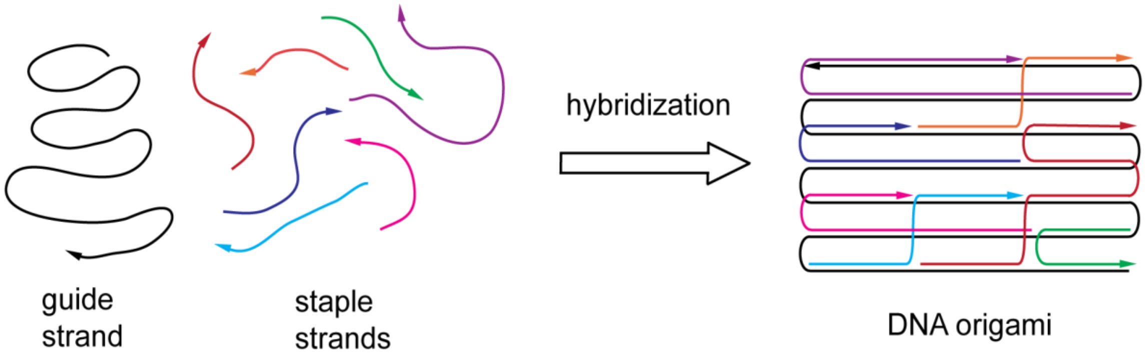

Fig. 3 Schematic display of the DNA origami principle: a long guide strand hybridizes with a set of shorter staple strands to form a DNA origami of defined structure.

In order to generate a defined folding of the given guide strand sequence, the sequences of the staple strands have to be designed in a way, that only one interaction of staple strand and guide strand is made possible, without any interactions among the staple strands themselves. Computer programs like *caDNAno* have emerged as elaborate tools, which only need the sequence of the guide strand and the desired structure to calculate the sequences of a set of staple strands, which, since being relatively short (usually 20 to 60 bases), are accessible by DNA solid phase synthesis.[14] With this approach Shih and coworkers were able to generate arbitrary three-dimensional structures based on honeycomb-like lattices.[15] Later on, square[16] or even hybrid lattices[17] were demonstrated, which showed many different possible ways for DNA to be aggregated to defined structures.

As beautiful and astonishing the possibilities of DNA origami is, a major flaw prevails, which keeps it being only limited applicable. All DNA origami design strategies have in common to pack DNA helices in a rather compact parallel manner. Due to its polyanionic backbone, a strong electrostatic repulsion forces the helices apart from each other. To overcome the ionic repulsion of the backbone, a tremendous amount of counter-ions are needed to keep the helices in proximity in order to keep the DNA origami structure intact. Since needed salt concentration usually exceed intracellular salt levels, the application of DNA origami *in vivo* is rather limited.[18] To overcome this limit novel strategies to create less tight structures like wire-frames[19] and length-variable multi arm junctions[20] were elaborated. Högberg, former coworker of Shih, established a method in his group to generate wire-frame structures based on triangulated polyhedral meshes. To optimize scaffold routing an algorithm based on the 3D-rendering program *Autodesk Maya* called *vhelix* was designed to create any arbitrary three-dimensional structure like the famous Stanford bunny.[21] Due to its wireframe nature, the polyhedral mesh DNA structure involves less DNA per structural volume created and is thereby more stable under physiological salt concentrations.[21,22]

In addition to the established DNA origami approach to fix a large single strand into a defined structure, Yang and coworkers demonstrated to generate higher ordered structures, only using single stranded units in a building brick-like manner. Due to its modular approach, very versatile structures can be created without the need for staple strands.[23,24] Although the yield of correctly formed structures is lower and the bricks are less stable than a completely interconnected DNA origami, the modularity offers great opportunities to create a large set of different structures. Additionally, the usage of L-DNA in the DNA brick approach improves the nuclease stability for *in vivo* applications (Fig. 4).[24]

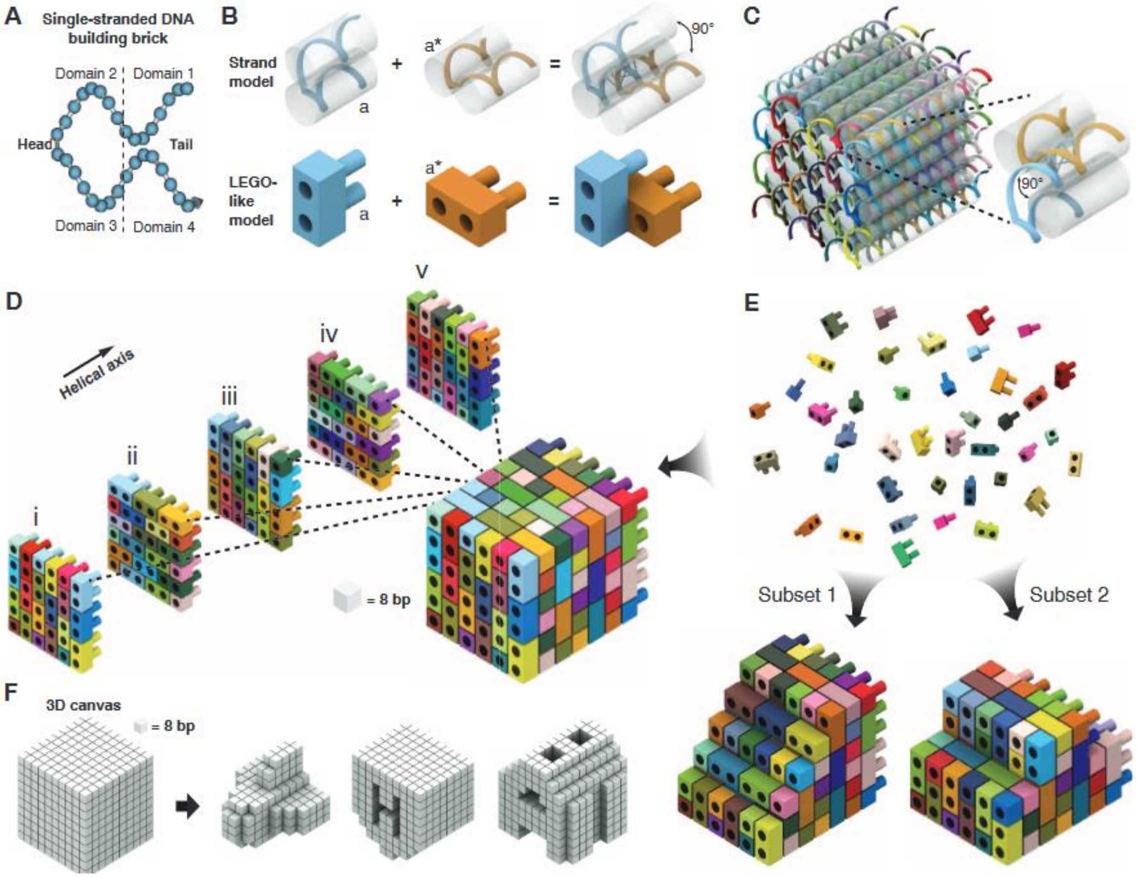
A
Single-stranded DNA building brick
Domain 2
Domain 1
Head
Tail
Domain 3
Domain 4
B
Strand model
a
a*
90°
LEGO-like model
a
a*
C
90°
D
Helical axis
i
ii
iii
iv
v
= 8 bp
E
Subset 1
Subset 2
F
3D canvas
= 8 bp

Fig. 4 Schematic representation of the DNA brick approach with a 32 nucleotide long building brick (A), orthogonal assembly of two building bricks (B), a molecular model of 48 interconnected building units ("48B cuboid", C), a LEGO® like model of the same 48B cuboid (D), display of the modularity of the DNA brick approach (E) and different shapes created from 10x10x10 voxels (F). Reprinted with permission from Ke et al.[23]

For completeness it shall be mentioned, that RNA nanostructures have also been reported in 2013 by the groups of Sugiyama[25] and Mao[26,27], but the field of RNA nanostructures stays behind its DNA counterpart due to the frailness of RNA in solution. It needs to be noted here, that RNA-RNA or RNA-DNA duplexes tent to hybridize in an A-helical form, which needs to be taken into consideration while designing three-dimensional structures.

This brief summary of the development of DNA nanostructures shall give the reader an overview of the different strategies and approaches in creating such. For a more detailed comprehension of the development of DNA nanostructures, the reader is advised to take insight into the review articles of Seeman[12], Wang[28] and Hong[29].

1.2 Azobenzene in an oligonucleotide context

Oligonucleotides like RNA and DNA play a major role in the propagation of life, since the sequence of nucleobases encrypt for all necessary gene products to keep a cell functioning. Since not all gene products are needed in the same amount throughout the lifetime of a cell, certain mechanisms have developed to alter the availability of genetic information in dependence of their need. Most of these mechanisms involve translocation of oligonucleotides and "masking" of their sequence, which, in the easiest way, is done by hybridizing the sequence of interest with a counterstrand. To manipulate biological processes on a molecular level, scientist aspire to gain control of the hybridization of oligonucleotides *in situ*. In order to gain control of an oligonucleotide of interest and its function an external stimulus would be desired, which selectively addresses said oligonucleotide and does not interact with any other cell compartment. Such an external stimulus could be light. In contrast to most chemical stimuli, light does not pollute the system and is harmless, if biocompatible wavelength and light doses are used. Due to the advances in optical and photophysical technology, light can be applied with high spatiotemporal control and dose precision.[30–32] To utilize light, the incorporation of light responsive moieties into the oligonucleotide is needed. Depending on the aim, reversible or irreversible photocontrol can be achieved by either photoswitches or photolabile protection groups. Photolabile protecting groups (PPG's) are covalently attached bulky residues, which block hybridization of an oligonucleotide by sterically hindering the formation of attractive interaction like hydrogen bonds. Upon irradiation with a certain wavelength, a bond break is provoked, causing the PPG to leave and revealing the nucleotide for hybridization again (Fig. 5). PPG's tend to have a very high on/off-ratio, but as already said, can be used one time only. Photolabile protecting groups are not part of this overview, for more details about this topic the reader is advised to take insight into the review of Klán *et al.*[30,32]

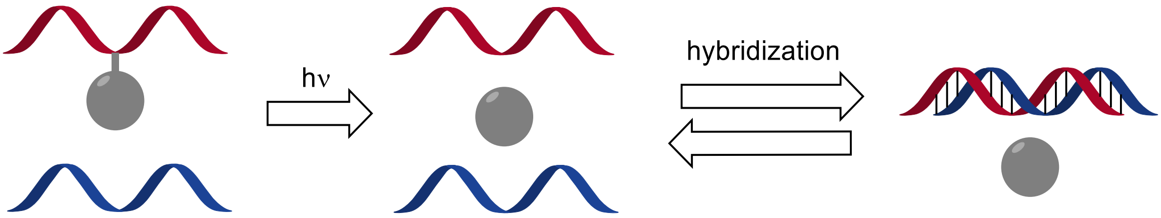

Fig. 5 Schematic representation of the operating principle of a photolabile protecting group. After irreversible photocleavage oft he PPG, the oligonucleotides can reversibly hybridize.

To gain reversible photocontrol over oligonucleotide hybridization, the incorporation of photochromic molecules is needed. The underlying principle is that the chromophore can exist in two or more isoforms, which differ, aside from their morphology, electronegativity distribution and solubility, in their light absorption. The energy needed for the transformation is taken from light of the corresponding wavelength itself. This phototransformation can either involve a *cis* to *trans* (*Z* to *E*) isomerization of a C=C-double bond, like in stilbenes, azobenzenes or (hemithio)indigos, or a ring opening or closure, like in spiropyranes, dithienylethenes or fulgides/fulgimides (Fig. 6).[33]

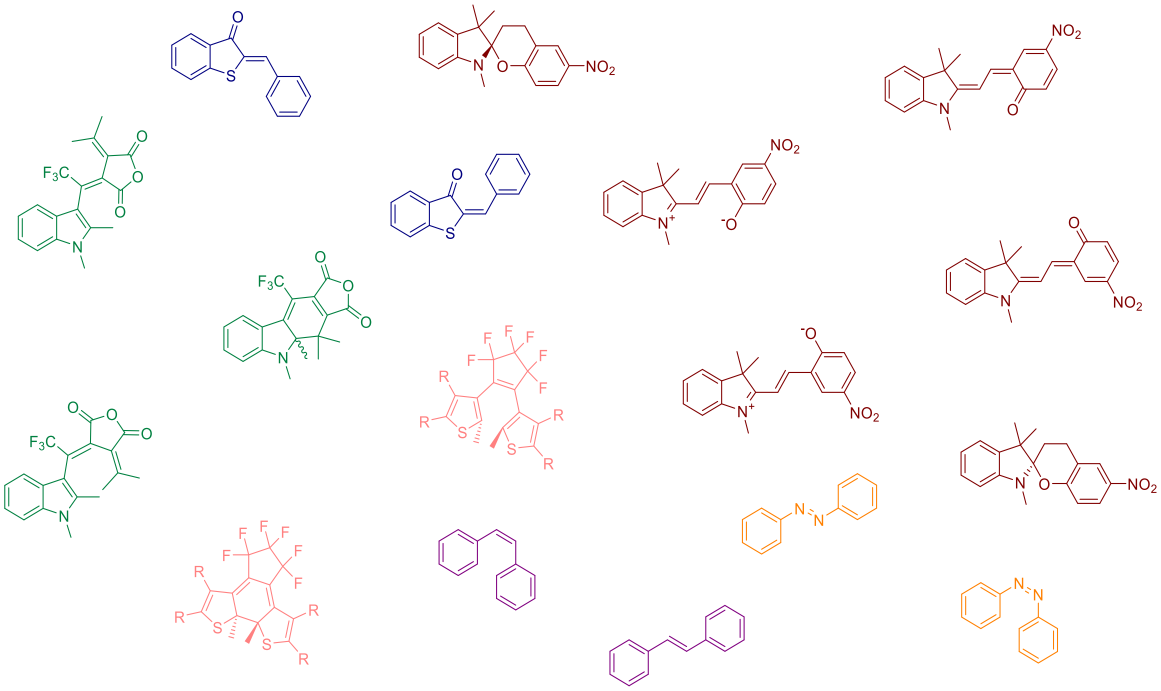

Fig. 6 Structures of chosen photoswitches and their isomers (fulgides in green, hemithioindigos in blue, dithienylethenes in peach, spiropyrans/merocyanines in brown, stilbenes in purple and azobenzenes in orange).

The underlying principle of the application of photoswitches in oligonucleotides is that the different photoisomers alter the possibility of attached oligonucleotide to hybridize to a different extend. This effect is usually less dominant, than in the case of photolabile protecting groups, but therefore is reversible (Fig. 7).

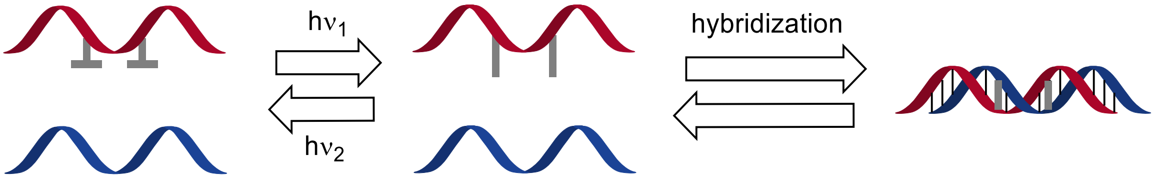

Fig. 7 Schematic representation of the operating principle of a photoswitch. Upon reversible photoisomerization, hybridization of the oligonucleotides is enabled.

Most of the named photoswitches have already been used in an oligonucleotide context, but certain key features limit their application. The perfect photoswitch would have two isoforms, which differ greatly in their morphology and are both stable in the applied medium over a long range of time. The needed wavelength for photoisomerization should be in the visible to near infrared range, since ultraviolet light tends to have certain phototoxicity and far infrared light is absorbed by water. Additionally, the absorption spectra of the isoforms should overlap little to none, since this defines, how much of one photoisomer can be accumulated by irradiation. Finally, photoswitching should be fatigue resistant, so that the switching process can be repeated as often as desired. The thermal back isomerization might as well be considered, but is a matter of application and therefore excluded here. Ogasawara *et al.* synthesized diarylethene derivatives from purine bases to regulate G-quadrupex structures and gene expression, but needed UV-light of around 310 nm, which is only limited applicable in biological systems.[34–37] Spiropyrans undergo a significant change in morphology and polarity distribution due to its ring opening isomerization to form merocyanines. It is believed that, due to its twisted structure, spiropyran causes steric repulsion in an oligonucleotide, whereas the open merocyanine form could interact with the base stack neatly.[38–41] Also, its photoisomerization wavelength in the visible range makes it a promising specimen for optogenetics and has been incorporated into oligonucleotides by the group of Wagenknecht.[42,43] Unfortunately, these studies showed, that spiropyrans tend to decompose in aqueous buffer solutions and the photoisomerization appears to be hindered by the oligonucleotide, limiting its use for oligonucleotide applications. The photoisomerization of diarylethenes is highly fatigue-resistant, but the morphological change upon isomerization is rather small and have only been used once to switch optochemical properties in oligonucleotides.[38]

The by far most utilized photoswitch for oligonucleotide applications is azobenzene. Azobenzene is a photoswitch, which exists in two isoforms. One is the *trans*-isomer, which is defined by its low polarity, a dihedral angle of 17.5° (for the C,N,N,C-dieder) and an end-to-end distance of 0.9 nm.[44] The *cis*-isomer on the other hand has an increased polarity, a dihedral angle of around 7° and an end-to-end distance of 0.5 nm (Figure 8).[45,46] The absorption spectra of the azobenzene-isomers are defined by three absorption maxima. The first results of a π-π*-transition of the isolated aromats themselves, which is located at around 230-250 nm, the symmetry-allowed π-π*-transition delocalized throughout the whole molecule including the nitrogens, which is located at 300-350 nm, and the symmetry forbidden n- π*-transition occurring at the central nitrogen atoms, located at 400-450 nm (Figure 8).[45]

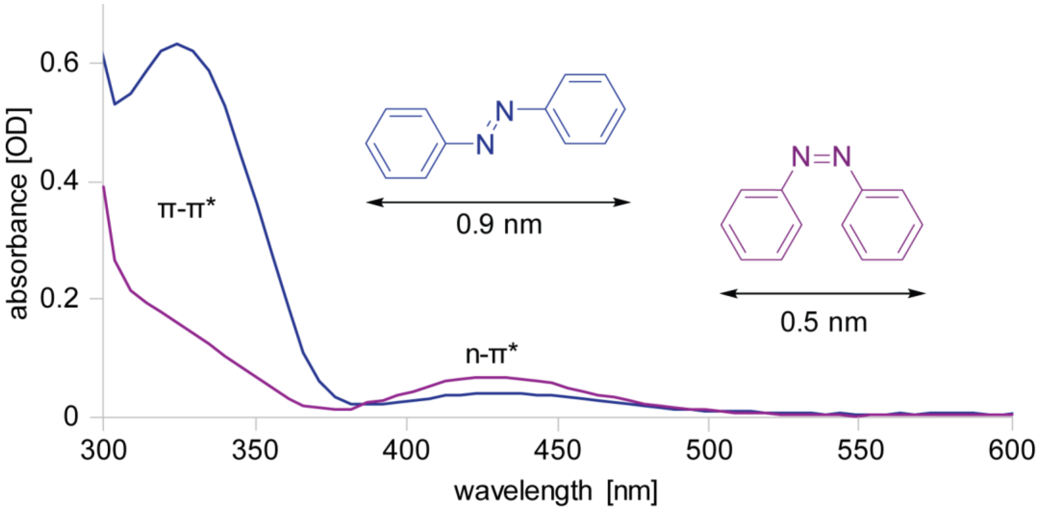

Fig. 8 Schematic display of the azobenzene-isomers and selected cut-out of their absorption spectra (trans-azobenzene and corresponding spectrum in blue, cis-azobenzene and corresponding spectrum in purple, shown spectra are from an azobenzene-modified oligonucleotide in PBS-buffer).

If an azobenzene in its thermal ground state, which is predominantly its *trans*-state, is irradiated with light of 300-350 nm, the π-π*-transition will induce the isomerization to the energetically elevated *cis*-state. The *cis*-isomer can either convert back to the energetically favored *trans*-state by thermal relaxation or by excitation of the n-π*-transition. The exact mechanism of the photoisomerization has been researched in a certain amount of studies, but can be summed up to three possible mechanisms. A torsion-like motion around the central double bond, an inversion, which moves the phenyl rings closer to each other in plane and the hula twist, which is a pedal-like motion, where one *C,N,N,C*-angle rotates 180°, while the phenyl rings move closer to each other, similar to the inversion. The hula twist can also be seen as a combination of torsion and inversion mechanism (Fig. 9).[47,48]

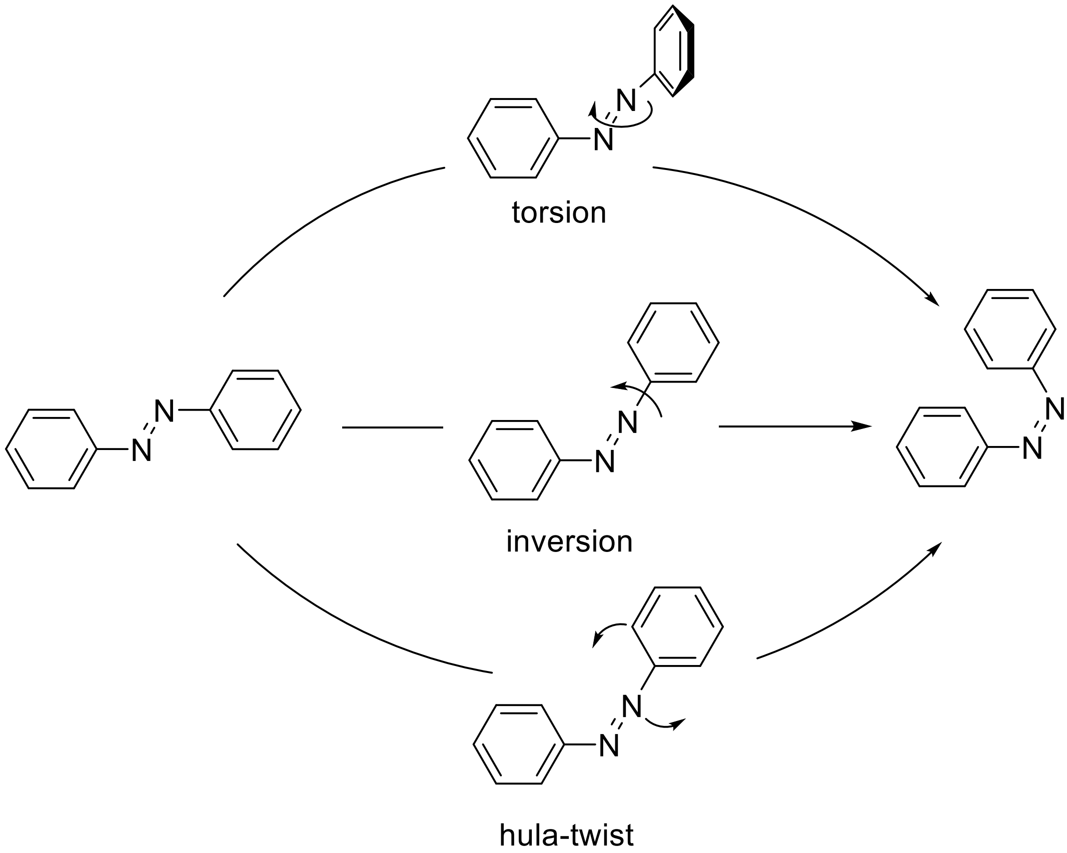

Fig. 9 Possible isomerization mechanisms for the photoisomerization of azobenzene.

It is believed, that the *trans* to *cis* isomerization is mediated by a torsion or hula-twist-movement, whereas the back-isomerization, especially in the case of the thermal relaxation, is inversion mediated. The isomerization mechanism also highly depends on the surrounding of the azobenzene, as it has been suggested, that torsion and hula-twist movements appear to be sensitive to oligonucleotide environments, whereas the inversion is not.[49–51]

The method of incorporating the azobenzene in the oligonucleotide plays a crucial role in its effectivity. An azobenzene linking system has to fulfill several characteristics. It needs to be positioned in a way, that one isomer does little to no harm to the hybridization, whereas the other should provide as much perturbance as possible. Additionally, the linking system should reduce the degree of freedom of the chromophore in a way, that only desired motions are possible. To harness the photochromicity of the azobenze and use it in oligonucleotides, several ways of incorporation of azobenzene have been developed, which shall be divided in six different strategies and explained in the following section (Fig. 10). 5'-modifications, like the use of dabcyl-fluorescence quenchers, will not be matter of this survey.

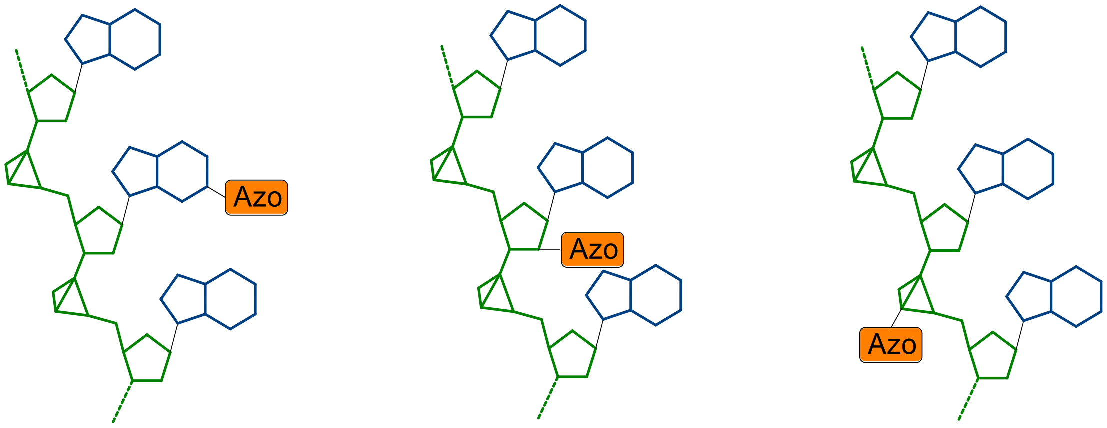

1 - nucleobase attached 2 - ribose attached 3 - phosphate attached

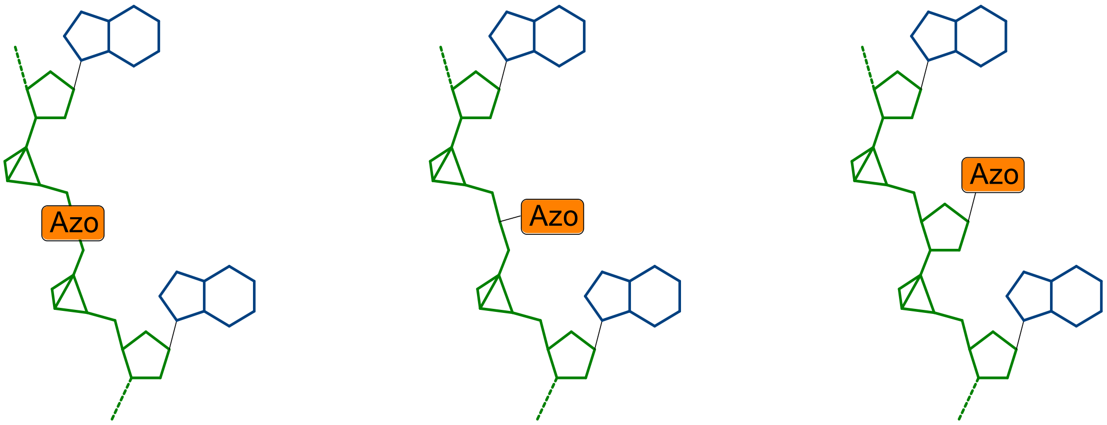

4 - backbone included 5 - nucleoside surrogate 6 - nucleobase surrogate

Fig. 10 Schematic display of different modes to covalently attach azobenzenes to oligonucleotides.

The attachment of an azobenzene-residue to a nucleobase has the advantage of keeping the duplex structure rather unaltered, compared to in the natural duplex structure. In addition, this approach gives the opportunity to introduce the azobenzene rather late stage in the synthetic route, opening the method for screening of different photochromic modifications. The Ito group introduced azobenzene via amide bond to the amino function of adenine, creating a photoresponsive RNA-aptamer to hemin (Fig. 11A).[52] The Obika group introduced azobenzene via alkynyl linkage at the *C*5-position of 2’-deoxyuridine[53] (Fig. 11B) and the locked nucleic acid analogue[54] (Fig. 11C) by palladium catalyzed cross coupling of an alkynylated azobenzene with the *C*5-iodinated uridine-counterpart. These modifications where easy to obtain and introduce in oligonucleotides, but had very little effect on the hybridization upon irradiation, as they pointed into the major groove.

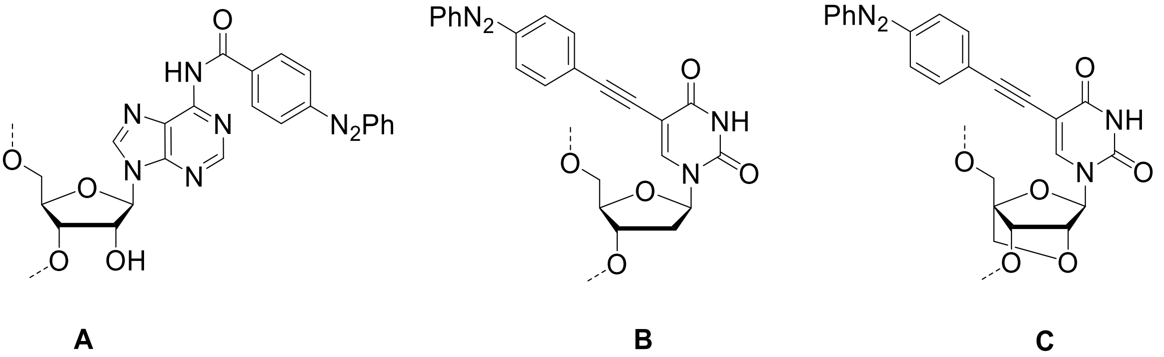

Fig. 11 Azobenzene modifications attached to the nucleobases as introduced by Ito (A) and Obika (B, C).

Azobenzenes have also been attached to the ribose moiety, but only to the 2'-position via ether or amide linkage to this date. The attachment via amide bond was performed by Keiper *et al.* for reversible photocontrol of a DNA-ribozyme to catalyze RNA-cleavage (Fig. 12A).[55] Asanuma *et al.* introduced azobenzene on the 2'-*O*-position for photocontrol of duplex-formation (Fig. 12B).[56]

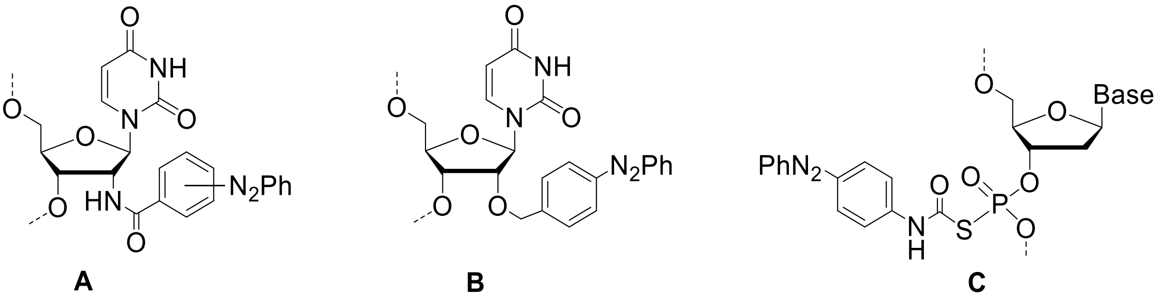

Fig. 12 Azobenzene modifications attached to the ribose moiety as introduced by Keiper (A) and Asanuma (B) and the phosphorothioate-modification of Patnaik et al. (C).

The attachment of azobenzene to the phosphate moiety in the backbone is a less prominent method, as it has only been used once by Patnaik *et al.* (Fig 12C). The introduction to the thiol-modification of a phosphorothiate gave the opportunity for this postsynthetic modification. Interestingly, although photocontrol is almost unchanged by the position of the modification in the oligonucleotide, overall duplex stability decreases, as the modification is installed closer to the center of the sequence.[57]

Including the azobenzene into the backbone of an oligonucleotide is a rather unique way of incorporation compared to the other approaches, which brings certain advantages and disadvantages. Either incorporated by ether or amide linker of variable length, backbone included azobenzenes imply great disturbance compared to the natural backbone. The main strategy would be using this modification in hairpin structures, since the rather planar trans azobenzene would form a hydrophobic cap structure at the turn of the hairpin, which would be stabilized by π-interaction with the adjacent nucleobases. Upon irradiation, optimal hairpin size would be lost, resulting in a distortion of the B-helical structure (Fig. 13).[58,59]

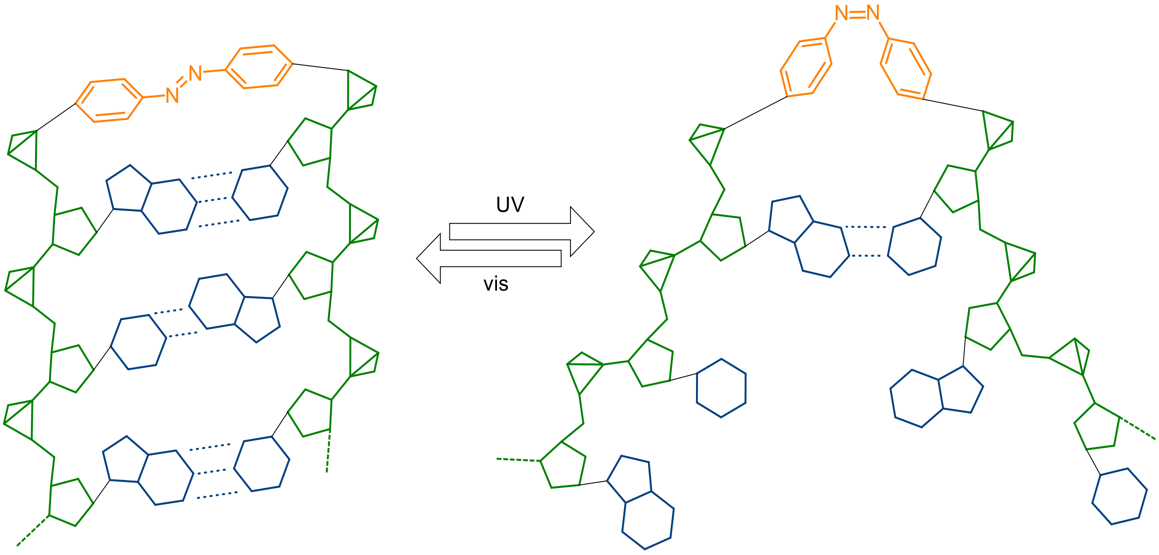

Fig. 13 Schematic mechanism of action of an azobenzene-incorporated hairpin structure. The trans-state stabilizes the hairpin neatly, whereas the cis-state causes perturbation.

This approach has been used to control the RNAse H digestion of RNA by modulating the hybridization of an antisense-oligonucleitode, which had two photoresponsive hairpin ends[60], as well as to control G-quadruplex formation[61] and has been utilized as molecular motor, to translate the irradiation into a directed movement.[62]

The approach to use a nucleoside surrogate is the best investigated and most used due to its favorable ratio of synthetical simplicity and high effect in application. The modification usually consists of a diol linker to incorporate the modification easily by solid phase synthesis and a side chain to attach the azobenzene to the linker. Since DNA is a chiral molecule due to its winding (right-handed winding for B-helix), the chirality of the linker is of importance to maintain natural winding. Several acyclic linker systems have been developed, which will be listed in the following (Fig. 14).

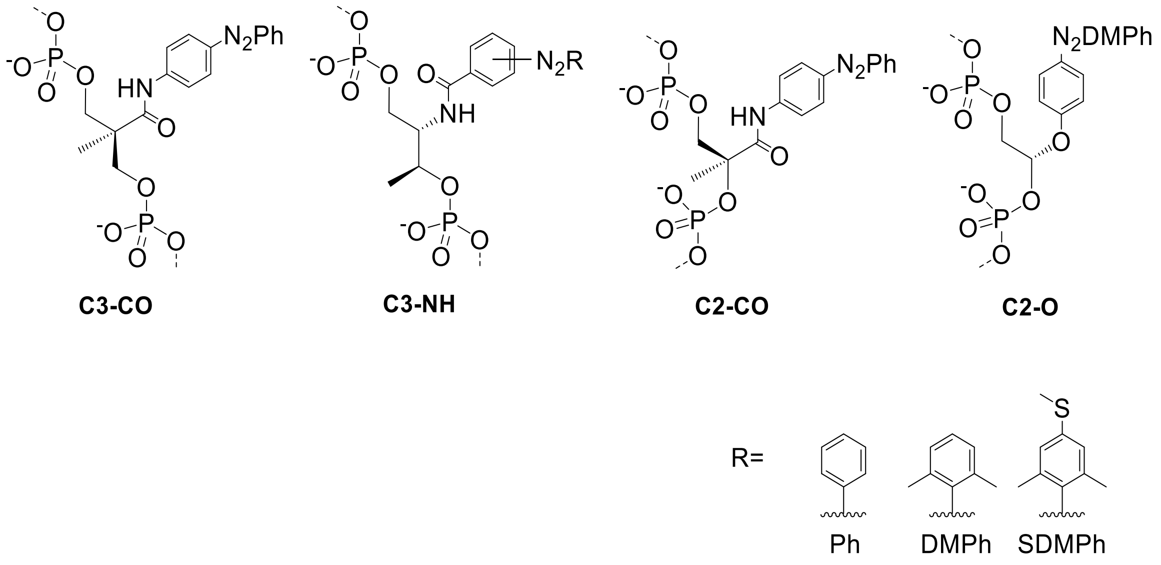

Fig. 14 Different acyclic linking systems and their azobenzene modifications.

The concept of the acyclic linker systems was introduced first by Asanuma *et al.* in 1998 with the C3-CO-linker.[63,64] The *trans*-state can intercalate into the nucleobase stack, whereas the *cis*-state causes a protrusion due to sterical perturbation in close proximity, hereby altering the duplex structure and weakening attractive interactions of the strands. Problematic for the C3-CO-linker was the racemic synthesis, leading to the necessity to purify the linker via HPLC prior to solid phase synthesis. The design of the linker was then improved by using *D*-threoninol (Fig. 14, C3-NH), which is commercially available in its enantiomeric pure form.[65] For the threoninol-azobenzene (*t*Azo) the idea could be verified by showing that both, the *D*-form and the *L*-form, can be used to incorporate azobenzenes, but the *L*-form causes more perturbation with less photocontrol. The right handed winding of the DNA is supported by *D*-threoninol, whereas *L*-threoninol supports a counter-clockwise turn.[66] Asanuma *et al.* have shown by 2D-NMR analysis, that *D*-threoninol supports a turn angle of 35-36°, which fits neatly to the stepwise angular change of 36° in DNA, whereas *L*-threoninol only supports 30-31°.[67] Although photocontrol has widely been reproduced using *t*Azo,[64,68,69] the quantity of photocontrol depends largely on sequence context, oligonucleotide type and incorporation motif. It was shown that, in contrary to DNA, *t*Azo destabilizes RNA in both forms, although this seems negligible for the *trans*-state, but still is less dominant for the *cis*-state than in DNA.[70] As expected, mismatches in close proximity also tend to improve photocontrol in duplexes, as opposed to fully complementary oligonucleotides.[71] Acyclic linking systems can be incorporated into an oligonucleotide either additionally, or in exchange of a nucleoside (Fig. 15). The replacement of a nucleobase for an azobenzene moiety causes a mismatch in the oligonucleotide, as the azobenzene is not capable to form hydrogen bonds with nucleobases. In addition azobenzene tends to be bigger in size than even purine bases, causing sterical hindrance in the local environment. The replacement motif is scarcely used, compared to the second motif, the wedge.[72]

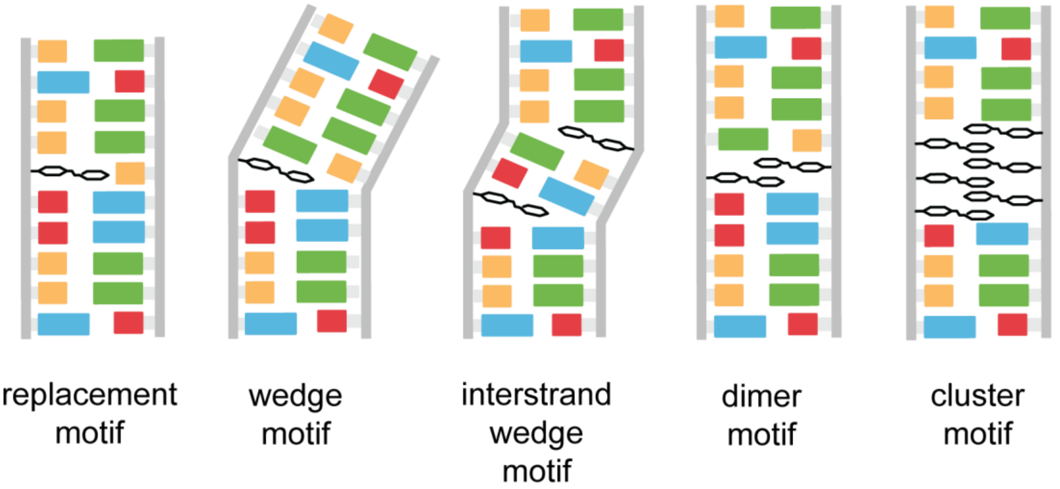

Fig. 15 Different strategies to incorporate nucleosidic surrogates into oligonucleotides (backbone in grey, nucleobases colored, azobenzene-modifications in black).

If *t*Azo is additionally incorporated into the strand, it will be one nucleotide longer than the counter strand, causing the duplex to bulge on one side, as the azobenzene forces itself like a wedge into the duplex. So-called wedge motif is by far the most prominent strategy, as the *trans*-azobenzene in the wedge can stabilize the duplex by π-π-interactions and causes great disturbance in the *cis*-state. In the wedge state only one strand is modified with *t*Azo, whereas the other strand consist of only natural nucleosides. In order to not destabilize the duplex by heavily modifying one strand, it is advised to keep at least two natural nucleosides in between every *t*Azo modification.[66,73] If the wedge motif is applied to both strands, the so called interstrand wedge motif is created. In contrast to asymmetric wedge motif, the interstrand wedge motif is symmetric and remarkably stable and NMR studies have shown that canonical Watson-Crick-base pairing is maintained of natural nucleosides in the interstrand wedge motif.[74] If the *t*Azo modifications are placed opposing each other, so called dimer motif is formed. In this motif, a new attractive force is present, which would be the π-π-interactions of the azobenzenes to each other. NMR-studies have shown that in the case of DNA, the azobenzene moieties will align to the nucleobases in 5'-direction, whereas in RNA, they will align in 3'-direction.[75,76] Due to their attractive interactions, the inclusion of dimers will stabilize the oligonucleotide compared to the natural one. If the dimer motif is repeated, the so called comb or cluster motif is formed. As with the dimer motif, the repetition of dimer units increases attractive interactions proportionally.

Unfortunately, the cluster motif tends to be so stable that photocontrol of duplex formation is lost.[77]

As noted before, the positioning of the methyl-group in the C3-scaffold seems to be of importance as explained for C3-CO, *D*-threoninol and *L*-threoninol. Recent studies have shown, that creating an inverse form of the *L*-threoninol scaffold (*iL*-threoninol, Fig. 16), duplexes can be stabilized even better in certain motifs, than with established *D*-threoninol. In wedge motif, *iL*-threoninol appears to further stabilize the duplex, but for dimer or cluster motifs, *D*-threoninol stays superior. Nevertheless, the photocontrol of oligonucleotide stability appeared to be greater with *iL*-threoninol, leaving room for future applications. Removing the methyl-group, the serinol linker system appeared to be inferior to *D*-threoninol in all cases and to *iL*-threoninol in some.[78]

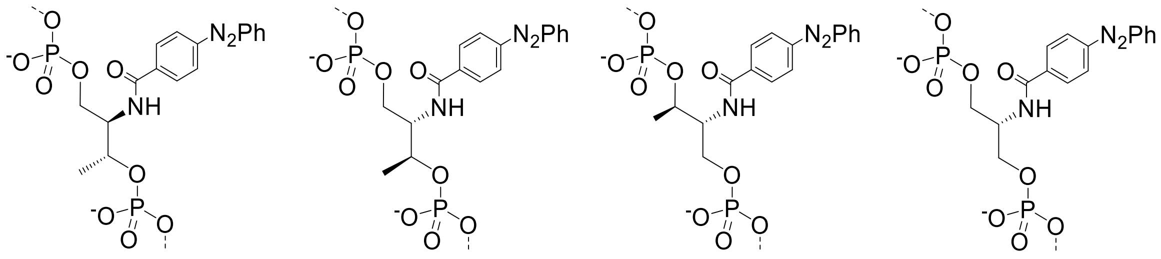

L*-threoninol** ***D*-threoninol** ***iL*-threoninol** ***serinol

Fig. 16 C3-NH-derived linker systems.

If the number of linking atoms is reduced to two (Fig. 14, C2-CO and C2-O) a stable duplex can be formed, although less stable than *t*Azo. Glycerol based C2-O linker has been used to generate a photoinduced toehold displacement, which could be monitored by fluorophore-quencher-assay and could be used in future applications. [79] One of the biggest drawbacks of acyclic linking systems is the fact, that elevated temperatures are needed to quantitatively isomerize the azobenzene. It was calculated, that the quantum yield of the *trans* to *cis* photoisomerization is lower for fully intact duplexes, since the constraining environment of the azobenzene hinderes it from isomerizing.[49,71,80] The *cis* to *trans* conversion on the other hand seems to be unhindered by this effect, since this isomerization comes with a loss of constrain. This results have also been confirmed empirically by several groups.[72,73,81–84] The explanation for this phenomenon lies in the isomerization mechanism. As mentioned before, *in silico* studies have shown that the *trans* to *cis* isomerization is mediated by the sterically demanding pedal-like hula twist, whereas the back-isomerization is performed by inversion, which takes less space.[71] Only upon weakening of the attractive interactions of the oligonucleotides to one another by heating, full photocontrol can be restored.[85] The only other way to gain full photocontrol even at low temperatures is by incorporating an unusually high number of *t*Azo residues incorporated.[86]

As a still rather new approach, Goldau *et al.* installed azobenzene as a nucleobase surrogate on a ribose linker by Heck-coupling reaction. So called azobenzene *C*-nucleosides have been used in DNA[84] and RNA[72] to compare their photocontrol capabilities to established *t*Azo linking system. It could be shown, that azobenzene attached as *C*-nucleoside is less temperature dependent in its *trans* to *cis* isomerization, yielding the photostationary isomer distribution of 80% *cis* even at 20 °C, whereas *t*Azo only reached about 50% at 20 °C. Elevating the irradiation temperature to at least 60 °C also improved the photostationary distribution, but only due to being close to the melting temperature of the duplex. Azobenzene *C*-nucleosides have been with either *para* (Fig. 17, *p*Azo) or *meta* (Fig. 17, *m*Azo) substituted azobenzene and it could be shown that, in almost every sequence context, *m*Azo appeared to be superior to *p*Azo in the means of photocontrol, which might be caused by the positioning in the base stack (Fig. 17).[72] Similar results have been obtained in a DNA context, proving clear superiority of *m*Azo in mismatched replace motif over *t*Azo.[84] For a deeper insight into photoresponsive modifications of oligonucleotides, effects and applications the reader is advised to the reviews of Liang[87] and Feringa[88].

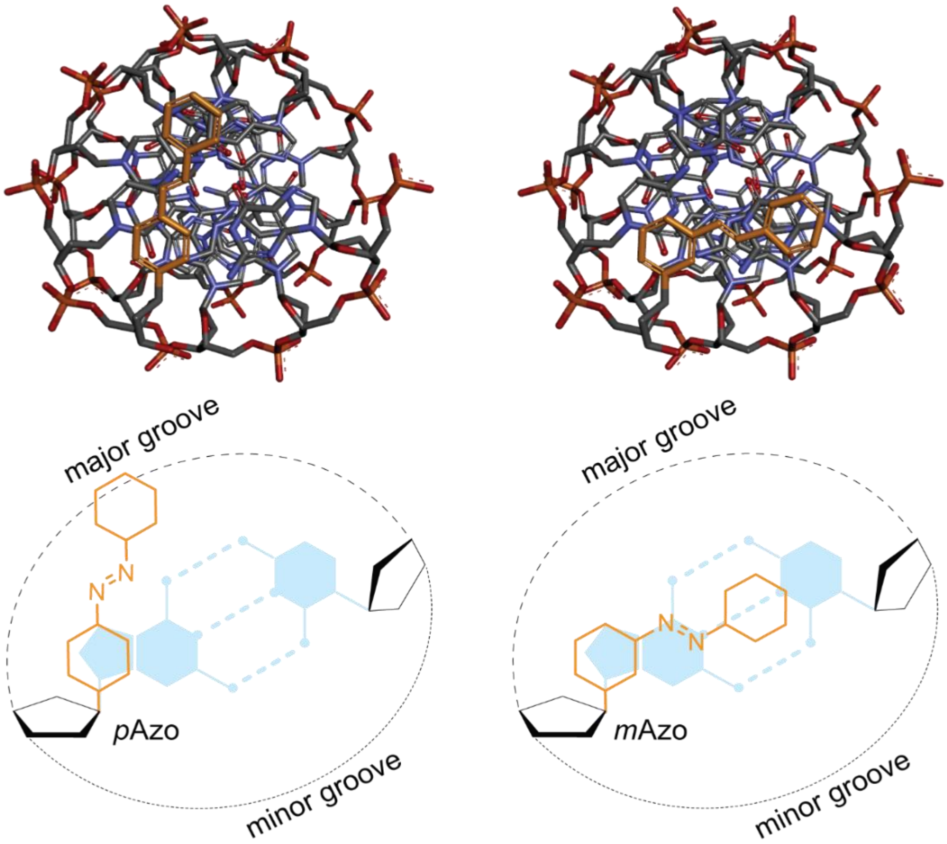

Fig. 17 Schematic representation of the positioning of azobenzene residues in duplexes caused by pAzo (left) or mAzo (right). Top structures are 3D-rendered structures of azobenzenes (orange) in an oligonucleotide duplex (top view) drawn with Discovery Studio Visualizer, bottom structures are simplified models.

1.3 Light-responsive DNA-nanostructures

Chapter 1.1 gave us insight into the fast developing field of DNA-nanostructures. It showed us, that with the help of sophisticated algorithms and programs and the possibility to generate customized DNA-sequences by solid phase synthesis, almost any arbitrary two- or three-dimensional structure in the nano- to micrometer-scale can be fabricated.[12,28] Albeit the possibilities, the structure does not directly dictate a function. Adding function to DNA-nanostructures is a field as elaborately researched as designing the structures themselves. The possible applications of DNA-nanostructures are vast and therefore several categories can be formulated. Harvesting external stimuli and translating them into directed motions is the objective of nanomachines and nanomotors, which can be fueled by strand displacement, buffer concentrations, pH or other chemical stimuli.[89–91] Single-molecule recognition and fluorescence studies, conformational analysis as well as chemical or enzymatic reactions on nanostructures are part of the single-molecule analytics field.[92] There are many more applications to name, but for scarcely any field, nanostructures can be designed without further modification. This can be achieved in many ways, like DNA-protein-hybrids[93,94], nanoparticle doped DNA-motifs[95–97] organochemical conjugates[98], lipophilic modifications for membrane-based applications[99–106] and many other[107]. Compared to these functionalization-strategies, the incorporation of photochromic elements is a rather small field. In the following, a summary of established modifications sorted by application shall be given.

The first approaches towards light sensitive DNA nanostructures where made in 2008 by Liang *et al.*[108] They designed a DNA-nanotweezer, which could be opened or closed, based on the photostationary state of a *t*Azo-modified counterstrand (Fig.18A). Following this idea, DNAzymes (Fig. 18B) and ribozymes (Fig. 18C) have been constructed, with the ability to gain photocontrol over RNA digestion.[109,110]

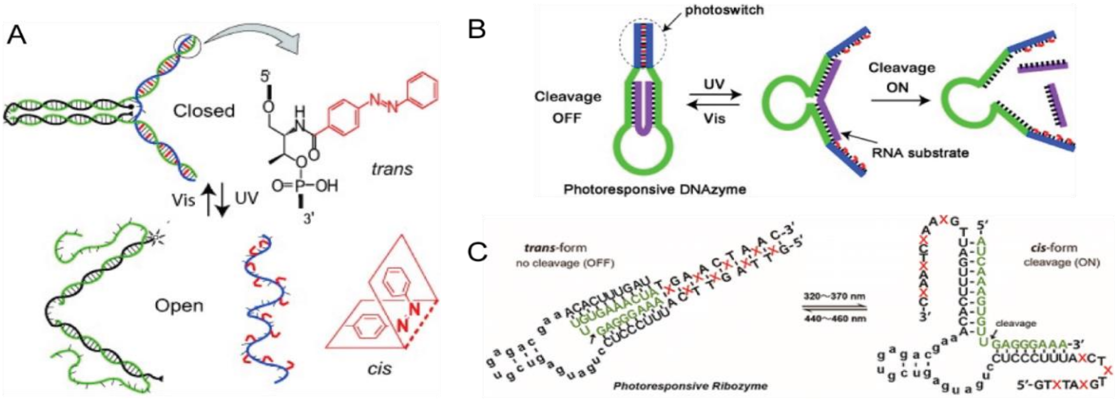

Fig. 18 Schematic representations of a photoswitchable DNA nanotweezer (A), a DNAzyme (B) and a ribozyme (C). Reprinted with permission from the publishers.[108–110]

Harvesting light and converting it into directed motions was achieved in the approach creating a molecular seesaw with bilateral movement. By incorporating azobenzenes with different absorption maxima for the trans to cis conversion, the seesaw structure could hybridize with different strands on either side, moving it back and forth (Fig. 19). The movement could be visualized by a fluorophor quencher assay, using different fluorophores for both ends.[111] Willner et al. have created nanoscopic scissor made from helix bundles with a flexible joint. Utilizing tAzo-modified DNA strands, they were able to manipulate the crossing angle of the trusses in isolated structures and in aggregates and image the changes with AFM.[112]

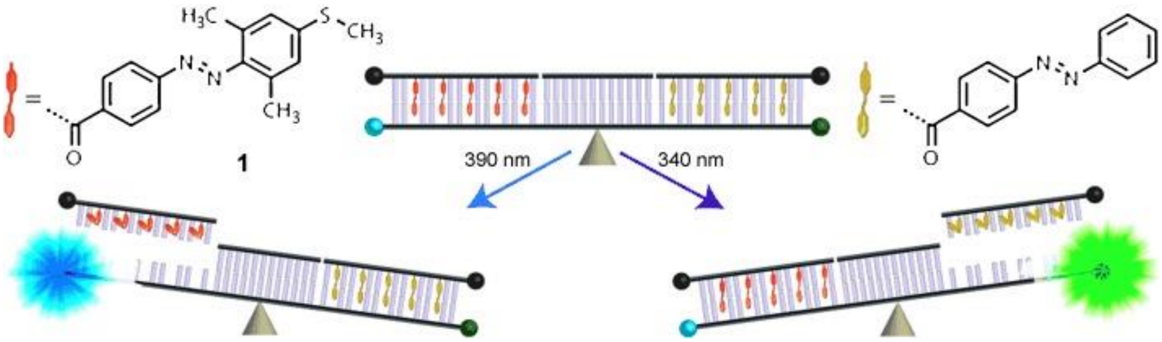

Fig. 19 Schematic display of the operating mode of the molecular seesaw. Reprinted with permisson from Nishioka et al.[111]

If the directed movement is repeatable along a surface, molecular walkers can be created. Two different approaches have been developed in this context. The first one has pyrene residues incorporated in the walker strand to harvest light and translate it into a reduction potential, which is then transmitted to disulfide bond containing immobilized strands (Fig. 20A). Upon reduction and thereby cleavage of the disulfide containing strands, migration of the walker strand towards the next disulfide containing strand takes place. Immobilization platform for this experiment was a DNA origami tile and was visualized by AFM.[113] The second one utilizes azobenzenes of different absorption maxima for the *trans*-*cis*-conversion again. Altering the hybridization affinity of the two different “legs” of this walker, a directed movement along a surface could be achieved.[114]

Not only linear, but also rotational movements can be achieved on the nanoscale. Fixing a DNA-made rod in parallel to a DNA origami platform over a rigid and linear molecular axle, the directed rotation was achieved by locking the rotor via hybridization to oligonucleotide anchors around it. Four of those anchors where placed on the platform, to which the rotor could bind depending on the photostationary state of the azobenzenes incorporated (Fig. 20B). With this, the rotor could perform 90° turn for every irradiation, which could be monitored by AFM imaging.[115]

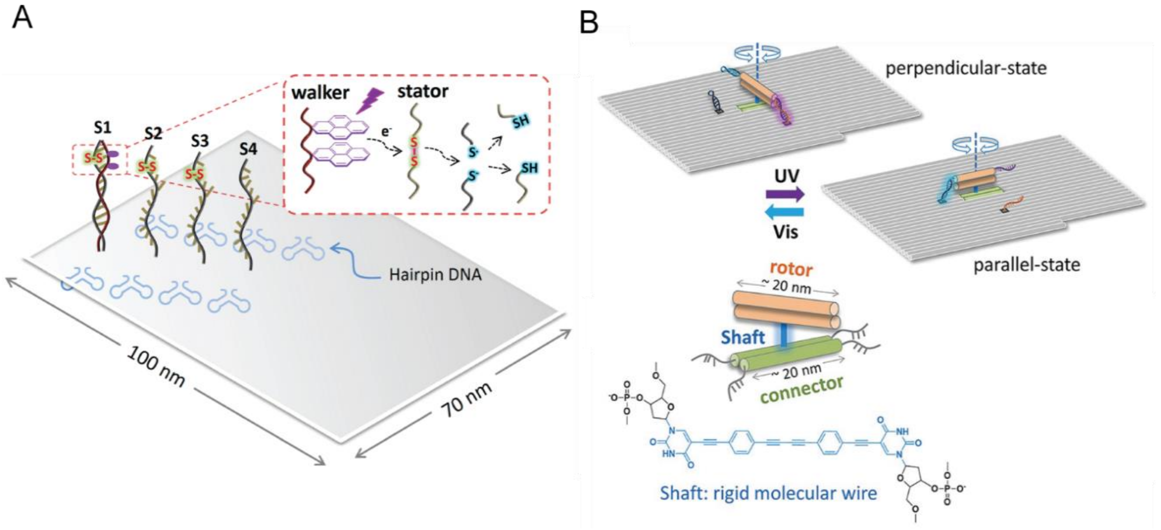

Fig. 20 Schematic display of the operation mode of a light-driven molecular walker (A) and a rotor (B). Reprinted with permission from the publishers.[113,115]

Utilizing photoresponsive nanostructures for the biomedical field, azobenzene-doped aptamer structures have been developed. The first approach utilizes *in vitro* selection of an azobenzene modified RNA library against hemin as target in a SELEX process. The aim was to select the aptamer in a way, that only the favored *trans*-state allowed efficient binding to the ligand, whereas upon *trans* to *cis* photoconversion the binding affinity to the ligand is reduced.[52] In a similar way Prusty *et al.* selected a photoresponsive riboswitch against cytostatic doxorubicin, by incorporating 2',6',dimethylazobenzene mounted to *D*-threoninol. A lipophilic modification to the photoresponsive aptamer was introduced, so that it could bind to hepatocyte growth factor cMet, which is overexpressed by H1838 tumors. Upon internalization of the lipophilic aptamers, doxorubicin could be released into the cytosol by UV irradiation. This significantly increased cell mortality, paving the way for a new class of aptamer-based therapeutics.[116] Utilizing DNA-origami scaffolds for immobilization of photoresponsive transcription factor GAL4 gave insight into its photo-dependant mode of operation. With the help of high-speed AFM Raghavan and coworkers where able to show, that upon activation under blue light, the VVD-subunit of the transcription factor dimerizes which is necessary for the adhesion to the GAL4 binding site. A series of different movements like binding, sliding, stalling and dissociation could be elucidated on the nanometer level in this study.[117]

The combination of DNA-nanostructures and nanoparticles is often used to create plasmonic devices for nanooptics and single molecule spectroscopy.[118–120] Combining gold nanorods with the idea of the molecular scissor established by Willner *et al.*[112] gave the possibility to control chirality of a nanoparticle assembly upon irradiation. The two domains of the functionalized nanoscissor where equipped with to *t*Azo-modified strands. In *trans* state, the strands would hybridize, resulting in a conformationally restricted position, fixing the nanostructure and thereby aligning the nanorods in a chiral way. If the *t*Azo residues were switched to the *cis* state, conformational restriction is released and thereby annulating the chirality of the structure (Fig. 21). This effect, which was characterized by CD-spectroscopy and TEM, gave rise for chiroptical elements on the nanoscale for future plasmonic applications.[121]

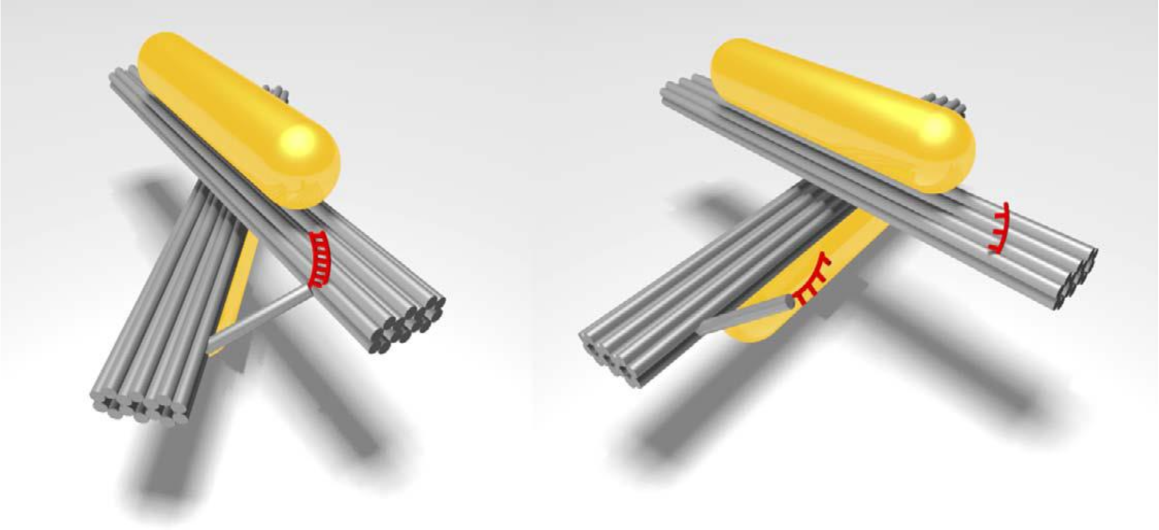

Fig. 21 Schematic representation of a gold nanorod-modified DNA nanoscissor in its chiral, tensed state (left) and its non-chiral, relaxed state (right). Reprinted with permission from Kuzyk et al.[121]

The controlled cargo release from photoresponsive nanocapsules appears to be one of the dominant applications for photoresponsive nanostructures. Using mesoporous silica nanoparticles as carrier, the Tan group demonstrated, that the pores of the silica particles could be sealed with *t*Azo-modified DNA-strands. Upon UV-irradiation, the dehybridization of the sealing DNA-strands lead to an opening of the pores, causing a release of the loaded cargo by diffusion (Fig. 22). This idea has been utilized to release doxorubicin as cytostatic to target viability of CEM cancer cells or to release fluorescent dyes.[122]

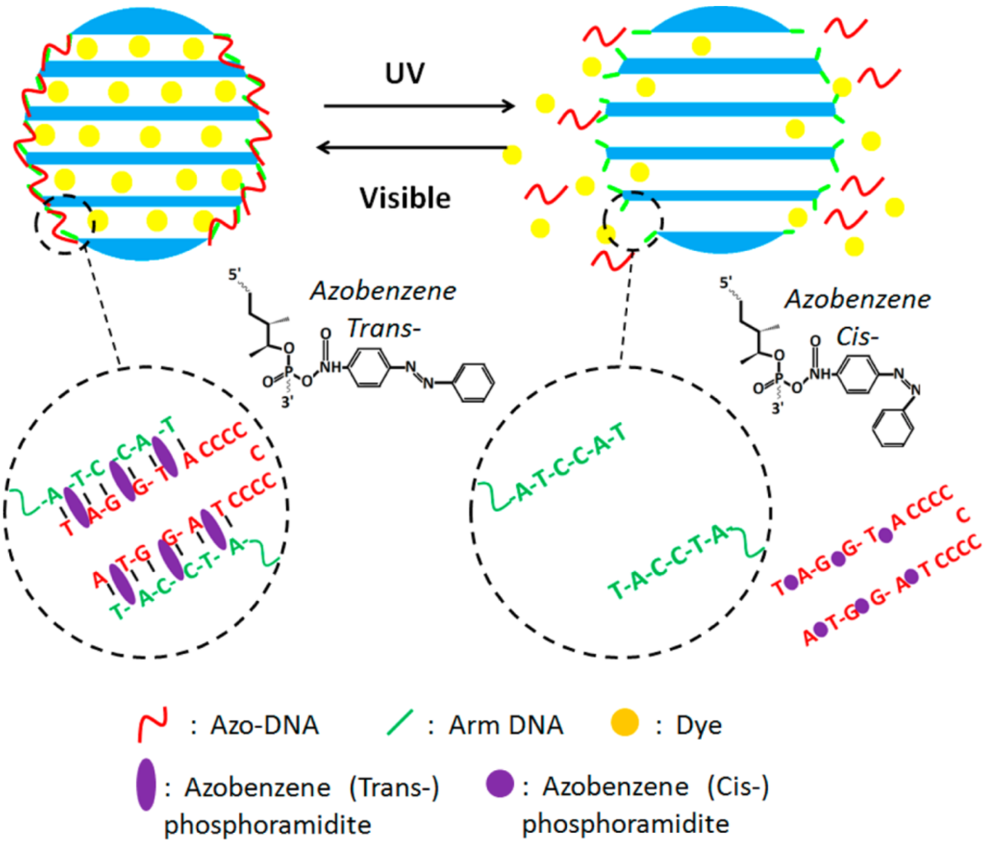
UV
Visible
Azobenzene
Trans-
Azobenzene
Cis-
5'
3'
: Azo-DNA
: Arm DNA
: Dye
: Azobenzene (Trans-) phosphoramidite
: Azobenzene (Cis-) phosphoramidite

Fig. 22 Schematic display of the mode of operation of photoresponsive mesoporous silica nanoparticles. Upon irradiation with UV light, red azobenzene-doped strands dissociate from green counterstrands opening the pores. Reprinted with permission from Yuan et al.[122]

Constructing DNA-made nanocapsules from three-way junctions have first been developed by Tanaka *et al.*. They showed that, although consisting of small three-point subunits, robust and size-precise cages could be formed. Additionally, the incorporation of *t*Azo moieties in the sticky ends of the three-point-junction motif allowed degradation of the nanostructures upon UV-irradiation and its observation via high-speed AFM.[123] This approach has been refined by Kamiya *et al.* with the use of azobenzene and 4’-Methylthio-2’,6’-dimethylazobenzene mounted to the *D*-threoninol carrier for photocontrol at different wavelength. In addition, they were able to demonstrate the release of fluorescent dyes and doxorubicin from the capsules upon irradiation (Fig. 23).[124]

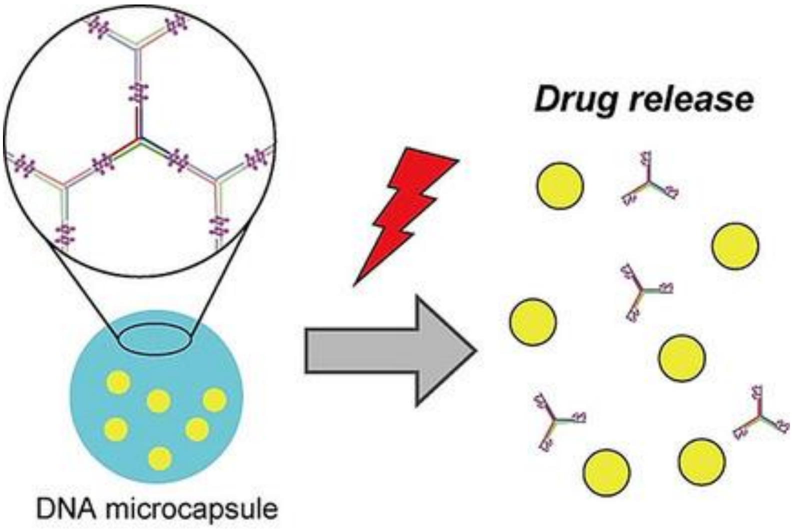

Fig. 23 Schematic display of the photocollapsible DNA-nanocapsule. Upon UV-irradiation azobenzene residues (purple) decreased hybridization affinity of the subunits, thereby causing disintegration of the structure and release of the cargo. Reprinted with permission from Kamiya et al.[124]

Utilizing the DNA-origami technique, DNA octahedrons have been created, which can open up with a hinge to form a capsule. The opening of the octahedral nanocapsule could be controlled with a *t*Azo-modified locking mechanism similar in function, as previously described and could be characterized by AFM. For a proof of principle, DNA-capsules where loaded with gold nanoparticles, to monitor the release via cryo-EM.[125] This capsule was later modified by the same group, by using photocages instead of azobenzenes, for an improved photoresponse. Additionally, the lid of the structure was equipped with a fluorophore-quencher-system to monitor the opening on a single molecule level. The capsules where also introduced into cells, to show that no cytotoxicity was caused by the structure and its operation.[126]

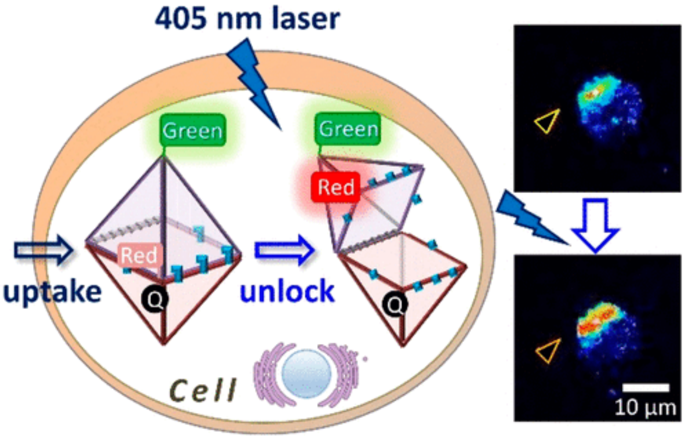

Fig. 24 Schematic display of the octahedral nanocapsule and its photoresponsive opening mechanism. Upon opening, fluorescence was restored, which could be monitored by fluorescence microscopy in real-time (right). Reprinted with permission from Tohgasaki et al.[126]

The approach to use photocleavable linker to release cargo upon irradiation has also been used in a RNA-nanopyramid. They could demonstrate, that paclitaxel-loaded nanopyramids could alter cell viability of breast cancer cells *in vitro*.[127]
The control of molecular shapes was demonstrated by Han *et al.* as they developed a shapeshifting DNA-tetrahedron. One edge of this tetrahedron consisted of a *t*Azo-modified strand, with the ability to shorten or lengthen this edge depending on the photostationary state of the azobenzenes. Modifying the edges of the tetrahedron with gold nanoparticles, a significant change of the edge length of 7 nm could be shown by TEM.[128]

The direct visualization of an azobenzene-incorporated strand hybridization was achieved in the Sugiyama group. Building a frame in a DNA origami manner, the inside of the frame structure accommodated two DNA duplexes, which spanned the frame in parallel. At half height, the duplexes bore single stranded protrusions, which were modified with *t*Azo residues for altering hybridization behavior. In the *trans* state, both single stranded overhangs could hybridize, forming a crossing of the parallel duplexes resulting in an X-like shape. Under UV light, hybridization ceased, opening up the crossing again (Fig. 25). With the help of high speed AFM imaging they could demonstrate this switching event in solution and dry on mica substrate.[129]

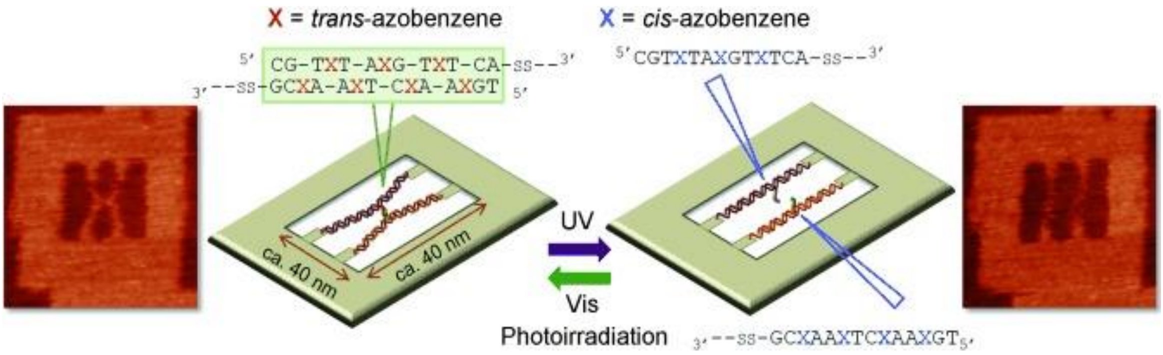

Fig. 25 Schematic view of the photoswitchable DNA-frame. In the center of the frame, the two duplexes can either be crossed under visible light (left) or released under UV-light (right). Reprinted with permission from Endo et al.[129]

To gain photocontrol over molecular association and dissociation processes is another aim for photoresponsive nanostructures. The group of Sugiyama developed DNA-origami-based hexagonal frames with the capability for directed aggregation on the edges. For aggregation *t*Azo modified single strands were installed to gain photocontrol over the process. In the *trans*-state the association of the structures was possible, which could easily be degraded again upon UV-irradiation. With this approach, higher-ordered DNA-motifs built from simple hexagonal subunits can be fabricated in a unilateral way, which only needs light as external stimulus (Fig. 26A).[130] This approach was later adapted to lipid membranes by installing cholesterol anchors in the bottom side of the hexagonal subunits.[131] The aggregation and deaggregation of nanoparticles can also be steered with the help of azobenzene-modified oligonucleotides. Suzuki *et al.* modified gold nanoparticles with oligonucleotides over thiol-bonds, which could readily hybridize with another. With the help of the azobenzene moieties, the aggregation of the colloidal gold nanoparticles could be controlled, so that the photophysical features of the dispersion could be altered upon irradiation (Fig. 26B).[132]

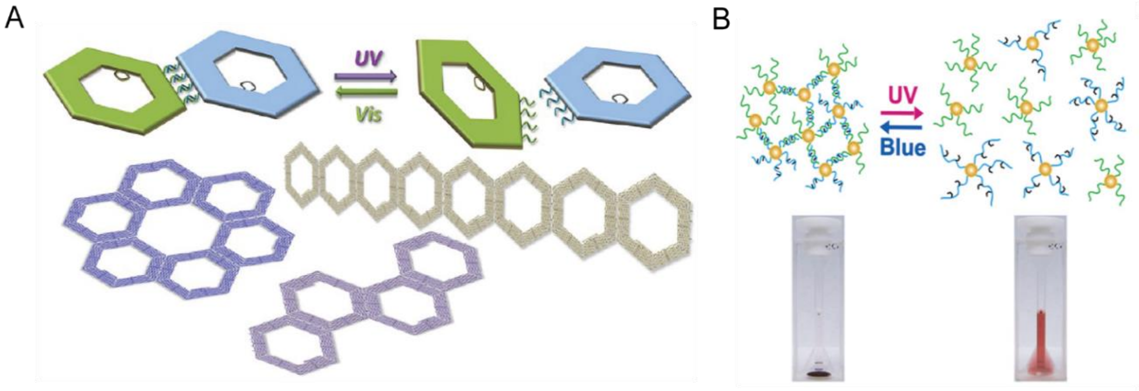

Fig. 26 Schematic display of hexagonal DNA-origami structures and possible aggregations (A) and photocontrollable colloidalization of gold nanoparticles (B). Reprinted with permission from the publishers.[130,132]

DNA-modified microtubule-filaments where used by Keya *et al.* to investigate swarming behavior of nanoconstructs. Propelled by surface-adhered kinesin motors, directed motions and aggregations of the filaments could be shown, if fueled by defined oligonucleotides. The translational and circular motion of the microtubule-arrays can be addressed by altering the stiffness of the arrays. In addition photoresponsive *t*Azo groups enabled switching between solitary and swarming behavior in response to stimulation with visible or UV-light.[133]

2. DNA-minicircles as model system for light responsive DNA-nanostructures

2.1 Motivation and objective

The interaction of oligonucleotides are very precise and well defined. The knowledge of the interaction patterns, the hybridization of oligonucleotides, gave us insight into fundamental biological processes such as transcription of genetic information into gene products and regulation of this process. Due to its precise way of hybridization, DNA can be used as a building material on the nanoscale. By hybridizing DNA with selected counterstrands, it can be bent and held it into position. With this, two- or three-dimensional structures can be formed, as it is used in techniques like DNA-origami.[12,28,29] Although any two or three-dimensional shape can be formed on the nanoscale nowadays, these constructs do not inherit a function on their own. In order to utilize these structures, certain modifications have been made, like DNA-protein-hybrids[93,94], nanoparticle doped DNA-motifs[95–97] organochemical conjugates[98], lipophilic modifications for membrane-based applications[99–106] and many other[107]. The modification with light responsive elements bear certain advantages. In contrast to most chemical stimuli, light does not pollute the system and is harmless, if biocompatible wavelength and light doses are used. Due to the advances in optical and photophysical technology, light can be applied with high spatiotemporal control and dose precision.[30–32] To utilize light, the incorporation of light responsive moieties into the oligonucleotide is needed. In contrast to photocleavable protecting groups, photoswitches can be used reversibly and cleaved-off photoproducts do not pollute the medium. The most relevant photoswitch for oligonucleotide applications by far is azobenzene. In its favored *trans*-state it intercalates neatly in between nucleobase pairs, whereas in its *cis*-state, it causes a protrusion within adjacent basepairs, distorting hydrogen bond distances and thereby lowering the hybridization affinity of the strands. The way of incorporating the azobenzene into the oligonucleotide is of crucial importance and needs to fulfill several characteristics. It needs to be positioned in a way, that one isomer does little to no harm to the hybridization, whereas the other should provide as much disturbance as possible. Additionally, the linking system should reduce the degree of freedom of the chromophore in a way that only desired motions are possible. The most frequently used linking system, especially for nanostructure applications, is the *D*-threoninol azobenzene *t*Azo. Its acyclic linker system, additionally incorporated into an oligonucleotide in wedge motif leads to high photocontrol of hybridization affinity. Unfortunately, *t*Azo modifications have the major drawback that elevated temperatures are needed to weaken the duplex, before feasible *trans* to *cis* isomerization can take place, since the chromophore is fixed in a constrained position. Recently, azobenzene *C*-nucleosides have been developed, which tackle this exact problem. It could be shown, that by exchanging a natural nucleoside with an azobenzene *C*-nucleoside photocontrol at room temperature can be achieved. This effect has been studied in an DNA- and RNA-context to show that at elevated temperatures, photocontrol of *t*Azo prevails, whereas at lowered temperatures, the *C*-nucleosidic linker causes a greater difference between the photoisomers with regard to hybridization affinity than established *t*Azo system.[72,84] Although azobenzene *C*-nucleosides have been proven to increase photocontrol at room temperature, they have not been used in DNA-nanostructures yet, although retaining low temperatures for DNA-nanostructures is crucial for their integrity. In order to establish the utilization of azobenzene *C*-nucleosides for DNA-nanostructures, a nanostructure model system needs to be developed. The model system should help to get insights into the photocontrol of the aggregation of complex structures and how to quantify this effect. With the knowledge gained of the evaluation of a photocontrolled nanostructure model system, the path to better photocontrol with the help of azobenzene *C*-nucleosides in DNA-nanostructures shall be paved.

2.2 Results and discussion

2.2.1 In search of a model system

As shown in chapter 1.3 many different functions can be steered with the help of hybridization-affinity-altering azobenzene photoswitches in DNA nanostructures. The binding of a modified strand can cause conformational changes[108–110], aggregation or deaggregation can be triggered[130,132], azobenzene doped strands can be used to restrain conformations[115,121] or as locking mechanism for controlled cargo release[122,124,126]. As unique these functions are, the mechanism of action is the same for all, which is based on altering the hybridization affinity of two strands via photoswitching the incorporated azobenzene. In order to establish a DNA-nanostructure model system for evaluation of the influence of different azobenzene linker systems preliminary requirements have to be set.

The model system needs to have a certain size, so that it can be imaged with a scanning microscopy technique such as AFM. On the other hand, increasing size also means that the constructs complexity rises. With the complexity of the construct, the amount of DNA-sequences needed to create the shape increases. Since the formation process of nanostructures is a highly complex arrangement of strands driven by thermodynamics, the probability to form fully assembled structures decreases and thereby the total yield of correctly formed structures. Additionally, with the amount of strands needed for forming the construct, the expenses in synthesizing or buying these strands also increase. Even in the academic field, money should be taken into consideration when planning a scientific project. A modular composition of the structure would allow the exchange of small subunits, like the azobenzene doped site, so that the construct can either be preassembled without the interchangeable position or assembled more easily when changes are needed. In addition, a modular approach would also lead to a higher degree of resemblance and thereby improving comparability of differently substituted constructs. As an optional request, DNA-nanostructures should be two-dimensional. Depending on the imaging technique the nanostructures can either be measured in solution or in air, although certain three-dimensional constructs tend to collapse when exposed to air.[134]

Taking these requirements into consideration several options as seen in the literature can be evaluated. Two-dimensional DNA-lattice structures[135] or crystalline arrays[136] are very simple to fabricate, as the subunits consist of a very limited amount of strands needed and are cheap to produce. They are flat and of appropriate size for the imaging process and can even be designed to be modular. The drawback of these structures for this project is also their main feature. The multifacial aggregation sites, which are responsible for the two-dimensional composition of this constructs, would be main target for photochromic modification in order to assemble and disassemble the two-dimensional constructs. The fact, that the aggregation is multidirectional makes it difficult to evaluate binding control caused by the azobenzenes, which would be definded by a ratio of aggregated structures to total amount of structures in a certain image section. This leads to the conclusion, that the aggregation of a nanostructure model system should be monodirectional for optimal evaluation (Fig. 27).

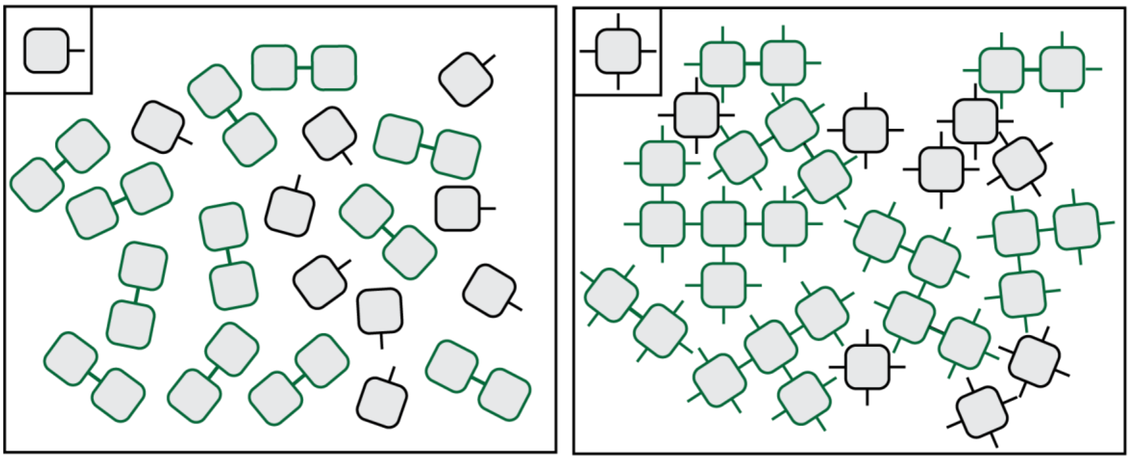

Fig. 27 Schematic display of a nanostructure for monodirectional (left) and multidirectional (right) assembly and their exemplary assembly on an imaging surface. Monomeric units with black edges, aggregated units with green edges.

The hexagonal structures demonstrated by Yang *et al.* 2012[130] (Fig. 26A) would be an interesting option for a nanostructure model system, as it combines a flat design, which is easy to image and monodirectional binding sites for defined characterization. But due to the fact, that the structure is built in a classic DNA-origami manner, the structure tends to be large and expensive in production, rendering it impractical for this application.

A very interesting model system are the so-called DNA-minicircles, which consist of relatively short, double stranded and circularized DNA. These minicircles have already been used by Schmidt *et al.* to investigate the binding abilities of polyamide-based minor-groove binders[137,138] (Fig. 28A), in DNA-rotaxanes[139], G-quadruplex-forming minicircles[140] (Fig. 28B) and other minor-groove binders[141,142]. Especially an approach for dimerization of minicircles upon irradiation and cleavage of photolabile protecting groups has been developed (Fig. 28C).[143] In this approach, a lariat shaped double stranded protrusion from the ring ends in a single stranded overhang for dimerization. The nucleobases of this sticky end was masked with photolabile protecting groups which, only upon irradiation, released the nucleobases for hydrogen bonding.

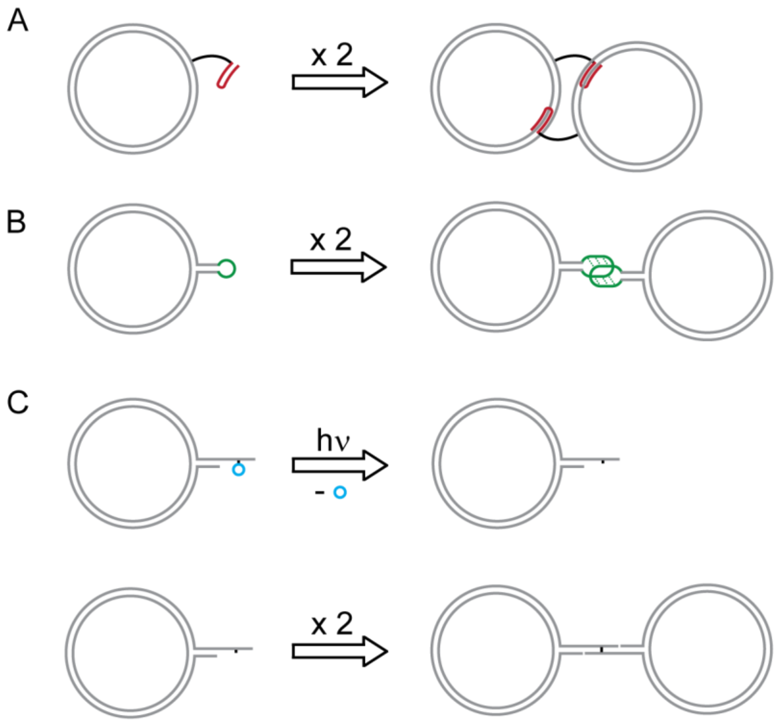

Fig. 28 Schematic minicircles and their use as model systems (minicircles in grey, minor groove binding polyamides in red, G-rich region for G-quadruplex formation in green, photolabile protecting group in blue).

As this model system has already been used to investigate aggregation of nanoscale objects after photoirradiation, it appears to be perfectly suited to evaluate photoswitch-mediated aggregation on the nanoscale. The minicircles are with 168 basepairs and a diameter of approximately 18 nm in the appropriate size window in between “too small to resolve” and “too expensive and complicated to assemble”, which makes them ideal for imaging via AFM or other scanning microscopy techniques[143]. The bending of the DNA into a strongly curved minicircle is made possible with the so called A-tracts[144]. These are sequences of 4-6 repeating A-T-pairs, which repeat once every helix turn. These A-tracts are responsible for a high degree of bending in an oligonucleotide hybrids like in chromatines and was first characterized by Trifonov *et al.*[145]*.* In addition, the minicircles are flat and relatively rigid due to persistency length of the B-helix, giving them a rather uniform morphology for easy recognition during evaluation. All these facts make DNA-minicircles a promising model structure for azobenzene dependent hybridization-tests.

2.2.2 Synthesis and purification of single stranded DNA-minicircles

The minicircle consists of a 168 base-long inner circle and the corresponding outer circle. At a certain point, a double strand protrudes out of the ring via a three-point junction, which is 10 bases long. This double stranded protrusion ends in a 10-base-long single strand, which is responsible for the hybridization of the structures (Fig. 29).

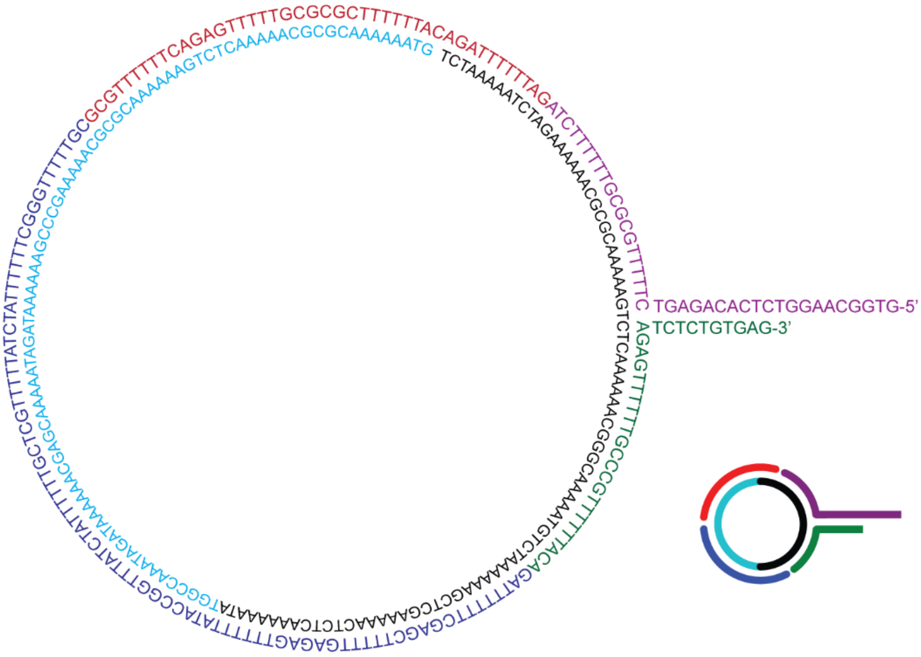

Fig. 29 Display of the unmodified DNA-minicircle used for this study, its sequences and a simplified representation (bottom right corner).

A stepwise approach to creating the fully assembled minicircle is by creating a fully ligated "inner circle", purifying it and hybridize the outer circle to it. To create a fully ligated circular single stranded DNA the method of splint ligation seems to be the most appropriate approach.[146] For the splint ligation, two linear strands, which will form the inner circle, need to be hybridized to splints. These splints are DNA-strands which are partially complementary to the joining ends of both strands and have the only function to keep both ends in close proximity. For an enzymatic ligation of two strands under splint ligation conditions, a phosphate residue at the 5'-end is necessary. In order to "attach" a phosphate to a 5'-hydroxy group either chemical phosphorylation or enzymatic phosphorylation can be used. Following previous studies in the preparation method[140–143] enzymatic phosphorylation with T*4*-polynucleotide kinase (T*4*PNK) is used, followed by ligation with T*4* ligase. Upon ligation, enzymes need to be deactivated at elevated temperatures, followed by purification of the single stranded product (Fig. 30).

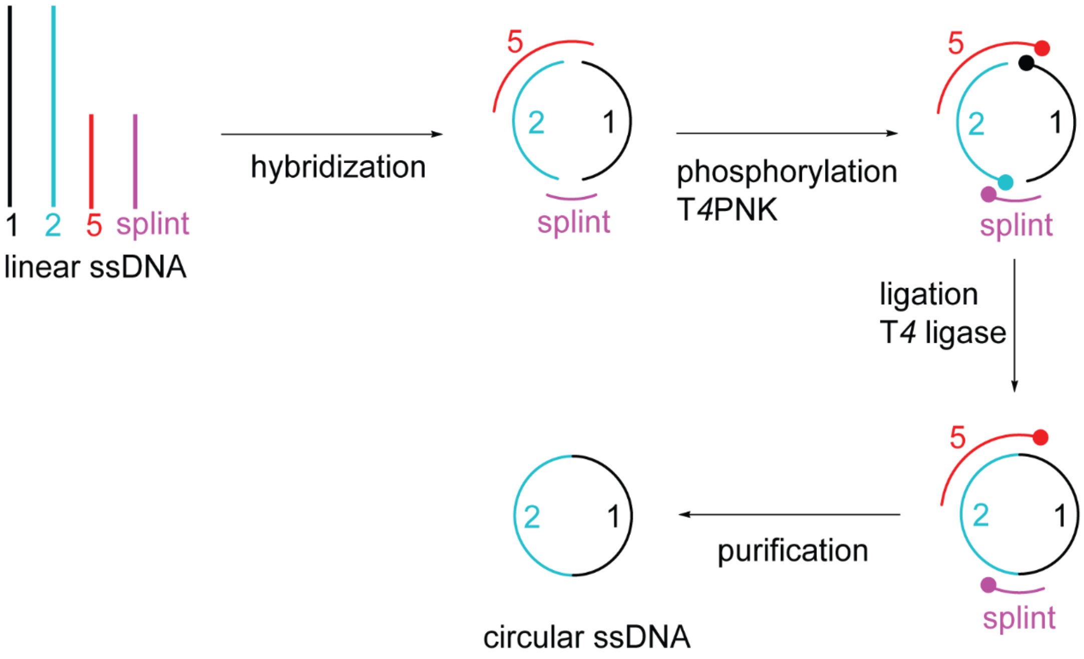
1
2
5
splint
linear ssDNA
hybridization
5
2
1
splint
phosphorylation
T4PNK
5
2
1
splint
ligation
T4 ligase
5
2
1
splint
purification
2
1
circular ssDNA

Fig. 30 Schematic approach for an enzymatic synthesis of a circular single stranded DNA under splint ligation conditions.

For the hybridization, the main strands (1 and 2, Fig. 30) are mixed with the two splints in a 1:1.5 ratio. The second splint (5, Fig. 30) is also part of the outer ring to save on sequences needed for monetary reasons. Since oligonucleotide hybridization is known to be depending on the cation concentration[147], several buffer systems have been tried. Highly concentrated buffers like phosphate buffered saline (PBS) have been avoided, in order to not disturb following enzymatic reactions. As suggested in previous works[140–143] a buffer of 50mM *tris*(hydroxymethyl)aminomethane (TRIS) and 100mM sodium acetate was used as standard condition, but it could be shown that even in deionized water the synthesis of single stranded DNA-rings was possible. For determination of the influence of divalent cations, series of magnesium chloride concentration has been tested, but without reproducible results. For the annealing process itself strands where pipetted into one tube under corresponding conditions, heated to 90 °C for 5 minutes and cooled passively to room temperature again within 1 hour. Using less-steep temperature ramps did not alter the resulting yield significantly.

The kits for the phosphorylation and the ligation step provided by *New England Biolabs* come with their own stock buffer solutions, which would implement that upon phosphorylation in its corresponding buffer system, a rebuffering step would be necessary. As first experiments showed, that the phosphorylation with T*4*PNK also works in ligation buffer, the rebuffering step was skipped in order to streamline the production of minicircles. Following the provided manual for the phosphorylation step, the stock buffer solution and the kinase were added to the annealed construct and incubated at 37 °C for 30 minutes. Longer incubation times of up to 3 h were also tested, but did not increase the yield. Upon completion of the phosphorylation, T*4* ligase was added to the mixture and incubated at 37 °C for 2 hours. Over-night ligations at room temperature were also suggested, but did not increase the yield. For deactivation of the enzymes by denaturation, samples were heated to 65 °C for 20 minutes.

When the ligation reaction is completed, the single stranded minicircle needs to be separated from the splints, the enzymes and additives like ATP and corresponding monophosphates. As the circularized product has neither a 3'- nor 5'-end, enzymatic digestion of side products and splints with the help of exonuclease III seemed as logical approach. Fueled by ATP, Exo III digests oligonucleotides from 3'- to 5'-end and should improve purification. Samples were incubated with the corresponding buffer and Exo III at 37 °C for one hour followed again by a deactivation step (65 °C, 20 min). As it can be seen in analytical denaturing polyacrylamide gel electrophoresis (a-dPAGE, Fig. 31), a new band formed (middle lanes), which migrates slower through the gel, than strand 1, 2 and the splints (side lanes).

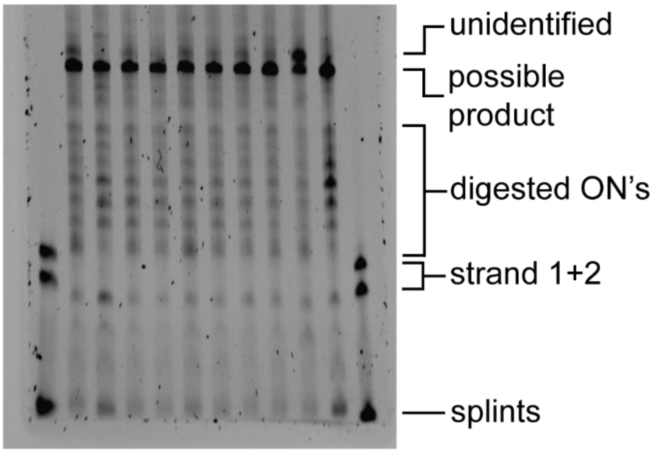

Fig. 31 An a-dPAGE (5% AA, 30 min, 3 W) of ligated single stranded minicircles after Exo III digestion. Explanations to the bands on the right side.

For the reaction mixtures (middle lanes) it can be seen that strand 1 and 2 almost completely vanished and a new band on top formed. In addition, several weak bands have been forming in between the newly formed top lane and the bottom. The lanes in between strand 1 and 2 and the splints were expected, as Exo III should digest these and traces of partially degraded strand 1 and 2 should still be present. The weak bands in between the product band and the bands of strand 1 and 2 on the other hand were surprising, as this means non-circularized ss-DNA longer than strand 1 and 2 appear to have formed. A possible explanation for this would be, that only on one end the ligation of strand 1 and 2 has been successful, were on the other end ligation failed. This would lead to both linear and circular full-length products to be formed, with the linear full-length product being digested by Exo III (Fig. 32).

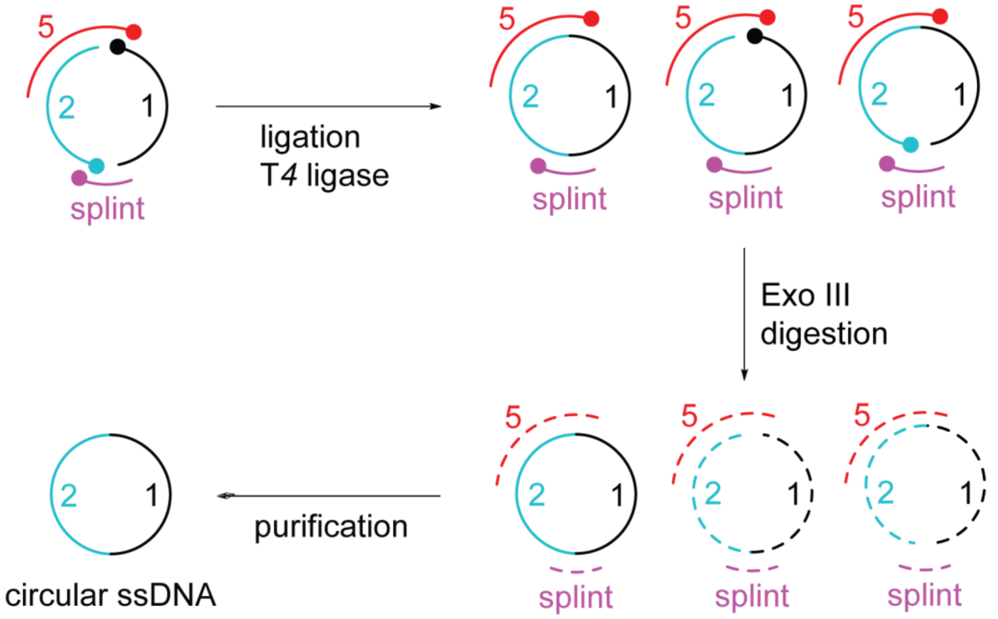

Fig. 32 Possible ligation products, their digestion through Exo III and the remaining product after purification.

In order to purify the single stranded minicircle, preparative denaturing PAGE is one of the main choices. It separates the oligonucleotides by size through a mesh of polymerized acrylamide cross-linked with *bis*acrylamide. As “size” in this context is a combination of molecular weight and morphology of the sample, linear full-length product moves faster in the electric field than the circular full-length product due to the reptation effect.[148] After running the gel, the corresponding bands will be visualized by UV-shadowing, which means the gel is placed on a fluorescent background and irradiated with UV-light. Dark spots will appear, where the nucleobases absorb the UV-light and can be cut out of the gel. An exemplary preparative denaturing PAGE is shown in Fig. 33.

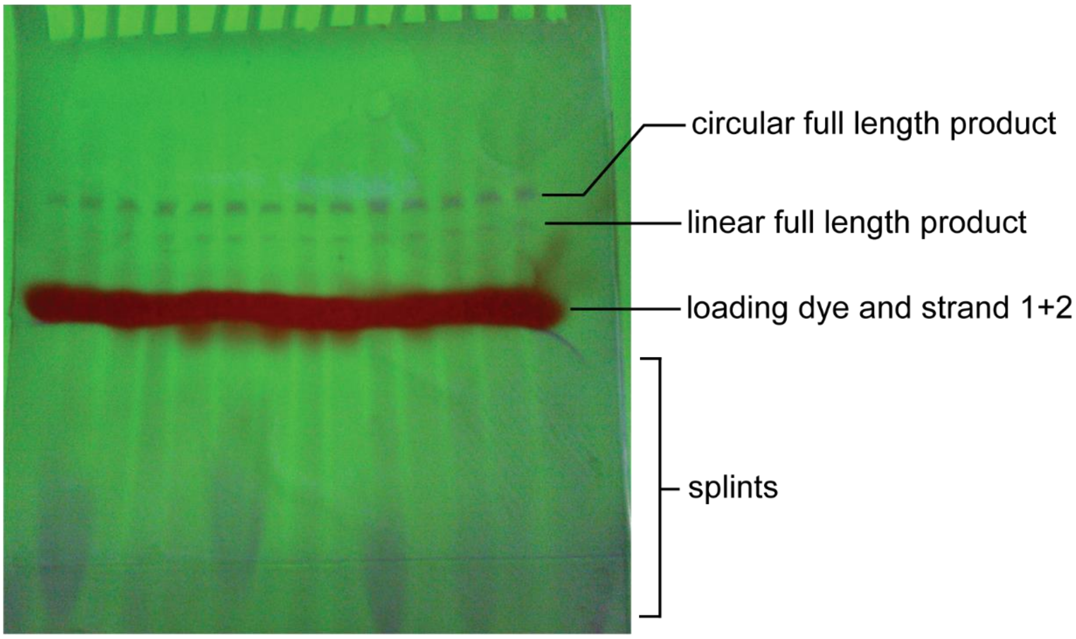
circular full length product
linear full length product
loading dye and strand 1+2
splints

Fig. 33 A p-dPAGE (5% AA, 2 h, 5 W) of a minicircle ligation reaction. Dark spots on the fluorescent background are caused by UV-absorption of the DNA.

In order to extract the DNA out of the PAGE gel, corresponding bands needed to be cut out of the gel using a scalpel. It needs to be noted that UV-irradiation should be kept to a minimum in order to avoid photodamage to the DNA. It has been shown, that exonuclease digestion of linear fragments anterior to the PAGE purification is not necessary, since the conditions during PAGE are denaturing enough to separate the oligonucleotides neatly on the gel, especially if the PAGE is run at elevated temperatures.

The cut out gel pieces are being placed in reaction tubes, crushed with a small pestle and soaked with an elusion buffer, which elutes DNA out of the gel into solution with detergents. Following this so called “crush & soak” strategy, the eluted minicircles need to be separated from gel particles and eluents. This was carried out with a purification kit provided by *Macherey* + *Nagel* after prevenient spin-filtration, to separate the product from large gel pieces. The underlying principle of the purification kit is the adsorption of the oligonucleotide onto a silica-membrane under chaotropic conditions, then eluting all dissolved impurities by spin-filtration. After washing the adsorbed sample several times with an alcoholic solution, resolvation of the sample with a buffer of low ionic strength and spin filtration will separate the product from small gel particles. The overall yield over the two enzymatic reactions followed by the clean-up procedure varied strongly. It could occasionally reach 86%, but usually was around 20-25%. Possible reasons for the fluctuation in quantity are manifold, as for example enzyme quality, timing or reagents. To evaluate all possibly problematic parameters and their combinations would take much more time than granted and would not be goal-oriented.

As an alternative for the gel electrophoresis followed by crush & soak purification, RP-HPLC was tested. Separating the product from short DNA-fragments, proteins and other contaminants showed to work surprisingly well, as they differed greatly in retention time. The only problem was the separation of circular or linear full-length product. The corresponding peaks in the chromatogram could not be baseline separated, leading to impurities of the other species in the product (Fig. 34).

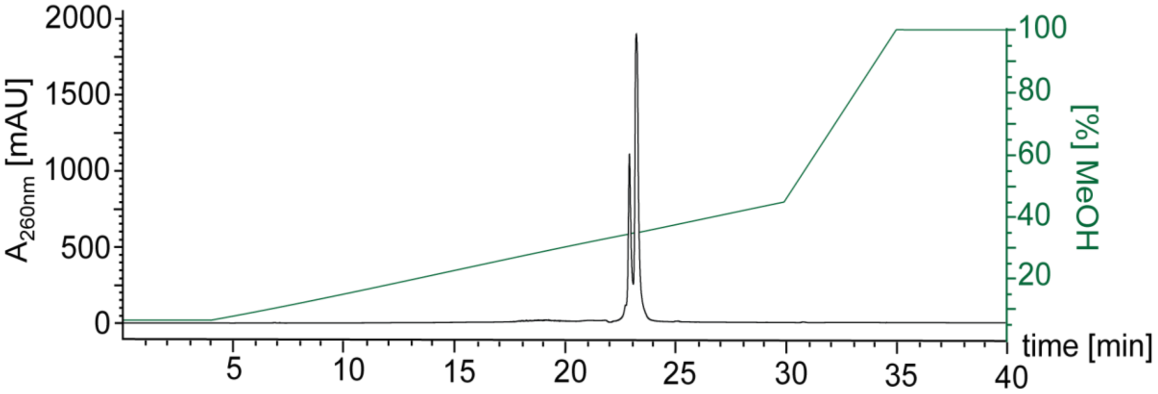

Fig. 34 Exemplary HPLC chromatogram of a mixture of linear (first peak) and circular (second peak) full-length product. HFIP-Buffer (0.4 M HFIP, 15 mM TEA) against methanol, gradient shown in green.

Comparing both purification-methods, the PAGE method included noticeably more work steps than the HPLC purification. This is compensated by the mount of HPLC-runs needed to purify the same amount of reaction mixture, as the resolution of the peaks increase with the dilution of the sample. It can be stated, that with both approaches, exonuclease digestion is not needed, since the purification methods themselves denature the sample sufficiently. The PAGE-method has the big drawback, that it consumes a noticeable amount of disposables during the process, making it less cost-efficient than the HPLC-purification. The biggest drawback of the HPLC-method on the other hand is, that the column used was not able to fully separate the two possible products, although being optimized for biomolecules. As the possible products are easily visible on the p-dPAGE and could be separated by a steady hand, the PAGE method was the weapon of choice in regard of single stranded minicircle purification.

2.2.3 Synthesis and purification of double stranded DNA-minicircles

After streamlining the synthetic pathway to create single stranded minicircles, an “outer ring” needs to be annealed. Two possible variations can be concluded, either annealing the 4 individual strands without further connecting them (Fig. 35A), or to ligate them as well, creating one linear fragment of the four strands forming the outer ring (Fig. 35B).

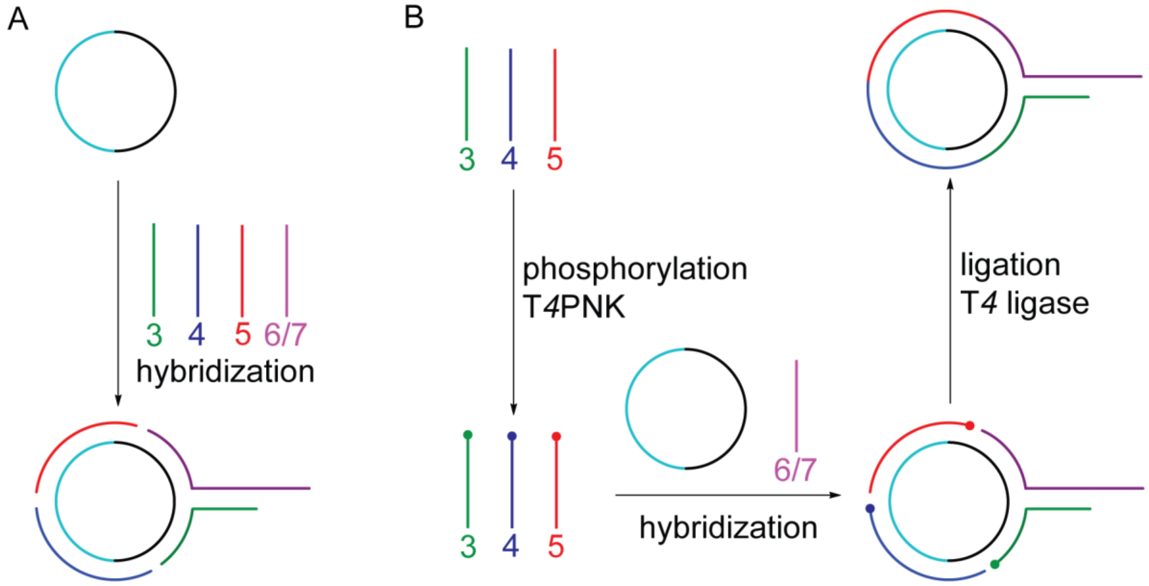

Fig. 35 Fabrication scheme to create a double stranded minicircle with either a non-ligated outer ring (A) or a fully ligated outer ring (B).

The formation of a double stranded minicircle with a non-ligated outer ring is rather simple, by adding corresponding strands to an aliquot of single stranded minicircle, heating it to 90 °C for 5 minutes and passively cooling it down like mentioned before. For the formation of a fully ligated outer ring, corresponding strands need to be phosphorylated and ligated with the minicircle acting as splint. On this point it needs to be taken in account that if all four strands forming the outer ring are being phosphorylated, the 5’-end of the lariat on the completed construct would also be phosphorylated. In case, that the upcoming purification of this construct after the enzymatic reactions is not quantitative, by mixing the construct with its counterpart chances are that the lariats might get ligated together, which would form a covalently connected minicircle dimer. Covalent dimers would not act like non-covalently connected minicircles, as they can’t deaggregate again. This would falsify the survey when estimation aggregation rate and should be avoided by any cost. For this reason, strand 3, 4 and 5 need to be phosphorylated separately in the same manner as mentioned before. Upon deactivation of the kinase, single stranded minicircle and corresponding strand are added and hybridized as before, followed by the known ligation procedure.

An evaluation of created constructs by gel electrophoresis showed that the outcome following either of the procedures described differed substantially as expected. Under denaturing conditions, no additional band was seen for the hybridized non-ligated outer ring, whereas for the ligated outer ring, an additional band could be seen less retarded than the single stranded minicircle (Fig. 36A), which could be the ligated outer circle. With 198 nucleotides it would be 30 nucleotides longer than the inner circle and therefore plausible to be this retarded in the gel.

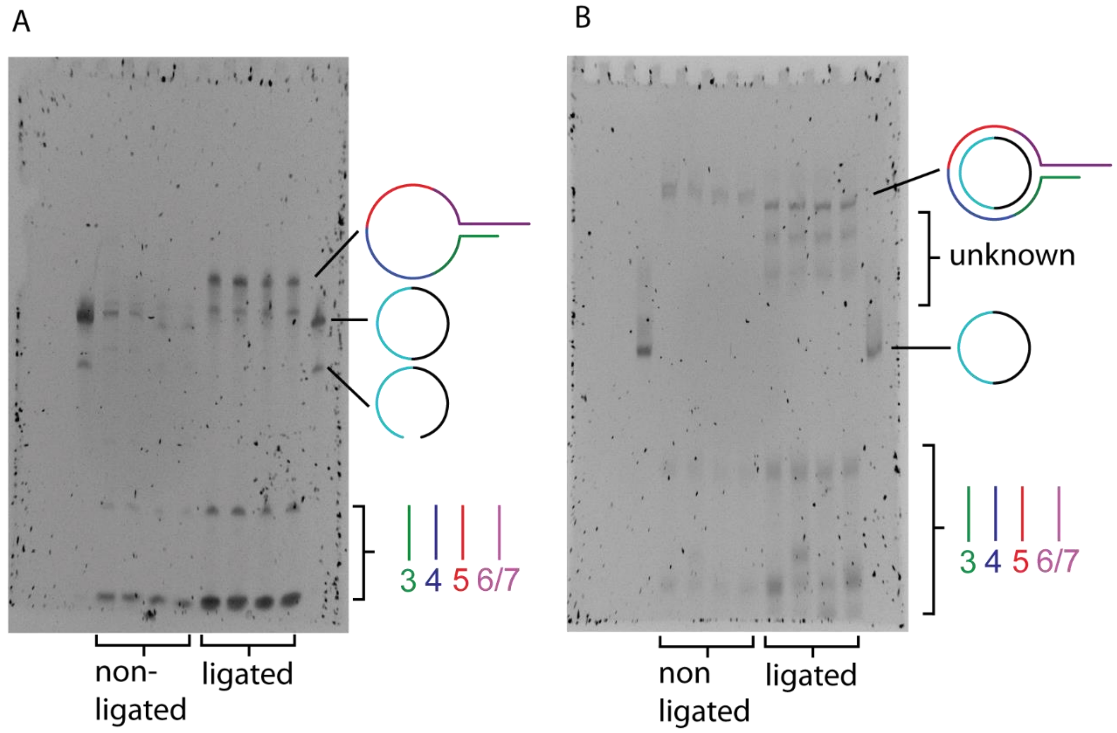

Fig. 36 Denaturing (5% AA, 30 min, 3 W, A) and native (5% AA, 30 min, 3 W, 10 °C, B) PAGE of non-ligated and ligated double stranded DNA minicircles with corresponding explanations.

In the case of native PAGE (Fig. 36B), the band of the single stranded minicircle vanished in both cases, resulting in a new band on top. Since this band appeared in both cases it is very likely to be the desired construct. The biggest difference in between the two approaches on a native gel is two additional bands in between the single stranded and the double stranded minicircle in the case of the ligated outer ring. It could not be cleared what exactly might have formed here, but it can be assumed to either be partly assembled rings or topological isoforms of the ring. For this reason and the increased materials and disposables consumption, only constructs with non-ligated outer rings will be used in this study from this point on.

As purification of assembled DNA-nanostructures without destroying their integrity is of utmost importance, many different strategies have evolved to fulfill this request.[149] Several strategies have been deployed in order to purify assembled DNA-minicircles and shall be illustrated in the following. Chromatographic purification methods have the advantage of high reproducibility and throughput with a minimum of effort and expenses needed. The biggest task is to establish a method of purification for the individual problem. As suggested by Shu *et al.* anion exchange chromatography can be an interesting tool to purify nanostructures, as they have been using to purify nanocages and tetrahedrons.[150] The underlying principle is that the nanostructures should migrate along the column in the exact ion concentration which is needed to keep the structure intact. In the case of DNA-minicircles a clear difference could be seen in the retention times of ss-minicircles and ds-minicircles (Fig. 37). Even under optimized conditions, double stranded minicircles tend to have rather broad peaks. The implication from this fact is that it stays unclear, whether this peak originates from a uniform species or hides several species under one peak, as the peaks feature a significant tailing. Unfortunately, no intact structures could be retrieved from the AE-HPLC. The reasons for this remain unclear, but it can be assumed that the minicircles deaggregated during the HPLC runs due to high salt gradients. Therefore AE-HPLC appeared to be unsuitable for this purification problem and has not been investigated any further.

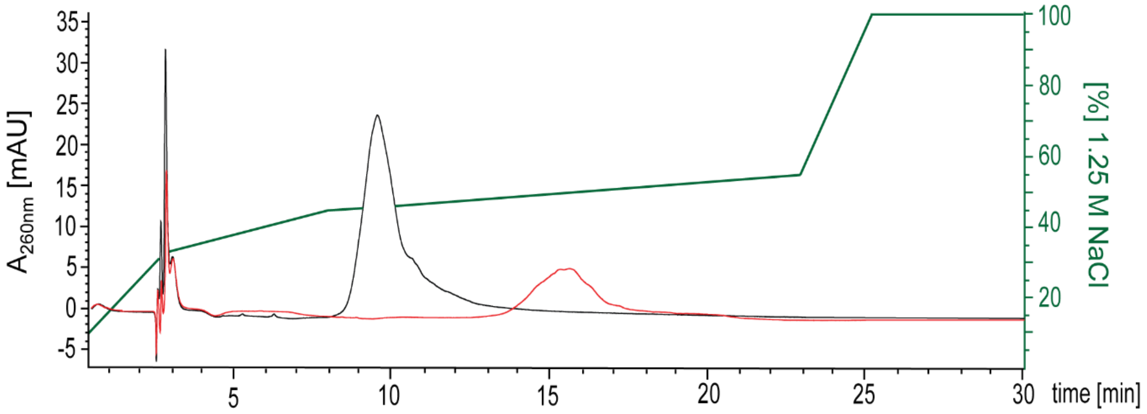

Fig. 37 Expemplary AE-HPLC chromatogram of 5 pmol ss-minicircle (red) and 5 pmol ds-minicircle (black). Deionized water against 1.25 M NaCl, gradient shown in green.

As RP-HPLC gave sufficient results for the single stranded minicircles, it seemed promising to evaluate the purification capabilities for hybridized constructs. The samples usually resulted in two peaks, which could be isolated separately. Unfortunately, the fractions did not show intact structures, as being proved by native PAGE. It can be assumed, that the amount of methanol in the eluent needed for migration of the sample along the column disturbs hydrogen bonding in the construct causing them to deaggregate. Even at lowered temperatures no positive outcome could be observed, which renders this method inapt for this application.

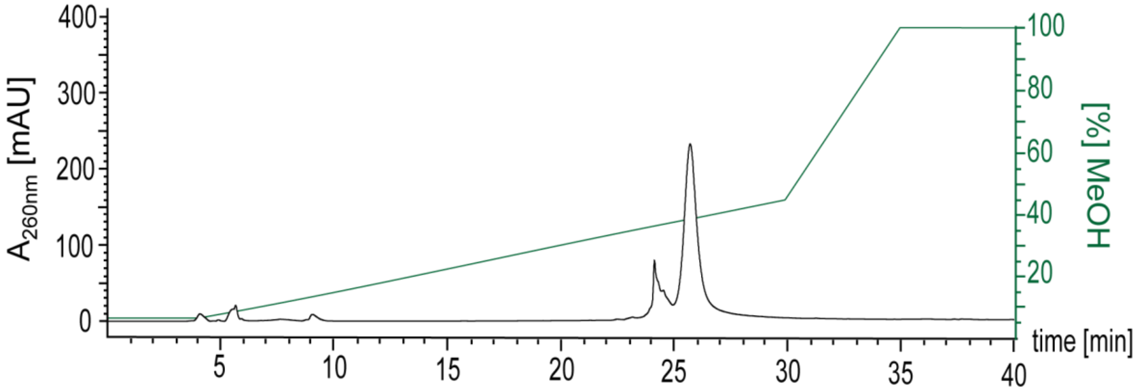

Fig. 38 Exemplary RP-HPLC chromatogram of an assembled double-stranded minicircle. HFIP-Buffer (0.4 M HFIP, 15 mM TEA) against methanol, gradient shown in green.

The weapon of choice for most DNA-nanostructure oriented studies is size exclusion chromatography.[149,151–153] The idea here in this context is that the single stranded oligonucleotides would be more compact in their morphology and thereby being more retarded by interactions with the surface within the column than a rather rigid, double stranded structure. To choose an appropriate column, the suggested average molecular weight needs to be met by the sample. Two columns have been tested, a *Bio SEC-3* from *Agilent* and a *Superdex 200 increase* from *GE Healthcare*. The first column with a molecular weight range of 100 Da to 100 kDa would be appropriate for the minicircles, with the double stranded minicircle being around 83 kDa and the single stranded minicircle being 38 kDa in mass. The SEC-runs were carried out with different buffers under isocratic conditions, with PBS-buffer resulting in the sharpest peaks. Unfortunately, retention time of ss- and ds-minicircle did not differ (Fig. 39A). A more size specific separation was promised for the second column with a molecular weight range from 10 kDa to 600 kDa. Unfortunalety, the results were the same, with double stranded minicircles having the same retention time as single stranded minicircles (Fig. 39B). Apparently, size exclusion chromatography did not improve the purity of the sample, but the structures were not damaged in the purification process like in the other methods before. Most size exclusion techniques are tailored for purification problems of proteins and enzymes, which are of a more globular and thereby predictable in shape. Appropriate chromatography methods for DNA-nanostructures still have to be developed.

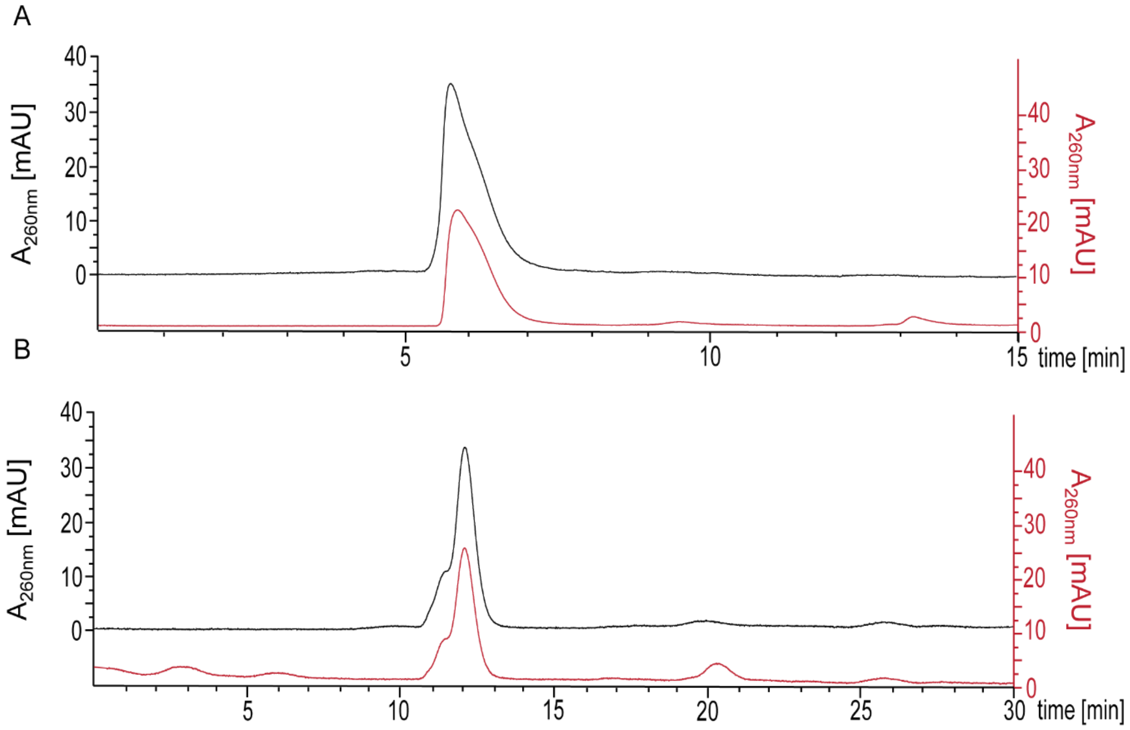

Fig. 39 Exemplary size exclusion chromatograms with the columns from Agilent (A) and GE Healthcare (B). Single stranded minicircle samples in red, double stranded minicircle samples in black.

A purification method closely related to size exclusion is the molecular weight cut-off by spin-filtration. Samples will be loaded in a tube onto a mesoporous membrane and only particles surpassing the pore diameter will be retained on top of the membrane. Several pore diametres are available and have been tested for the system. It could be shown, that spin-filters for 10 kDa (not shown) and 30 kDa (Fig. 40) did not purify the minicircles from low-molecular impurities, as their band intensity did not decrease in analytical native PAGE. This is reasonable, since ss-minicircles for example still exceed the MWCO-limit with 38 kDa. A different result could be achieved with MWCO spin-filter with a cut-off of 50 kDa (Fig. 40) and 100 kDa (not shown). It appeared that the impurity bands decreased, while target structure bands did not alter significantly. Since samples retrieved from the filters still appeared to yield intact bands in native PAGE, it can be said that an appropriate purification method had been found for the purification of the DNA-minicircles. As long as samples are not spin-filtered to dryness on the membrane, structures stay intact and can be used for further applications. In addition MWCO spin-filters are a convenient method for rebuffering of nanostructures, are fast and easy to use and moderate in expense.

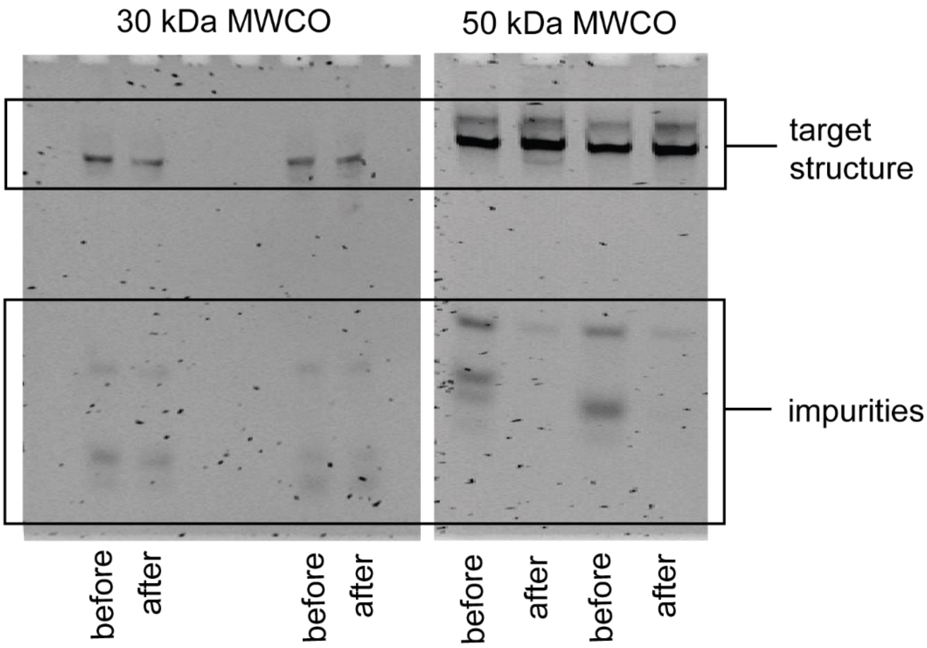
30 kDa MWCO
50 kDa MWCO
target structure
impurities
before
after
before
after
before
after
before
after

Fig. 40 Exemplary a-nPAGE gels (5% AA, 30 min, 3 W, 10 °C) of minicircle samples before and after MWCO spin-filtration.

2.2.4 AFM-imaging of DNA-minicircles

Since its development in the 1980's by *IBM* scientists[154] atomic force microscopy (AFM) made huge advances in resolving structures beyond the Abbe-limit imposed on light microscopes up to resolving individual molecules and atoms.[155–157] Since then, AFM also became a powerful tool in the life sciences for mapping, imaging and characterizing biomolecules like proteins on surface[158] and in membranes[159]. Even in the field of DNA imaging, the contribution of AFM still rises among other imaging techniques.[160] Especially for DNA-nanostructures the AFM technique offers great opportunities to investigate structural integrity and interactions of the structures on a surface.[134,161]

As for all microscopy techniques, good sample preparation is the key to successful imaging. In an AFM context this means that the DNA-nanostructures need to be adsorbed to a surface with a topology-profile less rough than the adsorbed structures for proper imaging. As most biomolecules are of polar or even ionic character, polar surfaces like muscovite (mica) have proven to be the sample carrier of choice. Being a phyllosilicate, cleaning the surface for sample preparation can easily be achieved just by exfoliating the top layer with adhesive tape. The simplest way of sample preparation is by just pipetting the diluted sample directly onto the freshly cleaved mica and incubate it for some minutes on the surface. The area of interest was encircled with a felt pen. The hydrophobic ink formed a barrier for the aqueous sample, so that it could not spread over the entire surface. With this technique multiple samples could be prepared onto one mica surface with ease. No reproducible differences could be observed if the incubation time was merely one minute or even extended to ten minutes (Fig. 41A). This gave already images of high quality with a very homogenous structure morphology and low background topology (Fig. 41B). However, as the samples were measured on air, remeasuring the same area 30 minutes after first imaging, structural differences could be observed (Fig. 41C). It appeared that the minicircles contracted and even aggregated to some extend. This might be due to the reason, that silicate surfaces are highly anionic on the surface. The anionic silicate oxygen atoms cause a serious repulsion against the polyanionic backbone of the DNA. In order to reestablish a valency saturation for the backbone, morphological changes of the DNA to aggregate into complex structures with the nucleobases might be a reason for this rearrangement. This is merely a theoretical approach to explain this phenomenon, experimental evidence is yet to be found. From this experiment it can be concluded, that the minicircles appear to have more structural flexibility as the persistency length would predict. This finding is surprising and needs to be kept in mind for future experiments. With the sample "aging" very fast on the surface and non-natural interactions due to high electrostatic repulsion of the sample material with the surface, this method was not used for qualitative or quantitative analysis of minicircles or their dimerization on a surface.

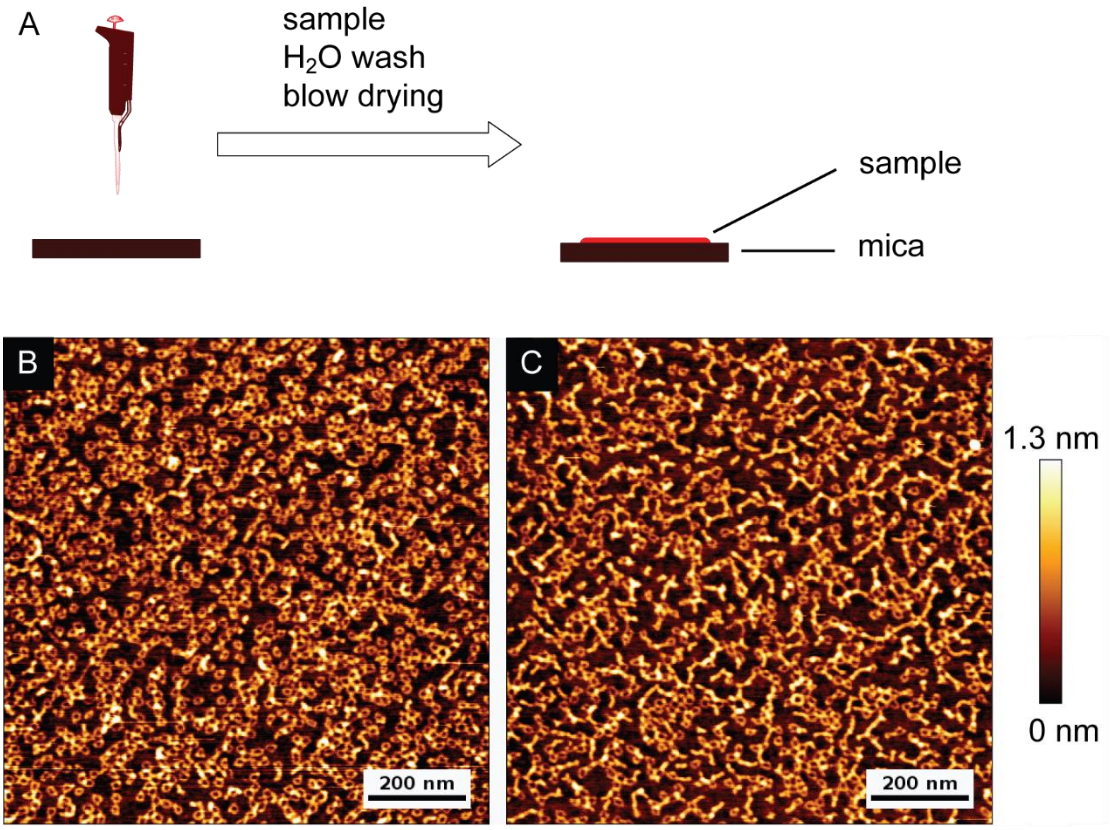

Fig. 41 Sample preparation for AFM imaging by simply adding the sample (100 nM minicircles in DNA storage buffer) onto the freshly cleaved mica (A) and image of the sample on air directly after sample preparation (B) and 30 minutes later (B).

It is advised in many studies to incubate the freshly cleaved mica with a positively charged substrate to cover the negatively charged silicate-anions. This so called positivation of anionic imaging surfaces is mostly achieved with divalent metal cations like Mg^{2+}, Ca^{2+} or Ni^{2+}-Ions.[162] Additionally, cationic polymers like poly-*L*-lysine[163] or poly-*L*-ornithine[164] have been used to successfully adhere biomolecules to mica surfaces. In regard of minicircle immobilization divalent cations Mg^{2+} and Ni^{2+} as aqueous solutions of their corresponding chlorides have been used in this work as well as aqueous poly-*L*-ornithine solutions. Since the outcome was genuinely better when poly-*L*-ornithine was used, all following results shown here were positivized with that substrate. In order to prepare an imaging sample with a positivated surface, two major strategies are reasonable. The first being combining the sample and positivation agent on the surface followed by rinsing with ultrapure water and blow-drying (Fig. 42A). Following the first procedure, large heterogenous structures could be seen on all imaging samples (Fig. 42B). By enlarging the images, it could clearly be seen that these globular structures of heterogenous size distribution were covered with minicircles (Fig. 42C).

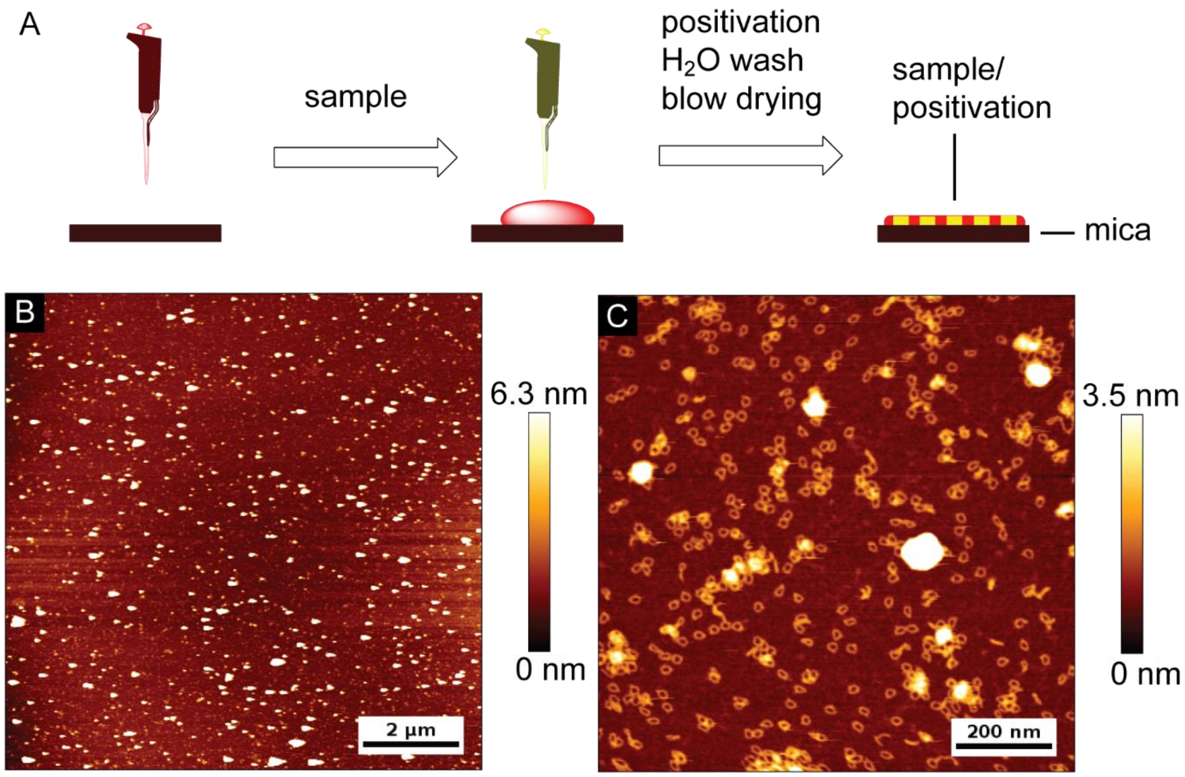
A
sample
positivation
H_2O wash
blow drying
sample/
positivation
mica
B
6.3 nm
0 nm
2 µm
C
3.5 nm
0 nm
200 nm

Fig. 42 Sample preparation by combining minicircles (10 nM) and positivation agent (10 µL of 0.1 mg poly-L-ornithine in 1 mL ultrapure water) in solution, rinsing it off and blow-drying (A), exemplary AFM-image of a sample prepared under this conditions (B) and a zoomed image of the same sample (C).

It appears, that the poly-*L*-ornithine and the minicircles formed aggregates in solution, which deposited on the surface. This would be logical, since structures of opposite polarity would attract each other by forming ionic bonds. With this aggregations, this method also fails to represent native structures quantitatively and can not be applied to investigate minicircle dimerization, since the samples aggregate even without interaction partner. However, this method can be used to take a detailed look at the minicircles themselves (Fig. 43).

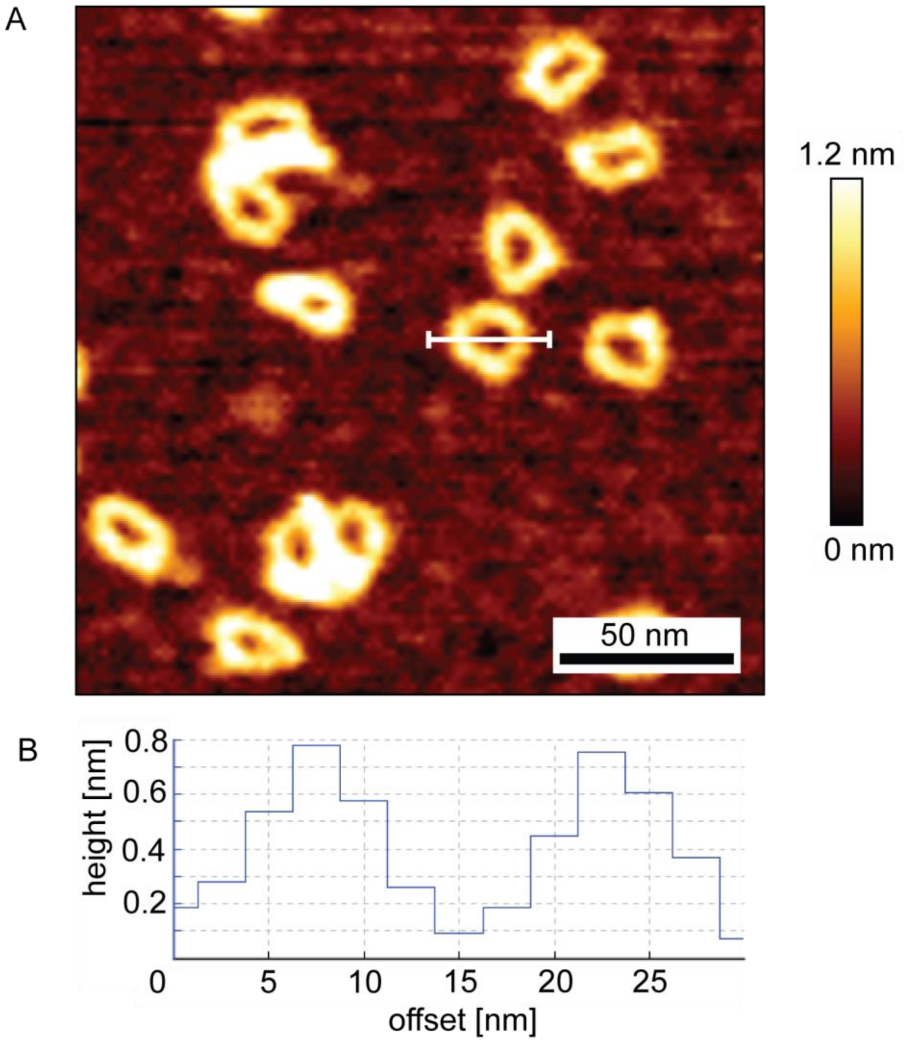

Fig. 43 Detailed AFM image of DNA-minicircles from Fig. 42C (A). The white bar across one ring in the center indicates path of the cross-section shown in B.

The minicircles appear to be of uniform circumference but with some degree of conformational freedom, as already seen in Fig. 42. Taking a close look at a rather round shaped ring in the center of the image a histographical cross section can be made for evaluation of size dimensions of the ring. The ring appears to be 0.8 nm in height on the surface with a diameter of around 15-20 nm on the highest positions. This is in accordance with theoretical calculations and previous studies working with this set of minicircles.[140–143]

The second method for sample preparation would be incubating the surface with the positivation agent followed by rinsing with ultrapure water and blow-drying, then incubating the treated surface with the sample solution followed by rinsing with ultrapure water and blow-drying again (Fig. 44A). This usually resulted in appropriate images with rings in high uniformity on the surface. Apparently, the background pollution of the sample rose significantly. This might be due to the fact, that the affinity of the DNA to the positively coated surface was much higher than in the non-pre coated case. Especially in cases without using molecular weight cut-off spin-filtration to purify the sample prior to imaging sample preparation a noticeable amount of defect structures, loose strands and other undefined objects could be seen among the rings (Fig. 44B). This makes it problematic to distinctively identify minicircles and their possible interactions on the surface. This problem could partly be condemned by MWCO spin-filtration. With the minicircles not “aging” on the surface over a relevant time span and not aggregating during sample preparation, this sample preparation method appeared to be the most useful for further minicircle imaging and was used on all samples from this point on.

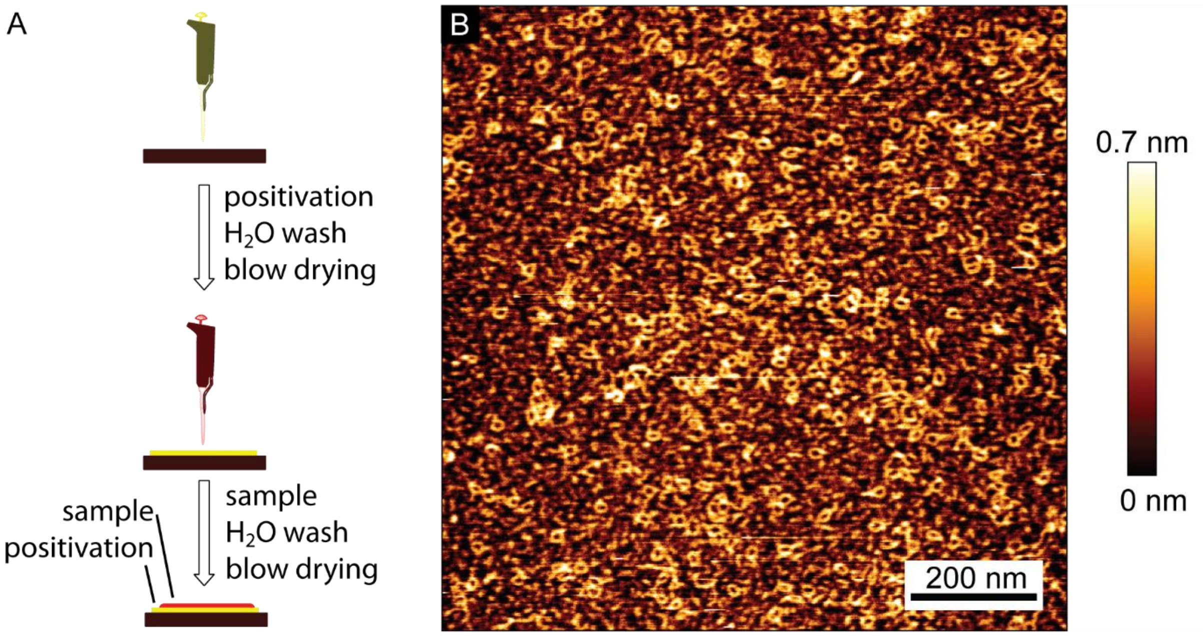

Fig. 44 Sample preparation by positivizing (10 µL of 0.1 mg poly-L-ornithine in 1 mL ultrapure water) the surface prior to sample adsorption (A). The result of this procedure can be hard to interpret, if samples have not been thoroughly purified by molecular weight cut-off spin-filtration before sample preparation (B).

The minicircles were designed in a way, that a single stranded overhang of 10 bases at the end of the lariat structure can bind to a second ring, carrying a single stranded overhang with the complementary sequence (Fig. 45A). For the evaluation of minicircle dimerization with AFM, samples of two corresponding rings, one modified with strand 6, one with strand 7, were mixed and applied onto the surface as previously described. Apparently, it did not matter whether the samples were mixed prior to the application or directly in the droplet on the surface. This seems plausible, as the hybridization event of short oligonucleotides takes place within seconds under appropriate buffer conditions.[165–167] With the exceeding incubation time of the sample on the surface of around 10 minutes, no differences are to be expected. Despite purifying the samples prior to sample preparation, a low signal to noise ratio could be achieved making analysis of the images difficult (Fig. 45B). Aside from this fact, these images provided a detailed view on the dimerized minicircle structures (Fig. 45C).

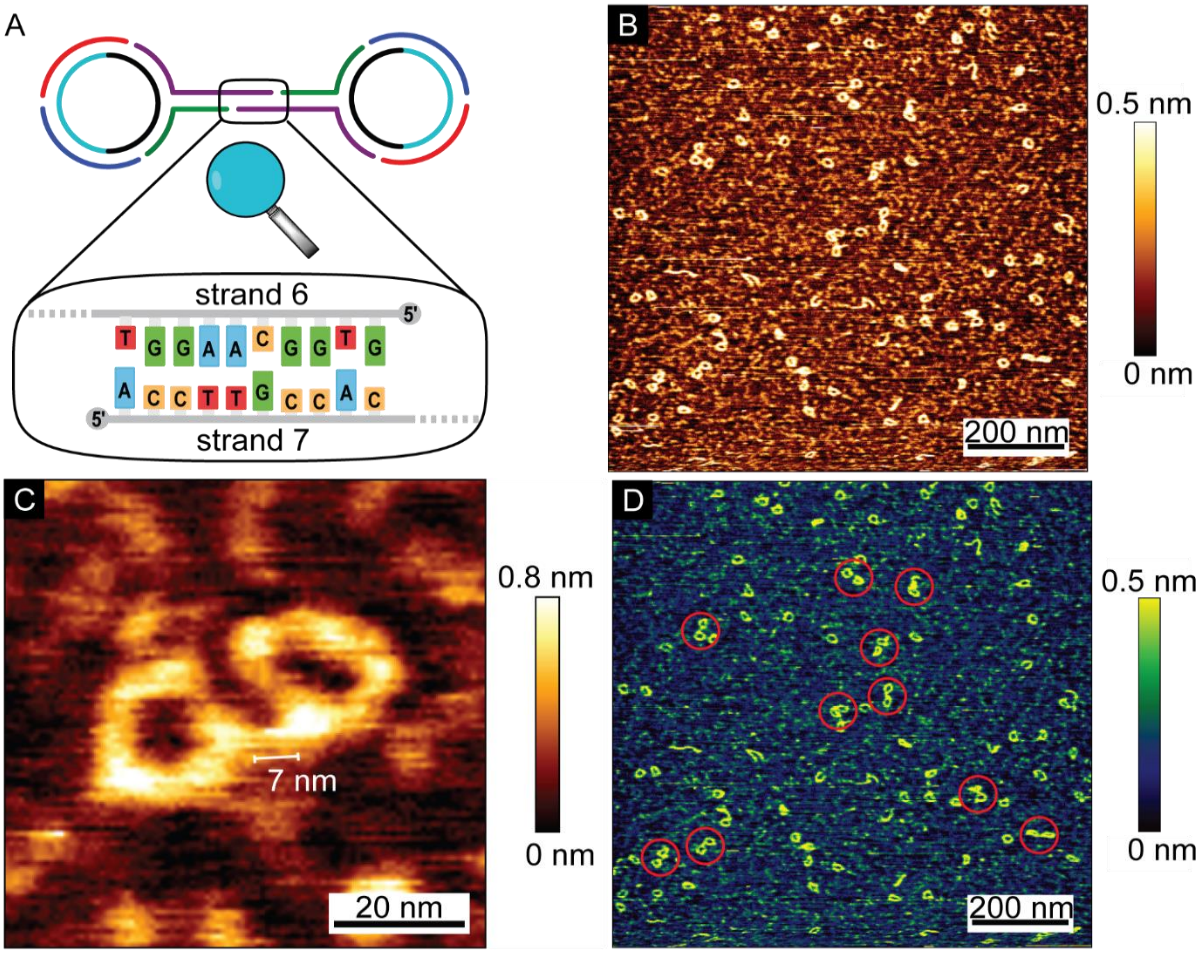

Fig. 45 Schematic representation of the minicircle dimers and the zoomed-in binding region (A), exemplary image of a minicircle dimer sample (B), magnified image of a minicircle dimer with the white bar indicating the length of the bridge (C) and contrast-improved image shown in B with the dimers encircled in red (D).

The length of the bridge has been measured at being around 7 nm, as the white bar in Fig. 45C indicates. With the bridge being 30 nucleotides long, this coincides with theoretical values, which estimates a B-DNA to grow 0.34 nm in length per nucleotide summing up to 7.2 nm for 30 nucleotides. After contrast-improvement of Fig. 45B with special color filters for low-profile images provided by *JPK*-software, the adsorbed structures can be seen clearly (Fig. 45D).

After interpreting several images of samples prepared by the same procedure, following conclusions can be made. The image quality is highly heterogenous and reproducing an image with the same quality is close to impossible, which leads to the need for high imaging throughput with producing a substantial amount of images not meeting the standard for quantitative analysis. The dimerization ratio of the minicircles on the surface, which is defined by the amount of circles being part of a dimer divided by the total amount of minicircles in the corresponding image section, also varied to a certain degree. As example, the dimers in Fig. 45D are indicated with red circles. With 20 dimer-minicircles out of 78 minicircles in total within this 1 µm^2 image section, a dimerization rate of 26% can be calculated. This image was among the best images obtained with this method with dimerization ratios usually being in the range of 0-30% and was independent from factors like sample temperature, handling speed or using nitrogen instead of air for drying. This is a clear contradiction to the behavior as seen in PAGE-experiments. Additionally, a noticeable amount of fractured minicircles can be seen along other linear DNA contaminants. As the linear fragments should have been removed by the purification prior to the sample preparation, it can be assumed that some minicircles were destroyed in this process. Indeed, it can be assumed that the sample preparation is a harsh process for the fragile DNA constructs as for example the drying of the surface with pressurized air puts the adhered sample under mechanical stress. As it was not possible to measure the structures in solution, a certain degree of denaturation could not be avoided. As a conclusion from this observations it can be conducted, that AFM-imaging offers rather a qualitative form of sample analysis rather than a quantitative one, if native conditions can not be guaranteed for the sample throughout the entire measuring process. All experiments quantifying dimerization ratio for unmodified and modified DNA-minicircles were performed with native PAGE from this point on.

2.2.5 Synthesis of azobenzene *C*-nucleosides

As mentioned in chapter 1.2 the main objective of an azobenzene linker system is to position the azobenzene within the oligonucleotide in a way, that minimal disturbance is caused in favored *trans*-state. Upon photoisomerization to the *cis*-state, maximum perturbation within the duplex should be caused by shifting the adjacent nucleobases in their position resulting in a distortion of the hydrogen bonds and ultimately decreasing hybridization affinity of the pairing strands. Additionally, the linker should provide mechanical support through rigidity, so that the isomerization is supported in its movement to stay in the base pairing region and not evade into minor or major groove. As azobenzene *C*-nucleosides fulfill all the criteria named above, a closer look at them through the perspective of a synthetic chemist is necessary. The interesting step in creating azobenzene *C*-nucleosides is fusing the chromophore onto the ribose linker. The first synthesis of azobenzene *C*-nucleosides as published by Goldau *et al.* utilized a palladium-catalyzed Heck-cross-coupling reaction of an iodinated azobenzene with a glycal (Fig. 46A).[72,84] This reaction is highly stereospecific, however, the yield decreases when the reaction is upscaled. This nuisance creates a bottleneck in this synthetic pathway, as the reaction has to be repeated several times in the low sub-gram scale in order to accumulate enough material for phosphoramidite synthesis. During the master thesis of current works author, the 2'-methoxy-RNA version of the azobenzene *C*-nucleoside has been developed. For this work, iodinated azobenzene has been transformed into the highly reactive lithiated azobenzene species by lithium-halogen-exchance with *n*-butyl lithium. Following this step, nucleophilic addition of the negatively charged azobenzene to a protected ribonolactone (Fig. 46B) and subsequent dehydroxylation gave the *C*-nucleoside in high yield in multi-gram scale.

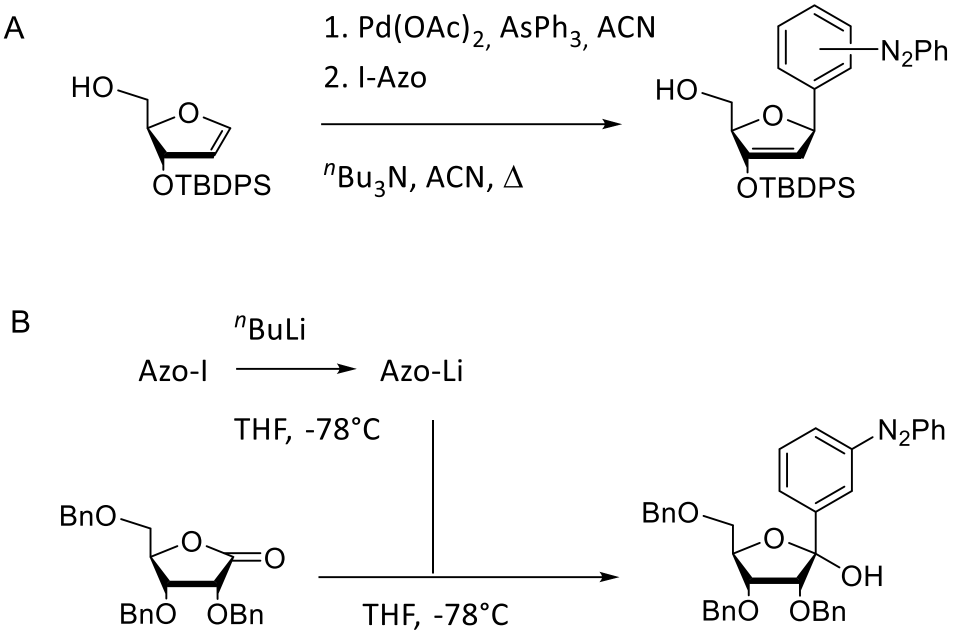

Fig. 46 Synthetic approach on attaching azobenzene to the sugar moiety by Heck-reaction (A) and nucleophilic addition of lithiated azobenzene (B).

As this synthetic pathway appeared to be highly efficient, it should also be adapted to the 2’-deoxy azobenzene *C*-nucleosides. For this, a 2’-deoxyribonolactone with protecting groups for the 3’- and 5’-alcohols needs to be generated. Starting with commercially available 2’-deoxyribose, initial reduction of the sugar with bromine in water resulted in the cyclized 2-deoxyribonolactone with up to 73% yield (Fig. 47, **1**). In analogy to the synthesis shown in Fig. 46B, benzyl ether protection of the alcohols has been tried, only to find that it appeared to be impossible to isolate desired product. It stays unclear, why benzyl protection of the 2’-deoxyribonolactone was not possible, although different bases for deprotonation have been tried like sodium hydroxide or sodium hydride. Exchanging the leaving group of the benzylation agent from benzyl chloride to the corresponding bromide or even iodide did not result in product formation. Since the alcohol protecting groups in this synthetic pathway have to be stable under very basic, acidic and even nucleophilic conditions but on the other hand should be cleaved under orthogonal conditions, the reorientation towards silyl protecting groups appeared to be logical. Since nucleophilic attack of lithiated azobenzene followed by dihydroxylation in presence of boron trifluorate are rather harsh conditions for the protecting groups, silyl ethers of high stability like *tri-iso*propyl silyl ethers (TIPS) were chosen. Introducing the TIPS-ether as corresponding chloride in presence of imidazole as activating base produced the protected species in quantitative yield (Fig. 47, **2**).

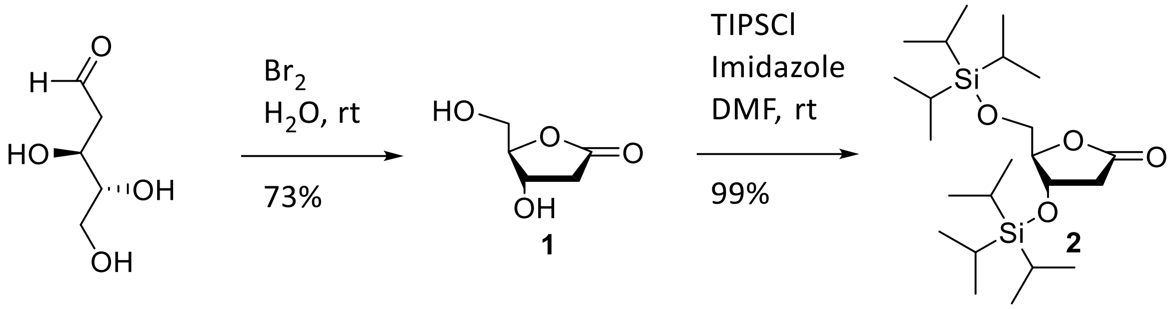

Fig. 47 Reaction of 2'-deoxyribose to corresponding ribonolactone with subsequent TIPS-protection.

No nucleophilic addition of lithiated azobenzene to species **2** was possible. The reaction has been tested in diethylether and tetrahydrofuran in ratios ranging from 1:1 to 1:10 of lactone to azobenzene in a temperature range from -90 °C to -40 °C and different timescales without any success. Higher temperatures have been avoided, since it is known for lithiated azobenzene species to degrade at higher temperatures.[168] As all endeavors were in vain, mechanistic contemplation of the reaction seemed necessary.

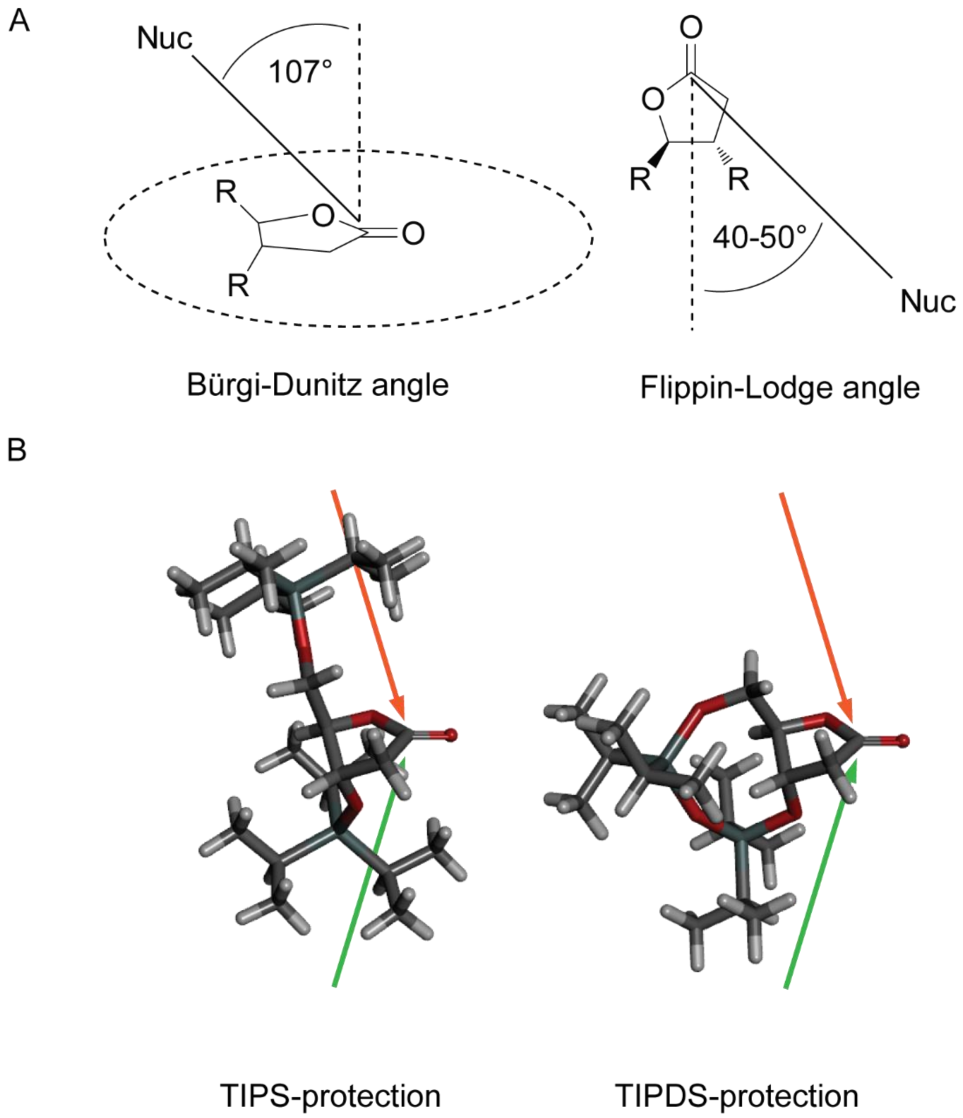

Bürgi-Dunitz angle

Flippin-Lodge angle

TIPS-protection

TIPDS-protection

Fig. 48 Schematic explanation of the Bürgi-Dunitz angle and the Flippin-Lodge angle (A) and 3D-rendered models of the TIPS-protected (B, left) or TIPDS-protected (B, right) ribonolactone. Orange arrows indicate si-site attack, green arrows re-side attack of a possible nucleophile following geometries depicted in A.

The attack of a nucleophile on the carbonyl functionality of the ribonolactone is carried out in an angle, that the σ-bond can be formed while simultaneously breaking the C-O-π-bond. This so called Bürgi-Dunitz angle defines the trajectory a nucleophile has to take in order to gain optimal orbital overlap and is usually around 107° (Fig. 48 A, left).[169,170] In addition to this, electron density and bulkiness of the nearest neighboring atoms to the carbonyl function also influence the trajectory greatly and can make up to 40-50°.[171] Due to the electronegative 4'-oxygen-brigde, the so-called Flippin-Lodge angle for the ribonolactone will force the nucleophile to attack from approximately the direction of the 2'-carbon (Fig. 48A, right). Taking a closer look on the TIPS-protected ribonolactone, it is clear to see that the protecting groups provide a tremendous amount of sterical hindrance for the possible nucleophile. Considering this fact it does not surprise, that nucleophilic addition of azobenzene could not be achieved. As a similar protecting group 1,1,3,3-(Tetraisopropyl)disiloxanediyl-protecting group (TIPDS) offers similar stability towards other reagents as TIPS, but with less steric hindrance. This so-called Markiewicz-group has been introduced to the ribonolactone similar to the TIPS-group by reaction with the corresponding chloride in DMF and imidazole as auxiliary base with a yield of 73% (Fig. 49, **3**). Upon lithium-halogen-exchange of the iodinated azobenzene and nucleophilic attack of the *in situ* formed lithiated species to **3**, a new species was formed displaying characteristics of an azobenzene covalently attached to the sugar moiety. Unexpectedly, hemiacetal **4** has not formed, but rather ketone **5** (Fig. 49).

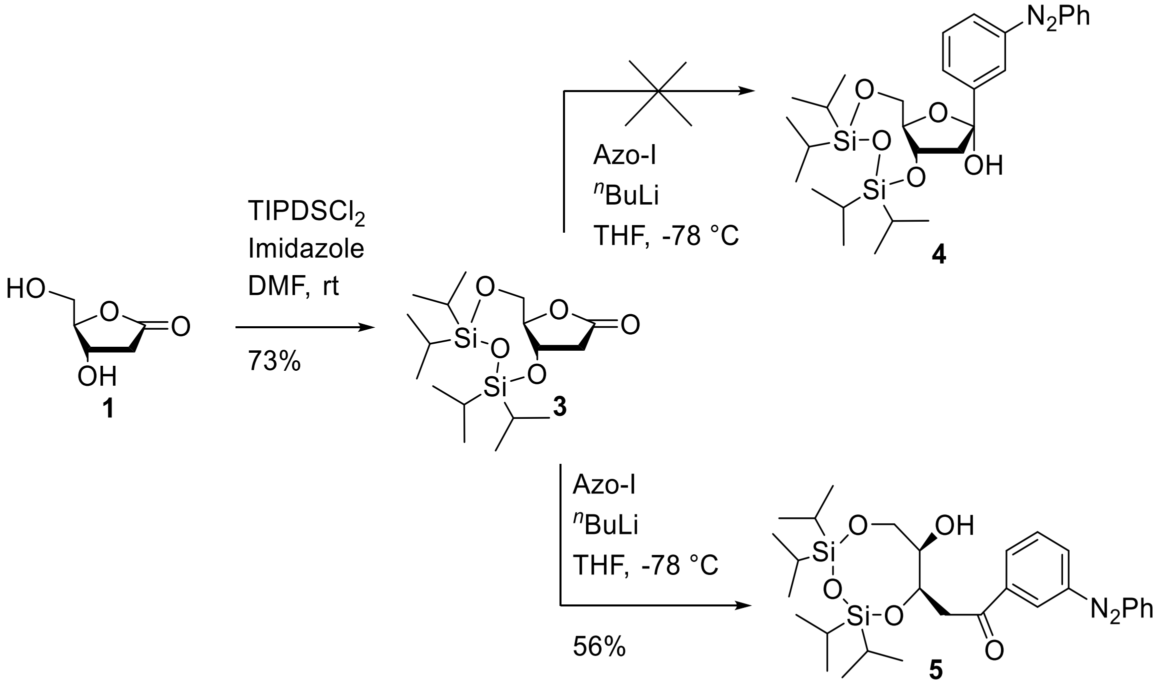

Fig. 49 Formation of the TIPDS-protected ribonolactone and subsequent addition of the nucleophilic azobenzene.

A possible reason for the unexpected ring opening might be conformational tension in the five-membered ring caused by the eight-membered cyclic silyl-ether. The biggest implication the formation of **5** brings, is that stereogenic control over product formation is lost in this process, as the newly-formed 1'-carbonyl can rotate without restriction. Providing *si*-site preference for the nucleophilic attack of the lithiated azobenzene by hypothetically installing protecting groups on the 3'- and 5'- positions with different steric demand would have been naught. The anomeric position will only be defined upon ring closure during following dehydroxylation.

The ring closure and subsequent dehydroxylation of *in situ* forming hemiacetal is being achieved by reaction with boron trifluoride etherate and triethyl silane in DCM at -78 °C. During this step α- and β-anomers of **6** was formed, which could be converted to the free nucleoside **7** by TBAF-deprotection (Fig. 50).

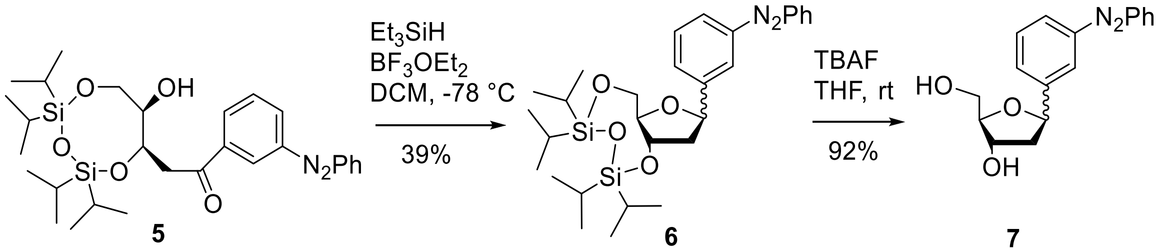

*Fig. 50 Dehydroxylation of **5** and subsequent deprotection to form free nucleoside **7**.*

The conformation of the anomeric position can be determined by several methods, as for example X-ray crystallographic structure analysis or NMR-methods. As crystallization appeared to be tricky for this kind of molecules and NMR-methods utilizing nuclear Overhauser-effect (NOESY, ROESY) did not bring a sufficient signal to noise ratio, a detailed look at the proton-NMR gave the answer (Fig. 51A). Looking at the 1'-H signal it can be seen that two species emerged, one giving a doublet of doublets, the other a triplet. Drawing the two anomers in Newman-projection along the bond of interest (Fig. 51B) it can be seen that the 1'-proton of the β-anomer is syn-clinal and anti-periplanar to the 2'-protons. The 1'-proton of the α-anomer on the other hand is syn-clinal to both 2'-protons. According to Karplus-relation this means that the 1'-proton of the β-anomer results in a second order coupling whereas the α-anomeric 1'-proton would give a first order coupling. Indeed, it can be seen, that the α-results in a triplet with a ^3J-coupling of 7.5 Hz, whereas the ^3J-coupling of the β-anomers 1'-proton is 10.1 and 5.7 Hz. This is in accordance to the literature, as for angles of 180° the coupling needs to be higher than 10 Hz. Since assignment of the signals is without contradiction, it can be stated that only about 21% of α-anomer have been formed during ring closure. During this work it was not possible to separate the anomers on a preparative scale. Even on analytical scale, only an enrichment of either anomer was possible. As the anomers appeared to be too similar in polarity to separate, the mixture of anomers has been used for further studies if not stated otherwise.

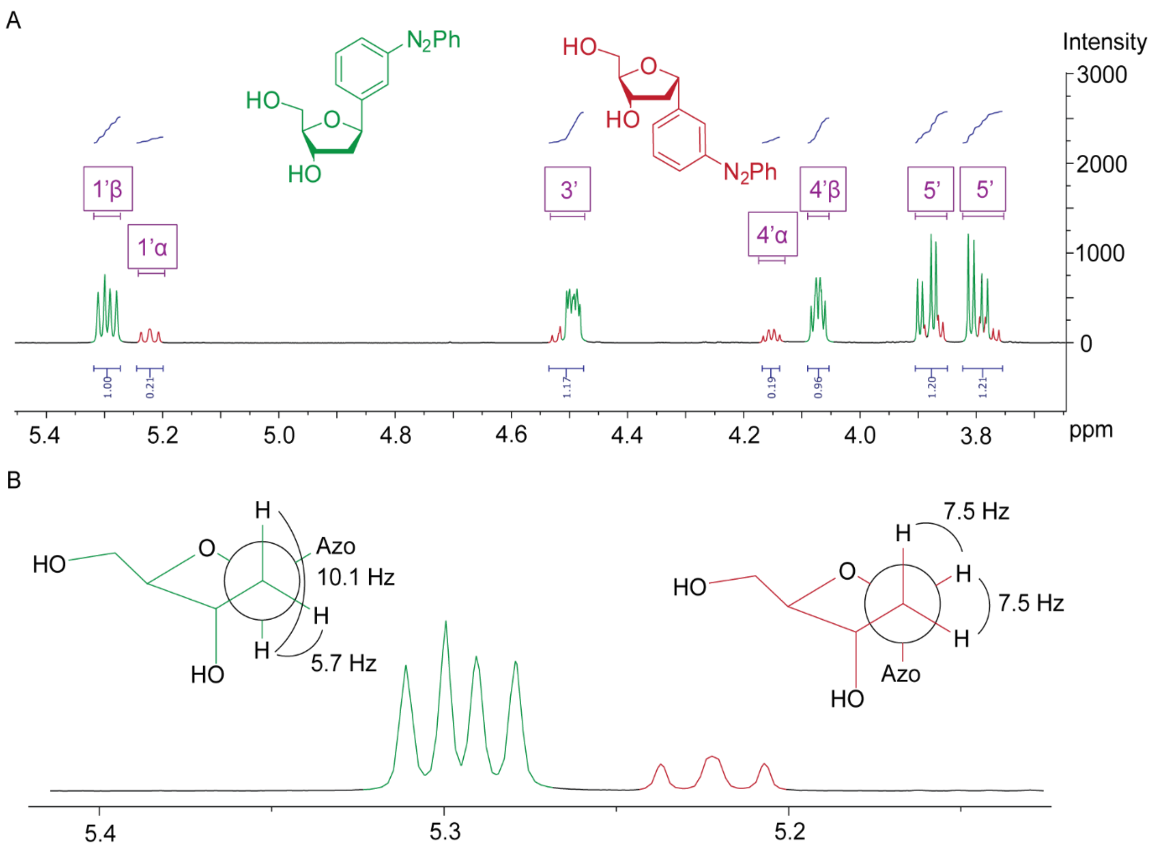

*Fig. 51 Selected region of the ^{1}H-NMR spectrum of **7** in $CDCl_3$ and its signal assignment (A). The Newman-projections of the two anomers with a magnification of the 1'-H signal from spectrum in A are shown for explaining the assignment (B).*

From the free nucleoside **7** tritylation of the 5'-position and phosphitylation of the 3'-position were carried out according to literature-known procedures without any complications to afford phosphoramidite **9** for solid phase synthesis (Fig. 52).

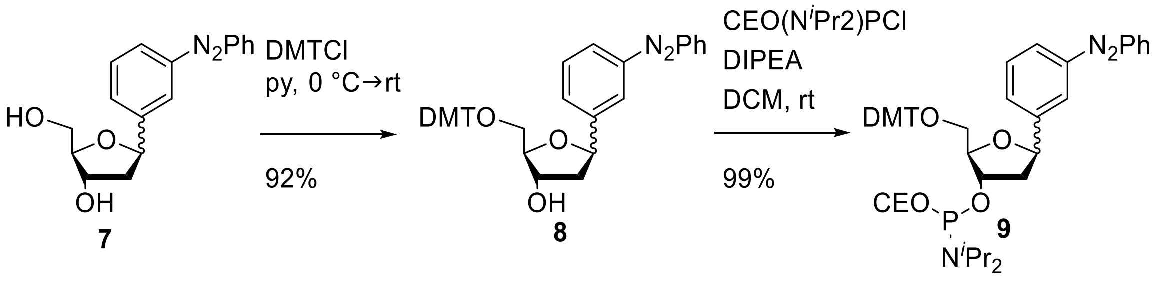
N₂Ph
HO
O
OH
7
DMTCl
py, 0 °C→rt
92%
DMTO
N₂Ph
O
OH
8
CEO(NⁱPr2)PCl
DIPEA
DCM, rt
99%
DMTO
N₂Ph
O
CEO
P
O
9
NⁱPr₂

*Fig. 52 Tritylation and phosphitylation of **7** to obtain phosphoramidite **9**.*

As this method successfully produced an azobenzene *C*-nucleoside in a multi gram scale on the cost of minor contamination with the α-anomer, this method should be applied to other azobenzenes as well. As mentioned in the beginning of chapter 1.2, the photophysical properties of an azobenzene can be subdivided into different categories. The absorption wavelength should be close to the optical window of biological tissue (600 to 1300 nm).[172] The absorption spectra of photoisomers should overlap as little as possible, so that nearly quanitative switching could be possible. With this, the photonic energy can be translated as best as possible into kinetic motion. The photofatigue of the *cis*-isomer is a matter of desired application, but should either be almost non-existent or super-fast. To apply a bathochromic shift to the absorption spectra of azobenzenes, the π-system needs to be expanded.[173] As this usually means the azobenzene gets larger in size, this contradicts the requirement of the azobenzene to fit into a B-DNA helix. Alternatively, heteroarene-modified azobenzenes have emerged as a large class of photoswitches with custom-tailored photophysical properties to meet the desired requirements.[174,175] Especially 1,3,5-trimethyl-4-(phenyldiazenyl)-1H-pyrazole has drawn certain attention since its introduction in 2014.[176] With photostationary distributions of 98% *cis* at 355 nm and 99% *trans* at 532 nm, a nearly quantitative enrichment can be achieved. In addition, the n-π*-transition band is bathochromically shifted into the green part of the spectrum. This and the fact that its morphological dimensions are approximately the same as for normal azobenzene makes it a promising photoswitch for oligonucleotide applications. This pyrazol-based azobenzene has recently been used in the Famulok-group to create a DNA-hairpin with switchable fluorescence and a DNAzyme with orthogonal light switchability.[177,178] As this azobenzene also has been incorporated into the oligonucleotides by *D*-threoninol-linkage recently, this novel synthetic pathway should be utilized to create arylazopyrazole-based *C*-nucleosides.

In contrast to *meta*-iodoazobenzene, which is synthesized by Mills reaction, the arylazopyrazoles have been prepared according to literature by diazotation of the corresponding iodo-anilines and subsequent addition to acetylacetone to form intermediates **10** and **11**, which then were treated with methylhydrazin in a Knorr-pyrazole synthesis to yield **12** and **13** (Fig. 53).

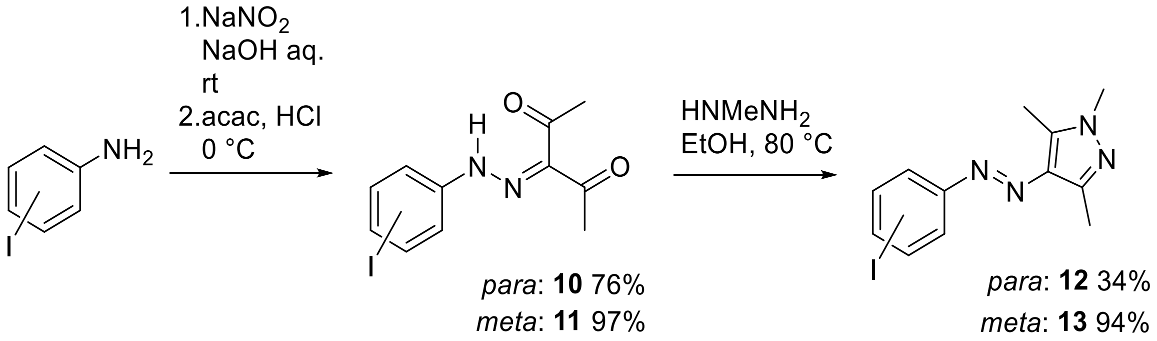
1.NaNO2
NaOH aq.
rt
2.acac, HCl
0 °C
HNMeNH2
EtOH, 80 °C
para: 10 76%
meta: 11 97%
para: 12 34%
meta: 13 94%

Fig. 53 Synthesis of iodinated 1,3,5-trimethyl-4-(phenyldiazenyl)-1H-pyrazoles by diazotation of iodoanilines and subsequent Knorr-pyrazole synthesis.

Analogue to the synthesis of the *meta*-azobenzene *C*-nucleoside (mAzo) arylheteropyrazole iodides (p-pyrAzo and m-pyrAzo) have been lithiated with *n*-butyl lithium and used in a subsequent addition to lacton **3** to form open adducts **14** and **15** as desired. Ring-closure and TBAF-deprotection gave free nucleosides **18** and **19**, which was followed by tritylation and phosphitylation under standard conditions to yield the corresponding phosphoramidites (Fig. 54).

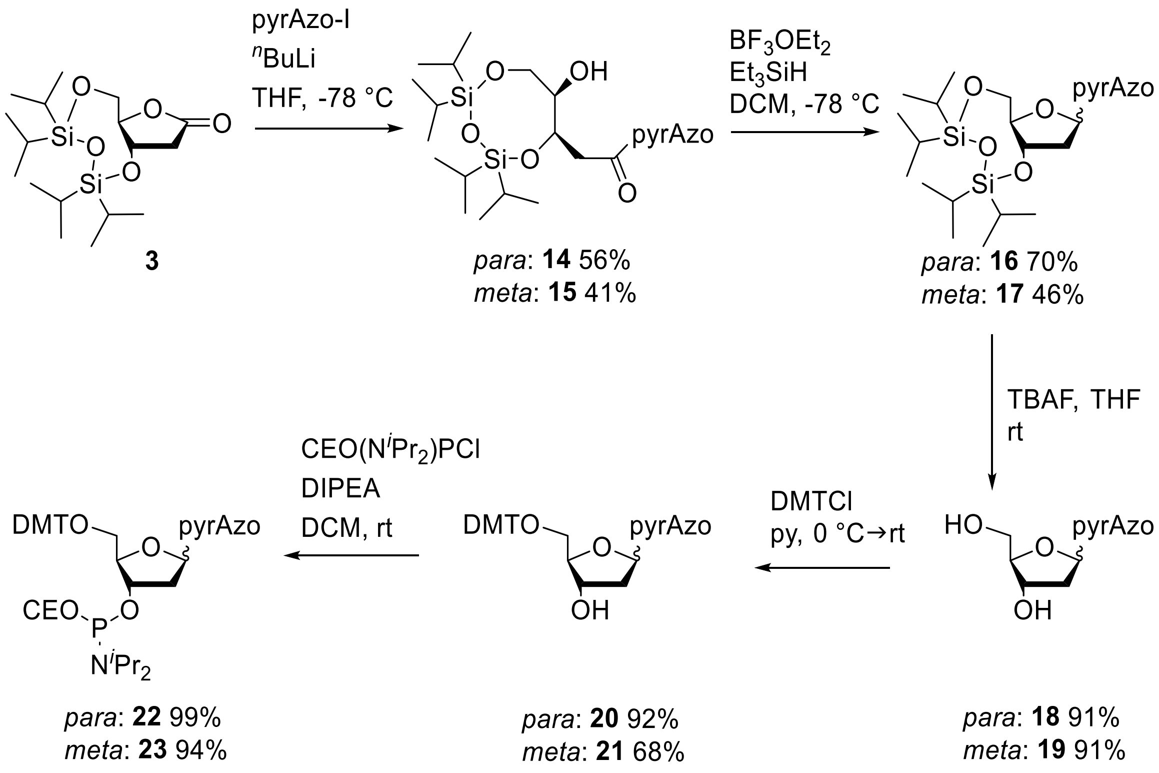
pyrAzo-I
nBuLi
THF, -78 °C
3
para: 14 56%
meta: 15 41%
BF3OEt2
Et3SiH
DCM, -78 °C
para: 16 70%
meta: 17 46%
TBAF, THF
rt
para: 18 91%
meta: 19 91%
DMTCl
py, 0 °C→rt
para: 20 92%
meta: 21 68%
CEO(NiPr2)PCl
DIPEA
DCM, rt
para: 22 99%
meta: 23 94%

*Fig. 54 Synthetic pathway of obtaining 1,3,5-trimethyl-4-(phenyldiazenyl)-1H-pyrazole (pyrAzo) C-nucleosides starting from lactone **3**.*

Additionally, it was possible to crystallize the free nucleoside **18** in order to confirm anomeric conformation in addition to NMR-studies *via* X-ray crystallography. The crystal structure was determined by Dr. Michael Bolte from the crystallographic service department of the Goethe University in Frankfurt am Main. The data were collected at 173 K on a STOE IPDS-II diffractometer equipped with a Genix microfocus tube and mirror optics using Mo*K*α radiation. The structure was solved by direct methods and refined against F^2 by full-matrix least-squares techniques. All hydrogen atoms were refined using a riding model. The torsion angles of the OH groups and methyl groups were refined. There are two molecules of **18** and one water molecule in the asymmetric unit. Both molecules have essentially the same conformation. Due to the absence of anomalous scatterers, the absolute configuration could not be determined. The data have been deposited with the Cambridge Crystallographic Database: CCDC 1561178. Fig. 55 shows a perspective view of one of the two molecules in the asymmetric unit with displacement ellipsoids at the 30% probability level.

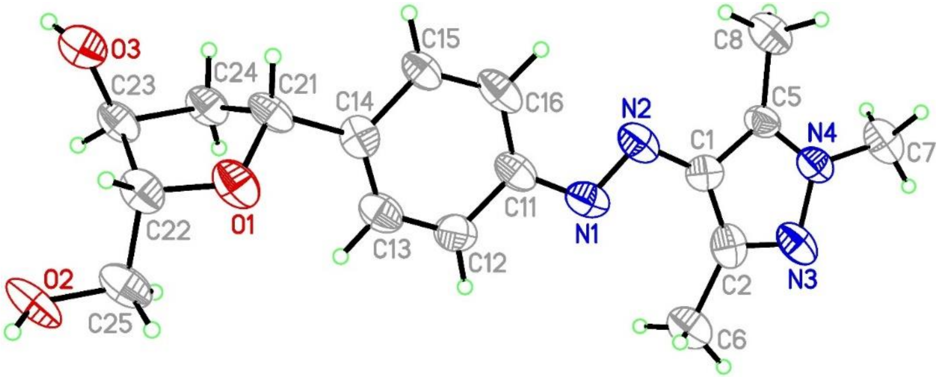

Fig. 55 Perspective view of the structure of ***18*** *calculated from crystallographic data (image provided by Dr. Michael Bolte).*

2.2.6 Light-dependent dimerization studies

To estimate the amount of photocontrol to be observed during PAGE-experiments, *D*-threoninol azobenzene (*t*Azo) has been utilized for preliminary experiments, since photocontrol of nanostructures with *t*Azo are well described (see chapter 1.3). For the 10mer binding region, a modification with four *t*Azo residues in wedge motif has been recommended by Prof. Dr. Hiroyuki Asanuma in a personal communication (Fig.56A). The corresponding strand (strand 8) has been purchased and incorporated into DNA-minicircles alongside wild type strands 6 and 7 to form three different minicircles for dimerization experiments (ring 6, 7, 8). Ring samples were separately irradiated until photostationary states were reached, then mixed at room temperature in equal amounts. For the preliminary experiment, single ring samples were placed in the first and last pocket as reference, a mixture of Ring 7 and 8 as negative control and Ring samples 6 and 8 in alternating PSS for photocontrol of dimerization (Fig. 56B).

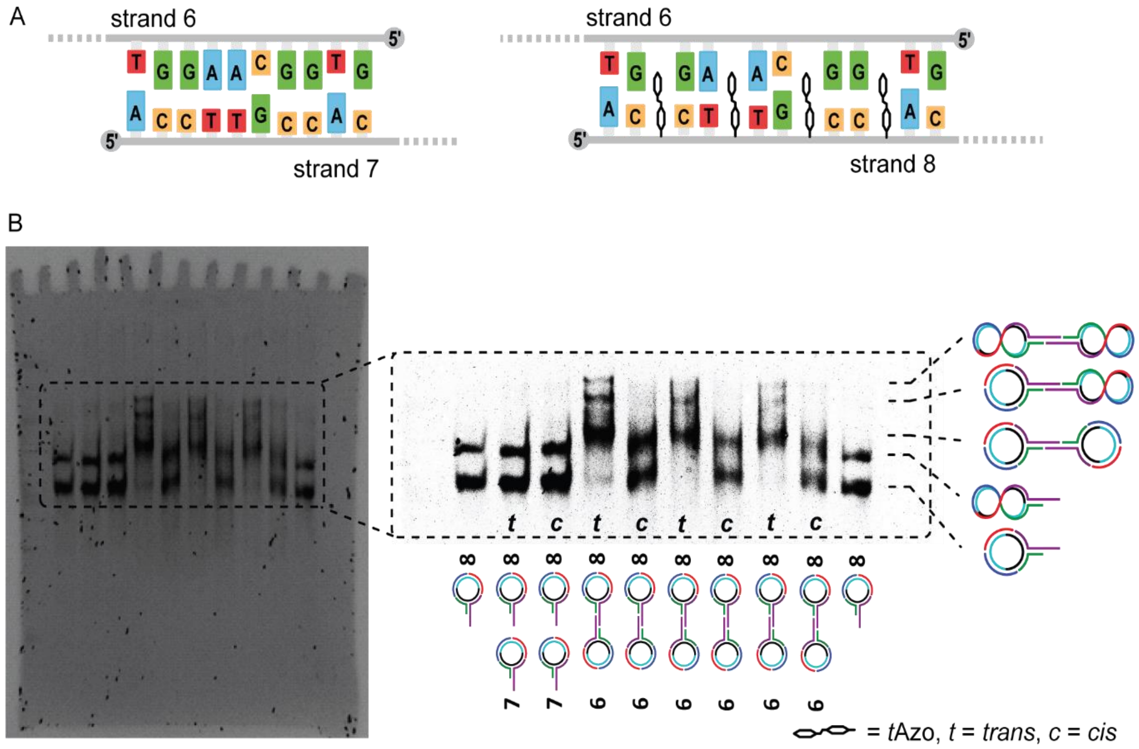

Fig. 56 schematic display of the binding regions of the different rings (A), preliminary irradiation experiment in an a-nPAGE (5% AA, 60 min, 3 W) involving azobenzene-doped minicircles (B, left), its magnification and explanation of the lanes (B, center). Plausible topoisomers as possible explanation of the different bands observed are schematically shown on the right.

As expected, mixing ring 7 and 8 did not lead to hybridization due to their non-complementary binding region and bands were at the same height as for single minicircle samples. In the lanes containing ring 6 and 8 additional bands could be seen when azobenzene was switched to *trans*-state and almost none in the *cis*-state. This experiment showed that photocontrol of minicircle dimerization could be achieved and monitored with PAGE. Interestingly, the lanes bore more bands than expected. In the case of a single minicircle two lanes could be observed and for dimers even 3 or more lanes could be seen. This was perplexing in the beginning, as this behavior is usually displayed for contaminated or impure samples. To check, whether or not additional bands might origin from rings which are not completely assembled, strand-deficient constructs were annealed and subjected to an analytical native PAGE-experiment (Fig. 57).

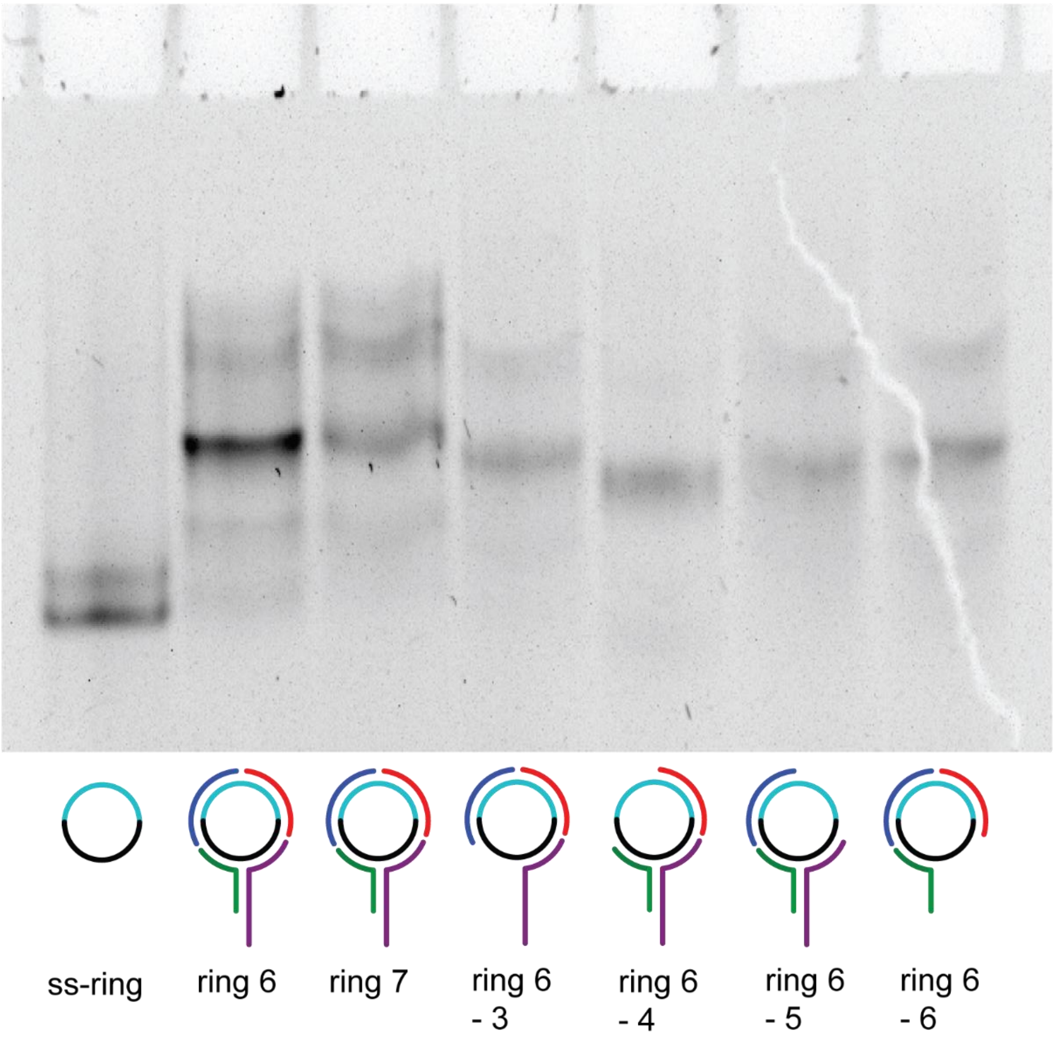

Fig. 57 An a-nPAGE experiment (5% AA, 60 min, 3 W) for determining band height of strand-deficient ring-constructs.

The experiment showed that intact rings 6 and 7 displayed a set of bands with one central dominant band, similar to the behavior of the strand-deficient constructs. Important to note here is that none of the dominant bands of the strand deficient-construct migrate to the same height as any of the bands in the complete constructs. This proves that the additional bands for the complete constructs do not come from malfunctioned minicircles. Even single stranded minicircles display more than one band in native PAGE experiments, which draws the idea of topoisomerism in minicircles closer. This theory could neither be approved nor disproved until the end of this work, but appears to be the most logical explanation for the additional bands in native PAGE-experiments. Possible schematic structures for minicircle-topoisomers have been drawn exemplary into Fig. 56B on the right.

As a feasible method for photoinduced dimerization control in minicircles has been established for *t*Azo-modifications, DNA strands with azobenzene *C*-nucleoside modifications have to be synthesized in order to incorporate them into minicircles. The rules of how to efficiently incorporate nucleosidic linkers into an oligonucleotide differ from the acyclic scaffolds. Wedge-motif appears to be inefficient and replacing natural nucleotides is advised.[72,84,179] In order to estimate how many modifications are needed for efficiently controlling the dimerization of the minicircles, three different strands containing one to three mAzo-modifications were synthesized by solid phase synthesis and incorporated into minicircles (Fig. 58A). As it can be seen in Fig. 58B, a difference in retention is achieved in between a single minicircle (lane 1) and a native dimer (lane 2). Photocontrol for *t*Azo-modified dimers in lane 3 and 4 can be seen, as the lower monomer-band is more dominant in the *cis*-state rather than the *trans*-state. In the case of one mAzo-modification (lane 5 and 6, strand 11-1) almost quantitative dimerization could be achieved, but no photocontrol could be seen. It appears that one modification is not sufficient to control hybridization of a 10mer DNA, but does not perturb hybridization affinity significantly. Two mAzo-modifications (lane 7 and 8, strand 11-2) on the other hand display a clear photocontrol. Almost no dimerization is seen in the *cis*-state, whereas an approximate 50% dimerization can be seen in the *trans*-state. Three mAzo-modifications do not show photocontrol of the minicircle-dimerization, as no hybridization can be observed in either photostationary state. It can be assumed that 3 mAzo-modifications imply steric stress in such an extend, that hybridization is no longer possible under given conditions. With this, two *C*-nucleosidic modifications per 10 bases appear to be the most useful for this model system and will be used from here on.

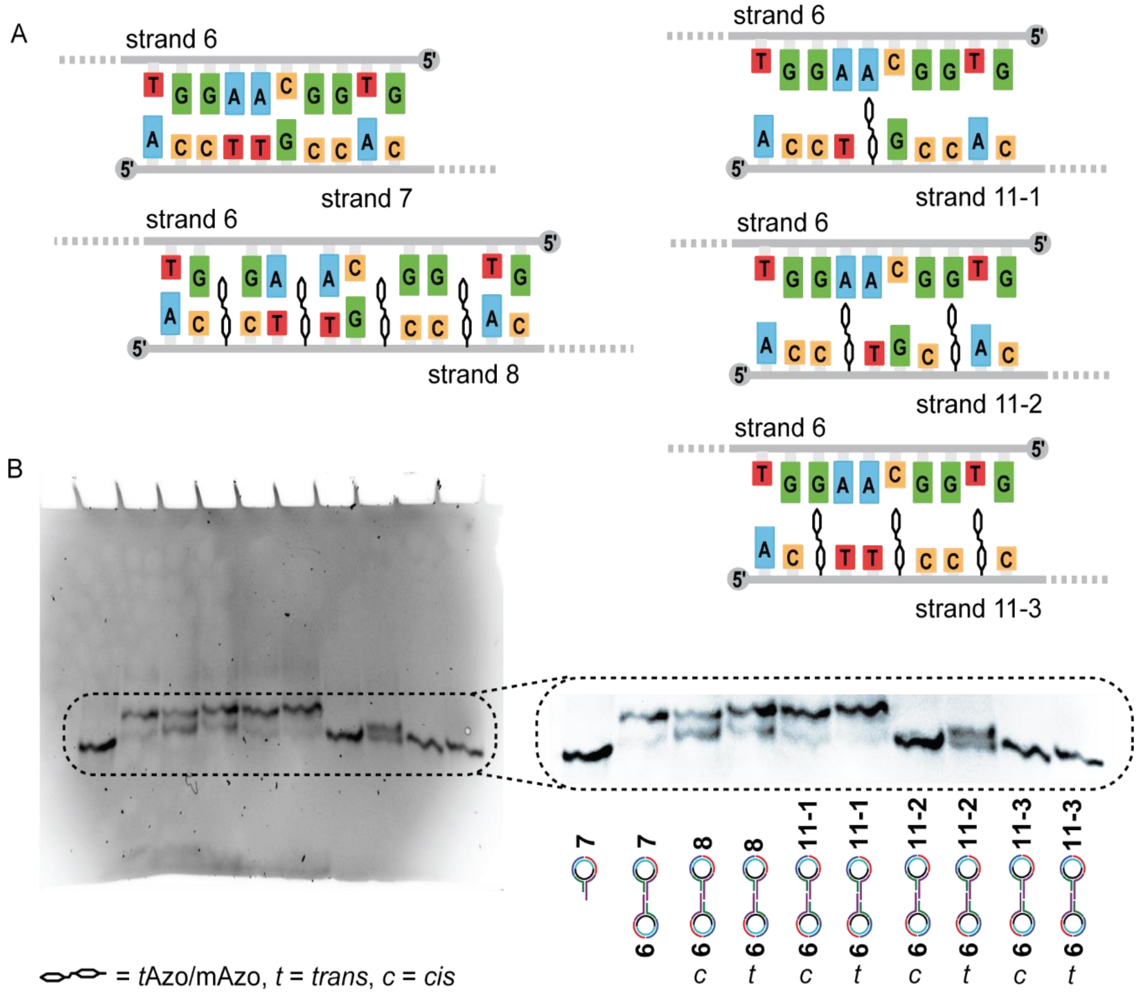
A
strand 6
5'
T G G A A C G G T G
A C C T T G C C A C
5'
strand 7
strand 6
5'
T G G A A C G G T G
A C C T T G C C A C
5'
strand 8
strand 6
5'
T G G A A C G G T G
A C C T G C C A C
5'
strand 11-1
strand 6
5'
T G G A A C G G T G
A C C T G C A C
5'
strand 11-2
strand 6
5'
T G G A A C G G T G
A C T T C C C
5'
strand 11-3
B
7
6 7
6 8 c
6 8 t
6 11-1 c
6 11-1 t
6 11-2 c
6 11-2 t
6 11-3 c
6 11-3 t
= tAzo/mAzo, t = trans, c = cis

Fig. 58 Strand motifs used for the screening experiment with strand 8 containing tAzo and strands 11 containing mAzo (A). The PAGE-experiment (5% AA, 2.5 h, 3 W) with explanation of the single lanes can be seen in B.

Since two mAzo units seemed to be the most fitting degree of modification, evaluation of the optimal position of the residues needed to be done. As it could be seen in Fig. 58, favored strand 11-2 was lacking dimerization, whereas strand 11-1 displayed nearly quantitative dimerization. To mimic a compromise in between two and one modification, distance in between the modification should be narrowed. It could be assumed, that by narrowing the distance between the mAzo moieties, longer parts of undisturbed hybridization would alleviate dimerization in general. For this matter, strands have been synthesized with one or no natural nucleoside in between the modifications (Fig. 59A). Evaluation in gel after incorporation into rings showed, that none of the two new motifs would allow dimerization (Fig. 59B).

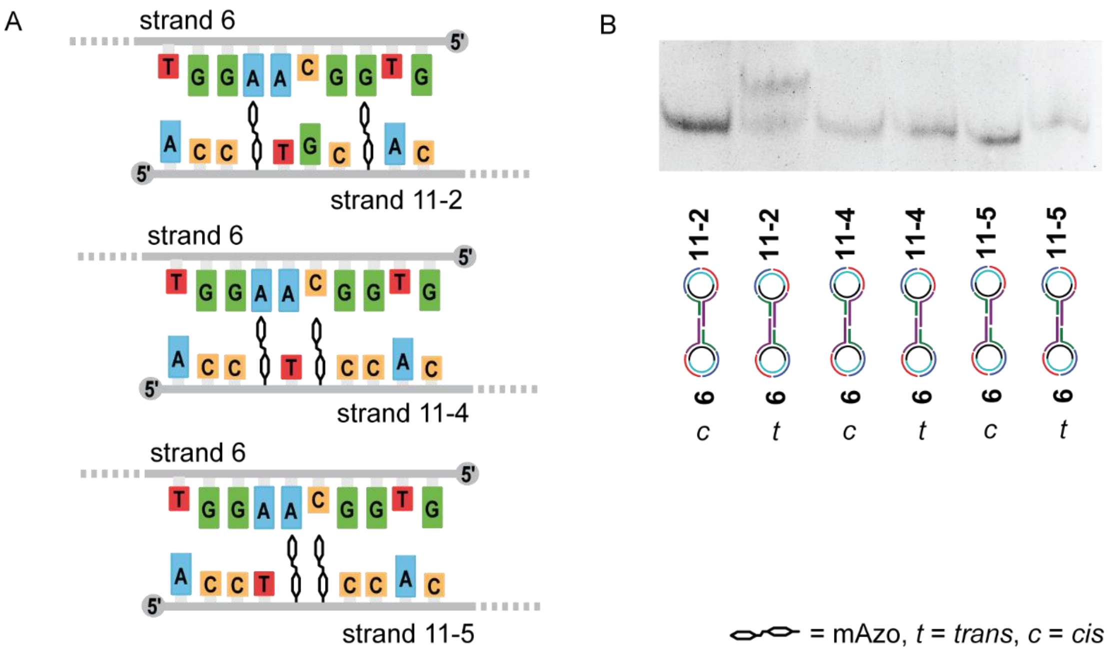
A
strand 6
5'
T G G A A C G G T G
A C C T G C A C
5'
strand 11-2
strand 6
5'
T G G A A C G G T G
A C C T C C A C
5'
strand 11-4
strand 6
5'
T G G A A C G G T G
A C C T C C A C
5'
strand 11-5
B
11-2 6 c
11-2 6 t
11-4 6 c
11-4 6 t
11-5 6 c
11-5 6 t
= mAzo, *t* = *trans*, *c* = *cis*

Fig. 59 Strand motifs (A) and PAGE cut-out (5% AA, 2.5 h, 3 W) with annotations of the lanes (B).

In the next iteration, additional base pairs on the edges of the binding region should be implemented in order to raise dimerization ratio. Since G-C-pairs form three hydrogen bonds, they were chosen to cause maximum effect with minimal amount of modification. Strands and counterstrands with two or four more G-C-pairs were synthesized and incorporated into minicircles (Fig. 60A). Apparently, no photocontrol could be observed for the two new motifs. Aside of that, the amount of dimers with four additional basepairs appeared to be higher than with two as expected (Fig. 60B).

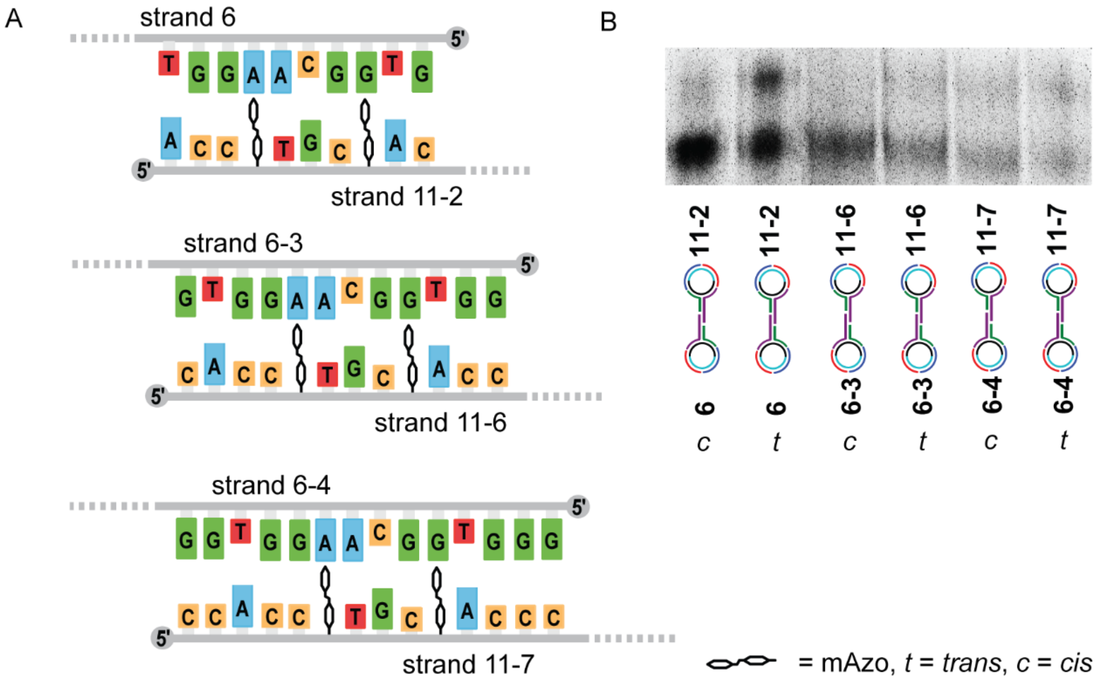
A
strand 6
5'
T G G A A C G G T G
A C C T G C A C
5'
strand 11-2
strand 6-3
5'
G T G G A A C G G T G G
C A C C T G C A C C
5'
strand 11-6
strand 6-4
5'
G G T G G A A C G G T G G G
C C A C C T G C A C C C
5'
strand 11-7
B
11-2 6 c
11-2 6 t
11-6 6-3 c
11-6 6-3 t
11-7 6-4 c
11-7 6-4 t
= mAzo, t = trans, c = cis

Fig. 60 Strand motifs (A) and PAGE cut-out (5% AA, 2.5 h, 3 W) with annotations of the lanes (B).

As this variation of the binding site also did not result in elevated dimerization in addition to feasible photocontrol, returning to the initial motif involving two modifications seemed reasonable. As azobenzene *C*-nucleosides replace a natural nucleotide, the photoswitch points directly to the opposing nucleobase, which leads to steric repulsion. One way to decrease steric repulsion is to imply non-natural nucleotides into the opposing strand, which are lacking a nucleobase. These abasic sites would lead to a gap in the strand, which could be filled by the sterically demanding chromophore. In this regard, abasic counter strands have been synthesized for strand 11-2 and 11-3 (strand 6-5 and 6-6, Fig. 61A). Strand 11-1 was not considered to improve with this attempt, as dimerization with native counterstrand 6 already gave almost quantitative dimerization. In order to compare hybridization rates for these systems with the already established systems shown in Fig. 58, new PAGE experiments has been performed (Fig. 61B). This experiment showed that for strand 11-2 dimerization could be turned off in the same degree with or without abasic sites in the opposing strand in the *cis*-state. In the *trans*-state on the other hand, dimerization appeared to be slightly more alleviated in the system with abasic sites. For strand 11-3 on the other hand introduction of abasic sites did not alter the behavior significantly, almost no dimerization could be observed for both photostationary states.

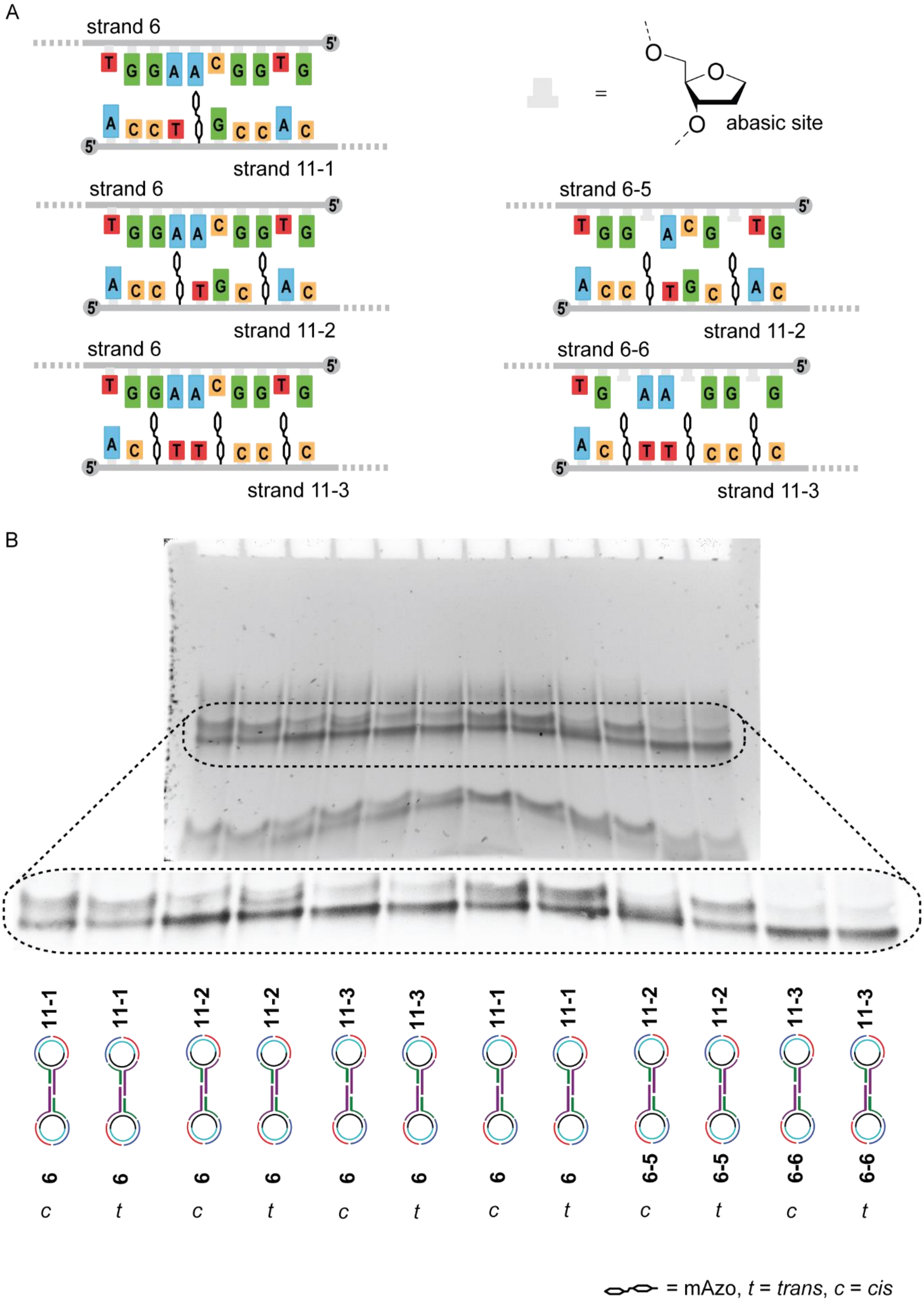
A
strand 6
5'
T G G A A C G G T G
A C C T G C C A C
5'
strand 11-1
strand 6
5'
T G G A A C G G T G
A C C T G C A C
5'
strand 11-2
strand 6
5'
T G G A A C G G T G
A C T T C C C
5'
strand 11-3
=
O
O
O
abasic site
strand 6-5
5'
T G G A C G T G
A C C T G C A C
5'
strand 11-2
strand 6-6
5'
T G A A G G G
A C T T C C C
5'
strand 11-3
B
11-1 11-1 11-2 11-2 11-3 11-3 11-1 11-1 11-2 11-2 11-3 11-3
6 6 6 6 6 6 6 6 6-5 6-5 6-6 6-6
c t c t c t c t c t c t
= mAzo, t = trans, c = cis

Fig. 61 Strand motifs of the tested systems with and without abasic sites (A) and PAGE-experiment including cut-out (5% AA, 2.5 h, 3 W) with annotations of the lanes (B).

The optimization of the binding motif with azobenzene *C*-nucleosides incorporated came to a halt after this iteration. The dimerization ratios are far from quantitative, but it appears to be that under these circumstances, a certain threshold can not be overcome. This became clear during the several attempts in creating mAzo-doped strands with the higher affinity to the counterstrand without losing photocontrol. In order to overcome the threshold of dimerization ratio, an overall redesigning of the hybridization site would be needed. It might also be the case that the limit in hybridization is also bound to these types of *C*-nucleosides. Since time consumption for completely redesigning the hybridization site would exceed the time limits of this project, the combination of strand 11-2 and 6-5 has been descried as the best working one in regards of dimerization rate and photocontrol of it.

As the comparison of *t*Azo and mAzo was one of the central objectives in this study, the incorporation of four *t*Azo moieties in contrast to two mAzos appeared to be not very alike. In addition, the threoninol-scaffold has been incorporated in a wedge motif, whereas the nucleosidic linkers replaced natural nucleosides. Basically, it can be said that there is nothing comparative at all in this approach aside of incorporating azobenzenes into oligonucleotides. As already mentioned several times in this work, both linking systems work under very different conditions and swapping the requirements of the linkers would lead to malfunctioned performance. The only way of relevant comparison in between the two linking systems is when the binding regions are optimized according to their own rules. This establishes the common ground to compare the systems in their best possible performance. As a final test before comparing all linkers and azobenzenes available for this study, a strand was synthesized with two *t*Azo modifications to see how the same amount of photoswitches per binding region would perform (Fig. 62A). From the PAGE-experiment shown in Fig. 62B it can be claimed that two *t*Azo-modifications display a mediocre dimerization rate but almost no photocontrol. This compared to the systems of rings including strands 8/6 or strands 11-2/6-5 demonstrates, that the four *t*Azo-modifications are necessary in order to gain optimal photocontrol with *t*Azo in this minicircle context and to be comparable on the performance level.

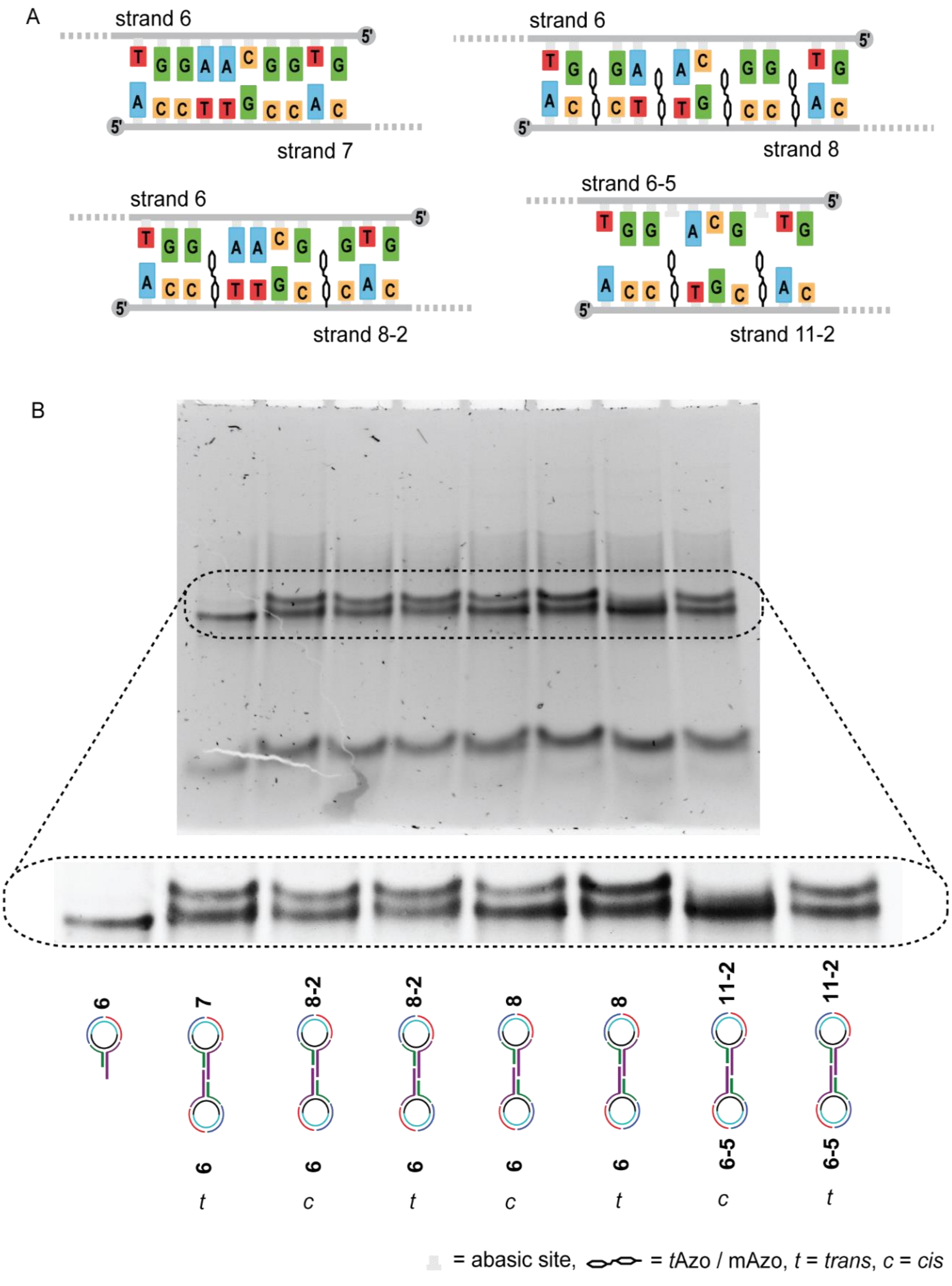
A
strand 6
5'
strand 7
strand 6
strand 8
strand 6
strand 8-2
strand 6-5
strand 11-2
B
6
7
6
t
8-2
6
c
8-2
6
t
8
6
c
8
6
t
11-2
6-5
c
11-2
6-5
t
= abasic site, = tAzo / mAzo, t = trans, c = cis

Fig. 62 Strand motifs of the tested systems with two or four tAzo residues compared to wild type references and mAzo reference (A) and PAGE-experiment (5% AA, 2.5 h, 3 W) including cut-out with annotations of the lanes (B).

After establishing the most fit binding motifs for the two different linking systems, strands in analogy to strand 11-2 containing 2’-methoxy RNA analogous MeO-mAzo and the two arylazopyrazoles p-pyrAzo and m-pyrAzo have been synthesized by solid phase synthesis. Following the incorporation into minicircles, a comparative study on the base of PAGE was performed. For this study, minicircle samples were irradiated until photostationary states were reached, then 2-3 pmol of each ring sample were mixed with the dimerization partner in equimolar proportions before applying it on the gel. For the modifications *t*Azo, mAzo and MeO-mAzo photostationary states of the wavelength 365 nm for *cis* and 420 nm for *trans* were tested. For the modifications p-pyrAzo and m-pyrAzo the photostationary state at 530 nm was tested in addition to the previously named. All PAGE-experiments were executed under red light and run under complete darkness to ensure isomeric distributions in the samples did not change throughout the experiment. Additionally, all gels carried two lanes with a single minicircle and native minicircle dimer 6+7 as internal reference for migration height of corresponding monomer and dimer bands. The irradiation experiments were repeated ten times for statistic relevance. The analysis of the gels was carried out with the open source program *GelBandFitter* published by Mitov *et al.* according to their described procedure.[180] The underlying principle of this method of analysis is that the grey-scale (densitometry) of a selected pathway along a lane is plotted against the pathway. The program then fits Gaussian functions to the corresponding bands and calculates a ratio. If the bands fitted are the corresponding monomer and dimer bands, the dimerization rate can be calculated directly. Fig. 63 displays the binding regions of the minicircles and the corresponding photochromic modifications (Fig. 63A and B) followed by one exemplary PAGE-gel with a close-up of the bands of interest and their annotations (Fig. 63C).

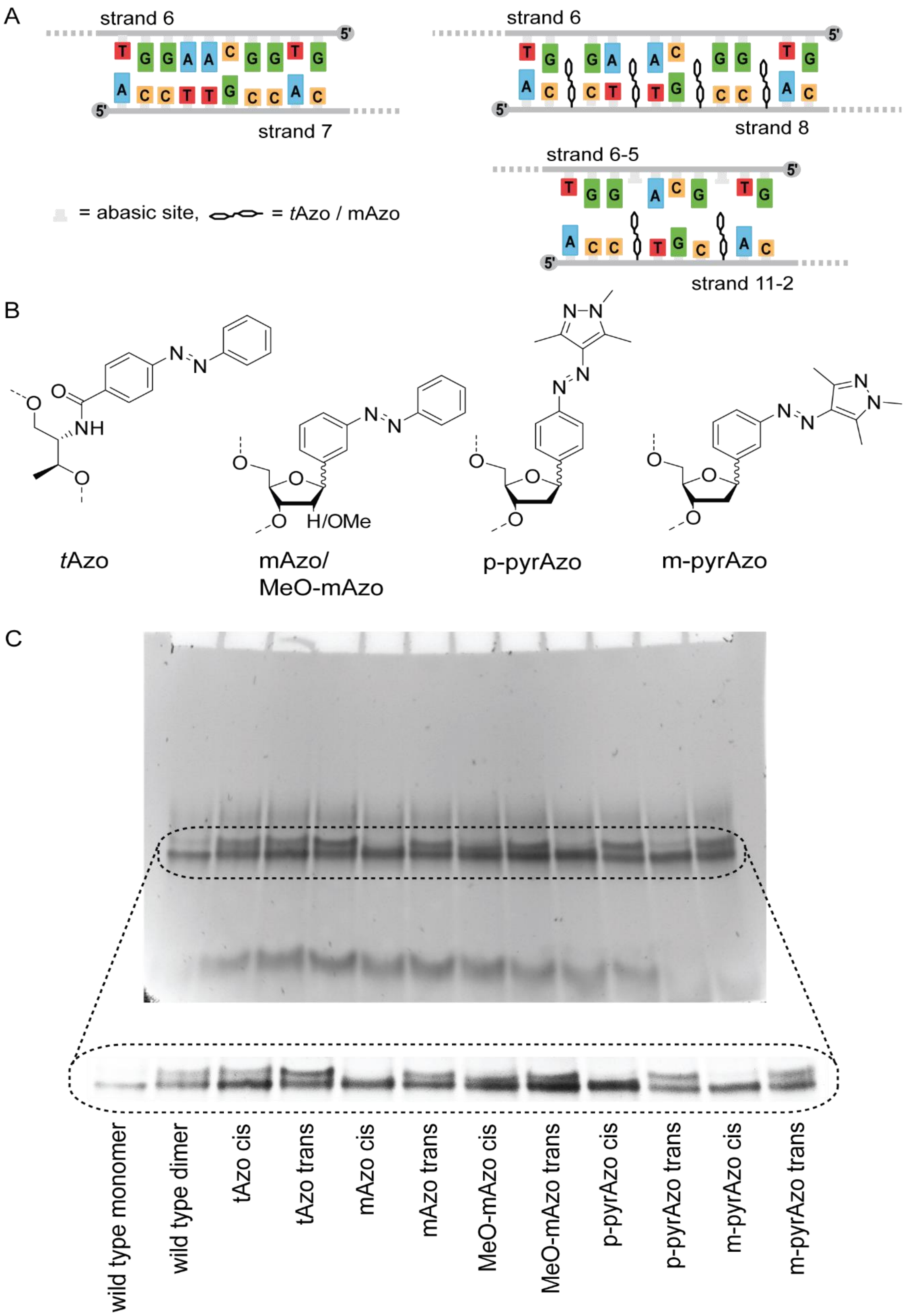
A
strand 6
5'
T G G A A C G G T G
A C C T T G C C A C
5'
strand 7
strand 6
5'
T G G A A C G G T G
A C C T T G C C A C
5'
strand 8
strand 6-5
5'
T G G A C G T G
A C C T G C A C
5'
strand 11-2
= abasic site,
= tAzo / mAzo
B
tAzo
mAzo/
MeO-mAzo
p-pyrAzo
m-pyrAzo
H/OMe
C
wild type monomer
wild type dimer
tAzo cis
tAzo trans
mAzo cis
mAzo trans
MeO-mAzo cis
MeO-mAzo trans
p-pyrAzo cis
p-pyrAzo trans
m-pyrAzo cis
m-pyrAzo trans

Fig. 63 Strand motifs used in the PAGE irradiation experiments (A) with corresponding modifications (B). One exemplary PAGE-experiment (5% AA, 2.5 h, 3 W) is shown with the area of interest magnified and contrast improved (C).

The results of all ten individual PAGE irradiation experiments have been summarized in one bar graph with the error bars calculated from the individual results by mean standard deviation (Fig. 64). With the native 10mer a dimerization degree of 44% could be achieved in 1xTA-buffered native PAGE. The *t*Azo modification in wedge motif even surpasses the wild type in *trans*-state with a dimerization ratio of 51%. On the contrary, switching *t*Azo to the *cis*-state is only able to lower dimerization to 38%, which makes 13% difference in between the photosationary states. With two mAzo residues installed in the replacement motif and with abasic sites on the counter strand a dimerization of 39% was achieved in the *trans*-state. This dimerization degree is slightly smaller compared to the wild type and shows, that even in the optimized binding region with abasic sites some sterical repulsion remains. After irradiation with 365 nm the dimerization ratio could be decreased to only 6% in the *cis*-state. Exchanging the mAzo residues for MeO-mAzo units resulted in a somewhat reduced dimerization switching amplitude with only 30% dimerization in the *trans* and 11% in the *cis*-state. Under same conditions, the p-pyrAzo and the m-pyrAzo residues both led to a switching performance almost identical to the one of mAzo within error limits when operated with 530 nm for the *cis* to *trans* isomerization to account for the different light absorbance properties. Both the overall decreased binding affinity in *trans*-state compared to the native binding sequence as well as the high photocontrol on the dimerization ratio can be explained by the rigidity of the nucleosidic linker. Visualizing the azobenzene as a photoswitchable lever, the *C*-nucleosidic linker system resembles a rigid anchor point, which supports the prying movement of the lever better than a flexible anchor point of acyclic linker systems. It keeps the photoswitch in place, avoiding evasion by alternative placements in the major or minor groove of the duplex or a reduction of dimerization switching amplitude by loss of conformational perturbation due to too many internal degrees of freedom. In this series of investigated photoswitchable *C*-nucleoside residues MeO-mAzo showed a less optimal performance. This shows once more that subtle changes in the linker can have significant effects on the performance of the photoswitch.

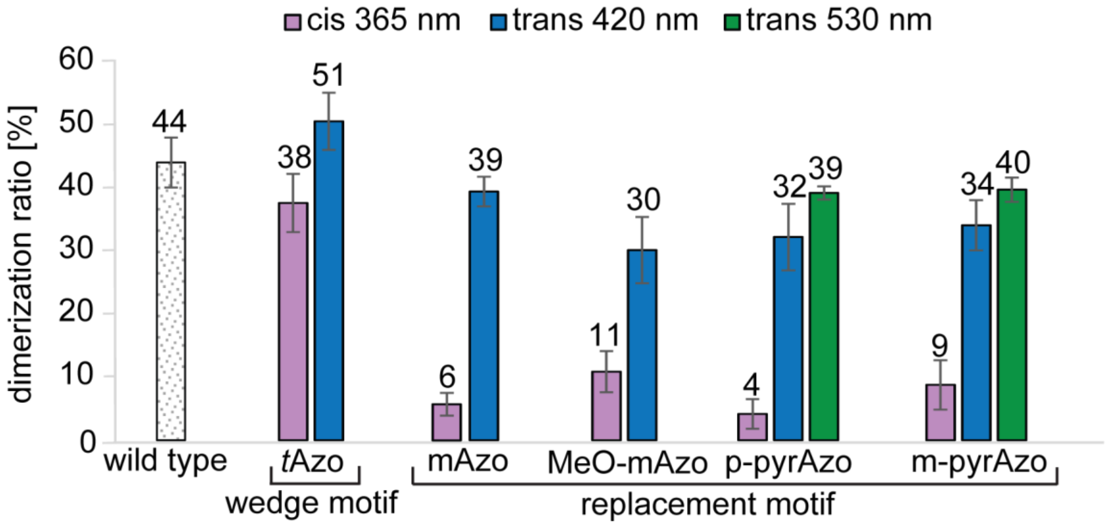

Fig. 64 Bar graph showing the results of the PAGE-irradiation-experiments as shown in Fig. 63.

During the PAGE-experiments it became clear that there is a strong dependency in between hybridization affinity and the temperature of the system. For temperature control during PAGE-irradiation-experiments, a PAGE setup from *Biometra* has been used. This allows active temperature control by connecting it to commercially available thermostats, which cool or heat one side of the gel during the experiments. Although the temperature could be set between 5 and 60 °C with this setup for the experiments, the actual temperature has not been measured during the experiment. In order to elucidate the in-gel temperature, a temperature probe with 0.5 mm diameter has been covered with a conventional melting point glass capillary and been stuck directly into the central lane of the gel for real-time measurement (Fig. 65A). Three temperature curves have been measured with the temperatures on the thermostat being set to 5, 20 or 37 °C and the power to 3 W as in the irradiation experiments. Temperatures measured for a time course of 60 minutes showed that a noticeable raise of the temperature could be observed within the gel, although the thermostat maintained the set temperature on the outside (Fig. 65B). Especially for the set 20 °C as in the irradiation experiments, an increase of 8.1 °C implies a tremendous change of conditions during the experiment, which needs to be taken into consideration.

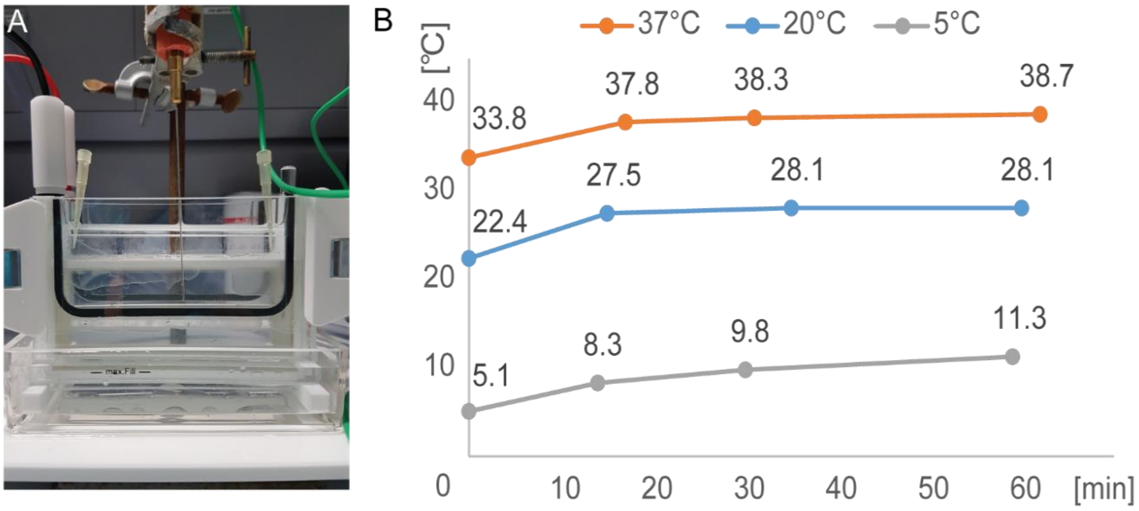

Fig. 65 Photograph of the PAGE-setup used with the temperature probe piercing into the gel from atop (A) and measured temperature change within the gel with 5, 20 and 37 °C set on the thermostat and a current of 3 W applied on the gel(B).

With this findings the gel experiment was repeated with the thermostat set to 5 and 37 °C to estimate the temperature dependence of the systems used (Fig. 66A). It could be shown, that at 38.7 °C in-gel temperature the dimerization of rings containing *C*-nucleosidic modifications almost seized to exist in either state, whereas the photocontrol of *t*Azo containing rings even improved. On the other end of the temperature scale at 11.3 °C in-gel temperature dimerization ratios of all systems increased to a certain degree in both states, but photocontrol of the minicircle hybridization was diminished to a certain extend. Plotting the dimerization ratios against the in-gel temperature (Fig. 66B) a certain trend within all light-dependent results can be seen. The *cis*- and *trans*-states frame a certain space in which photocontrol of hybridization affinity can be controlled. This ellipsoid resembling a lense defines the optimal photocontrol of a system with its broadest part defining the temperature for optimal photocontrol. It can be seen that optimal photocontrol for the systems containing azobenzene *C*-nucleosides is somewhere around the initially used 28.1 °C whereas for *t*Azo containing rings it appears not to be reached even at 38.7 °C. In order to gain deeper understanding of the photocontrol of hybridization affinity, additional experiments for exploring the underlying kinetics and thermodynamics would be needed, but have not been executed for the minicircle project. This project has been published in *Chemistry – A European Journal* in 2018.[181]

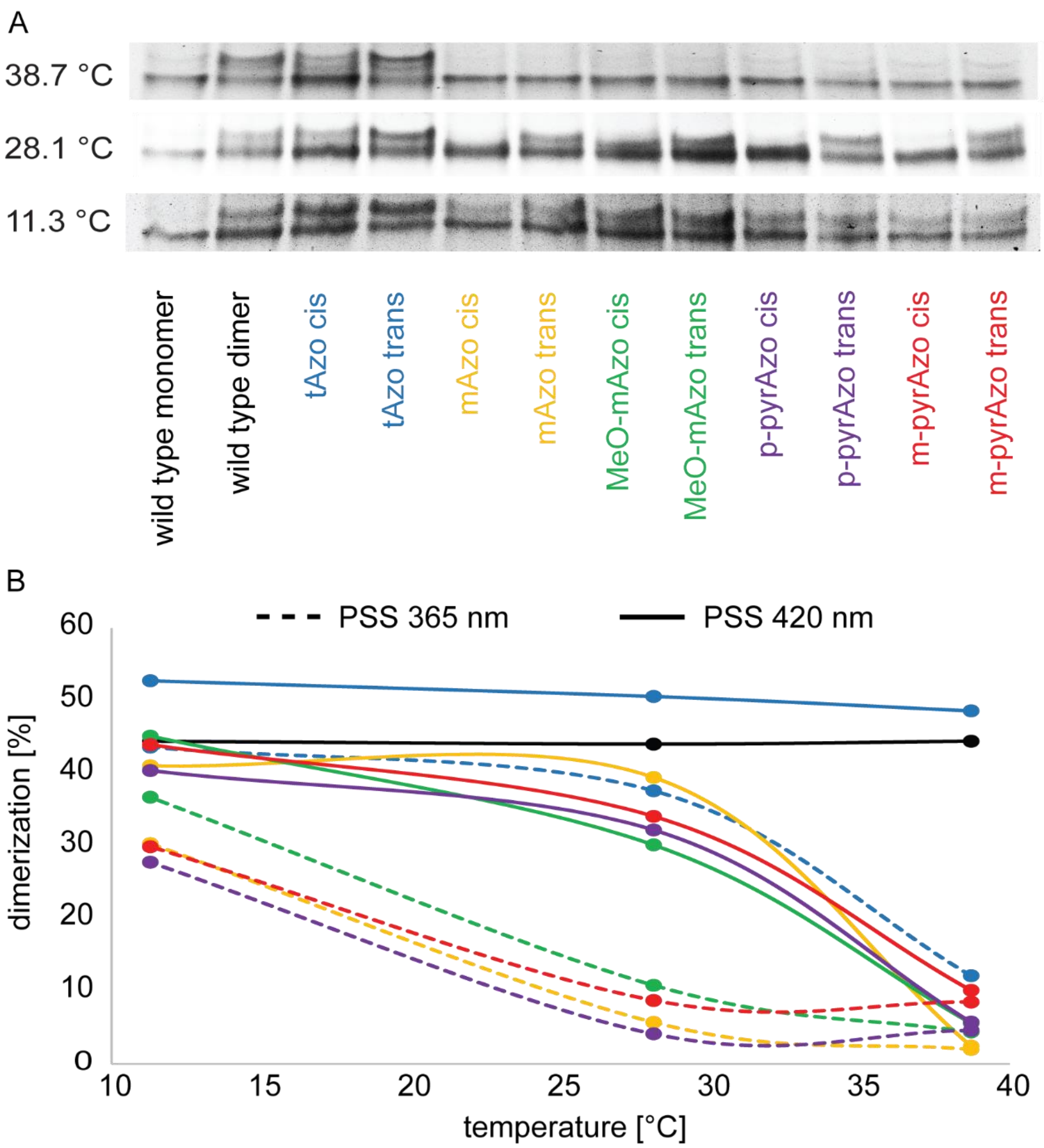

Fig. 66 Cut-outs of PAGE-irradiation-experiments (5% AA, 2.5 h, 3 W) set on different temperatures (A) and calculated dimerization ratios from it (B). The color code in B resembles annotations in A.

2.3 Summary and outlook

Regulating the hybridization of oligonucleotides is a goal sought-after for many decades by now. Utilizing light is a delightful way to gain control over hybridization processes. Light does not pollute the system of interest, can be applied with high spatio-temporal resolution and is not harmful in a biological context, if power and wavelength is controlled. To gain reversible photocontrol over the hybridization, photoswitchable molecules like azobenzene can be incorporated into the oligonucleotide. The planar *trans*-azobenzene intercalates neatly in between neighboring base pairs causing minimal perturbance. Upon irradiation with light of 365 nm, the *trans*-to-*cis* isomerization is induced. The angled *cis*-azobenzene is sterically more demanding and forces neighboring nucleobases to shift out of optimal distance for hydrogen bonding, thereby weakening the hybridization of the duplex. The way of incorporating the azobenzene into the oligonucleotide is of utmost importance, as the linker system has to provide a rigid base for the isomerization movement without allowing the chromophore to slip out of the base pairing region. Azobenzene *C*-nucleosides have been proven to do exactly that with its rigid ribosidic linker, which mimics the natural backbone of an oligonucleotide. This azobenzene *C*-nucleosides have previously been only synthesized by Heck-coupling reaction, which limits the synthesis scale to mere milligrams, making it hard to accumulate enough material for solid phase synthesis. The synthesis of azobenzene *C*-nucleosides has been reinvented utilizing the lithiation of iodinated azobenzenes and subsequent addition to protected ribonolactones. This synthetic pathway offered an almost unlimited upscaling of the crucial reactions with a small drawback of minor side products.

The fact that the interaction of oligonucleotides follows strict rules has been utilized to create two- or three-dimensional objects made of DNA. With computer-assisted design of DNA sequences, any arbitrary structure on the nanometer- to micrometer-scale can be generated just by hybridization of the needed strands. As astonishing these structures are, without any modification of the DNA strands involved no function can be assigned to them. Many different ways of functionalizing DNA-nanostructures have been developed with light-responsive nanostructures having a rather subordinated role as it requires expertise in the field of DNA-nanostructures and oligonucleotide-associated photochemistry. Almost all light responsive DNA-nanostructures involve the acyclic azobenzene-linking system *t*Azo which is known to work best at elevated temperatures to ensure optimal switching. As the structure of DNA-constructs is mainly maintained by hydrogen-bonding, variation of the temperature should be avoided in order to keep the structure intact. To develop a light-responsive nanostructure model system with low-temperature operating azobenzene *C*-nucleosides, DNA-minicircles have been utilized. Those minicircles bear a lariat-like protrusion with a 10 base long single-stranded overhang, which is responsible for the dimerization with a ring bearing a complementary binding region.

DNA-minicircles have been produced in a sequential manner by building and purifying the single stranded minicircle first followed by annealing it to the outer ring. The single stranded ring has been produced by splint ligation of a preassembled construct by enzymatic phosphorylation and ligation. For the purification either preparative denaturing PAGE or RP-HPLC proved themselves as methods of choice, without a clear preference of one over the other. For the annealed double stranded minicircle many different purification methods have been tested with only molecular weight cut-off by spin-filtration purified the samples without destroying them. Imaging of DNA-minicircles by atomic force microscopy was possible with several methods of sample preparation leading to images of varying quality. With the help of AFM, qualitative analysis of the minicircles was possible. It could be shown, that theoretical and empirical size dimensions of the rings and their interactions were in great accordance.

Designing the interaction site of the minicircles proved to be the main task in this project. The amount of *C*-nucleosidic modifications was identified by screening, followed by a screening of their optimal position and binding partners in the counterstrand. Two azobenzene *C*-nucleosides with three natural bases in between and abasic sites opposing to them appeared to give the best compromise between absolute dimerization ratio and photocontrolled change of it, as identified by native PAGE. Comparing the dimerization ratios of minicircles containing azobenzene *C*-nucleosides with minicircles containing *t*Azo and unmodified minicircles it could be shown, that the *t*Azo-modification leads to an elevated binding affinity compared to the unmodified minicircles, but the change upon irradiation is relatively humble compared to the *C*-nucleosides. For the *C*-nucleosidic modification dimerization ratios reached a maximum of 40% in favored *trans*-state, but could be almost completely turned-off when switching into *cis*-state. In addition, arylazopyrazole-modified *C*-nucleosides could be switched into *trans*-state by 530 nm wavelength irradiation, which is an improvement compared to standard azobenzene for shifting irradiation wavelength closer to the phototherapeutic window. The temperature dependence of the dimerization results reveals that more investigation on the thermodynamic characteristics of nanoconstruct-aggregation needs to be done in order to fully understand and fine-tune a system to fit to the desired application.

With the light-responsive minicircle dimerization it could be shown that azobenzene *C*-nucleosides can be utilized for photocontrol of DNA-nanostructures in future. Many possible projects could be approached involving gained knowledge from this project, such as nanomachines or –motors. As a closing remark the application of azobenzene *C*-nucleosides in DNA-nanopores as a concrete application shall be mentioned. Membrane pores entirely made of DNA have drawn a lot of attention recently, as they are easy to design and to produce compared to their proteinogenic analogues. Especially hexagonal nanopores published by Burns *et al.* have drawn interest, as they are especially simple in design and incorporated a gating mechanism to control fluorophore leakage of small unilamellar vesicles.[106] Unfortunately, the gating mechanism could only be controlled by strand displacement upon adding the complementary sequence to the system. Utilizing photochromic elements to steer the gating mechanism with light would be much more elegant and application relevant, as there would not be the need for possibly polluting stimulants aside of light itself. The pore could be closed with two azobenzene doped strands hybridizing to each other in the azobenzenes *trans*-state. Upon irradiation with UV-light, the *trans*-to-*cis*-isomerization would then cease the hybridization of the gating oligonucleotides, thereby releasing the cargo from within vesicles or generally allowing trans-membrane transport of small molecules such as dyes, pharmaceuticals or other xenobiotica (Fig. 67).

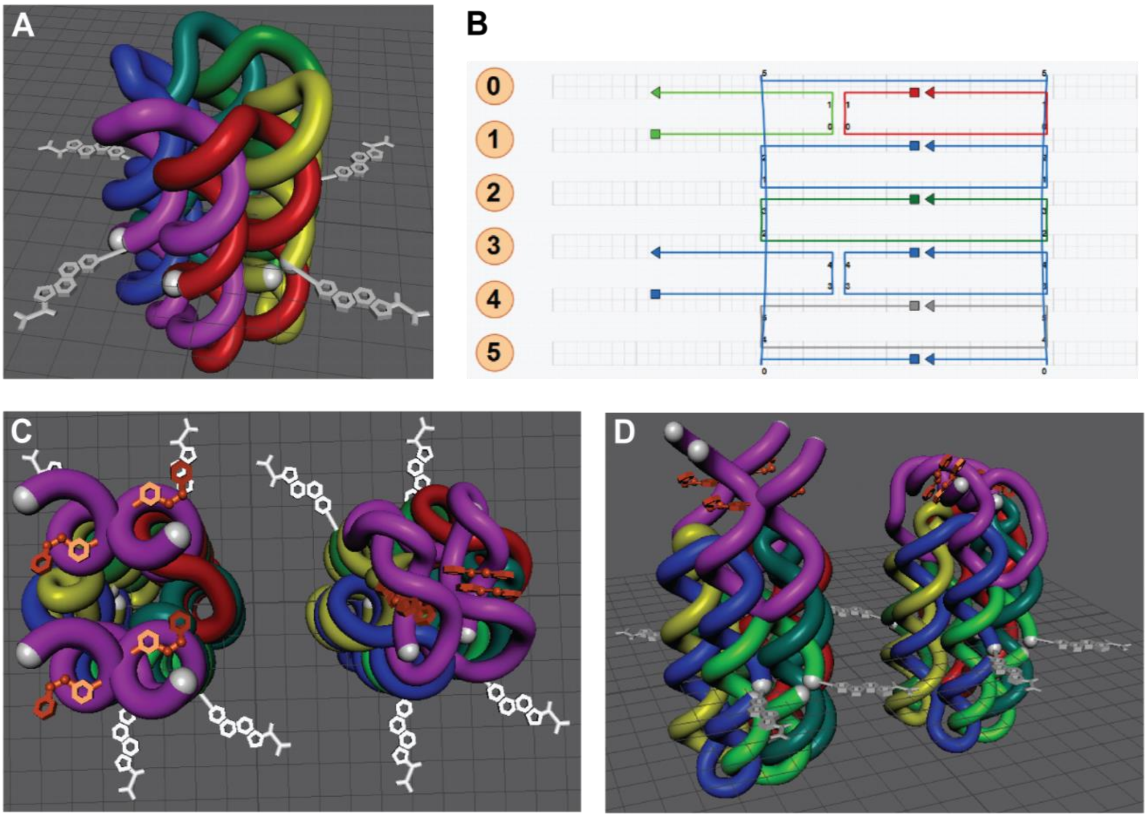

Fig. 67 Hexagonal DNA-nanopore as used by Burns et al.[106] *(A), cadnano-projection of a modified nanopore (B) and the 3D-rendered models in top view (C) and side view (D). Each strand is individually colored, azobenzene-modified strands are colored purple (C, D), azobenzenes are colored orange, cholesterol-anchors for membrane association are white. Pores on the left are open, pores on the right closed (C, D). 3D-rendered models created with the vHelix plug-in and Autodesk Maya.*

3. Locked azobenzene *C*-nucleosides

3.1 Motivation and objective

As seen in chapter 1.2 and 2, oligonucleotide hybridization can be controlled with light as external stimulus, when the oligonucleotides are modified with photochromic moieties. Especially the *cis-trans*-isomerization of azobenzene with the accompanying morphological changes are an often used tool as it leads to significant rearrangements within the duplex. In order to harness the morphological changes of the azobenzene to the fullest, the way of incorporation into the oligonucleotide is of utmost importance. Several linking strategies have been described in chapter 1.2. *D*-threoninol-derived *t*Azo is the most prominent one, as it has been used in many studies to date since it is easy to synthesize and versatile in applications.[87,88] The major drawback of *t*Azo modifications is the need for elevated temperatures, as the *trans*-azobenzene residue appears to be trapped in the base stacking region.[72,84,179,182] The elevated temperature is needed to overcome attractive interactions of the nucleobases to the azobenzene in order to carry out the isomerization movement. The acyclic *D*-threoninol linker is very flexible and therefore does not support the leverage of the azobenzene moiety during the isomerization sufficiently.

Recently developed azobenzene *C*-nucleosides offer a different approach to incorporate azobenzenes into oligonucleotides. Replacing the nucleobase on the 1'-position with the chromophore, it mimics natural nucleosides. In addition, the ribosidic linker offers a strong base for the isomerization movement. As a result, the azobenzenes full switching potential can already be harnessed at room temperature.[72,84] In chapter 2 it could be demonstrated, that azobenzene *C*-nucleosides can be utilized to create light responsive nanostructures, which can be operated at room temperature. During this project, the major drawback of the ribosidic linkers became clear again. Due to the rigidity of the ribosidic linker and the end to end distance of *trans*-aztobenzene, the azobenzene penetrates deep into the opposing base stack, causing steric repulsion even in favored *trans*-state. This limits the scope of application for the *C*-nucleoside, as incorporating it into an oligonucleotide leads directly to decreased duplex stability.

In order to increase duplex stability and thereby diminishing the drawback of the ribosidic linker, chemical modifications of the linker seems to be a reasonable approach. A huge variety of oligonucleotide modifications exist to choose from, all with different effects. The main goal would be to identify the best-suited modification to improve duplex stability while maintaining photoswitching efficiency of the azobenzene *C*-nucleoside, followed by synthesis of the improved linker and thorough testing in oligonucleotides.

3.2 Results and discussion

3.2.1 Identification of suitable *C*-nucleoside modifications

The modification of oligonucleotides in order to tune certain functions is a well-established field. Many modifications have been identified to improve duplex stability, stability against enzymatic digestion or cellular uptake just to name a few. As the modifications are manifold, arranging them into certain categories appears to be helpful (Fig. 68).

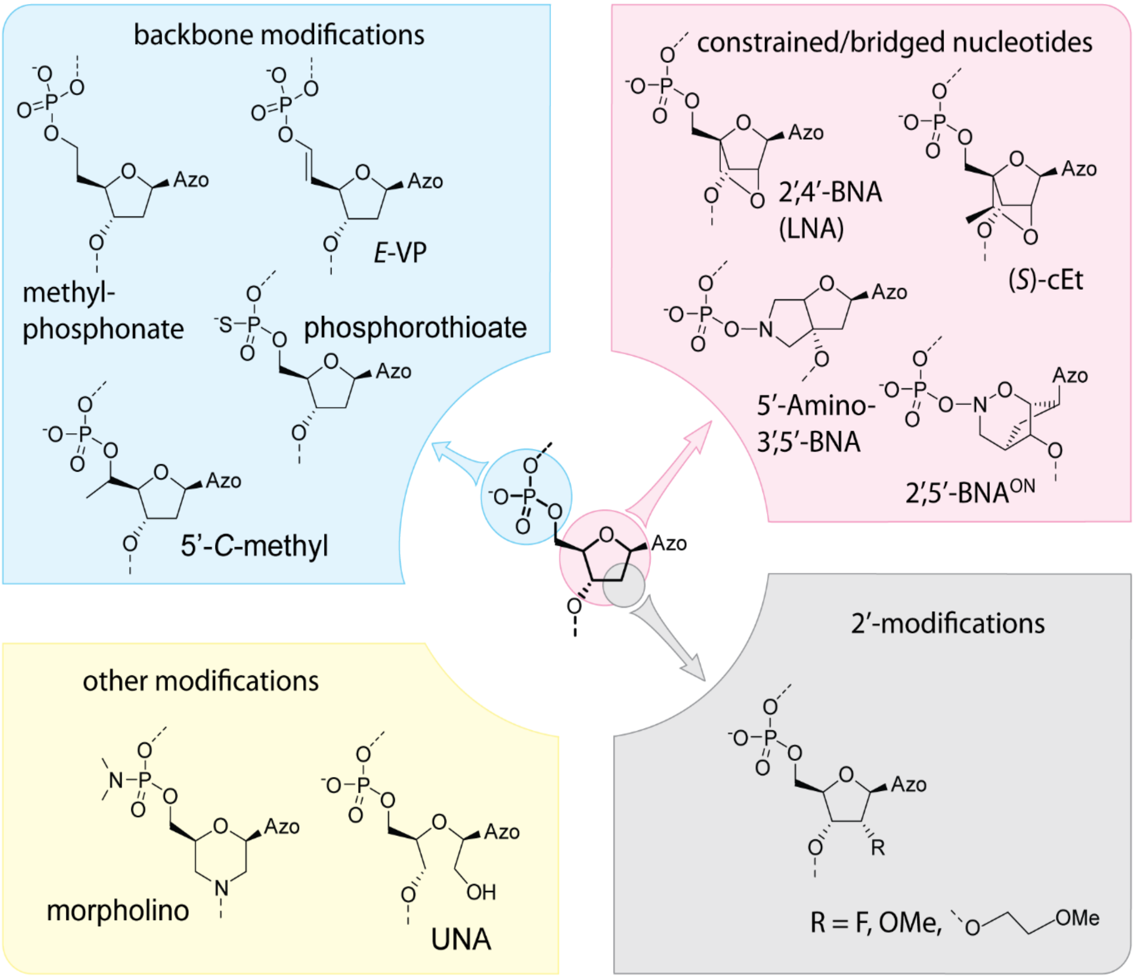
backbone modifications
Azo
methyl-
phosphonate
E-VP
phosphorothioate
5'-*C*-methyl
constrained/bridged nucleotides
2',4'-BNA
(LNA)
(*S*)-cEt
5'-Amino-
3',5'-BNA
2',5'-BNA^ON
2'-modifications
R
R = F, OMe, O OMe
other modifications
morpholino
UNA
OH

Fig. 68 An azobenzene C-nucleoside and selected ways to modify it, sorted by backbone modifications, constrained/bridged nucleotides, 2'-modifications and other.

Backbone modifications almost exclusively tackle the problem of exonuclease digestion of RNA *in vivo*.[183] Even 2'-modifications stabilize mainly against nuclease digestion, but in addition propagate A-helix formation. With a bulky residue on the 2'-position, 3'-endo conformation of the ribose moiety is facilitated, which is a necessity for A-helix formation in RNA duplexes and DNA-RNA hybrids. Morpholinos as non-natural nucleic acid have become very famous since the approval of the first morpholino-based antisense RNA to treat Duchenne's muscular dystrophy.[184,185] Since their benefit mainly concerns nuclease resistance and duplex stability is similar to natural nucleosides, they are no option for stability improvement. Unlocked nucleic acids (UNA) imply a gain of conformation freedom, similar to that of *D*-threoninol linker, but rather decrease duplex stability in DNA and RNA.[186] The opposite happens, if a nucleotide is constrained with an additional bridge like in the bridged/constrained nucleotides. Depending on which atoms in the ribose ring are interlocked, 2'- or 3'-endo conformation is enforced. Where 2',5'-BNA^{ON} and 5'-Amino-3',5'-BNA lock the sugar moiety in 2'-endo position, (*S*)-cET and 2',4'-BNA lock the sugar in 3'-endo conformation. Especially 2',4'-BNA, which coined the name locked nucleic acid (LNA) became famous for duplex stabilization and nuclease resistance improvement[187]. Since synthesis and influence of locked nucleic acids is well characterized, the development of 2',4'-locked azobenzene *C*-nucleosides appears reasonable. Locking the sugar moiety in one conformation would also tackle another possible problem: Previous studies involving azobenzene *C*-nucleosides reported less effect of the chromophore on duplex stability, than expected when attached on a rigid base like ribose.[72,84] Since the sugar moiety is not conformationally locked it is possible, that the geometry of the ribose changes upon isomerization of the azobenzene. The intended tension caused by the photoisomerization of azobenzene is possibly lost due to these degrees of conformational freedom rather than being used to force hydrogen bonds out of optimal distance in the base pairing region (Fig. 69A). In the contrary, locked azobenzene *C*-nucleoside could not rearrange itself during isomerization of the azobenzene moiety and therefore the energy of the isomerization movement would not be lost in conformational rearrangements of the sugar moiety but rather would go directly into rearrangement of the duplex shape itself (Fig. 69B).

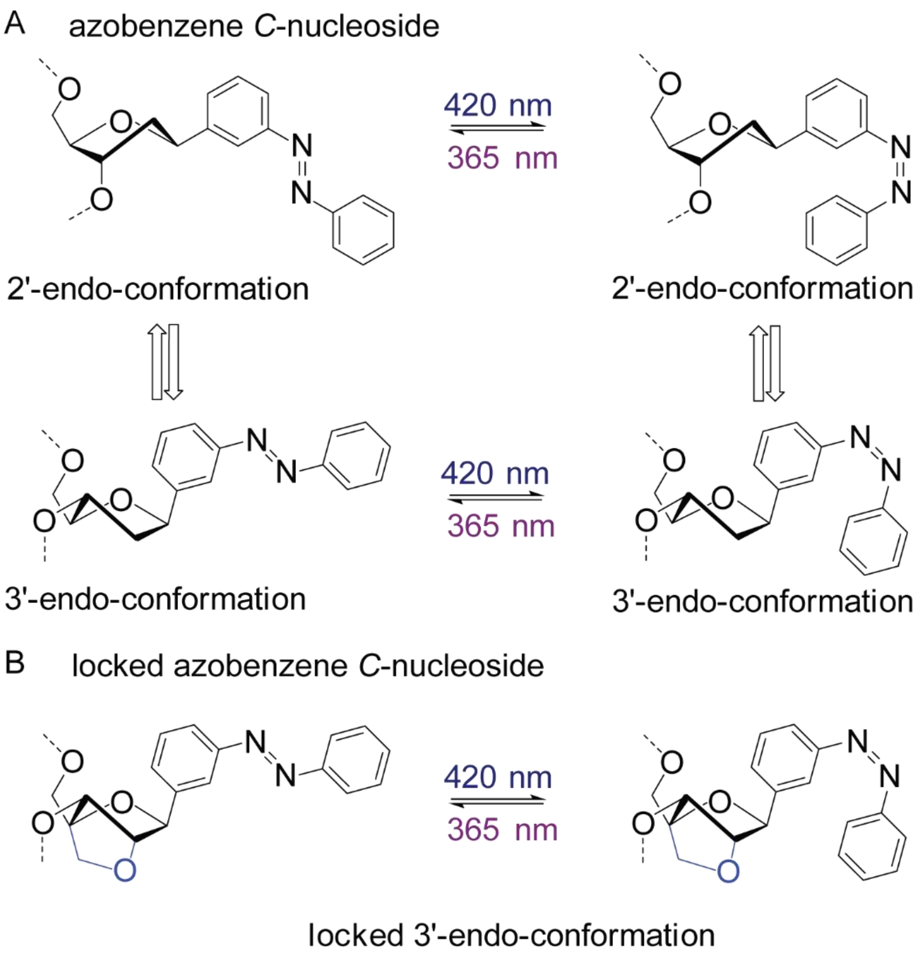
A azobenzene C-nucleoside
420 nm
365 nm
2'-endo-conformation
2'-endo-conformation
3'-endo-conformation
3'-endo-conformation
B locked azobenzene C-nucleoside
locked 3'-endo-conformation

Fig. 69 Display of the photoisomers of azobenzene C-nucleosides with different sugar conformations (A) and the photoisomers of locked azobenzene C-nucleoside (B).

Azobenzenes have previously been incorporated into LNA by attachment via an alkynyl-linker at the C5-position of a locked uridine nucleoside[54] In this study, positioning and length of the linker causes the azobenzene to be oriented into the major groove, which leads to little change of the hybridization behavior upon irradiation with ΔT_M-values of 1 °C (Fig. 70). In this matter, locked azobenzene *C*-nucleosides are expected to yield more promising results. The *trans*-azobenzene moiety has to be positioned in the stacking region and a migration of the intentionally bulky *cis*-photoisomer into the minor or major groove has to be prevented.

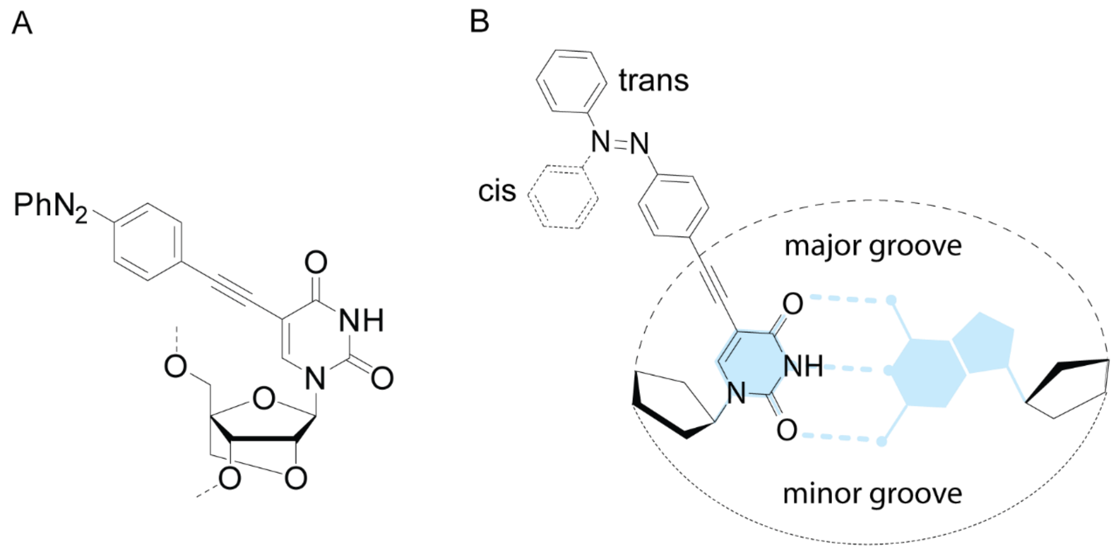
A
B
PhN2
O
NH
N
O
O
O
O
O
trans
N=N
cis
major groove
O
NH
N
O
minor groove

Fig. 70 Locked uridine nucleoside with an azobenzene attached via alkynyl linker to the C5-position (A) and its positioning in an oligonucleotide duplex (B).

3.2.2 Synthesis of the locked azobenzene *C*-nucleoside LNAzo

The synthesis of locked *C*-nucleosides is not as established as for *N*-nucleosides due to their commercial significance. Obika *et al.*[188] and Babu *et al.*[189] have established synthetic pathways for locked *C*-nucleosides following a similar approach, but with different protection group strategies. The key step is a nucleophilic attack of a negatively charged aryl onto a pre-locked, open sugar aldehyde (Fig. 71). The approach of Babu *et al.* was chosen over Obika *et al.*, as the hydrogenolitic cleavage of benzyl protecting groups might also reduce the azobenzene to corresponding hydrazine. *Para*-methoxybenzyl groups can be cleaved by single electron transfer from DDQ, which is orthogonal to the substrates functionalities.

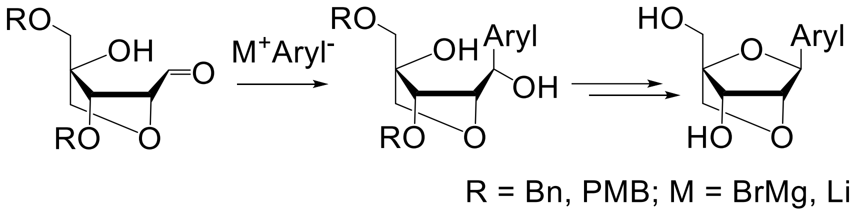

R = Bn, PMB; M = BrMg, Li

Fig. 71 Essential steps in the formation of locked C-nucleosides.

Starting from commercially available 1,2:5,6-di-O-isopropylidene-α-*D*-allofuranose **24**, the first synthetic steps involve the protection of the 3’-position with para-methoxybenzyl chloride to form **25**, followed by deprotection of the 5’- and 6’-OH groups to give **26** in almost quantitative yield (Fig. 71). Cleavage of the vicinal diol and oxidation of the 5’-position with sodium periodate gave aldehyde **27.** A successive Cannizzaro reaction and simultaneous aldol-like addition on the 4’-position formed diol **28** (Fig. 72).

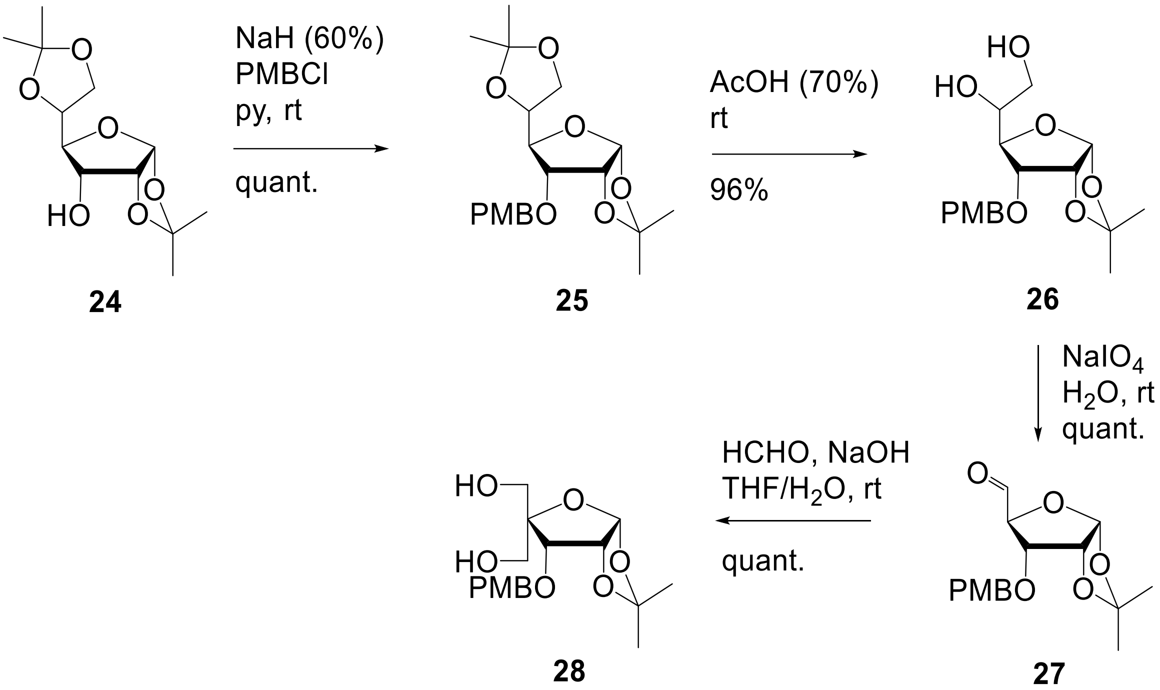
NaH (60%)
PMBCl
py, rt
quant.
AcOH (70%)
rt
96%
NaIO$_4$
H$_2$O, rt
quant.
HCHO, NaOH
THF/H$_2$O, rt
quant.
HO
PMBO
24
25
26
27
28

Fig. 72 First four steps in the synthetic pathway to create locked azobenzene C-nucleosides.

The formation of the diol **28** is followed by mesylation of the two hydroxylic groups with mesyl chloride to form **29**. The acidic methanolysis forming compound **30** is followed by the base induced closure of the 2'-*O*,4'-*C* bridge to form conformationally locked compound **31**. The interconversion of 5'-mesyl to 5'-acetyl with potassium acetate and crown ether in dioxane is followed by ammonolysis to deprotect the 5'-position, which is protected in the following with *para*-methoxybenzyl to form **34**. Acid catalyzed ether cleavage on the anomeric position leads to the constrained sugar aldehyde **35**, which is then used for nucleophilic attack of the azobenzene.

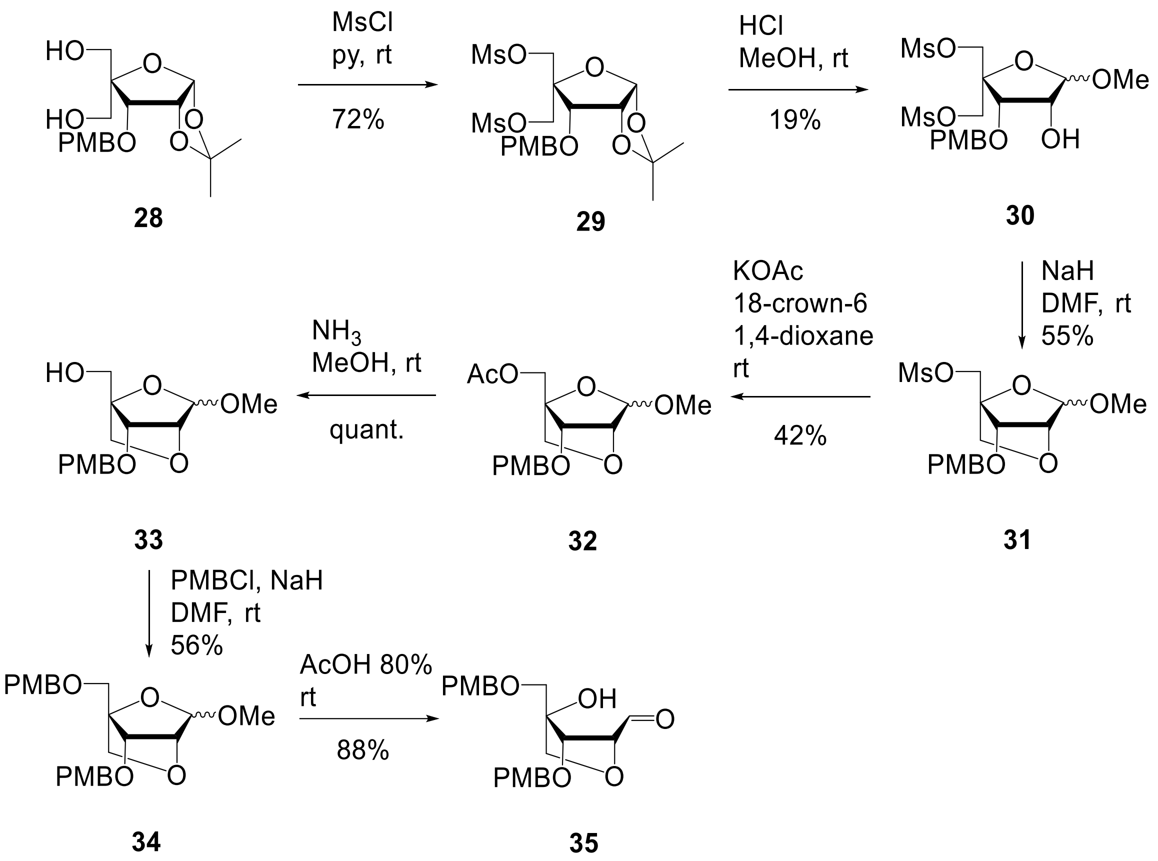

Fig. 73 Step five to eleven of the synthetic pathway to create locked azobenzene C-nucleosides.

In analogy to the synthesis established in chapter 2, *meta*-iodoazobenzene is activated by lithium halogen exchange utilizing ^{n}butyl lithium at temperatures below -78 °C. Unfortunately, the nucleophilic addition of lithiated azobenzene to aldehyde **35** appeared to be difficult. The reason for this is that the first equivalent of lithiated azobenzene deprotonates the alcoholic group at the 4'-position, which then subsequently attacks the aldehyde to form a closed ribose ring with a 1'-alcoholate (Fig. 74). This structure is not susceptible for nucleophilic attacks anymore and stands in equilibrium with the open sugar with a 4'-alkoholate. Since the equilibrium is strongly shifted to the 1'-alcoholate, product formation is deprived under these conditions. Following the rules of Le Chatelier, the removal of 4'-alcoholate by subsequent reaction with the azobenzene should shift the equilibrium towards the favored 4'-alcoholate. This is a long lasting process, which does not match instability of highly reactive lithiated species in the reaction. The best option is to scale the reaction down to find the best compromise in between reaction time and substrate conversion. This fits empirical observations, as the reaction gave yields up to 20% in a 50-200 mg scale. Yields dropped significantly or product formation could not be observed at all for larger scales.

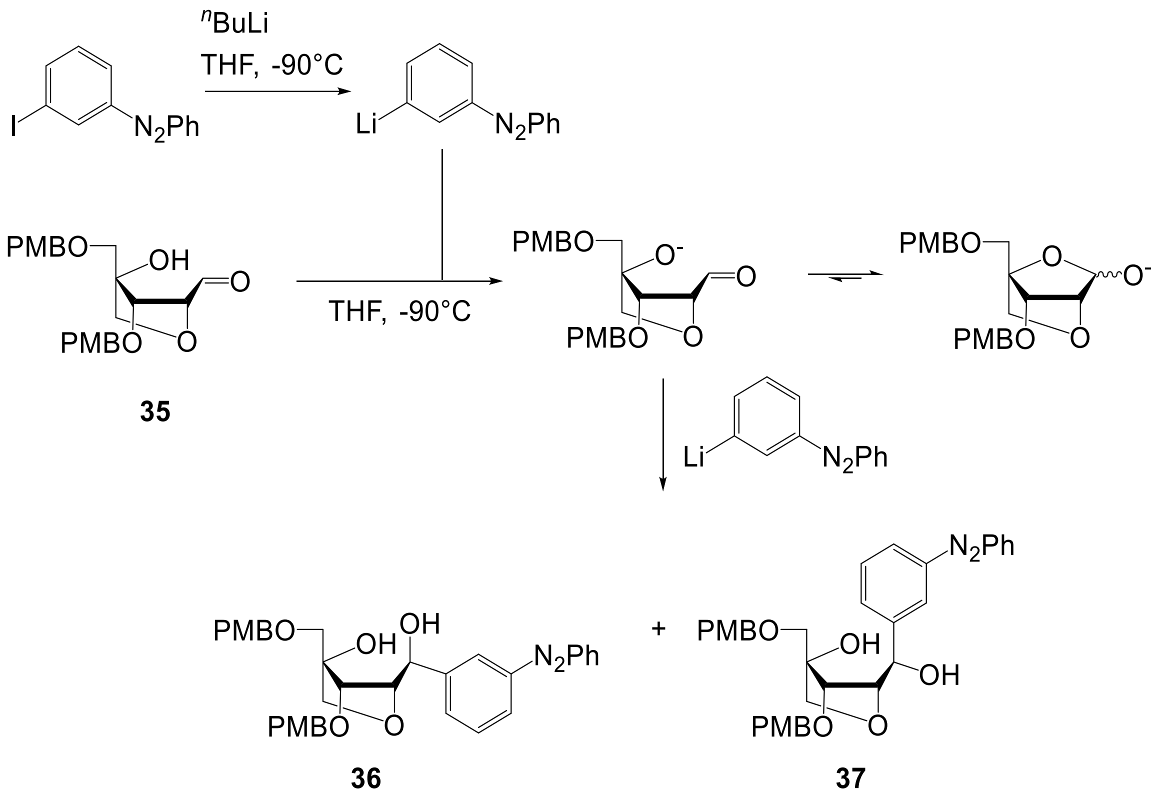

Fig. 74 Nucleophilic addition of lithiated azobenzene to aldehyde ***35*** *and transition state equilibrium.*

After initial direct phase column chromatography to separate the products from other contaminants, two conformational isomers could be separated by reverse phase column chromatography. In order to assign (*R*)- or (*S*)-configuration to the products several attempts have been tried, but without success. ^{1}H-NMR data only gave multiplet singals for the 1'-hydrogen without distinguishable coupling constants and with similar shift of the signal. Nuclear Overhauser effect based NMR methods to estimate proximity relations in NOESY or ROESY experiments were not successful, even with water suppression. Crystallization of the compounds was tried in all accessible solvents without success. Chiral derivatization with the Mosher approach was not possible, since very little amounts of material could be synthesized and where needed for the following steps.[190] As these approaches failed for all following steps, it was only possible to name them compounds X and Y. However, as soon as anomer X and anomer Y were incorporated into oligonucleotides, it became quite clear which compound was the more natural β-anomer and which compound was the deviant α-anomer. As the difference in behavior was consistent in all oligonucleotide systems, assignment of the conformation could be concluded from these findings. All assignments for the synthesis of LNAzo phosphoramidites from this point on are based on these findings.

In the following step, ring closure was carried out under Mitsunobu-conditions using triphenylphosphine and DIAD. This leads to the formation of compound **38** and **39**, which were then deprotected with DDQ to give free nucleosides **40** and **41**. In order to incorporate LNAzo building blocks into oligonucleotides, 5'*O*-tritylation and 3'*O*-phosphitylation were carried out under standard conditions to give amidites **44** and **45** (Fig. 75).

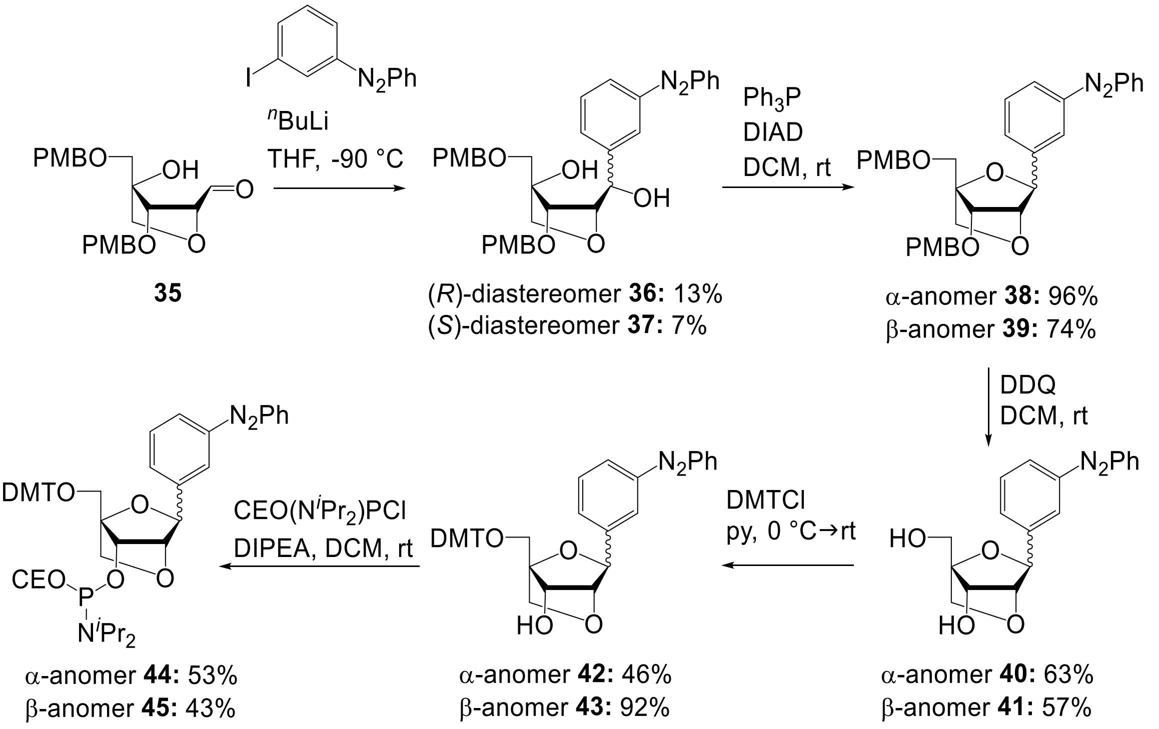

N₂Ph
I
ⁿBuLi
THF, -90 °C
PMBO
OH
O
PMBO
35
(*R*)-diastereomer **36:** 13%
(*S*)-diastereomer **37:** 7%
Ph₃P
DIAD
DCM, rt
α-anomer **38:** 96%
β-anomer **39:** 74%
DDQ
DCM, rt
HO
α-anomer **40:** 63%
β-anomer **41:** 57%
DMTCl
py, 0 °C→rt
DMTO
α-anomer **42:** 46%
β-anomer **43:** 92%
CEO(NⁱPr₂)PCl
DIPEA, DCM, rt
CEO
P
NⁱPr₂
α-anomer **44:** 53%
β-anomer **45:** 43%

Fig. 75 Synthesis of LNAzo phosphoramidites starting from aldehyde ***35****.*

3.2.3 Influence of LNAzo in oligonucleotides

In order to test influence and capabilities of the two LNAzo anomers, an oligonucleotide model systems was needed. The choice fell onto the 10mer binding region of the minicircles in chapter 2, as experience gained from that study might benefit the current one. The length of ten bases with a GC-content of 60% offers to evaluate the influence of a single modification and its two photostationary states by temperature dependent UV/vis absorption and CD-spectroscopy. In addition to this, Prof. Asanuma suggested to support spectroscopic studies by temperature dependent fluorescence analysis, if fluorophore-quencher-pairs 6-fluorescein (FAM) and dabcyl (DAB) were installed on one end of the duplex. DNA-analogue mAzo residue was included in this study for a direct comparison between the DNA- and LNA-linker system.

For melting point measurements 1 mL samples were prepared with 1µM of strand and counterstrand in 1x PBS-buffer for each modification and each system (16 in total). The absorbance changes at 260 nm were measured against the temperature with a gradient of 1 °C per minute. Samples were irradiated as single strands at elevated temperatures with either 365 nm or 420 nm until the photostationary state was reached to prevent mismatches. To avoid effects of hysteresis, melting points were calculated by a sigmoidal fit from cooling and heating measurements. At least five independent heating and cooling measurements were performed for precise results.

The unmodified DNA wild type had a melting point of 49.8 °C in 1x PBS buffer (Fig. 76). Introducing azobenzene *C*-nucleoside decreased the melting temperature by 16.6 °C, which demonstrates again the huge impact the steric repulsion of the azobenzene brings. Utilizing the photochromicity of the azobenzene, a melting point difference between the photostationary states of 365 nm and 420 nm of 4.1 °C could be achieved. Incorporating the α-anomer of LNAzo a melting point similar to that of the *cis*-isomer of mAzo could be achieved, but no photocontrol of the duplex stability could be observed within error limits. The β-anomer on the other hand displayed a behavior similar to that of mAzo, with overall increased melting points by approximately 2 °C and a ΔT_M of 4.8 °C, which is 0.7 °C greater than for mAzo.

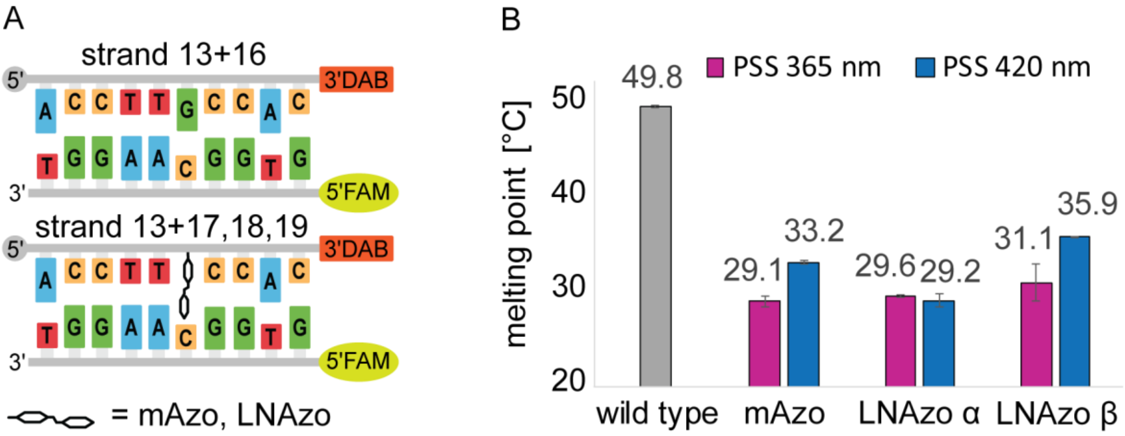

Fig. 76 System 1: DNA-DNA duplexes used in this study with the unmodified wild type (A, top), the modified duplexes (A, bottom) and resulting melting points (B).

In chapter 2 it could be showed, that the steric repulsion caused by the rigid linker and the end-to-end distance of the azobenzene can partly be compensated by removing the nucleobase in the opposing strand, so that the azobenzene can fill up the space of two nucleobases. In an analogue approach it should also be demonstrated, how big the influence of the abasic site on the melting points of the oligonucleotides is. The overall performance of the modifications did not change much (Fig. 77). Melting points of the modified strands increased by approximately 2 °C with similar differences in between the *trans*- and the *cis*-state of the azobenzene moieties. Again, the LNAzo β-anomer increases duplex stability compared to mAzo by 3-4 °C with ΔT_M values 0.9 °C greater than for mAzo. The α-anomer of LNAzo displayed no photocontrol within error limits, just as in system 1 before. The behavior of the wild type on the other hand was more than surprising, as melting point plummeted by almost 30 °C compared to the wild type from system 1.

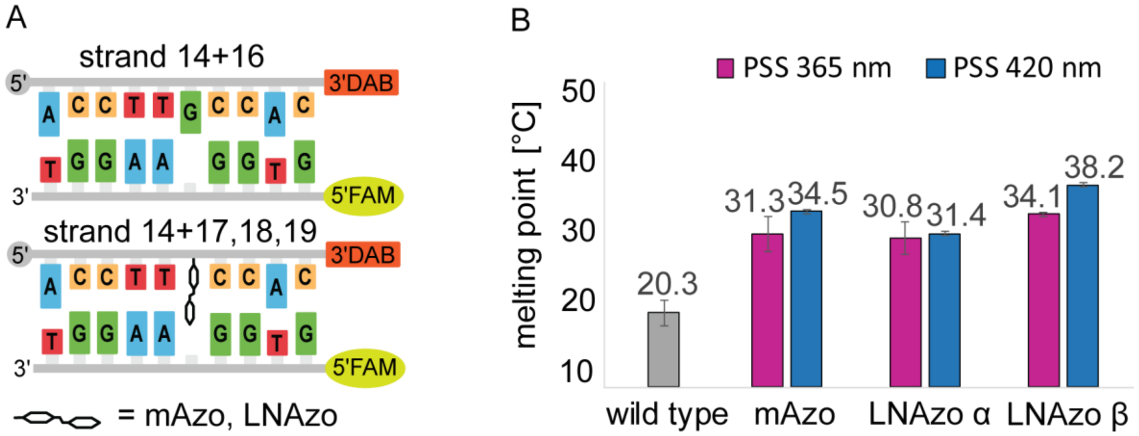

Fig. 77 System 2: DNA-abasic DNA duplexes used in this study with the unmodified wild type (A, top), the modified duplexes (A, bottom) and resulting melting points (B).

To gain further insight into base deprived DNA, the wild type strands of system 1 and 2 were compared with their analogues without fluorophore-quencher-pairs in order to exclude them to be responsible for the drop in duplex stability (Fig. 78). As to bee seen from the melting points, the same behavior could be observed without fluorophore-quencher-pairs. The melting points without FAM or DAB modification were in general lower than with. The reason for this might be attractive interaction between these two groups, which also need to be broke by temperature so that the strands could dissociate. CD-spectra (Fig. 78, B and C) suggest that B-helicity is not as developed in base-deficient strands than in native strands.

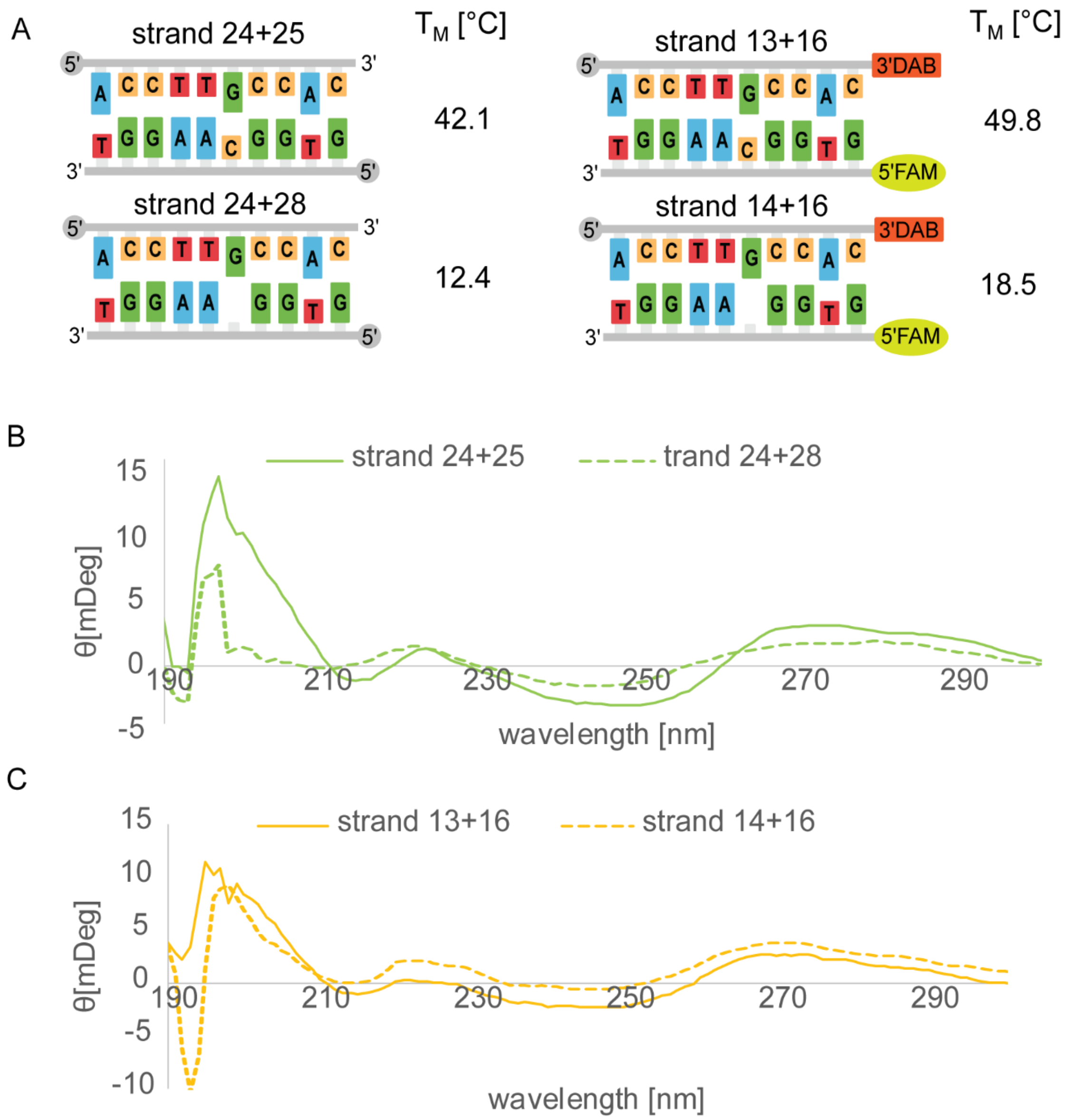

Fig. 78 Structures of DNA-duplexes without (A, left) or with (A, right) fluorophor-quencher-pairs attached to them and corresponding melting points, and CD-spectra of such (B, C).

A reasonable explanation for these phenomena might be that upon removing a nucleobase out of the center of this 10mer duplex, the system gets separated into 5mer duplex with a 4mer duplex appendix, only held together via a guanosine residue. The separated duplexes would dehybridize independently from one another, which also would explain, why helicity is decreased. To close this survey, a permutation of 4 base-deficient 10mer duplexes were compared by melting points and CD-spectra to one another and the wild type 10mer duplex (Fig. 79).

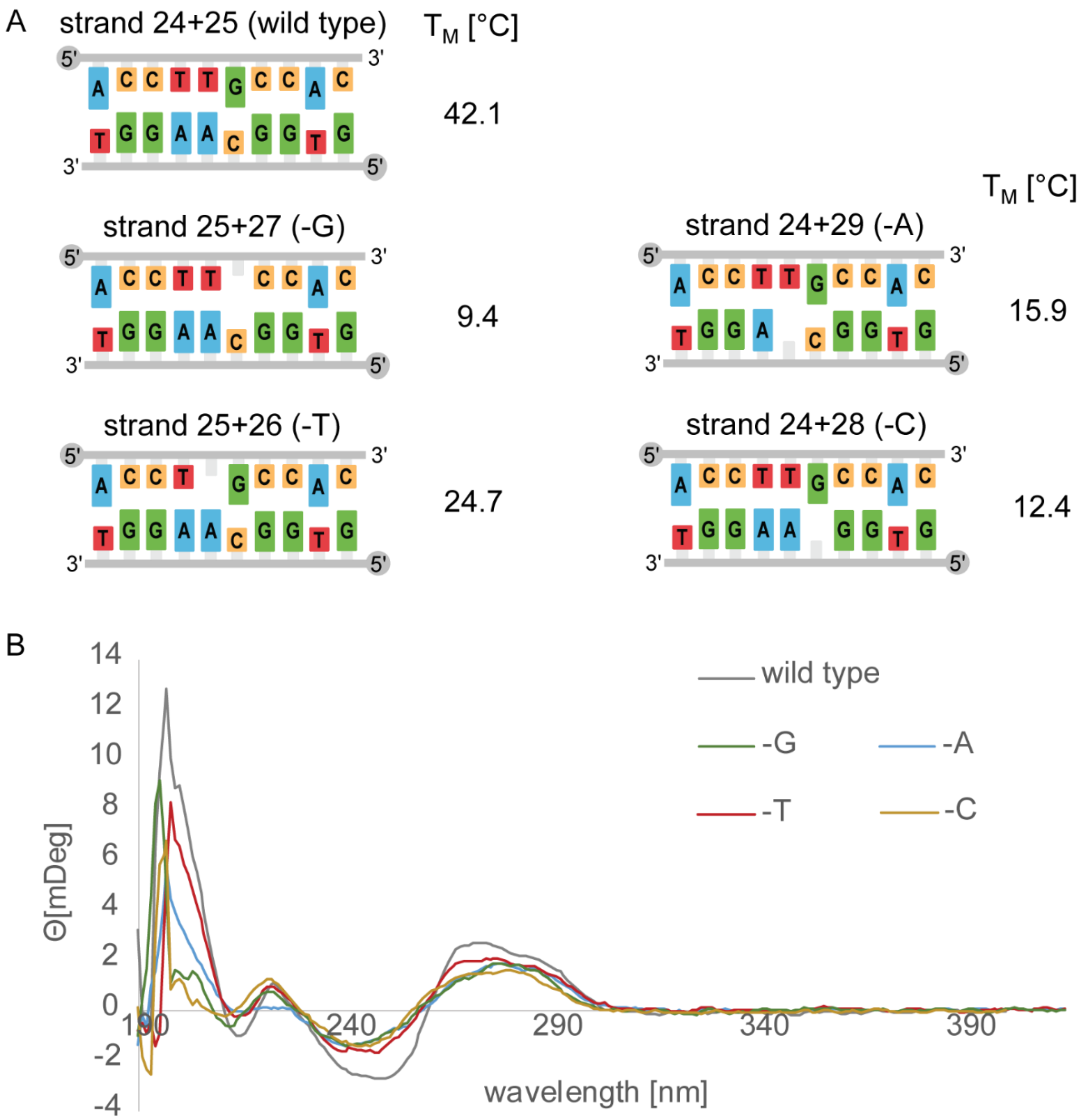

Fig. 79 Structures of base-defficient duplexes, corresponding melting points (A) and their CD-spectra (B).

The trend as seen before seems to repeat for all four duplexes with slight differences. Removing bases partaking in three hydrogen bonds decreases duplex stability more, than removing bases partaking in two hydrogen bonds, as expected. In addition contribution to π-stacking interactions in the duplex appear to be significant as well, since removing purines decrease duplex stability more than removing pyrimidines. The CD-spectra all display a reduction of B-helicity in base-defficient duplexes compared to the wild type.

The results of system 1 and 2 shown in Fig.76 and 77 did not yield the desired effect of LNAzo β compared to established mAzo. In general, LNAzo β increases duplex stability by approximately 2 °C and photocontrol of duplex stability by around 1 °C if used in a DNA context. As it is known, the 3’-endo conformation of LNA promotes the A-helical character of a duplex as seen in RNA duplexes. It could be the case that the true potential of LNAzo can not unfold unless it is used in a RNA-context. To test this hypothesis, existing azobenzene-modified DNA strands were hybridized with a RNA-counterstrand to form DNA-RNA-hybrids (Fig. 80). The melting point of system 3 wild type was with 55.7 °C almost 6 °C higher than that of system 1 wild type, which appears to be plausible. The melting points of mAzo modified duplex still displays a strongly decreased melting point, but is approximately 4 °C higher than in system 1 with a ΔT_M value of 4 °C as high as for the DNA setting. LNAzo α displays for the first time photocontrol of a duplex with melting points in the same order of magnitude as for mAzo and with a ΔT_M of 2 °C. LNAzo β on the other hand increased overall melting points by almost 7 °C with a ΔT_M of 5.8 °C. This is almost 50% higher as for mAzo and 1 °C higher than for the DNA setting, which gives a hint that the A-helical context is needed for LNAzo in order to unfold its true potential. CD-spectroscopic data also suggest this, as the duplexes of system 3 display a strong A-helical character, compared to the duplexes of system 1 and 2, which were clearly B-helical. CD-spectra of all duplexes can be seen in the experimental part, section 5.5.1.

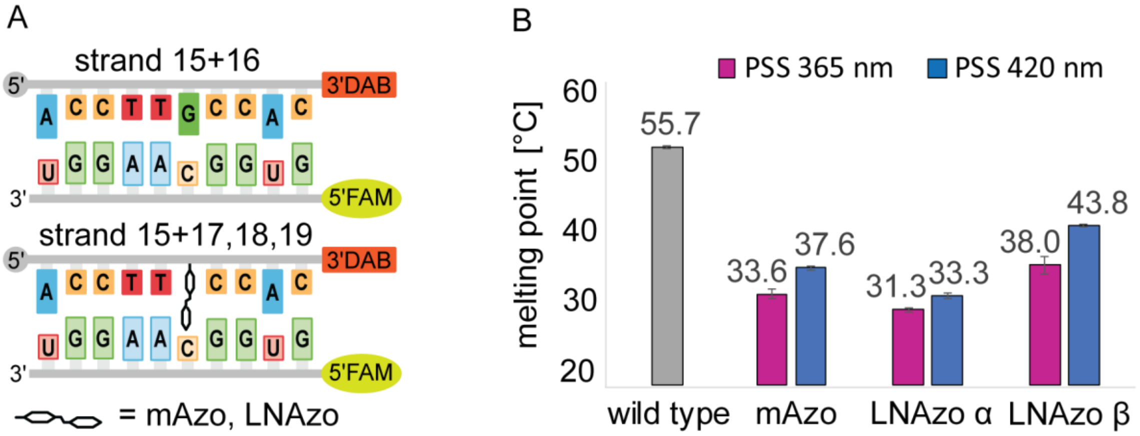

Fig. 80 System 3: DNA-RNA duplexes used in this study with the unmodified wild type (A, top), the modified duplexes (A, bottom) and resulting melting points (B).

The next logical step in this study was the incorporation of all photochromic modifications into RNA-strands (Fig. 81). As before, the melting point of the RNA wild type rose again by several degrees to 62.4 °C, displaying the strong attractive interactions of RNA compared to DNA. The melting points for the mAzo modified strands were around 4 °C higher than for the DNA-RNA hybrids of system 3, but the melting point differences ΔT_M of around 4 °C did not change throughout all systems, in which mAzo has been applied. This shows, that the photocontrol capabilities of azobenzene attached to a DNA-analogue ribosidic linker do not depend on the type of nucleotide where it is incorporated. The influence of LNAzo α worsened again compared to system 3 as it destabilizes the duplex more than any other modification with half of the photocontrol compared to system 3. The approach to incorporate LNAzo β into RNA proved to be the right decision, as duplex destabilization sank by almost 3 °C. The biggest surprise was that the photocontrol of duplex formation could be increased to ΔT_M values of 8.8 °C. For a single modification in a 10mer duplex this is an incredibly high ΔT_M value is almost 2.3 times greater than for the mAzo reference.

With the development and characterization of novel LNAzo β, a tool for improved reversible photocontrol has been found. Unfortunately, the improvement through this modification for DNA applications is rather limited as the photocontrol is only increased by 17% compared to established mAzo. For the application in a RNA context, LNAzo β appears to be just right, since photocontrol of duplex stability could be improved over 100% compared to established mAzo. With this, a useful tool for photocontrolling RNA interference and reversible photocontrol of possible RNA therapeutics is at hand. Data from this project have been published in *Chemistry – A European Journal* in 2019.[191]

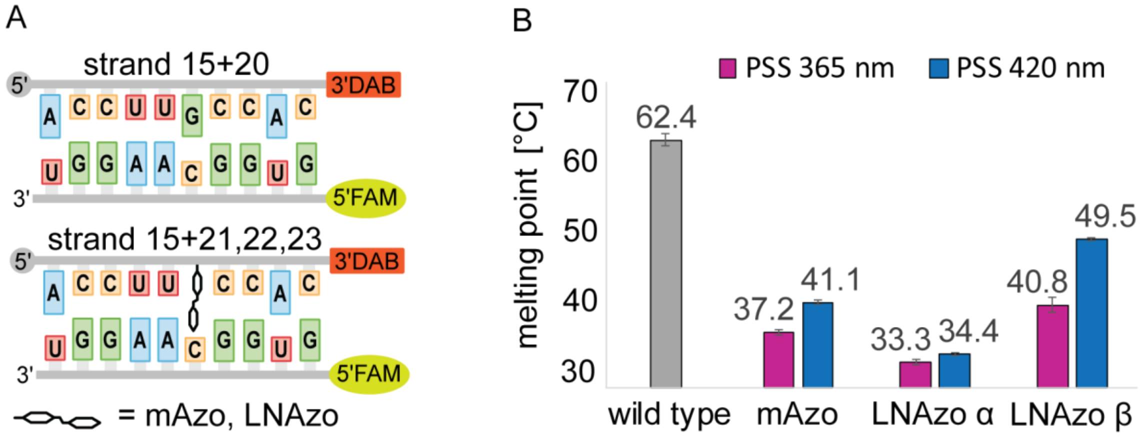

Fig. 81 System 3: RNA-RNA duplexes used in this study with the unmodified wild type (A, top), the modified duplexes (A, bottom) and resulting melting points (B).

3.3 Summary and outlook

Controlling duplex stability with light as a strategy to create light responsive DNA-nanostructures can be achieved by incorporating photochromic compounds like azobenzene into the oligonucleotide. The way the azobenzene is incorporated into the oligonucleotide is here of utmost importance, as the linking system has to fulfill several criteria: The *trans*-state needs to be positioned in the base pairing region of the duplex causing least possible steric perturbation. Upon photoisomerization, the *cis*-state should form easily without hindrance. The evasion from the base pairing region into major or minor groove needs to be prevented at any cost. Shifting the sterically demanding *cis*-isomer into the free space of the major or minor groove would discharge the steric stress on adjacent basepairs, which is needed to decrease duplex stability. *D*-threoninol derived *t*Azo linker fulfills most of these criteria, but needs elevated temperatures to gain full switching potential. The *trans*-azobenzene gets stacked by surrounding nucleobases and can not isomerize, since the isomerization movement is not supported by the flexible diol linker.

To tackle this problem, azobenzene *C*-nucleosides have been developed. The stiff ribosidic linker represents firm base for the isomerization movement and it has been shown, that photocontrol over duplex stability could also be achieved at room temperature. But the utilization of DNA-analogous *C*-nucleosides brings two drawbacks with it: the ribose units includes the flexibility of the sugar conformation and it is reasonable to think, that upon isomerization of the azobenzene, part of the steric stress generated is compensated by the sugar reconfiguration, which is lost for duplex destabilization. In addition, the combination of the rigid ribosidic linker and the end-to-end distance of *trans*-azobenzene causes the chromophore to penetrate deep into the base stack of the opposing strand, causing a serious destabilization even in favored *trans*-state. The goal would be to find a linker system, that combines the benefits of the azobenzene *C*-nucleoside without the possibility to change sugar conformation and the strong destabilization in the *trans*-state. For this reason locked azobenzene *C*-nucleosides in analogy to LNA nucleotides have been synthesized and characterized in several oligonucleotide test systems.

The synthesis of LNA analogous azobenzene *C*-nucleosides (LNAzo) was possible over a 16 step synthesis, with the critical step being the addition of *in situ* lithiated azobenzene to protected sugar aldehyde **35**. Upon deprotonation, the open aldehyde stands in equilibrium with its closed acetal form, which is not susceptible for nucleophilic attack of the azobenzene. Due to this equilibrium, the critical step could only be performed in small scales, which limited the total amount of LNAzo synthesized. Both anomers of LNAzo and mAzo as reference where incorporated into different oligonucleotide test systems by solid phase synthesis for thorough evaluation.

It could be shown, that LNAzo β has a similar performance to mAzo in DNA with overall slightly increased melting points and ΔT_M-values. Even if steric stress is reduced by using abasic sites in the counterstrand opposing the azobenzene performance of LNAzo β was similar to mAzo. Only in a RNA context, the true potential of LNAzo β could be observed. If azobenzene modifications where incorporated into DNA to hybridize with a RNA strand, photocontrol could be improved by almost 50%, if incorporated into RNA to hybridize with a RNA counterstrand even by over 100% (Fig. 82).

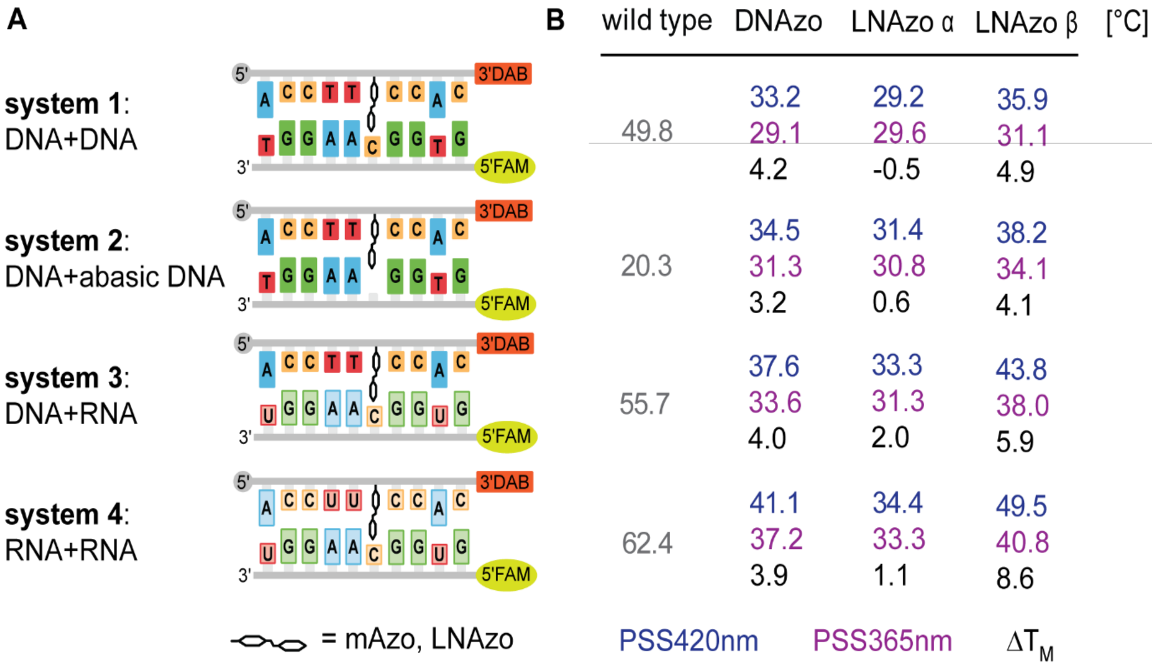

wild type	DNAzo	LNAzo α	LNAzo β	[°C]
49.8	33.2 29.1 4.2	29.2 29.6 -0.5	35.9 31.1 4.9	
20.3	34.5 31.3 3.2	31.4 30.8 0.6	38.2 34.1 4.1	
55.7	37.6 33.6 4.0	33.3 31.3 2.0	43.8 38.0 5.9	
62.4	41.1 37.2 3.9	34.4 33.3 1.1	49.5 40.8 8.6	

Fig. 82 Schematic drawing of the four different oligonucleotide test systems used (A) and the melting points gathered from them (B).

Although the primary goal was the improvement of the azobenzene *C*-nucleoside for a DNA-nanostructure context, LNAzo β proved not to give a sufficient improvement in regard to the cost-value ratio. Never the less, the invention of the locked azobenzene *C*-nucleoside was a huge success for reversible photoregulation of RNA hybridization. With this, a new way to regulate RNA hybridization has been found, which could be used to create RNA therapeutics in an antisense-approach.

Characterizing the influence of photochromic modifications on oligonucleotides merely by melting point analysis of a duplex in one concentration and one buffer system can not give the information needed for *in vivo* applications. Mapping the influence of factors like temperature, oligonucleotide and ion concentration would give the ability to describe the behavior of a duplex in solution by thermodynamic parameters like enthalpy, entropy and dissociation constants. Several methods to measure certain thermodynamic parameters of oligonucleotides exist to date like isothermal titration calorimetry[192], fluorescence correlation spectroscopy[193] or surface plasmon resonance[194] just to name a few. It would be elegant to extract thermodynamic parameters just from analyzing temperature dependent fluorescence of a series of different oligonucleotide concentrations. Development of such a technique would give an approach of thermodynamic characterization of oligonucleotides without the need for specialized instrumentation other than a fluorescence spectrometer or a suitable real-time PCR device. With this, a deeper understanding of oligonucleotide hybridization could be gained and used to customize oligonucleotide drugs and probes to the specifications of any possible application.

4. 2-Phenyldiazenyl purines

4.1 Motivation and objective

Applying reversible light control on oligonucleotide hybridization can be achieved by incorporation of photochromic moieties like azobenzene into the strands. As stated before, the way of incorporating the azobenzene is of utmost importance, as the linker system needs to position the favored *trans*-state in the least disturbing way in the base pairing region. Upon *trans*-to-*cis*-isomerization, the linker needs to support the prying movement of the distal aromat to weaken hydrogen bonds of adjacent basepairs. During the isomerization, the evasion of the azobenzene from the base pairing region needs to be prevented, otherwise the movement will not be translated in a desired motion to weaken adjacent base pairing but rather be in vain. The utilization of azobenzene *C*-nucleosides has shown that the ribosidic linker is rigid enough to allow photocontrol of duplex stability even at room temperature, whereas for acyclic linkers like *t*Azo elevated temperatures are needed. Nevertheless, azobenzene *C*-nucleosides have the drawback of decreasing duplex stability even in favored *trans*-state to a noticeable amount. The reason for this could be, that the rigid ribosidic linker combined with the end-to-end distance of a *trans*-azobenzene shifts the distal aromat far into the opposing base stacking region causing significant (Fig. 83).

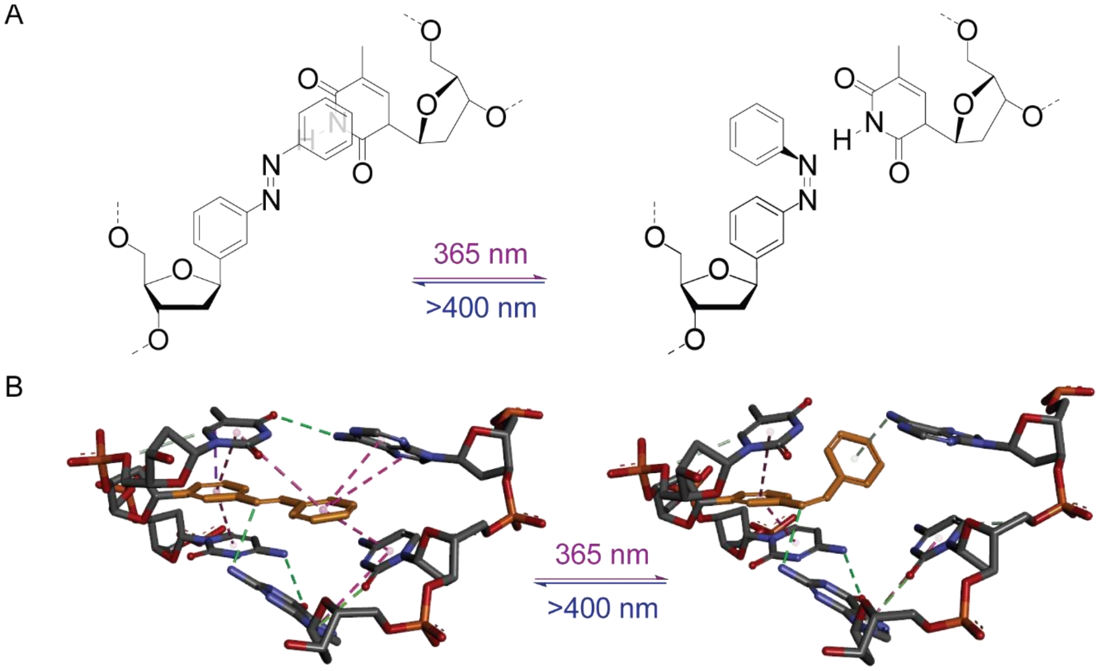

Fig. 83 Schematic drawing of an azobenzene C-nucleoside opposing a cytosine in a duplex (A) and the same situation with the closest neighboring basepairs included as three-dimensional schematic representation animated with Discovery

Studio Visualizer (B). Azobenzene in orange, π-interactions in dashed purple lines, hydrogen bonds in dashed green lines, other interactions as dashed grey lines.

To decrease the steric repulsion caused by the azobenzene *C*-nucleoside, a conformationally locked azobenzene *C*-nucleoside (LNAzo) has been synthesized and incorporated into oligonucleotides. As described in chapter 3, the conformational lock should increase binding affinity of the strands and should prevent conformational changes in the ribosidic linker during azobenzene isomerization. It could be shown that LNAzo could improve overall duplex stability and photocontrol to a certain extend in the different oligonucleotide test systems. As LNA units promote the formation of an A-helical structure, the biggest improvements could be seen in DNA-RNA and RNA-RNA duplexes. Unfortunately, the improvement for B-helical DNA systems was rather limited, as it could be shown by UV/vis-absorption and melting point comparison.

As it appears that the ribosidic linker is only capable to improve duplex stability to a limited extend, modification of the photochromic moiety would be the next logical step. Two major features on the interaction pattern of the azobenzene could be targeted for improvement. First, as shown in Fig. 83, the distal aromat of the azobenzene moiety is responsible for the steric repulsion in the opposing strand, as it is positioned in the base pairing region. A major improvement could be achieved, if the distal aromat would be positioned in the open space of either major or minor groove and only would shift into the confined base pairing region upon *trans*-to-*cis*-isomerization. This would cause a great difference of steric demand of the distal ring between the two photoisomers, which would improve duplex stability of the *trans*-state and photocontrol of duplex stability. It needs to be noted here, that shifting the distal aromat from the less restricted space of either major or minor groove back to the base pairing region would have a particular activation barrier, as attractive interactions of the nucleobases need to be weakened or broken in order to migrate back into the base pairing region. The rigidity of the ribosidic would be needed here to support the translation of photonic energy into a useful kinetic motion of the azobenzene in order to overcome the activation barrier. The second feature standard azobenzene is missing, is that azobenzene can only partake in aromatic interaction to the neighboring nucleobases, which is only a small contribution to all the attractive interactions of two oligonucleotides. If the photoswitch could also partake in hydrogen bonding within the duplex, the additional attractive interactions would increase duplex stability and would compensate the incorporation of unnatural moieties. It needs to be taken into consideration, that hydrogen bonding capabilities of the two photoisomers should differ in quality as much as possible. Unfortunately, the estimation of all possible interactions of the two photoisomers in a duplex is difficult to predict, even with computational methods. The amount of interaction partners involved and the amount of energetically possible conformations makes the computational evaluation of the situation rather complicated.

In this regard, a photoswitch needs to be found, which can be incorporated as *C*-nucleoside, can shift a sterical demanding residue from the open major or minor groove into the confined space of the base pairing region. In addition, a photoswitch, which is capable of forming hydrogen bonds would improve duplex stability and could compensate the deformation caused by its own incorporation.

4.2 Results and discussion

4.2.1 Choosing a suitable photochromic nucleobase-modification

As stated before, the ability to contribute to hydrogen bonding with nucleobases in closest proximity would diminish the steric disturbance caused by the incorporation of a photoswitch into an oligonucleotide. An elegant way to create such a compound would be the combination of a nucleobase and a photoswitch. Photochromic derivatives of natural nucleobases offer a great tool for applying light control to base pairing. The nucleobase moiety provides attractive interaction for hybridization, whereas the photochromic moiety can alter the interaction upon irradiation due to conformational changes. Several photoswitches exist to choose from, as they all come along with their genuine features. Spiropyrans imply a great morphological change upon its isomerization to form merocyanines, unfortunately they can decompose in water and are not very fatigue resistant.[42,43] Diarylethenes offer more stability in aqueous solutions, but undergo no significant morphological changes upon isomerization.[38] Stilbene modifications of purines and pyrimidines are well described. The *cis*-*trans*-photoisomerization of stilbene-modified nucleobases have been used in photochemical studies,[34,35,195] to regulate G-quadruplex formation[196] and even as a photoresponsive 5'-cap structure to control protein expression.[37] Unfortunately, *trans*-to-*cis*-photoisomerization requires wavelength of around 310 nm, which could cause photodamage in biological tissue.

Azobenzenes have a great potential for oligonucleotide applications. They are easily accessible,[197] photophysical properties can be custom-tailored to the application requirements[173] and therefore have already been used in numerous studies involving oligonucleotides.[88] However, azobenzene-modified nucleobases are scarce and not well-described to date. Wang *et al.* added a thymidine-like residue to the distal aromat of an azobenzene *C*-nucleoside to allow hydrogen bonding in the *trans*-state, whereas the *cis*-state decreases base pairing affinity by sterical hindrance (Fig. 84A). It could be shown to regulate oligonucleotide hybridization, although the large photochromic nucleobase of so-called dzT causes a lot of sterical hindrance in the base pairing region as it spans the entire base pairing region (Fig. 84B).[198]

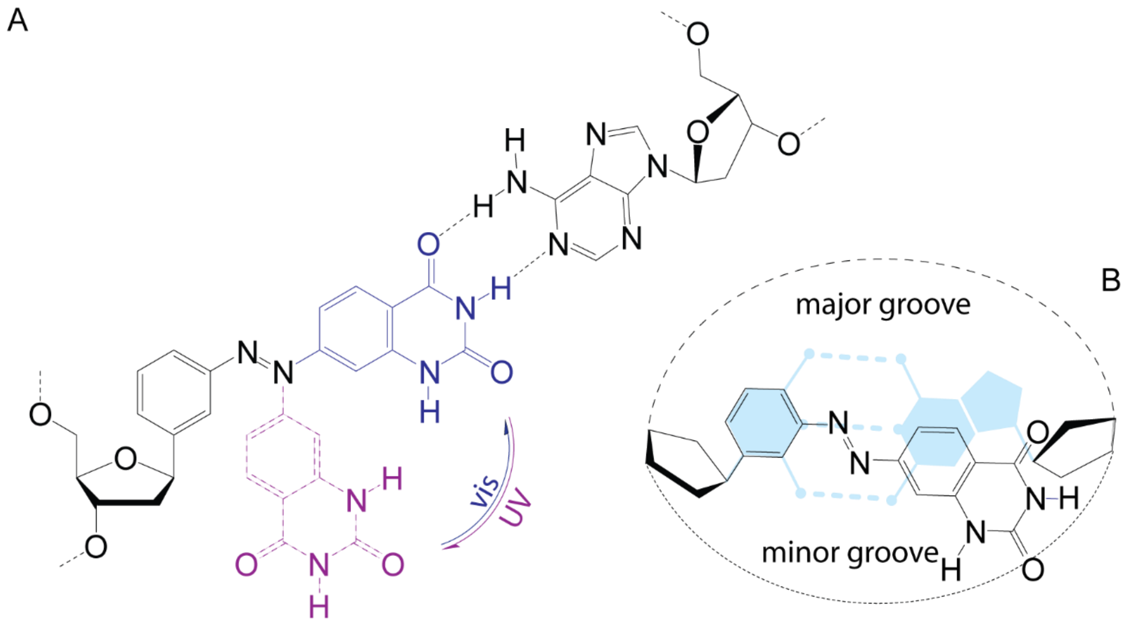

Fig. 84 Artificial photochromic thymidine-analogous C-nucleoside dzT and its proposed mechanism of action (A). The photochromic moiety of dzT spans the entire base pairing region and therefore causes a lot of steric stress in the duplex (B).

Recently, 2-phenyldiazenyl-adenosine has been developed and used as a photoresponsive 5'-cap *in vivo* to control protein expression time resolved.[199] Upon *trans*-to-*cis* isomerization expression of squint protein in zebrafish embryos could be increased 7.1 times, demonstrating that the position of the distal aromat on the 2-phenyldiazenyl-adenosine has great impact on enzyme recognition of the 5'-cap region. Although demonstrated for enzymatic interactions, the effect on oligonucleotide hybridization stays unclear to this date. It can be assumed, that 2-phenyldiazenyl substituted purines could fulfill all requirements a photochromic nucleobase for manipulating duplex stability has. They can contribute to base pairing in a certain extend in the *trans*-state, while in the *cis*-state the distal aromat would position itself in between the bases causing a bulge in the duplex, thereby lowering duplex stability (Fig. 85). For these reasons, investigation on the influence of 2-phenyldiazenyl purines shall be synthesized and influence of their photoisomers on duplex stability shall be explored.

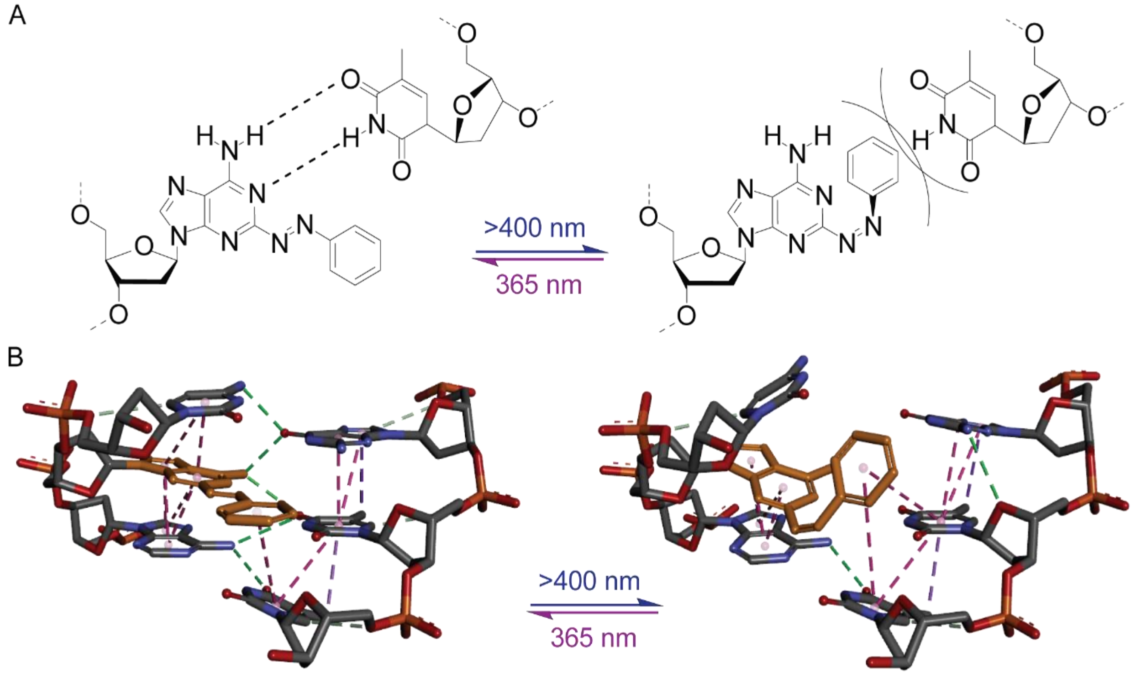

Fig. 85 Schematic drawing of 2-phenyldiazenyl-2’-deoxyadenosine opposing a 2’-deoxythymidine in a duplex (A) and the same situation with the closest neighboring base pairs included as three-dimensional schematic representation animated with Discovery Studio Visualizer (B). 2-Phenyldiazenyl-adenosine in orange, π-interactions in dashed purple lines, hydrogen bonds in dashed green lines, other interactions as dashed grey lines.

4.2.2 Synthesis of 2-phenyldiazenyl purine nucleotides

In order to prepare 2-aryldiazenylpurine compounds by Mills-reaction, the reaction of an electron deficient amine and a nitroso-compound under acidic conditions is needed. The direct Mills coupling of 2-amino group of 2'-deoxyguanosine and nitrosobenzene was not possible under any condition, screening several acetic acid concentrations and reaction temperatures. The reason for this is an electron rich aniline derivative is needed, so that the lone pair of the amino function can perform a nucleophilic attach onto the acid activated nitroso group of nitrosobenzene. Apparently, guanosine is to electron deficient at the *C*2-position, so that nucleophilic attack is not possible this way. To circumvent this issue, a conversion into 2-nitroso purines is needed. In analogy to the approach of Wanner *et al.*[200] 2-nitrosopurines were prepared from standard 2'-deoxyadenosine (Fig. 86).

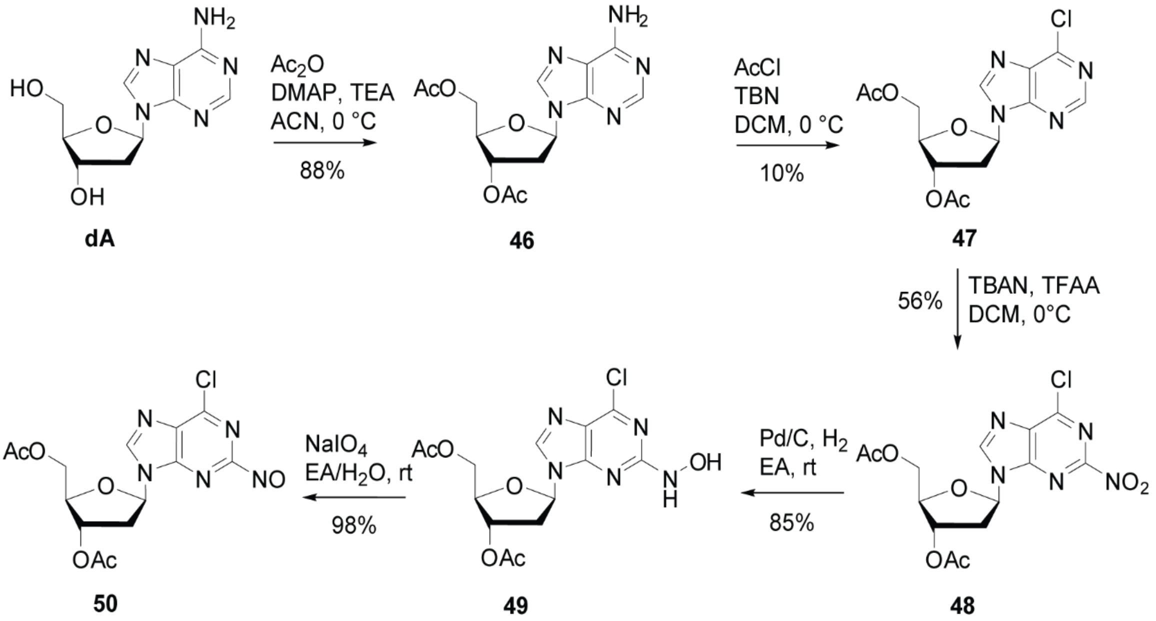

Fig. 86 Synthesis of protected 2-nitroso-4-chloropurine ***50*** *starting from commercially available 2'-deoxyadenosine (****dA****).*

The acetylation of 2'-deoxyadenosine under standard conditions went neat giving compound **46** with 88% yield. The chlorination of the *C*4-position appeared to be problematic. Using phosphoryl chloride as standard reagent for purine chlorination did only result in compound decomposition. For this reason *in situ* nitration of the *C*4-position and subsequent substitution for chlorine donated by acetyl chloride has been performed, although only yielding 10% of chlorinated product **47**. Several methods have been developed for installing nitroso groups on aromats for subsequent Mills-reaction,[197] Wanner *et al.* established a redox-method suitable for sensitive compounds like protected nucleosides. Nitration on the *C*2-position under acidic conditions to give compound **48** provides the necessary nitrogen atom on this position. The 2-nitro group is then reduced under hydrogen atmosphere in presence of palladium on charcoal to give highly reactive hydroxylamine **49**. It can be purified by direct phase column chromatography for analytical purposes, but it is suggested to be used immediately for the follow-up reaction. A subsequent oxidation with sodium periodate in a bifacial solvent mixture gave the 2-nitroso compound in almost quantitative yield. Although being susceptible to decomposition, the nitroso-compound is shelf stable for several days under argon atmosphere. The reason for this might be, that the 2-nitroso purines tend to dimerize in concentrated solutions and in solid state and are thereby less reactive.[199,200] From there on, Mills-reaction of protected nitrosopurine **50** could be coupled with aniline in acetonitrile with catalytic amounts of acetic acid to form 2-phenyldiazenyl-4-chloropurine **51** with 70% yield (Fig. 87).

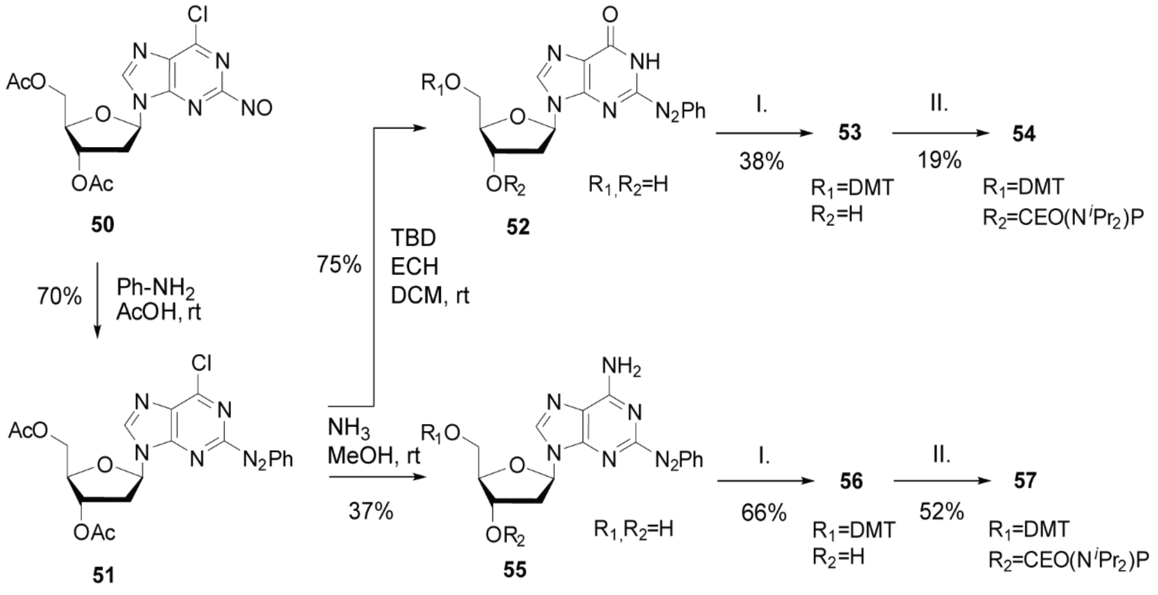

Fig. 87 Synthesis of 2-phenyldiazenyl-2'-deoxyguanosine and -adenosine from protected 2-nitroso-4-chloropurine and subsequent preparation of corresponding phosphoramidites for solid phase synthesis (I.: DMTCl, py, 0 °C → rt; II.: CEO(N^{i}Pr$_2$)PCl, DIPEA, DCM, rt).

In contrast to previously published synthetic approaches,[199,200] conversion of the *C*4-chloride into corresponding natural functionalities was set to be carried out after Mills-reaction. With this, late stage modification could be established, so that an universal synthetic route could be established for individualization according to desired application from an unspecified stock-compound with as few steps as possible. The conversion chloropurine **51** to the guanosine analogue could be commenced with 3-hydroxyproprionitrile and 1,5,7-triazabicyclo(4.4.0)dec-5-ene as catalytic base to give compound **52** with 75% yield. The ammonolysis of chloropurine **51** in methanol on the other hand yielded adenosine analogue compound **55** with only 37% yield. Formation of an unidentified side product limited the product formation here, which could not be tackled with additional amounts of ammonia-saturated methanol. The benefit of acetyl-protection of sugar alcohols could be seen in both reactions, as chloride-conversion was always accompanied by acetyl cleavage. With this, no additional deprotection reaction was needed to give free nucleosides **52** and **55**. To incorporate 2-phenyldiazenylpurines into oligonucleotides, corresponding phosphoramidites have been prepared by tritylation and subsequent phosphitylation under standard conditions. Additional protection of the nucleobase functionalities to protect them from solid phase synthesis conditions was not necessary, as mass spectra of synthesized oligonucleotides showed (see chapter 5.2).

4.2.3 Influence of 2-phenyldiazenyl purines in a DNA test system

As for evaluation of the LNAzo nucleotides, single 2-phenyldiazenyl purine modifications have been incorporated into a 10mer DNA test sequence in order to estimate the influence of a single modification. Again, test duplexes were equipped with a FAM/DAB fluorophore-quencher-pair, to gain melting point data from temperature dependent fluorescence read-out in addition to UV/vis absorption. As the modified purines should form hydrogen bonds with their natural counterparts according to Watson-Crick-base pairing, modified purines replaced their analogues (dA or dG) in the center of the duplex (Fig. 88). In addition, hybridization of the 2-phenyldiazenyl purine modified DNA strands to test the effect of a dimer motif in a 10mer duplex has been carried out. As a reference, unmodified wild type duplex and the mAzo-modified duplex has been used to set the melting points into perspective.

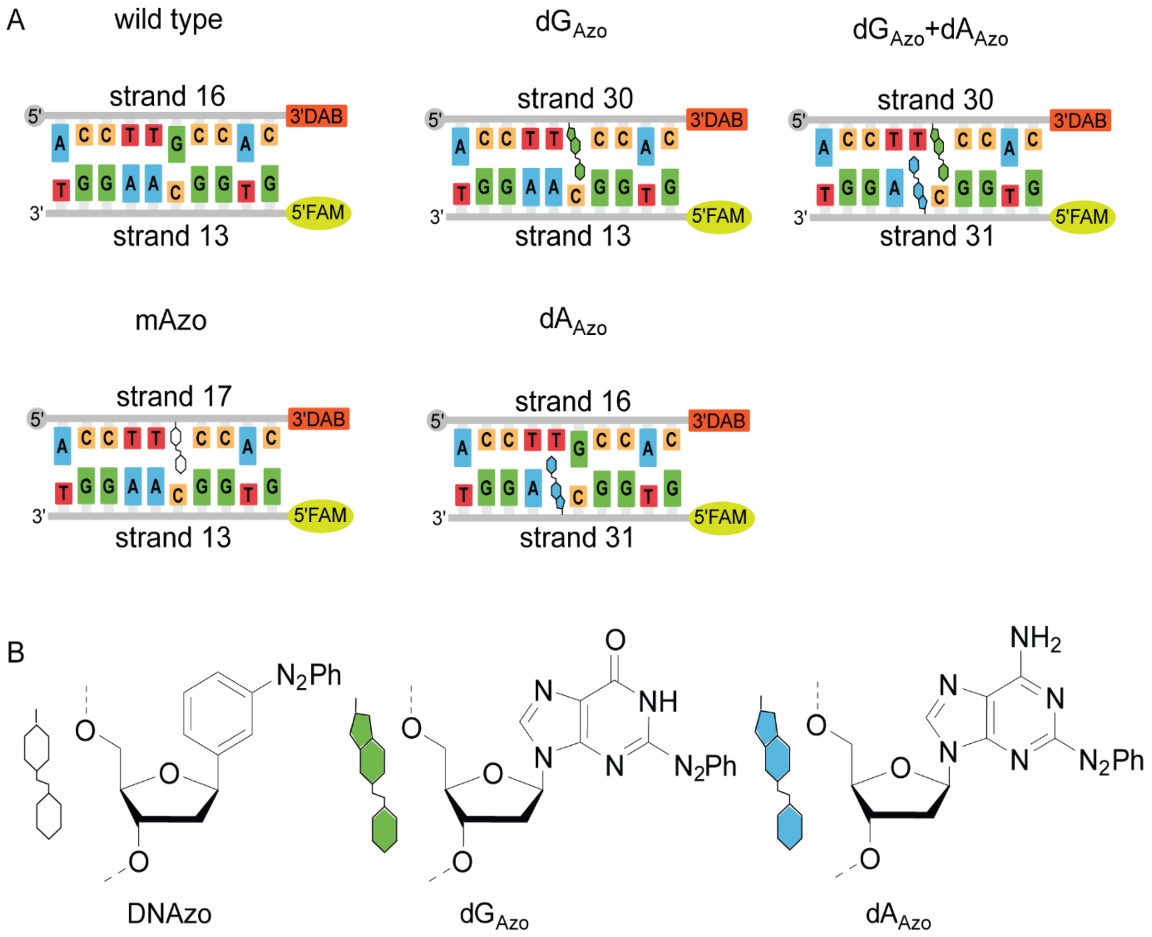
A
wild type
strand 16
5'
3'DAB
A C C T T G C C A C
T G G A A C G G T G
3'
5'FAM
strand 13
dGAzo
strand 30
strand 13
dGAzo+dAAzo
strand 30
strand 31
mAzo
strand 17
strand 13
dAAzo
strand 16
strand 31
B
N2Ph
O
O
O
DNAzo
O
N
NH
N
N
N2Ph
dGAzo
NH2
N
N
N
N
N2Ph
dAAzo

Fig. 88 DNA strands used in this study (A), and corresponding modifications (B).

As it could be identified by UV/vis-spectroscopy of free nucleosides **52** and **55**, the highest difference in photostationary distribution of *cis*- and *trans*-photoisomers could be achieved by irradiation with 365 nm for *cis* and 455 nm for *trans* (the spectra are shown in the experimental part, section 5.3.3).

From the UV/vis-absorption data it could be seen that mAzo as a reference system decreases the melting point by 16.4 °C compared to the unaltered wild type (Fig. 89). This again shows the great impact an azobenzene *C*-nuceoside has on duplex stability. Exchanging the mAzo residue for the guanosine-analogue dG$_{\mathrm{Azo}}$, melting point increased by 3.4 °C, incorporating adenosine-analogue dA$_{\mathrm{Azo}}$ into opposing position led to an overall increase of 7.5 °C. This appears to fit expectations, as 2-phenyldiazenylpurines should increase affinity with their own base pairing capabilities. The melting points for dG$_{\mathrm{Azo}}$ are slightly lower than when dA$_{\mathrm{Azo}}$ is used. This is comprehensible, since introducing the phenyldiazenyl moiety replaces the *C*2-amine in 2'-deoxyguanosine, which reduces hydrogen bonding capabilities. 2'-deoxyadenosine carries no functionality on the *C*2-position, so that addition of the phenyldiazenyl moiety does not alter hydrogen bonding capabilities. The influence of the photoswitching for literature known mAzo residue in this sequence context is a difference of 1.5 °C between the photostationary states at 455 nm and 365 nm (ΔT_{M}). The melting point difference is only 0.5 °C for dG$_{\mathrm{Azo}}$ and 1.3 °C for dA$_{\mathrm{Azo}}$. The photoisomerization of dA$_{\mathrm{Azo}}$ is less effective than for mAzo, but influences hybridization more than dG$_{\mathrm{Azo}}$. As final test, dG$_{\mathrm{Azo}}$- and dA$_{\mathrm{Azo}}$-including strands were hybridized to test their joint influence in a so-called dimer-motif. The melting point is even lower than for mAzo by 2.6 °C and photoswitching implies as much difference as dG$_{\mathrm{Azo}}$ alone. CD-spectroscopy revealed that the strongest difference in helicity between the photostationary states could be seen for DNAzo (see experimental part, section 5.5.2). 2-phenyldiazenylpurines did not alter B-DNA helicity compared to the wild type significantly, which might give a hint why they do not influence hybridization behavior in the same extend as DNAzo. In addition to measuring melting curves with UV/vis-absorbance, temperature-dependent fluorescence was measured in a real-time PCR device for all duplexes in a concentration range of 0.1 µM to 5 µM. The results were in overall accordance with values from UV/vis-absorbance. Some of the fluorescence curves from dG$_{\mathrm{Azo}}$ and most of the curves from dG$_{\mathrm{Azo}}$+dA$_{\mathrm{Azo}}$ could not be interpreted due to their signal to noise ratio and were therefore excluded. Fluorescence-based melting points are listed in the experimental part, section 5.7.

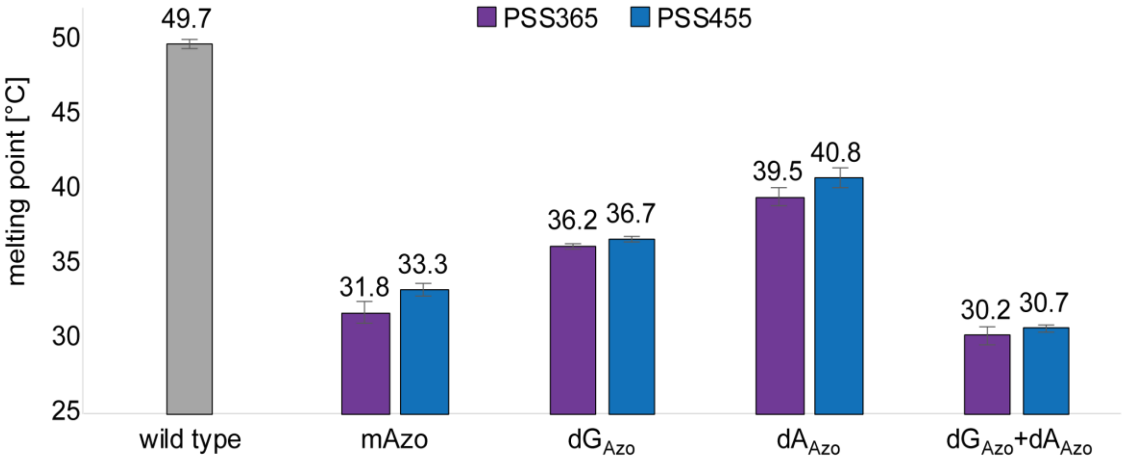

Fig. 89 Melting points of DNA-duplexes shown in Fig. 88, gathered by temperature dependent UV/vis-absorption measurement.

To explain the lack of sufficient photocontrol caused by 2-phenyldiazenylpurines a detailed look into the possible configurations of the distal aromat needs to be taken. Although been shown as planar and linear, *trans*-azobenzenes can exist in two different conformations within a duplex. As the distal aromat is shifted in parallel to the proximal aromat, it can be shifted towards the center of the duplex (the base pairing region) or to the outside. For clarification, the terms *exo*- or *endohelical* shall be used from here on (Fig. 90). In both exo- or endo-helical *trans*-states the distal aromat is positioned in the minor groove, although being closer to the opposing nucleobase in the endo- rather than the exo-state. During *trans*-to-*cis* isomerization, the distal aromat flips into familiar *cis*-conformation according to one of the mechanisms described in chapter 1.2. As it is not possible, that distal and proximal aromat residue in one plane, the distal aromat undergoes a shift above or below the plane of the proximal aromat, becoming axially chiral. Due to the right-handedness of B-DNA, only *P*-*cis*-conformations are allowed, since *M*-*cis*-conform distal aromats would pierce directly into the ribose moieties of the strands. Considering all proposed isomerization mechanisms of azobenzene, a transition of endo-*trans*-conformation can only result in endo-*P*-*cis*-conformation and exo-*trans*-conformation can only result in exo-*P*-*cis*-conformation. Since the energy harvested by photon absorption can only be translated into a useful kinetic motion in the endo-states, exo-states do not contribute photoresponsive duplex stability control and their formation should be avoided. It appears to be more likely, that 2-phenyldiazenyl purines adapt the exo-*trans*-conformation, as it appears to be less sterically hindered than corresponding endo-conformation, thus resulting in a futile switching event. Modification of the distal aromat, as for example the installation of substituents partaking in hydrogen bonding, might change the situation, but such endeavors have not been made in this project.

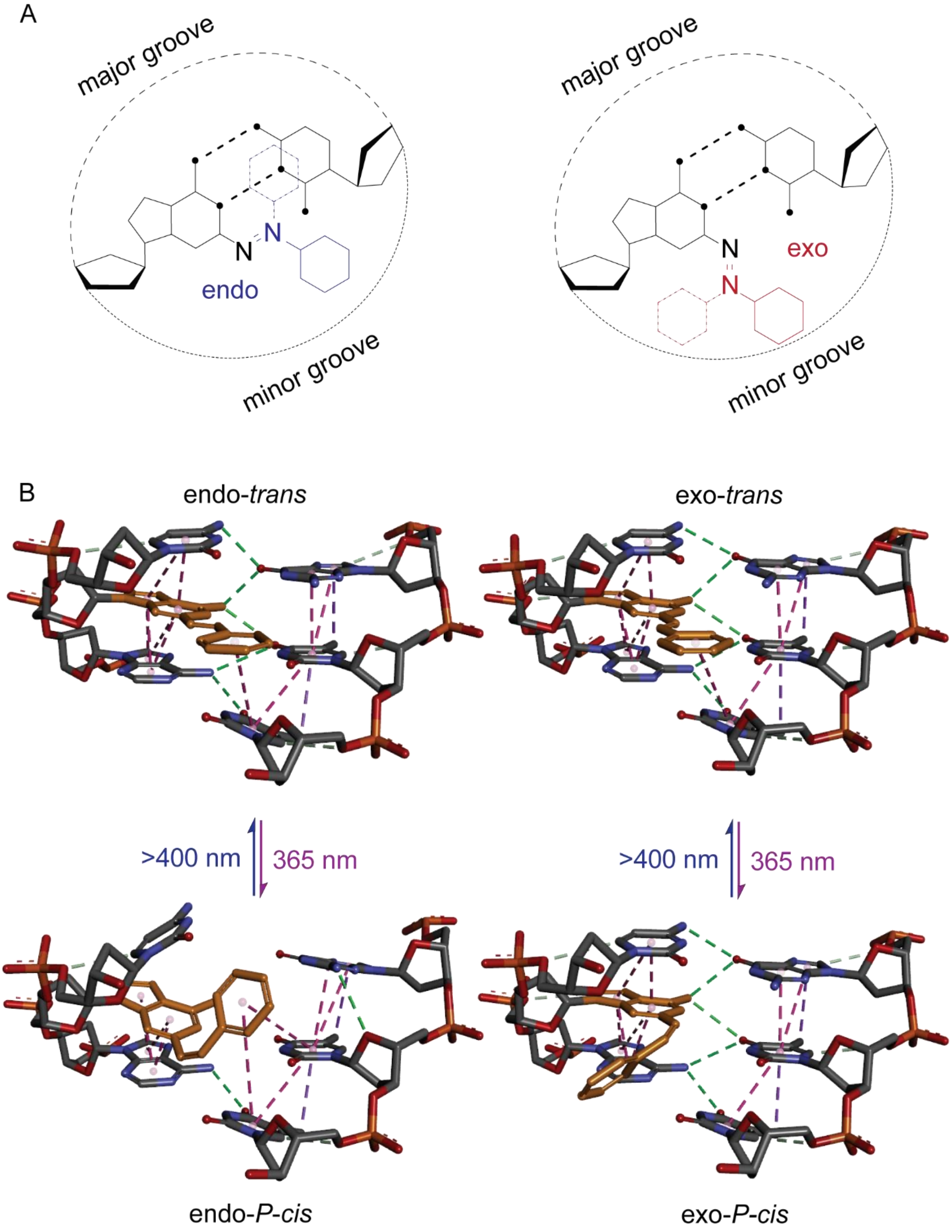
A
major groove
minor groove
N
N
endo
major groove
minor groove
N
N
exo
B
endo-*trans*
exo-*trans*
>400 nm
365 nm
>400 nm
365 nm
endo-*P*-*cis*
exo-*P*-*cis*

Fig. 90 Possible conformations of the distal aromat of a 2-phenyldiazenyl purine during base pairing in a DNA duplex (A). The same situation with the closest neighboring basepairs included as three-dimensional schematic representation animated with Discovery Studio Visualizer (B). 2-Phenyldiazenyl adenosine in orange, π-interactions in dashed purple lines, hydrogen bonds in dashed green lines, other interactions as dashed grey lines.

4.3 Summary and outlook

The reversible light control of duplex formation can be achieved by incorporation of photochromic molecules like azobenzene into the oligonucleotide strands. The *trans*-azobenzene intercalates in between adjacent nucleobases causing minimal perturbation, whereas the *cis*-azobenzene applies conformational stress on its surrounding by increasing its steric demand. The linkage between chromophore and oligonucleotide plays a major role, as it has to provide a rigid base for the isomerization movement and needs to position the azobenzene into the base pairing region for optimizing its effect on base pairing. Azobenzene *C*-nucleotides fulfill these demands, but imply the drawback of serious steric repulsion even in favored *trans*-state. The rigid ribosidic linker and the end-to-end distance of *trans*-azobenzene cause the distal aromat to be shifted deep into the opposing base stacking region. To diminish steric repulsion, conformationally locked *C*-nucleosides have been employed. It could be shown that duplex stability and photocontrol of it could partly be improved by so-called LNAzo β unit. A serious improvement could be shown in an RNA context, whereas duplex stability and its photocontrol only slightly improved for DNA. This is reasonable, as the employment of LNA units in oligonucleotides promote A-helix formation.

As LNAzo β improved duplex stability only in a limited amount, further improvements on the backbone have been declared futile and focus shifted onto optimization of the chromophore. First, the azobenzene as it is installed on the ribosidic linker decreases duplex stability by forcing its distal aromat deep into opposing base stacking region. It would be an improvement, if in favored *trans*-state the distal aromat would be positioned in the less confined space of either major or minor gap and only upon isomerization would shift into base pairing region. Second, the azobenzene itself is not able to contribute to attractive interactions aside from relatively weak π-interactions to adjacent nucleobases. A reasonable improvement could be expected, if the chromophore could partake in hydrogen bonding, as they make up a major amount of attractive interactions in oligonucleotides.

For those apparent reasons, 2-phenyldiazenyl-modified purines have been selected as targets. They combine the ability to contribute to hydrogen bonding of nucleobases with the photochomicity of azobenzenes. Both 2'-deoxyadenosine- and 2'-deoxyguanosine-analogue photoswitches dA_{Azo} and dG_{Azo} have been synthesized and incorporated into 10mer DNA test systems by solid phase synthesis. It could be shown, that duplex stability could be increased compared to established azobenzene *C*-nucleoside. The improvement was stronger for dA_{Azo} than for dG_{Azo} as in the case for guanosine the amino function on the *C*2-position had to be replaced by the phenyldiazenyl function, reducing its ability to form hydrogen bonds. Photocontrol of duplex stability caused by 2-phenyldiazenyl purines was rather limited. A reason for this could be the positioning of the distal aromat within the duplex, which can be close to the opposing nucleobase (endo-helical) or in greater distance (exo-helical). The exo-helical conformation of the *trans*-isomer can only switch to the exo-*P*-*cis*-conformation, which relocates the distal aromat in the minor groove, without significant impact on duplex stability. Nevertheless, the general idea of creating a photoswitch, which can partake in hydrogen bonding and which switches its distal aromat from less-confined minor groove into the confined base pairing region is promising. As an additional criterium, it should be assured, that the photoswitch can not exist in more than one isoforms, especially if the quality of photocontrol provided by these isoforms is as heterogenous as for the 2-phenyldiazenyl purines. An emerging, but still underestimated class of photoswitches could have the potential to fulfill all mentioned criteria.

Hemithioindigos (HTI) are a class of photoswitches derived from the indigo dye and undergo *E*/*Z*-isomerization upon irradiation or under thermal relaxation, similar to azobenzenes.[33] Their high stability, photostationary distributions and red shifted absorption spectra make them a promising class of photoswitches for biological applications. Hemithioindigos have previously been used to manipulate hydrogen bond formation in peptides and as photoinducible inhibitor of lipoxygenase LOX-12/15.[201,202] As hemithioindigo *C*-nucleosides are not capable to undergo conformational changes other than the described *E*/*Z*-photoisomerization they would be optimal for photocontrolling duplex stability in oligonucleotides (Fig. 91A). As photochemical and sterical features of hemithioindigos accompany each other in this context, other modifications than standard phenyl substitution might be interesting as well. In the best case, a distal aromat could be selected, which is planar enough to intercalate into minior groove in favored *Z*-state, but would cause most possible steric repulsion in the *E*-state. In addition, it has to be considered, that attractive interactions can commence as soon as distal aromat is brought into proximity of the base pairing region. For this reason a julolidine-substituted hemithioindigo could be of particular interest (Fig. 91B). Compared to phenyl-substituent, a julolidine-substituent provides the same amount of aromatic π-interaction possibilities, with the steric demand being three times as high. In addition, as the wavelength of *Z*-to-*E*-isomerization is between 450 and 500 nm for the julolidine derivative compared to the phenyl derivative, the possibility for *in vivo* applications comes at hand (Fig. 91C and D). Even the fast thermal relaxation into favored *Z*-state with a half-life time of 9 minutes at room temperature could be used to create oligonucleotide therapeutics or DNA-nanostructures, which are only active during irradiation.[203]

Planning the development of novel molecules to control duplex stability with light can always lead to failure, if the task is not elucidated from every possible perspective. Even then, small unimportant appearing details can decide over the fate of a project, might it be the conformation of the distal ring of a 2-phenyldiazenyl purine or the fact, that hydrogen bonding can change the entire isomerization mechanism in hemithioindigos.[204] Nevertheless, every step taken to broaden the knowledge of mankind is worth taking, even if it might lead nowhere.

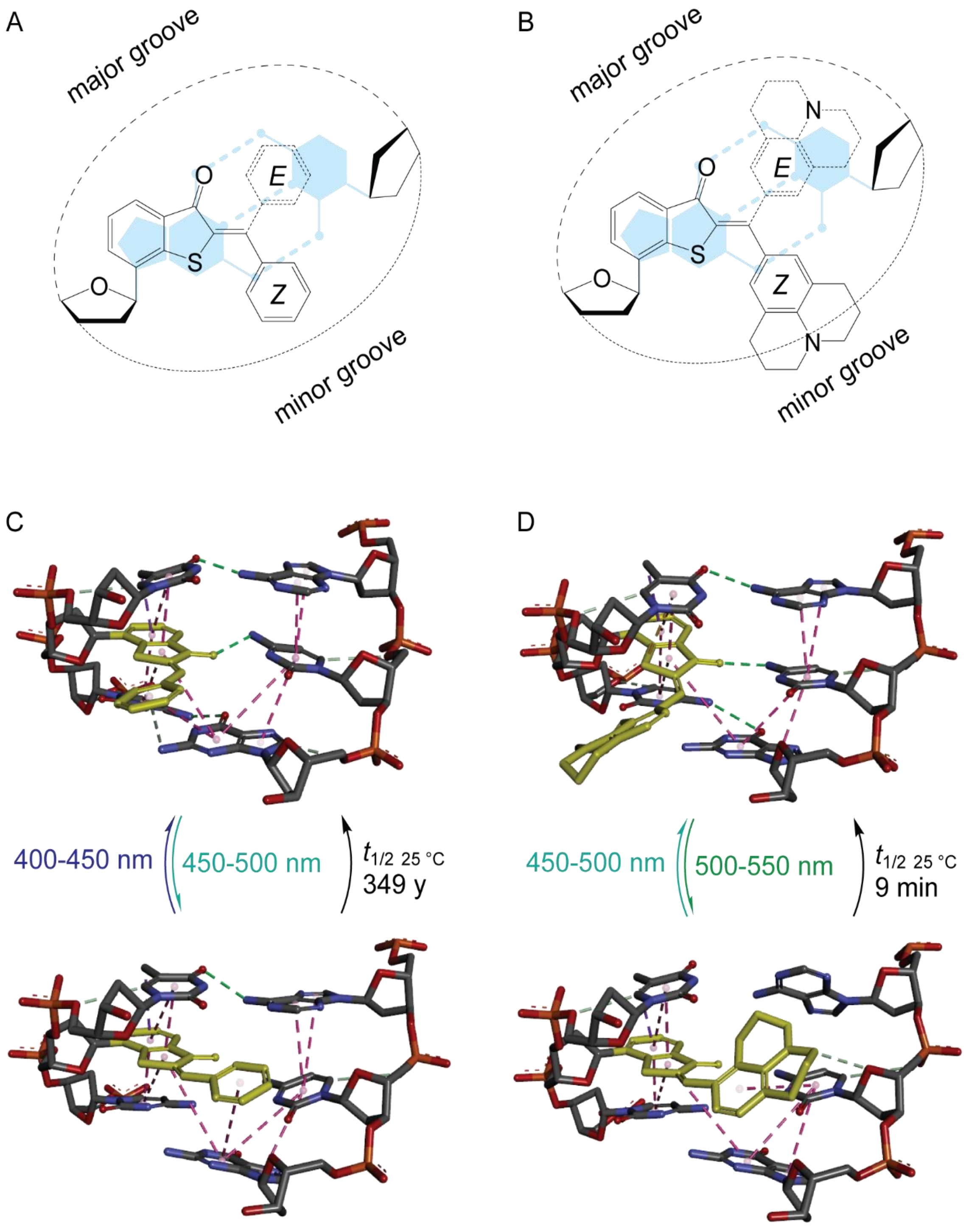
A
major groove
O
E
S
Z
O
minor groove
B
major groove
N
O
E
S
Z
O
N
minor groove
C
D
400-450 nm
450-500 nm
$t_{1/2\ 25\ °C}$
349 y
450-500 nm
500-550 nm
$t_{1/2\ 25\ °C}$
9 min

Fig. 91 Schematic positioning of phenyl- (A) and julolidine-substituted HTI (B) integrated into an oligonucleotide duplex. The same situation with the closest neighboring basepairs included as three-dimensional schematic representation animated with Discovery Studio Visualizer for phenyl- (C) and julolidine-substituted HTI (D). HTI in yellow, π-interactions in dashed purple lines, hydrogen bonds in dashed green lines, other interactions as dashed grey lines.

5. Experimental section

5.1 Chemical syntheses

5.1.1 Devices and materials

Conditions

If necessary, reactions were carried out under Schlenk conditions, which means only dry solvents stored over molecular sieve were used in oven-dried Schlenk glassware. In these cases, reactions were carried out under argon atmosphere to exclude moisture.

Solvents

Dry solvents were purchased from the company Acros and used without any further purification in the synthesis. If not stated otherwise, solvents of technical grade were used.

Reagents

All chemicals were purchased from *Sigma-Aldrich, Fluka, Alfa Aesar, TCI, ChemPur, Carbosynth* or *Fluorochem* and used without any further purification in the synthesis.

NMR-Spectroscopy

The NMR spectra were measured on the devices DPX 250, AV 300, AV 400 and AV 500 from Bruker. As suitable solvents for the NMR sample DMSO-*d*6 (^{1}H, δ = 2.49 ppm, ^{13}C, δ = 39.52 ppm) and $CDCl_3$ (^{1}H, δ = 7.26 ppm, ^{13}C, δ = 77.16 ppm) were used. The chemical shift is given in ppm. The abbreviations of the multiplicity of the signals are as follows: singlet = s, doublet = d, triplet = t, quartet = q, quintet = qn, multiplet = m. Corresponding combinations are used deductively, for example, dt for doublet of triplets.

TLC

To check the reaction progress of all reactions, thin layer chromatography plates silica gel 60 F254 on aluminum foil from Macherey-Nagel were used. The evaluation was performed visually using a UV light at 254 nm or 365 nm or with staining reagents.

Column-Chromatography

Purification by column chromatography was performed using silica gel 60 (particle size: 40-63 µm) from Macherey-Nagel and technical solvents.

Mass-Spectrometry

ESI-MS were measured on a VG Platform II Fisons and high resolution mass spectra were measured on a MALDI LTQ Orbitrap XL from Thermo Fisher Scientific. Mass spectra were measured by the MS service department of the Goethe University Frankfurt (Matthias Brandl, Andreas Münch, Uwe Hener and Simon Zenglein), who we would like thank for their work.

5.1.2 Chemical syntheses of the DNA-minicircle project

2’-Deoxy-*D*-ribono-1’,4’-lactone **1**

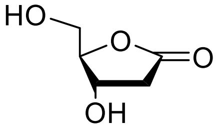

1

$C_5H_8O_4$

132.12 g/mol

Synthesis has been carried out according to literature.[205] To an ice-cooled solution of 2’-Deoxy-*D*-ribose (30.0 g, 223.8 mmol) in 200 mL Water, bromine (40 mL, 1.56 mol, 7.0 eq) was added via dropping funnel and stirred for 8 hours at room temperature. The exceeding bromine was removed by pressurized airflow into the solution and deactivated by passing through sodium thiosulfate solution. The pale yellow to colorless solution was neutralized by addition of sodium carbonate before removal of the solvent under reduced pressure. The crude product was adsorbed on silica and subjected to flash column chromatography (EA/MeOH 9:1) to afford the product as colorless oil. Yield: 21.41 g (0.16 mol, 73%), R_f = 0.57 (EA/MeOH 9:1), Spectroscopic data were in accordance with literature.[205] ^{1}H NMR (250 MHz, DMSO-d_6) δ = 5.48 (d, *J* = 4.1 Hz, 1H, 3‘-OH), 5.05 (t, *J* = 5.4 Hz, 1H, 5‘-OH), 4.35 – 4.16 (m, 2H, 3‘-H + 4‘-H), 3.60 – 3.50 (m, 2H, 5‘-H), 2.80 (dd, *J* = 17.7, *J* = 2.4 Hz, 1H, 2‘-H), 2.22 (dd, *J* = 17.7, 2.4 Hz, 1H, 2‘-H).

3’,5’-*O*-Di(triisopropylsilyl)-2’-deoxy-*D*-ribono-1’,4’-lactone **2**

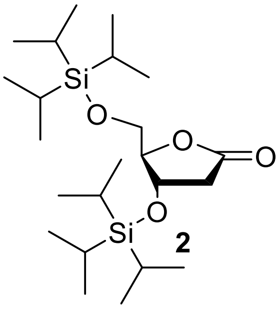

2

$C_{23}H_{48}O_4Si_2$
444.80 g/mol

Compound **1** was dissolved with 12.358 g (181.631 mmol, 3.5 eq) imidazole in 60 mL dry DMF. 22 mL (103.789 mmol, 2.0 eq) triisopropylsilyl chloride were added and the reaction was left to stir over night at room temperature. Upon addition of 10 mL methanol, the reaction was evaporated to dryness, then dissolved in ethyl acetate. The organic phase was washed successively with 0.1 M HCl, saturated $NaHCO_3$ solution and water. After drying over sodium sulfate, solvent was evaporated to dryness and crude product was subjected to flash column chromatography (Cy/EA 19:1→100% EA) to afford product as colorless oil. Yield: 22.991 g (51.745 mmol, 99%), R_f = 0.67 (cyclohexane/ethyl acetate 4:1), ^{1}H NMR (400 MHz, DMSO-*d*$_6$) δ 4.59 (dt, *J* = 6.3, 2.0 Hz, 1H, 4’-H), 4.38 (dd, *J* = 5.2, 3.4 Hz, H, 3’-H), 3.85 (qd, *J* = 11.5, 3.6 Hz, 2H, 2’-H), 2.96 (d, *J* = 6.4 Hz, 1H, 5’-H), 2.36 (d, *J* = 2.3 Hz, 1H, 5’-H), 1.40 (s, 2H, CH), 1.15 – 0.96 (m, 18H, CH_3). ^{13}C NMR (101 MHz, DMSO-*d*$_6$) δ 175.03, 87.72, 69.58, 62.71, 26.32, 17.69, 17.68, 17.66, 17.64, 11.39, 11.23. ^{29}Si NMR (60 MHz, DMSO-*d*$_6$) δ 14.91, 14.83. HRMS: Calculated for $C_{23}H_{48}O_4Si_2Na$ ($[M+Na]^+$) *m/z* 467.29833, found *m/z* 467.7608.

3’,5’-*O*-((1,1,3,3-Tetraisopropyl)disiloxanediyl)-2’-deoxy-D-ribono-1’,4’-lactone **3**

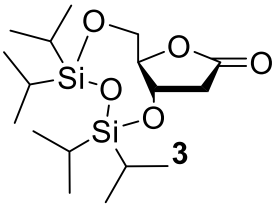

3

$C_{17}H_{34}O_5Si_2$
374.62 g/mol

Synthesis has been carried out according to literature.[206] To a solution of 21.41 g (0.162 mol, 1.0 eq) of compound **1** and 38.58 g (0.567 mol, 3.5 eq) imidazol in 40 mL dry DMF, 51.84 mL (0.162 mol, 1.0 eq) $TIPDSCl_2$ have been added and stirred over night at room temperature. Upon completion, 20 mL methanol have been added before evaporating the solvents under reduced pressure. The residue was dissolved in ethyl acetate and subsequently washed with 0.1 M hydrochloric acid, saturated sodium hydrogen carbonate solution, brine and dried over sodium sulfate before evaporation under reduced pressure. The crude product was subjected to flash column chromatography (Cy/EA 19:1→9:1) to afford the product as colorless oil. Yield: 21.41 g (0.16 mol, 73%), R_f = 0.57 (EA/MeOH 9:1). Spectroscopic data were in accordance with literature.[206] ^{1}H NMR (600 MHz, DMSO-d_6) δ 4.68 (dd, ^3J = 16.1 Hz, ^3J = 8.0 Hz, 1H, 3‘-H), 4.19 (td, J = 6.8, J = 3.6 Hz, 1H, 4‘-H), 3.99 (qd, J = 12.2, 5.1 Hz, 2H, 5‘-H), 2.86 (dd, J = 16.9, 8.0 Hz, 1H, 2‘-H), 2.71 (dd, J = 16.9, 9.1 Hz, 1H, 2‘-H), 1.10 – 0.94 (m, 28H, ^{i}Pr-H).

2-(7-Hydroxy-2,2,4,4-tetraisopropyl-1,3,5,2,4-trioxadisilocan-6-yl)-1-(3-(phenyldiazenyl)phenyl)ethanone **5**

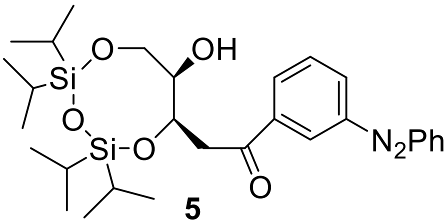

5

$C_{29}H_{44}N_2O_5Si_2$
556.85 g/mol

To a solution of 11.75 g (38.13 mmol, 1.0 eq) *meta*-iodo-azobenzene in 500 mL dry THF where added 16.02 mL (40.04 mmol, 1.05 eq) of a 2.5 M ^{n}BuLi solution in hexane at -78 °C and stirred for 30 minutes. The reaction mixture was transferred to a -78 °C prechilled solution of 10.0 g (26.69 mmol, 0.7 eq) of **3** in 200 mL dry THF via cannulation and stirred for an additional hour. The reaction was quenched by addition of saturated ammonium chloride solution, then extracted with DCM and dried over sodium sulfate before evaporation under reduced pressure. The crude product was subjected to flash column chromatography (Cy/EA 19:1→9:1 + 1% TEA) to afford the product as orange foam. Yield: 9.45 g (14.90 mmol, 56%), R_f = 0.59 (cyclohexane/ethyl acetate 3:1), ^{1}H NMR (500 MHz, $CDCl_3$) δ 8.52 (t, *J* = 1.7 Hz, 1H, Ar-H), 8.14 – 8.08 (m, 2H, Ar-H), 7.98 – 7.93 (m, 3H, Ar-H), 7.62 (td, *J* = 7.8, 3.9 Hz, 1H, Ar-H), 7.57 – 7.47 (m, 5H, Ar- H), 4.53 (ddd, *J* = 9.6, 6.3, 4.3 Hz, 1H, 3'-H), 4.21 (dd, *J*=11.7, 1.1 Hz, 1H, 5'-H), 3.84 (dt, *J*=6.7, 3.4 Hz, 1H, 5'-H), 3.58 (dd, *J*=16.0, 4.3 Hz, 1H, 2'-H), 3.46 (t, *J*=9.8 Hz, 1H, 4'-H), 3.34 – 3.28 (m, 1H, 2'-H), 2.30 (d, *J*=10.7 Hz, 1H, 4'-OH), 1.11 – 0.99 (m, 28H, ^{i}Pr-H). ^{13}C{^{1}H} NMR (126 MHz, $CDCl_3$-*d*) δ 198.75, 154.43, 153.09, 152.87, 152.78, 152.59, 138.54, 130.43, 129.55, 129.32, 127.38, 123.18, 123.06, 122.85, 109.55, 106.73, 75.72, 67.73, 62.25, 57.95, 45.14, 27.06, 17.48, 17.39, 13.55, 13.49, 13.37, 13.09, 12.73. δ ^{29}Si-INEPT NMR (99 MHz, DMSO-d_6) δ -12.84, -15.07. HRMS: Calculated for $C_{29}H_{44}N_2O_5Si_2Na$ ($[M+Na]^+$) *m/z* 579.26810, found *m/z* 579.26682.

1-Phenyl-2-(3-(2,2,4,4-tetraisopropyltetrahydro-6H-furo[3,2-f][1,3,5,2,4]trioxadisilocin-8-yl)phenyl)diazene **6**

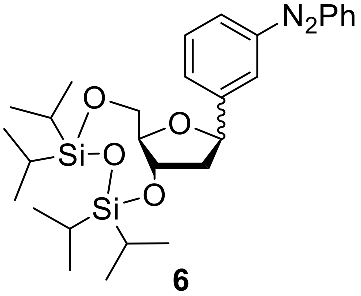

6

$C_{29}H_{44}N_2O_4Si_2$
540.85 g/mol

To a solution of 5.01 g (8.99 mmol, 1.0 eq) **5** in 100 mL dry DCM 7.44 mL (26.98 mmol, 3.0 eq) BF_3OEt_2 and 4.30 mL (26.98 mmol, 3.0 eq) Et_3SiH were added at -78°C and stirred for 90 minutes. After quenching with saturated sodium hydrogen carbonate solution, the aqueous layer was extracted with DCM, dried over sodium sulfate and evaporated under reduced pressure. The crude product was subjected to flash column chromatography (Cy/EA 19:1→4:1) to afford the product as orange oil. Yield: 1.88 g (3.48 mmol, 39%), R_f = 0.77 (Cy/EA 4:1), ^{1}H NMR (500 MHz, $CDCl_3$) δ 7.93 – 7.88 (m, 3H, Ar-H), 7.84 – 7.80 (m, 1H, Ar-H), 7.55 – 7.47 (m, 5H, Ar-H), 5.20 (t, *J*=7.4 Hz, 1H, 1'-H), 4.57 (dt, *J*=7.9, 4.6 Hz, 1H, 3'-H), 4.20 – 4.13 (m, 1H, 5'-H), 3.98 – 3.90 (m, 2H 4'+5'-H), 2.45 (ddd, *J*=12.8, 6.9, 4.5 Hz, 1H, 2'-H), 2.18 – 2.11 (m, 1H, 2'-H), 1.14 – 1.00 (m, 40H, ^{i}Pr-H). ^{13}C{^{1}H} NMR (126 MHz, $CDCl_3$-*d*) δ 152.88, 152.79, 144.28, 143.55, 131.14, 129.22, 128.56, 123.00, 122.02, 120.50, 86.68, 83.84, 78.88, 73.42, 63.80, 43.34, 27.06, 17.75, 17.62, 17.60, 17.56, 17.41, 17.26, 17.23, 17.14, 13.66, 13.55, 13.16, 12.70. ^{29}Si-INEPT NMR (99 MHz, $CDCl_3$-*d*) δ -12.32, -15.18. HRMS: Calculated for $C_{29}H_{44}N_2O_4Si_2$ ([M+H]$^+$) *m/z* 541.29124, found *m/z* 541.28896.

1'-(3-(Phenyldiazenyl)phenyl)-2'-deoxyribose **7**

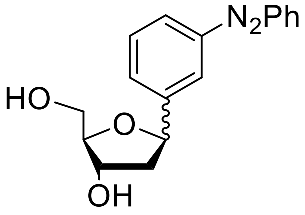

7

$C_{17}H_{18}N_2O_3$
298.34 g/mol

To a solution of 2.22 g (4.10 mmol, 1.0 eq) of **6** in 10 mL THF 12.0 mL (12.30 mmol, 3.0 eq) of a 1.0 M TBAF solution in THF was added and stirred over night at room temperature. After addition of aqueous ammonium chloride solution, the organic phase was extracted with DCM, dried over sodium sulfate and evaporated under reduced pressure. The crude product was subjected to flash column chromatography (Cy/EA 2:1→1:1) to afford the product as orange foam. Yield: 1.13 g (3.78 mmol, 92%), R_f = 0.57 (EA 100%). Spectroscopic data in accordance with literature.[72] ^{1}H NMR (500 MHz, DMSO-d_6) δ 7.92 – 7.87 (m, 3H, Ar-H), 7.80 – 7.76 (m, 1H, Ar-H), 7.64 – 7.54 (m, 5H, Ar-H), 5.14 (dd, *J* = 10.4, 5.4 Hz, 1H, 1'-H), 5.11 (d, *J* = 3.9 Hz, 1H, 3'-OH), 4.81 (t, *J* = 5.5 Hz, 1H, 5'-OH), 4.25 – 4.20 (m, 1H, 3'-H), 3.84 (td, *J* = 5.3, 2.2 Hz, 1H, 4'-H), 3.54 (dt, *J* = 10.3, 5.1 Hz, 1H, 5'-H), 3.47 (dt, *J* = 11.3, 5.7 Hz, 1H, 5'-H), 2.17 (m, 1H, 2'-H), 1.88 – 1.80 (m, 1H, 2'-H). ^{13}C{^{1}H} NMR (126 MHz, DMSO-d_6) δ 151.93, 144.44, 131.55, 129.50, 129.31, 129.12, 128.83, 122.56, 121.10, 120.27, 119.70, 119.41, 87.99, 78.80, 72.42, 62.42, 43.65.

1‘-(3-(Phenyldiazenyl)phenyl)-5‘-((bis(4-methoxyphenyl)(phenyl)methoxy)methyl)-2’-deoxyribose **8**

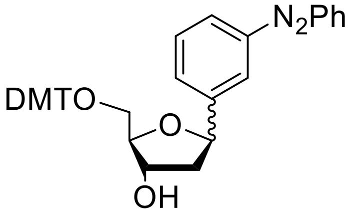

8

$C_{38}H_{36}N_2O_5$
600.71g/mol

To a solution of 1.72 g (5.77 mmol, 1.0 eq) of **7** in 20 mL pyridine, a solution of 2.15 g (6.35 mmol, 1.1 eq) 4,4‘-dimethoxytrityl chloride in 10 mL pyridin was added dropwise, then stirred over night at room temperature. After adding aqueous ammonium chloride solution, the aqueous layer was extracted with DCM, dried over sodium sulfate and evaporated under reduced pressure. The crude product was subjected to flash column chromatography (Cy/EA 4:1) on silica, which has previously been neutralized with triethylamine, to afford the product as orange foam. Yield: 2.712 g (4.301 mmol, 75%), R_f = 0.58 (Cy/EA 1:1). Spectroscopic data in accordance with literature.[72] ^{1}H NMR (500 MHz, $CDCl_3$-*d*) δ 7.79 – 7.71 (m, 3H, Ar-H), 7.50 – 7.40 (m, 4H, Ar-H), 7.39 – 7.33 (m, 2H, Ar-H), 7.33 – 7.24 (m, 5H, Ar-H), 7.20 – 7.14 (m, 5H, Ar-H), 6.87 – 6.80 (m, 7H, Ar-H), 5.24 (dd, ^3J = 10.2, 5.7 Hz, 1H, 1’-H), 4.46 (ddd, ^3J = 10.4, 7.0, 4.0 Hz, 1H, 3’-H), 4.05 (td, ^3J = 4.5, 3.0, 1H, 4’-H), 3.86 (m, 7H, 4H, 5’-H+CH_3), 3.38-3.92 (m, 1H, 5’-H), 2.30 (ddd, ^3J=13.3, 5.7 Hz, ^4J = 1.9 Hz, 1H, 2’-H), 2.06 (m, 1H, 2’-H). $^{13}C\{^1H\}$ NMR (126 MHz, $CDCl_3$-*d*) δ 158.75, 158.60, 153.39, 153.23, 147.45, 144.98, 143.25, 142.48, 139.58, 138.94, 135.26, 130.23, 129.26, 127.99, 127.90, 127.22, 126.62, 126.59, 122.03, 113.33, 113.30, 113.26, 87.47, 86.56, 86.37, 85.63, 81.57, 79.98, 73.96, 63.58, 60.55, 55.40, 55.35, 44.37, 36.13, 14.35, 13.97, 10.12.

2-((Bis(4-methoxyphenyl)(phenyl)methoxy)methyl)-5-(3-(phenyldiazenyl)phenyl)tetrahydrofuran-3-yl(2-cyanoethyl)diisopropyl phosphoramidite (**9**)

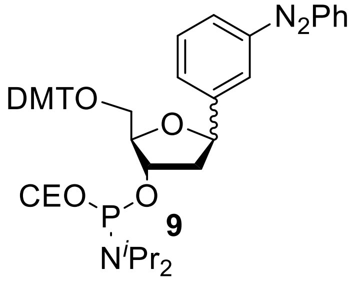

9

$C_{47}H_{53}N_4O_6P$
800.94 g/mol

To a solution of 2.712 g (4.301 mmol, 1.0 eq) of **8** and 3.75 mL (21.505 mmol, 5.0 eq) of *N,N*-diisopropylethylamine in 8 mL DCM 1.44 mL (6.452 mmol, 1.5 eq) 2-cyanoethyl-*N,N*-diisopropylchlorphosphoramidite were added and stirred for 45 minutes at room temperature. Upon addition of sodium hydrogen carbonate solution, the aqueous layer was extracted with DCM, the organic layer dried over sodium sulfate and evaporated under reduced pressure. The crude product was subjected to flash column chromatography (Cy/acetone 4:1→1:1 + 1% TEA) to afford the product as orange foam. Yield: 3.424 g (4.275 mmol, 99%). R_f = 0.31 (Cy/acetone 4:1). Spectroscopic data in accordance with literature.[72] ^{1}H NMR (500 MHz, $CDCl_3$-*d*) *δ* 7.87 – 7.80 (m, 3H, Ar-H), 7.53 – 7.43 (m, 6H, Ar-H), 7.39 (m, 4H, Ar-H), 7.32 – 7.23 (m, 3H, Ar-H), 7.21 – 7.12 (m, 1H, Ar-H), 6.87 – 6.77 (m, 5H, Ar-H), 5.29 (ddd, *J* = 10.7, 5.1, 2.5 Hz, 1H, 1'-H), 4.58 – 4.51 (m, 1H, 3'-H), 4.31 – 4.26 (m, 1H, 4'-H), 3.79 (m, 2H), 3.74 (m, 4H, CH_2), 3.68 – 3.53 (m, 2H, CH), 3.42 – 3.24 (m, 2H, 5'-H), 2.55 – 2.38 (m, 2H, 2'-H), 2.13 (m, 1H, 2'-H), 1.23 – 0.99 (m, 12H, CH_3). $^{13}C\{^1H\}$ NMR (126 MHz, $CDCl_3$-*d*) δ 158.54, 152.91, 152.73, 144.99, 143.25, 136.22, 131.06, 130.33, 130.28, 130.24, 129.23, 129.13, 128.75, 128.45, 128.39, 127.92, 126.81, 123.01, 122.13, 120.58, 117.61, 113.21, 86.26, 80.15, 64.38, 58.56, 58.41, 55.31, 55.30, 55.29, 43.55, 43.40, 43.35, 43.30, 43.24, 27.05, 24.82, 24.80, 24.75, 24.63, 24.60, 24.57, 20.81, 20.55, 20.48, 20.37, 20.31. $^{31}P\{^1H\}$ NMR (121 MHz, $CDCl_3$-*d*) δ 148.12, 147.90.

3-(2-(4-Iodophenyl)hydrazono)pentan-2,4-dion **10**

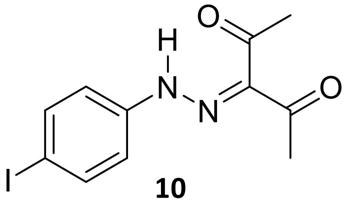

10

$C_{11}H_{11}IN_2O_2$
330.13 g/mol

Synthesis has been carried out according to literature.[207] To a 0°C prechilled solution of 7.0 g (32 mmol, 1.0 eq) 4-iodoanilin, 1.3 g (32 mmol, 1.0 eq) sodium hydroxide and 2.2 g (32 mmol, 1.0 eq) sodium nitrite in 50 mL water, 5.3 mL (64 mmol, 2.0 eq) concentrated hydrochloric acid was added dropwise, leaving the temperature below 5°C. The resulting emulsion was transferred to a mixture containing 3.3 mL (32 mmol, 1.0 eq) acetylacetone and 1.3 g (32 mmol, 1.0 eq) sodium hydroxide in 50 mL water and stirred for 20 hours at room temperature. The precipitate was filtered, dried and used for the follow up reaction without further purification. Yield: 8.04 g (24.4 mmol, 76%). R_f = 0.55 (Cy/EA 3:1). Spectroscopic data in accordance with literature.[207] ^{1}H NMR (250 MHz, $CDCl_3$-*d*) δ = 7.79-7.72 (m, 2H, Ar-H), 7.51 (s, 1H, NH), 7.45-7.38 (m, 2H, Ar-H), 2.47 (s, 3H, CH_3), 2.40 (s, 3H, CH_3).

3-(2-(3-Iodophenyl)hydrazono)pentan-2,4-dion **11**

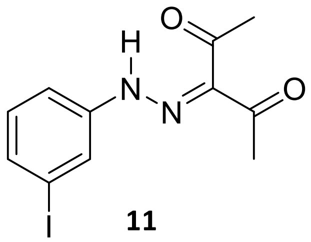
11

$C_{11}H_{11}IN_2O_2$
330.13 g/mol

To a 0°C prechilled solution of 19.72 g (90 mmol, 1.0 eq) 3-iodoanilin, 2.60 g (64 mmol, 1.0 eq) sodium hydroxide and 7.45 g (108 mmol, 1.2 eq) sodium nitrite in 100 mL water, 20 mL (242 mmol, 7.5 eq) concentrated hydrochloric acid was added dropwise, leaving the temperature below 5°C. The resulting emulsion was transferred to a mixture containing 11.7 g (117 mmol, 1.3 eq) acetylacetone and 4.9 g (121 mmol, 1.3 eq) sodium hydroxide in 100 mL water and stirred over night at room temperature. The precipitate was filtered, vacuum dried and used for the follow up reaction without further purification. Yield: 28.94 g (88 mmol, 97%). R_f = 0.54 (Cy/EA 3:1). ^{1}H NMR (250 MHz, DMSO-d_6): δ = 13.68 (s, 1H, N-H), 7.94 (t, ^4J = 1.8 Hz, 1H, Ar-H), 7.62 – 7.58 (m, 1H, Ar-H), 7.54 – 7.51 (m, 1H, Ar-H), 7.20 (t, ^3J = 8.0 Hz, 1H, Ar-H), 2.46 (s, 3H, CH3), 2.42 (s, 3H, CH3).

1,3,5-Trimethyl-1*H*-pyrazol-*para*-iodazobenzene **12**

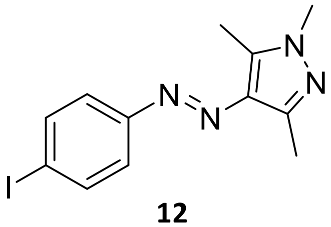

12

$C_{12}H_{13}IN_4$
340.17 g/mol

Synthesis has been carried out according to literature.[207] A solution of 7.9 g (24.0 mmol, 1.0 eq) **10** and 1.5 mL (28.8 mmol, 1.2 eq) methylhydrazine in 200 mL ethanol was heated for 5 hours at 80 °C. Upon completion, the solvent was evaporated under reduced pressure and the crude product subjected to flash column chromatography (Cy/EA 9:1→4:1) to afford the product as orange solid. Yield: 2.76 g (8.10 mmol, 34%). Spectroscopic data in accordance with literature.[207] R_f = 0.52 (Cy/EA 3:1). ^{1}H NMR (400 MHz, DMSO-d_6) δ 7.87 (d, ^3J = 5.4 Hz, 2H, Ar-H), 7.52 (d, ^3J = 5.4 Hz, 2H, Ar-H), 3.74 (s, 3H, CH_3), 2.55 (s, 3H, CH_3), 2.36 (s, 3H, CH_3). ^{13}C{^{1}H} NMR (126MHz, DMSO-d_6) δ 152.35, 140.51, 140.07, 138.07, 134.34, 123.42, 121.97, 95.93, 35.99, 13.80, 9.51, -7.92.

1,3,5-Trimethyl-1*H*-pyrazol-*meta*-iodazobenzene **13**

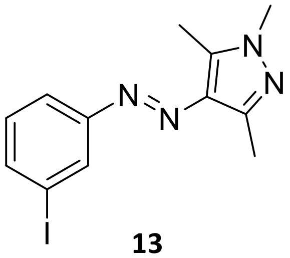

13

$C_{12}H_{13}IN_4$
340.17 g/mol

A solution of 28.94 g (87.7 mmol, 1.0 eq) **11** and 5.6 mL (106.8 mmol, 1.2 eq) methylhydrazine in 700 mL ethanol was heated for 5 hours at 80 °C. Upon completion, the solvent was evaporated under reduced pressure and the crude product subjected to flash column chromatography (Cy/EA 9:1→4:1) to afford the product as orange solid. Yield: 27.93 g (82.15 mmol, 94%). R_f = 0.50 (Cy/EA 3:1). ^{1}H NMR (500 MHz, $CDCl_3$-*d*): δ = 8.10 (t, ^3J = 1.7 Hz, 1H, Ar-H), 7.75 (ddd, ^3J = 7.9 Hz, ^4J=1.8, 1.0 Hz, 1H, Ar-H), 7.68 (ddd, ^3J = 7.8 Hz, ^4J=1.6, 1.0 Hz, 1H, Ar-H), 3.79 (s, 3H,CH_3), 2.58 (s, 3H,CH_3), 2.49 (s, 3H,CH_3). ^{13}C{^{1}H} NMR (126 MHz, $CDCl_3$-*d*) δ 154.62, 142.64, 139.65, 137.97, 135.24, 130.61, 129.94, 122.40, 94.71, 36.18, 14.06, 10.16. HRMS: Calculated for $C_{12}H_{13}IN_4$ ($[M+H]^+$) *m/z* 341.02577, found *m/z* 341.02586.

2-((6S,7R)-7-Hydroxy-2,2,4,4-tetraisopropyl-1,3,5,2,4-trioxadisilocan-6-yl)-1-(4-((1,3,5-trimethyl-1H-pyrazol-4-yl)diazenyl)phenyl)ethanone **14**

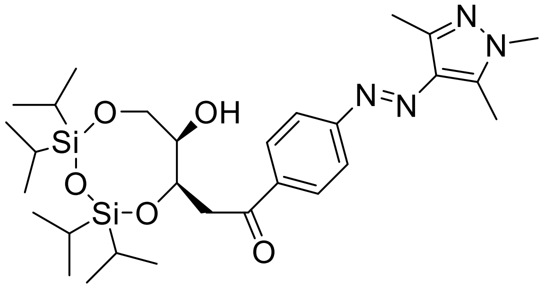

14

$C_{29}H_{48}N_4O_5Si_2$
588.90 g/mol

To a solution of 12.97 g (38.13 mmol, 1.0 eq) 4-((3-iodophenyl)diazenyl)-1,3,5-trimethyl-1H-pyrazole **12** in 500 mL dry THF were added 16.00 mL (40.04 mmol, 1.05 eq) of a 2.5 M ^{n}BuLi solution in hexane at -78°C and stirred for 30 minutes. The reaction mixture was transferred to a -78°C prechilled solution of 10.0 g (26.69 mmol, 0.7 eq) of **3** in 200 mL dry THF via cannulation and stirred for an additional hour. The reaction was quenched by addition of saturated ammonium chloride solution, then extracted with DCM and dried over sodium sulfate before evaporation under reduced pressure. The crude product was subjected to flash column chromatography (Cy/EA 9:1→4:1) on silica, which has previously been neutralized with triethylamine to afford the product as orange foam. Yield: 8.54 g (14.90 mmol, 56%), R_f = 0.36 (Cy/EA 1:1), ^{1}H NMR (500 MHz, $CDCl_3$-*d*) δ 8.08 (d, *J* = 8.6 Hz, 2H, Ar-H), 7.82 (d, *J* = 8.6 Hz, 2H, Ar-H), 4.54 – 4.49 (m, 1H, 3'-H), 4.20 (dd, *J* = 11.6, 0.8 Hz, 1H, 5'-H), 3.84 (dd, *J* = 11.7, 2.0 Hz, 1H, 5'-H), 3.79 (d, *J* = 4.2 Hz, 3H, NCH_3), 3.51 (dd, *J* = 16.1, 4.1 Hz, 1H, 2'-H), 3.44 (t, *J* = 9.9 Hz, 1H, 4'-H), 3.28 (dd, *J* = 16.1, 6.4 Hz, 1H, 2'-H), 2.60 (s, 3H, CH_3), 2.50 (s, 3H, CH_3), 2.33 (d, *J* = 10.6 Hz, 1H, 4'-OH), 1.13 – 1.00 (m, 28H, ^{i}Pr-H). $^{13}C\{^1H\}$ NMR (126 MHz, $CDCl_3$-*d*) δ 198.69, 156.40, 142.86, 139.98, 137.48, 135.79, 129.49, 121.93, 75.76, 67.66, 62.29, 45.00, 36.22, 27.06, 17.62, 17.54, 17.49, 17.47, 17.42, 17.39, 14.12, 13.55, 13.47, 12.75, 12.73, 10.17. ^{29}Si-INEPT NMR (99 MHz, $CDCl_3$) δ -11.25, -13.37. HRMS: Calculated for $C_{29}H_{48}N_4O_5Si_2$ ($[M+H]^+$) *m/z* 589.32360, found *m/z* 589.32258.

2-((6S,7R)-7-Hydroxy-2,2,4,4-tetraisopropyl-1,3,5,2,4-trioxadisilocan-6-yl)-1-(3-((1,3,5-trimethyl-1H-pyrazol-4-yl)diazenyl)phenyl)ethanone **15**

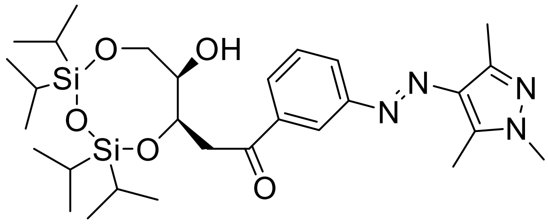

15

$C_{29}H_{48}N_4O_5Si_2$
588.90 g/mol

To a solution of 12.97 g (38.13 mmol, 1.0 eq) 4-((3-iodophenyl)diazenyl)-1,3,5-trimethyl-1H-pyrazole **13** in 250 mL dry THF, 16.00 mL (40.04 mmol, 1.05 eq) of a 2.5 M ^{n}BuLi solution in hexane were added at -78°C and stirred for 30 minutes. The reaction mixture was transferred to a -78°C prechilled solution of 10.0 g (26.69 mmol, 0.7 eq) of **3** in 200 mL dry THF via cannulation and stirred for an additional hour. The reaction was quenched by addition of saturated ammonium chloride solution, then extracted with DCM and dried over sodium sulfate before evaporation under reduced pressure. The crude product was subjected to flash column chromatography (Cy/EA 9:1→4:1) on silica, which has previously been neutralized with triethylamine to afford the product as orange foam. Yield: 6.36 g (10.81 mmol, 41%), ^{1}H NMR (400 MHz, $CDCl_3$-*d*) δ = 8.36 (m, 1H, Ar-H), 7.97 (tdd, *J*=7.9, 2.5, 1.2 Hz, 2H, Ar-H), 7.54 (t, *J*=7.9 Hz, 1H, Ar-H), 4.52 (ddd, *J* = 9.4, 6.3, 4.2 Hz, 1H, 3'-H), 4.20 (dd, *J* = 11.7, 1.3 Hz, 1H, 5'-H), 3.84 (dd, *J* = 11.7, 2.1 Hz, 1H, 5'-H), 3.80 (s, 3H, CH_3), 3.57 (dd, *J* = 16.1, 4.2 Hz, 1H, 2'-H), 3.45 (dt, *J*=9.6, 1.6 Hz, 1H, 4'-H), 3.29 (dd, *J* = 16.0, 6.4 Hz, 1H, 2'-H), 2.60 (s, 3H, CH_3), 2.51 (s, 3H, CH_3), 1.13 – 0.98 (m, 28H, ^{i}Pr-H). ^{13}C{^{1}H} NMR (126 MHz, $CDCl_3$-*d*) *δ* 199.05, 153.80, 142.68, 139.48, 138.38, 135.31, 129.24, 128.85, 125.62, 122.46, 75.72, 67.67, 62.26, 45.12, 36.18, 27.04, 17.62, 17.52, 17.47, 17.45, 17.38, 14.09, 14.06, 13.53, 13.47, 12.71, 10.18, 10.16. ^{29}Si-INEPT NMR (99 MHz, $CDCl_3$-*d*) δ -11.25, -13.35. HRMS: Calculated for $C_{29}H_{48}N_4O_5Si_2$ ($[M+H]^+$) *m/z* 589.32360, found *m/z* 589.32258.

(6aR,9aS)-4-Ethyl-2,2,4-triisopropyl-8-(4-((1,3,5-trimethyl-1H-pyrazol-4-yl)diazenyl)phenyl)tetrahydro-6H-furo[3,2-f][1,3,5,2,4]trioxadisilocin-8-ol **16**

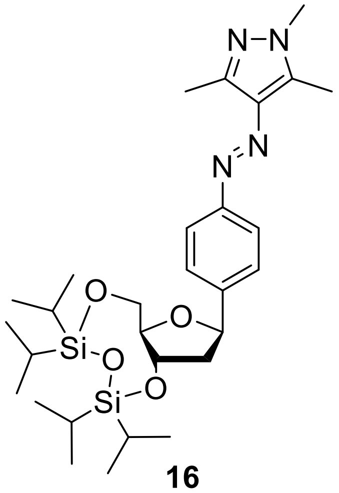

16

$C_{29}H_{48}N_4O_4Si_2$

572.90 g/mol

To a solution of 6.45 g (10.95 mmol, 1.0 eq) **14** in 100 mL dry DCM, 8.42 mL (32.74 mmol, 3.0 eq) BF_3OEt_2 and 5.25 mL (32.85 mmol, 3.0 eq) Et_3SiH was added at -78°C and stirred for 90 minutes. After quenching with saturated sodium hydrogen carbonate solution, the aqueous layer was extracted with DCM, dried over sodium sulfate and evaporated under reduced pressure. The crude product was subjected to flash column chromatography (Cy/EA 9:1→4:1) to afford the product as orange oil. Yield: 4.39 g (7.67 mmol, 70 %), R_f = 0.30 (Cy/EA 1:1), ^{1}H NMR (250 MHz, $CDCl_3$-*d*) δ 7.74 (d, *J* = 8.5 Hz, 1H, Ar-H), 7.42 (d, *J* = 8.3 Hz, 1H, Ar-H), 5.15 (t, *J* = 7.3 Hz, 1H, 1‘-H), 4.55 (dt, *J* = 7.5, 4.7 Hz, 1H, 3‘-H), 4.16 (dd, *J* = 7.1, 4.2 Hz, 1H, 5‘-H), 3.98 – 3.85 (m, 2H, 4‘-H + 5‘-H), 3.78 (s, 1H, NCH3), 2.57 (s, 3H, CH3), 2.49 (s, 3H, CH3), 2.41 (ddd, *J* = 12.7, 6.9, 4.6 Hz, 1H, 2‘-H), 2.10 (dt, *J* = 7.4, 4.7 Hz, 1H, 2‘-H), 1.14 – 1.00 (m, 28H, iPr). ^{13}C{^{1}H} NMR (126 MHz, $CDCl_3$-*d*) δ 153.25, 143.55, 142.64, 138.75, 135.32, 126.44, 121.92, 120.54, 86.65, 83.80, 78.93, 78.29, 73.43, 63.85, 43.41, 36.11, 17.74, 17.62, 17.60, 17.55, 17.41, 17.26, 17.23, 17.14, 13.94, 13.67, 13.57, 13.21, 12.74, 10.12., ^{29}Si-INEPT NMR (60 MHz, $CDCl_3$) δ -12.36, -15.23. HRMS: Calculated for $C_{29}H_{48}N_4O_5Si_2$ $[M+H]^+$ *m/z* 573.32086, found 573.32744.

(6aR,9aS)-4-Ethyl-2,2,4-triisopropyl-8-(3-((1,3,5-trimethyl-1H-pyrazol-4-yl)diazenyl)phenyl)tetrahydro-6H-furo[3,2-f][1,3,5,2,4]trioxadisilocin-8-ol **17**

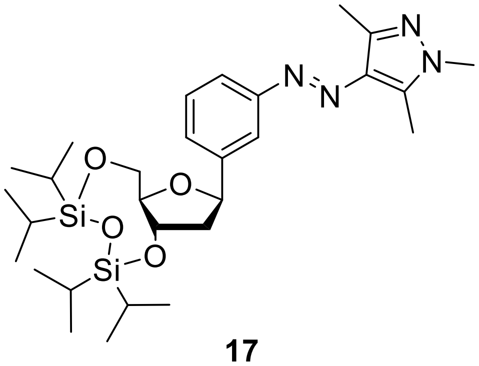

17

$C_{29}H_{48}N_4O_4Si_2$

572.90 g/mol

To a solution of 3.03 g (5.15 mmol, 1.0 eq) **15** in 50 mL dry DCM, was added 1.9 mL (15.44 mmol, 3.0 eq) BF_3OEt_2 and 2.45 mL (15.44 mmol, 3.0 eq) Et_3SiH at -78°C and stirred for one hour. After quenching with saturated sodium hydrogen carbonate solution, the aqueous layer was extracted with DCM, dried over sodium sulfate and evaporated under reduced pressure. The crude product was subjected to flash column chromatography (Cy/EA 9:1→4:1) to afford the product as orange oil. Yield: 1.37 g (2.39 mmol, 46%), ^{1}H NMR (500 MHz, $CDCl_3$-*d*) *δ* 7.73 (m, 1H, Ar-H), 7.67 (dt, *J* = 7.6, 1.7 Hz, 1H, Ar-H), 7.44 – 7.36 (m, 2H, Ar-H), 5.18 (t, *J* = 7.4 Hz, 1H, 1'-H), 4.56 (dt, *J* = 7.7, 4.6 Hz, 1H, 3'-H), 4.16 (dd, *J* = 10.9, 2.9 Hz, 1H, 5'-H), 3.98 – 3.89 (m, 2H, 4'+5'-H), 3.78 (s, 3H, CH_3), 2.58 (s, 3H, CH_3), 2.50 (s, 3H, CH_3), 2.42 (ddd, *J* = 12.8, 6.8, 4.3 Hz, 1H, 2'-H), 2.14 (dt, *J* = 12.8, 7.8 Hz, 1H, 2'-H), 1.15 – 0.89 (m, 28H, ^{i}Pr-H). ^{13}C{^{1}H} NMR (126 MHz, $CDCl_3$-*d*) *δ* 153.80, 143.13, 142.55, 142.55, 138.93, 135.23, 129.09, 126.84, 120.52, 119.88, 86.68, 79.06, 73.55, 63.87, 43.32, 36.11, 17.74, 17.59, 17.54, 17.41, 17.22, 17.13, 13.97, 13.65, 13.55, 13.20, 13.14, 12.69, 10.13. ^{29}Si INEPT-NMR (99 MHz, $CDCl_3$-*d*) δ -12.38, -15.28. HRMS: Calculated for $C_{29}H_{48}N_4O_5Si_2$ [M+H]$^+$ *m/z* 573.32869, found 573.32825.

1‘-(((1,3,5-Trimethyl-1H-pyrazol-4-yl)diazenyl)phenyl)2’-deoxyribose **18**

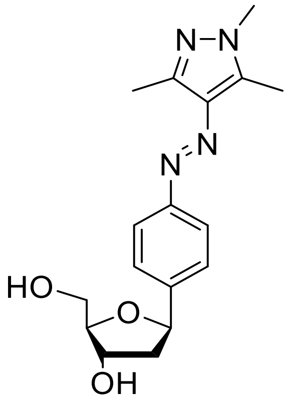

18

$C_{17}H_{22}N_4O_3$

330.39 g/mol

To a solution of 3.12 g (5.44 mmol, 1.0 eq) of **16** in 10 mL THF 16.3 mL (16.31 mmol, 3.0 eq) of a 1.0 M TBAF solution in THF was added and stirred for two hours at room temperature. After addition of aqueous ammonium chloride solution, the organic phase was extracted with DCM, dried over sodium sulfate and evaporated under reduced pressure. The crude product was subjected to flash column chromatography (DCM/MeOH 9:1) to afford the product as orange foam. Yield: 1.64 g (4.95 mmol, 91%), R_f = 0.47 (EA/MeOH 9:1), ^{1}H NMR (250 MHz, $CDCl_3$-*d*) *δ* 7.76 (d, *J* = 8.5 Hz, 1H, Ar-H), 7.44 (d, *J* = 8.3 Hz, 1H, Ar-H), 5.25 (dd, *J* = 10.1, 5.7 Hz, 1H, 1‘-H), 4.51 – 4.44 (m, 1H, 3‘-H), 4.14 (t, *J* = 7.2 Hz, 1H, 4‘-H), 4.06 (dd, *J* = 7.1, 4.5 Hz, 1H, 5‘-H), 3.88 (dd, *J* = 11.6, 4.1 Hz, 1H, 5-H‘), 3.79 (s, 3H, NCH_3), 2.58 (s, 3H, CH_3), 2.50 (s, 3H, CH_3), 2.31 (ddd, *J* = 13.3, 5.7, 2.0 Hz, 1H, 2‘-H), 2.06 – 2.03 (m, 1H, 2‘-H). ^{13}C{^{1}H} NMR (126 MHz, $CDCl_3$-*d*) *δ* 153.37, 142.56, 142.53, 138.96, 135.24, 126.62, 122.02, 87.50, 79.98, 73.86, 63.55, 44.27, 36.09, 13.93, 10.10. HRMS: Calculated for $C_{17}H_{22}N_4O_3$ $[M+H]^+$ *m/z* 331.17647, found 331.17711.

Crystal structure analysis: The data were collected at 173 K on a STOE IPDS-II diffractometer equipped with a Genix microfocus tube and mirror optics using Mo*K*α radiation. The structure was solved by direct methods and refined against F^2 by full-matrix least-squares techniques. All H atoms were refined using a riding model. The torsion angles of the OH groups and methyl groups were refined. There are two molecules of **18** and one water molecule in the asymmetric unit. Both molecules have essentially the same conformation. Due to the absence of anomalous scatterers, the absolute configuration could not be determined. The data have been deposited with the Cambridge Crystallographic Database: CCDC 1561178.

1‘-((3-(1,3,5-Trimethyl-1H-pyrazol-4-yl)diazenyl)phenyl)2’-deoxyribose **19**

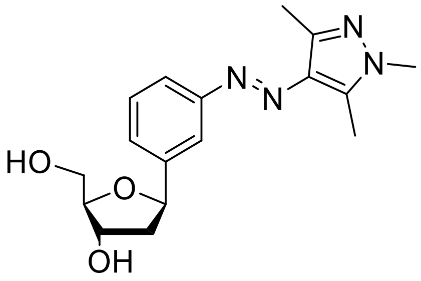

19

$C_{17}H_{22}N_4O_3$
330.39 g/mol

To a solution of 1.50 g (2.62 mmol, 1.0 eq) of **17** in 10 mL THF 7.9 mL (7.85 mmol, 3.0 eq) of a 1.0 M TBAF solution in THF was added and stirred over night at room temperature. After addition of aqueous ammonium chloride solution, the organic phase was extracted with DCM, dried over sodium sulfate and evaporated under reduced pressure. The crude product was subjected to flash column chromatography (EA/MeOH 9:1) to afford the product as orange foam. Yield: 1.64 g (4.95 mmol, 91%), ^{1}H NMR (500 MHz, DMSO-*d*$_6$) *δ* 7.72 (t, *J* = 1.8 Hz, 1H, Ar-H), 7.61 (ddt, *J* = 7.5, 3.8, 1.7 Hz, 1H, Ar-H), 7.48 – 7.41 (m, 2H, Ar-H), 5.14 – 5.08 (m, 2H, 1’-H, 3’-OH), 4.80 (t, *J* = 5.5 Hz, 1H, 5’-OH), 4.23 (m, 1H, 3’-H), 3.84 (td, *J* = 5.3, 2.2 Hz, 1H, 4’-H), 3.75 (s, 3H, CH_3), 3.50 (m, 2H, 5’-H), 2.56 (s, 3H, CH_3), 2.38 (s, 3H, CH_3), 2.16 (ddd, *J* = 12.7, 5.5, 1.7 Hz, 1H, 2’-H), 1.88 – 1.80 (m, 1H, 2’H). ^{13}C{^{1}H} NMR (126 MHz, DMSO-*d*$_6$) *δ* 152.97, 144.01, 140.29, 139.59, 134.34, 128.97, 127.02, 119.96, 119.18, 87.91, 78.97, 72.43, 62.45, 17.27, 17.24, 13.79, 9.48.HRMS: Calculated for $C_{17}H_{22}N_4O_3$ $[M+H]^+$ *m/z* 331,17647, found 331.17688.

1‘-(((1,3,5-Trimethyl-1H-pyrazol-4-yl)diazenyl)phenyl)-5‘-((bis(4-methoxyphenyl)(phenyl)methoxy)methyl)2’-deoxyribose **20**

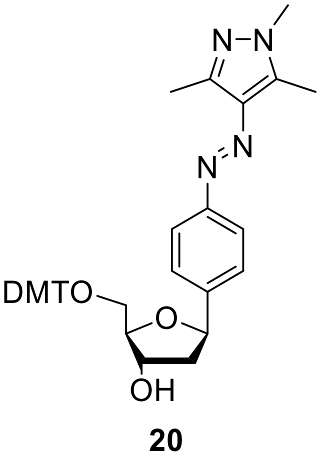

20

$C_{38}H_{40}N_4O_5$

632.76 g/mol

To a solution of 1.345 g (4.071 mmol, 1.0 eq) of **18** in 20 mL pyridin a solution of 1.517 g (4.478 mmol, 1.1 eq) 4,4‘-dimethoxytrityl chloride in 10 mL pyridin was added dropwise and stirred for 3.5 hours at room temperature. After adding aqueous ammonium chloride solution, the aqueous layer was extracted with DCM, dried over sodium sulfate and evaporated under reduced pressure. The crude product was subjected to flash column chromatography (Cy/EA 4:1) on silica, which has previously been neutralized with triethylamine, to afford the product as orange foam. Yield: 2.361 g (3.731 mmol, 92%), R_f = 0.69 (Cy/EA 9:1), ^{1}H NMR (500 MHz, $CDCl_3$-*d*) δ 7.79 – 7.72 (m, 2H, Ar-H), 7.50 – 7.42 (m, 4H, Ar-H), 7.39 – 7.31 (m, 4H, Ar-H), 7.31 – 7.24 (m, 6H, OCH3), 7.24 – 7.15 (m, 2H, Ar-H), 6.87 – 6.80 (m, 5H, Ar-H), 5.27 – 5.21 (t, J = 5.0 Hz, 1H, 1‘-H), 4.47 – 4.42 (m, 1H, 3‘-H), 4.10 – 4.03 (m, 1H, 4‘-H), 3.79 (s, 3H, NCH_3), 3.40 – 3.35 (dd, *J* = 10.0, 5.5 Hz, 1H, 5‘-H), 3.33 – 3.28 (dd, *J* = 10.1, 5.5 Hz, 1H, 5‘-H), 2.57 (s, 3H, CH_3), 2.49 (s, 3H, CH_3), 2.28 (ddd, *J* = 13.1, 5.7, 2.0 Hz, 1H, 2‘-H), 2.11 – 2.05 (m, 1H, 2‘-H). ^{13}C{^{1}H} NMR (126 MHz, $CDCl_3$-*d*) δ 158.78, 158.63, 153.26, 145.00, 143.24, 142.57, 139.59, 138.84, 136.19, 136.16, 135.28, 130.25, 129.28, 128.34, 128.00, 127.91, 126.94, 126.62, 126.59, 122.04, 121.91, 113.31, 113.29, 87.46, 86.55, 86.38, 79.91, 74.83, 64.59, 60.55, 55.40, 55.36, 44.13, 36.13, 21.21, 14.35, 13.98, 10.13. HRMS: Calculated for $C_{38}H_{40}N_4O_5$ $[M+H]^+$ *m/z* 633.30715, found 633.30675.

1‘-((3-(1,3,5-Trimethyl-1H-pyrazol-4-yl)diazenyl)phenyl)-5‘-((bis(4-methoxyphenyl)(phenyl)methoxy)methyl)2’-deoxyribose **21**

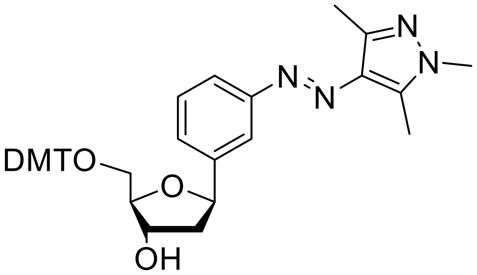

21

$C_{38}H_{40}N_4O_5$
632.76 g/mol

To a solution of 1.24 g (3.75 mmol, 1.0 eq) of **19** in 20 mL pyridin a solution of 1.40 g (4.13 mmol, 1.1 eq) 4,4‘-dimethoxytrityl chloride in 10 mL pyridin was added dropwise, then stirred over night at room temperature. After adding aqueous ammonium chloride solution, the aqueous layer was extracted with DCM, dried over sodium sulfate and evaporated under reduced pressure. The crude product was subjected to flash column chromatography (Cy/EA 4:1 + 1% TEA) to afford the product as orange foam. Yield: 1.60 g (2.55 mmol, 68%), ^{1}H NMR (500 MHz, DMSO-*d*$_6$) *δ* 7.82 (m, 1H, Ar-H), 7.62 (dt, *J* = 7.8, 1.5 Hz, 1H, Ar-H), 7.51 – 7.39 (m, 5H, Ar-H), 7.34 – 7.25 (m, 8H, Ar-H), 7.21 – 7.16 (m, 1H, Ar-H), 6.89 (m, 1H, Ar-H), 6.86 – 6.82 (m, 4H, Ar-H), 5.21 – 5.13 (m, 2H, 1’-H, 3’-OH), 4.18 (ddt, *J* = 6.1, 4.3, 2.0 Hz, 1H, 3’-H), 4.00 – 3.96 (m, 1H, 4’-H), 3.71 (s, 3H, CH_3), 3.69 (m, 6H, CH_3), 3.17 (dd, *J* = 9.9, 3.7 Hz, 1H, 5’-H), 3.10 (dd, *J* = 9.9, 5.5 Hz, 1H, 5’-H), 2.41 (s, 3H, CH_3), 2.27 (s, 3H, CH_3), 2.26 – 2.19 (m, 1H, 2’-H), 1.90 (ddd, *J* = 12.6, 10.1, 5.9 Hz, 1H, 2’-H). ^{13}C{^{1}H} NMR (126 MHz, DMSO-*d*$_6$) δ 170.33, 158.00, 157.99, 153.15, 144.93, 143.83, 140.29, 139.59, 135.70, 135.67, 134.36, 129.71, 128.98, 127.74, 126.94, 126.57, 119.67, 119.25, 113.12, 113.11, 86.24, 85.34, 84.64, 79.04, 78.55, 72.48, 72.33, 64.43, 59.76, 55.02, 54.96, 43.92, 35.92, 20.77, 14.09, 13.69, 9.50, 9.31. HRMS: Calculated for $C_{38}H_{40}N_4O_5$ $[M+H]^+$ *m/z* 633.30715, found 633.30728.

(2R,3S,5R)-2-((Bis(4-methoxyphenyl)(phenyl)methoxy)methyl)-5-(4-((1,3,5-trimethyl-1H-pyrazol-4-yl)diazenyl)phenyl)tetrahydrofuran-3-yl (2-cyanoethyl) diisopropyl phosphoramidite **22**

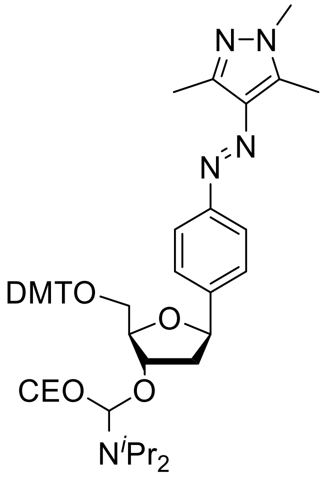

22

$C_{47}H_{57}N_6O_6P$

832.98 g/mol

To a solution of 2.361 g (3.731 mmol, 1.0 eq) of **20** and 3.25 mL (18.655 mmol, 5.0 eq) of *N,N*-diisopropylethylamine in 6 mL DCM 1.25 mL (5.597 mmol, 1.5 eq) 2-cyanoethyl-*N,N*-diisopropylchlorphosphoramidite have been added and stirred for 45 minutes at room temperature. After adding sodium hydrogen carbonate solution, the aqueous layer was extracted with DCM, the organic layer dried over sodium sulfate and evaporated under reduced pressure. The crude product was subjected to flash column chromatography (Cy/acetone 4:1→1:1) on silica, which has previously been neutralized with triethylamine, to afford the product as orange foam. Yield: 3.078 g (3.695 mmol, 99%). R_f=0.55 (Cy/acetone 1:1), ^{1}H NMR (400 MHz, $CDCl_3$-*d*) *δ* 7.75 (d, *J* = 8.1 Hz, 2H, Ar-H), 7.53 – 7.47 (m, 4H, Ar-H), 7.38 (dp, *J* = 9.8, 3.3 Hz, 5H, Ar-H), 7.33 – 7.18 (m, 6H, Ar-H), 6.86 – 6.79 (m, 5H, Ar-H), 5.27 – 5.19 (m, 1H, 1‘-H), 4.57 – 4.49 (m, 1H, 3‘-H), 4.25 (t, *J*=5.1 Hz, 1H, 4‘-H), 3.35 - 3.26 (m, 2H, 5‘-CH_2), 2.58 (s, 3H, CH_3), 2.50 (s, 3H, CH_3), 2.36 (dd, *J*=11.7, 5.4 Hz, 1H, 2’-CH_2), 2.06 (tdd, *J*=13.0, 6.2, 3.4 Hz, 1H, 2‘-CH_2), 1.18 (dt, *J*=6.7, 5.3 Hz, 9H, ^{i}Pr). ^{13}C{^{1}H} NMR (101 MHz, $CDCl_3$-*d*) *δ* 158.58, 153.29, 153.26, 145.03, 143.19, 143.16, 142.59, 138.79, 138.78, 136.30, 136.26, 136.23, 136.20, 135.31, 135.30, 130.32, 130.28, 128.46, 128.41, 127.94, 126.70, 121.89, 113.23, 86.26, 80.25, 58.57, 58.38, 55.36, 55.34, 43.39, 43.31, 43.27, 36.12, 27.06, 24.82, 24.74, 24.64, 24.57, 13.96, 10.12. ^{31}P{^{1}H} NMR (121 MHz, $CDCl_3$-*d*) δ 148.09, 147.92. MS (ESI): $[M+H]^+$ *m/z* 833.57.

2-((Bis(4-methoxyphenyl)(phenyl)methoxy)methyl)-5-(3-((1,3,5-trimethyl-1H-pyrazol-4-yl)diazenyl)phenyl)tetrahydrofuran-3-yl (2-cyanoethyl) diisopropyl phosphoramidite **23**

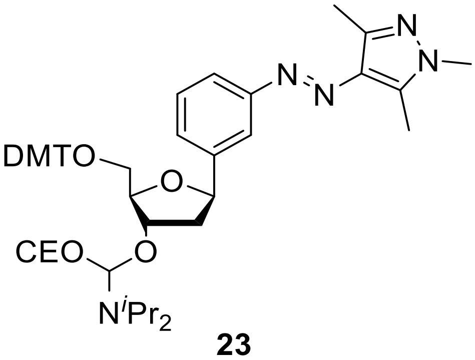

23

$C_{47}H_{57}N_6O_6P$

832.98 g/mol

To a solution of 1.51 g (2.39 mmol, 1.0 eq) of **21** and 2.10 mL (11.93 mmol, 5.0 eq) of *N,N*-diisopropylethylamine in 4 mL DCM 0.8 mL (3.58 mmol, 1.5 eq) 2-cyanoethyl-*N,N*-diisopropylchlorphosphoramidite have been added and stirred for 45 minutes at room temperature. After adding sodium hydrogen carbonate solution, the aqueous layer was extracted with DCM, the organic layer dried over sodium sulfate and evaporated under reduced pressure. The crude product was subjected to flash column chromatography (Cy/acetone 4:1→2:1 + 1% TEA) to afford the product as orange foam. Yield: 1.90 g (2.24 mmol, 94%). ^{1}H NMR (500 MHz, $CDCl_3$-*d*) δ 7.89 (m, 1H, Ar-H), 7.69 (m, 1H Ar-H), 7.50 (m, 2H, Ar-H), 7.47 – 7.41 (m, 2H, Ar-H), 7.41 – 7.34 (m, 5H, Ar-H), 7.29 – 7.20 (m, 3H, Ar-H), 6.81 – 6.76 (m, 4H, Ar-H), 5.26 (ddd, *J* = 10.6, 5.0, 3.2 Hz, 1H, 1'-H), 4.59 – 4.51 (m, 1H, 3'-H), 4.29 – 4.23 (m, 1H, 4'-H), 3.80-3.77 (m, 2H, CH) 3.76 – 3.73 (m, 9H, CH_3), 3.66 – 3.52 (m, 2H, CH_2), 3.38 (m, 1H, 5'-H), 3.24 (ddd, *J* = 9.9, 7.7, 4.3 Hz, 1H, 5'-H), 2.49 – 2.44 (s, 3H, CH_3), 2.37 (m, 4H, CH_3+2'-H), 2.12 (m, 1H, 2'-H), 1.22 – 1.06 (m, 12H, ^{i}Pr-H). ^{13}C{^{1}H} NMR (126 MHz, $CDCl_3$-*d*) δ 158.51, 153.92, 145.01, 142.84, 142.43, 139.16, 136.30, 136.18, 135.23, 130.25, 130.22, 129.01, 128.38, 127.91, 127.08, 126.78, 120.69, 119.98, 117.61, 113.22, 113.19, 86.19, 80.28, 64.21, 58.56, 58.41, 55.30, 43.58, 43.38, 43.33, 43.28, 43.23, 36.08, 31.08, 24.82, 24.79, 24.76, 24.73, 24.64, 24.62, 24.58, 24.56, 20.53, 20.36, 13.99, 10.16, 9.86. ^{31}P{^{1}H} NMR (202 MHz, $CDCl_3$-*d*) δ 147.97, 147.79. HRMS: Calculated for $C_{47}H_{57}N_6O_6P$ $[M+H]^+$ *m/z* 833.41500, found 833.41694.

5.1.3 Chemical syntheses of the LNAzo project

6-Di-*O*-isopropyliden-3-*O*-*p*-methoxybenzyl-α-*D*-*allo*-furanose **25**

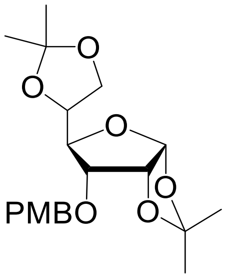

25

$C_{20}H_{28}O_7$
380.44 g/mol

Synthesis has been carried out according to literature.[208] Compound **24** (100.0 g, 384.2 mmol, 1.0 eq) was dissolved in 450 mL DMF. 15.52 g sodium hydride (60%, 388.03 mmol, 1.01 eq) was added and reaction was left to stir for one hour. PMBCl (60.77 g, 388.03 mmol, 1.01 eq) was added dropwise and the reaction was stirred for additional two hours. Upon completion, reaction was quenched by addition of water. After evaporation of the solvent, reaction mixture was dissolved in DCM, washed with water, dried over sodium sulfate and evaporated dryness. The crude product (brown viscous oil) was used without further purification. R_f = 0.52 (Cy/EA 1:1). Spectroscopic data were in accordance with literature.[208] ^{1}H NMR (400 MHz, $CDCl_3$-*d*) δ 7.32 (dt, *J* = 8.6 Hz, 2H, Ar-H), 6.88 (dt, *J* = 8.6 Hz, 2H, Ar-H), 5.74 (d, *J* = 3.7 Hz, 1H, 1'-H), 4.70 (d, *J* = 11.4 Hz, 1H, PMB-CH_2), 4.56-4.50 (m, *J* = 9.8, 7.9 Hz, 2H, PMB-CH_2+2'-H), 4,36 (td, *J* = 7.1, 3.1 Hz, 1H, 5'-H), 4.12 (dd, *J* = 8.7, 3.1 Hz, 1H, 4'-H), 3.97 (dt, *J* = 15.4, 8.2 Hz, 2H, 6'-H), 3.86 (dd, *J* = 8.7, 4.5 Hz, 1H, 3'-H), 3.80 (s, 3H, PMB-OMe), 1.58 (s, 3H, CH_3), 1.40-1.33 (m, 9H, CH_3). ^{13}C{^{1}H} NMR (101 MHz, $CDCl_3$-*d*) δ 159.67, 130.00, 129.71, 114.00, 113.03, 109.79, 104.00, 78.10, 77.98, 77.48, 77.24, 76.84, 74.89, 71.98, 65.13, 55.44, 26.99, 26.73, 26.33, 25.27.

1,2-*O*-Isopropyliden-3-*O*-*p*-methoxybenzyl-α-*D*-*allo*-furanose **26**

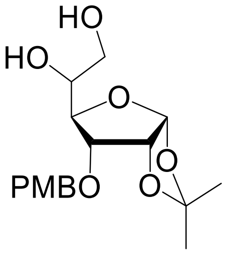

26

$C_{17}H_{24}O_7$
340.37 g/mol

Synthesis has been carried out according to literature.[208] Compound **1** (146.2 g, 384.2 mmol, 1.0 eq) was dissolved in 70% acetic acid and stirred overnight. Solvent was coevaporated with toluene, then the crude product was subjected to flash column chromatography (Cy/EA 1:1) to afford product as pale yellow viscous oil. Yield: 125.4 g (368.4 mmol, 96%). R_f = 0.2 (DCM/MeOH 19:1). Spectroscopic data were in accordance with literature.[208] ^{1}H NMR (500 MHz, $CDCl_3$-*d*) δ 7.32-7.28 (m, 2H, Ar-H), 6.91-6.87 (m, 2H, Ar-H), 5.76 (d, *J* = 3.8 Hz, 1H, 1‘-H), 4.72 (d, *J* = 11.1 Hz, 1H, PMB-CH_2), 4.60 (t, *J* = 4.0 Hz, 1H, 2‘) 4.49 (d, *J* = 11.1 Hz, 1H, PMB-CH_2), 4.09 (dd, *J* = 8.9, 3.3 Hz, 1H, 4‘-H), 3.99 (td, *J* = 4.9, 3.3 Hz, 1H, 5‘-H), 3.90 (dd, *J* = 8.9, 4.3 Hz, 1H, 3‘-H), 3.80 (s, 3H, PMB-OMe), 3.72-3.62 (m, 2H, 6‘-CH_2), 1.59 (s, 3H, CH_3), 1.37-1.35 (m, 3H, CH_3). ^{13}C{^{1}H} NMR (126 MHz, $CDCl_3$-*d*) δ 159.84, 130.14, 130.14, 128.79, 114.13, 114.11, 113.31, 104.30, 79.25, 77.35, 76.44, 71.93, 70.82, 63.17, 55.41, 26.91, 26.68.

4-Formyl-1,2-*O*-isopropyliden-3-*O*-*p*-methoxybenzyl-α-*D*-*ribo*-pentofuranose **27**

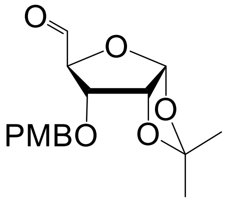

27

$C_{16}H_{20}O_6$
308.33 g/mol

Synthesis has been carried out according to literature.[208] Compound **26** (125.4 g, 368.8 mmol, 1.0 eq) was dissolved in water, sodium periodate (86.7 g, 409.3 mmol, 1.1 eq) was added and reaction was left to stir for two hours. Upon deactivation with 20 mL ethylene glycol, product was exrtracted with DCM, dried over sodium sulfate and evaporated to dryness to yield the product as pale yellow viscous oil. Yield: 112.9 g (366.4 mmol, 99%). R_f = 0.18 (Cy/EA 1:1). Spectroscopic data were in accordance with literature.[208] ^{1}H NMR (500 MHz, $CDCl_3$-*d*) δ 9.60 (d, *J* = 1.7 Hz, 1H, CHO), 7.29-7.27 (m, *J* = 5.4 Hz, 2H, Ar-H), 6.91-6.86 (m, 2H, Ar-H), 5.81 (d, *J* = 3.4 Hz, 1H, 1‘-H), 4.68 (d, *J* = 11.9 Hz, 1H, PMB-CH_2), 4.59-4.55 (m, *J* = 8.1, 4.2 Hz, 2H, PMB-CH_2+2‘-H), 4.47 (dd, *J* = 9.3,1.7 Hz, 1H, 4‘-H), 3.84-3.80 (m, 4H, PMB-OMe+3‘-H), 1.60 (s, 3H, CH_3), 1.37 (s, 3H, CH_3). ^{13}C{^{1}H} NMR (126 MHz, $CDCl_3$-*d*) δ 198.65, 159.81, 129.93, 129.87, 128.86, 114.13, 114.05, 114.05, 104.79, 104.76, 82.39, 78.02, 77.68, 72.22, 55.44, 27.10, 26.73.

4-*C*-Hydroxymethyl-1,2-*O*-isopropyliden-3-*O*-*p*-methoxybenzyl-α-*D*-*ribo*-pentofuranose **28**

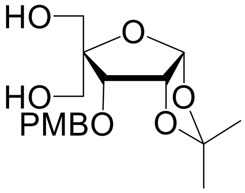

28

$C_{17}H_{24}O_7$
340.37 g/mol

Synthesis has been carried out according to literature.[208] Compound **27** (112.9 g, 366.4 mmol, 1.0 eq) was dissolved in a 1:1 mixture of water and THF. 330 mL of 37% formaldehyde solution and 400 mL 1 M NaOH was added and left to stir overnight at room temperature. Reaction mixture was extracted with DCM, combined organic phases were dried over sodium sulfate and evaporated to dryness. Crude product was subjected to flash column chromatography (Cy/EA 1:2 → 100% EA) to afford the product as yellow viscous oil. Yield: quantitative. R_f = 0.17 (Cy/EA 1:2). Spectroscopic data were in accordance with literature.[208] ^{1}H NMR (500 MHz, $CDCl_3$-*d*) δ 7.29 (d, *J* = 8.6 Hz, 2H, Ar-H), 6.89 (d, *J* = 8.5 Hz, 2H, Ar-H), 5.79-5.70 (m, 1H, 1‘-H), 4.77-4.71 (m, *J* = 8.0 Hz, 2H, PMB-CH_2), 4.64-4.59 (m, *J* = 9.1, 4.6 Hz, 1H, 2‘-H), 4.49 (d, *J* = 11.2 Hz, 1H, PMB-CH_2), 4.19 (d, *J* = 5.2 Hz, 1H, 3‘-H), 3.89 (s, 2H, 5‘-CH_2), 3.81 (s, 3H, PMB-OMe), 3.77-3.72 (m, 1H, 6‘-H), 3.54 (d, *J* = 12.1 Hz, 1H, 6‘-H), 1.63 (s, 3H, CH_3), 1.33 (s, 3H, CH_3).

1,2-*O*-Isopropylidene-5-*O*-methansulfonyl-4-*C*-methansulfonyloxymethyl-3-*O*-(*p*-methoxybenzyl-α-*D*-*erythro*-pentofuranose **29**

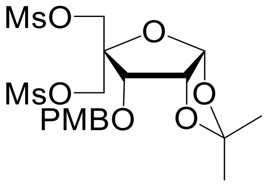

29

$C_{19}H_{28}O_{11}S_2$
496.54 g/mol

Synthesis has been carried out according to literature.[189] Compound **28** (84.19 g, 247.33 mmol, 1.00 eq) was dissolved in 300 mL dry pyridin. Mesyl chloride (56.7 g, 494.7 mmol, 2.0 eq) was added and reaction mixture was stirred for one hour at room temperature. The solvent was coevaporated with toluene, crude product was dissolved in DCM, washed with saturated $NaHCO_3$ solution, dried over sodium sulfate and evaporated to dryness. Crude product was subjected to flash column chromatography (Cy/EA 2:1 → 1:1) to afford the product as brownish viscous oil. Yield: 88.43 g (178.09 mmol, 72%). R_f = 0.30 (Cy/EA 99:1). Spectroscopic data were in accordance with literature.[189] ^{1}H NMR (400 MHz, $CDCl_3$-*d*) δ 7.30 (d, *J* = 8.4 Hz, 2H, Ar-H), 6.91 (d, *J* = 8.5 Hz, 2H, Ar-H), 5.78 (d, *J* = 3.6 Hz, 1H, 1‘-H), 4.86 (d, *J* = 12.0 Hz, 1H, PMB-CH_2), 4.70 (d, *J* = 11.4 Hz, 1H, CH_2), 4.61 (t, *J* = 4.3 Hz, 1H, 2‘-H), 4.50 (d, *J* = 11.3 Hz, 1H, PMB-CH_2), 4.39 (d, *J* = 12.0 Hz, 1H, CH_2), 4.30 (d, *J* = 11.0 Hz, 1H, CH_2), 4.17 (d, *J* = 5.0 Hz, 1H, 3‘-H), 3.82 (s, 3H, PMB-OMe), 3.08 (s, 3H, Ms-CH_3), 2.99 (s, 3H, Ms-CH_3), 1.68 (s, 3H, CH_3), 1.34 (s, 3H, CH_3).

Methyl-5-*O*-methansulfonyl-4-*C*-methansulfonyloxymethyl-3-*O*-(*p*-methoxybenzyl)-α,β-*D*-*erythro*-pentofuranosid **30**

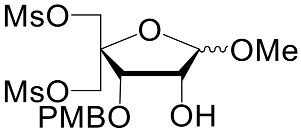

30

$C_{17}H_{26}O_{11}S_2$
470.50 g/mol

Synthesis has been carried out according to literature.[189] Compound **29** (181.92 g, 366.61 mmol, 1.00 eq) was dissolved in 700 mL MeOH. 200 mL 0.1 M hydrochloric acid was added and stirred overnight at room temperature. Reaction was neutralized with sodium hydroxide solution and evaporated to dryness. The crude product was subjected to flash column chromatography (Cy/EA 1:2 → EA/MeOH 1:1 + 1% TEA) to afford the product as pale yellow viscous oil. Yield: 33.19 g (70,54 mmol, 19%). R_f = 0.47 (DCM/MeOH 9:1). Spectroscopic data were in accordance with literature.[189] ^{1}H NMR (500 MHz, $CDCl_3$-*d*): δ 7.28 (d, *J* = 8.6 Hz, 2H, Ar-H), 6.91 (d, *J* = 8.6 Hz, 2H, Ar-H), 4.89-4.85 (m, 1H, 1'-H), 4.63 (d, *J* = 11.4. Hz, 1H, Ar-CH_2), 4.53 (d, *J* = 11.4 Hz, 1H, Ar-CH_2), 4.43 (d, *J* = 11.1 Hz, 1H, CH_2), 4.37 (d, *J* = 11.1 Hz, 1H, CH_2), 4.31 (d, *J* = 9.8 Hz, 1H, CH_2), 4.25 (d, *J* = 4.7 Hz, 1H, 2'-H), 4.06 (d, *J* = 9.8 Hz, 1H, CH_2), 3.96 (d, *J* = 4.7 Hz, 1H, 3'-H), 3.81 (d, *J* = 5.5 Hz, 3H, Ar-OMe), 3.33 (s, 2H, 1'-OMe), 3.07 (s, 3H, Ms-CH_3), 3.03 (s, 3H, Ms-CH_3). $^{13}C\{^1H\}$ NMR (126 MHz, $CDCl_3$-*d*) δ 171.32, 160.10, 130.18, 128.54, 114.40, 107.89, 81.77, 81.30, 69.76, 69.63, 60.55, 55.60, 55.47, 37.65, 37.57, 21.21, 14.35. MS (ESI) $[M+Na]^+$: *m/z* = 493.04.

(1*R*,3*RS*,4*R*,7*S*)-1-Methylsulfonyloxymethyl-3-methoxy-7-(*p*-methoxybenzyloxy)-2,5-dioxabicyclo[2.2.1]heptan **31**

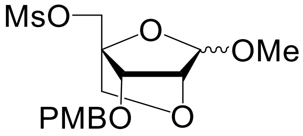

31

$C_{16}H_{22}O_8S$

374.40 g/mol

Synthesis has been carried out according to literature.[189] Compound **30** (33.19 g, 70,54 mmol, 1.00 eq) was dissolved in 100 mL dry DMF. Sodium hydride (60%, 6.8 g, 282.1 mmol, 4.0 eq) was added at 0 °C and stirred for 2.5 hours. Upon quenching with water, the reaction was evaporated to dryness. The residue was dissolved in ethyl acetate, washed with water, dried over sodium sulfate and evaporated to dryness. The crude product was subjected to flash column chromatography (Cy/EA 4:1 → EA/MeOH 9:1) to afford the product as yellowish viscous oil. Yield: 14.6 g (38.9 mmol, 55%). R_f = 0.42 (Cy/EA 1:1). Spectroscopic data were in accordance with literature.[189] ^{1}H NMR (250 MHz, $CDCl_3$-*d*) δ 7.29-7.22 (m, 2H, Ar-H), 6.91-6.86 (m, 2H, Ar-H), 4.80 (s, 1H, 1‘-H), 4.62-4.46 (m, *J* = 10.5, 9.9, 5.4 Hz, 4H, CH_2+6‘-H), 4.10 (d, *J* = 2.4 Hz, 2H, 2‘-H+3‘-H), 3.98 (s, 1H, 5‘-H), 3.81 (s, 3H, Ar-OMe), 3.69 (d, *J* = 7.4 Hz, 1H, 5‘-H), 3.37 (s, 3H, 1‘-OMe), 3.05 (s, 3H, Ms-CH_3). MS (ESI) $[M+ACN]^+$ m/z = 415.22.

(1*R*,3*RS*,4*R*,7*S*)-1-Acetoxymethyl-3-methoxy-7-(*p*-methoxybenzyloxy)-2,5-dioxabicyclo[2.2.1]heptan **32**

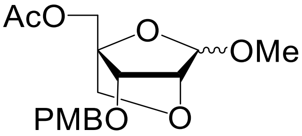

32

$C_{17}H_{22}O_7$

338.36 g/mol

Synthesis has been carried out according to literature.[189] Compound **31** (14.6 g, 38.9 mmol, 1.0 eq) was dissolved in 85 mL dry dioxan. Upon addition of 18-crown-6 (20.67 g, 78.19 mmol, 2.01 eq) and potassium acetate (19.28 g, 196.45 mmol, 5.05 eq) the reaction mixture was heated to 110 °C for 12 hours. Upon completion, reaction was evaporated to dryness. The residue was dissolved in DCM, washed with water, dried over sodium sulfate and evaporated to dryness. The crude product was subjected to flash column chromatography (Cy/EA 99:1 → 9:1) to yield the product as yellowish viscous oil. Yield: 5.49 g (16.23 mmol, 42%). R_f = 0.75 (Cy:EA 2:3). Spectroscopic data were in accordance with literature.[189] ^{1}H NMR (500 MHz, $CDCl_3$-*d*) δ 7.27 – 7.24 (m, 3H, Ar-H), 6.90 – 6.86 (m, 2H, Ar-H), 4.80 (s, 1H, 1‘-H), 4.59 (d, *J* = 11.5 Hz, 1H, 6‘-H), 4.50 – 4.45 (m, *J* = 11.9, 8.6 Hz, 2H, PMB-CH_2+6‘-H), 4.27 (d, 1H, PMB-CH_2), 4.10 (s, 1H, 2‘-H), 4.05 (s, 1H, 3‘-H), 3.99 (d, *J* = 7.4 Hz, 1H, 5‘-H), 3.81 (s, 3H, PMB-OMe), 3.71 (d, *J* = 7.4 Hz, 1H, 5‘-H), 3.37 (s, 3H, 1‘-OMe), 2.06 (s, 3H, Ms-CH_3). ^{13}C{^{1}H} NMR (126 MHz, $CDCl_3$-*d*) δ 170.78, 159.58, 129.48, 114.01, 105.21, 83.40, 78.97, 72.14, 72.06, 61.18, 55.55, 55.43, 20.87.

(1*R*,3*RS*,4*R*,7*S*)-1-Hydroxymethyl-3-methoxy-7-(*p*-methoxybenzyloxy)-2,5-dioxabicyclo[2.2.1]heptan **33**

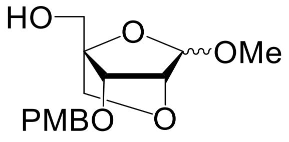

33

$C_{15}H_{20}O_6$
296.32 g/mol

Synthesis has been carried out according to literature.[189] Compound **32** (5.49 g, 16.23 mmol 1.00 eq) was dissolved in 200 mL of a methanolic ammonia solution (7 M) and stirred over night at room temperature. Upon completion, solvent was evaporated to dryness. Crude product has been used without further purification. Yield: quantitative. R_f = 0.30 (Cy/EA 1:1). Spectroscopic data were in accordance with literature.[189] ^{1}H NMR (500 MHz, $CDCl_3$-*d*): δ 7.27 – 7.25 (d, *J* = 8.6 Hz, 2H, Ar-H), 6.89 – 6.87 (m, 2H, Ar-H), 4.80 (s, 1H, 1‘-H), 4.59 (d, *J* = 11.5 Hz, 1H, 6‘-H), 4.53 (d, *J* = 11.5 Hz, 1H, 6‘-H), 4.09 (d, *J* = 2.9 Hz, 1H, 2‘-H), 3.97 (d, *J* = 7.5 Hz, 2H, CH_2), 3.85 (d, 2H, CH_2+3‘-H), 3.80 (s, 4H, Ar-OMe+CH_2), 3.64 (d, *J* = 7.4 Hz, 1H, CH_2), 3.37 (s, 3H, CH_3). ^{13}C{^{1}H} NMR (126 MHz, $CDCl_3$-*d*) δ 159.51, 129.79, 129.43, 113.98, 105.28, 85.63, 78.37, 77.46, 72.05, 71.88, 58.84, 55.61, 55.40.

(1*R*,3*RS*,4*R*,7*S*)-3-Methoxy-7-(*p*-methoxybenzyloxy)-1-(*p*-methoxybenzyloxymethyl)-2,5-dioxabicyclo[2.2.1]heptan **34**

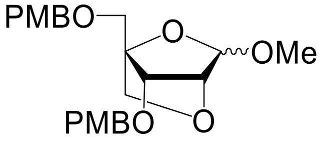

34

$C_{23}H_{28}O_7$
416.47 g/mol

Synthesis has been carried out according to literature.[189] Compound **33** (5.08 g, 17.14 mmol, 1.00 eq) was dissolved in 10 mL dry DMF. Sodium hydride (60%, 0.45 g, 18.84 mmol, 1.10 eq) was added at 0 °C and the reaction mixture was stirred for 15 minutes at room temperature. PMBCl (2.95 g, 18.84 mmol, 1.00 eq) was added and the reaction was stirred for an additional two hours. Upon completion, reaction was quenched with water and evaporated to dryness. The residue was dissolved in DCM, washed with water, dried over sodium sulfate and evaporated to dryness. The crude product was subjected to flash column chromatography (Cy:EE 4:1 → 1:1) to afford the product as colorless viscous oil. Yield 3.99 g (9.58 mmol, 56%). R_f = 0.64 (Cy/EA 1:1). Spectroscopic data were in accordance with literature.[189] ^{1}H NMR (250 MHz, $CDCl_3$-*d*,) δ 7.31 – 7.22 (m, *J* = 8.3, 6.9 Hz, 4H, Ar-H), 6.93 – 6.86 (m, 4H, Ar-H), 4.82 (s, 1H, 1'-H), 4.53 (dd, *J* = 16.6, 7.3 Hz, 3H, CH_2+6'-CH_2), 4.10 (s, 1H, 2'-H), 4.07 (s, 1H, 3'-H), 3.99 (d, *J* = 7.5 Hz, 1H, CH_2), 3.83 (s, 6H, Ar-OMe), 3.77 (dd, *J* = 7.2, 4.6 Hz, 3H, 5'-CH_2+CH_2), 3.38 (s, 3H, 1'-OMe).

(2*R*,3*S*,4*S*)-4-Hydroxy-3-(*p*-methoxybenzyloxy)-4-(*p*-methoxybenzyloxymethyl)-tetrahydrofuran-2-carbaldehyd **35**

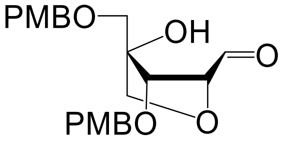

35

$C_{22}H_{26}O_7$
402.44 g/mol

Synthesis has been carried out according to literature.[189] Compound **34** (3.99 g, 9.58 mmol, 1.00 eq) was dissolved in 50 mL 70% acetic acid and stirred for 12 hours at room temperature. The solvent was coevaporated with toluene and subjected to flash column chromatography (Cy/EA 4:1 → 1:1) to afford the product as colorless viscous oil. Yield: 3.40 g (8.45 mmol, 88%). R_f = 0.26 (Cy/EA 1:1). Spectroscopic data were in accordance with literature.[189] ^{1}H NMR (500 MHz, $CDCl_3$-*d*) δ 9.64 (d, *J* = 0.8 Hz, 1H, 1'-H), 7.19 (d, *J* = 8.6 Hz, 4H, Ar-H), 6.88 – 6.84 (m, 4H, Ar-H), 4.59 (d, *J* = 11.4 Hz, 1H, CH_2), 4.51 – 4.46 (m, *J* = 10.0 Hz, 2H, CH_2), 4.45 – 4.42 (m, 1H, CH_2), 4.36 (s, 1H, 2'-H), 3.96 – 3.88 (m, *J* = 9.1 Hz, 4H, CH_2+3'-H), 3.80 (s, 3H, Ar-OMe), 3.78 (d, *J* = 9.2 Hz, 1H, CH_2), 3.45 (d, *J* = 9.2 Hz, 1H, CH_2). $^{13}C\{^1H\}$ NMR (126 MHz, DMSO-d_6) δ 202.75, 158.82, 158.71, 130.17, 129.41, 129.35, 129.28, 128.92, 128.22, 125.33, 113.66, 113.59, 86.50, 86.37, 80.26, 75.44, 72.37, 70.30, 69.63, 55.05, 55.03, 21.06.

(2*S*,3*S*,4*S*)-Hydroxy-2-[(*R*)-hydroxy-1‘-(*m*-azobenzyl)methyl]-4-(*p*-methoxybenzyloxy)-3-(*p*-methoxybenzyloxymethyl)-tetrahydrofuran (**36**, **37**)

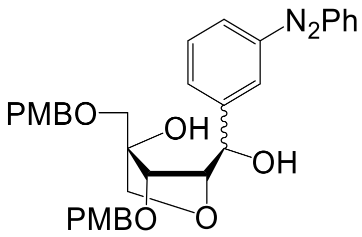

(*R*)-diastereomer **36**
(*S*)-diastereomer **37**

$C_{34}H_{36}N_2O_7$
584.67 g/mol

Meta-iodoazobenzene (17.64 g, 57.29 mmol, 7.10 eq) was dissolved in 100 mL dry THF and cooled to -90 °C. *N*-Butyllithium (2.5 M in hexane, 22.6 mL, 59.98 mmol, 7.0 eq) was added dropwise while stirring vigorously. After 30 minutes the solution was transferred to a solution of compound **1** (3.247 g, 8.069 mmol, 1.0 eq) in 35 mL of dry THF at -90 °C and stirred for 1 hour. The reaction was quenched by addition of aqueous NH_4Cl-solution. The organic layer was extracted with DCM, dried over Na_2SO_4 and evaporated to dryness. Crude product was subjected to flash column chromatography (Cy/EA + 1% TEA 2:1 → 1:1) and successive reverse phase column chromatography (MeOH/H_2O 4:1 → 9:1) for diastereomer separation to afford orange viscous oils as products.

(*R)*-diastereomer **36**: Yield: 0.332 g (0.568 mmol, 7%). R_f = 0.39 (Cy:EA 1:1). ^{1}H NMR (500 MHz, $CDCl_3$-*d*) δ 7.93 (dd, *J* = 7.1, 1.3 Hz, 3H, Ar-H), 7.87 (dt, *J* = 7.5, 1.6 Hz, 1H, Ar-H), 7.58 – 7.44 (m, 5H, Ar-H), 7.28 – 7.19 (m, 2H, Ar-H), 6.93 (d, *J* = 8.6 Hz, 2H, Ar-H), 6.88 (d, *J* = 8.6 Hz, 2H, Ar-H), 6.74 (d, *J* = 8.7 Hz, 2H, Ar-H), 4.85 (d, *J* = 6.0 Hz, 1H, 1‘-H), 4.51 (s, 2H, CH_2), 4.20 (d, *J* = 5.9 Hz, 1H, 2‘-H), 4.15 (dd, *J* = 6.0, 2.3 Hz, 1H, CH_2), 3.92 (d, *J* = 9.4 Hz, 1H, CH_2), 3.80 (s, 6H, CH_2+3‘-H, Ar-OMe), 3.76 (d, *J* = 9.3 Hz, 1H, CH_2), 3.71 (s, 3H, Ar-OMe), 3.53 (d, *J* = 9.3 Hz, 1H, CH_2). $^{13}C\{^1H\}$ NMR (126 MHz, $CDCl_3$-*d*) δ 159.54, 159.37, 152.77, 152.74, 142.15, 131.15, 129.71, 129.59, 129.34, 129.20, 114.01, 113.87, 89.27, 84.42, 81.90, 75.37, 74.37, 73.56, 71.85, 69.11, 55.38, 55.27. HRMS (MALDI) $[M+H]^+$ m/z = calculated: 585.25953, found: 585.23724.

(*S)*-diastereomer **37**: Yield: 0.654 g (1.119 mmol, 13%). R_f = 0.52 (Cy:EA 1:1). ^{1}H NMR (500 MHz, $CDCl_3$-*d*) δ 8.05 (s, 1H, Ar-H), 7.95 – 7.92 (m, 2H, Ar-H), 7.87 (d, *J* = 7.7 Hz, 1H, Ar-H), 7.60 – 7.45 (m, 5H, Ar-H), 7.25 – 7.19 (m, 2H, Ar-H), 6.90 – 6.83 (m, 2H, Ar-H), 6.71 (d, *J* = 8.8 Hz, 2H, Ar-H), 6.63 (d, *J* = 8.7 Hz, 2H, Ar-H), 5.20 (d, *J* = 2.9 Hz, 1H, 1‘-H), 4.49 (s, 2H, CH_2), 4.29 – 4.27 (m, 1H, 2‘-H), 3.95 (d, *J* = 9.4 Hz, 1H, CH_2), 3.84 (d, *J* = 1.3 Hz, 1H, 3‘-H), 3.79 (s, 4H, CH_2+Ar-OMe), 3.75 – 3.70 (m, 3H, CH_2+CH_2), 3.66 (s, 3H, Ar-OMe), 3.52 (d, *J* = 9.4 Hz, 1H, CH_2). $^{13}C\{^1H\}$ NMR (126 MHz, $CDCl_3$-*d*) δ 159.59, 159.21, 152.98, 152.74, 142.14, 131.26, 129.77, 129.32, 129.25, 128.73, 123.08, 122.32, 120.62, 114.04, 113.71, 90.85, 81.91, 81.35, 73.07, 71.28, 68.79, 55.41, 55.24. HRMS (MALDI) $[M+H]^+$ m/z = calculated: 585.25953, found: 585.25759.

(1*S*,3*S*,4*R*,7*S*)-1‘-(*m*-Azobenzyl)-7-(*p*-methoxybenzyloxy)-1-(*p*-methoxybenzyloxymethyl)-2,5-dioxabicyclo[2.2.1]heptan (**38**, **39**)

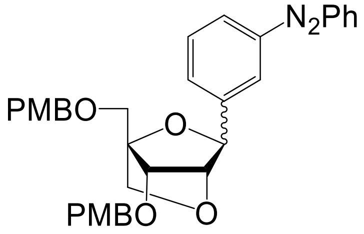

α-anomer **38**
β-anomer **39**

$C_{34}H_{34}N_2O_6$
566.65 g/mol

Tetramethylazodicarboxamide (0.289 g, 1.679 mmol, 1.5 eq / 0.148 g, 0.852 mmol, 1.5 eq) was dissolved in 10 mL dry benzene at 0 °C. Tributylphosphine (0.340 g, 1.679 mmol, 1.5 eq / 0.172 g, 0.852 mmol, 1.5 eq) and compound **36**/**37** (0.654 g, 1.119 mmol, 1.0 eq / 0.332 g, 0.568 mmol, 1.0 eq) dissolved in 1 mL dry benzene was added successively and stirred at room temperature overnight. The reaction was quenched by pouring into an aqueous NH_4Cl-solution. The organic phase was extracted with DCM, dried over sodium sulfate and evaporated to dryness. The crude product was subjected to flash column chromatography (Cy/EA + 1% TEA 4:1 → 1:1) to afford the product as viscous orange oil.

α-anomer **38**: Yield: 0.606 g (1.069 mmol, 96%). R_f = 0.50 (Cy/EA 1:1). ^{1}H NMR (500 MHz, $CDCl_3$-*d*) δ 7.93 – 7.89 (m, 3H, Ar-H), 7.86 – 7.82 (m, 1H, Ar-H), 7.54 – 7.46 (m, 5H, Ar-H), 7.32 – 7.27 (m, 4H, Ar-H), 6.92 – 6.85 (m, 5H, Ar-H), 5.26 (s, 1H, 1’-H), 4.67 – 4.56 (m, 4H, CH_2+CH_2), 4.43 (s, 1H, 2’-H), 4.32 (s, 1H, 3’-H), 4.04 – 3.98 (m, 1H, CH_2), 3.82 (s, 3H, Ar-OMe), 3.81 (s, 3H, Ar-OMe), 3.83 – 3.72 (m, 1H, CH_2). $^{13}C\{^1H\}$ NMR (126 MHz, $CDCl_3$-*d*) δ 159.53, 152.83, 140.11, 131.06, 129.83, 129.60, 129.45, 129.20, 129.09, 122.97, 122.15, 120.72, 114.02, 113.95, 87.62, 82.07, 80.79, 73.58, 71.84, 65.83, 55.44, 55.42. HRMS (MALDI) $[M+H]^+$ m/z = calculated: 567.24896, found: 567.24702.

β-anomer **39** Yield: 0.239 g (0.422 mmol, 74%). R_f = 0.71 (Cy/EA 1:1). ^{1}H NMR (500 MHz, $CDCl_3$-*d*) δ 7.94 – 7.90 (m, 2H, Ar-H), 7.90 – 7.87 (m, 1H, Ar-H), 7.82 (d, *J* = 7.9 Hz, 1H, Ar-H), 7.55 – 7.46 (m, 4H, Ar-H), 7.32 – 7.29 (m, 2H, Ar-H), 7.12 – 7.09 (m, 2H, Ar-H), 6.88 (dd, *J* = 10.8, 8.2 Hz, 3H, Ar-H), 6.78 – 6.73 (m, 2H, Ar-H), 5.26 (s, 1H, 1‘-H), 4.60 (dd, *J* = 19.6, 8.4 Hz, 2H, CH_2), 4.47 – 4.42 (m, 1H, CH_2), 4.37 (d, *J* = 11.3 Hz, 1H, CH_2), 4.25 (s, 1H, 2‘-H), 4.11 (d, *J* = 1.4 Hz, 1H, CH_2), 4.04 (s, 1H, 3‘-H), 3.85 (dd, *J* = 23.4, 11.5 Hz, 2H, CH_2), 3.78 (s, 3H, Ar-OMe), 3.73 (s, 3H, Ar-OMe). $^{13}C\{^1H\}$ NMR (126 MHz, $CDCl_3$-*d*) δ 159.44, 159.33, 152.86, 152.71, 140.71, 131.30, 130.29, 129.58, 129.36, 129.26, 127.97, 123.07, 122.97, 121.75, 120.18, 113.93, 113.86, 86.21, 83.76, 71.98, 66.33, 55.38. HRMS (MALDI) $[M+H]^+$ m/z = calculated: 567.24896, found: 567.24634.

(1*S*,3*S*,4*R*,7*S*)-1'-(*m*-Azobenzyl)-7-hydroxy-1-hydroxymethyl-2,5-dioxabicyclo[2.2.1]heptan (**40**, **41**)

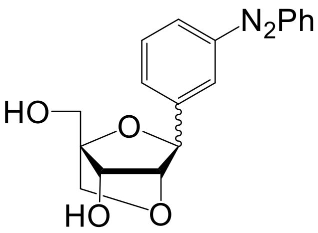

α-anomer **40**
β-anomer **41**

$C_{18}H_{18}N_2O_4$
326.35 g/mol

Compound **38** (0.606 g, 1.069 mmol, 1.0 eq) or **39** (0.239 g, 0.422 mmol, 1.0 eq) was dissolved in 10 mL DCM. Upon addition of 0.5 mL water and DDQ (0.335 g, 1.476 mmol, 3.5 eq / 0.850 g, 3,743 mmol, 3.5 eq) the reaction was left to stir over night. The reaction was filtered, the organic phase washed with an aqueous $NaHCO_3$ solution and brine successively, dried over sodium sulfate and evaporated to dryness. The crude product was subjected to flash column chromatography (DCM/MeOH 19:1→9:1) to afford the product as viscous orange oil.

α-anomer **40**: Yield: 0.221 g (0,677 mmol, 63%). R_f = 0.52 (Cy/EA 1:1). ^{1}H NMR (400 MHz, DMSO-*d*$_6$) δ 7.96 – 7.88 (m, 3H, Ar-H), 7.79 (dq, *J* = 7.0, 2.8, 2.2 Hz, 1H, Ar-H), 7.64 – 7.55 (m, 5H, Ar-H), 5.62 (d, *J* = 4.3 Hz, 1H, 3'-OH), 5.27 (s, 1H, 1'-H), 4.84 (t, *J* = 5.7 Hz, 1H, 5'-OH), 4.30 – 4.24 (m, 2H, 2'-H+3'-H), 3.86 (d, *J* = 7.6 Hz, 1H, 6'-H), 3.76 (t, *J* = 6.9 Hz, 3H, 6'-H+5'-CH_2). ^{13}C{^{1}H} NMR (126 MHz, $CDCl_3$-*d*) δ 152.78, 152.76, 139.65, 131.23, 129.25, 128.44, 123.01, 122.28, 120.54, 88.32, 81.88, 81.69, 72.66, 58.89. HRMS (MALDI) $[M+H]^+$ m/z = calculated: 327.13393, found: 327.13383.

β-anomer **41**: Yield: 0.078 g (0,239 mmol, 57%). R_f = 0,44 (Cy/EA 1:1). ^{1}H NMR (400 MHz, DMSO-*d*$_6$) δ 7.94 – 7.88 (m, 3H, Ar-H), 7.77 (dt, *J* = 6.5, 2.2 Hz, 1H, Ar-H), 7.65 – 7.55 (m, 5H, Ar-H), 5.35 (d, *J* = 4.4 Hz, 1H, 3‘-OH), 5.08 (s, 1H, 1‘-H), 4.95 (t, *J* = 5.7 Hz, 1H, 5‘-OH), 4.15 (s, 1H, 2‘-H), 3.94 (d, *J* = 4.3 Hz, 1H, 3‘-H), 3.91 (d, *J* = 7.5 Hz, 1H, 6‘-H), 3.81 (d, *J* = 7.5 Hz, 1H, 6‘-H), 3.78 (dd, *J* = 5.7, 1.9 Hz, 2H, 5‘-CH_2). ^{13}C{^{1}H} NMR (126 MHz, $CDCl_3$-*d*) δ 152.90, 152.66, 139.94, 131.42, 129.55, 129.29, 127.77, 123.09, 122.35, 119.82, 86.84, 83.88, 83.33, 72.45, 71.69, 59.59. HRMS (MALDI) $[M+H]^+$ m/z = calculated: 327.13393, found: 327.13374.

(1*R*,3*S*,4*R*,7*S*)-1-(4,4‘-Dimethoxytrityloxymethyl)-1‘-(*m*-azobenzyl)-3-hydroxy-2,4-dioxabicyclo[2.2.1]heptan (**42**, **43**)

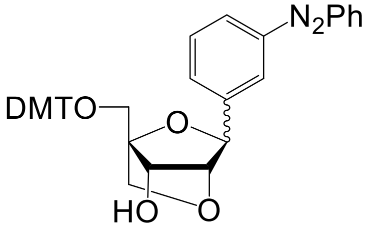

α-anomer **42**
β-anomer **43**

$C_{39}H_{36}N_2O_6$
628.73 g/mol

Compound **40** (0.078 g, 0,239 mmol, 1.0 eq) or **41** (0.221 g, 0,677 mmol, 1.0 eq) was dissolved in 5 mL dry pyridine. DMTCl (0.089 g, 0.262 mmol, 1.1 eq / 0.221 g, 0.745 mmol, 1.1 eq) dissolved in 5 mL of dry pyridine was added dropwise over a time of 45 minutes at 0 °C and left to stir for 4 hours. Upon completion of the reaction pyridine was coevaporated with toluene. The residue was extracted with DCM, the organic layer was dried over Na_2SO_4 and evaporated to dryness. The crude product was subjected to flash column chromatography (Cy/EA 2:1 + 1% TEA) to afford the product as orange foam.

α-anomer **42**: Yield: 0.195 g (0.310 mmol, 46%). R_f = 0.67 (Cy/EA 1:1). ^{1}H NMR (500 MHz, DMSO-*d$_6$*) δ 8.01 (s, 1H, Ar-H), 7.92 – 7.88 (m, *J* = 8.1, 1.5 Hz, 2H, Ar-H), 7.85 – 7.82 (m, 1H, Ar-H), 7.66 – 7.57 (m, 5H, Ar-H), 7.46 (d, *J* = 7.3 Hz, 2H, Ar-H), 7.37 – 7.20 (m, 5H, Ar-H), 7.08 – 7.04 (m, 1H, Ar-H), 6.94 – 6.88 (m, 4H, Ar-H), 6.85 – 6.82 (m, 1H, Ar-H), 5.68 (d, *J* = 4.6 Hz, 1H, 3’-OH), 5.34 (s, 1H, 1’-H), 4.32 (s, 1H, 2’-H), 4.29 (d, *J* = 4.6 Hz, 1H, 3’-H), 4.01 (d, *J* = 7.7 Hz, 1H, 5’-H), 3.88 (d, *J* = 7.7 Hz, 1H, 5’-H), 3.77 – 3.69 (m, 6H, Ar-OMe), 3.39 – 3.29 (m, 2H, 6’-CH_2). ^{13}C{^{1}H} NMR (126 MHz, DMSO-*d$_6$*) δ 158.10, 129.78, 129.51, 128.92, 127.73, 122.54, 113.24, 55.63, 55.03, 54.93. HRMS (MALDI) $[M+H]^+$ m/z = calculated: 629.26461, found: 629.26536.

β-anomer **43**: Yield: 0.138 mg (0.221 mmol, 92%). R_f = 0.63 (Cy/EA 1:1). ^{1}H NMR (500 MHz, DMSO-*d$_6$*) δ 8.02 (s, 1H, Ar-H), 7.80 (t, *J* = 7.5 Hz, 1H, Ar-H), 7.76 – 7.72 (m, 2H, Ar-H), 7.62 (dd, *J* = 16.1, 7.6 Hz, 2H, Ar-H), 7.55 (dt, *J* = 4.6, 2.5 Hz, 3H, Ar-H), 7.50 (d, *J* = 7.4 Hz, 2H, Ar-H), 7.38 – 7.25 (m, 3H, Ar-H), 7.21 (m, *J* = 16.9, 7.2, 5.8 Hz, 2H, Ar-H), 7.10 – 7.05 (m, 2H, Ar-H), 6.88 (m, *J* = 9.6, 7.0, 2.4 Hz, 2H, Ar-H), 6.86 – 6.82 (m, 2H, Ar-H), 5.42 (d, *J* = 4.7 Hz, 1H, 3‘-OH), 5.18 (s, 1H, 1‘-H), 4.25 (s, 1H, 2‘-H), 4.05 – 4.03 (m, 1H, 3‘-H), 3.94 (d, *J* = 7.2 Hz, 1H, 5‘-H), 3.85 (d, *J* = 7.4 Hz, 1H, 5‘-H), 3.70 (d, *J* = 4.9 Hz, 6H, Ar-OMe), 3.41 – 3.26 (m, 2H, 6‘-CH_2). ^{13}C{^{1}H} NMR (126 MHz, DMSO-*d$_6$*) δ 158.07, 157.81, 148.36, 140.24, 135.61, 129.78, 129.36, 128.92, 127.85, 127.65, 127.43, 126.45, 122.57, 113.20, 112.77, 85.78, 82.40, 79.91, 70.06, 59.77, 55.01, 54.92, 20.78. HRMS (MALDI) $[M+H]^+$ m/z = calculated: 629.26461, found: 629.26530.

(1*R*,3*S*,4*R*,7*S*)-7-[2-Cyanoethoxy(diisopropylamino)phosphinoxyl]-1-(4,4‘-dimethoxytrityloxymethyl)-1‘-(*m*-azobenzyl)-2,5-dioxabicyclo[2.2.1]heptan (**44**,**45**)

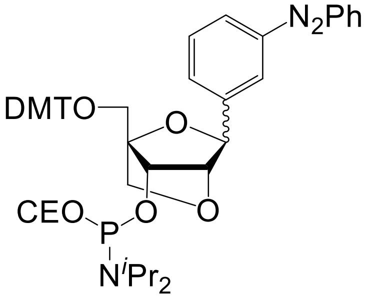

α-anomer **44**
β-anomer **45**

$C_{48}H_{53}N_4O_7P$
828.95 g/mol

Compound **42** (0.195 g, 0.310 mmol, 1.0 eq) or **43** (0.138 g, 0.221 mmol, 1.0 eq) was dissolved in 3 mL of dry DCM. DIPEA (0.200 g, 1.545 mmol, 5.0 eq / 0.143 g, 1.105 mmol, 5.0 eq) and CEO(N^{i}Pr$_2$)PCl (0.110 g, 0.465 mmol, 1.5 eq / 0.079 g, 0.332 mmol, 1.5 eq) were added successively and left to stir at room temperature for 2 hours. Upon quenching with methanol the reaction was evaporated to dryness, extracted with DCM, dried over Na_2SO_4 and evaporated to dryness again. The crude product was subjected to flash column chromatography (n-hexane/acetone 9:1 → 2:1) to afford the product as orange foam.

α-anomer **44**: Yield: 0.158 g (0.191 mmol, 51%). R_f = 0.53 (Cy/Aceton 2:1). ^{1}H NMR (500 MHz, DMSO-*d*$_6$) δ 8.01 (s, 1H, Ar-H), 7.93 – 7.89 (m, 2H, Ar-H), 7.87 – 7.83 (m, 1H, Ar-H), 7.66 – 7.58 (m, 4H, Ar-H), 7.48 – 7.44 (m, 2H, Ar-H), 7.35 – 7.29 (m, 4H, Ar-H), 7.27 – 7.22 (m, 2H, Ar-H), 6.93 – 6.87 (m, 5H, Ar-H), 6.87 – 6.83 (m, 1H, Ar-H), 5.43 (d, *J* = 4.4 Hz, 1H, 1’-H), 4.60 – 4.48 (m, 2H, 2’-H+3’-H), 4.05 (dd, *J* = 16.8, 7.9 Hz, 2H, CH_2+CH_2), 3.86 – 3.81 (m, 1H, CH_2), 3.79 – 3.71 (m, 7H, Ar-OMe+CH_2), 3.59 – 3.41 (m, 2H, CEO-CH_2), 2.67 – 2.60 (m, 2H, CH_2), 1.25 – 0.92 (m, 14H, ^{i}Pr). ^{13}C{^{1}H} NMR (126 MHz, DMSO-*d*$_6$) δ 158.11, 151.97, 151.84, 144.74, 137.73, 136.89, 136.57, 135.46, 134.91, 129.75, 129.71, 129.51, 127.87, 127.63, 126.72, 122.54, 113.20, 55.01, 24.32, 19.81, 19.75. ^{31}P{^{1}H} NMR (121 MHz, DMSO-*d*$_6$) δ 148.23, 148.10, 146.92, 146.80. HRMS (MALDI) $[M+H]^+$ m/z = calculated: 829.37246, found: 829.73083.

β-anomer **45**: Yield: 0.079 g (0.095 mmol, 43%). R_f = 0.53 (Cy/Aceton 2:1). 1H NMR (500 MHz, DMSO-*d*$_6$) δ 7.84 – 7.80 (m, 1H, Ar-H), 7.73 – 7.64 (m, 3H, Ar-H), 7.55 – 7.47 (m, 4H, Ar-H), 7.40 – 7.32 (m, 5H, Ar-H), 7.31 – 7.25 (m, 3H, Ar-H), 7.23 – 7.16 (m, 2H, Ar-H), 6.92 – 6.83 (m, 4H, Ar-H), 5.28 (d, *J* = 10.6 Hz, 1H, 1‘-

H), 4.56 (s, 1H, 2‘-H), 4.39 (s, 1H, 3‘-H), 4.11 – 3.96 (m, 4H, CEO-CH_2+CH_2), 3.70 – 3.66 (m, 6H, Ar-OMe), 3.49 – 3.40 (m, 3H, 6‘-H+CH_2), 3.24 (d, 10.7 Hz, 1H, CH_2), 2.89 (t, *J* = 5.9 Hz, 2H, CEO-CH_2), 1.21 – 1.16 (m, 14H, iPr). $^{13}C\{^1H\}$ NMR (126 MHz, DMSO-*d6*) δ 158.05, 152.16, 151.74, 141.09, 135.36, 129.82, 129.77, 129.72, 129.32, 129.26, 127.84, 127.79, 127.73, 126.67, 122.52, 118.60, 113.13, 113.08, 112.76, 112.29, 85.53, 82.61, 82.50, 58.17, 58.13, 54.93, 46.16, 44.46, 22.82, 22.65, 22.63, 22.60, 19.39, 19.33, 18.82. $^{31}P\{^1H\}$ NMR (121 MHz, DMSO-*d6*) δ 147.60, 147.56, 147.18, 146.54. HRMS (MALDI) $[M]^+$ m/z = calculated: 828.36464, found: 828.92814.

5.1.4 Chemical syntheses of the 2-phenyldiazenyl purine project

3’,5’-Di-*O*-acetyl-2’-deoxy-adenosine **46**

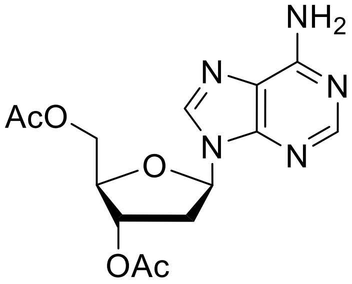

46

$C_{14}H_{17}N_5O_5$

335.32 g/mol

To a solution of 62.190 g (247.5 mmol, 1.0 eq) of 2’-deoxyadenosine, 1,512 g (12,377 mmol, 0.05 eq) 4-*N*,*N*-dimethylamino-pyridine and 137 mL (0.99 mol, 4.0 eq) triethylamine in 270 mL acetonitrile, 49 mL (53.068 mmol, 2.1 eq) acetic acid anhydride was added dropwise at 0 °C, then stirred for 3 h at room temperature. Upon completion, excess anhydride was quenched with methanol and solvents where evaporated at a rotary evaporator. Residue was dissolved in DCM, washed with 10 mM hydrochloric acid, dried over Na_2SO_4, and evaporated to dryness. Flash column chromatography (DCM/MeOH 19:1 → 9:1) afforded the product as colorless powder. Yield: 72.65 g (216.657 mmol, 88%). R_f = 0.48 (DCM/MeOH 9:1). ^1H NMR (500 MHz, DMSO-*d6*) δ 8.34 (s, 1H, 8), 8.15 (s, 1H, 2), 7.32 (s, 2H, NH_2), 6.36 (dd, *J* = 8.0, 6.3 Hz, 1H, 1’), 5.40 (dt, *J* = 5.2, 2.3 Hz, 1H, 3’), 4.31 (dt, *J* = 11.2, 5.6 Hz, 1H, 5’), 4.25 – 4.22 (m, 1H, 4’), 4.20 (dd, *J* = 10.8, 5.9 Hz, 1H, 5’), 3.16 (ddd, *J* = 14.4, 8.0, 6.6 Hz, 1H, 2’), 2.09 (s, 3H, CH_3), 2.01 (s, 3H, CH_3). $^{13}C\{^1H\}$ NMR (126 MHz, DMSO-*d6*) δ 170.17, 170.07, 156.13, 152.68, 149.21, 139.58, 119.23, 83.52, 81.60, 74.41, 63.61, 21.32, 20.84, 11.04. HRMS (MALDI) $[M+H]^+$ m/z = calculated: 336.13025, found: 336.13050.

6-Chloropurine-3‘,5‘-di-*O*-acetyl-2’deoxyriboside **47**

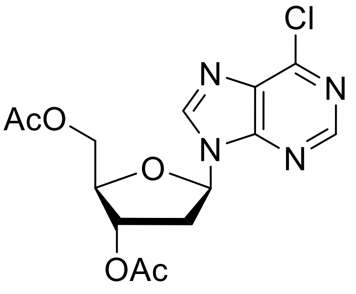

47

$C_{14}H_{15}ClN_4O_5$
354.75 g/mol

To a solution of 72.65 g (216,66 mmol, 1.0 eq) of compound **2** in 300 mL DCM, 87 mL (1.22 mol, 5.5 eq) acetyl chloride and 100 mL (1.12 mol, 4.5 eq) tert-butyl nitrite were added dropwise subsequently at 0 °C and then stirred at 0 °C. Upon completion, the reaction was quenched with 1 M NaOH, extracted with DCM, dried over Na_2SO_4 and evaporated to dryness. Flash column chromatography (Cy/EA 1:2 → 100% EA) afforded the product as pale yellow oil. Yield: 7.73 g (21.790 mmol, 10%). R_f = 0.66 (DCM/MeOH 9:1). ^{1}H NMR (500 MHz, DMSO-d_6) δ 8.90 (s, 1H, 8), 8.82 (s, 1H, 2), 6.51 (t, *J* = 6.9 Hz, 1H, 1’), 5.49 – 5.41 (m, 1H, 3’), 4.31 (ddd, *J* = 12.5, 8.4, 3.7 Hz, 2H, 4’+5’), 4.27 – 4.19 (m, 1H, 5’), 3.18 (dt, *J* = 14.2, 7.0 Hz, 1H, 2’), 2.68 – 2.59 (m, 1H, 2’), 2.10 (s, 3H, CH_3), 1.99 (s, 3H, CH_3). $^{13}C\{^1H\}$ NMR (126 MHz, DMSO-d_6) δ 170.13, 170.07, 151.78, 151.40, 149.44, 146.08, 131.55, 84.28, 81.99, 74.04, 63.44, 35.48, 20.81, 20.51. HRMS (MALDI) $[M+H]^+$ m/z = calculated: 355.08037, found: 355.08047.

2-Nitro-6-chloropurine-3‘,5‘-di-*O*-acetyl-2’deoxyriboside **48**

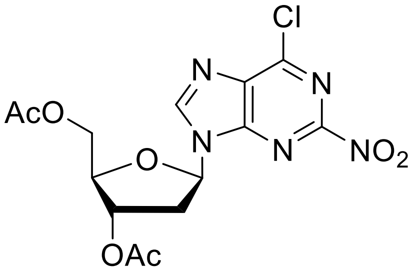

48

$C_{14}H_{14}ClN_5O_7$
399.74 g/mol

The nitration mixture was prepared by dropwise addition of 0.21 mL (1.450 mmol, 1.5 eq) of trifluoro acetic anhydride to a solution of 0.442 g (1.450 mmol, 1.5eq) of tetrabutyl ammonium nitrate in 10 mL of DCM at 0 °C and stirring for 20 minutes. The nitration mixture was then added to a solution of compound **47** in 20 mL DCM at 0 °C and was stirred for 2 hours at 0 °C. Upon completion, the reaction mixture as poured into an ice-cooled aqueous sodiumcarbonate solution, extracted with DCM, dried over Na_2SO_4 and evaporated to dryness. Flash column chromatography (DCM/MeOH 99:1 → 9:1) afforded the product as pale yellow foam. Yield: 262 mg (0,546 mmol, 56%). R_f = 0.5 (DCM/MeOH 19:1). ^{1}H NMR (500 MHz, DMSO-*d*$_6$) δ 9.22 (s, 1H, 8), 6.56 (q, *J* = 6.7 Hz, 1H, 1’), 5.51 – 5.46 (m, 1H, 3’), 4.37 – 4.31 (m, 2H, 4’+5’), 4.28 (td, *J* = 7.5, 1.9 Hz, 1H, 5’), 3.12 (dt, *J* = 14.0, 6.8 Hz, 1H, 2’), 2.70 (ddd, *J* = 14.4, 6.6, 3.5 Hz, 1H, 2’), 2.11 (s, 3H, CH_3), 1.99 – 1.97 (m, 3H, CH_3). ^{13}C{^{1}H} NMR (126 MHz, DMSO-*d*$_6$) δ 170.11, 170.06, 152.30, 151.62, 149.95, 149.73, 134.77, 84.70, 82.34, 73.81, 63.44, 54.93, 20.81, 20.51. HRMS (MALDI) [M+Na]$^+$ m/z = calculated: 422.04740, found: 422.04744.

2-Hydroxyamino-6-chloropurine-3‘,5‘-di-*O*-acetyl-2’deoxyriboside **49**

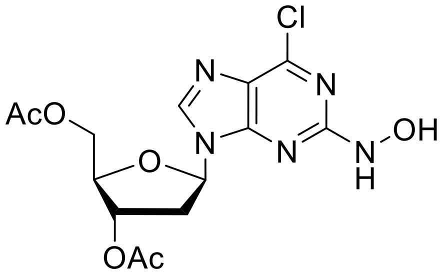

49

$C_{14}H_{16}ClN_5O_6$

385.76 g/mol

To a solution of 1.840 g (4.603 mmol, 1.0 eq) of compound **48** in a mixture of 10 mL EA and 5 mL EtOH, 0.211 g palladium on charcoal where added and was left to stir under hydrogen atmosphere for 2 hours. Upon completion, the catalyst was filtered off and the solution was evaporated to dryness. Crude product was directly used for subsequent reaction without further purification and yielded an off-white foam. Yield: 1.510 g (3.913 mmol, 85%). R_f = 0.29 (DCM/MeOH 19:1). ^{1}H NMR (400 MHz, DMSO-*d*$_6$) δ 9.85 (s, 1H, OH), 8.91 (s, 1H, NH) 8.44 (s, 1H, 8), 6.33 (t, *J* = 6.9 Hz, 1H, 1’), 5.37 (d, *J* = 4.3 Hz, 1H, 3’), 4.28 – 4.20 (m, 3H, 4’+5’), 3.19 – 3.03 (m, 1H, 2’), 2.69 (dt, *J* = 16.6, 6.7 Hz, 1H, 2’), 2.02 (s, 3H, CH_3), 1.98 (s, 3H, CH_3). $^{13}C\{^1H\}$ NMR (101 MHz, DMSO-*d*$_6$) δ 170.10, 161.78, 153.25, 151.58, 149.88, 141.87, 81.66, 73.77, 63.54, 55.99, 35.18, 20.78, 20.51, 18.52. HRMS (MALDI) $[M+H]^+$ m/z = calculated: 386.08619, found: 386.08493.

2-Nitroso-6-chloropurine-3‘,5‘-di-*O*-acetyl-2’deoxyriboside **50**

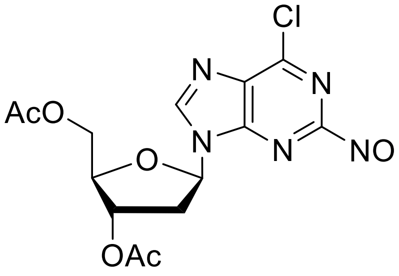

50

$C_{14}H_{14}ClN_5O_6$
383.75 g/mol

To a solution of 1.510 g (3.913 mmol, 1.0 eq) of compound **49** in 10 mL EA a solution of 1.181 g (5.523 mmol, 1.2 eq) of sodium periodate in 5 mL water was added and stirred for 30 minutes at room temperature. Upon completion, the mixture was extracted with EA, dried over Na_2SO_4 and evaporated to dryness. Flash column chromatography (Cy/EA 1:1 → 100% EA) afforded the product as pale yellow foam. Yield: 1.465 g (3.818 mmol, 98%). R_f = 0.43 (DCM/MeOH 19:1). ^{1}H NMR (400 MHz, DMSO-d_6) δ 9.26 (s, 1H, 8), 6.63 (t, *J* = 6.7 Hz, 1H, 1’), 5.55 – 5.47 (m, 1H, 3’), 4.31 (m, 3H, 4’+5’), 3.20 (dt, *J* = 14.2, 6.9 Hz, 1H, 2’), 2.72 (ddd, *J* = 14.1, 7.2, 3.5 Hz, 1H, 2’), 2.12 (s, 3H, CH_3), 1.97 (s, 3H, CH_3). ^{1}H NMR (500 MHz, $CDCl_3$-*d*) δ 8.61 (s, 1H, 8), 6.58 (t, *J* = 6.8 Hz, 1H, 1’), 5.45 (dd, *J* = 11.4, 8.5 Hz, 1H, 3’), 4.48 – 4.36 (m, 3H, 4’+5’), 2.91 – 2.84 (m, 1H, 2’), 2.79 (ddd, *J* = 14.2, 6.0, 2.7 Hz, 1H, 2’), 2.18 – 2.14 (m, 3H, CH_3), 2.09 (s, 3H, CH_3). $^{13}C\{^1H\}$ NMR (126 MHz, $CDCl_3$-*d*) δ 170.37, 170.32, 153.37, 152.85, 151.30, 147.18, 135.09, 85.71, 83.51, 74.07, 63.58, 38.47, 21.03, 20.90. HRMS (MALDI) $[M+H]^+$ m/z = calculated: 384.07058, found: 384.07058.

2-Phenyldiazenyl-6-chloropurine-3‘,5‘-di-*O*-acetyl-2’deoxyriboside **51**

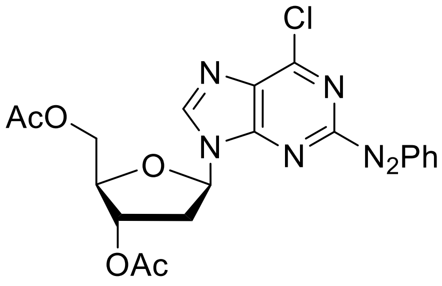

51

$C_{20}H_{19}ClN_6O_5$

458.86 g/mol

To a solution of 0.342 g (0.891 mmol, 1.0 eq) of compound **50** in 5 mL ACN, 80 µL (1.18 mmol, 1.2 eq) aniline where added and stirred for 10 minutes, before 100 µL acetic acid where added and stirred for 30 minutes. Upon completion, the solution was neutralized by addition of aqueous sodium carbonate solution, extracted with DCM, dried over Na_2SO_4 and evaporated to dryness. Flash column chromatography (Cy/EA 1:1 → 100% EA) afforded the product as orange foam. Yield: 0.286 mg (0.624 mmol, 70%). R_f = 0.28 (DCM/MeOH 19:1). ^{1}H NMR (500 MHz, DMSO-d_6) δ 9.03 (s, 1H, 8), 8.05 (dd, *J* = 7.9, 1.7 Hz, 2H, Ar), 7.72 – 7.66 (m, 3H, Ar), 6.57 (t, *J* = 6.8 Hz, 1H, 1’), 5.51 (dd, *J* = 6.3, 3.1 Hz, 1H, 3’), 4.38 – 4.27 (m, 3H, 4’+5’), 3.17 (dt, *J* = 14.1, 6.9 Hz, 1H, 2’), 2.68 (ddd, *J* = 14.3, 6.5, 3.3 Hz, 1H, 2’), 2.10 (s, 3H, CH_3), 1.98 (s, 3H, CH_3). $^{13}C\{^1H\}$ NMR (126 MHz, DMSO-d_6) δ 165.54, 165.51, 156.52, 147.85, 147.78, 147.42, 139.85, 128.66, 127.12, 124.52, 123.84, 122.26, 119.50, 80.27, 78.31, 69.54, 58.96, 33.69, 16.19, 16.09. HRMS (MALDI) $[M+Na]^+$ m/z = calculated: 481.09909, found: 481.09977.

2-Phenyldiazenyl-2'-deoxyguanosine **52**

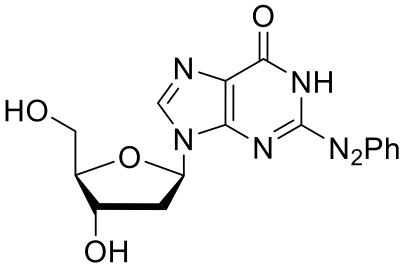

52

$C_{16}H_{16}N_6O_4$
356.34 g/mol

To a solution of 100 mg (0.218 mmol, 1.0 eq) of compound **51** and 58 µL (0.872 mmol, 4.0 eq) 3-hydroxypropionitrile in 5 mL DCM, 61 mg (0.436 mmol, 2.0 eq) 1,5,7-triazabicyclo(4.4.0)dec-5-ene was added and left to stir over night. Upon completion, solvents where evaporated and submitted to flash column chromatography (DCM/MeOH 19:1) to afford the product as orange solid. Yield: 58 mg (0.163 mmol, 75%). R_f = 0.22 (DCM/MeOH 9:1). ^{1}H NMR (500 MHz, DMSO-*d*$_6$) δ 12.54 (s, 1H, NH), 8.50 (d, *J* = 5.5 Hz, 1H, 8), 8.07 – 8.03 (m, 2H, Ar), 7.76 – 7.67 (m, 3H, Ar), 6.43 (dd, *J* = 13.6, 6.9 Hz, 1H, 1'), 5.40 (t, *J* = 4.6 Hz, 1H, 3'-OH), 5.01 (dd, *J* = 11.7, 6.2 Hz, 1H, 5'-OH), 4.44 (td, *J* = 6.9, 3.5 Hz, 1H, 3'), 3.94 – 3.88 (m, 1H, 4'), 3.67 – 3.61 (m, 1H, 5'), 3.59 – 3.53 (m, 1H, 5'), 2.72 – 2.65 (m, 1H, 2'), 2.42 – 2.35 (m, 1H, 2'). ^{13}C{^{1}H} NMR (126 MHz, DMSO-*d*$_6$) δ 156.12, 154.51, 151.01, 147.53, 140.42, 134.36, 129.89, 124.96, 123.80, 123.28, 88.12, 83.70, 70.60, 61.53, 20.93, 20.61. HRMS (MALDI) $[M+H]^+$ m/z = calculated: 357.13058, found: 357.13059.

2-Phenyldiazenyl-5’(4,4‘-dimethoxytrityloxymethyl)-2’-deoxyguanosine **53**

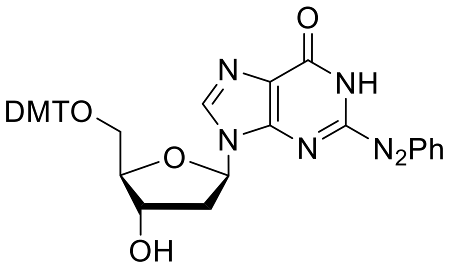

53

$C_{37}H_{34}N_6O_6$
658.72 g/mol

After coevaporating 1.139 g (3.196 mmol, 1.0 eq) compound **52** twice with pyridine and dissolving it in 40 mL pyridine, a solution of 1.191 g (3.516 mmol, 1.1 eq) of 4,4‘-dimethoxytrityloxymethylchloride in 20 mL pyridine were added dropwise at 0 °C and stirred for 3 hours at room temperature. Upon completion, reaction was quenched with methanol and solvents where coevaporated with toluene. The residue was dissolved in DCM, washed with aqueous sodium carbonate solution, dried over Na_2SO_4 and evaporated to dryness. Flash column chromatography (DCM/MeOH 49:1 → 19:1 + 1% TEA) afforded the product as orange foam. Yield: 0.806 g (1.223 mmol, 38%). R_f = 0.30 (DCM/MeOH 9:1). ^{1}H NMR (500 MHz, DMSO-d_6) δ 8.60 – 8.55 (m, 1H, Ar), 8.37 (s, 1H, 8), 8.03 – 7.97 (m, 1H, Ar), 7.82 – 7.76 (m, 1H, Ar), 7.76 – 7.67 (m, 2H, Ar), 7.38 (ddd, *J* = 7.6, 4.3, 1.4 Hz, 1H, Ar), 7.28 (dd, *J* = 7.8, 1.7 Hz, 2H, Ar), 7.20 – 7.10 (m, 6H, Ar), 6.71 (dd, *J* = 22.0, 8.9 Hz, 4H, Ar), 6.46 (t, *J* = 6.3 Hz, 1H, 1’), 5.39 (d, *J* = 4.7 Hz, 1H, 3’-OH), 4.52 – 4.46 (m, 1H, 3’), 4.05 – 3.99 (m, 1H, 4’), 3.37 – 3.34 (m, 1H, 5’), 3.12 (dd, *J* = 10.2, 3.1 Hz, 1H, 5’), 2.88 – 2.80 (m, 1H, 2’), 2.45 – 2.38 (m, 1H, 2’). ^{13}C{^{1}H} NMR (126 MHz, DMSO-d_6) δ 157.95, 157.91, 156.28, 154.39, 151.02, 149.63, 147.44, 144.91, 140.86, 136.15, 135.55, 135.45, 134.25, 129.85, 129.66, 129.58, 127.63, 127.59, 126.53, 125.43, 123.92, 123.71, 112.95, 112.88, 86.38, 85.31, 84.03, 70.56, 54.95, 54.92, 45.69, 10.60. HRMS (MALDI) $[M+Na]^+$ m/z = calculated: 681.24320, found: 681.24500.

2-Phenyldiazenyl-2’(cyanoethoxy(*N*,*N*-diisopropylamino)phosphinoxyl)-5’(4,4‘-dimethoxytrityloxymethyl)-2’-deoxyguanosine **54**

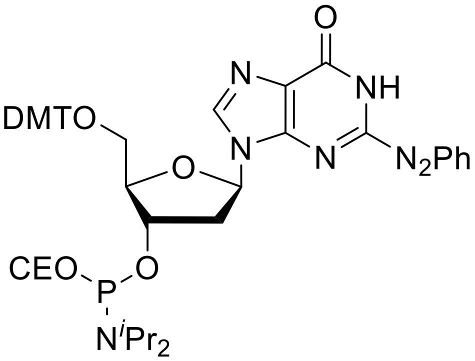

54

$C_{46}H_{51}N_8O_7P$
858.94 g/mol

To a solution of 806 mg (1.223 mmol, 1.0 eq) of compound **53** and 243 µL (6.118 mmol, 5.0 eq) *N*,*N*-diisopropylethylamine in 8 mL DCM, 348 µL (1.835 mmol, 1.5 eq) CEO(N^{i}Pr$_2$)PCl was added and left to stir at room temperature for 2 hours. Upon quenching with methanol the reaction was evaporated to dryness, extracted with DCM, dried over Na_2SO_4 and evaporated to dryness again. The crude product was subjected to flash column chromatography (DCM/MeOH 99:1 → 49:1) to afford the product as orange foam. Yield: 292 mg (0.340 mmol, 19%). R_f = 0.38 (DCM/MeOH 19:1). ^{1}H NMR (500 MHz, $CDCl_3$-*d*) δ 10.28 (s, 1H, NH), 8.11 – 8.05 (m, 1H, 8), 8.03 – 8.00 (m, 1H, Ar), 7.64 – 7.60 (m, 1H, Ar), 7.58 – 7.54 (m, 2H, Ar), 7.39 – 7.35 (m, 2H, Ar), 7.29 – 7.17 (m, 8H, Ar), 6.77 – 6.72 (m, 4H, Ar), 6.56 (t, *J* = 6.7 Hz, 1H, 1’), 4.75 – 4.66 (m, 1H, 3’), 4.34 – 4.26 (m, 1H, 4’), 3.73 (s, 3H, CH_3), 3.72 (s, 3H, CH_3), 3.62 – 3.53 (m, 2H, CH), 3.45 – 3.30 (m, 2H, 5’), 2.80 – 2.63 (m, 2H, 2’), 2.60 (t, *J* = 6.3 Hz, 2H, CH_2), 2.45 (t, *J* = 6.4 Hz, 2H, CH_2), 1.19 – 1.11 (m, 12H, CH_3). ^{13}C{^{1}H} NMR (126 MHz, $CDCl_3$-*d*) δ 158.62, 155.49, 152.88, 150.69, 148.03, 144.51, 140.17, 135.66, 135.55, 134.87, 130.18, 130.16, 129.79, 128.25, 128.18, 127.94, 127.01, 126.76, 124.76, 117.64, 117.53, 116.51, 113.23, 86.65, 86.40, 86.20, 84.86, 74.13, 73.42, 63.72, 58.54, 58.32, 55.29, 43.41, 43.37, 43.27, 40.54, 40.51, 40.49, 40.45, 24.76, 24.74, 24.68, 24.66, 24.59, 23.07, 23.05, 22.98, 22.96, 20.52, 20.46, 20.35, 20.29, 1.98. ^{31}P NMR (202 MHz, $CDCl_3$) δ 148.85, 148.83. HRMS (MALDI) [M+Na]$^+$ m/z = calculated: 881.35105, found: 881.35462.

2-Phenyldiazenyl-2’-deoxyadenosine **55**

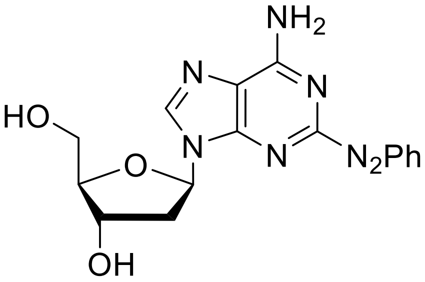

55

$C_{16}H_{17}N_7O_3$
355.36 g/mol

205 mg (0.447 mmol) of compound **51** was dissolved in ammonia saturated methanol (7 M) and stirred overnight at room temperature. After evaporation of the solvent the residue was submitted to flash column chromatography (DCM/MeOH 19:1 → 99:1) to afford the product as orange solid. Yield: 59 mg (0.166 mmol, 37%). R_f = 0.31 (DCM/MeOH 9:1). ^{1}H NMR (500 MHz, DMSO-*d*$_6$) δ 8.49 (d, *J* = 4.1 Hz, 1H, 8), 7.97 – 7.91 (m, 2H, Ar), 7.75 (s, 2H, NH_2), 7.67 – 7.61 (m, 3H, Ar), 6.42 (dd, *J* = 7.6, 6.2 Hz, 1H, 1’), 5.35 (d, *J* = 4.0 Hz, 1H, 3’-OH), 5.09 (t, *J* = 5.7 Hz, 1H, 5’-OH), 4.44 (d, *J* = 2.5 Hz, 1H, 3’), 3.93 – 3.88 (m, 1H, 4’), 3.65 (dt, *J* = 11.6, 4.5 Hz, 1H, 5’), 3.59 – 3.52 (m, 1H, 5’), 2.75 (ddd, *J* = 13.3, 7.7, 5.8 Hz, 1H, 2’), 2.35 – 2.29 (m, 1H, 2’). ^{13}C{^{1}H} NMR (126 MHz, DMSO-*d*$_6$) δ 162.34, 156.60, 151.99, 149.93, 141.06, 132.49, 129.63, 122.93, 119.00, 88.15, 83.88, 70.94, 61.88, 48.64, 39.61. HRMS (MALDI) $[M+H]^+$ m/z = calculated: 356.14656, found: 356.14677.

2-Phenyldiazenyl-5’(4,4‘-dimethoxytrityloxymethyl)-2’-deoxyadenosine **56**

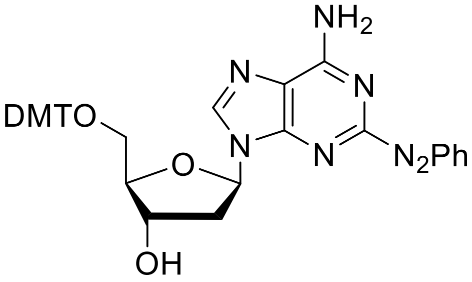

56

$C_{37}H_{35}N_7O_5$
657.73 g/mol

After coevaporating 100 mg (0.281 mmol, 1.0 eq) compound **55** two times with pyridine and dissolving it in 5 mL pyridine, a solution of 105 mg (0.310 mmol, 1.1 eq) of 4,4‘-dimethoxytrityloxymethylchloride in 5 mL pyridine were added dropwise at 0 °C and stirred for 3 hours at room temperature. Upon completion, reaction was quenched with methanol and solvents where coevaporated with toluene. The residue was dissolved in DCM, washed with aqueous sodium carbonate solution, dried over Na_2SO_4 and evaporated to dryness. Flash column chromatography (DCM/MeOH 49:1 → 19:1 + 1% TEA) afforded the product as orange foam. Yield: 122 mg (0.185 mmol, 66%). R_f = 0.58 (DCM/MeOH 9:1). ^{1}H NMR (500 MHz, DMSO-*d*$_6$) δ 8.59 – 8.55 (m, 1H, Ar), 8.39 (s, 1H, 8), 7.91 – 7.87 (m, 1H, Ar), 7.70 (s, 2H, NH_2), 7.67 – 7.62 (m, 2H, Ar), 7.38 (ddd, *J* = 7.6, 4.3, 1.5 Hz, 1H, Ar), 7.28 (dd, *J* = 8.0, 1.5 Hz, 1H, Ar), 7.21 – 7.13 (m, 7H, Ar), 6.71 (dd, *J* = 18.9, 8.9 Hz, 4H, Ar), 6.44 (t, *J* = 6.3 Hz, 1H, 1’), 5.36 (d, *J* = 4.7 Hz, 1H, 3’-OH), 4.51 (dt, *J* = 10.1, 4.9 Hz, 1H, 3’), 4.00 – 3.94 (m, 1H, 4’), 3.68 (s, 6H, CH_3) 3.28 (dd, *J* = 10.3, 6.5 Hz, 1H, 5’), 3.12 (dd, *J* = 10.3, 3.4 Hz, 1H, 5’), 2.87 (dt, *J* = 12.6, 6.1 Hz, 1H, 2’), 2.43 – 2.36 (m, 1H, 2’). ^{13}C{^{1}H} NMR (126 MHz, DMSO-*d*$_6$) δ 162.31, 157.95, 157.91, 156.52, 152.01, 149.94, 149.63, 148.64, 144.92, 136.15, 135.60, 135.46, 129.66, 129.59, 128.67, 127.74, 127.64, 126.52, 123.92, 122.85, 119.58, 119.06, 113.09, 112.98, 112.93, 86.09, 85.34, 83.79, 83.41, 70.79, 70.61, 64.29, 54.95, 45.70, 20.05, 13.99. HRMS (MALDI) $[M+Na]^+$ m/z = calculated: 680.25919, found: 680.26127.

2-Phenyldiazenyl-2’(cyanoethoxy(*N*,*N*-diisopropylamino)phosphinoxyl)-5’(4,4‘-dimethoxytrityloxymethyl)-2’-deoxyadenosine **57**

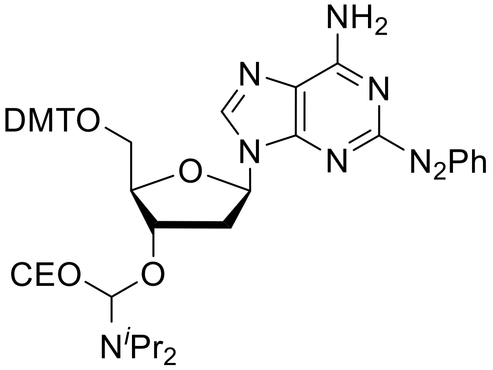

57

$C_{46}H_{52}N_9O_6P$
857.95 g/mol

To a solution of 122 mg (0.185 mmol, 1.0 eq) of compound **56** and 37 µL (0.927 mmol, 5.0 eq) *N*,*N*-diisopropylethylamine in 3 mL DCM, 44 µL (1.835 mmol, 1.5 eq) $CEO(N^iPr_2)PCl$ was added and left to stir at room temperature for 1 hour. Upon quenching with methanol the reaction was evaporated to dryness, extracted with DCM, dried over Na_2SO_4 and evaporated to dryness again. The crude product was subjected to flash column chromatography (DCM/MeOH 49:1 → 19:1) to afford the product as orange foam. Yield: 125 mg (0.146 mmol, 52%). R_f = 0.38 (DCM/MeOH 19:1). ^1H NMR (500 MHz, $CDCl_3$-*d*) δ 8.16 – 8.10 (s, 1H, 8), 8.03 (m, 2H, Ar), 7.52 – 7.48 (m, 2H, Ar), 7.40 – 7.34 (m, 2H, Ar), 7.29 – 7.14 (m, 6H, Ar), 6.81 – 6.71 (m, 6H, Ar), 6.64 – 6.59 (m, 1H, 1’), 6.38 (s, 2H, NH_2), 4.76 (dq, *J* = 6.1, 3.5 Hz, 1H, 3’), 4.25 (ddd, *J* = 10.9, 7.2, 3.6 Hz, 1H, 4’), 3.73 (s, 3H, CH_3), 3.72 (s, 3H, CH_3), 3.59 – 3.52 (m, 2H, CH), 3.43 – 3.38 (m, 1H, 5’), 3.27 (m, 1H, 5’), 2.79 – 2.73 (m, 1H, 2’), 2.73 – 2.69 (m, 1H, 2’), 2.57 (t, *J* = 6.4 Hz, 2H, CH_2), 2.43 – 2.39 (m, 2H, CH_2), 1.15 (m, 12H, CH_3). $^{13}C\{^1H\}$ NMR (126 MHz, $CDCl_3$-*d*) δ 162.29, 158.59, 156.20, 152.61, 150.64, 144.56, 140.57, 135.72, 132.52, 130.13, 129.17, 128.28, 128.21, 127.93, 126.98, 123.92, 120.17, 119.98, 117.67, 117.54, 113.23, 86.59, 86.59, 85.83, 84.97, 84.31, 74.20, 73.43, 63.67, 63.45, 58.49, 58.44, 58.34, 58.28, 58.25, 58.20, 55.28, 45.35, 43.39, 43.24, 24.66, 23.07, 20.50, 20.44, 20.31, 20.25, 20.15, 1.97. ^{31}P NMR (202 MHz, $CDCl_3$) δ 148.79, 148.76. HRMS (MALDI) $[M+H]^+$ m/z = calculated: 858.38509, found: 858.38488.

5.2 Oligonucleotide syntheses

DNA synthesis

For the synthesis of DNA containing azobenzene-*C*-nucleosides, standard phosphoramidites were purchased from Sigma–Aldrich. The strands were synthesized in the 4,4′-dimethoxytrityl (DMTr)-On mode on an ABI392 synthesizer by using standard protocols and columns (1.0 µmol; Applied Biosystems). For the cleavage of nucleobase protection groups, a wash with diethylamine (25% in acetonitrile, 20 minutes) followed by an acetonitrile wash and evaporation under reduced pressure were applied. Ammonia (25% in water) was used for resin-cleavage (over night, RT). After evaporation and resuspension in ultrapure water, the strands were purified by means of RP-HPLC with 0.4 M hexafluoroisopropanol and 15 mM trimethylamine in ultrapure water and methanol (column: Waters XBridge Peptide BEH C18, gradient: 5→40% methanol over 40 min). Incubation with 80 % acetic acid for 20 min at room temperature cleaved the DMT-group. After evaporation, the strands were purified again by means of RP-HPLC as mentioned before. Mass-spectrometric analyses were recorded on a Bruker micrOTOF-Q device. The strands containing no azobenzene modifications were purchased from biomers, strands containing the *t*Azo modification were provided by Hokkaido System Science Co., Ltd. (Japan).

RNA synthesis

For the synthesis of RNA containing azobenzene-*C*-nucleosides, standard phosphoramidites were purchased from Sigma–Aldrich. The strands were synthesized in the 4,4′-dimethoxytrityl (DMTr)-On mode on an ABI392 synthesizer by using standard protocols and columns (1.0 µmol; Applied Biosystems). For the cleavage of nucleobase protection groups, a wash with diethylamine (25% in acetonitrile, 20 minutes) followed by an acetonitrile wash and evaporation under reduced pressure were applied. A 3:1 mixture of ammonia (25% in water) and ethanol was used for resin-cleavage (over night, RT). After evaporation the crude oligonucleotide was resuspended in 115 µL DMSO, 60 µL TEA and 75 µL TEA·3HF and incubated at 65 °C for 2.5 hours. After cooling to room temperature 25 µL of aqueous sodium acetate (3 M) and 1 mL of *n*-butanol was added and left at -80 °C. After precipitation the sample was centrifuged for 30 minutes at 12.000 rpm and 4 °C, then supernatant was removed. The RNA-pellet was dried in a vacuum centrifuge, resuspended in ultrapure water and purified by means of RP-HPLC with 0.4 M hexafluoroisopropanol and 15 mM trimethylamine in ultrapure water and methanol (column: Waters XBridge Peptide BEH C18, gradient: 5→40% methanol over 40 min). Incubation with 80% acetic acid for 20 min at room temperature cleaved the DMT-group. After evaporation, the strands were purified again by means of RP-HPLC as mentioned before. Mass-spectrometric analyses were recorded on a Bruker micrOTOF-Q device. The strands containing no azobenzene modifications were purchased from biomers.

Oligonucleotide sequences and masses

	Oligo	Name	Sequence 5'→3'	**X** =	$M_{calculated}$ [g·mol^{-1}]	M_{found} [g·mol^{-1}]
DNA minicircle project	DNA	strand 1	TCT-AAA-AAT-CTA-GAA-AAA-ACG-CGC-AAA-AAG-TCT-CAA-AAA-ACG-GGC-AAA-AAT-GTC-TAA-AAA-AGC-TCG-AAA-AAC-TCT-CAA-AAA-ATA		25918	25921
	DNA	strand 2	TGG-CCA-AAT-AGA-TAA-AAA-ACG-AGC-AAA-AAT-AGA-TAA-AAA-AGC-CCG-AAA-AAC-GCG-CAA-AAA-AGT-CTC-AAA-AAC-GCG-CAA-AAA-ATG		26027	26025
	DNA	splint	TAT-TTG-GCC-ATA-TTT-TTT-GAG-AGT-TTT-TCG-A		9523	9524
	DNA	strand 3	ACA-TTT-TTG-CCC-GTT-TTT-TGA-GAT-CTC-TGT-GAG		10102	10104
	DNA	strand 4	CGT-TTT-TCG-GGC-TTT-TTT-ATC-TAT-TTT-TGC-TCG-TTT-TTT-ATC-TAT-TTG-GCC-ATA-TTT-TTT-GAG-AGT-TTT-TCG-AGC-TTT-TTT-AG		25449	25501
	DNA	strand 5	GAT-TTT-TAG-ACA-TTT-TTT-GCG-CGT-TTT-TGA-GAC-TTT-TTT-GCG		12912	12910
	DNA	strand 6	GTG-GCA-AGG-TCT-CAC-AGA-GTC-TTT-TTG-CGC-GTT-TTT-TCT-A		12284	12285
	DNA	strand 6-5	GT**X**-GCA-**X**GG-TCT-CAC-AGA-GTC-TTT-TTG-CGC-GTT-TTT-TCT-A	abasic site	12008	12009
	DNA	strand 6-6	G**X**G-G**X**A-A**X**G-TCT-CAC-AGA-GTC-TTT-TTG-CGC-GTT-TTT-TCT-A	abasic site	11908	11910
	DNA	strand 7	ACC-TTG-CCA-CCT-CAC-AGA-GTC-TTT-TTG-CGC-GTT-TTT-TCT-A		12124	12125
	DNA	strand 8-2	ACC-**X**TT-GC**X**-CAC-CTC-ACA-GAG-TCT-TTT-TGC-GCG-TTT-TTT-CTA	tAzo	12880	12883
	DNA	strand 8-4	AC**X**-CT**X**-TG**X**-CC**X**-ACC-TCA-CAG-AGT-CTT-TTT-GCG-CGT-TTT-TTC-TA	tAzo	13631	13633
	DNA	strand 11-1	ACC-T**X**G-CCA-CCT-CAC-AGA-GTC-TTT-TTG-CGC-GTT-TTT-TCT-A	mAzo	12317	12320
	DNA	strand 11-2	ACC-**X**TG-C**X**A-CCT-CAC-AGA-GTC-TTT-TTG-CGC-GTT-TTT-TCT-A	mAzo	12317	12324
	DNA	strand 11-3	AC**X**-TT**X**-CC**X**-CCT-CAC-AGA-GTC-TTT-TTG-CGC-GTT-TTT-TCT-A	mAzo	12186	12187
	DNA	strand 9-2	ACC-**X**TG-C**X**A-CCT-CAC-AGA-GTC-TTT-TTG-CGC-GTT-TTT-TCT-A	MeO-mAzo	12257	12259
	DNA	strand 10-2	ACC-**X**TG-C**X**A-CCT-CAC-AGA-GTC-TTT-TTG-CGC-GTT-TTT-TCT-A	p-pyrAzo	12279	12281
	DNA	strand 12-2	ACC-**X**TG-C**X**A-CCT-CAC-AGA-GTC-TTT-TTG-CGC-GTT-TTT-TCT-A	m-pyrAzo	12321	12323
LNAzo project	DNA	strand 13	FAM-GTG-GCA-AGG-T		3646	3645
	DNA	strand 14	FAM-GTG-G**X**A-AGG-T	abasic site	3535	3536
	RNA	strand 15	FAM-GUG-GCA-AGG-U		3777	3779
	DNA	strand 16	ACC-TTG-CCA-C-DAB		3408	3409
	DNA	strand 17	ACC-TT**X**-CCA-C-DAB	mAzo	3439	3440
	DNA	strand 18	ACC-TT**X**-CCA-C-DAB	LNAzo α	3467	3468
	DNA	strand 19	ACC-TT**X**-CCA-C-DAB	LNAzo β	3467	3468
	RNA	strand 20	ACC-UUG-CCA-C-DAB		3541	3541
	RNA	strand 21	ACC-UU**X**-CCA-C-DAB	mAzo	3556	3559
	RNA	strand 22	ACC-UU**X**-CCA-C-DAB	LNAzo α	3584	3587
	RNA	strand 23	ACC-UU**X**-CCA-C-DAB	LNAzo β	3584	3587
	DNA	strand 24	ACC-TTG-CCA-C		2948	2939
	DNA	strand 25	GTG-GCA-AGG-T		3108	3100
	DNA	strand 26	ACC-T**X**G-CCA-C	abasic site	2823	2827
	DNA	strand 27	ACC-TT**X**-CCA-C	abasic site	2798	2804
	DNA	strand 28	GTG-G**X**A-AGG-T	abasic site	2998	2999
	DNA	strand 29	GTG-GC**X**-AGG-T	abasic site	2974	2968
purine azo project	DNA	strand 13	FAM-GTG-GCA-AGG-T		3646	3645
	DNA	strand 16	ACC-TTG-CCA-C-DAB		3408	3409
	DNA	strand 17	ACC-TT**X**-CCA-C-DAB	mAzo	3439	3439
	DNA	strand 30	ACC-TT**X**-CCA-C-DAB	dG_{Azo}	3497	3496
	DNA	strand 31	FAM-GTG-GC**X**-AGG-T	dA_{Azo}	3746	3746

5.3 Spectroscopic studies

5.3.1 Spectroscopic studies of the DNA-minicircle project

Azobenzene-modified DNA-strands were dissolved in 1xPBS buffer and set to the stated concentration. Spectra were measured in a custom built setup including a custom built white light source, diverse *Thorlabs* LED's and an USB4000 detector from *Ocean Optics*. The software used for recording the spectra (Photoswitch Irradiation Test Suite – PHITS) has been programmed by Prof. Dr. Alexander Heckel himself. 1 mL samples were irradiated with the corresponding wavelength and powers for two minutes in a quartz glass cuvette, until absorption did not change anymore and photostationary state (PSS) was reached.

365 nm: Thorlabs M365L2 (310 mW, 700 mA)
420 nm: Thorlabs M420L2 (290 mW, 500 mA)
530 nm: Thorlabs M530L2 (400 mW, 1600 mA)

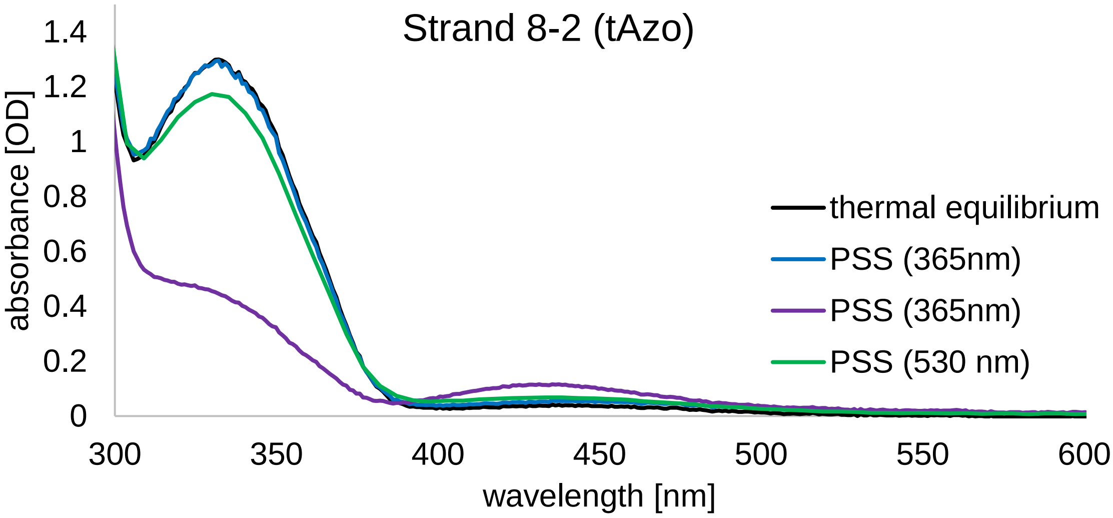

Fig. 92 Absorption spectra of strand 8-2 (sample: 22.8 µM, 1 mL; light source as described above).

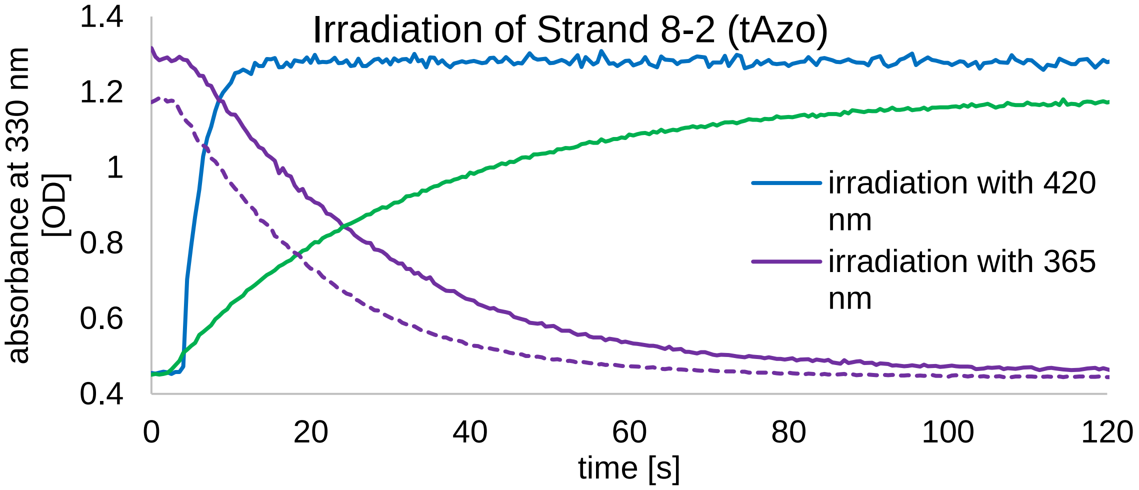

Fig. 93 Absorbance of strand 8-2 at 330 nm during irradiation (sample: 22.8 µM, 1 mL; light source as described above).

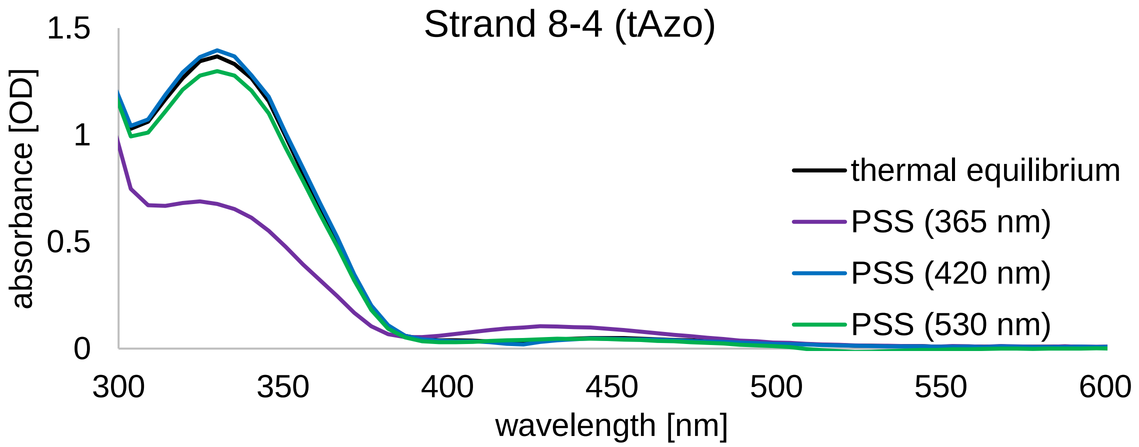

Fig. 94 Absorption spectra of strand 8-4 (sample: 12.8 µM, 1 mL; light source as described above).

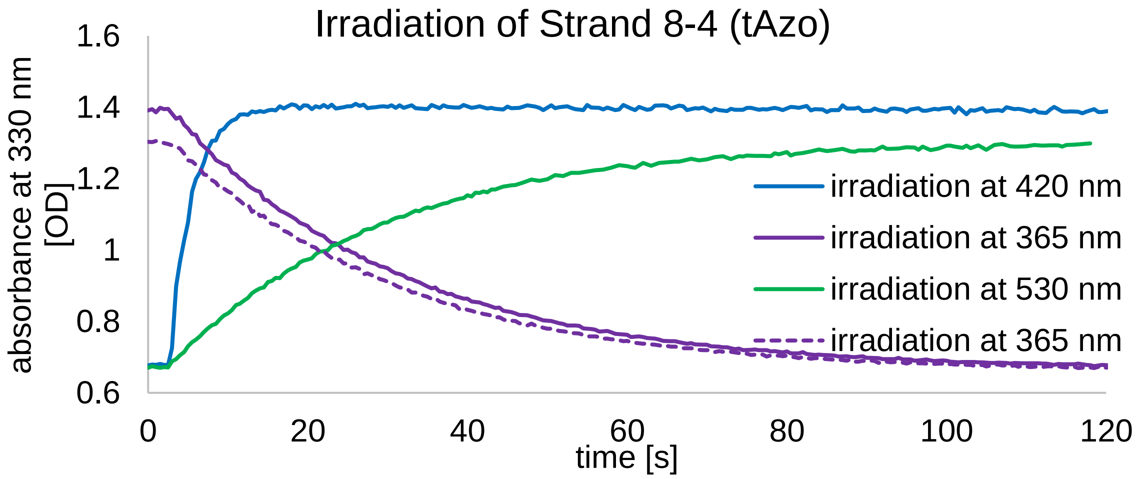

Fig. 95 Absorbance of strand 8-4 at 330 nm during irradiation (sample: 12.8 µM, 1 mL; light source as described above).

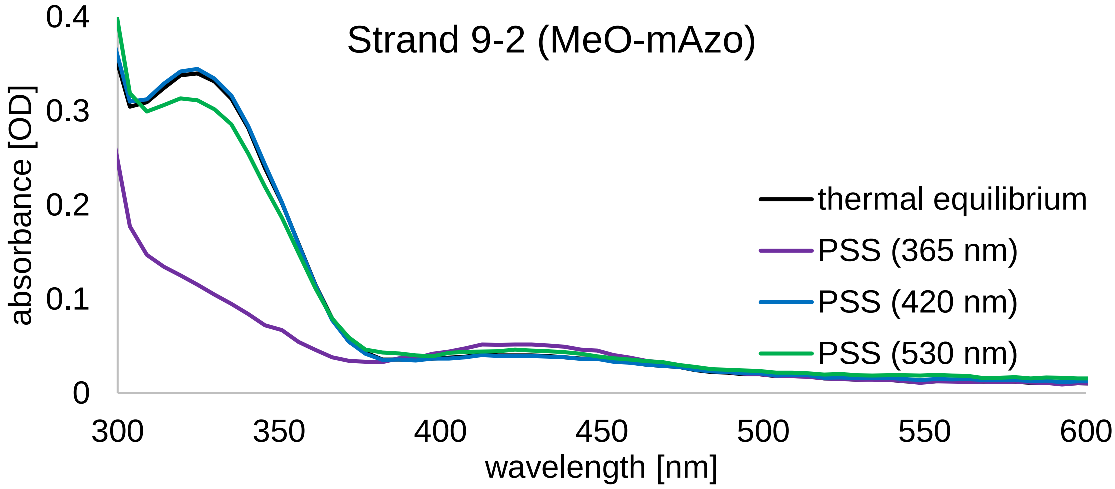

Fig. 96 Absorption spectra of strand 9-2 (Sample: 7.7 µM, 1 mL; light source as described above).

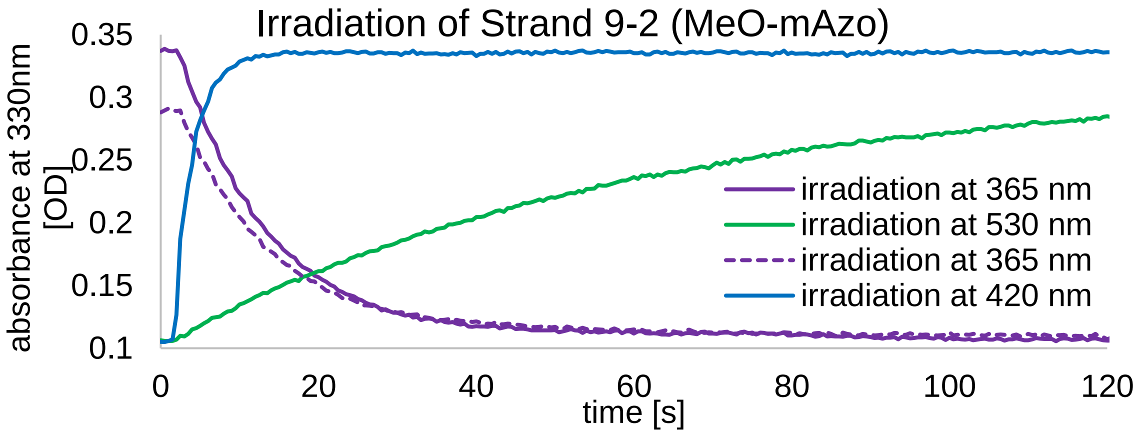

Fig. 97 Absorbance of strand 9-2 at 330 nm during irradiation (sample: 7.7 µM, 1 mL; light source as described above).

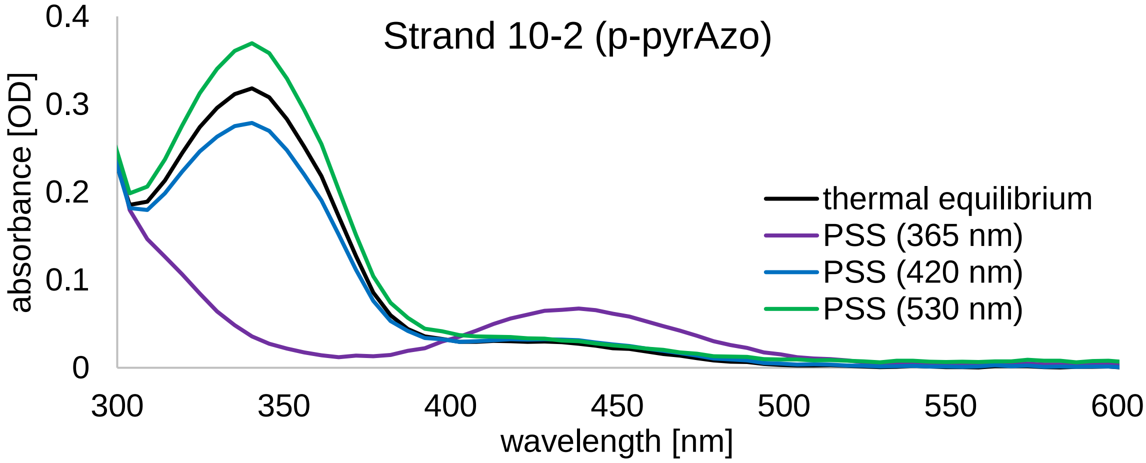

Fig. 98 Absorption spectra of strand 10-2 (sample: 5.9 µM, 1 mL; light source as described above).

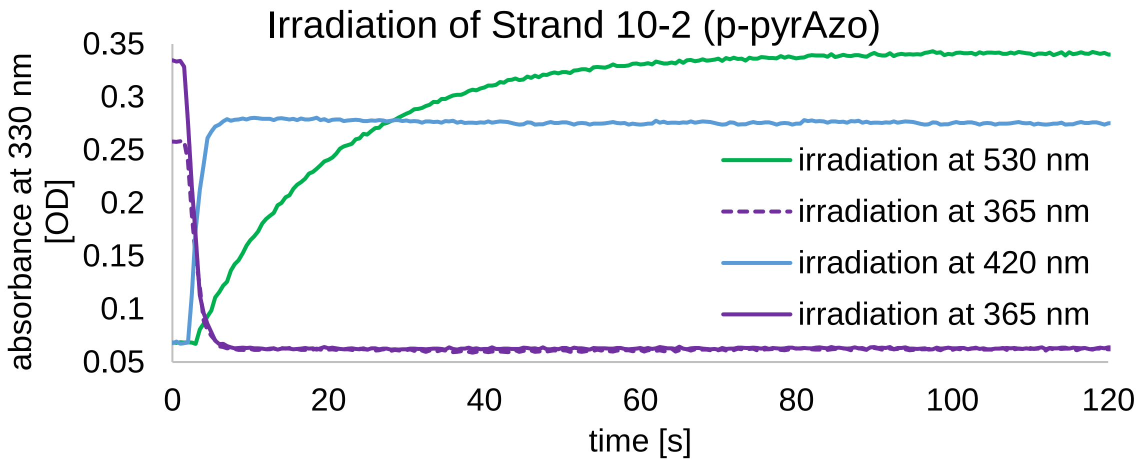

Fig. 99 Absorbance of strand 10-2 at 330 nm during irradiation (sample: 5.9 µM, 1 mL; light source as described above).

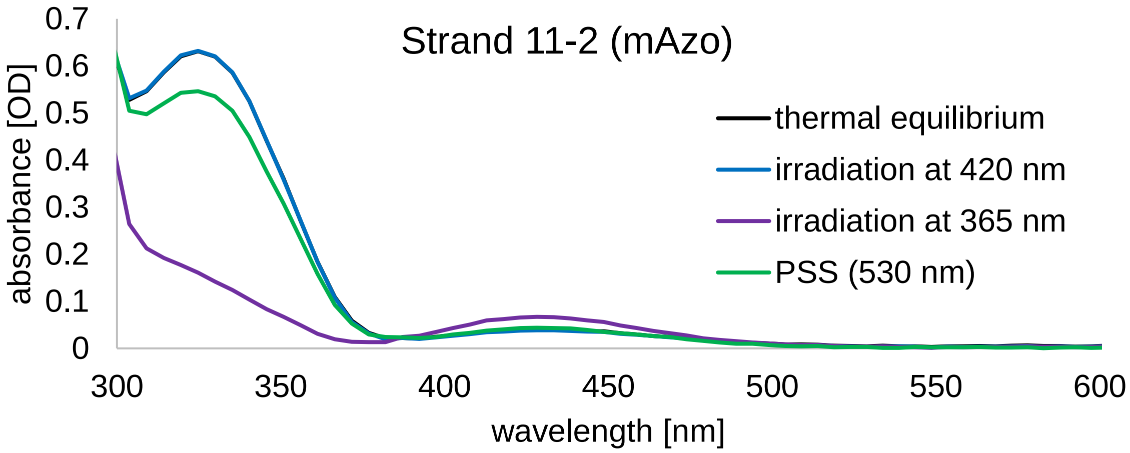

Fig. 100 Absorption spectra of strand 11-2 (sample: 14.5 µM, 1 mL; light source as described above).

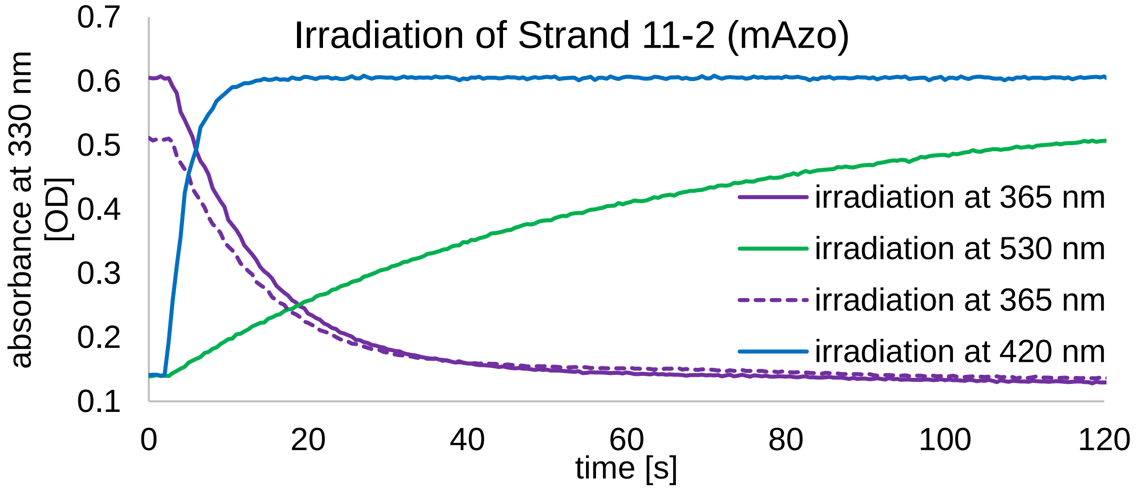

Fig. 101 Absorbance of strand 11-2 at 330 nm during irradiation (sample: 14.5 µM, 1 mL; light source as described above).

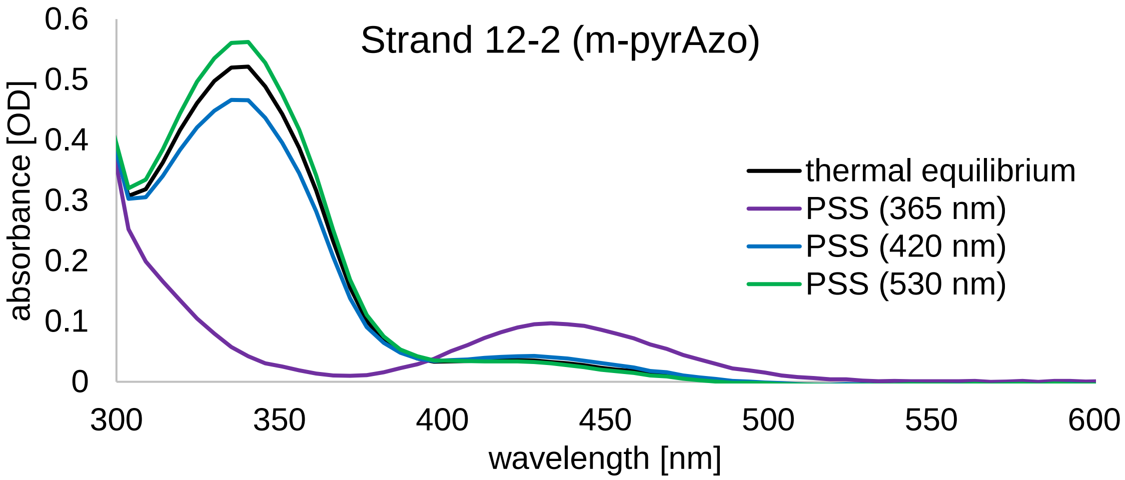

Fig. 102 Absorption spectra of strand 12-2 (sample: 11.7 µM, 1 mL; light source as described above).

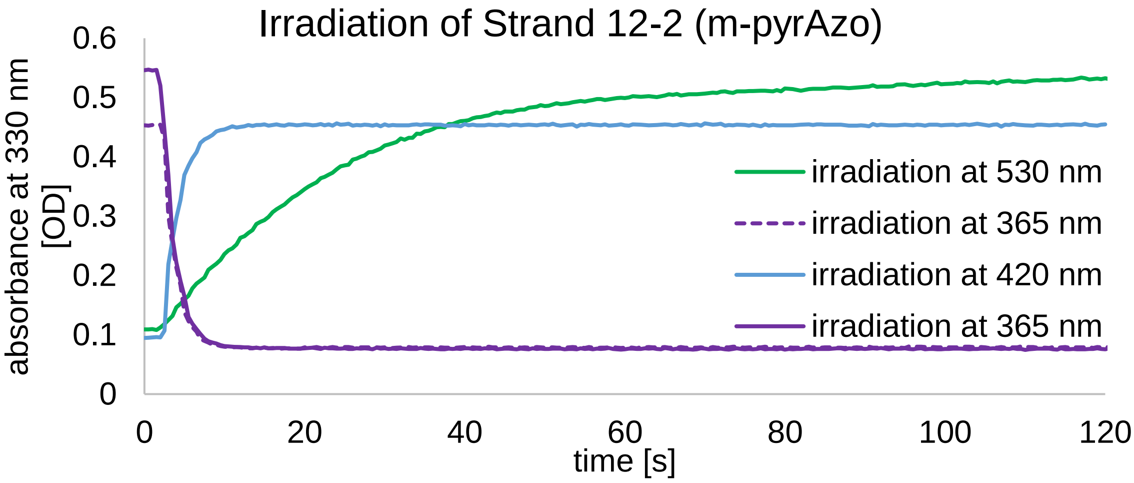

Fig. 103 Absorbance of strand 12-2 at 330 nm during irradiation (sample: 11.7 µM, 1 mL; light source as described above).

5.3.2 Spectroscopic studies of the LNAzo project

Spectra of LNAzo β

For spectra of free nucleoside LNAzo β **41**, three independent samples with a concentration of 36 µM, 63 µM and 90 µM in a solution of water and acetonitrile (95:5) were separated on a short precolumn under isocratic conditions. The spectra of baseline separated peaks from both photoisomers were superimposed to find an isosbestic point at 378 nm. From the three concentrations, the extinction coefficients at the isosbestic point could be calculated to normalize clean spectra (to be seen in Fig. 104).

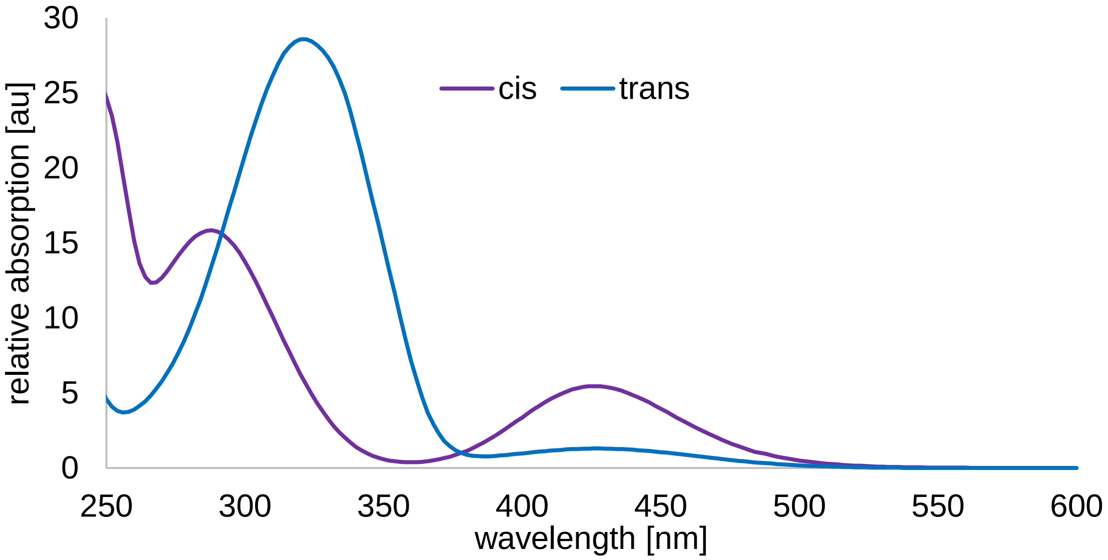

Fig. 104 Normalized spectra of the cis- and trans-photoisomers of nucleoside ***41****.*

Photostationary distributions of LNAzo β

Three independent samples of compound **41** (100 nmol) were irradiated either at 365 nm or 420 nm until the photostationary state was reached (365 nm: 220 mW, 60 s; 420 nm: 290 mW, 30 s). Photoisomers were then baseline-separated on a short precolumn by means of RP-HPLC under isocratic conditions (95% 0.4 M trimethylammonium acetate buffer pH 7, 5% ACN) and spectra were recorded with an inline diode array detector. A chromatogram trace at the isosbestic point (378 nm) was extracted (Fig. 105A). From the integrals of the peaks, the relative amount of the photoisomers was determined. Under these conditions, the photostationary state was determined to be at 80.0±0.5% cis isomer after irradiation at 365 nm and at 20.3±0.1% cis isomer after irradiation at 420 nm.

Alternatively, the photostationary distribution can be calculated from absorbance ratios of the n-π*-band at 420 nm (Fig. 105B). This analysis showed that the photostationary state after irradiation at 365 nm was composed of 79±1% cis isomer and the photostationary state after irradiation at 420 nm of 21±1% cis isomer, respectively.

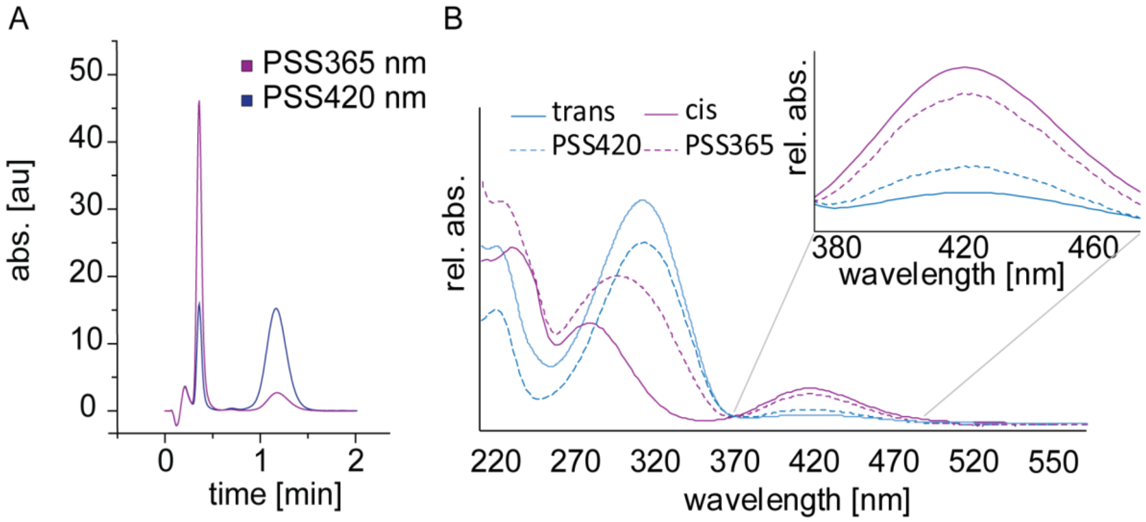

Fig. 105 Analysis of the photostationary distribution of the photostationary states at 365 nm and 420 nm with either RP-HPLC (A) or the absorption spectra of the photostationary states in comparison to the absorption spectra of the pure photoisomers (B).

Photofatigue studies of LNAzo β

For evaluation of the photofatigue resistance of **41**, a 100 µM sample in 1x PBS was alternately irradiated with 365 nm (220 mW, 60 s) and 420 nm (290 mW, 30 s) and absorption changes at 300 nm were recorded. Compound **7** showed no photofatigue over 100 switching cycles (Fig. 106).

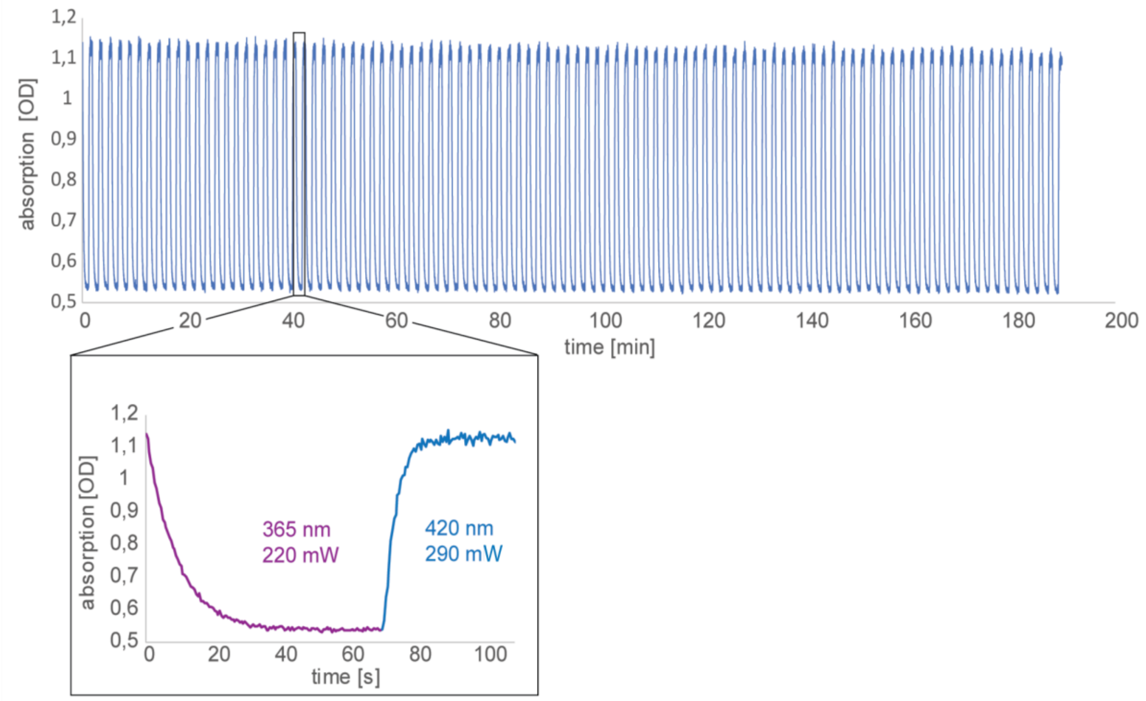

Fig. 106 Display of 100 switching cycles of 41 with a close-up of one cycle.

5.3.3 Spectroscopic studies of the 2-phenyldiazenyl purine project

Photostationary states of 2-Phenyldiazenylpurine-deoxyribosides

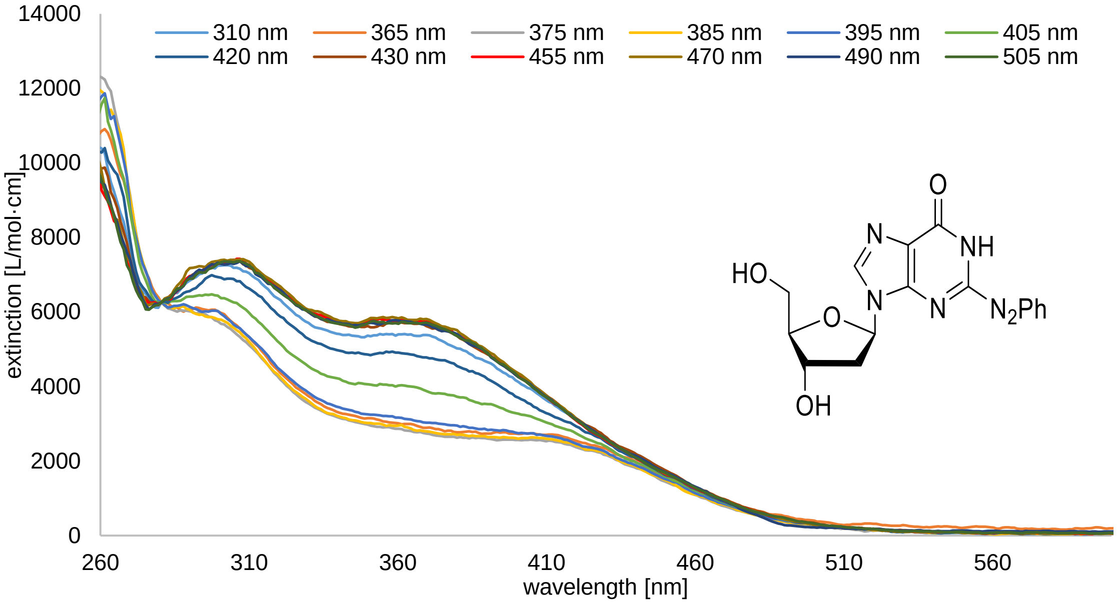

Fig. 107 Photostationary states of free dG$_{Azo}$ nucleoside ***52*** *(100 µM in 1x PBS). 1 mL sample was irradiated until no absorbance changes could be seen anymore, then the spectrum was recorded. Each spectrum corresponds to the wavelength stated above in nm.*

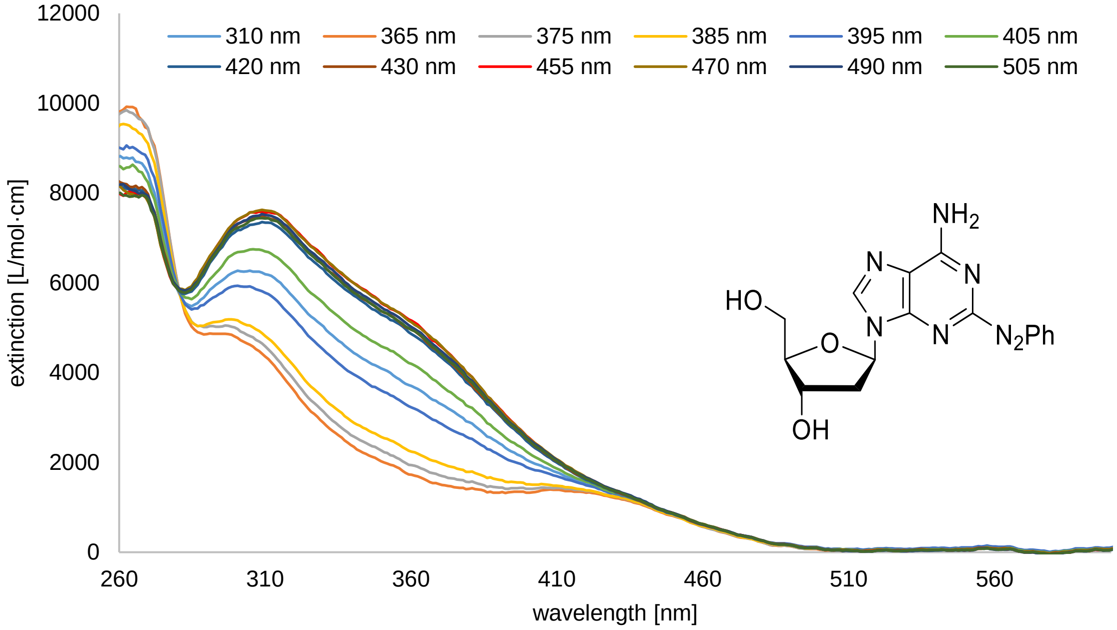

Fig. 108 Photostationary states of free dA$_{Azo}$ nucleoside ***55*** *(100 µM in 1x PBS). 1 mL sample was irradiated until no absorbance changes could be seen anymore, then the spectrum was recorded. Each spectrum corresponds to the wavelength stated above in nm.*

Spectra of the pure photoisomers of 2-phenyldiazenyl purines

Three independent samples of compound dG_{Azo} and dA_{Azo} (100 nmol) were irradiated either at 365 nm or 455 nm until the photostationary state was reached (365 nm: 220 mW, 60 s; 455 nm: 300 mW, 60 s). Photoisomers were then baseline-separated on a short precolumn by means of RP-HPLC under isocratic conditions (dG_{Azo}: 100% 0.4 M trimethylammonium acetate buffer pH 7; dA_{Azo}: 95% 0.4 M trimethylammonium acetate buffer pH 7, 5% ACN) and spectra were recorded with an inline diode array detector. The spectra of separate peaks from both photoisomers were superimposed and normalized to the extinction coefficient at the isosbestic point (278 nm; Fig. 109,110).

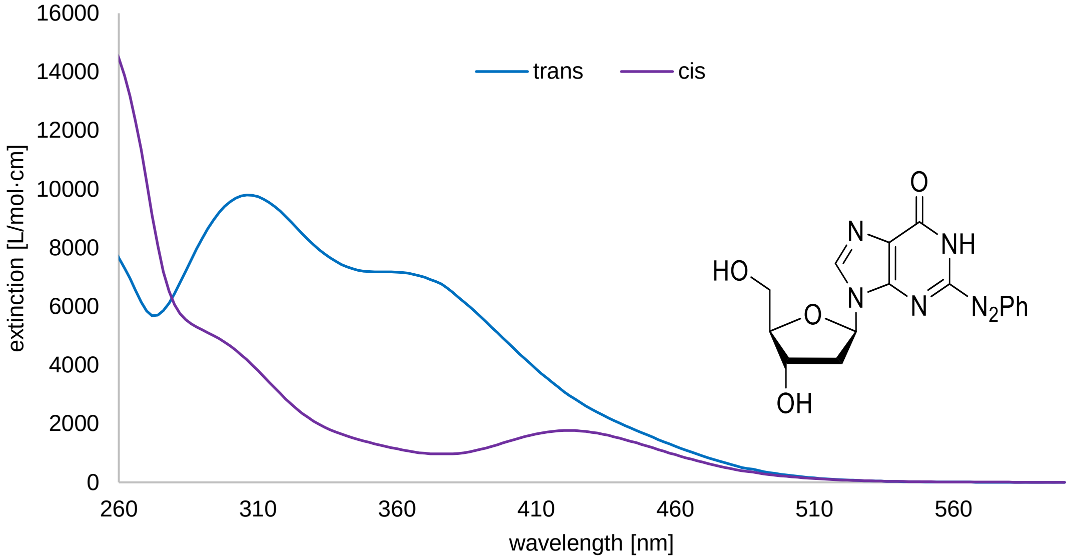

Fig. 109 Spectra of the pure photoisomers of dG_{Azo}.

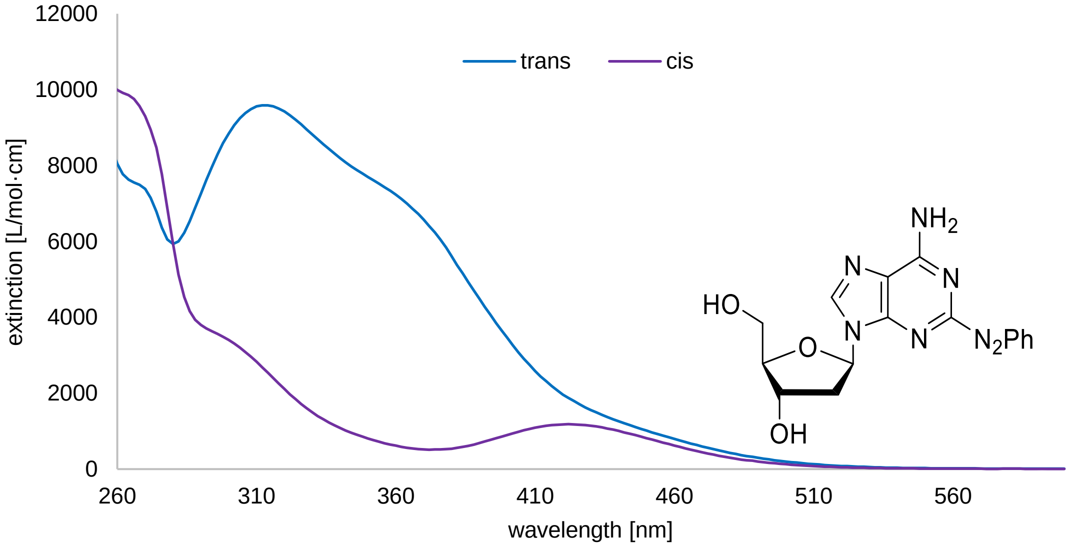

Fig. 110 Spectra of the pure photoisomers of dA_{Azo}.

Photostationary distributions of 2-phenyldiazenyl purines

Three independent samples of compound dG$_{Azo}$ and dA$_{Azo}$ (100 nmol) were irradiated either at 365 nm or 455 nm until the photostationary state was reached (365 nm: 220 mW, 60 s; 455 nm: 300 mW, 60 s). Photoisomers were then separated on a short precolumn by means of RP-HPLC under isocratic conditions (dG$_{Azo}$: 100% 0.4 M trimethylammonium acetate buffer pH 7; dA$_{Azo}$: 95% 0.4 M trimethylammonium acetate buffer pH 7, 5% ACN) and spectra were recorded with an inline diode array detector. A chromatogram trace at the isosbestic point (278 nm) was extracted (Figure S5). From the integrals of the peaks, the relative amount of the photoisomers was determined. Results including standard deviation are shown below, exemplary chromatograms can be seen in Figure S6.

	dG$_{Azo}$		dA$_{Azo}$	
	cis [%]	*trans* [%]	*cis* [%]	*trans* [%]
PSS 455 nm	38.2 ± 0.3	61.8 ± 0.3	34.8 ± 0.5	65.2 ± 0.5
PSS 365 nm	77 ± 1	23 ± 1	81.2 ± 0.8	18.8 ± 0.8

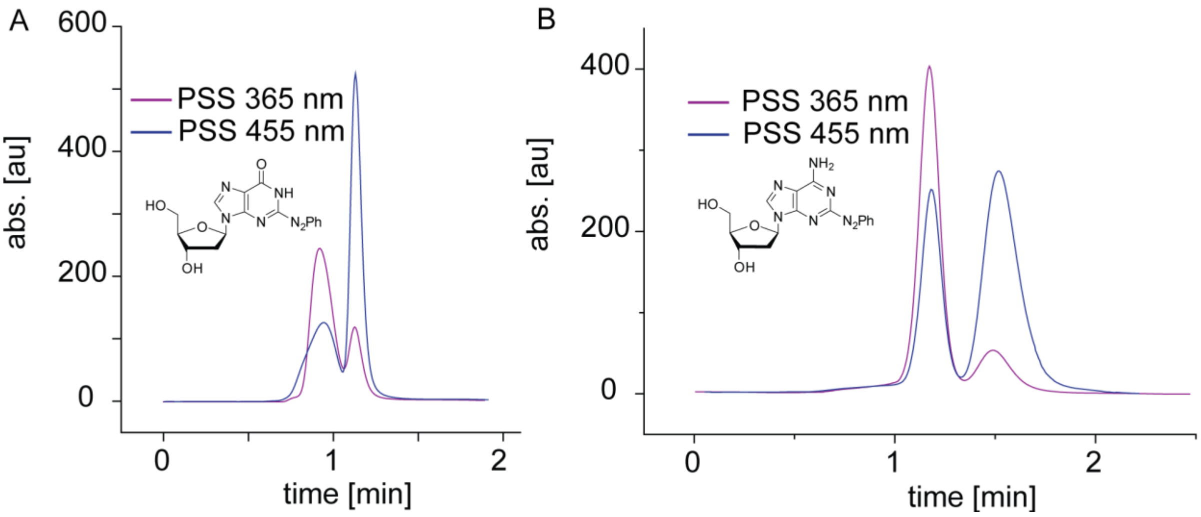

Fig. 111 RP-HPLC chromatograms of the photostationary states at 365 nm and 455 nm of dG$_{Azo}$ (A) and dA$_{Azo}$ (B).

Photofatigue studies of 2-Phenyldiazenylpurine-deoxyribosides

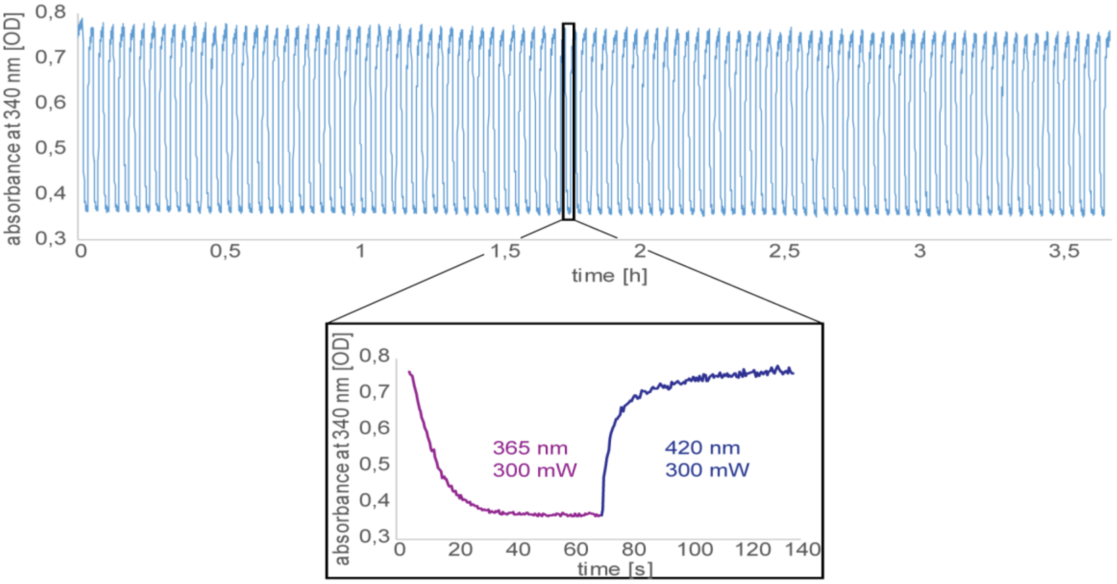

Fig. 112 Photofatigue-study of dG$_{Azo}$*. A 100 µM sample in 1x PBS-buffer was alternately irradiated at 365 nm (300 mW, 1 min) and at 420 nm (300 mW, 1 min) for 100 cycles, while absorbance change was monitored at 340 nm. No photofatigue could be observed over 100 switching cycles.*

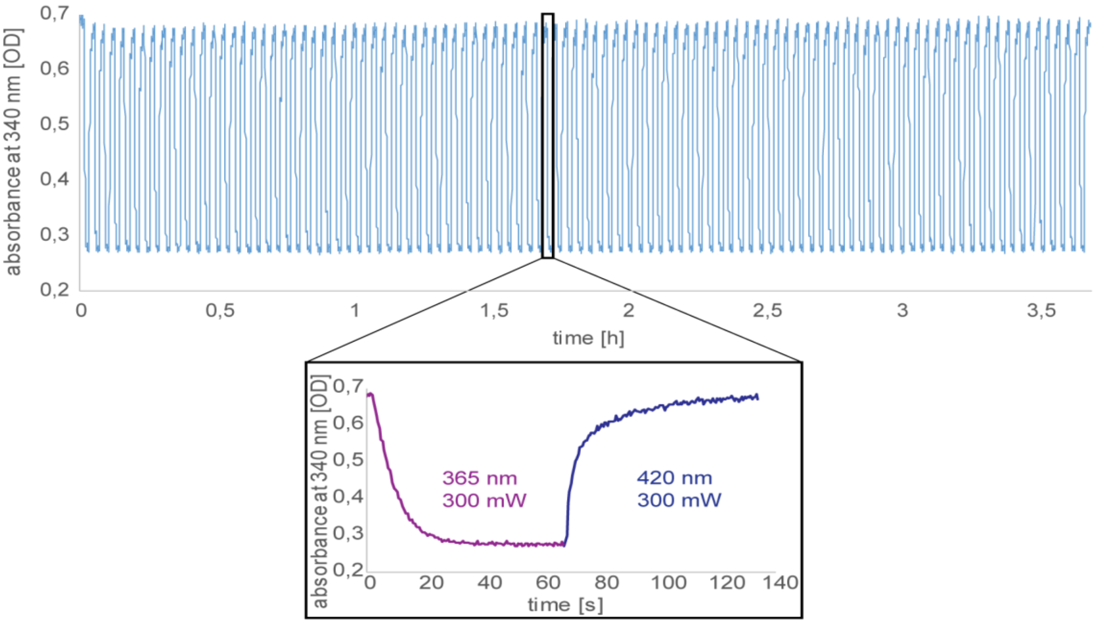

Fig. 113 Photofatigue-study of dA$_{Azo}$*. A 100 µM sample in 1x PBS-buffer was alternately irradiated at 365 nm (300 mW, 1 min) and at 420 nm (300 mW, 1 min) for 100 cycles, while absorbance change was monitored at 340 nm. No photofatigue could be observed over 100 switching cycles.*

Thermal relaxation of the *cis*-states

The thermal relaxation of the *cis*-state to the thermodynamically favored *trans*-state without irradiation follows a first order reaction kinetic. Formulating the reaction as $Azo_{cis} \rightarrow Azo_{trans}$ with the reaction rate k in [s^{-1}], the concentration of Azo_{cis} is proportional to the time dependent concentration change of Azo_{cis}.

$$-\frac{dAzo_{cis}}{dt} = k[Azo_{cis}] \qquad \text{(equation 1)}$$

To solve this first order differential equation, separation of variables and integration is necessary.

$$\frac{d[Azo_{cis}]}{[Azo_{cis}]} = -kdt \qquad \text{(equation 2)}$$

$$\ln[Azo_{cis}] - l\,n[Azo_{cis}]_0 = -ln\frac{[Azo_{cis}]_0}{[Azo_{cis}]} = -kt \qquad \text{(equation 3)}$$

The concentration of the *cis*-species can be determined with the absorption at 380 nm according to the following rearrangements.[209]

$$\frac{[Azo_{cis}]_0}{[Azo_{cis}]} = \frac{[Azo_{cis}]_0(\varepsilon_{trans,380}-\varepsilon_{cis,380})}{[Azo_{cis}](\varepsilon_{trans,380}-\varepsilon_{cis,380})} \qquad \text{(equation 4)}$$

$$= \frac{([Azo_{trans}]_0+[Azo_{cis}]_0)\varepsilon_{trans,380}-([Azo_{trans}]_0+[Azo_{cis}]_0)\varepsilon_{cis,380})}{([Azo_{trans}]_t+[Azo_{cis}]_t)\varepsilon_{trans,380}-([Azo_{trans}]_t+[Azo_{cis}]_t)\varepsilon_{cis,380})} \qquad \text{(equation 5)}$$

$$= \frac{\varepsilon_{trans,380}-([Azo_{trans}]_0\varepsilon_{trans,380}+[Azo_{cis}]_0\varepsilon_{cis,380})}{\varepsilon_{trans,380}-([Azo_{trans}]_t\varepsilon_{trans,380}+[Azo_{cis}]_t\varepsilon_{cis,380})} \qquad \text{(equation 6)}$$

$$= \frac{A_{\infty,380}-A_{0,380}}{A_{\infty,380}-A_{t,380}} \qquad \text{(equation 7)}$$

The absorption at the thermal ground state at 380 nm is defined as $A_{\infty,380}$, the absorption at 380 nm at the beginning of the measurement as $A_{0,380}$ and $A_{t,380}$ as the absorption at 380 nm during the time t. To calculate the thermal relaxation rate k, equation 8 and 3 are merged.

$$ln\frac{A_{\infty,380}-A_{0,380}}{A_{\infty,380}-A_{t,380}} = kt \qquad \text{(equation 8)}$$

Plotting $ln\frac{A_{\infty,350}-A_{0,350}}{A_{\infty,350}-A_{t,350}}$ against the time t gives the thermal relaxation rate k as the slope. Thermal relaxation has been measured at 25, 37 and 60 °C. As thermal relaxation at 25 and 37 °C has been very slow, time dependent absorption change has been extrapolated in order to calculate the relaxation rate and thermal half-life times.

The half-time of a first order reaction is defined by equation 9.

$$\boldsymbol{t_{\frac{1}{2}} = \frac{ln(2)}{k}} \qquad \text{(equation 9)}$$

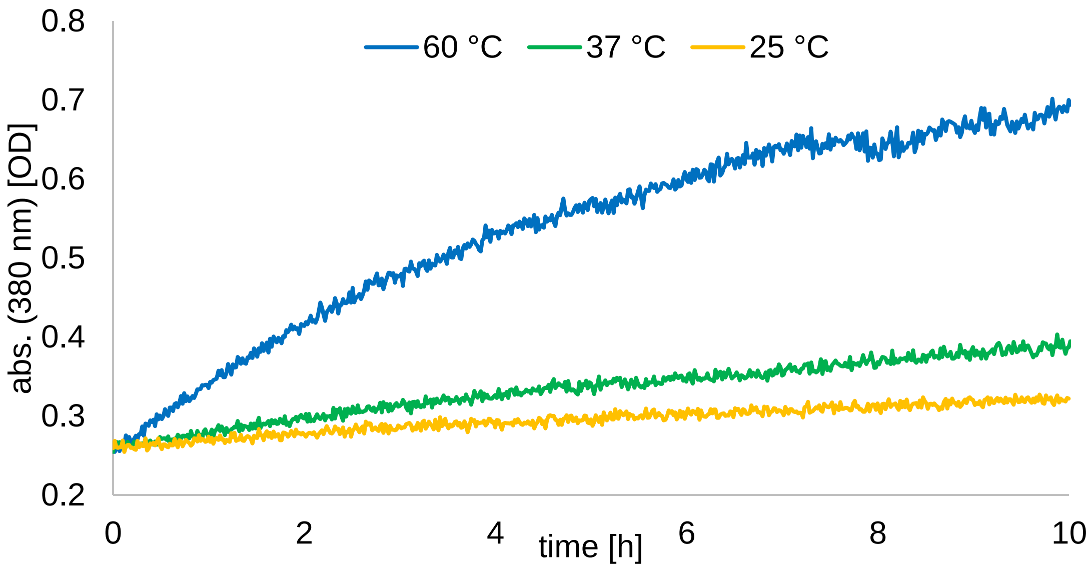

Fig. 114 Thermal relaxation of dG$_{Azo}$ observed as absorption change at 380 nm.

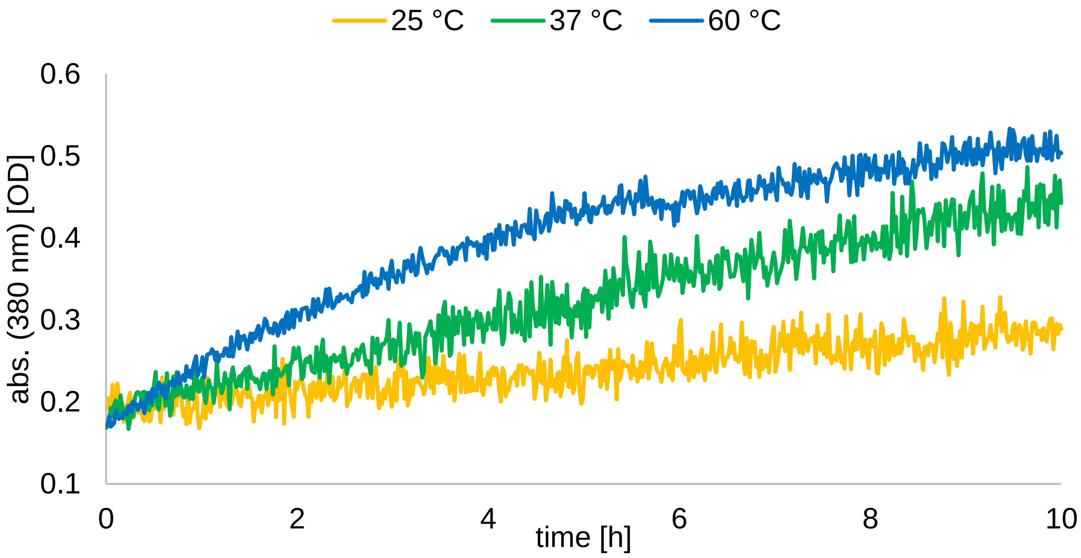

Fig. 115 Thermal relaxation of dA$_{Azo}$ observed as absorption change at 380 nm.

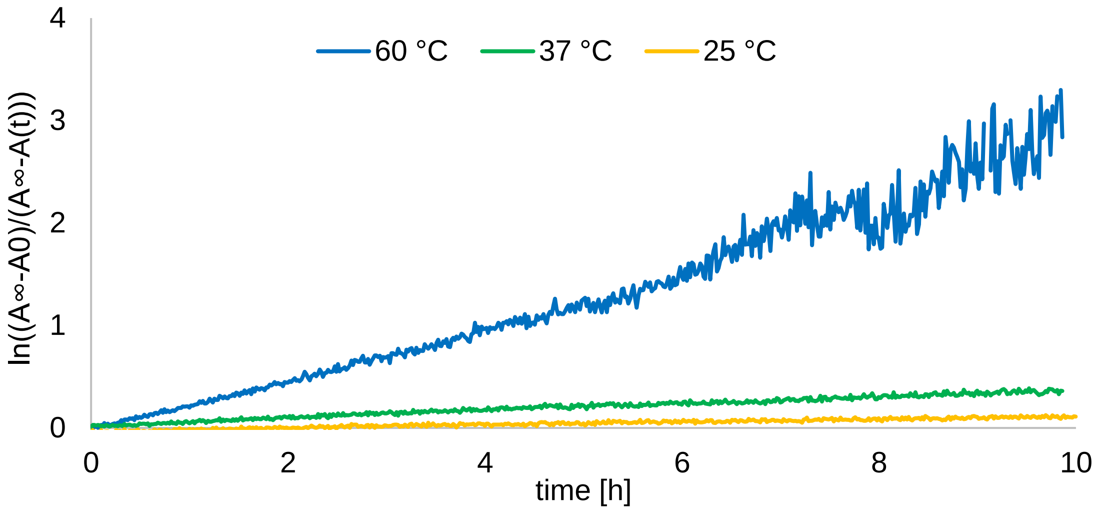

Fig. 116 Plot to calculate thermal relaxation rate k and half-life $t_{1/2}$ of dG_{Azo} in accordance to equation 8.

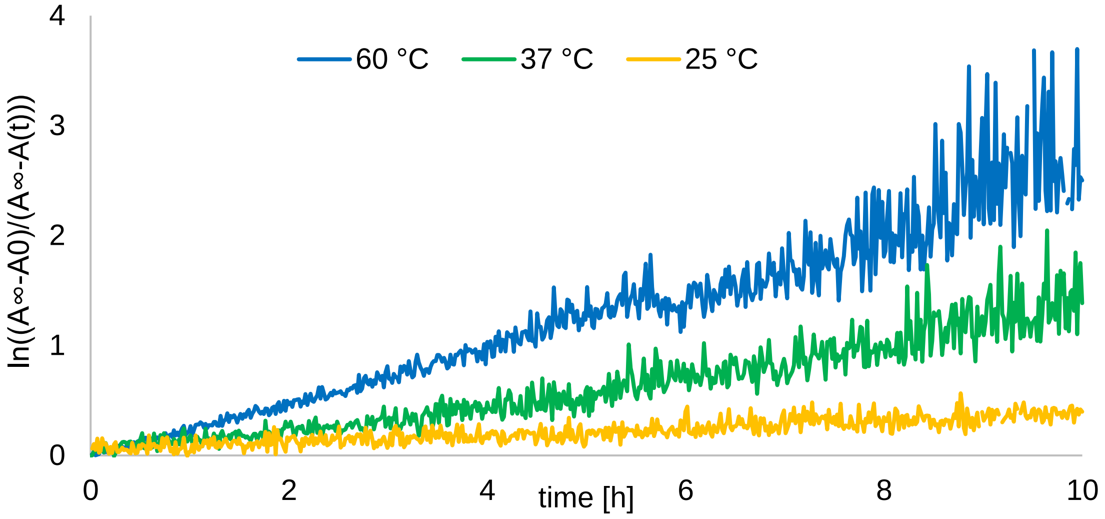

Fig. 117 Plot to calculate thermal relaxation rate k and half-life $t_{1/2}$ of dA_{Azo} in accordance to equation 8.

dG_{Azo}	k=	0.29±0.01 s^{-1}	(60 °C)	dA_{Azo}	k=	0.27±0.02 s^{-1}	(60 °C)
		0.034±0.001 s^{-1}	(37 °C)			0.14±0.02 s^{-1}	(37 °C)
		0.015±0.001 s^{-1}	(25 °C)			0.03±0.01 s^{-1}	(25 °C)
	$t_{1/2}$=	2.39±0.08 h	(60 °C)		$t_{1/2}$=	2.6±0.2 h	(60 °C)
		20.4±0.5 h	(37 °C)			5.0±0.6 h	(37 °C)
		46±3 h	(25 °C)			23±6 h	(25 °C)

Quantum yields of the photoisomerization processes

For calculation of the quantum yields the method of Reinfelds *et al.* was used.[210] The described fulgide was dissolved in toluene to give a solution with an OD of approximately 0.5, then irradiated between the photostationary states of 595 nm, 455 nm and 365 nm. With the known quantum yields and extinction coefficients for these processes, photon flux of used LED's could be calculated with a custom software (Photoswitch Irradiation Test Suite – PHITS). The photon flux was calculated from five independent irradiation processes each for best results.

wavelength λ [nm]	LED type	LED power [mW]	photon flux [nmol/s]
365	Thorlabs M365L2	44.3 (100 mA)	39.6 ± 0.5
455	Thorlabs M455L2	112.5 (100 mA)	21.1 ± 0.6

With the known photon flux the quantum yield of the 2-phenyldiazenyl purines could be calculated. Solutions of the 2-phenyldiazenyl purines (100 µM in 1x PBS, pH7.4, 2 mL) where irradiated, until photostationary states at 365 nm or 455 nm where reached. The quantum yield was calculated with the above mentioned software and the spectra of pure photoisomers from five independent irradiation processes each for best results.

	process	wavelength λ [nm]	quantum yield Φ [%]
dA_{Azo}	*cis* → *trans*	455	43.5 ± 0.5
	trans → *cis*	365	16.9 ± 0.2
dG_{Azo}	*cis* → *trans*	455	58.9 ± 0.2
	trans → *cis*	365	18.7 ± 0.1

5.4 Polyacrylamide gel electrophoresis

5.4.1 Buffer systems and general procedures

10X TBE-Buffer		1X TBE-Buffer		10X TA-Buffer		1X TA-Buffer		1X HFIP-Buffer	
Ingredient	mM	Ingredient	mM	Ingredient	mM	Ingredient	mM	Ingredient	mM
Tris	890	Tris	89	Tris	500	Tris	50	HFIP	400
B(OH)$_3$	890	B(OH)$_3$	89	NaOAc*3H$_2$O	1000	NaOAc*3H$_2$O	100	TEA	15
Na$_2$EDTA*2H$_2$O	20	Na$_2$EDTA*2H$_2$O	2						

denaturing PAGE			native PAGE		
Ingredient			Ingredient		
AA/BAA 40%	1,25	mL	AA/BAA 40%	1,25	mL
10x TBE	1	mL	10x TA	1	mL
Urea (7M)	4,2	g	fill with H$_2$O	7,75	mL
fill with H$_2$O	7,75	mL			
%	5	%	%	5	%
Vol. in mL	10	mL	Vol. in mL	10	mL
add before use:			add before use:		
TEMED	10	µL	TEMED	10	µL
10% APS	100	µL	10% APS	100	µL

denaturing loading buffer		native loading buffer	
Ingredient	mM		
Tris	89	sucrose	65%w
B(OH)$_3$	89	H$_2$O	35%w
Na$_2$EDTA*2H$_2$O	2	10xTA	10%w
		dye	
glycerol	30% vol	bromophenol blue	
H$_2$O	70% vol	xylene cyanol	
dye			
Crocein Orange B			

5.4.2 Standard procedure for poly acryl amide gel electrophoresis and PAGE-imaging

Acryl amide gels were cast according to the mixture mentioned above in either *Biometra* (*Multigel*), *VWR* (*Mini Vertical PAGE System*) or *Bio Rad* (*Protean II XL Cell*) device. Denaturing PAGE were run for 30 (*Biometra*/ *VWR* devices) or 90 minutes (*BioRad* device) with 3 or 5W, native PAGE were run at 3W for 90-150 minutes tempered at 20°C by attached thermostat (*Biometra* device) if not stated otherwise. After electrophoresis, gels where stained with SYBR Gold (*Thermo Fisher*, 2 µL diluted in 20 mL 1x TA-buffer) for 20 minutes before imaging at a transilluminator (*biostep Dark Hood DH-40/50* or *BioRad GelDoc XR+*).

5.4.3 Standard Procedure and evaluation of PAGE-irradiation experiments for the DNA-minicircle project

Analytical 5%-native PAGE was prepared according to mixtures as mentioned above. For irradiation experiments 2-3 pmol of each azobenzene-modified ring where mixed after irradiation at 365 nm (UVLED-365-250-SMD, 250 mW, 500 mA), 420 nm (H2A1-H420, 130 mW, 350 mA) or 530 nm (H-HP803PG , 600 mW, 500 mA) for 2 minutes each on a custom build multi LED device with the same amount of binding partner in MilliQ water, before mixing with loading buffer and pipetting into pockets, to ensure that needed salt concentration for sufficient dimerization of the 10mer binding site is present at approximately the same time for every sample. Gels were run at 3 W for 2.5 to 3 hours with the temperature kept at 20 °C by flow thermostat. After electrophoresis, gels were stained and imaged as mentioned above. The quantitative analysis of the narrow gel bands was carried out with the program GelBandFitter from Mitov *et al.* according to the described procedure.[180] To enable comparativity, three independent gels were run and analyzed for 365/420 nm and 365/530 nm experiments. For analysis, only fits were taken into consideration with a coefficient of determination exceeding $R^2 = 0.98$. The mean value of the three measurements were taken as value together with their standard deviation as error values. Unmodified images of the gels used for this study can be seen in Fig. 112-122 (nomenclature of the rings are according to the number of the dimerization relevant strand in the ring).

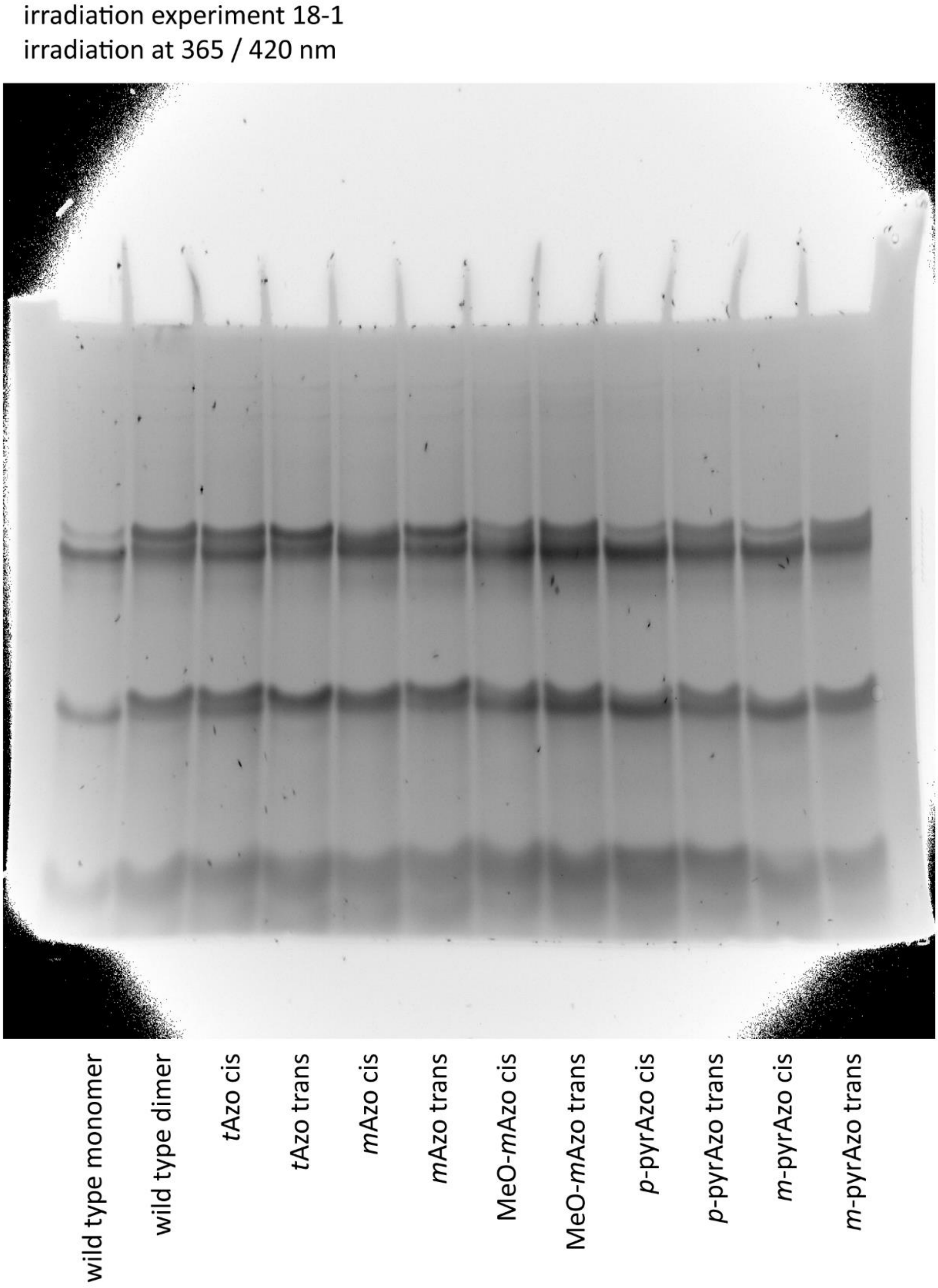
irradiation experiment 18-1
irradiation at 365 / 420 nm
wild type monomer
wild type dimer
*t*Azo cis
*t*Azo trans
*m*Azo cis
*m*Azo trans
MeO-*m*Azo cis
MeO-*m*Azo trans
p-pyrAzo cis
p-pyrAzo trans
m-pyrAzo cis
m-pyrAzo trans

Fig. 118 Unmodified image of the irradiation PAGE experiments (18-1) and description of the corresponding lines.

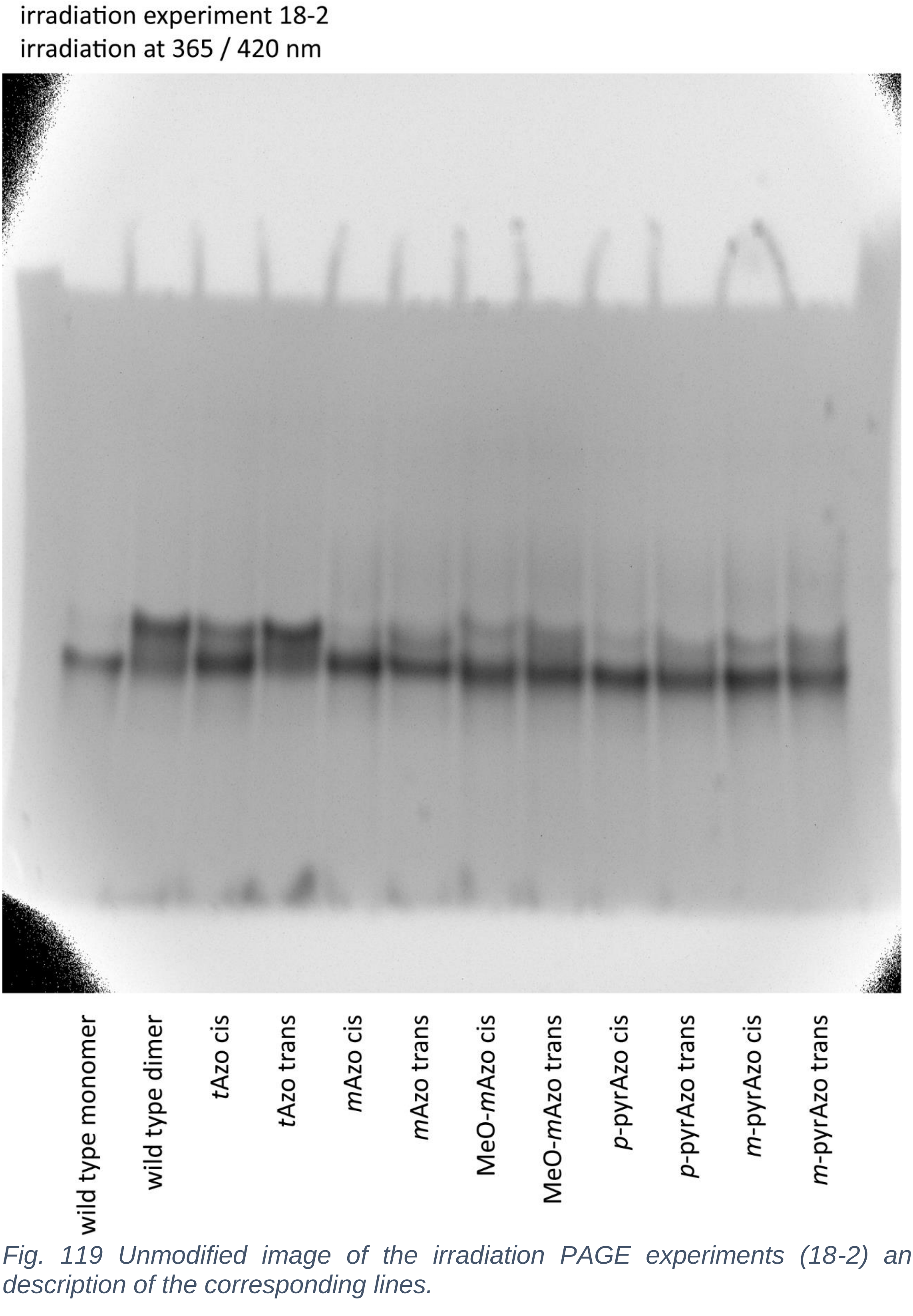
irradiation experiment 18-2
irradiation at 365 / 420 nm
wild type monomer
wild type dimer
tAzo cis
tAzo trans
mAzo cis
mAzo trans
MeO-mAzo cis
MeO-mAzo trans
p-pyrAzo cis
p-pyrAzo trans
m-pyrAzo cis
m-pyrAzo trans

Fig. 119 Unmodified image of the irradiation PAGE experiments (18-2) and description of the corresponding lines.

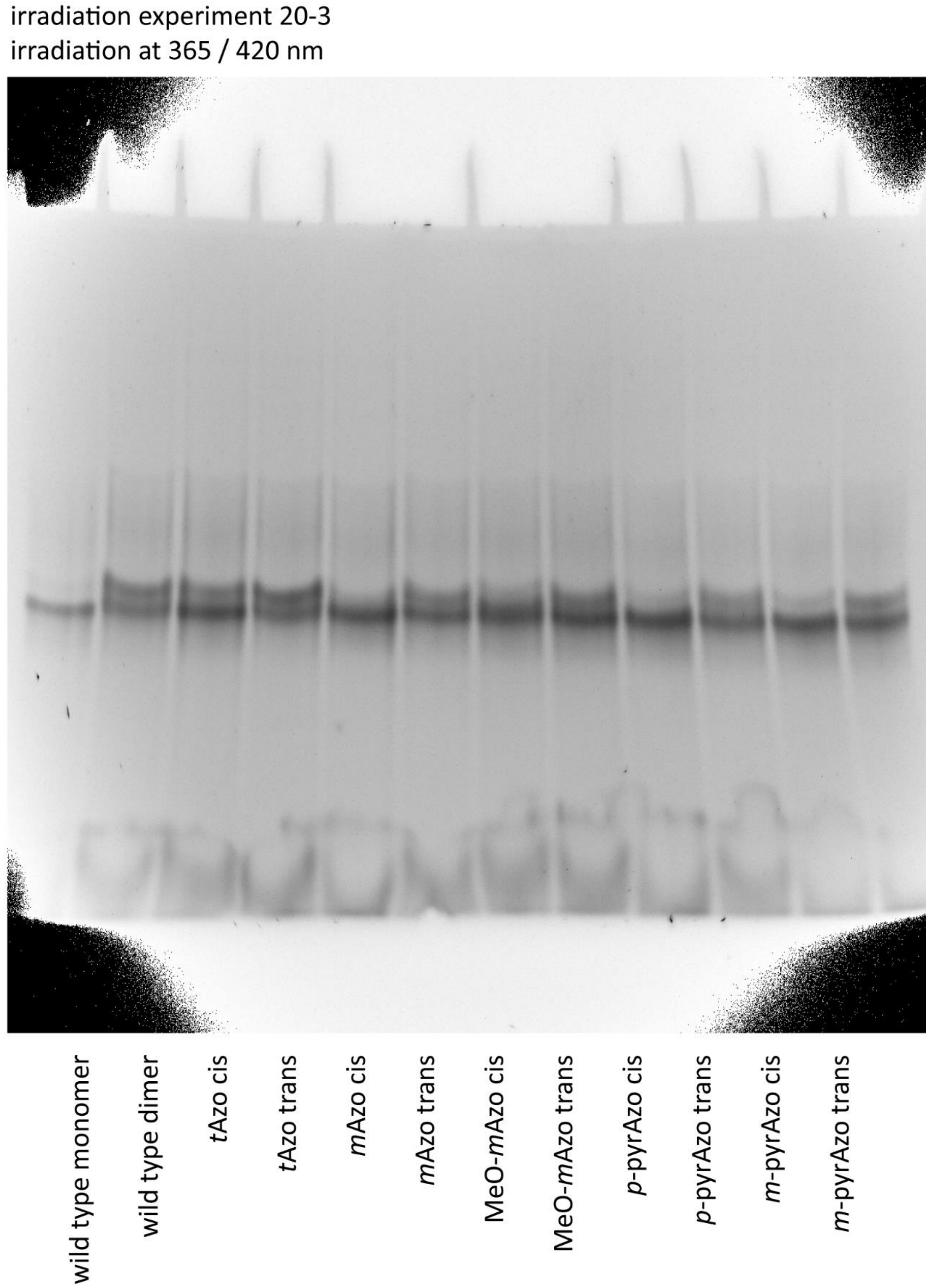
irradiation experiment 20-3
irradiation at 365 / 420 nm
wild type monomer
wild type dimer
tAzo cis
tAzo trans
mAzo cis
mAzo trans
MeO-mAzo cis
MeO-mAzo trans
p-pyrAzo cis
p-pyrAzo trans
m-pyrAzo cis
m-pyrAzo trans

Fig. 120 Unmodified image of the irradiation PAGE experiments (20-3) and description of the corresponding lines.

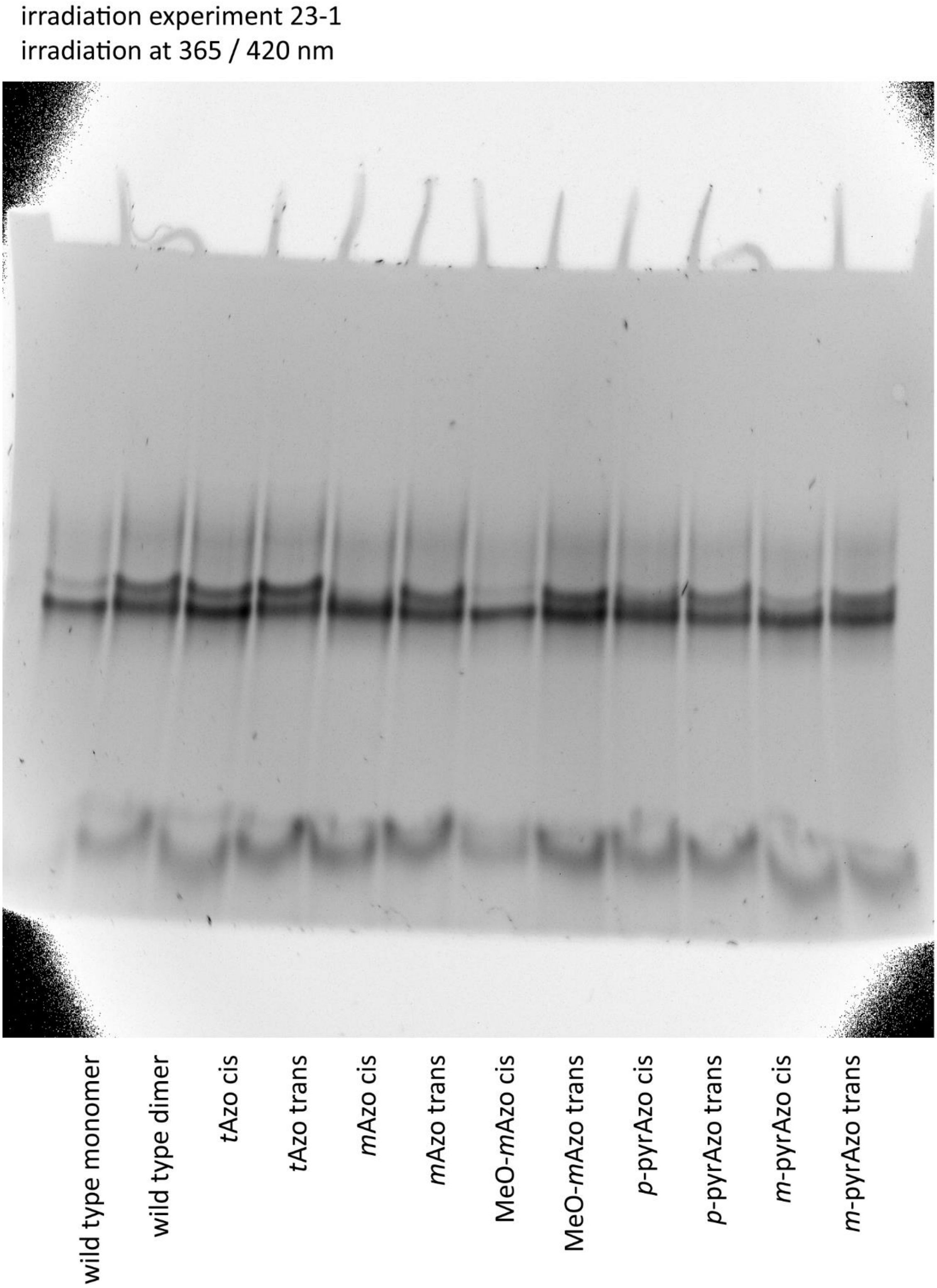
irradiation experiment 23-1
irradiation at 365 / 420 nm
wild type monomer
wild type dimer
*t*Azo cis
*t*Azo trans
*m*Azo cis
*m*Azo trans
MeO-*m*Azo cis
MeO-*m*Azo trans
p-pyrAzo cis
p-pyrAzo trans
m-pyrAzo cis
m-pyrAzo trans

Fig. 121 Unmodified image of the irradiation PAGE experiments (23-1) and description of the corresponding lines.

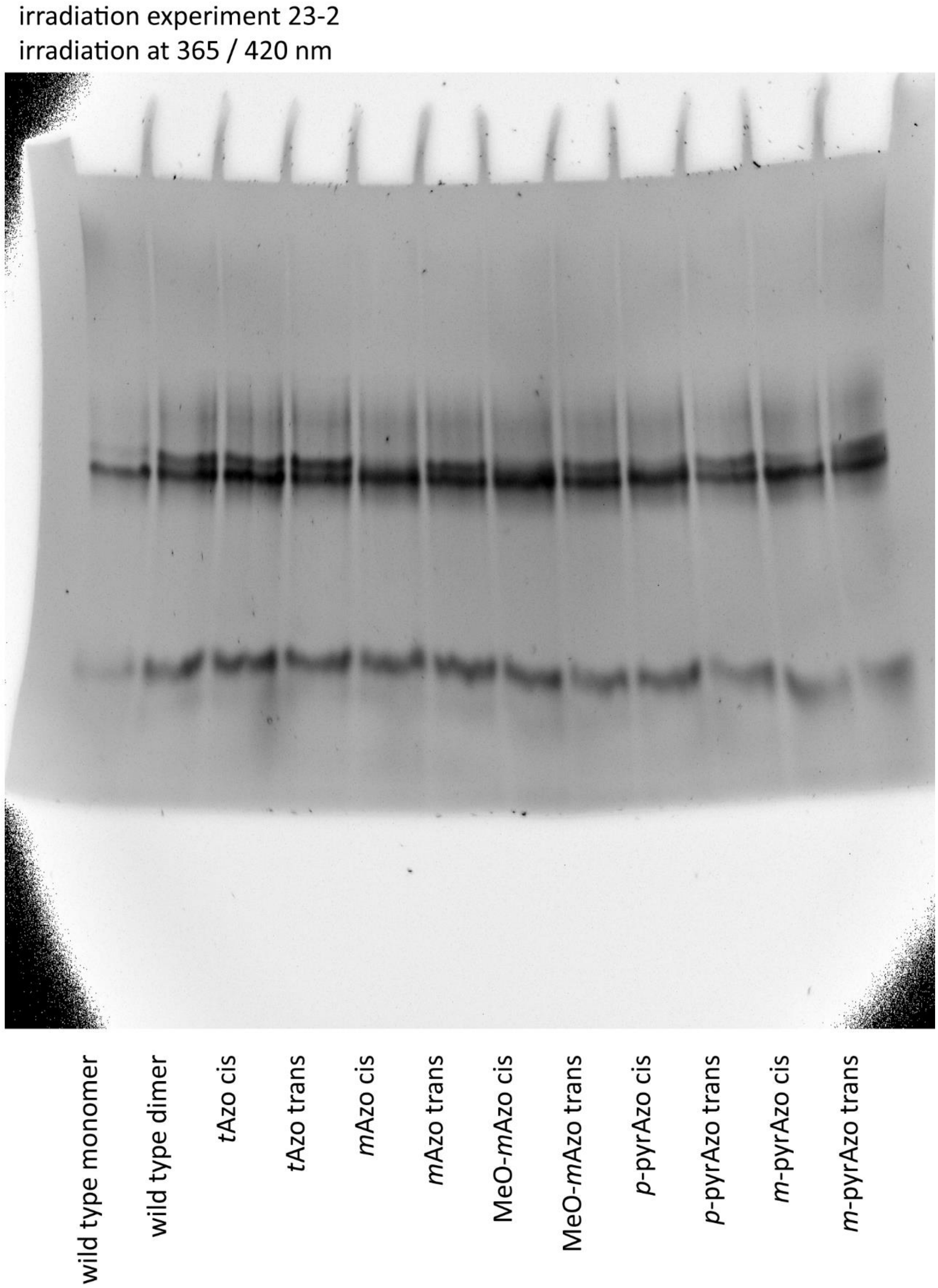
irradiation experiment 23-2
irradiation at 365 / 420 nm
wild type monomer
wild type dimer
tAzo cis
tAzo trans
mAzo cis
mAzo trans
MeO-mAzo cis
MeO-mAzo trans
p-pyrAzo cis
p-pyrAzo trans
m-pyrAzo cis
m-pyrAzo trans

Fig. 122 Unmodified image of the irradiation PAGE experiments (23-2) and description of the corresponding lines.

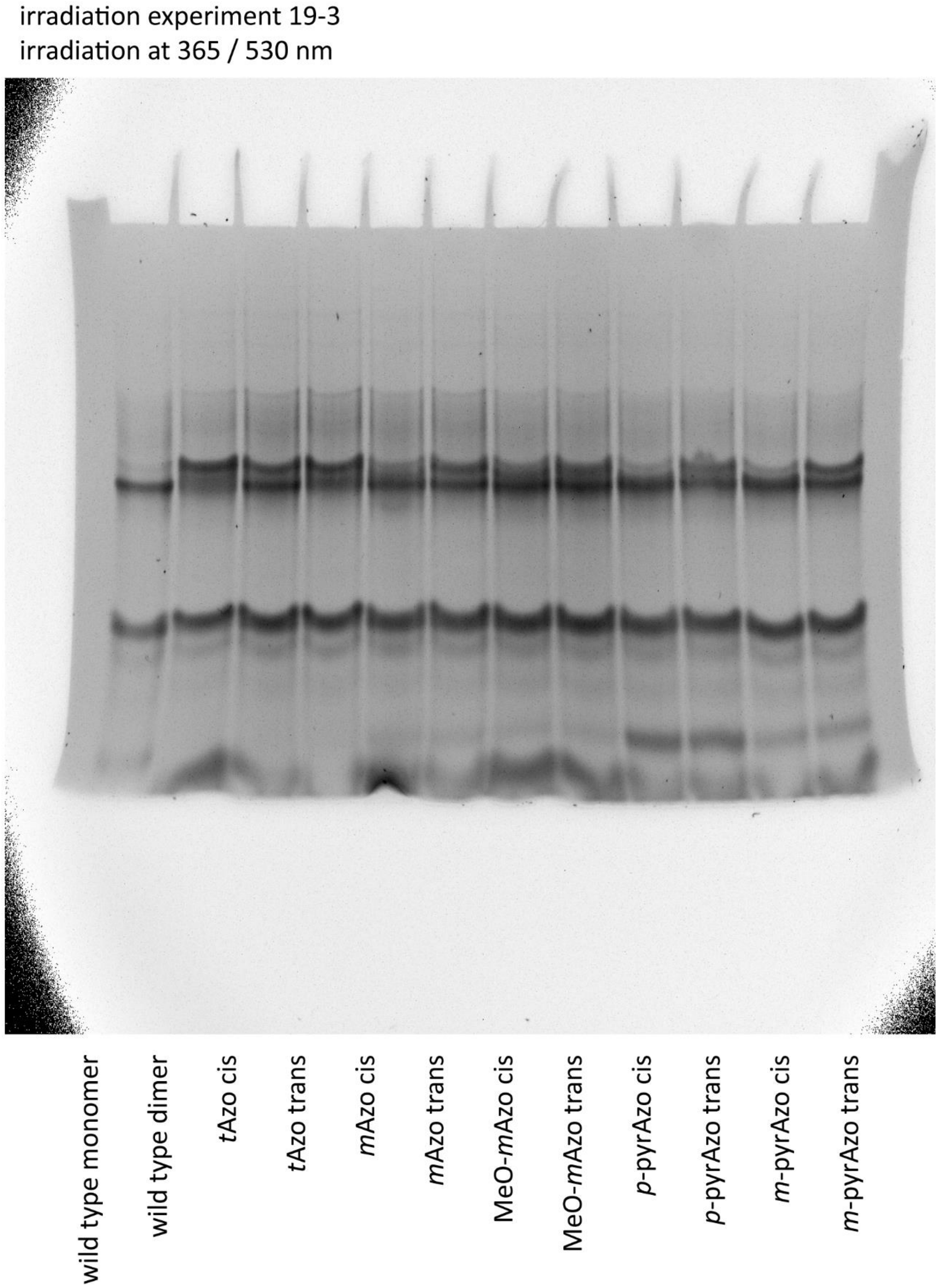
irradiation experiment 19-3
irradiation at 365 / 530 nm
wild type monomer
wild type dimer
*t*Azo cis
*t*Azo trans
*m*Azo cis
*m*Azo trans
MeO-*m*Azo cis
MeO-*m*Azo trans
p-pyrAzo cis
p-pyrAzo trans
m-pyrAzo cis
m-pyrAzo trans

Fig. 123 Unmodified image of the irradiation PAGE experiments (19-3) and description of the corresponding lines.

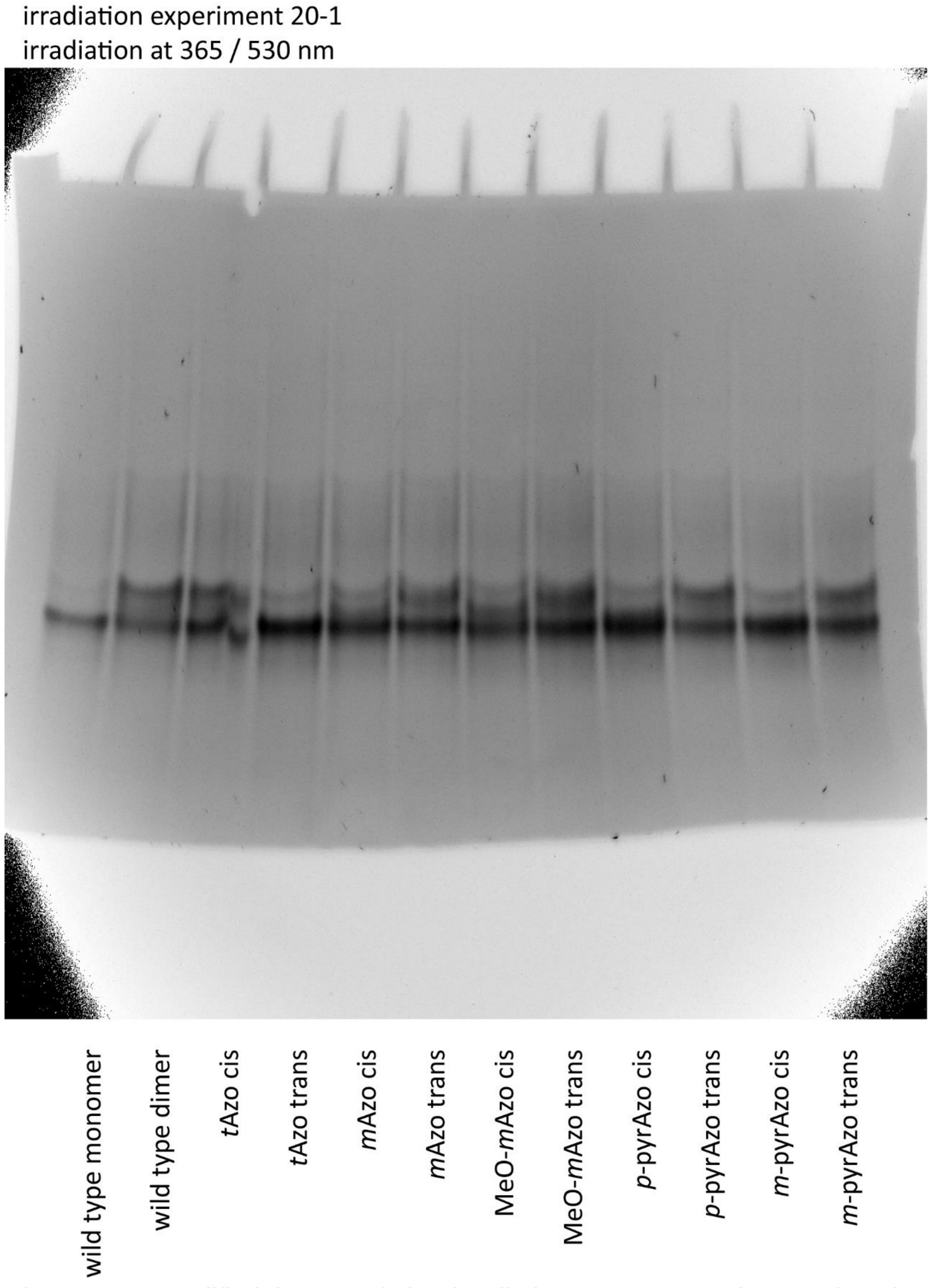
irradiation experiment 20-1
irradiation at 365 / 530 nm
wild type monomer
wild type dimer
*t*Azo cis
*t*Azo trans
*m*Azo cis
*m*Azo trans
MeO-*m*Azo cis
MeO-*m*Azo trans
p-pyrAzo cis
p-pyrAzo trans
m-pyrAzo cis
m-pyrAzo trans

Fig. 124 Unmodified image of the irradiation PAGE experiments (20-1) and description of the corresponding lines.

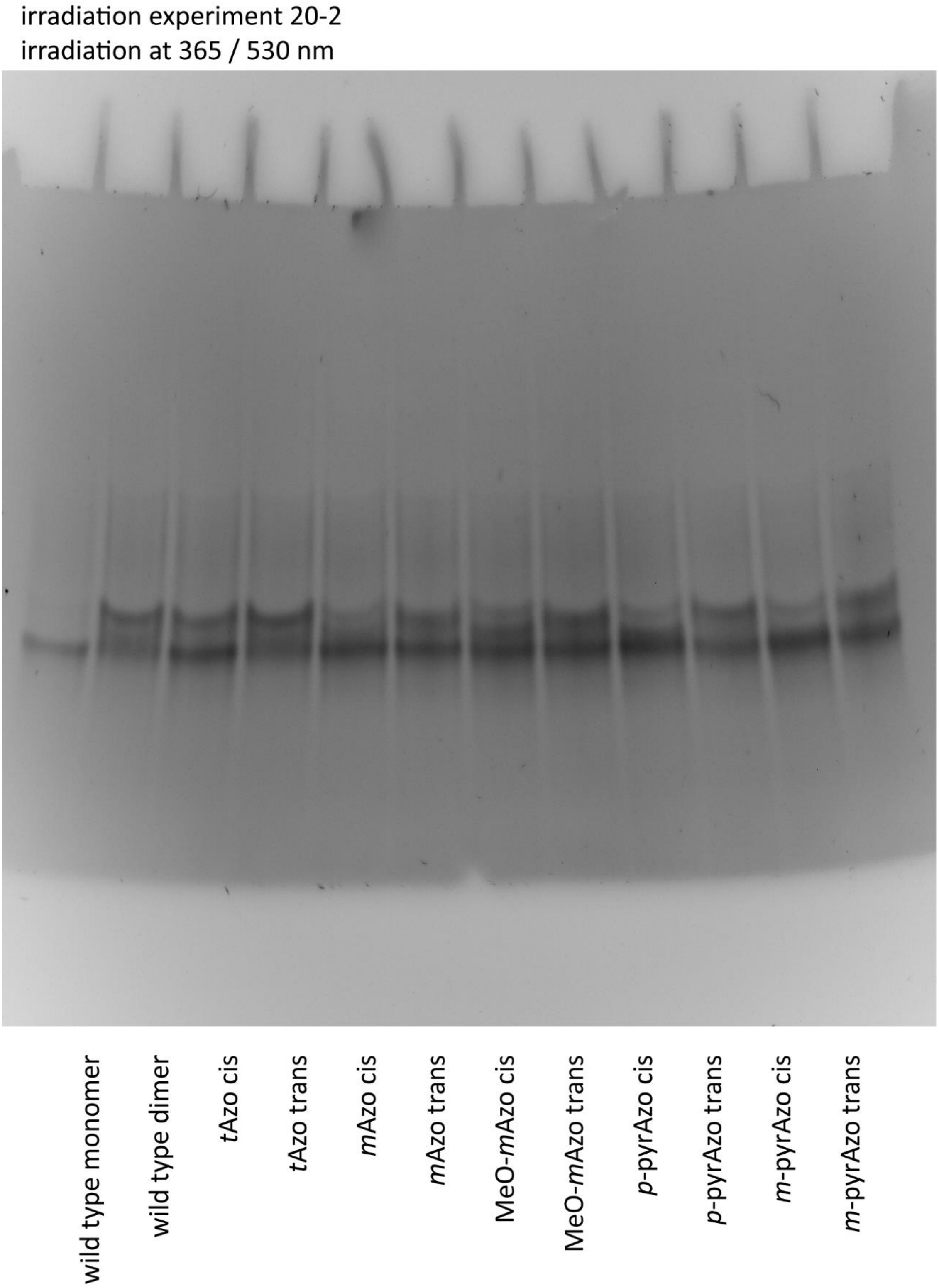
irradiation experiment 20-2
irradiation at 365 / 530 nm
wild type monomer
wild type dimer
tAzo cis
tAzo trans
mAzo cis
mAzo trans
MeO-mAzo cis
MeO-mAzo trans
p-pyrAzo cis
p-pyrAzo trans
m-pyrAzo cis
m-pyrAzo trans

Fig. 125 Unmodified image of the irradiation PAGE experiments (20-2) and description of the corresponding lines.

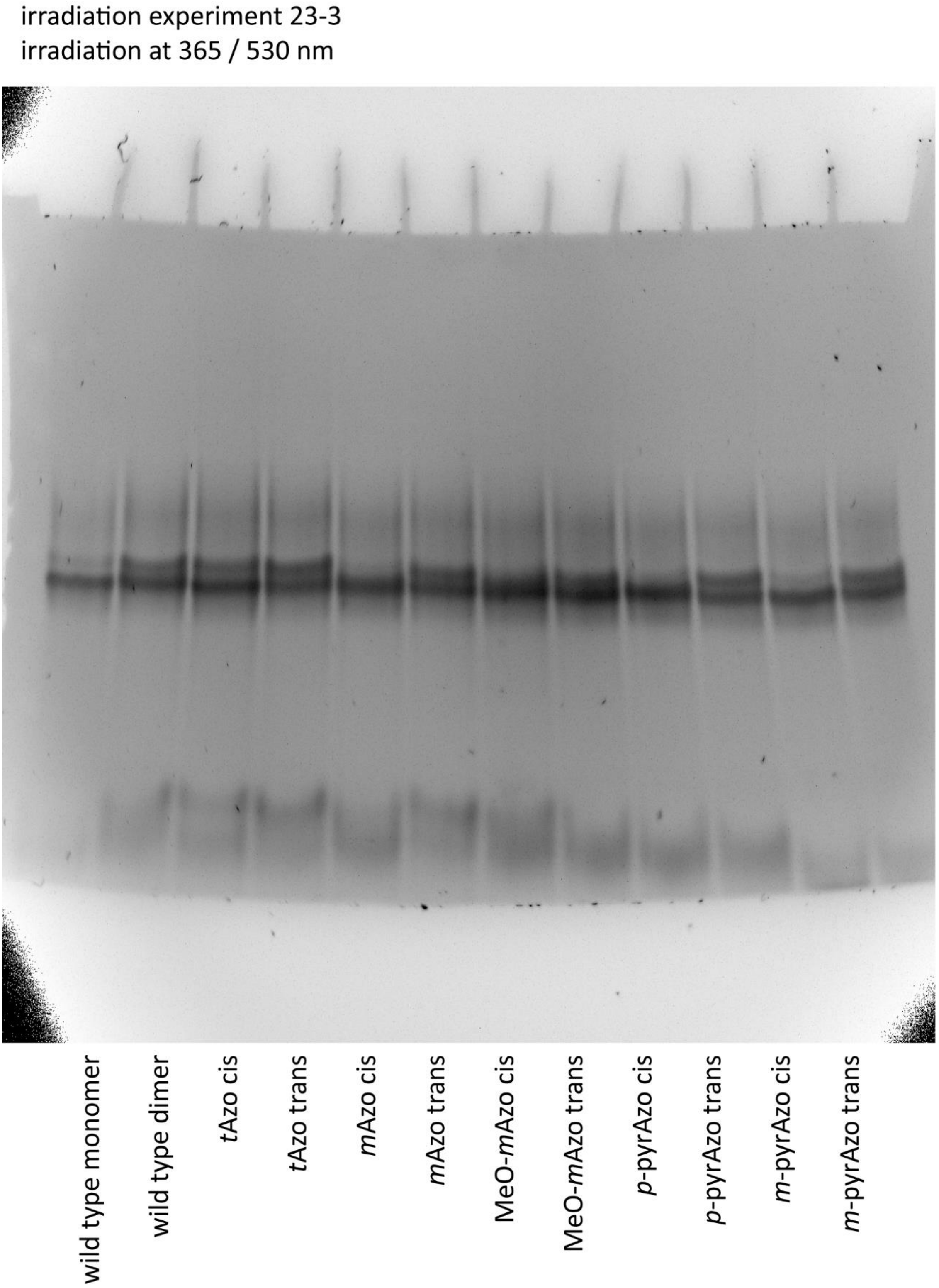
irradiation experiment 23-3
irradiation at 365 / 530 nm
wild type monomer
wild type dimer
tAzo cis
tAzo trans
mAzo cis
mAzo trans
MeO-mAzo cis
MeO-mAzo trans
p-pyrAzo cis
p-pyrAzo trans
m-pyrAzo cis
m-pyrAzo trans

Fig. 126 Unmodified image of the irradiation PAGE experiments (23-3) and description of the corresponding lines.

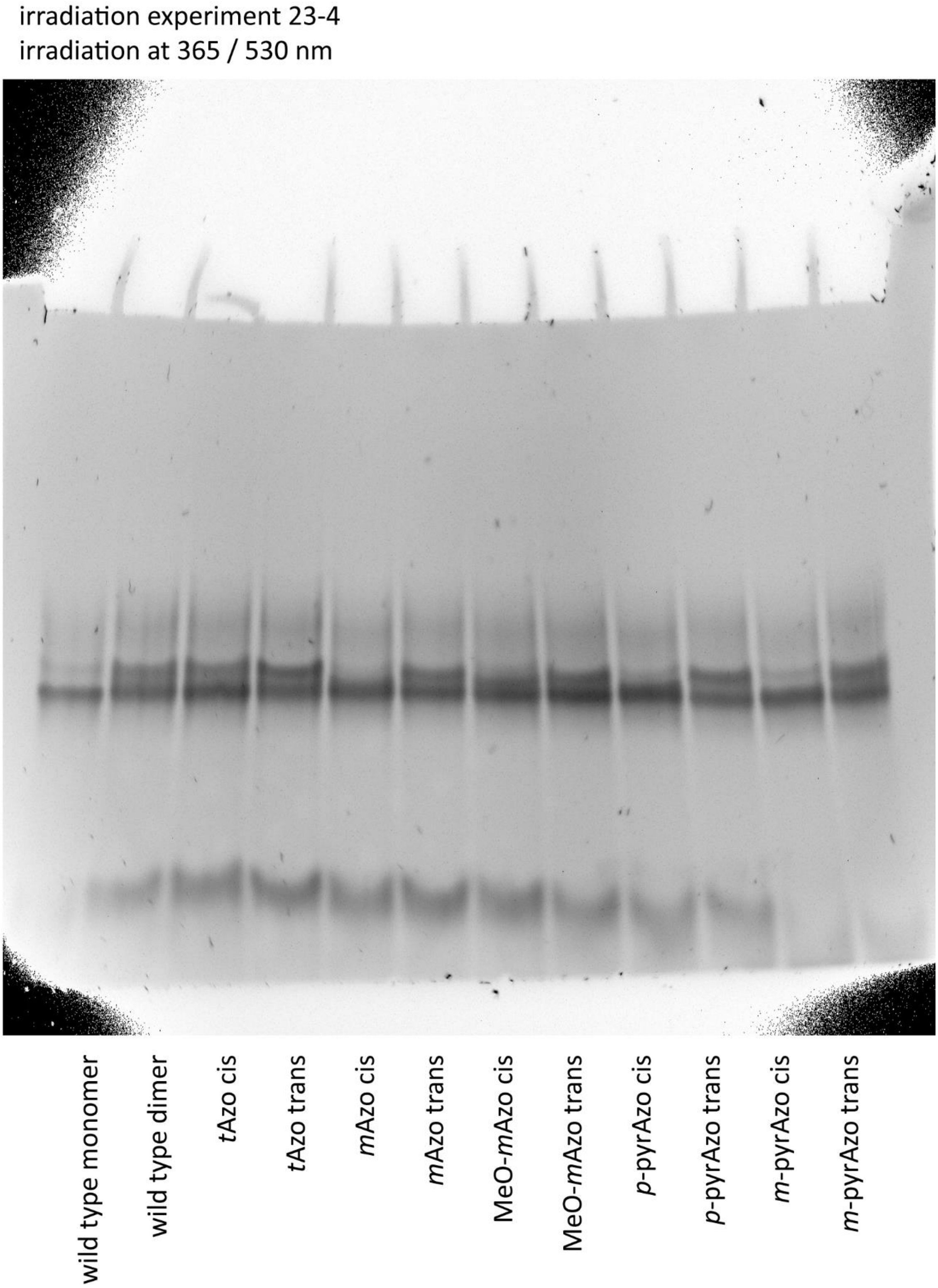
irradiation experiment 23-4
irradiation at 365 / 530 nm
wild type monomer
wild type dimer
*t*Azo cis
*t*Azo trans
*m*Azo cis
*m*Azo trans
MeO-*m*Azo cis
MeO-*m*Azo trans
p-pyrAzo cis
p-pyrAzo trans
m-pyrAzo cis
m-pyrAzo trans

Fig. 127 Unmodified image of the irradiation PAGE experiments (23-4) and description of the corresponding lines.

5.5 CD-spectroscopy

Samples for CD-measurements were 10 µM in 1x PBS-buffer, CD-spectra were recorded on a J-710 CD-spectrometer from JASCO. Samples were irradiated at 70 °C, then annealed and measured at 20 °C. Ten individual measurements for each sample were accumulated for best results.

5.5.1 CD-spectra of the LNAzo project

System 1

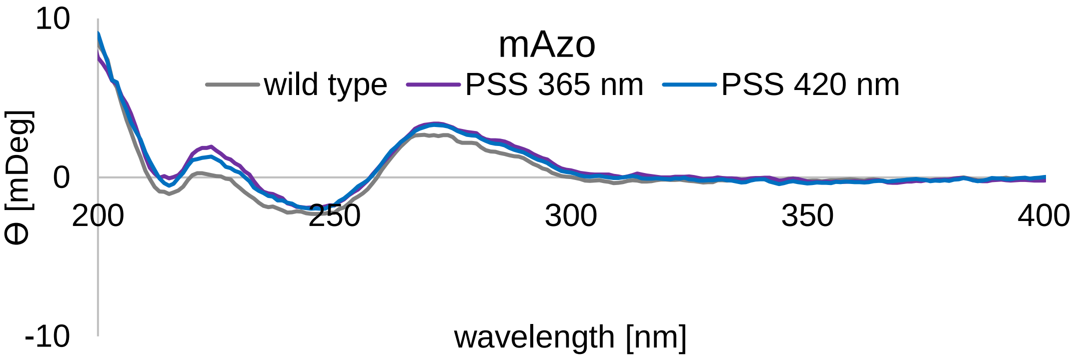

Fig. 128 CD-spectra of strand 13+17 compared to strand 13+16.

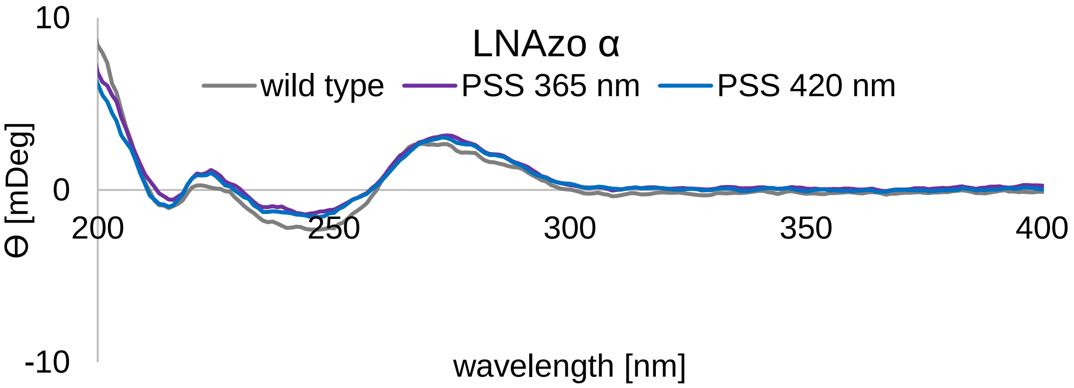

Fig. 129 CD-spectra of strand 13+18 compared to strand 13+16.

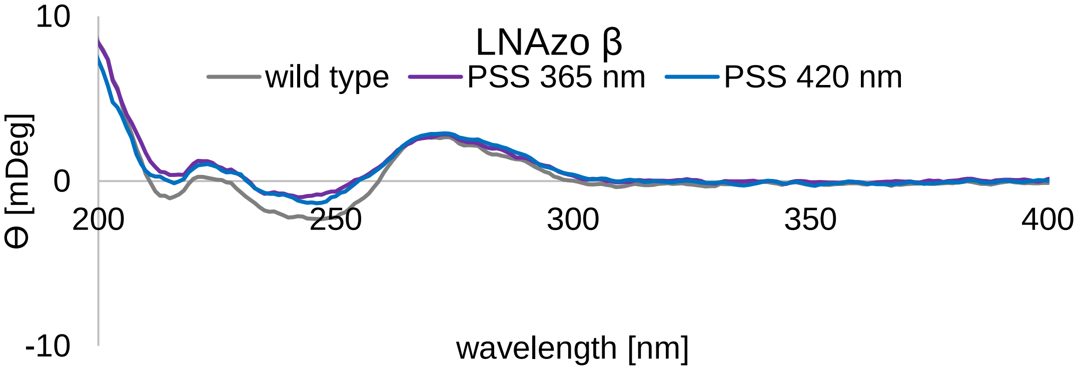

Fig. 130 CD-spectra of strand 13+19 compared to strand 13+16.

System 2

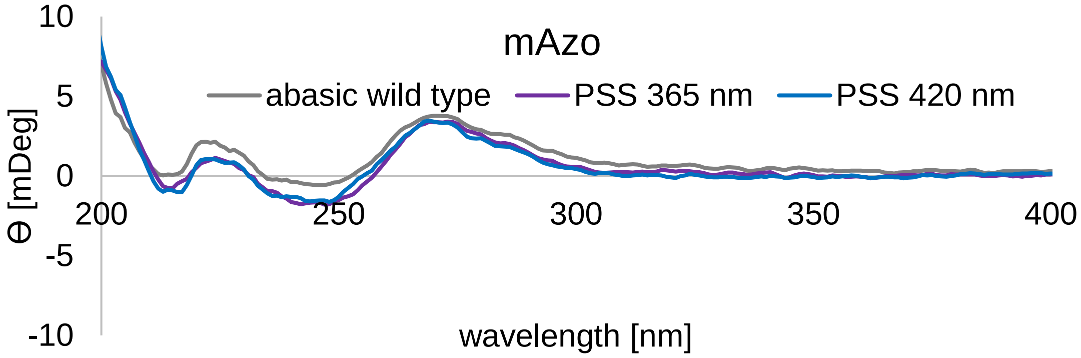

Fig. 131 CD-spectra of strand 14+17 compared to strand 14+16.

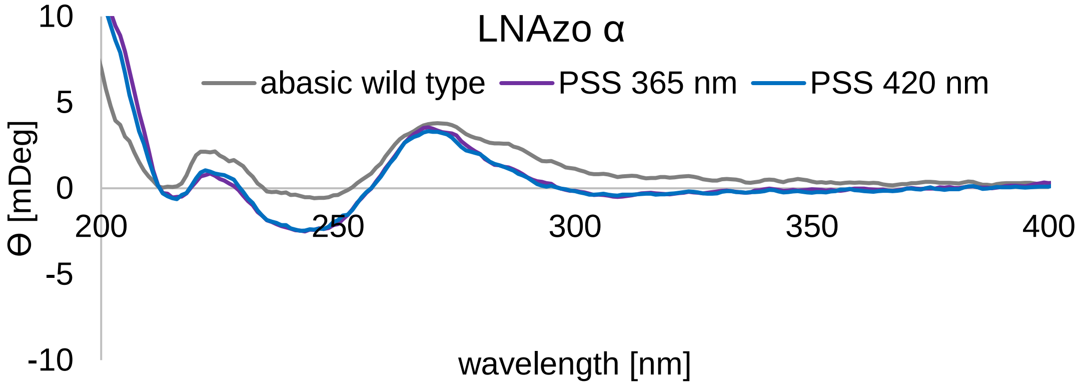

Fig. 132 CD-spectra of strand 14+18 compared to strand 14+16.

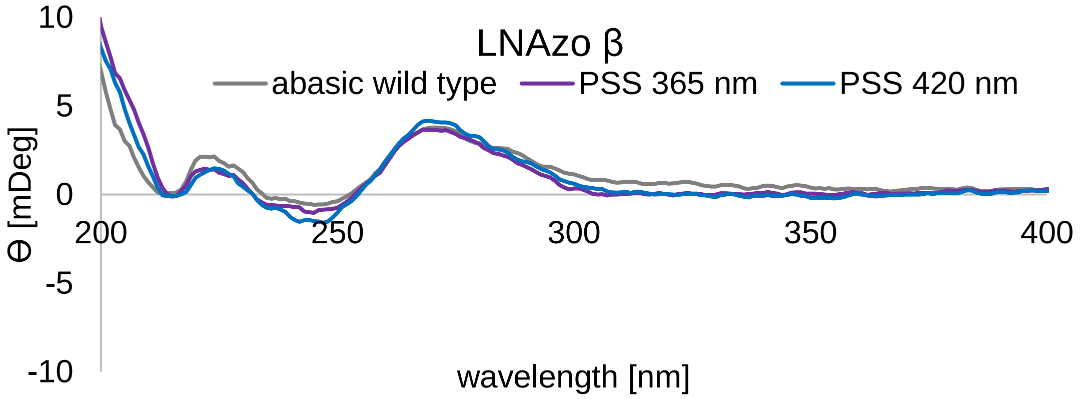

Fig. 133 CD-spectra of strand 14+19 compared to strand 14+16.

System 3

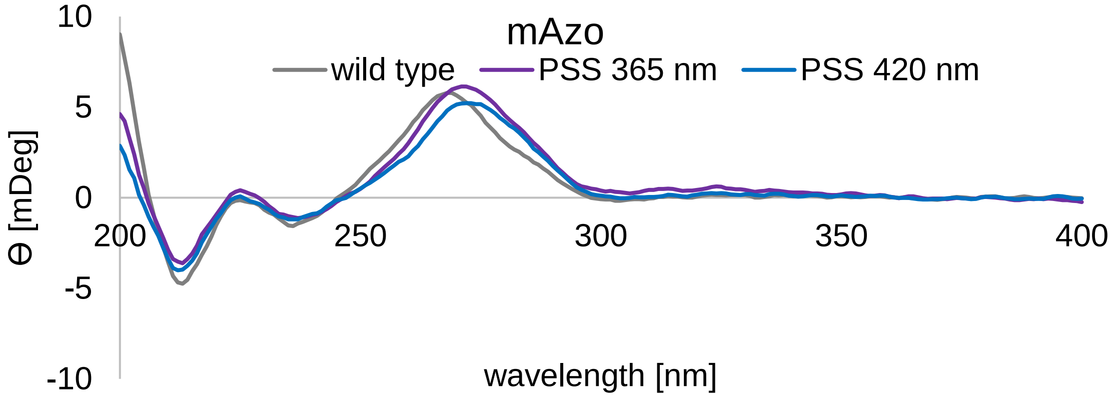

Fig. 134 CD-spectra of strand 15+17 compared to strand 15+16.

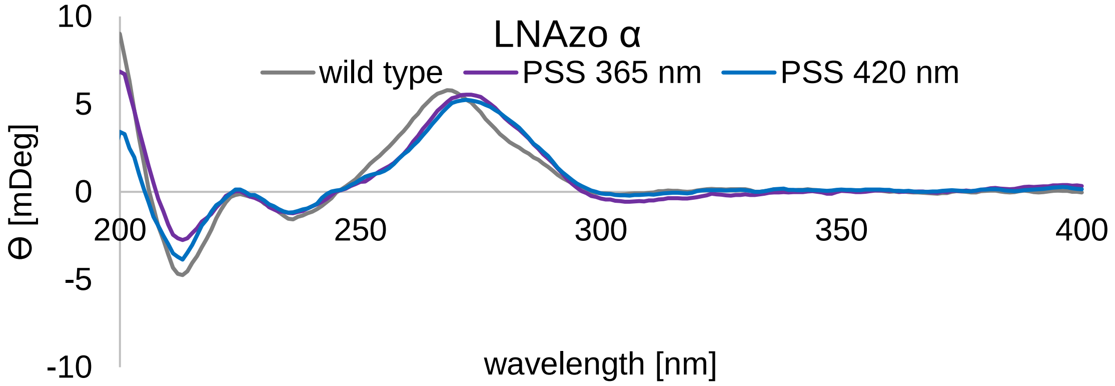

Fig. 135 CD-spectra of strand 15+18 compared to strand 15+16.

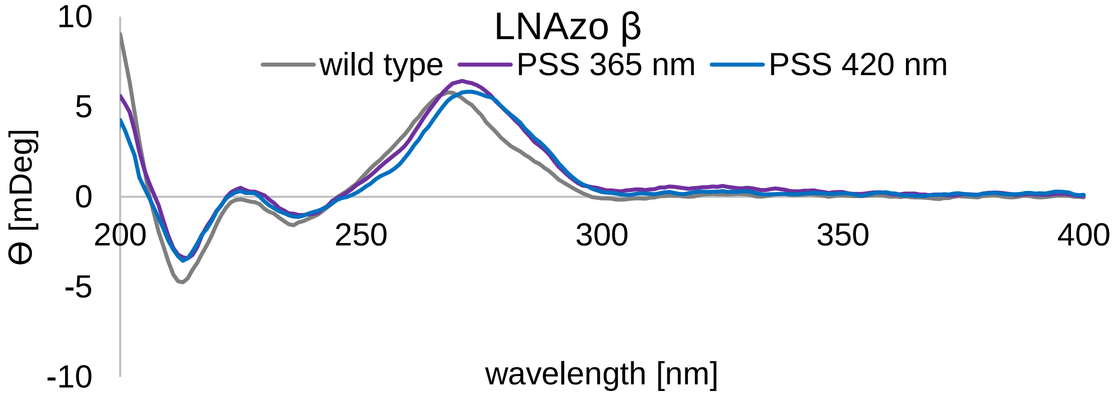

Fig. 136 CD-spectra of strand 15+19 compared to strand 15+16.

System 4

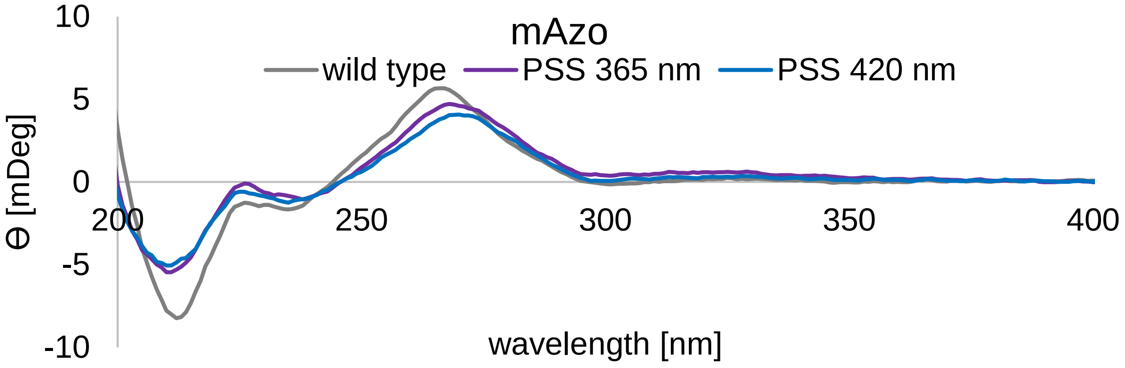

Fig. 137 CD-spectra of strand 15+21 compared to strand 15+20.

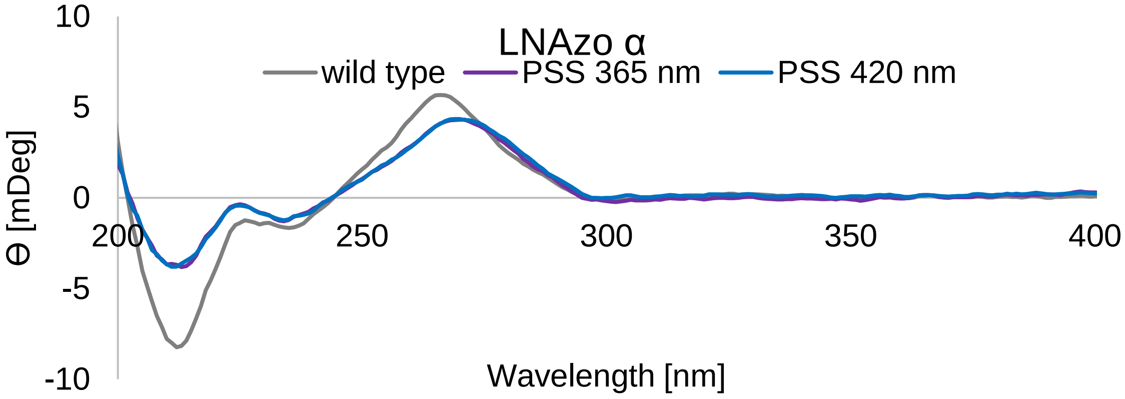

Fig. 138 CD-spectra of strand 15+22 compared to strand 15+20.

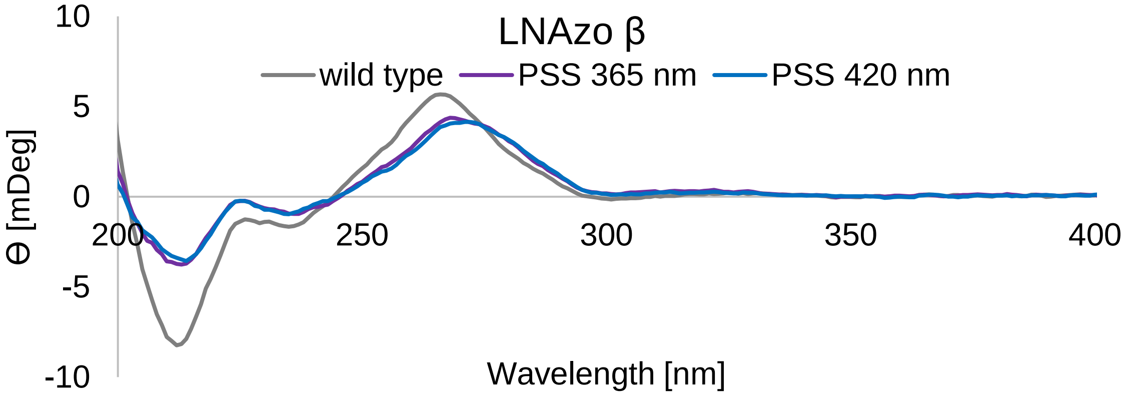

Fig. 139 CD-spectra of strand 15+23 compared to strand 15+20.

5.5.2 CD-spectra of the 2-phenyldiazenyl purine project

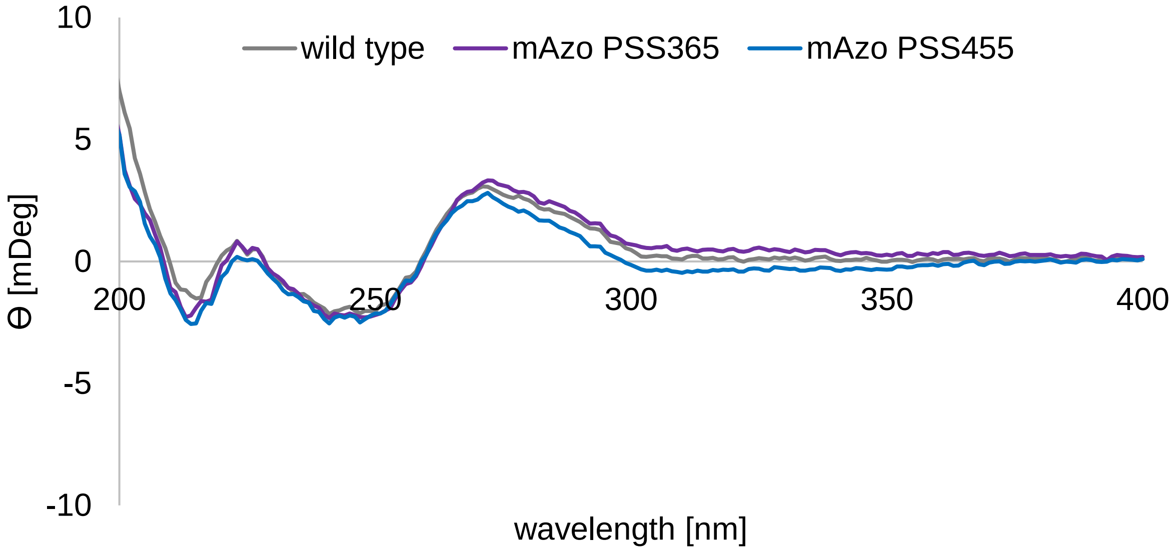

Fig. 140 CD-spectra of strand 13+15 compared to strand 13+16.

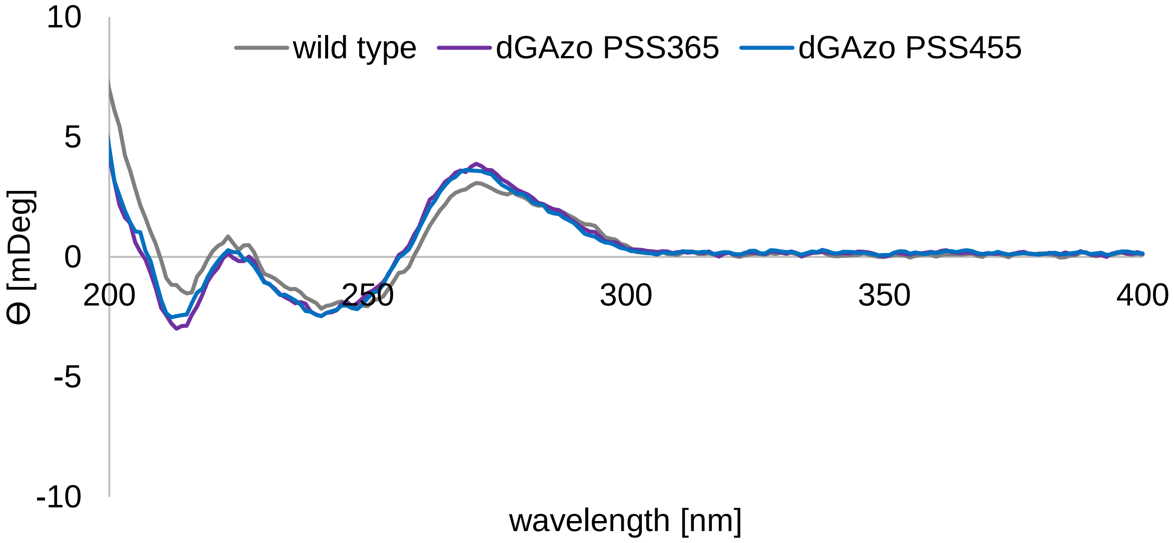

Fig. 141 CD-spectra of strand 13+30 compared to strand 13+16.

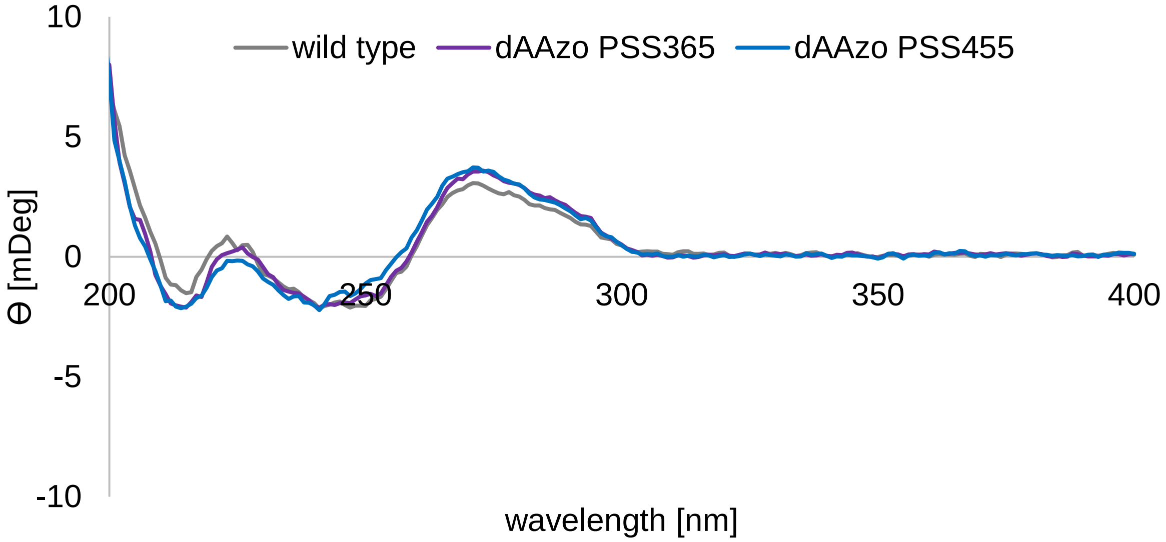

Fig. 142 CD-spectra of strand 15+31 compared to strand 13+16.

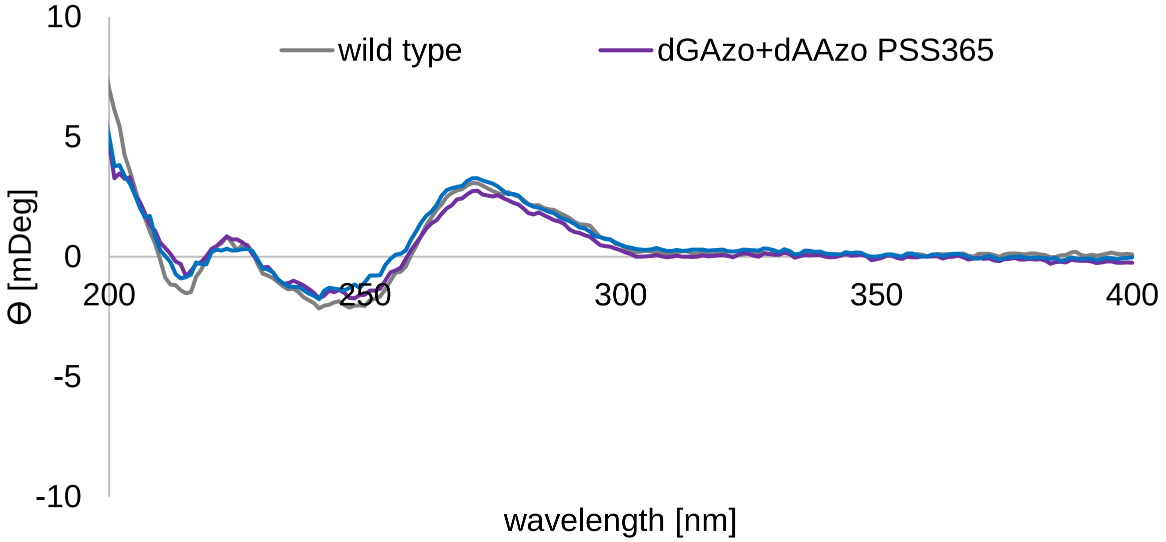

Fig. 143 CD-spectra of strand 30+31 compared to strand 13+16.

5.6 UV/vis absorption-based melting curves

5.6.1 Melting curves of the DNA-minicircle project

The absorbance changes of the samples (1 mL, 1 µM in PBS buffer, pH 7.4) at λ = 260 nm were measured within a temperature range of 5–80 °C. The samples were irradiated either with UV (λ = 365 nm, 250 mW, 500 mA, 2 minutes) or visible light (λ = 420 nm, 130 mW, 350 mA, 2 minutes or 530nm, 55 lm, 500 mA, 2 minutes) at room temperature to obtain the photostationary state. The melting point (T_{M}) was calculated by Origin via sigmoidal fit. At least five independent measurements were performed. Due to hysteresis, melting points are averaged between heating and cooling cycles. Although only irradiation in the double strand (20 °C) were of interest in this study, samples were additionally irradiated in single strand (60 °C) to do justice to their maximum switching capabilities. The most important melting curves of duplexes irradiated at 60 °C are shown below (Fig. 144-148), each containing five cooling (1-5) and heating (1r-5r) curves.

melting point	20 °C 365 nm	60 °C 365 nm	20 °C 420 nm	60 °C 420 nm	20 °C 530 nm	60 °C 530 nm
wild type			36.8			
*t*Azo	41.5	31.8	48.7	47.4		
*m*Azo	21.2	20.1	22.4	22.9		
MeO-*m*Azo	17.4	17.4	20.3	19.8		
p-pyrAzo	22.0	22.6	29.1	28.3	26.6	28.1
m-pyrAzo	18.4	19.8	25.7	25.1	26.0	26.8
error	20 °C 365 nm	60 °C 365 nm	20 °C 420 nm	60 °C 420 nm	20 °C 530 nm	60 °C 530 nm
wild type			0.63			
*t*Azo	0.70	0.20	2.53	1.03		
*m*Azo	2.20	1.34	0.22	0.45		
MeO-*m*Azo	0.26	0.15	0.21	0.08		
p-pyrAzo	0.21	0.31	0.07	0.06	0.07	0.03
m-pyrAzo	2.72	0.34	0.43	1.33	0.24	0.06

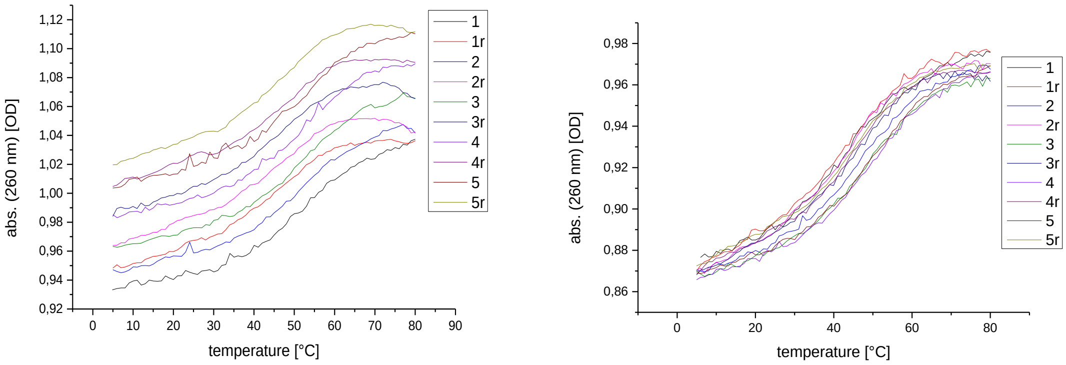

Fig. 144 Melting curves of strand 6+8 at PSS 420 nm (left) and PSS 365 nm (right).

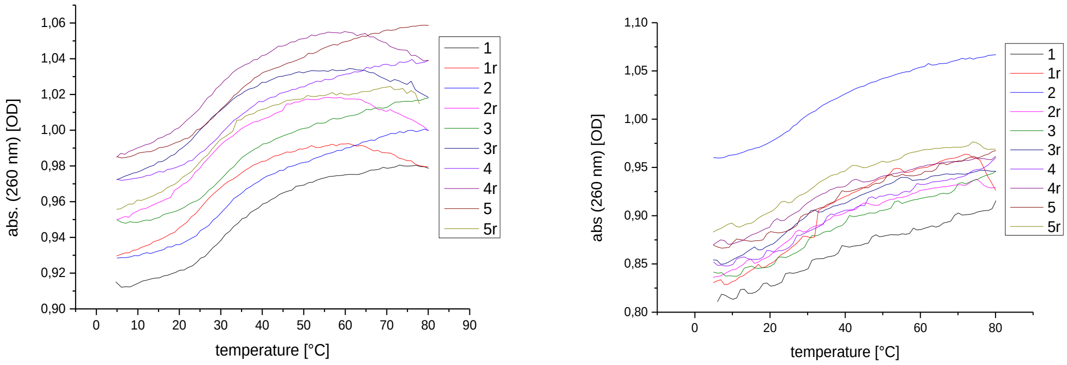

Fig. 145 Melting curves of strand 6-5+9-2 at PSS 420 nm (left) and PSS 365 nm (right).

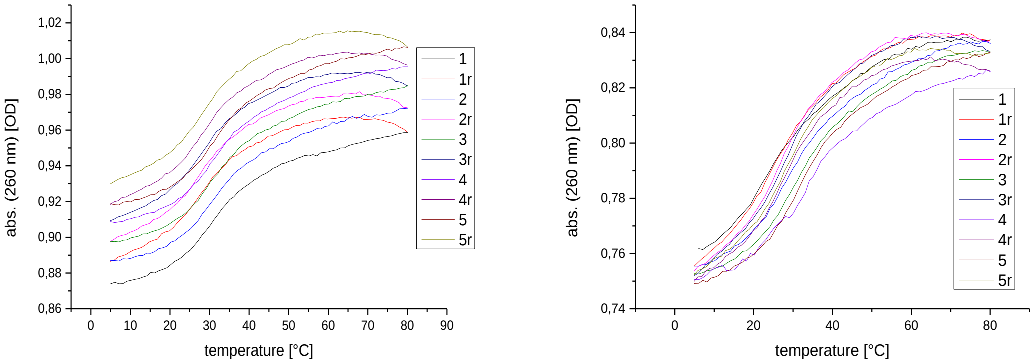

Fig. 146 Melting curves of strand 6-5+10-2 at PSS 530 nm (left) and PSS 365 nm (right).

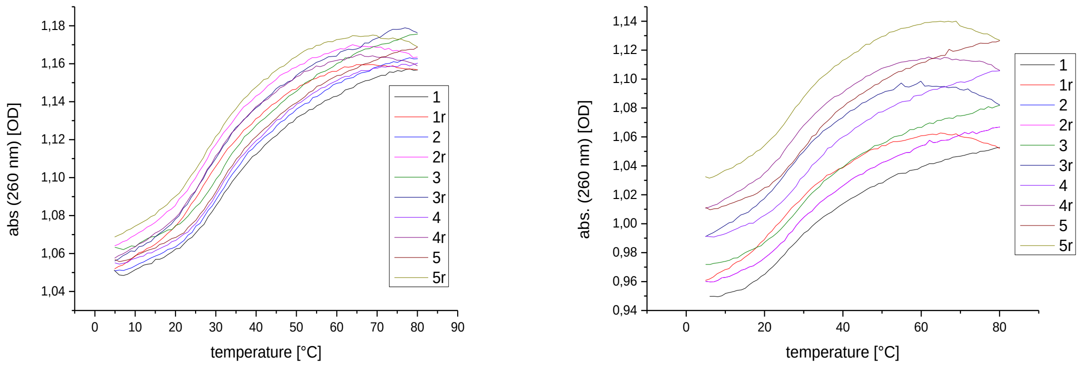

Fig. 147 Melting curves of strand 6-5+11-2 at PSS 420 nm (left) and PSS 365 nm (right).

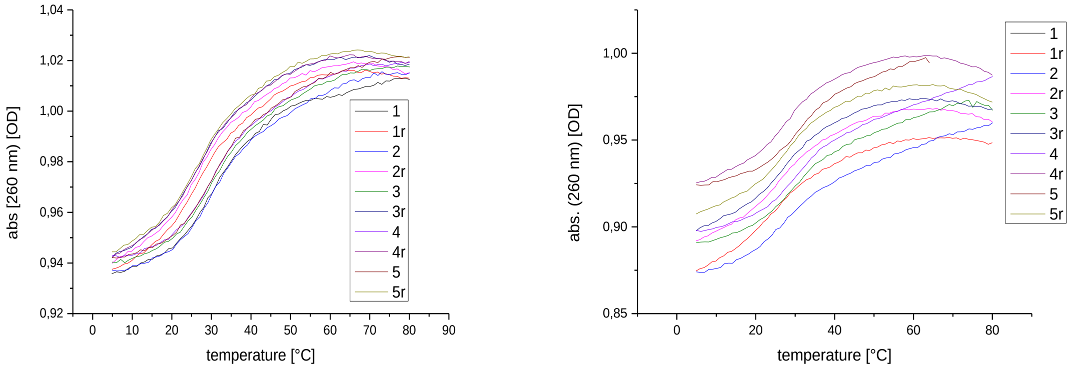

Fig. 148 Melting curves of strand 6-5+12-2 at PSS 530 nm (left) and PSS 365 nm (right).

5.6.2 Melting curves of the LNAzo project

For melting point measurements 1 mL samples were prepared with 1µM of strand and counterstrand in 1x PBS-buffer for each modification and each system (16 in total). The absorbance changes at 260 nm were measured by a V-650 UV/vis-spectrometer from JASCO. Samples were irradiated as single strands at elevated temperatures (system 1-3: 70°C, system 4: 80°C) with either 365 nm or 420 nm until the photostationary state (PSS) was reached to prevent mismatches. The temperature gradient was 1 °C per minute. To avoid effects of hysteresis, melting points were calculated by a sigmoidal fit from cooling and heating measurements. At least five independent heating and cooling measurements were performed for precise results. For experimental values with error bars see chapter 3.2.3. The most important melting curves of duplexes are shown below (Fig. 149-164), each containing five cooling (1-5) and heating (1r-5r) curves.

System 1

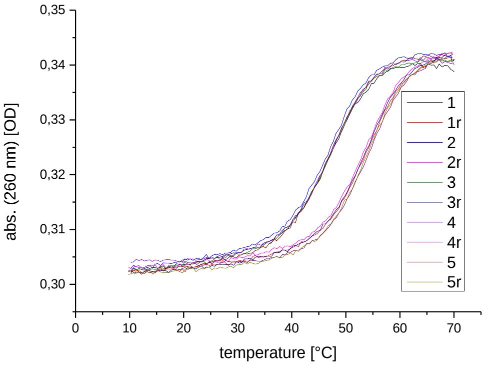

Fig. 149 Melting curves of system 1 wild type (strand 13+16).

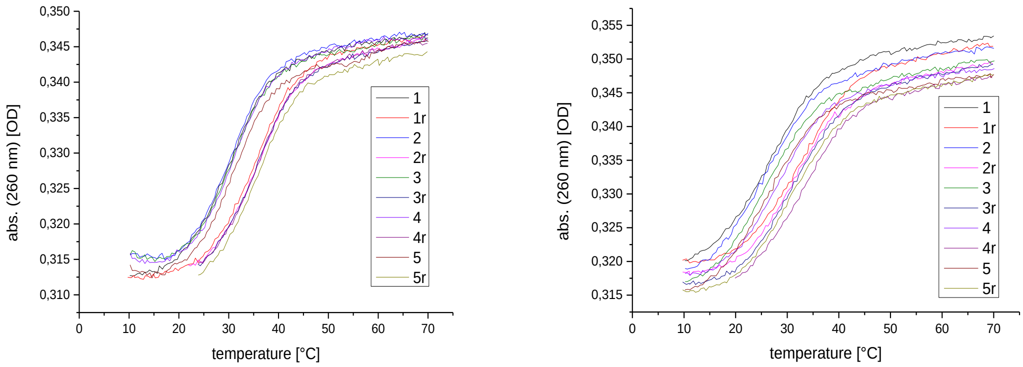

Fig. 150 Melting curves of system 1 mAzo (strand 13+17) in PSS 420 nm (left) and PSS 365 nm (right).

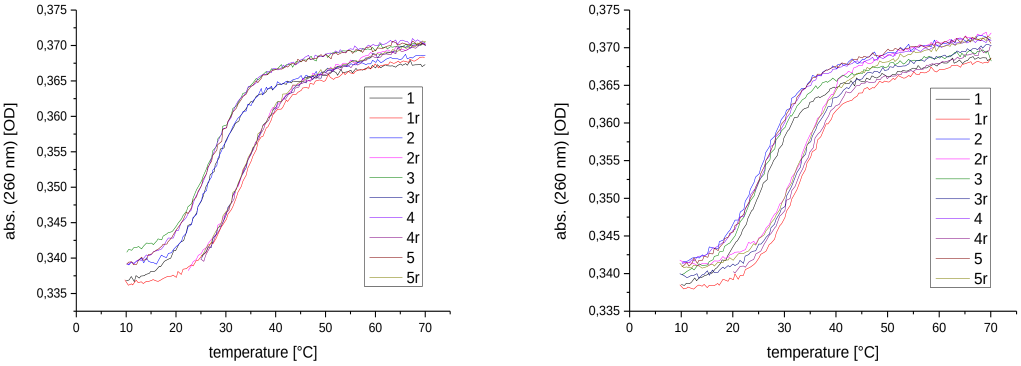

Fig. 151 Melting curves of system 1 LNAzo α (strand 13+18) in PSS 420 nm (left) and PSS 365 nm (right).

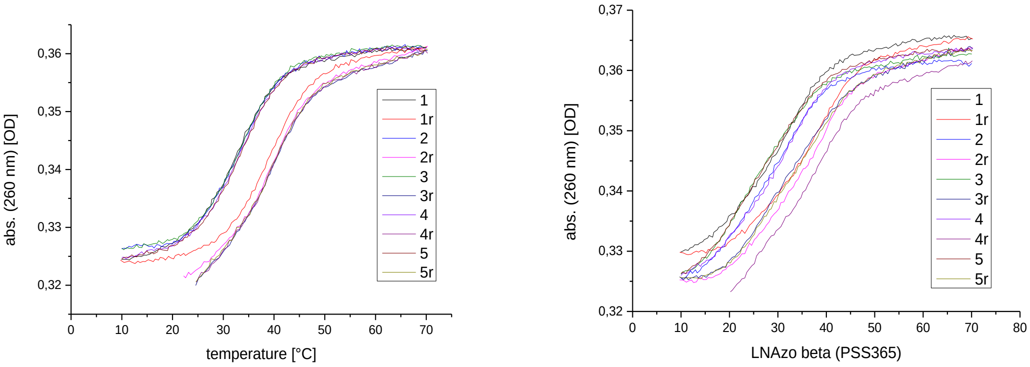

Fig. 152 Melting curves of system 1 LNAzo β (strand 13+18) in PSS 420 nm (left) and PSS 365 nm (right).

System 2

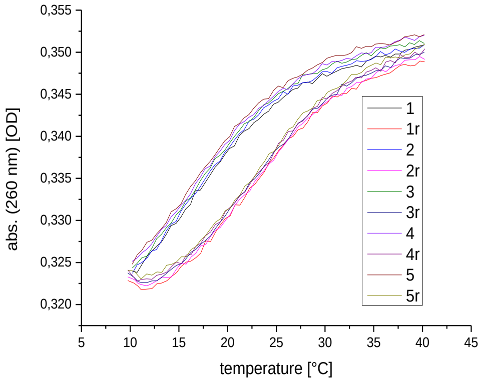

Fig. 153 Melting curves of system 2 wild type (strand14+16).

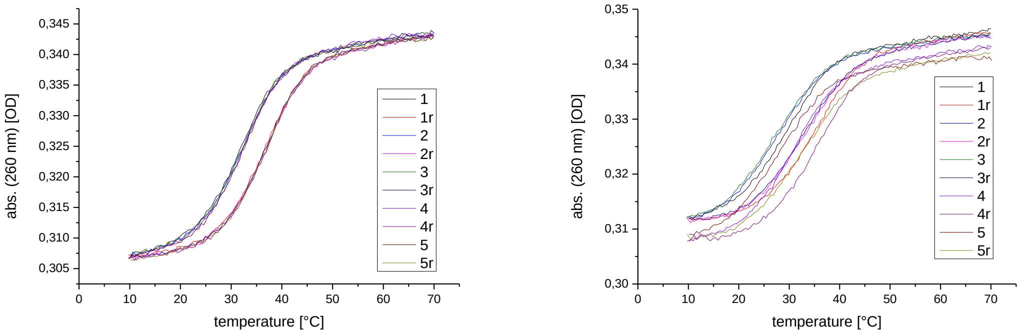

Fig. 154 Melting curves of system 2 mAzo (strand 14+17) in PSS 420 nm (left) and PSS 365 nm (right).

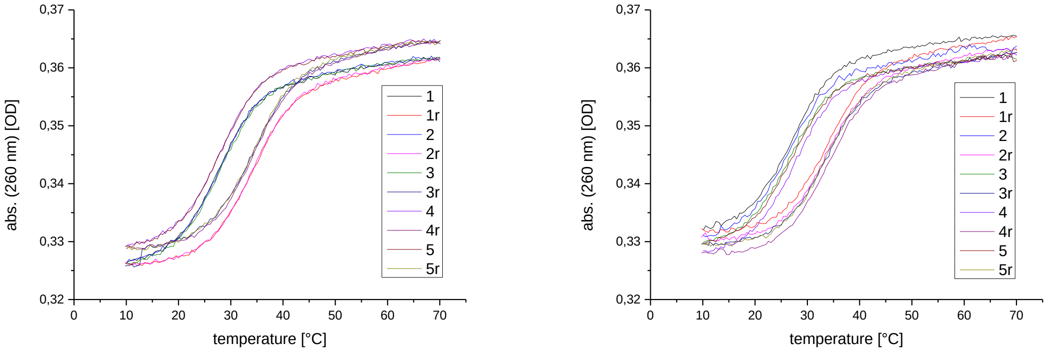

Fig. 155 Melting curves of system 2 LNAzo α (strand 14+18) in PSS 420 nm (left) and PSS 365 nm (right).

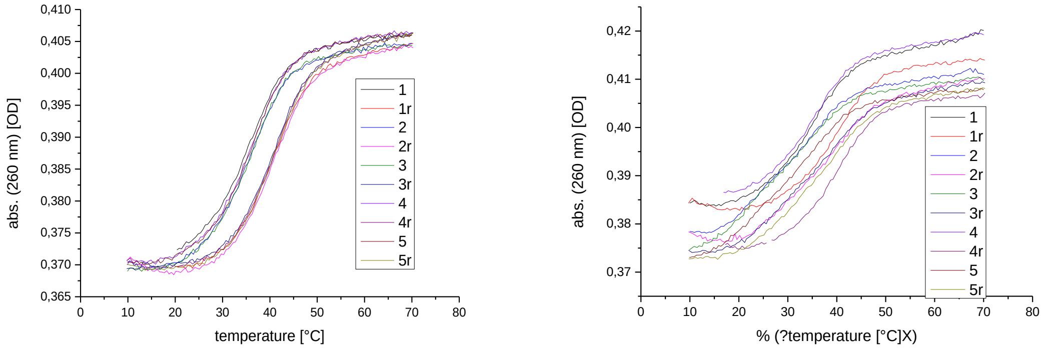

Fig. 156 Melting curves of system 2 LNAzo β (strand 14+18) in PSS 420 nm (left) and PSS 365 nm (right).

System 3

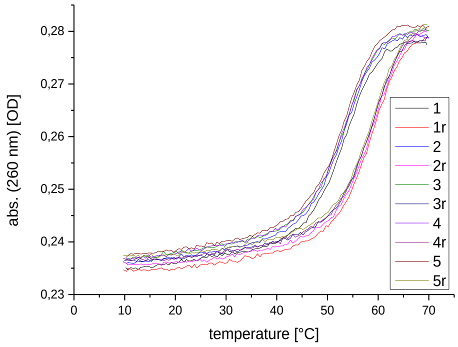

Fig. 157 Melting curves of system 3 wild type (strand15+16).

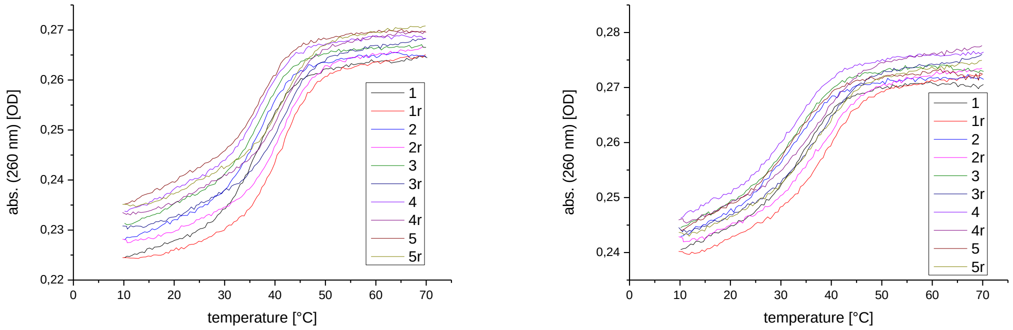

Fig. 158 Melting curves of system 3 mAzo (strand 15+17) in PSS 420 nm (left) and PSS 365 nm (right).

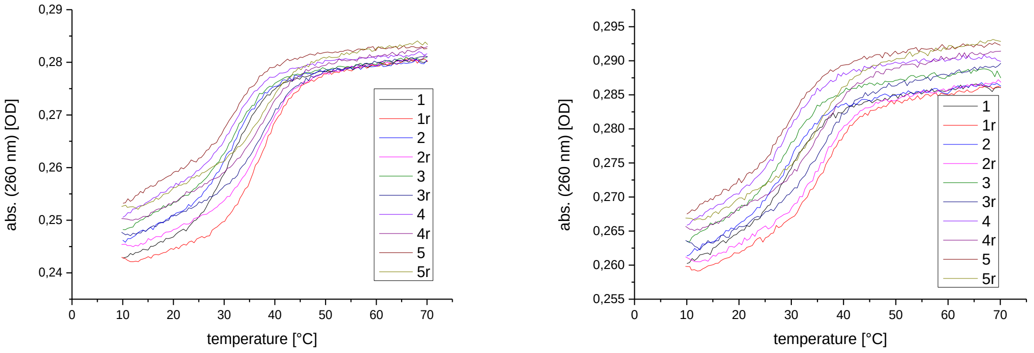

Fig. 159 Melting curves of system 3 LNAzo α (strand 15+18) in PSS 420 nm (left) and PSS 365 nm (right).

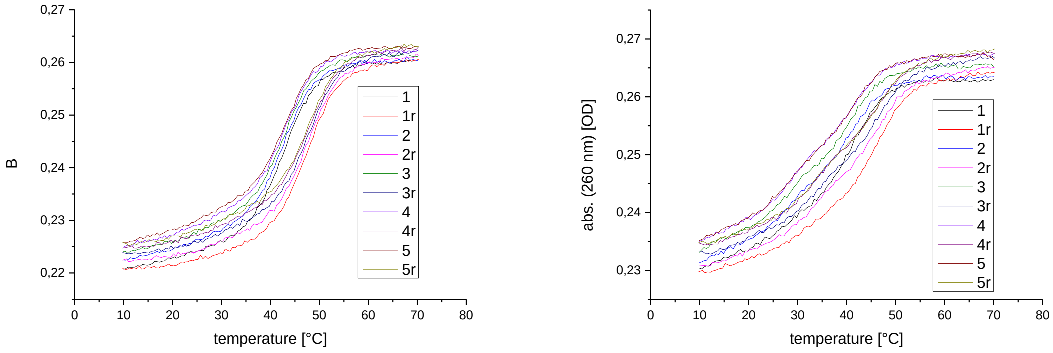

Fig. 160 Melting curves of system 3 LNAzo β (strand 15+18) in PSS 420 nm (left) and PSS 365 nm (right).

System 4

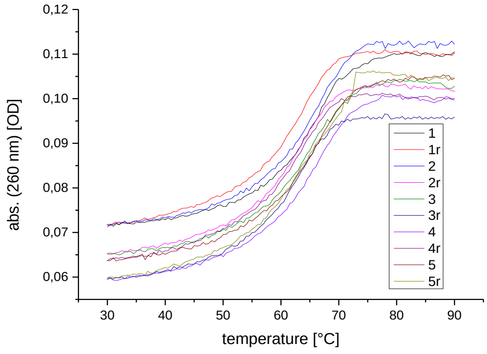

Fig. 161 Melting curves of system 4 wild type (strand15+20).

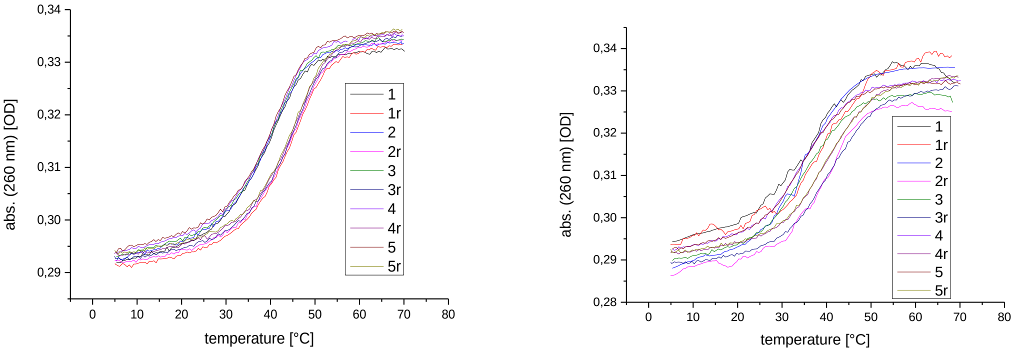

Fig. 162 Melting curves of system 4 mAzo (strand 15+21) in PSS 420 nm (left) and PSS 365 nm (right).

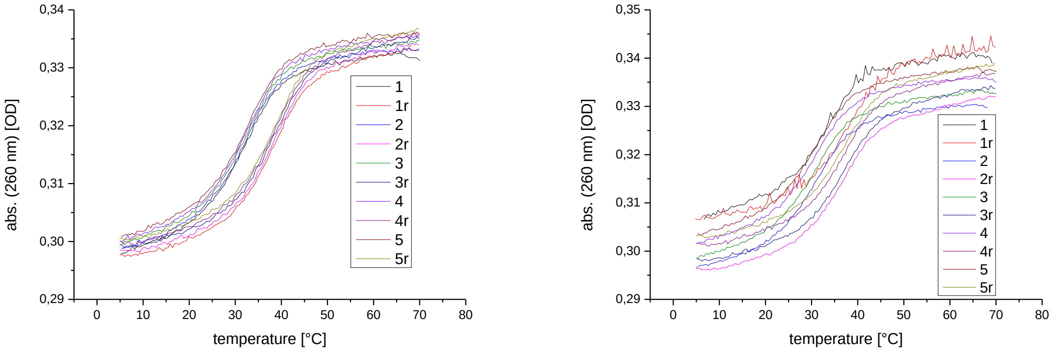

Fig. 163 Melting curves of system 4 LNAzo α (strand 15+22) in PSS 420 nm (left) and PSS 365 nm (right).

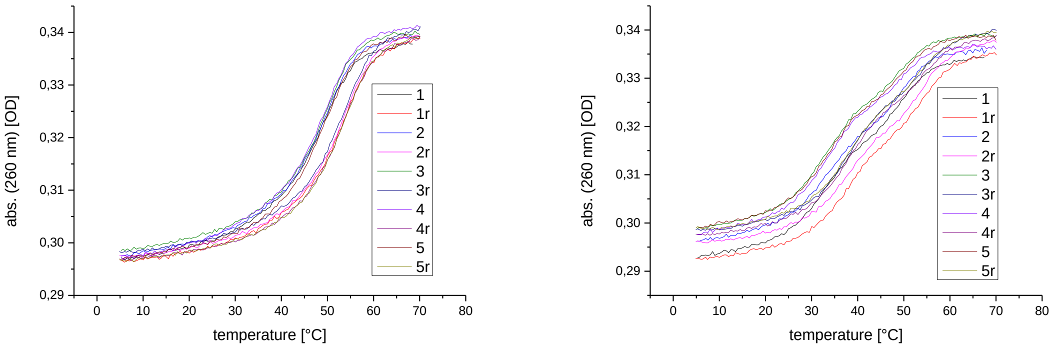

Fig. 164 Melting curves of system 4 LNAzo β (strand 15+23) in PSS 420 nm (left) and PSS 365 nm (right).

5.6.3 Melting curves of the 2-phenyldiazenyl purine project

For melting point measurements 1 mL samples were prepared with 1µM of strand and counterstrand in 1x PBS-buffer for each modification (5 in total). The absorbance changes at 260 nm were measured by a V-650 UV/vis-spectrometer from JASCO. Samples were irradiated as single strands at 70 °C with either 365 nm or 455 nm until photostationary state (PSS) was reached to prevent mismatches. Temperature gradient was 1 °C per minute. To avoid effects of hysteresis, melting points were calculated by sigmoidal fit from cooling and heating measurements. At least five independent heating and cooling measurements were performed for precise results. For experimental values with error bars see chapter 4.2.3. The most important melting curves of duplexes are shown below (Fig. 165-168), each containing five cooling (1-5) and heating (1r-5r) curves.

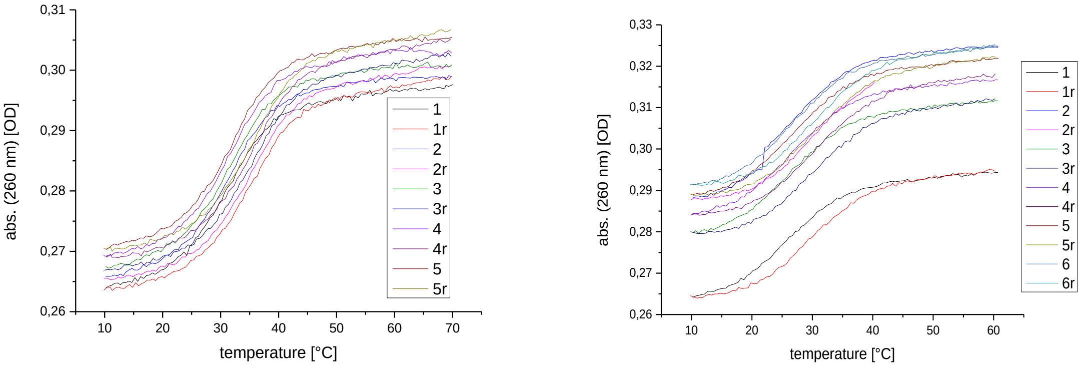

Fig. 165 Melting curves of mAzo-modified strands (strand 13+17) in PSS 455 nm (left) and PSS 365 nm (right).

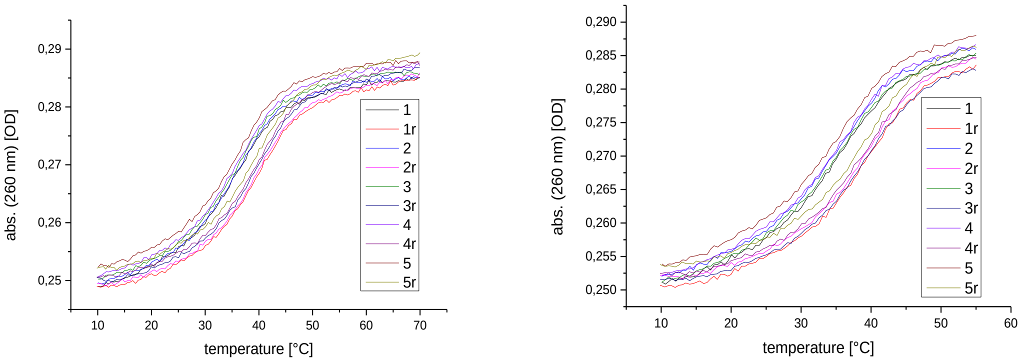

Fig. 166 Melting curves of dG_{Azo}-modified strands (strand 13+30) in PSS 455 nm (left) and PSS 365 nm (right).

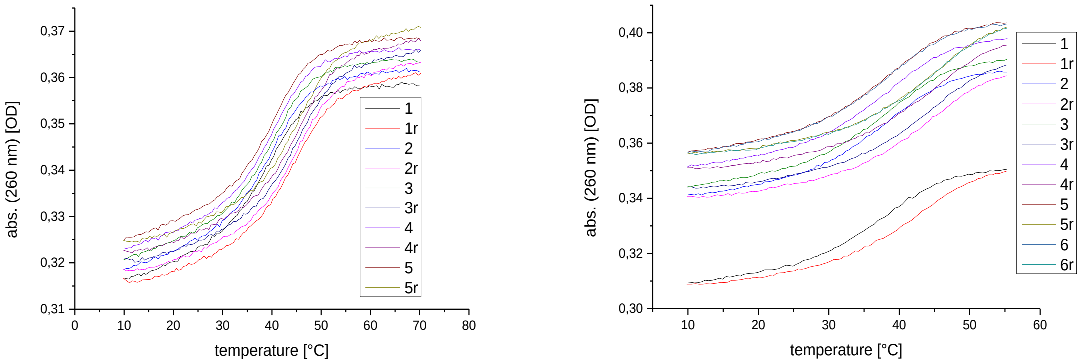

Fig. 167 Melting curves of dA$_{Azo}$-modified strands (strand 31+16) in PSS 455 nm (left) and PSS 365 nm (right).

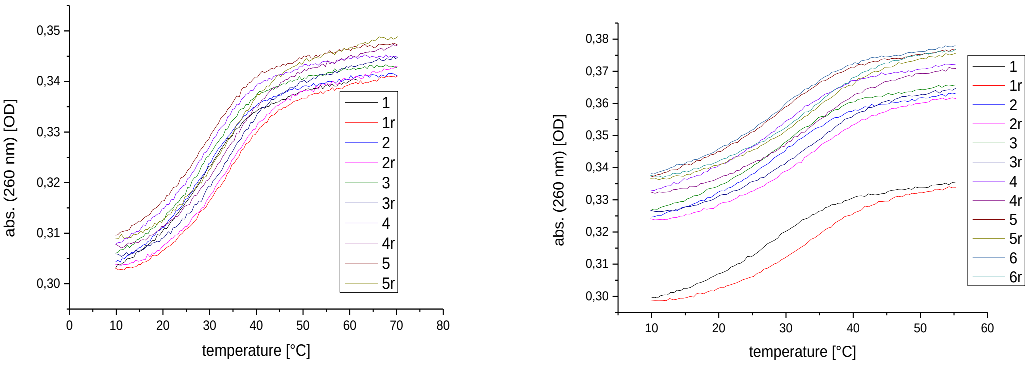

Fig. 168 Melting curves of dG$_{Azo}$+dA$_{Azo}$-modified strands (strand 31+30) in PSS 455 nm (left) and PSS 365 nm (right).

5.7 Fluorescence-based melting point studies

Temperature-dependent fluorescence measurements were recorded in a *PikoReal* real-time PCR system from *Thermo Scientific.* Triplicates were irradiated at 80 °C until photostationary state was reached, then temperature dependent fluorescence was measured from 80 °C to 5 °C within one hour. Values given are averaged over these three individual samples. Measured spectra were normalized with the spectra of free fluorescein in PBS buffer of the corresponding concentration to level out temperature-dependence of fluorescein fluorescence followed by sigmoidal fit with Origin. The inflection points of resulting fits are given as melting points. Melting points are given as column graphs in Figure S20-34, corresponding melting points in [°C] above the graphs, concentrations in [µM] below the graphs starting on the following page. The corresponding wild type was included as a negative control, as irradiation at different wavelength should not alter melting points. In some cases sigmoidal fit to curves with abnormal course could not be executed, indicated by missing columns. In the case of In the case of dG_{Azo} + dA_{Azo} combined, no reasonable values could be gained out of fluorescence spectra.

LNAzo-project System 1

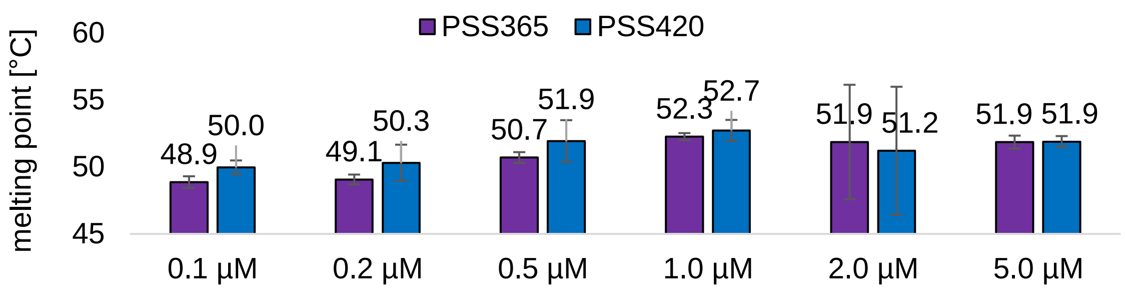

Fig. 139 Bar graph of fluorescence-based melting points of system 1 wild type.

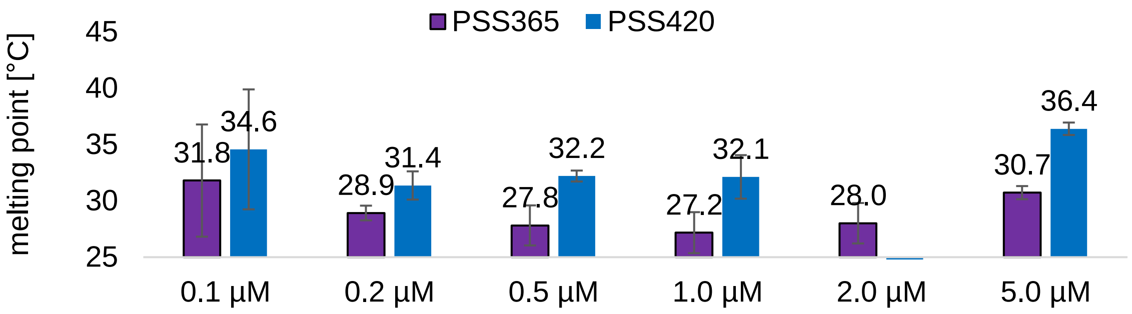

Fig. 140 Bar graph of fluorescence-based melting points of system 1 mAzo.

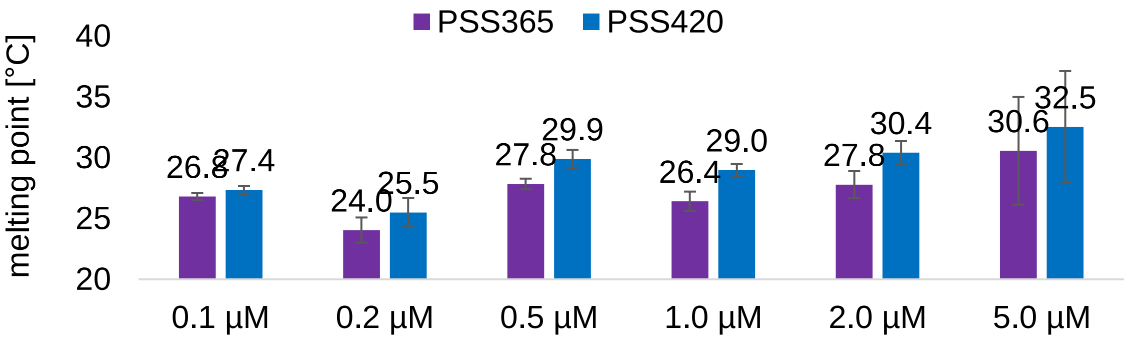

Fig. 141 Bar graph of fluorescence-based melting points of system 1 LNAzo α.

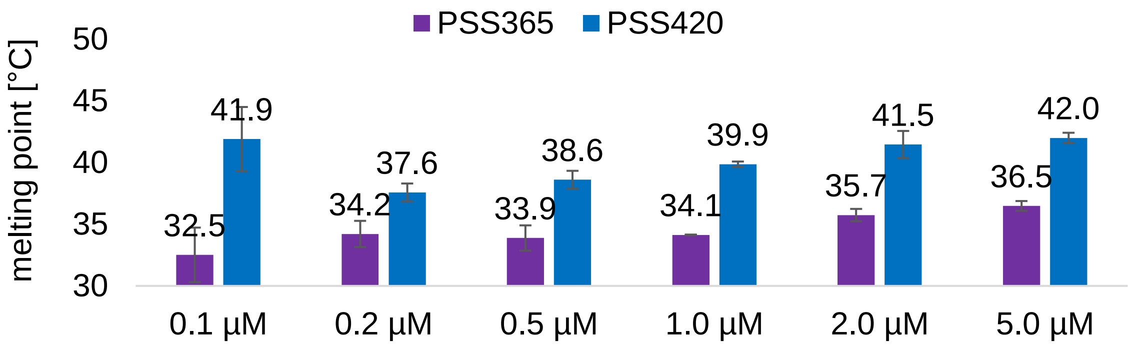

Fig. 142 Bar graph of fluorescence-based melting points of system 1 LNAzo β.

LNAzo project System 2

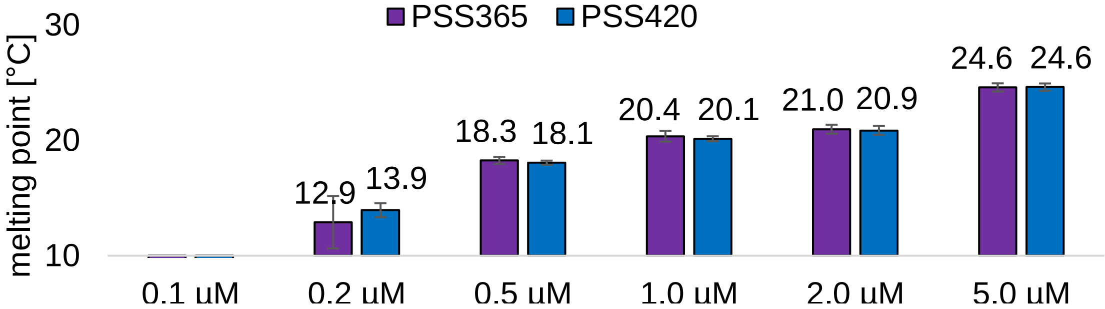

Fig. 125 Bar graph of fluorescence-based melting points of system 2 wild type.

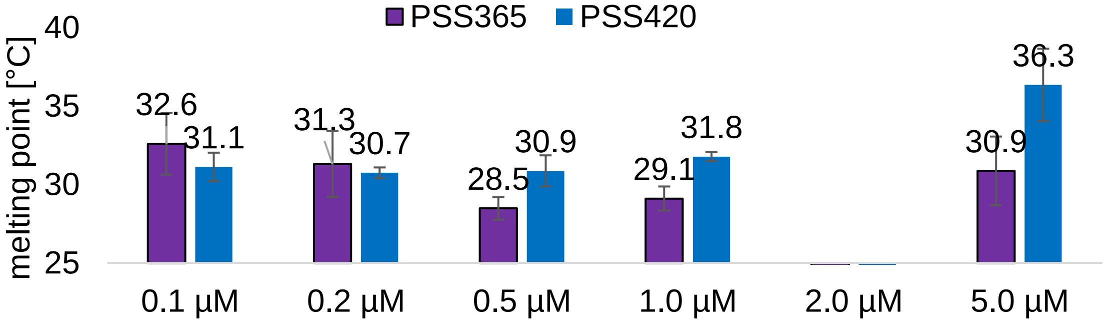

Fig. 126 Bar graph of fluorescence-based melting points of system 2 mAzo.

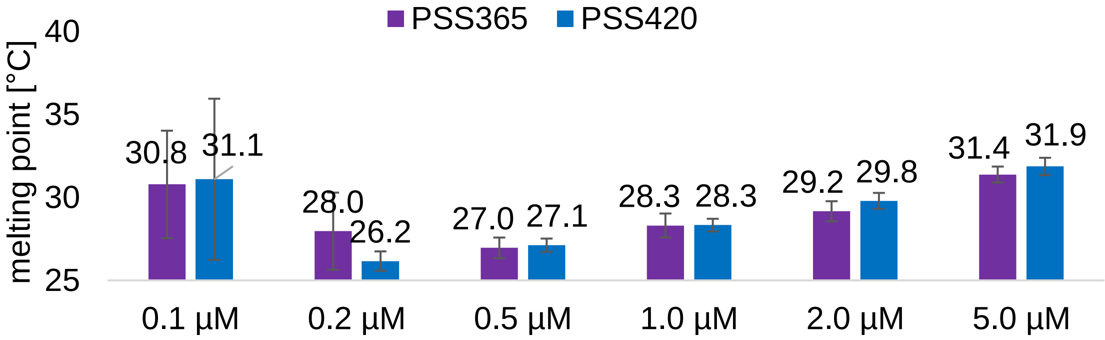

Fig. 127 Bar graph of fluorescence-based melting points of system 2 LNAzo α.

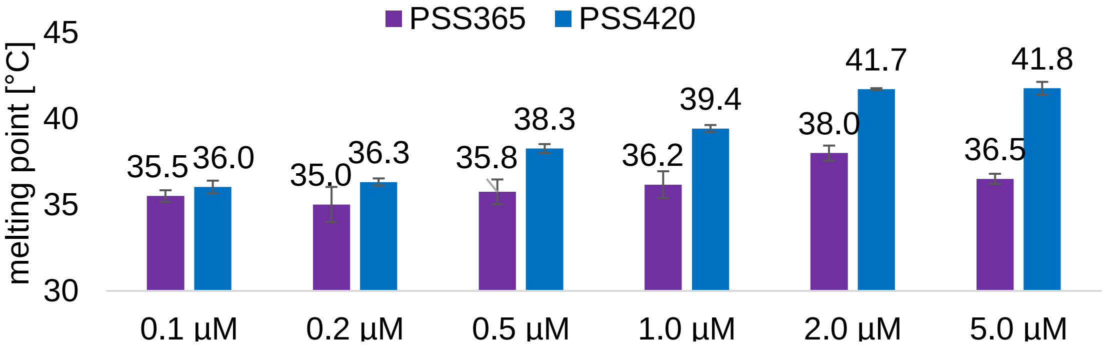

Fig. 128 Bar graph of fluorescence-based melting points of system 2 LNAzo β.

LNAzo project System 3

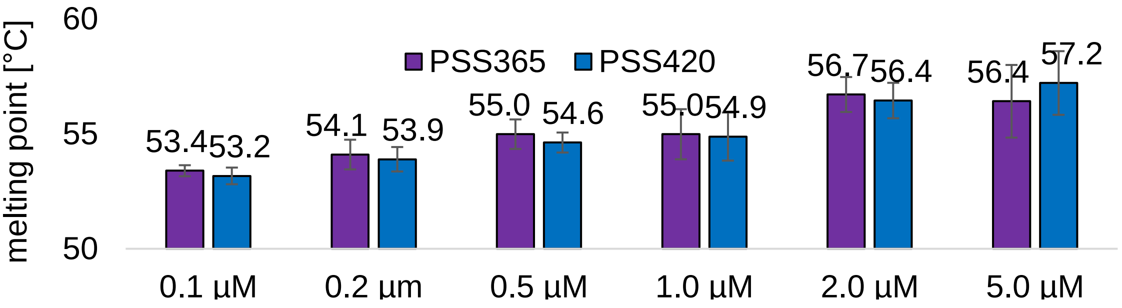

Fig. 129 Bar graph of fluorescence-based melting points of system 3 wild type.

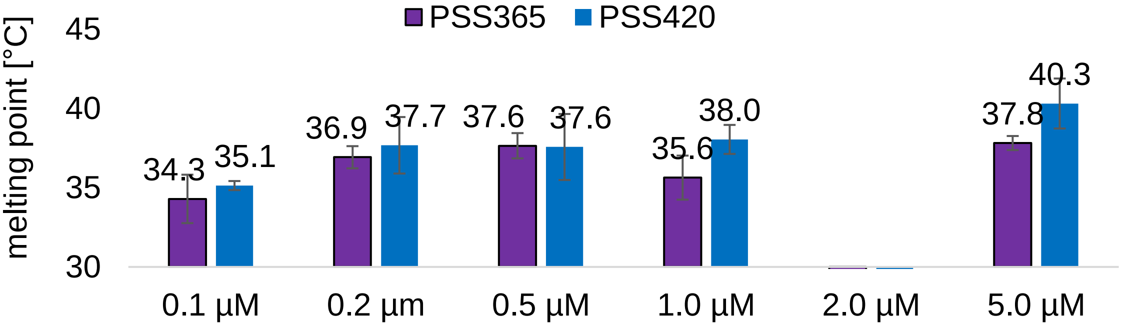

Fig. 130 Bar graph of fluorescence-based melting points of system 3 mAzo.

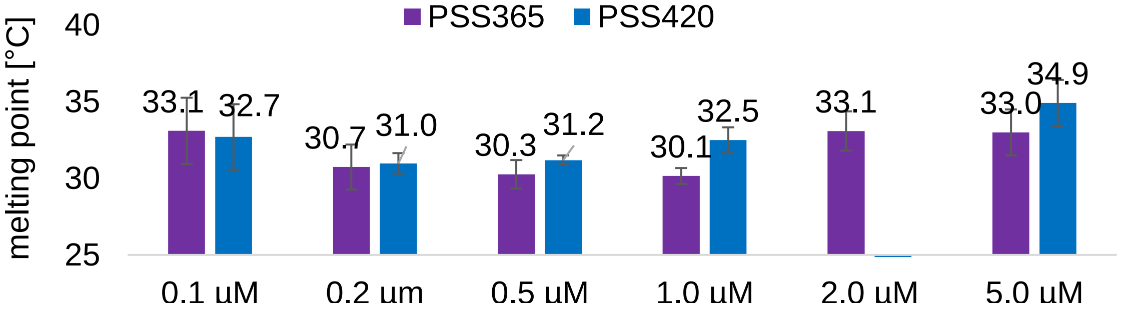

Fig. 131 Bar graph of fluorescence-based melting points of system 3 LNAzo α.

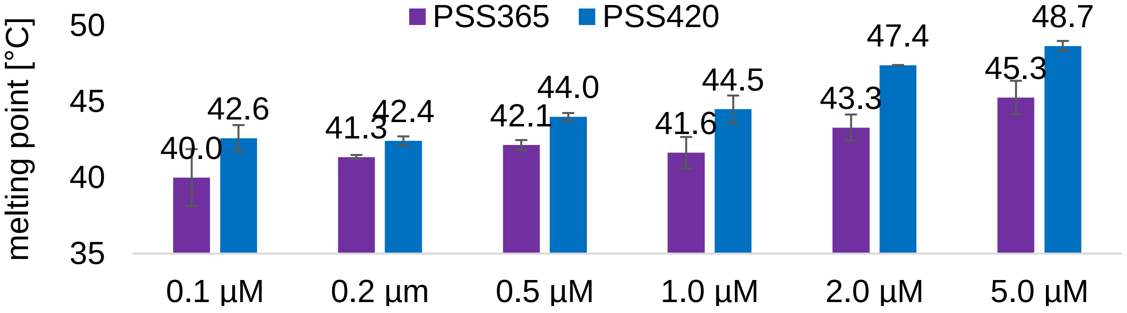

Fig. 132 Bar graph of fluorescence-based melting points of system 3 LNAzo β.

LNAzo project System 4

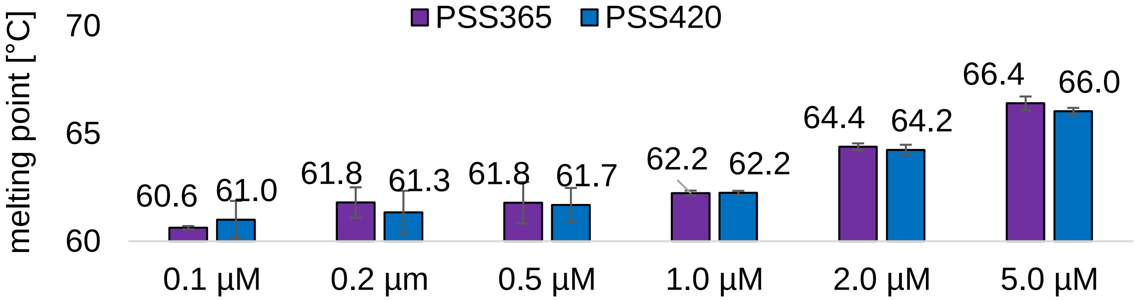

Fig. 133 Bar graph of fluorescence-based melting points of system 4 wild type.

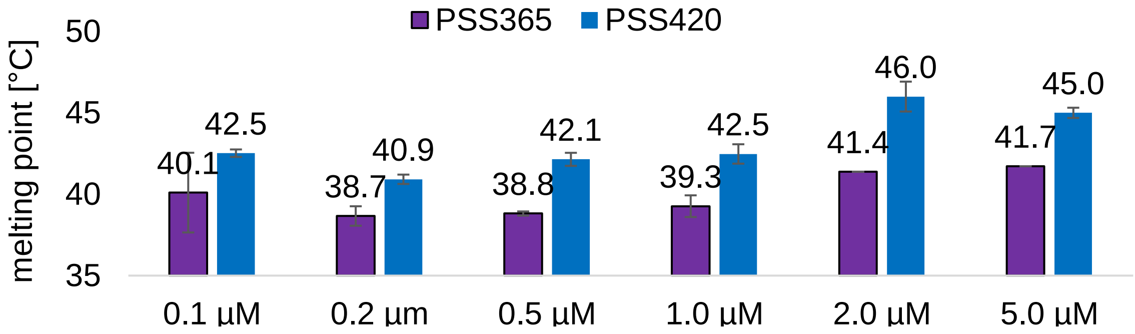

Fig. 134 Bar graph of fluorescence-based melting points of system 4 mAzo.

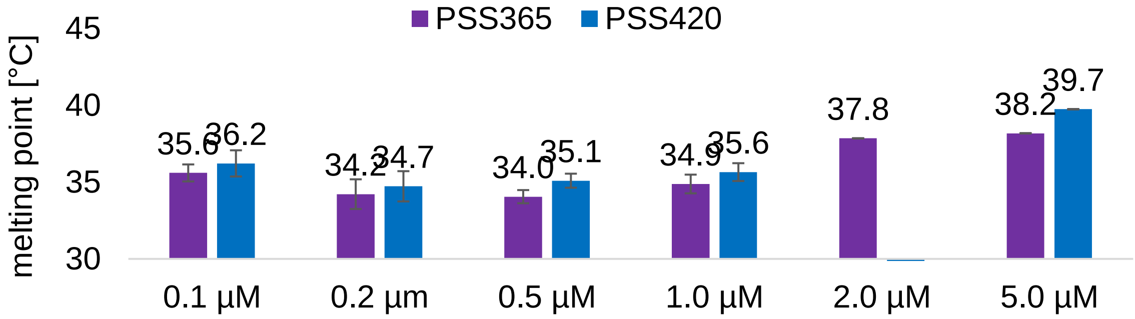

Fig. 135 Bar graph of fluorescence-based melting points of system 4 LNAzo α.

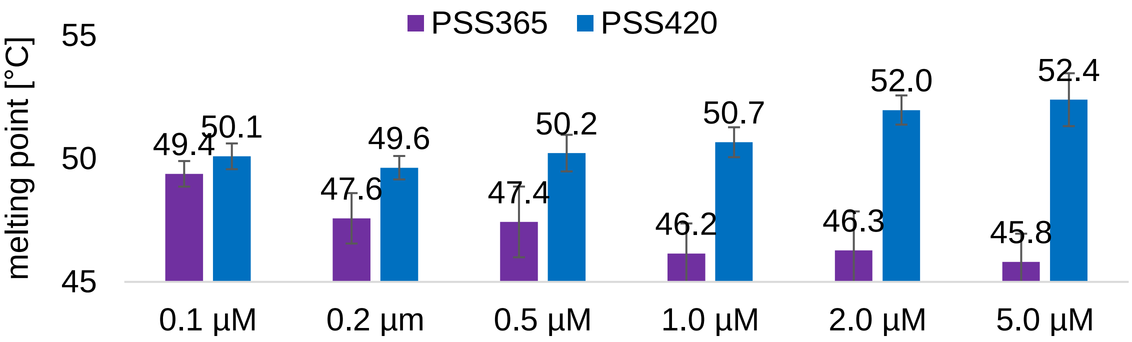

Fig. 136 Bar graph of fluorescence-based melting points of system 4 LNAzo β.

2-Phenyldiazenyl purine project

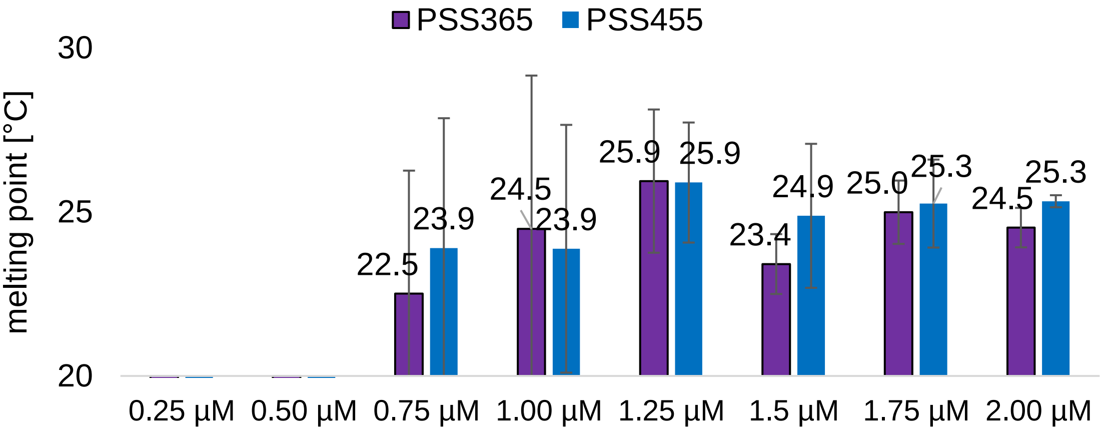

Fig. 137 Bar graph of fluorescence-based melting points of the dG$_{Azo}$-containing duplex.

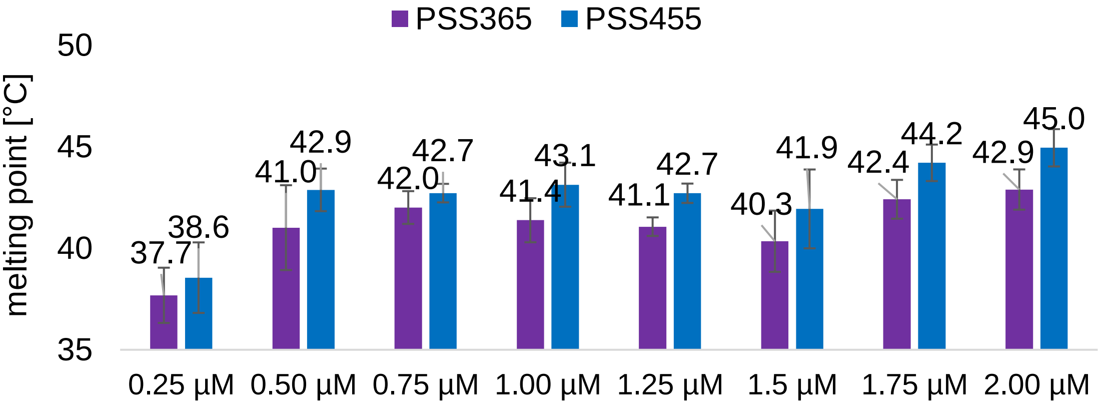

Fig. 138 Bar graph of fluorescence-based melting points of the dA$_{Azo}$-containing duplex.

5.8 Enzymatic synthesis of DNA-minicircles

A mixture of strand 1 (1 nmol, 1.0 eq), strand 2 (1 nmol, 1.0 eq), splint (1.5 nmol, 1.5 eq) and strand 5 (1.5 nmol, 1.5 eq) in 70 µL MilliQ-water was heated to 90 °C for 5 minutes and passively cooled down to room temperature over a time of 60 minutes to anneal the constructs. Upon addition of 7 µL 10x ligase-buffer (provided by *New England Biolabs* (*NEB*)) and 6 µL T4 polynucleotide kinase (10.000 U/mL, *NEB*), mixture was set for 60 minutes at 37 °C to enable 5'-phosphorylation, before adding 9 µL T*4* DNA ligase 2 (400.000 U/mL, *NEB*) and incubated for 120 minutes at 37 °C. After ligation, sample were mixed 1:1 with denaturing loading buffer (see section 5.4) and run in a 5% denaturing polyacrylamide gel electrophoresis. Corresponding bands were visualized by UV-shadowing on TLC-plates and cut out. Cut out gel part were extracted and purified with "*PCR clean-up Gel extraction*"-kit provided by *Macherey-Nagel* according to distributed procedure. Quality of synthesized single stranded DNA-rings was visualized by 5%-denaturing PAGE, yields are usually around 5-35%. For the annealing of double stranded minicircles single stranded DNA-ring (1.0 eq) was mixed with strand 3, 4, 5 (1.1 eq each) and a strand, which is responsible for the ring-dimerization (1.1 eq). The mixture was heated to 90 °C for 5 minutes and passively cooled down to room temperature over a time of 60 minutes to anneal the constructs. Resulting DNA-minicircles were used without further purification for PAGE experiments, for AFM-imaging samples were purified with a molecular weight cut-off spin filter provided by *Sartorius* (*vivaspin 500*, 50 kDa cut-off) according to the distributed procedure.

5.9 AFM-Imaging

A solution of 20 µL of 0.1 mg poly-*L*-ornithine in 1 mL of ultrapure water was applied on freshly cleaved mica and incubated for 3 minutes at ambient temperature. The surface was rinsed with ultrapure water and blown dry with pressurized air. From the stock, DNA-samples were prepared by diluting to a final concentration of 1-100 nM with ultrapure water. To the pretreated mica surface, 10 µL of the freshly prepared samples were added. The DNA was allowed to adsorb to the mica for 3 minutes, then the surface was rinsed with ultrapure water and blown dry with pressurized air. Then AFM images were taken on a *JPK Nanowizard 3* AFM in tapping mode, images were taken in air with ACTA probes (25-75 N/m) from APP Nano (Santa Clara, CA, USA). The free amplitude set point was set to 0.3 V, typical resonance frequencies of the cantilevers were between 200 and 400 kHz. Scanning frequencies were between 0.5 and 2 Hz. Muscovite mica was purchased from Plano GmbH (Germany), poly-*L*-ornithine hydrobromide was purchased from Sigma Aldrich GmbH (Germany).

6. Appendix

6.1 NMR-Spectra

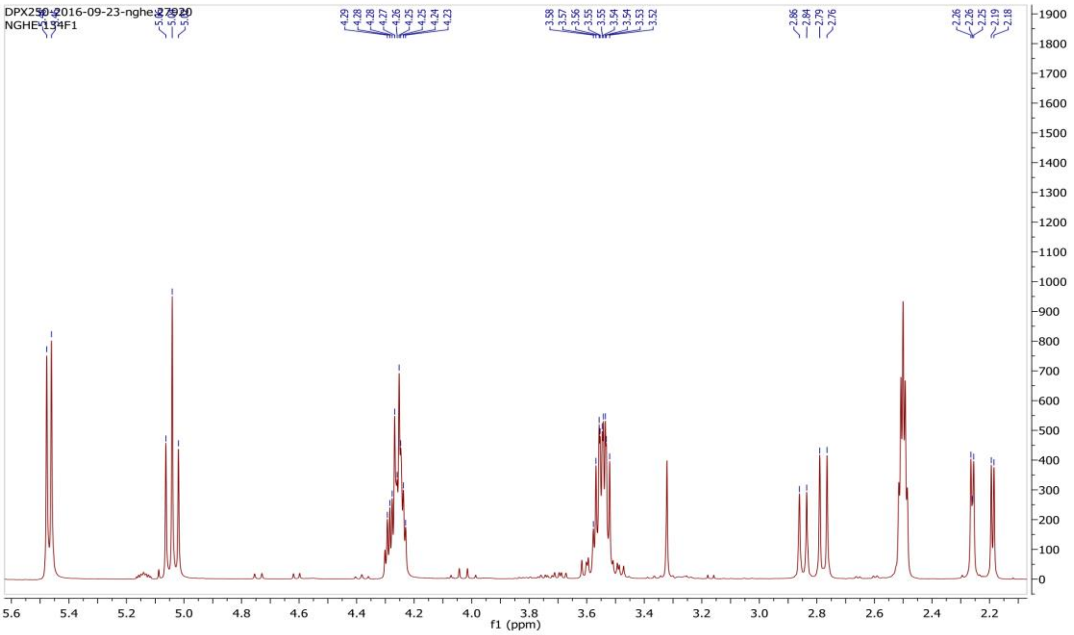

*Fig. 169 ^{1}H spectrum of compound **1**.*

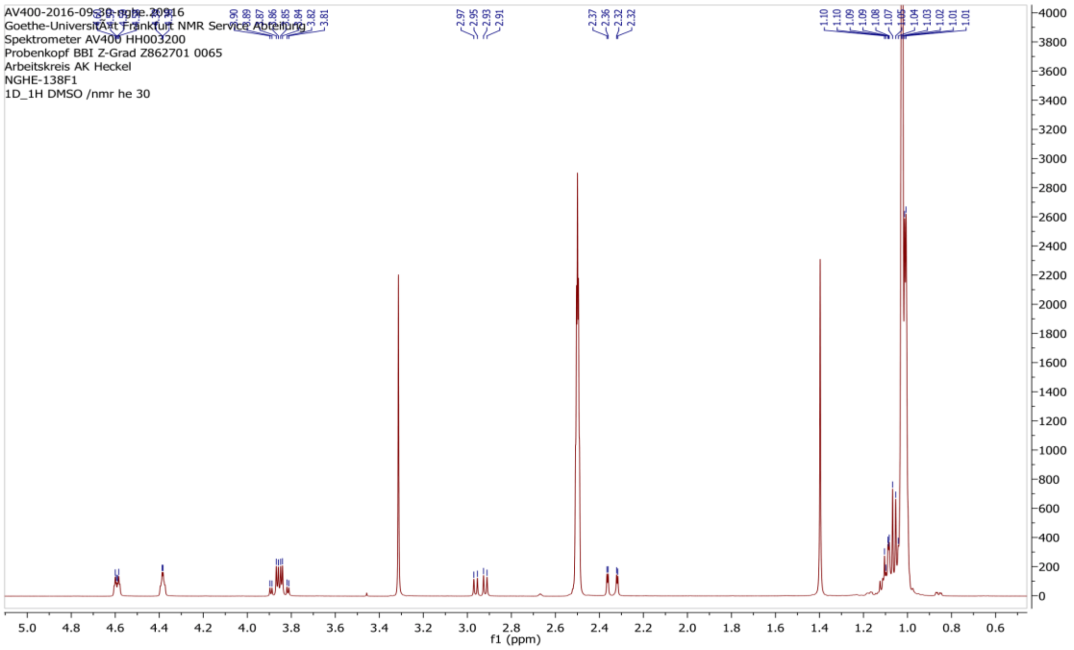

*Fig. 170 ^{1}H spectrum of compound **2**.*

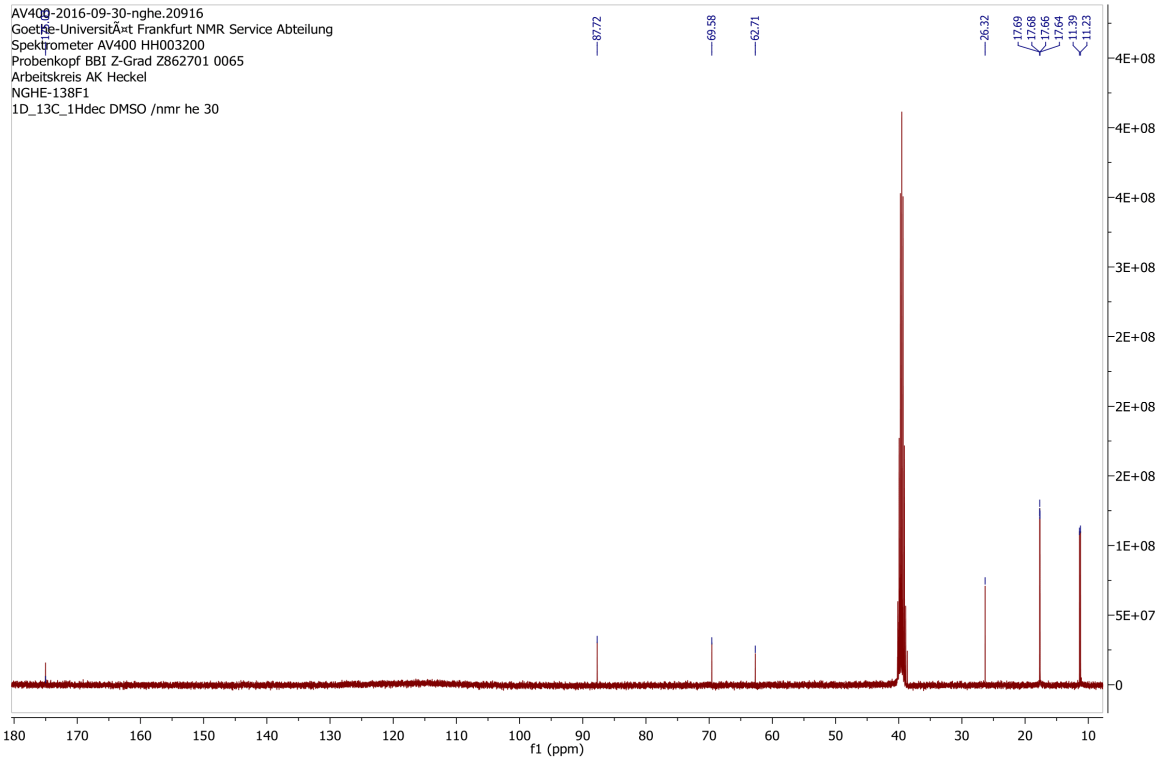

Fig. 171 ^{13}C spectrum of compound **2**.

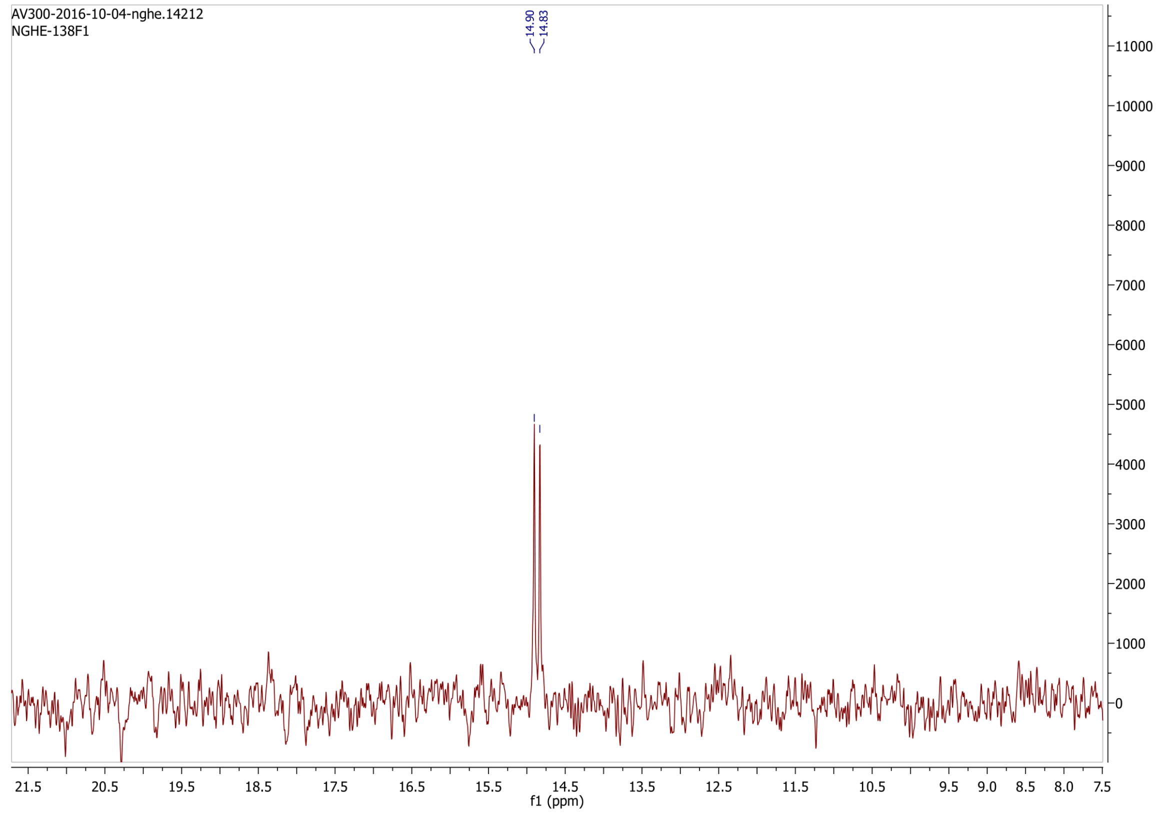

Fig. 172 ^{29}Si spectrum of compound **2**.

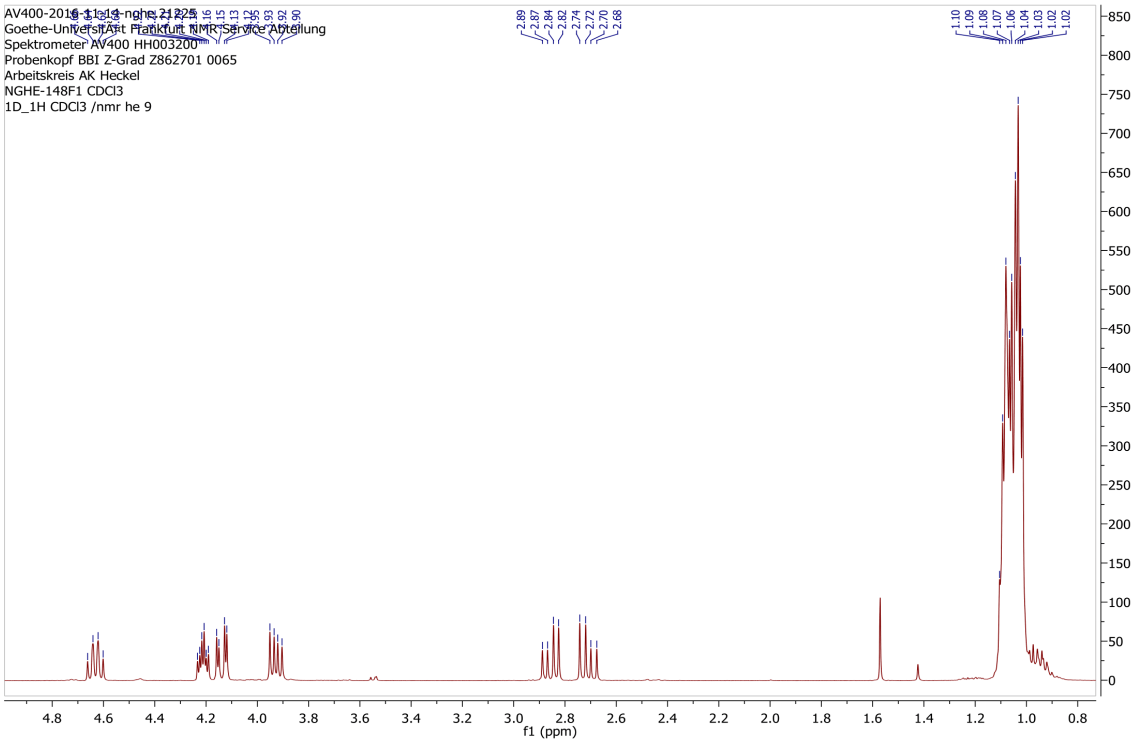

*Fig. 173 ^{1}H spectrum of compound **3**.*

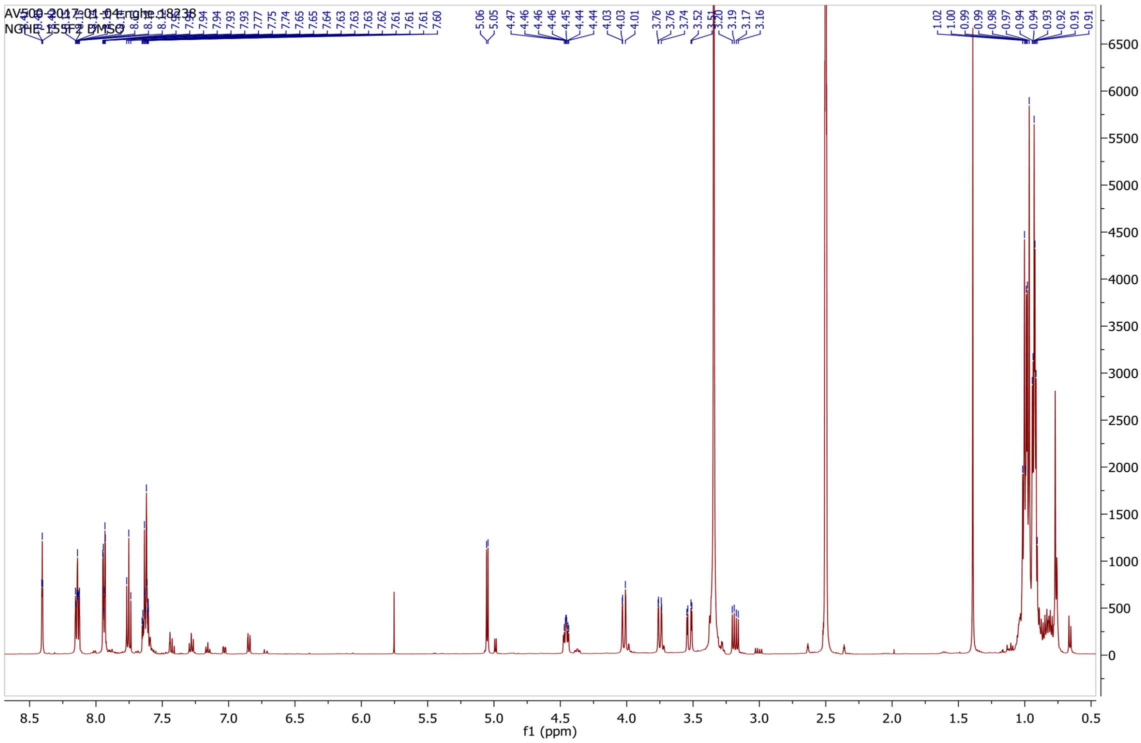

*Fig. 174 ^{1}H spectrum of compound **5**.*

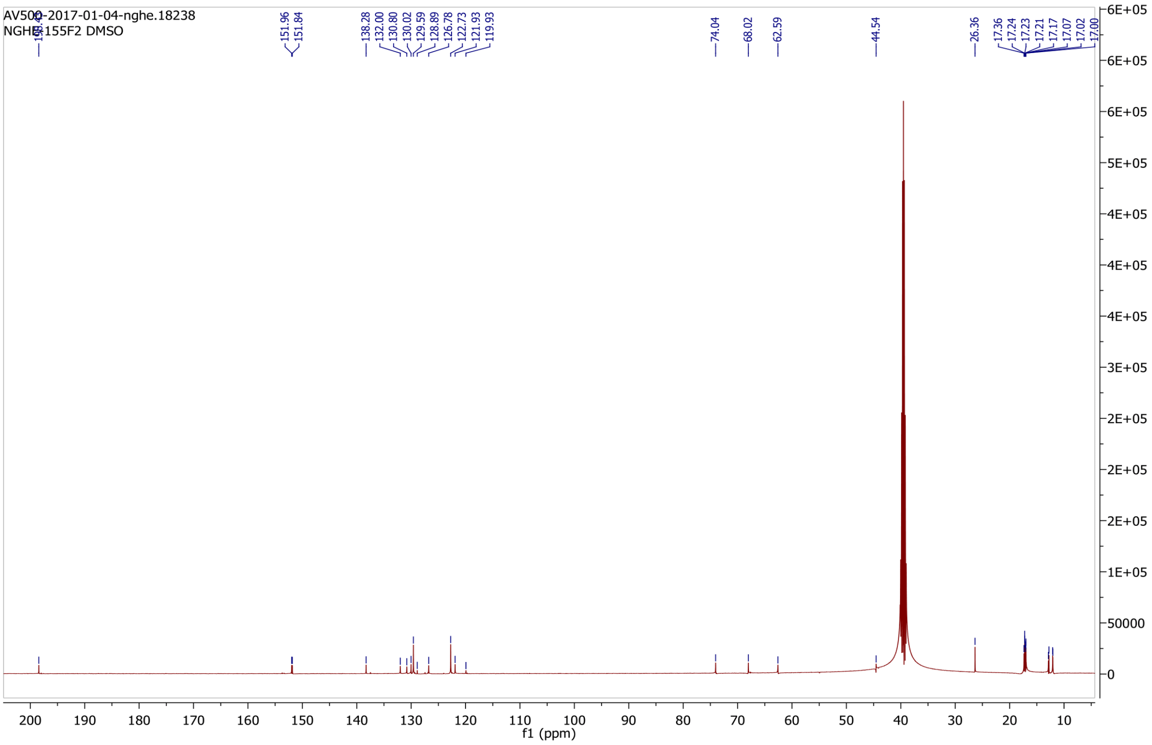

Fig. 175 ^{13}C spectrum of compound ***5****.*

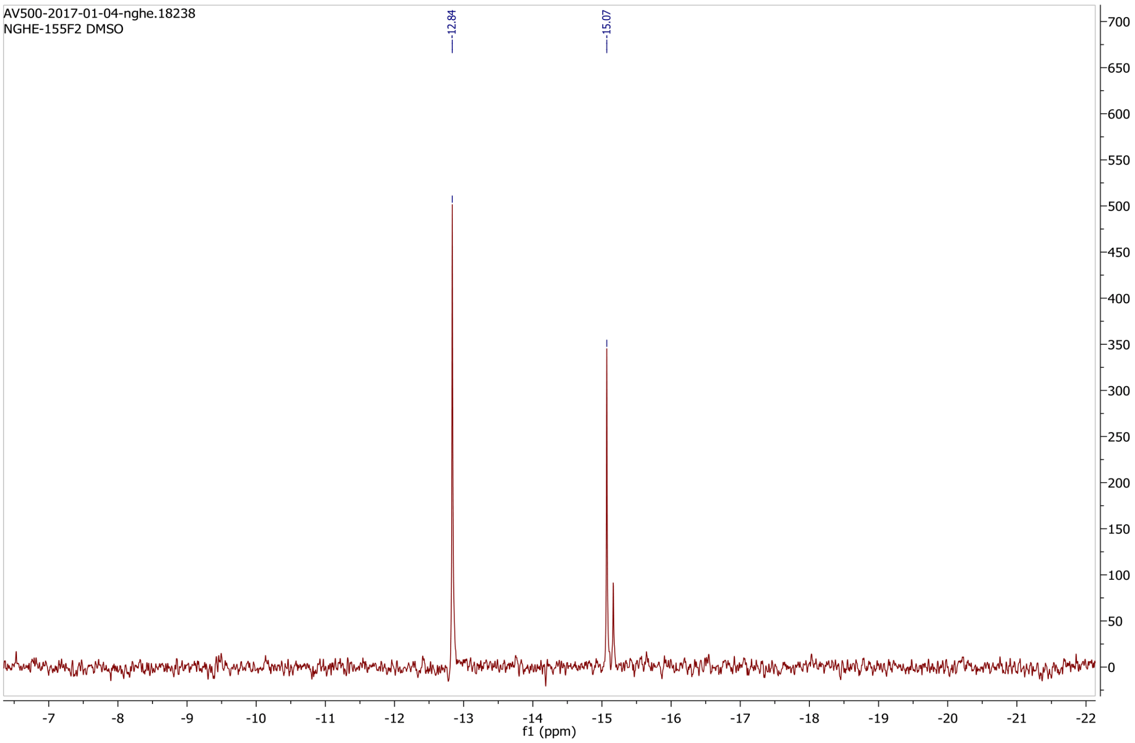

Fig. 176 ^{29}Si spectrum of compound ***5****.*

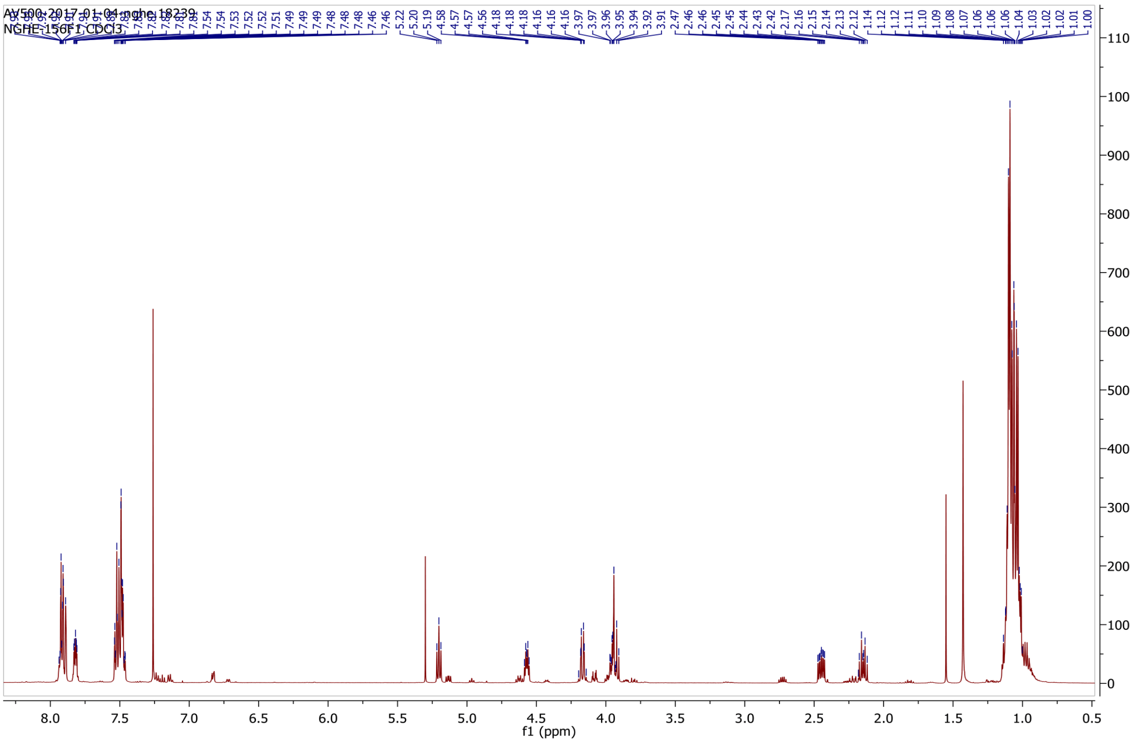

Fig. 177 ^{1}H spectrum of compound **6**.

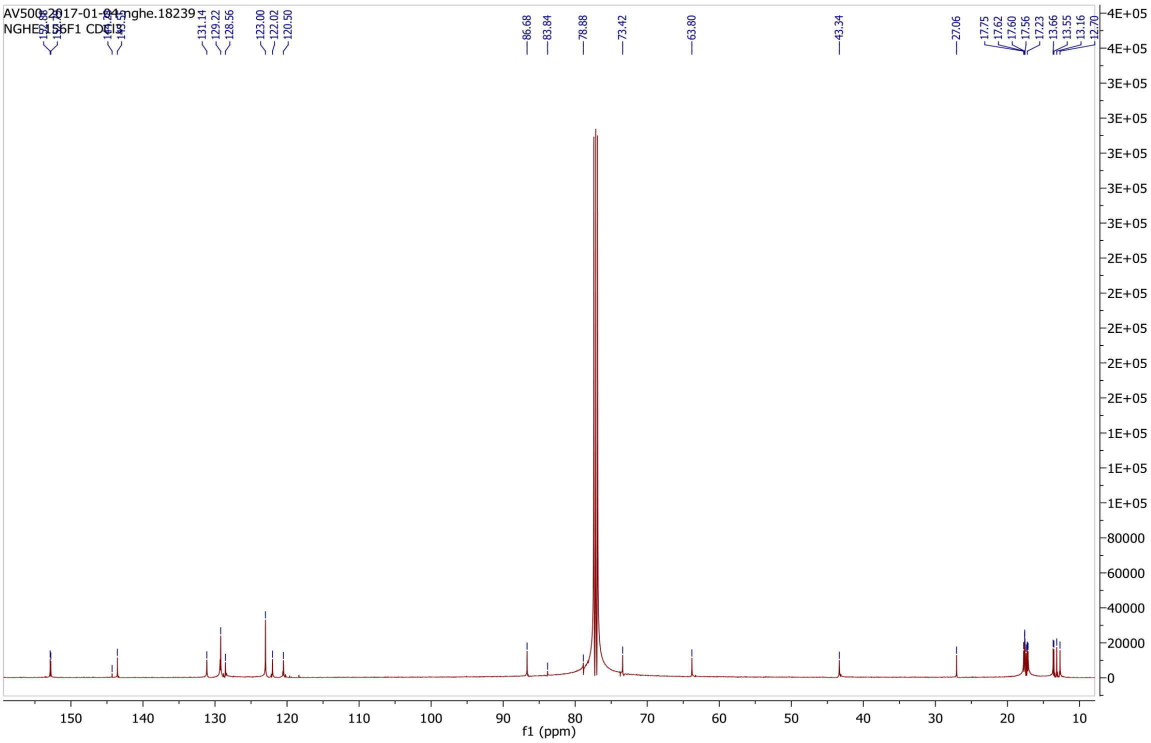

Fig. 178 ^{13}C spectrum of compound **6.**

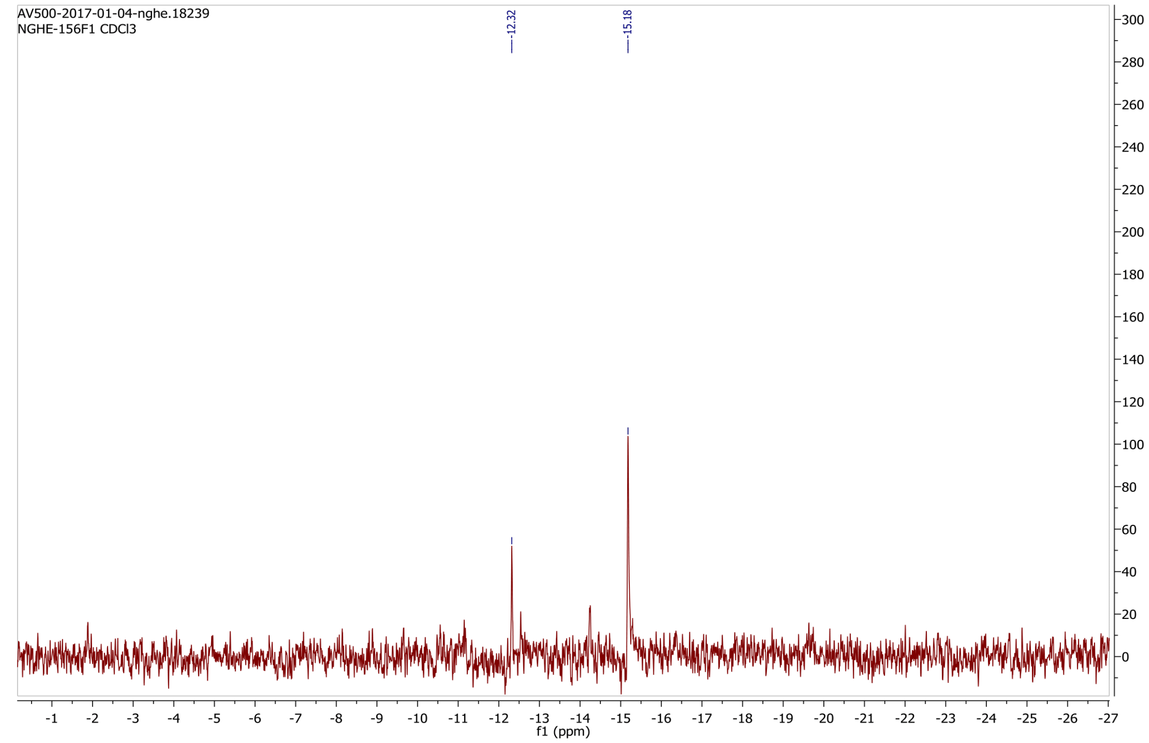

Fig. 179 ^{29}Si spectrum of compound **6**.

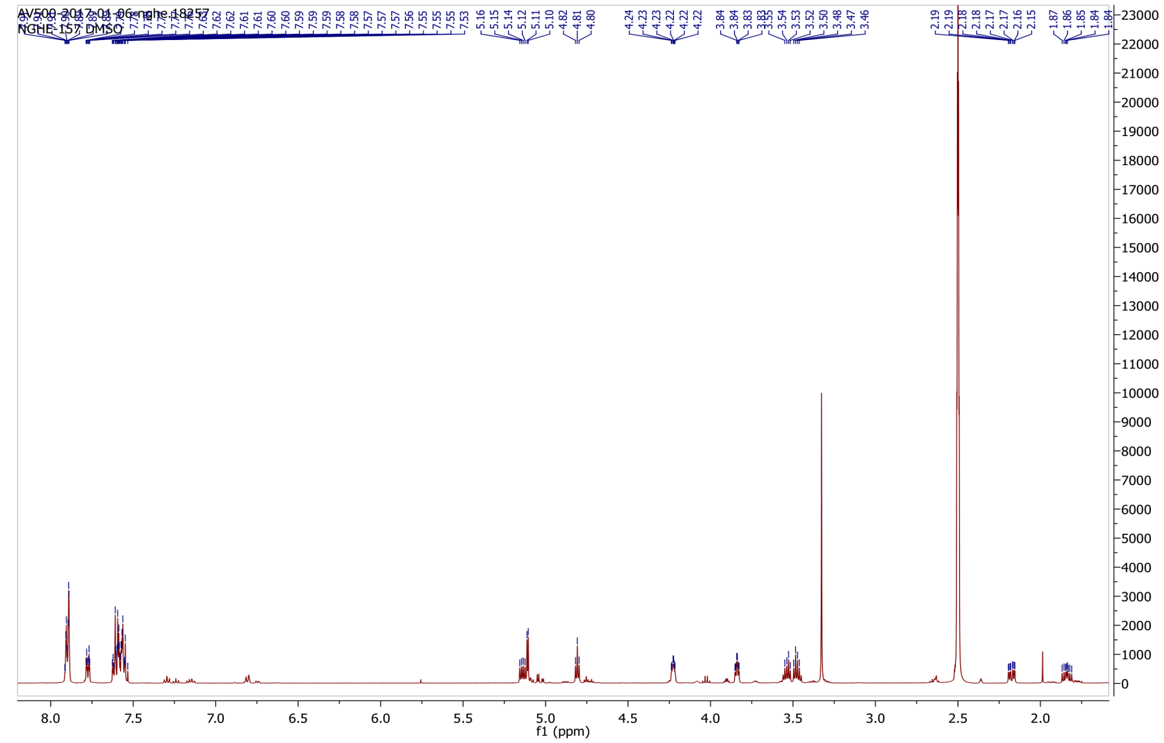

Fig. 180 ^{1}H spectrum of compound **7**.

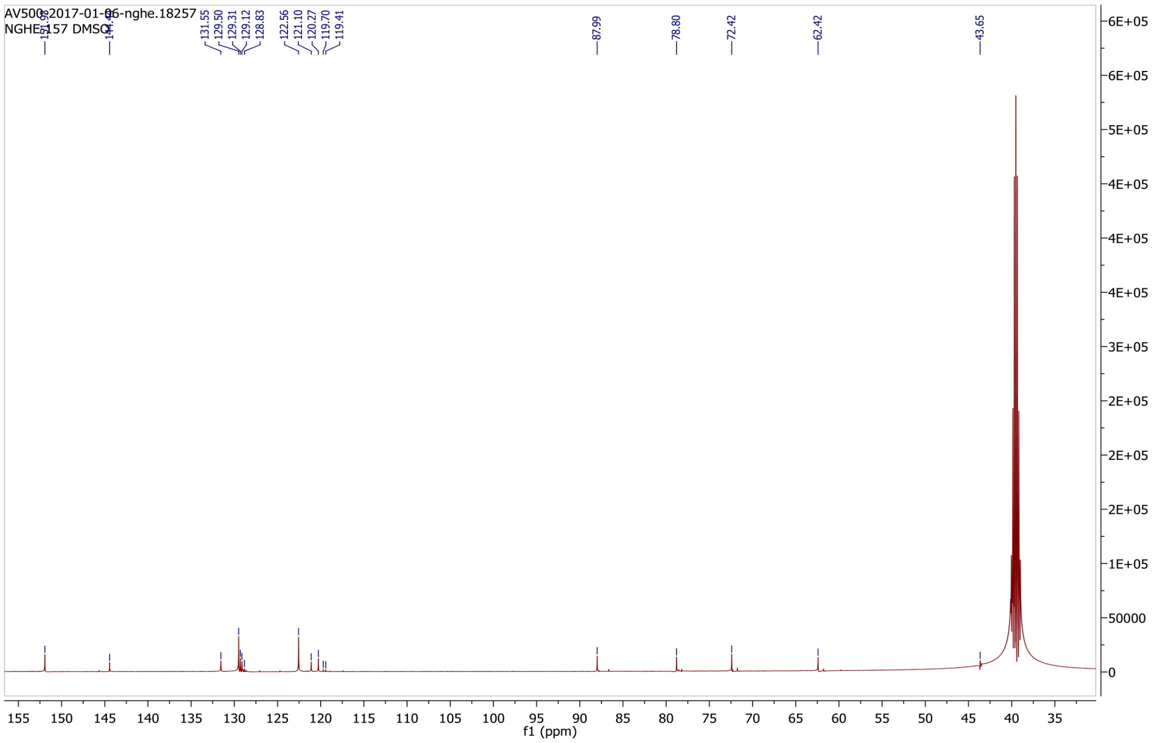

*Fig. 181 ^{13}C spectrum of compound **7**.*

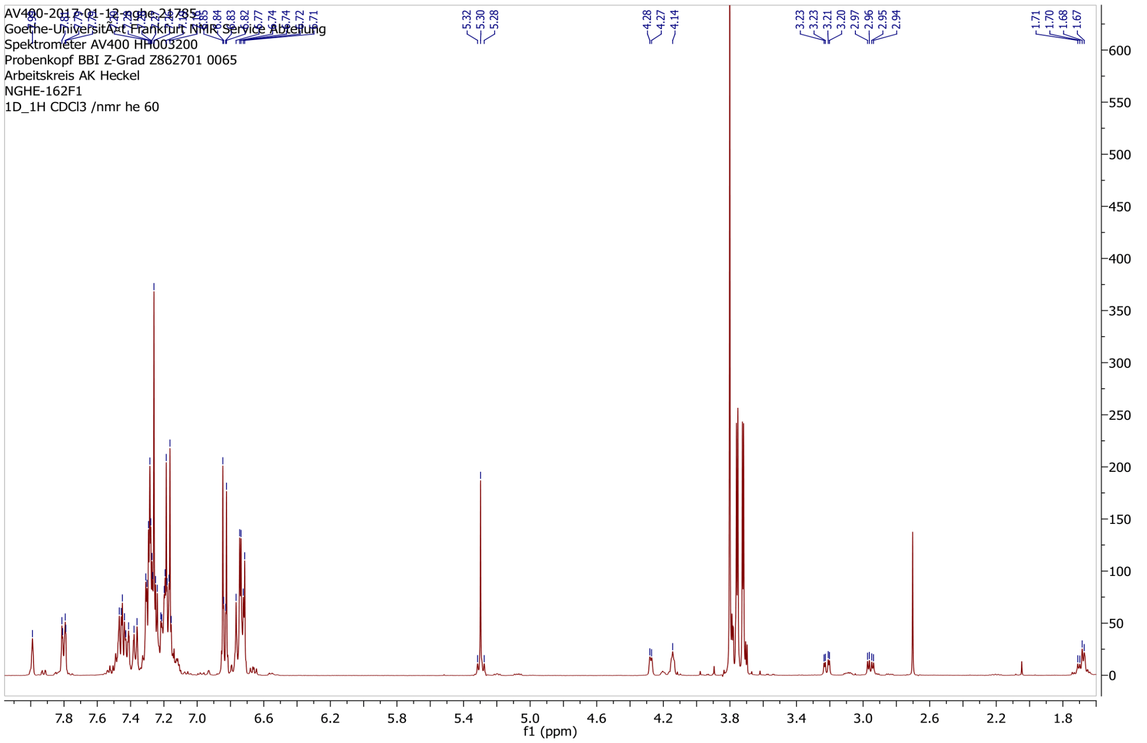

*Fig. 182 ^{1}H spectrum of compound **8**.*

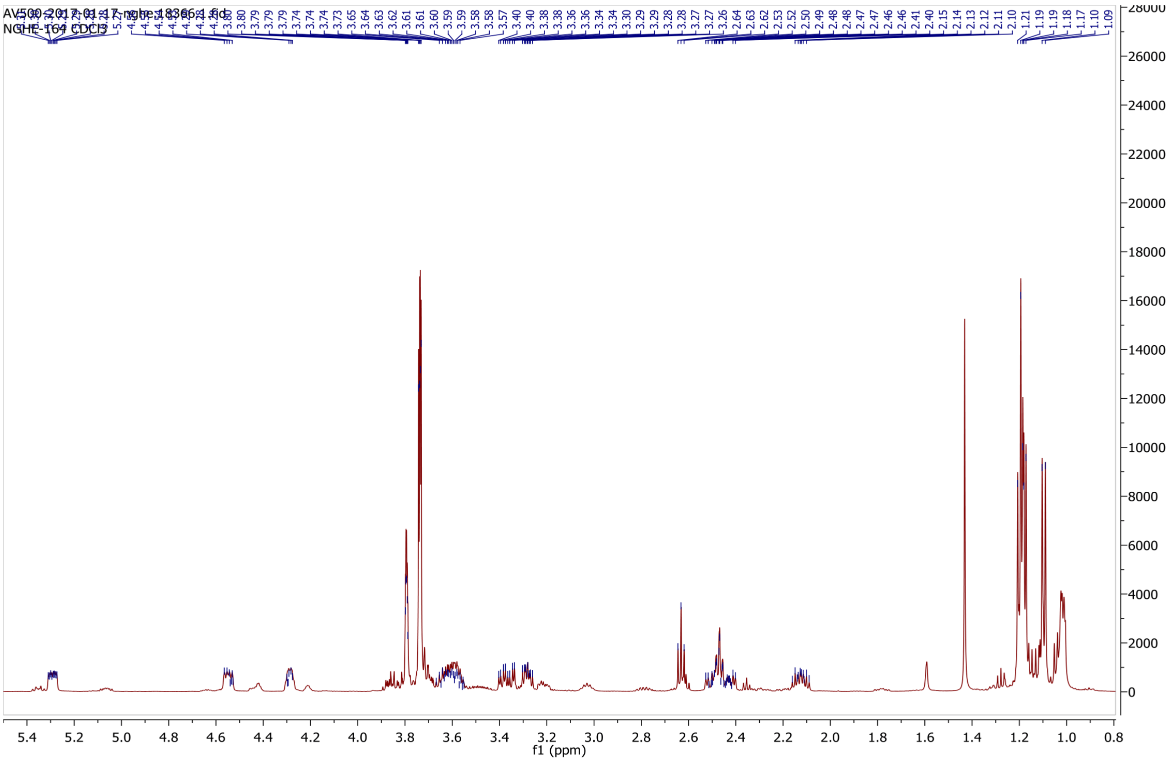

Fig. 183 ^{1}H spectrum of compound **9**.

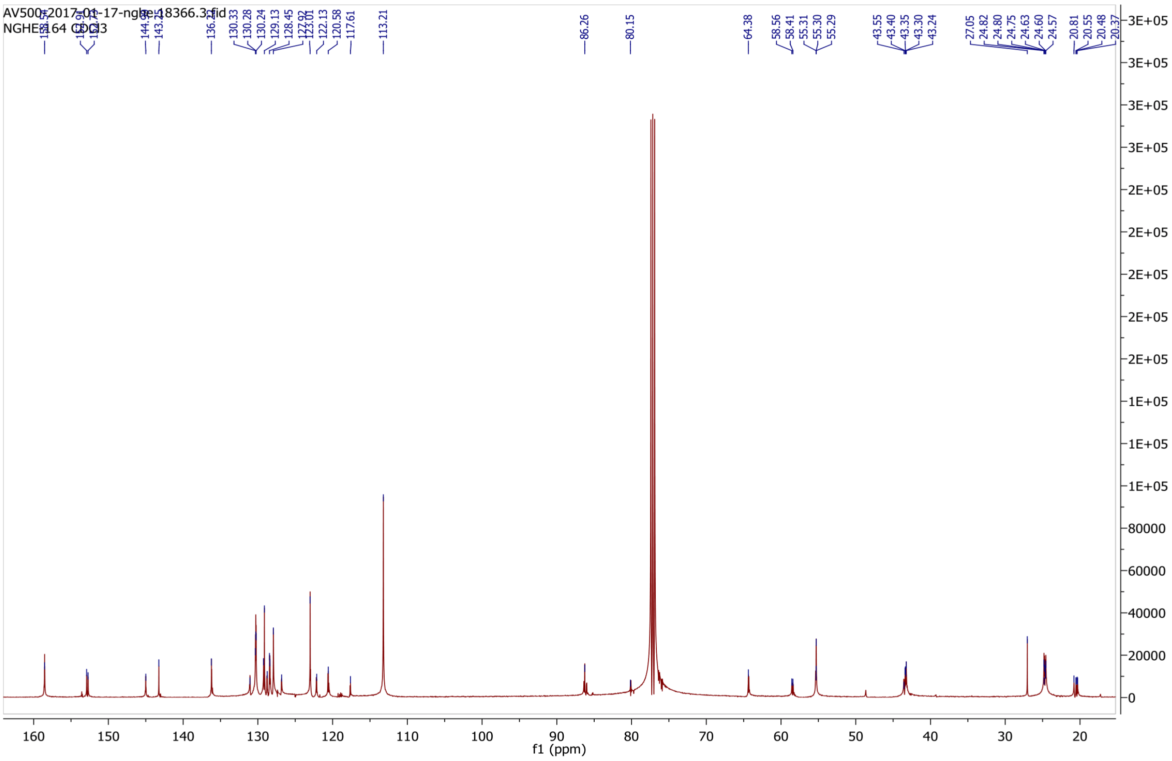

Fig. 184 ^{13}C spectrum of compound **9**.

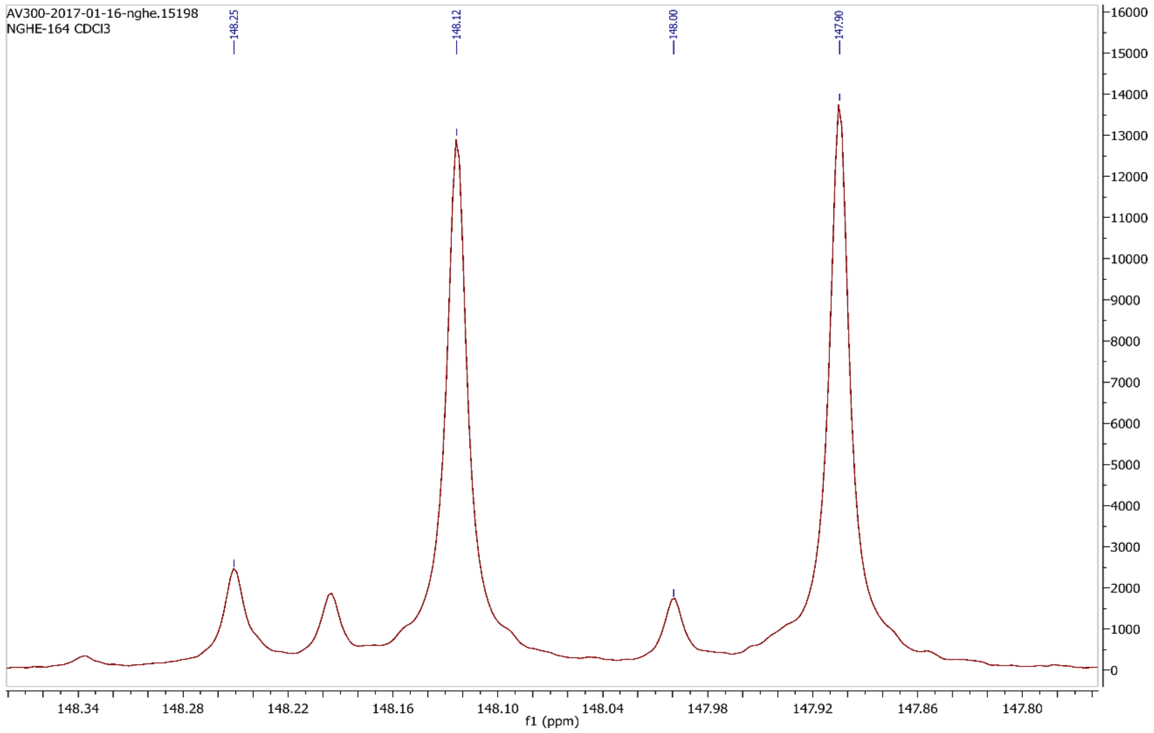

Fig. 185 ^{31}P spectrum of compound **9**.

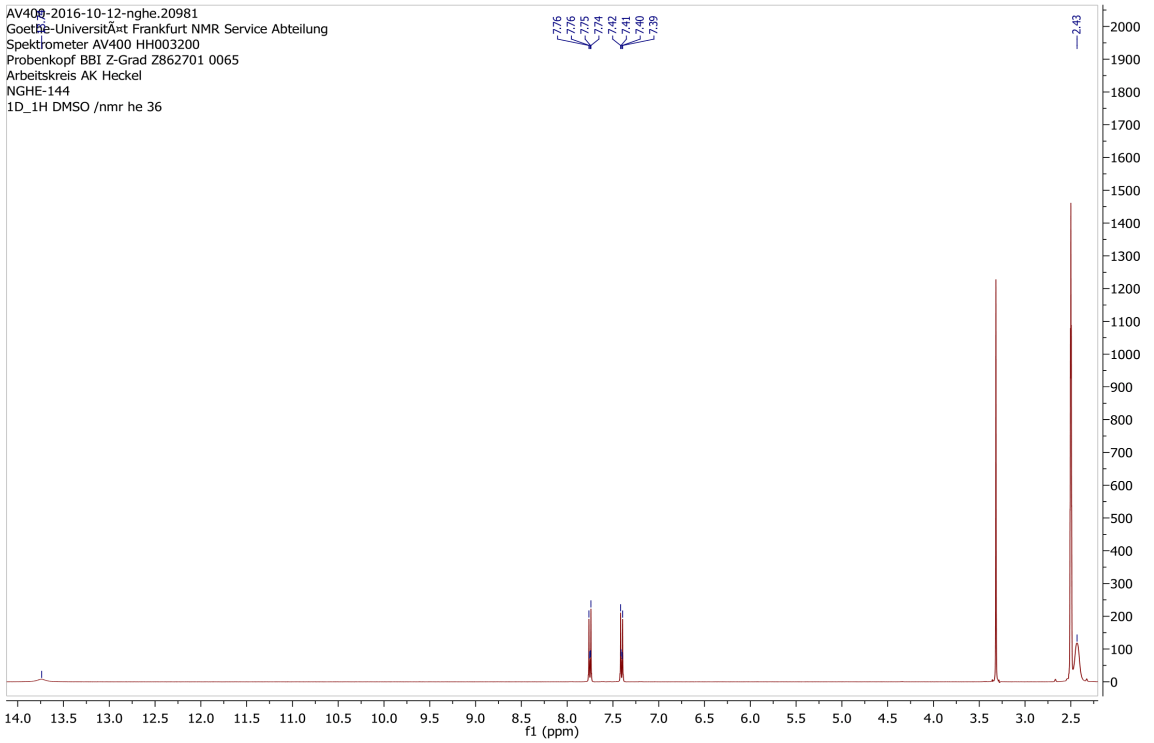

Fig. 186 ^{1}H spectrum of compound **10**.

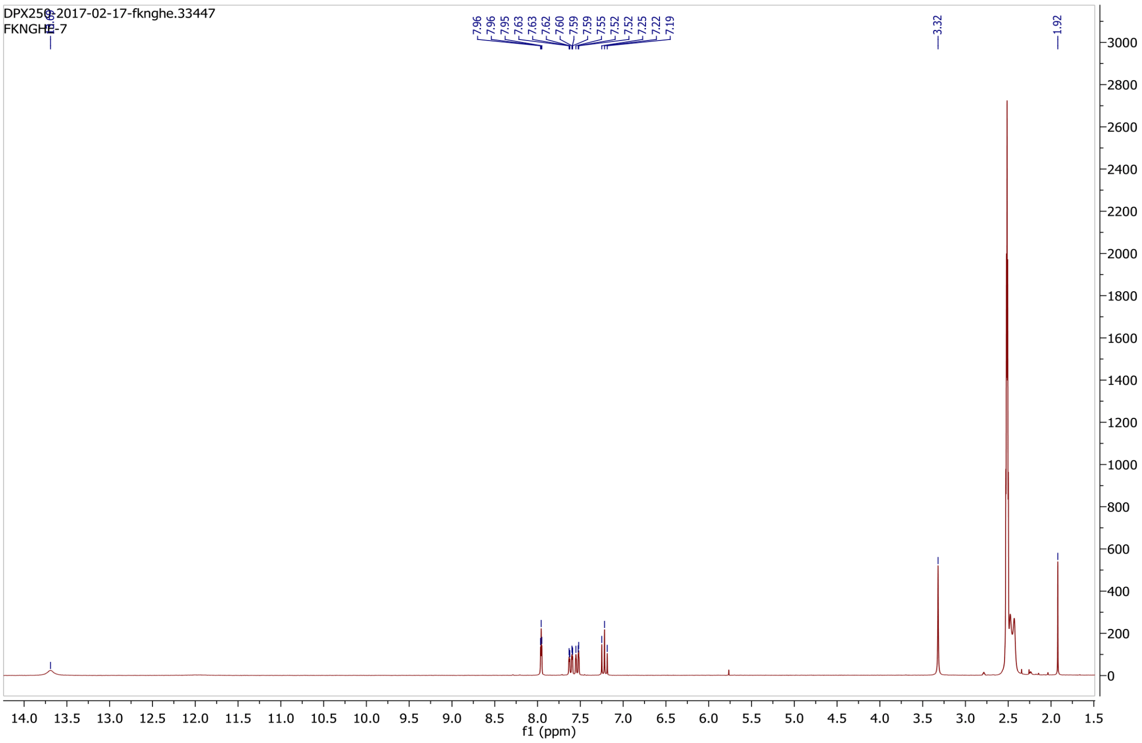

Fig. 187 ^{1}H spectrum of compound ***11****.*

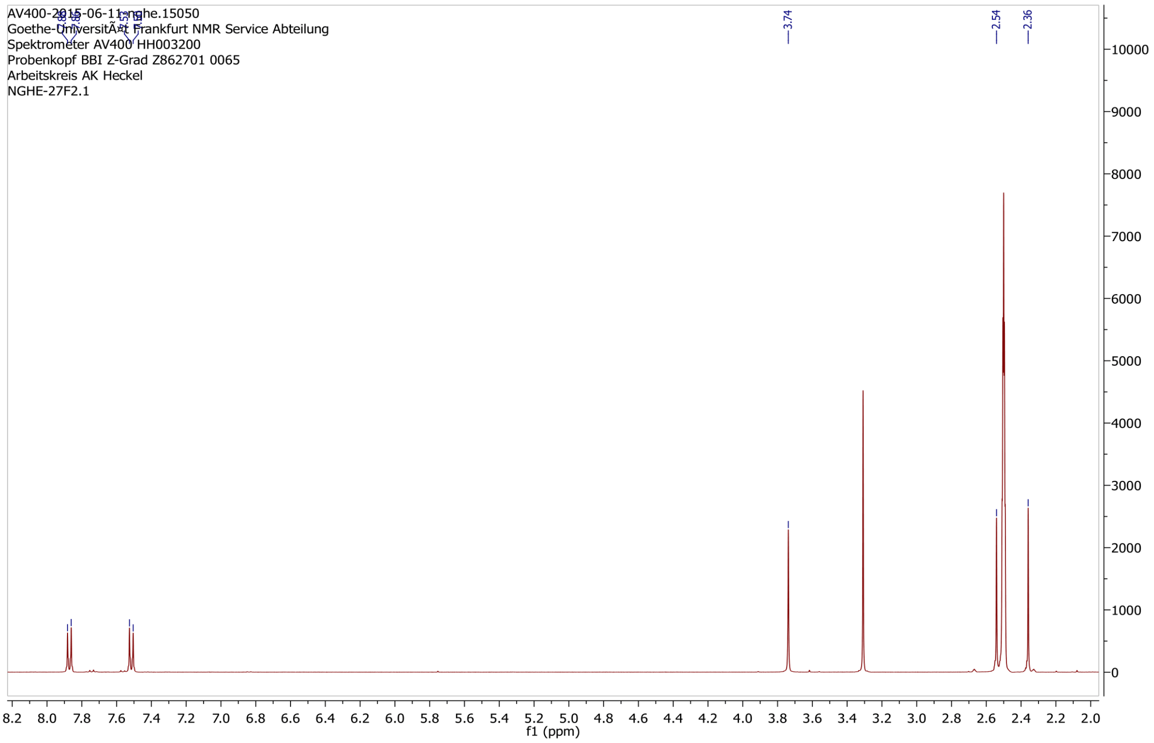

Fig. 188 ^{1}H spectrum of compound ***12****.*

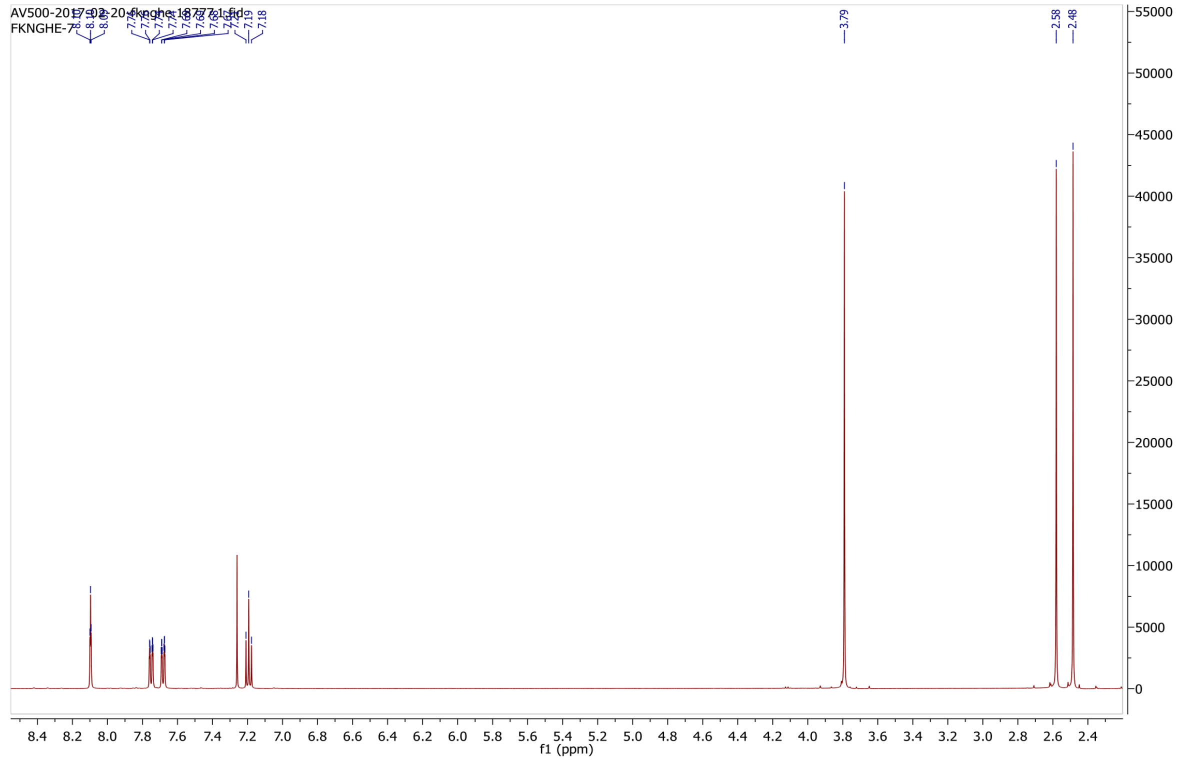

Fig. 189 ^{1}H spectrum of compound **13**.

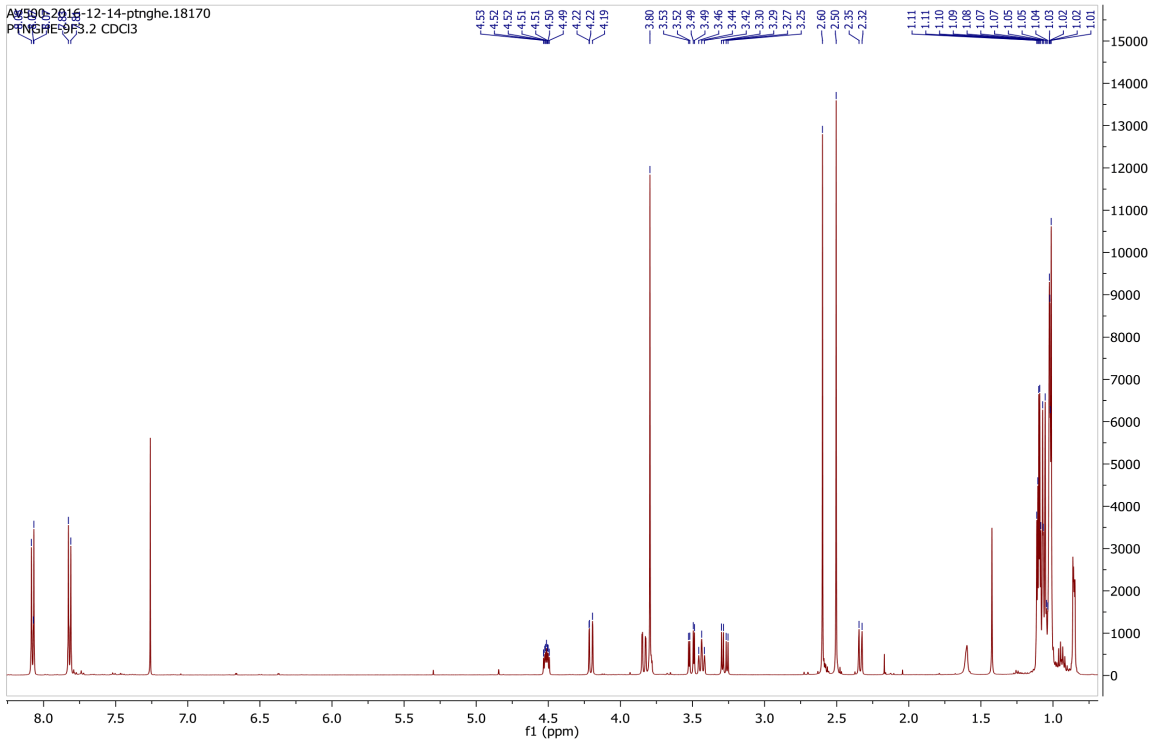

Fig. 190 ^{1}H spectrum of compound **14**.

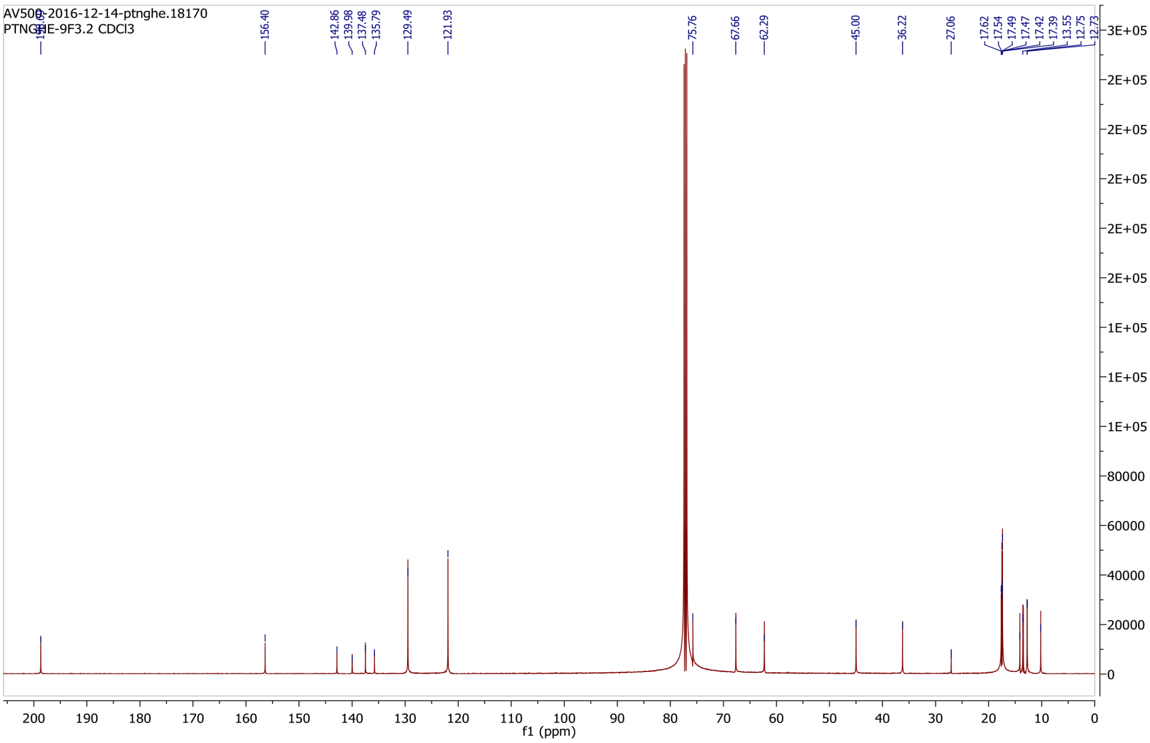

Fig. 191 ^{13}C spectrum of compound **14**.

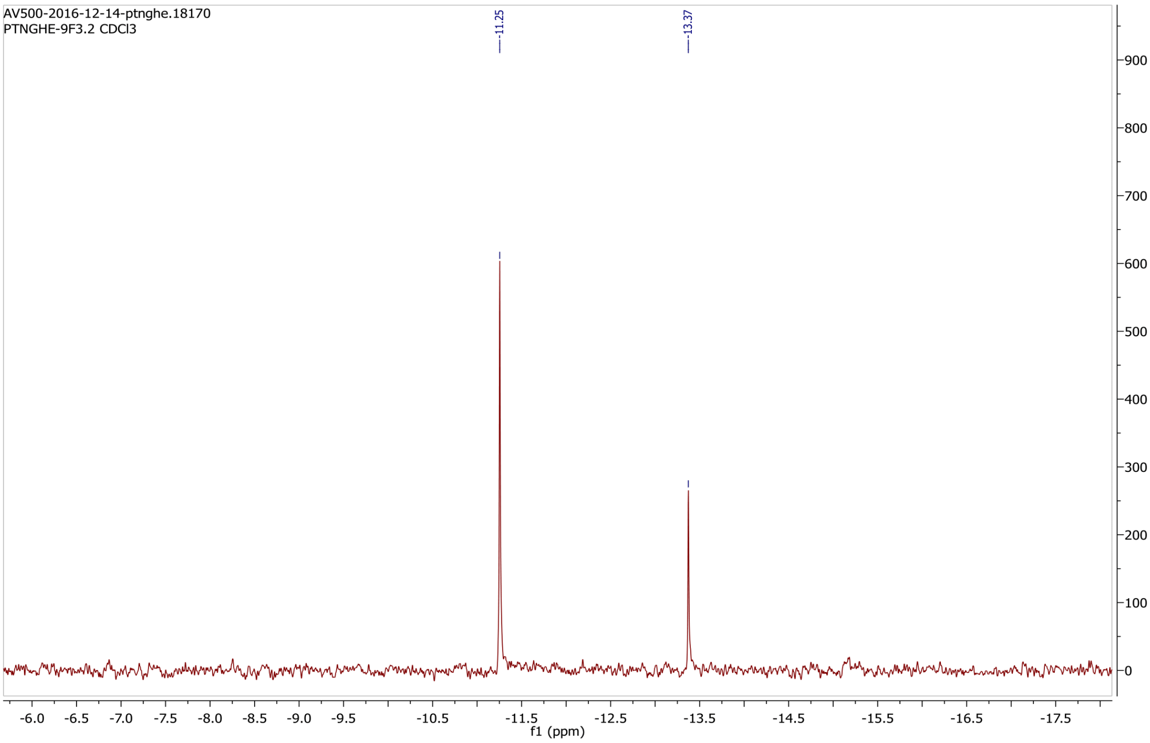

Fig. 192 ^{29}Si spectrum of compound **14**.

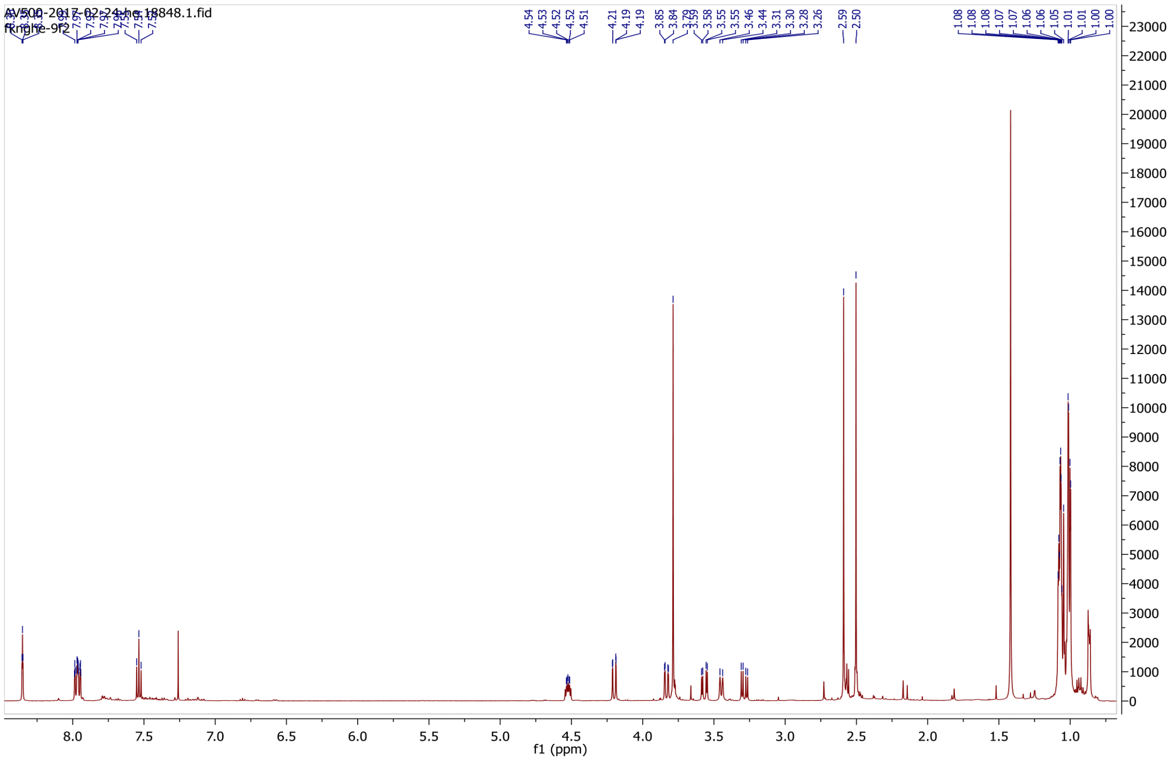

*Fig. 193 ^{1}H spectrum of compund **15**.*

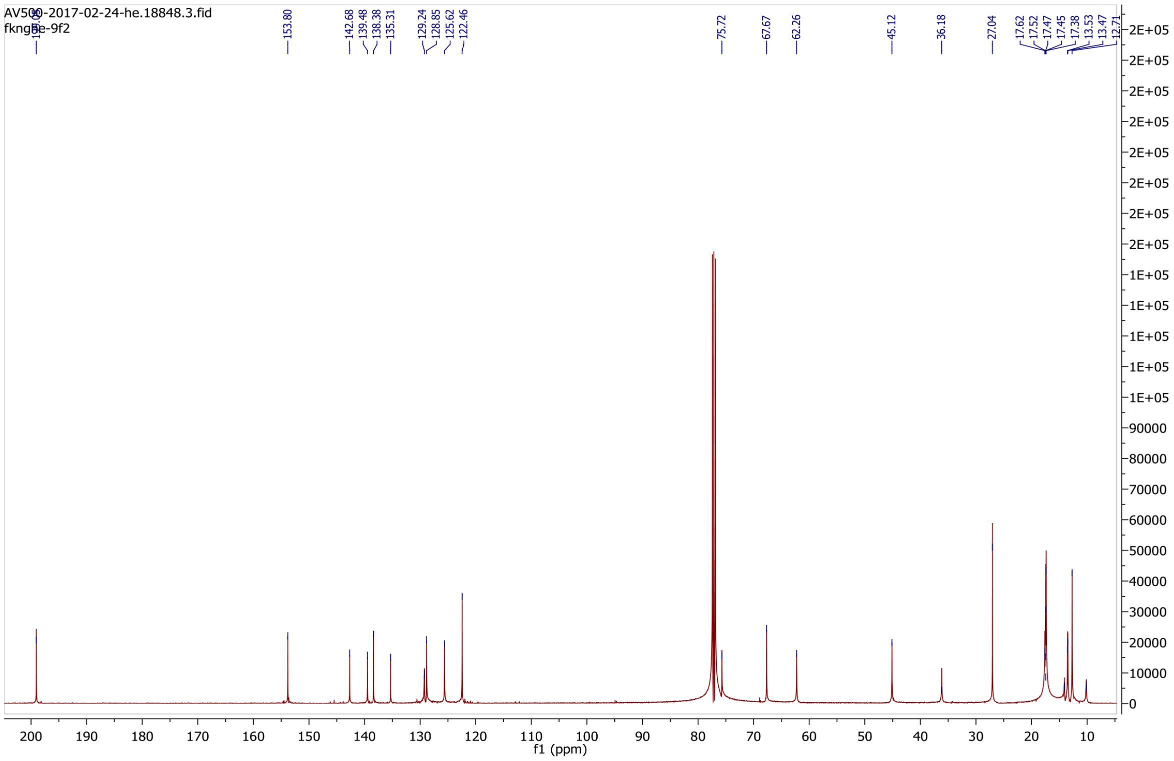

*Fig. 194 ^{13}C spectrum of compound **15**.*

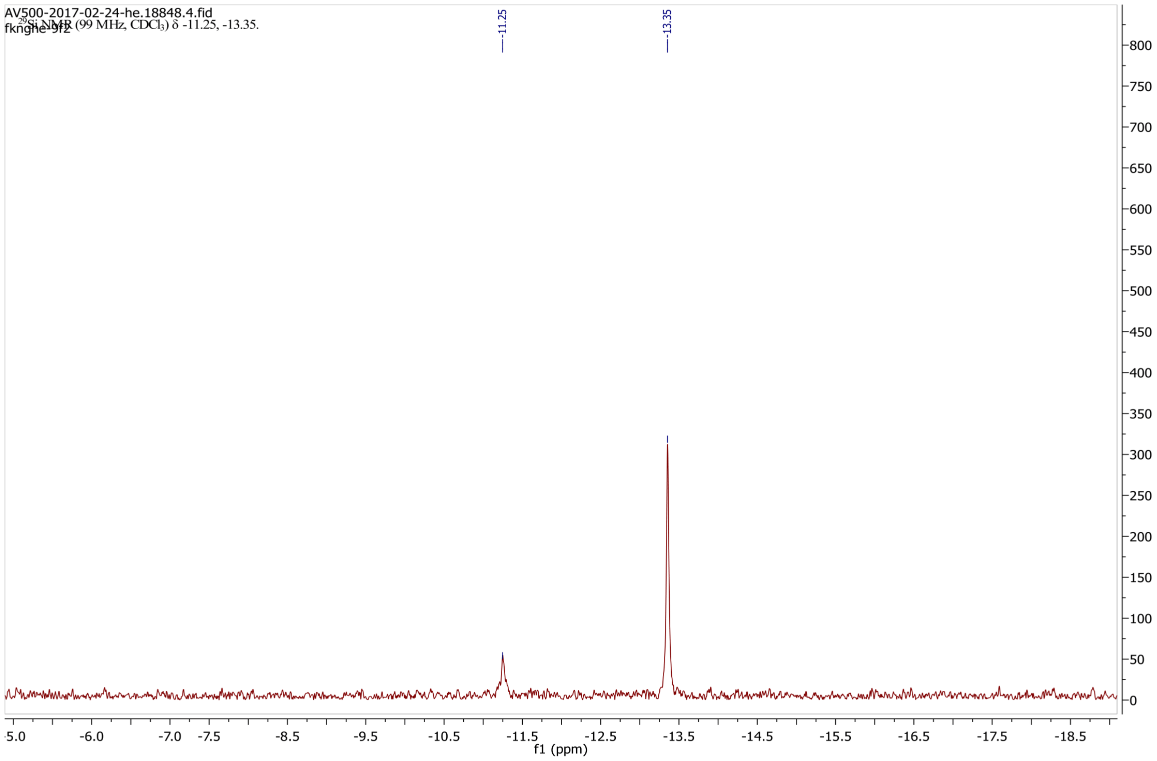

Fig. 195 ^{29}Si spectrum of compound ***15****.*

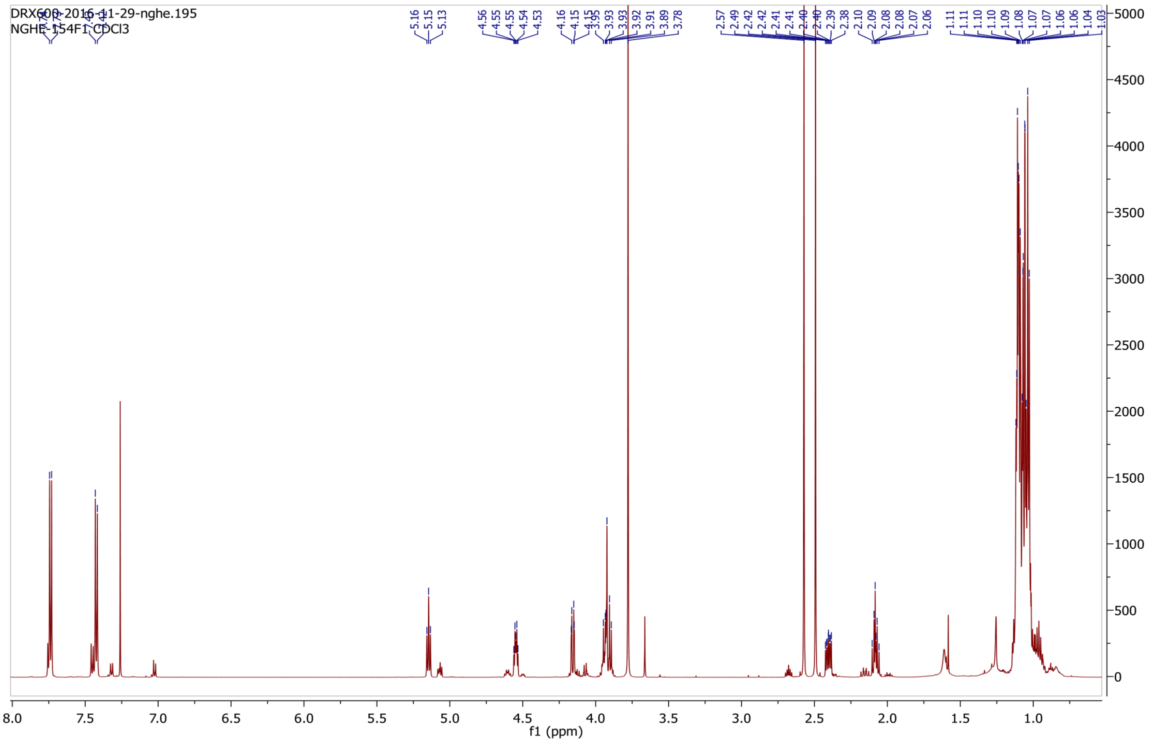

Fig. 196 ^{1}H spectrum of compound ***16****.*

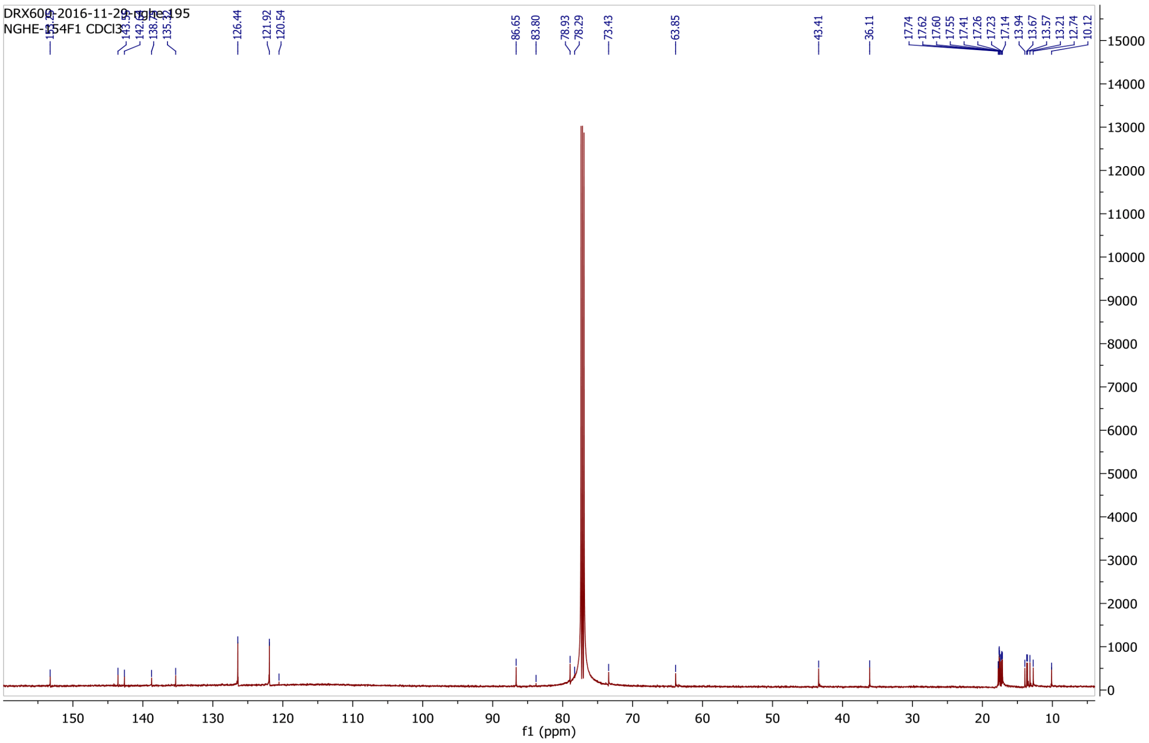

*Fig. 197 ^{13}C spectrum of compound **16**.*

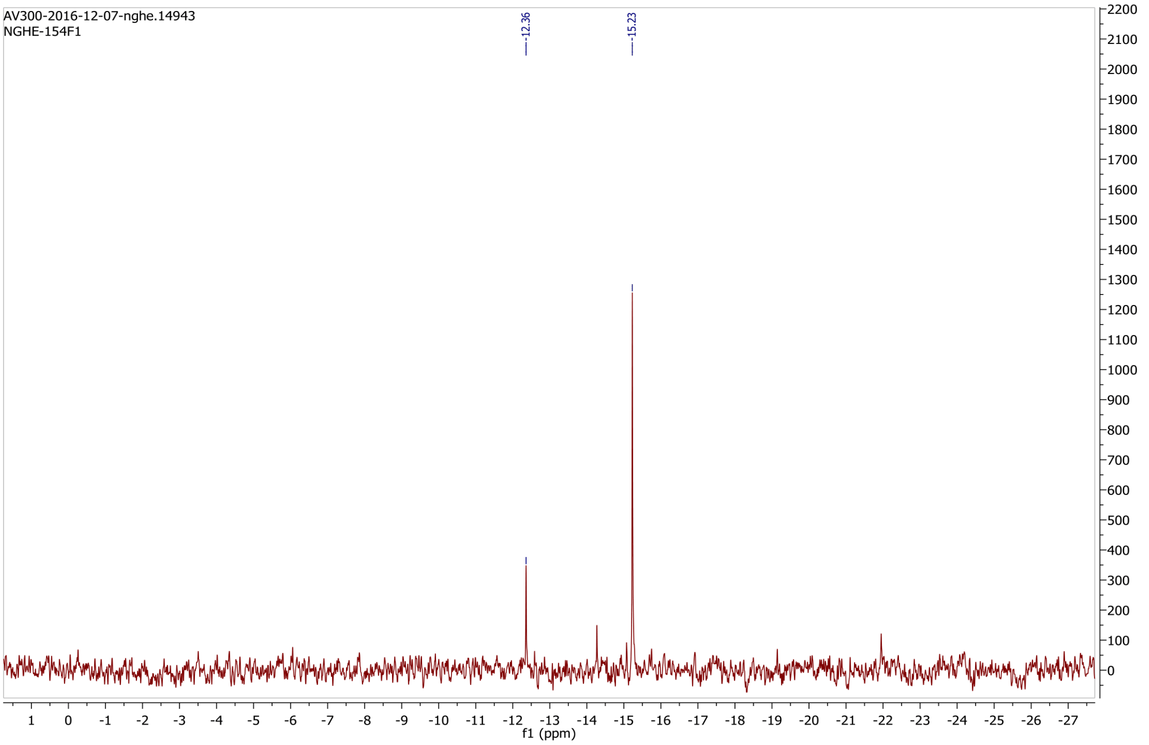

*Fig. 198 ^{29}Si spectrum of compound **16**.*

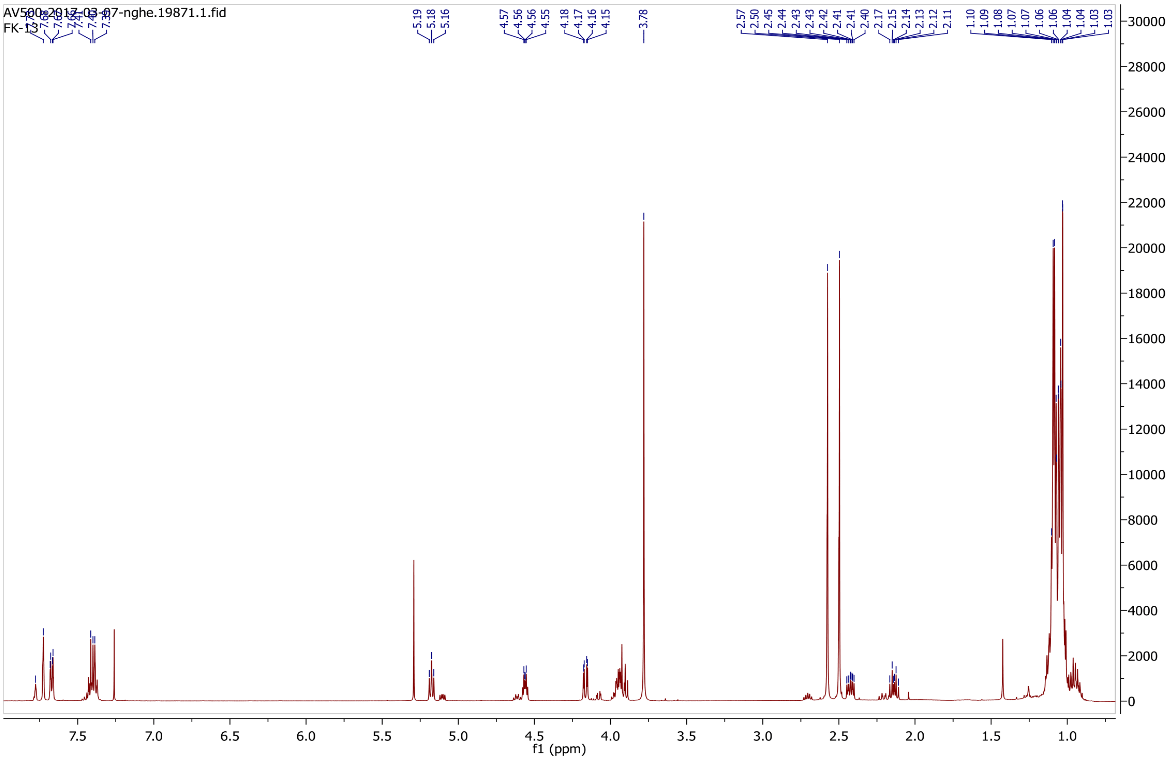

Fig. 199 ^{1}H spectrum of compound **17**.

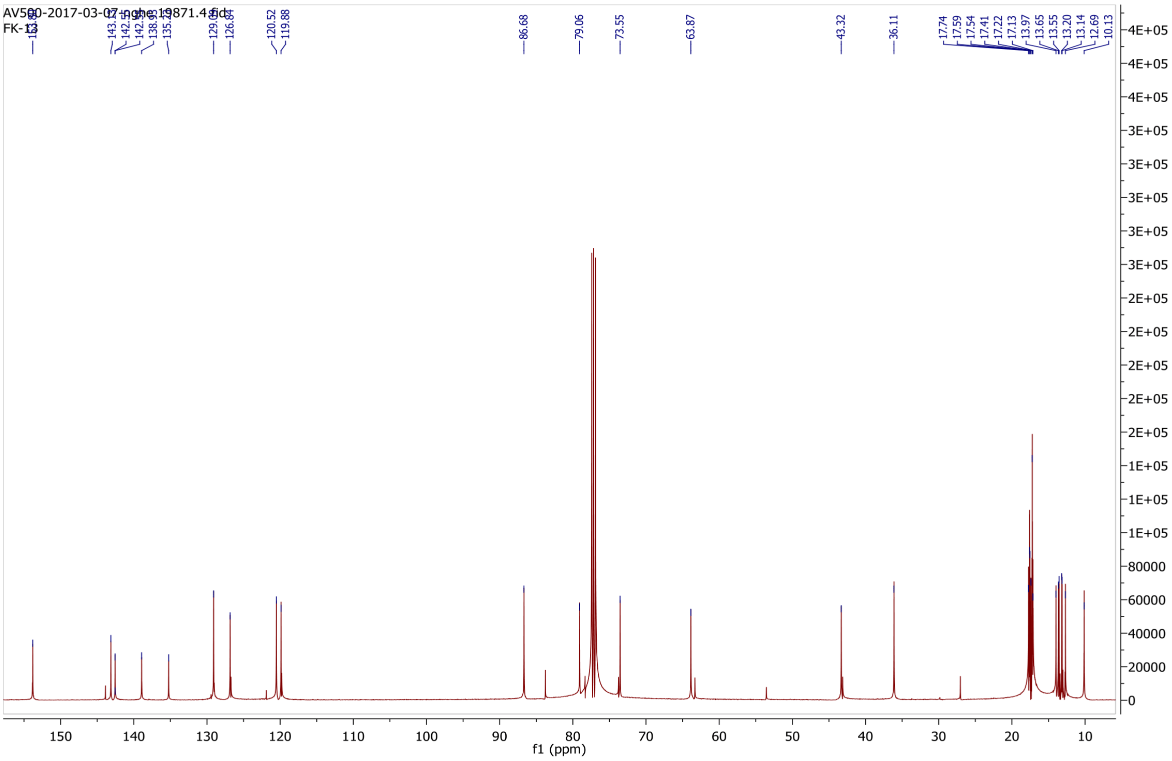

Fig. 200 ^{13}C spectrum of compound **17**.

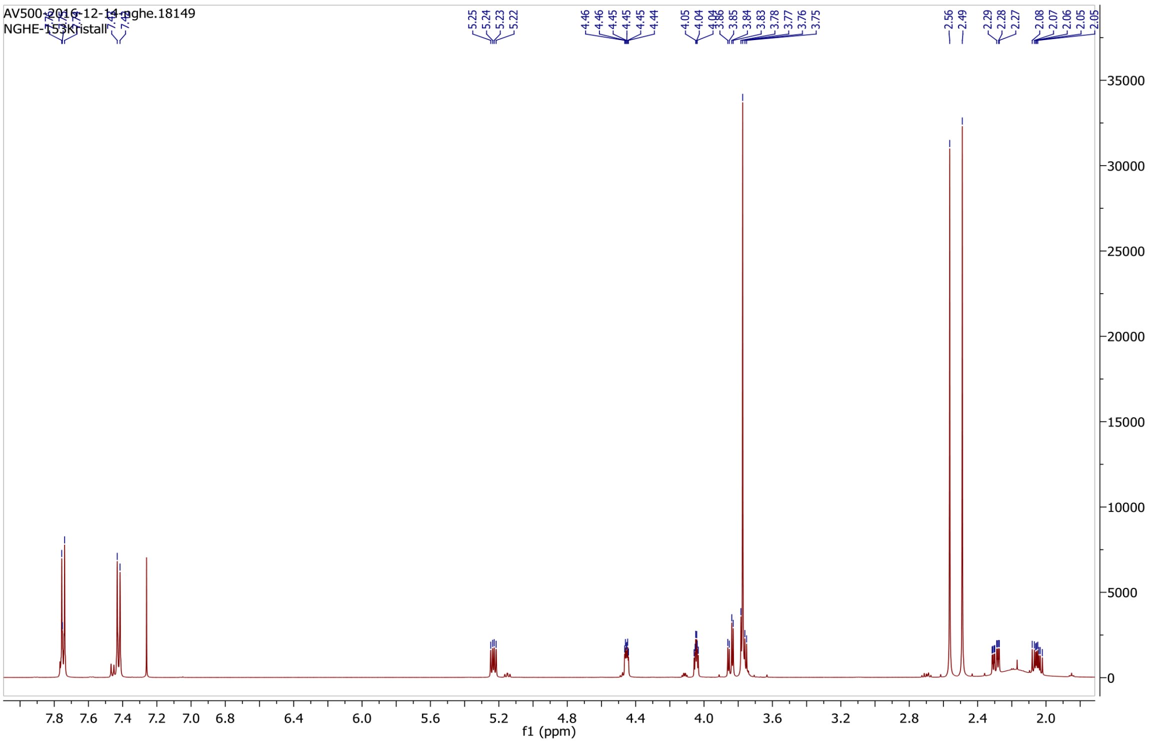

Fig. 201 ^{1}H spectrum of compound **18**.

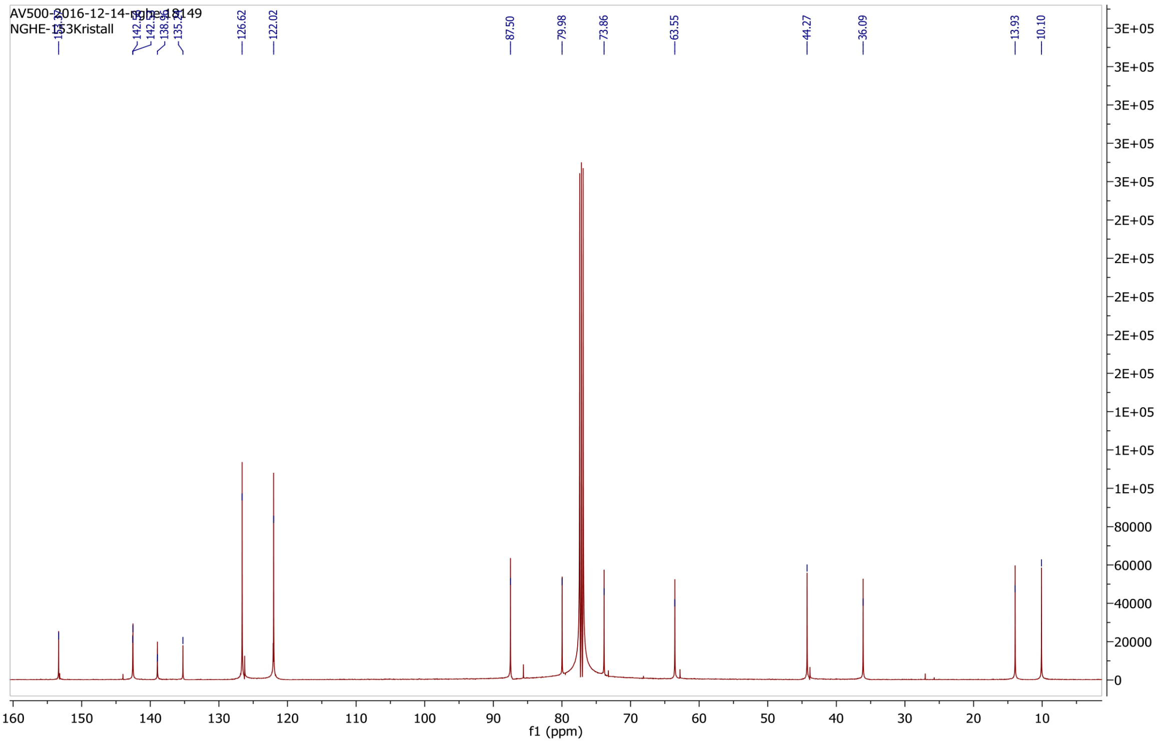

Fig. 202 ^{13}C spectrum of compound **18**.

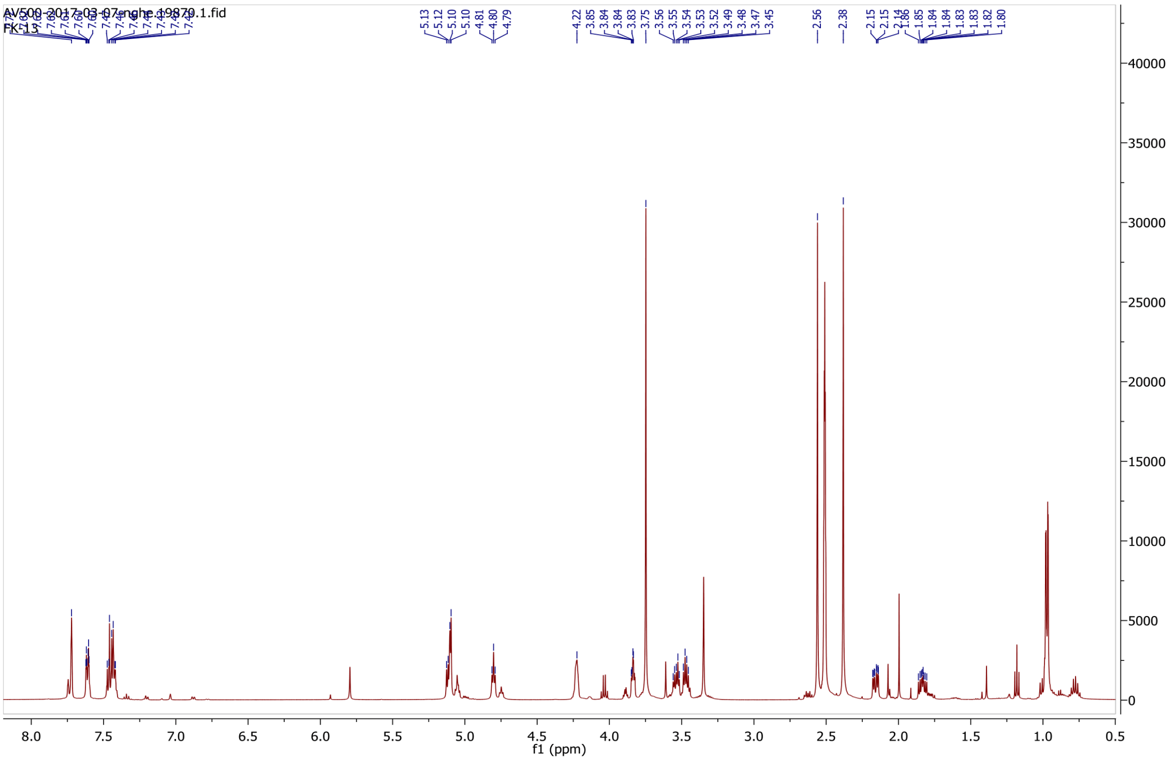

Fig. 203 ^{1}H spectrum of compound **19**.

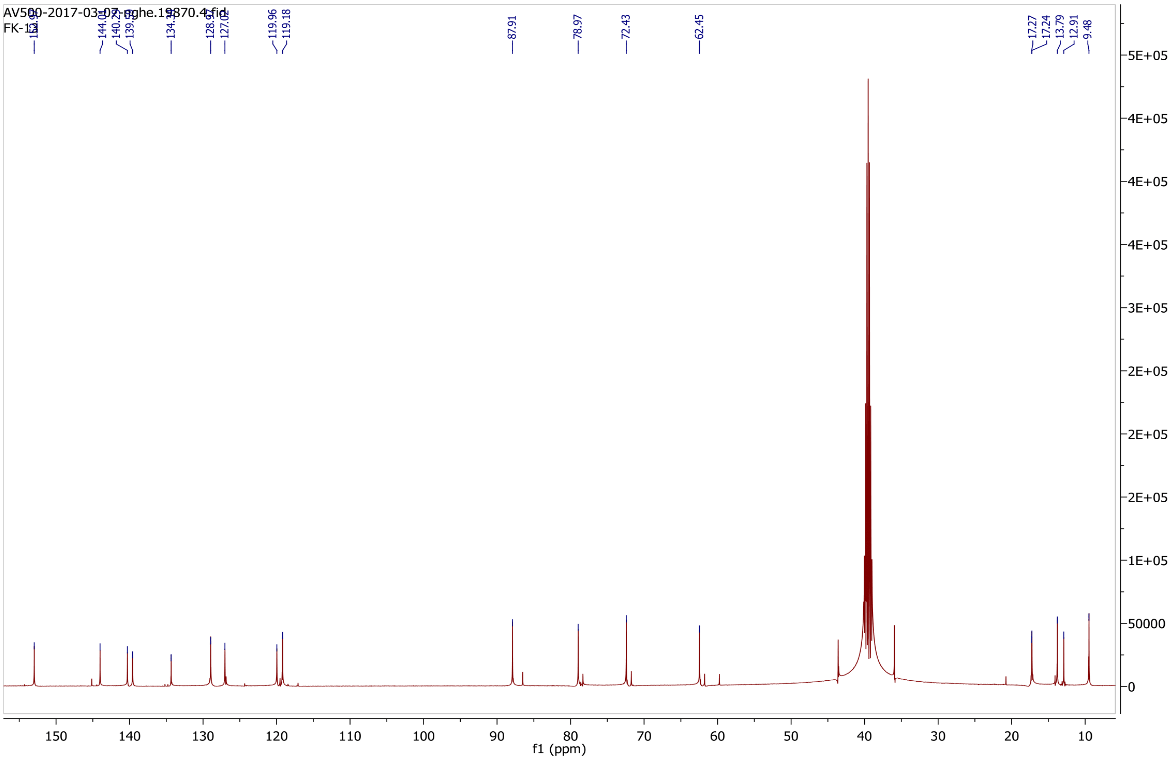

Fig. 204 ^{13}C spectrum of compound **19**.

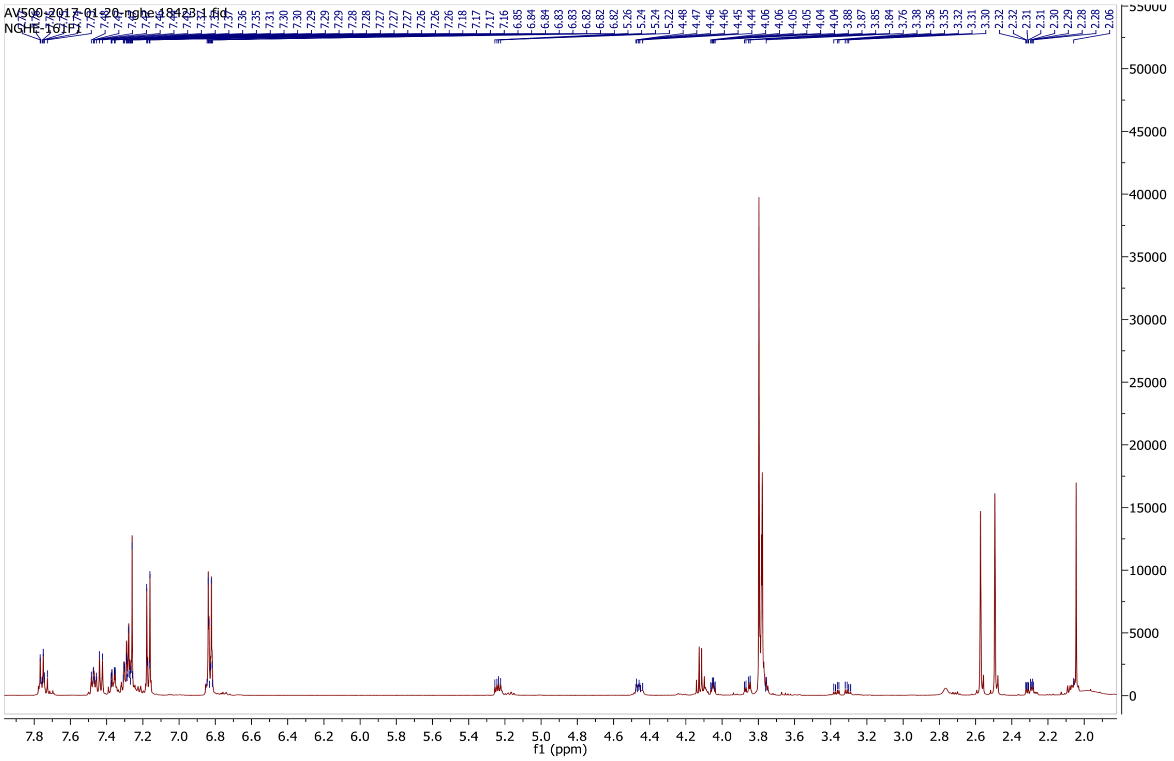

Fig. 205 ^{1}H spectrum of compound ***20****.*

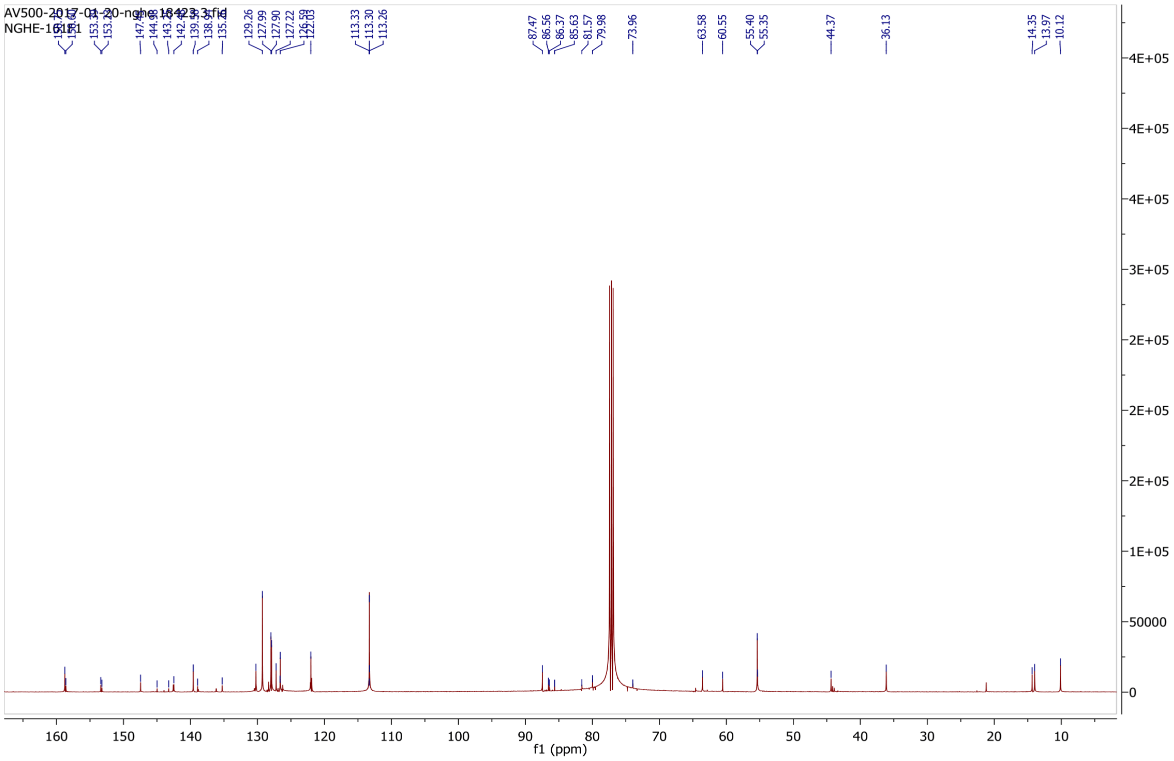

Fig. 206 ^{13}C spectrum of compound ***20****.*

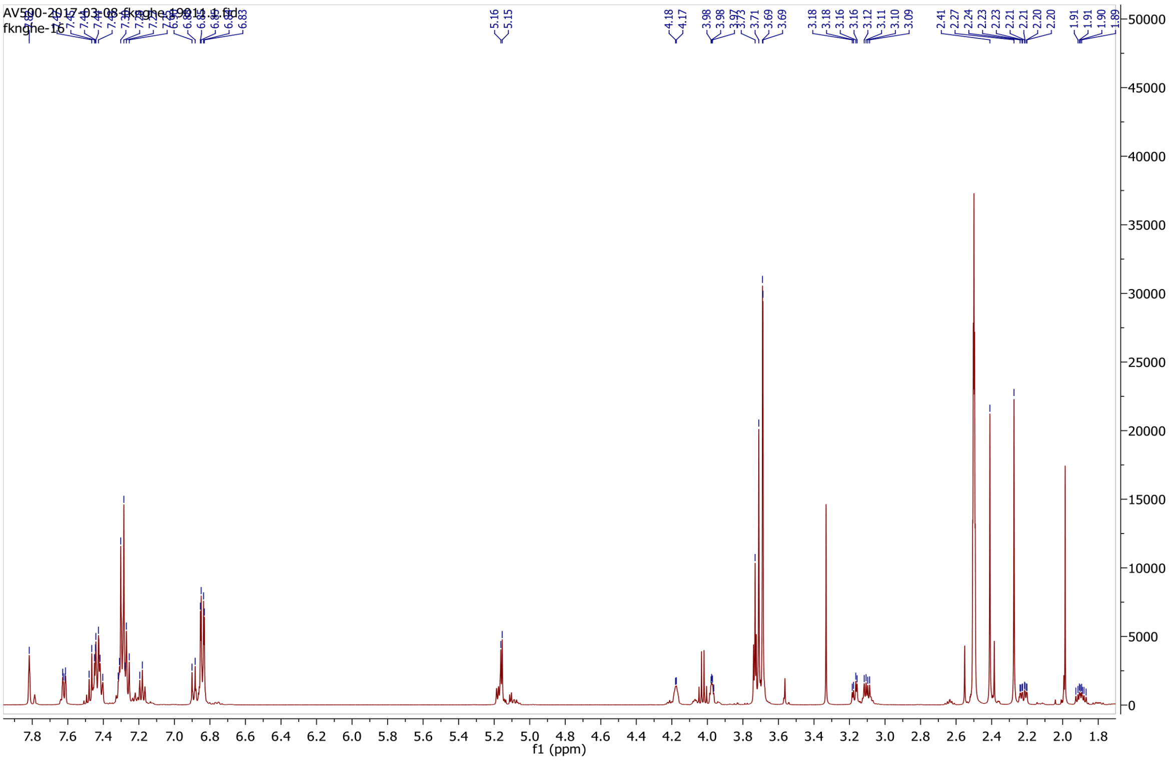

Fig. 207 ^{1}H spectrum of compound ***21****.*

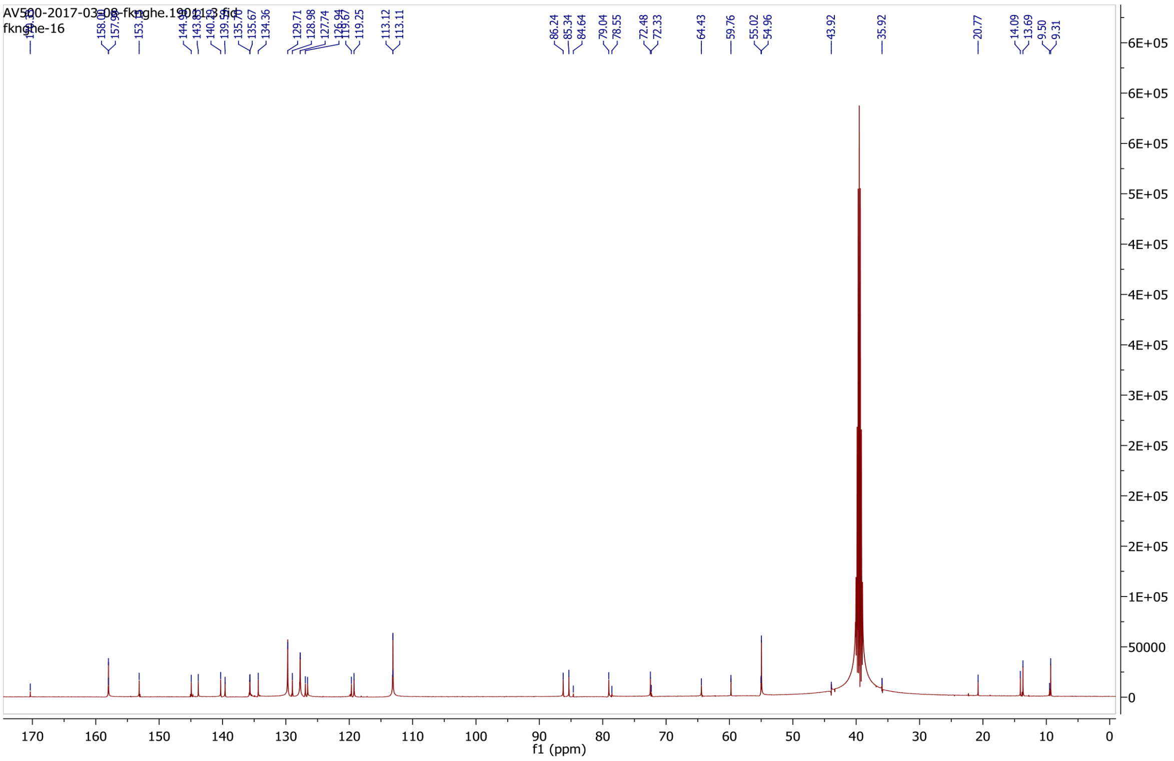

Fig. 208 ^{13}C spectrum of compound ***21****.*

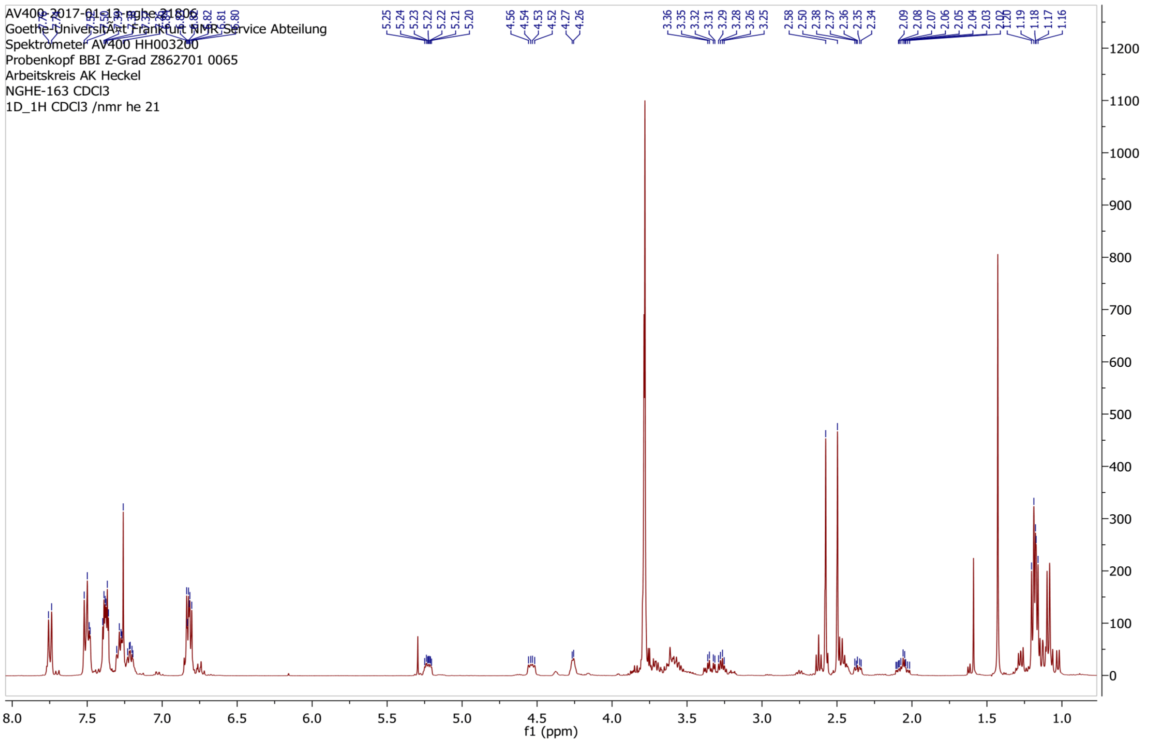

Fig. 209 ^{1}H spectrum of compound **22**.

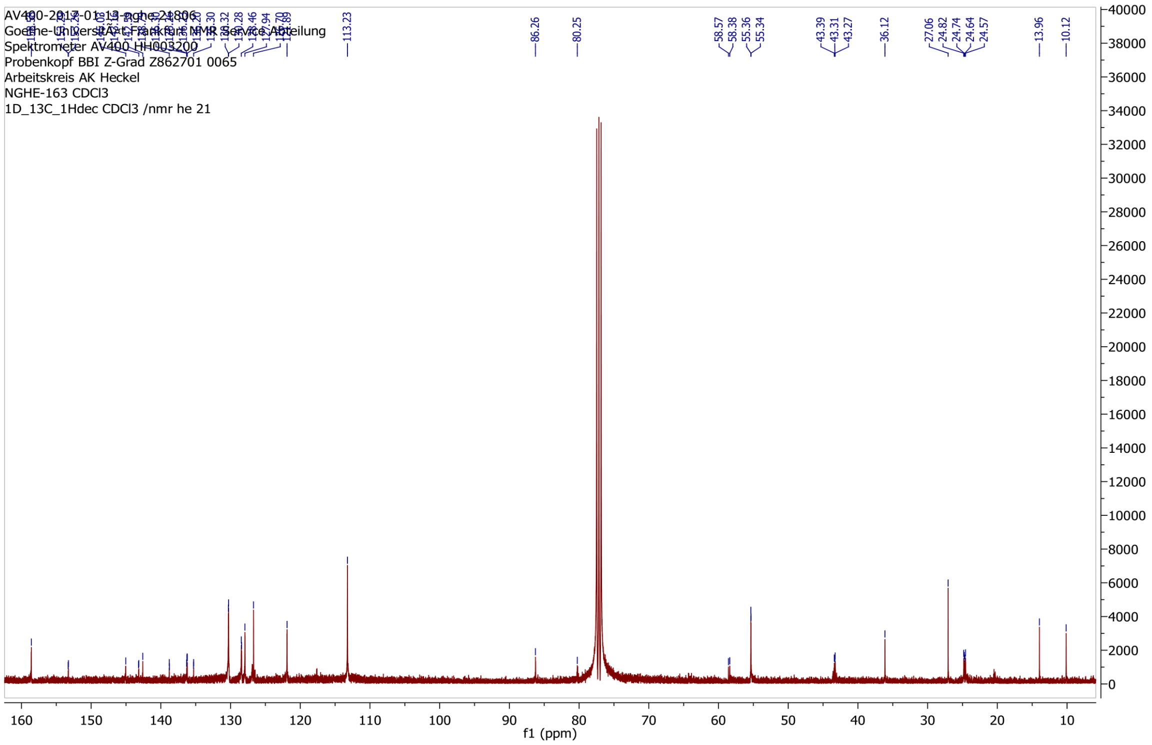

Fig. 210 ^{13}C spectrum of compound **22**.

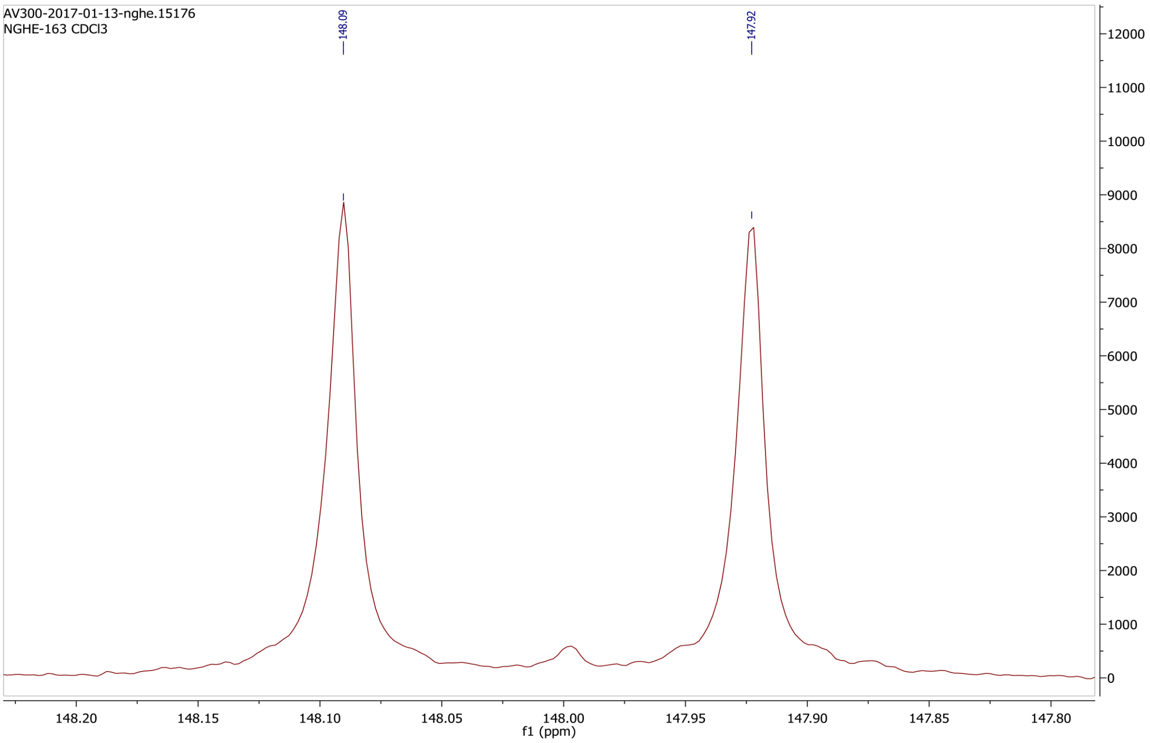

Fig. 211 ^{31}P spectrum of compound **22**.

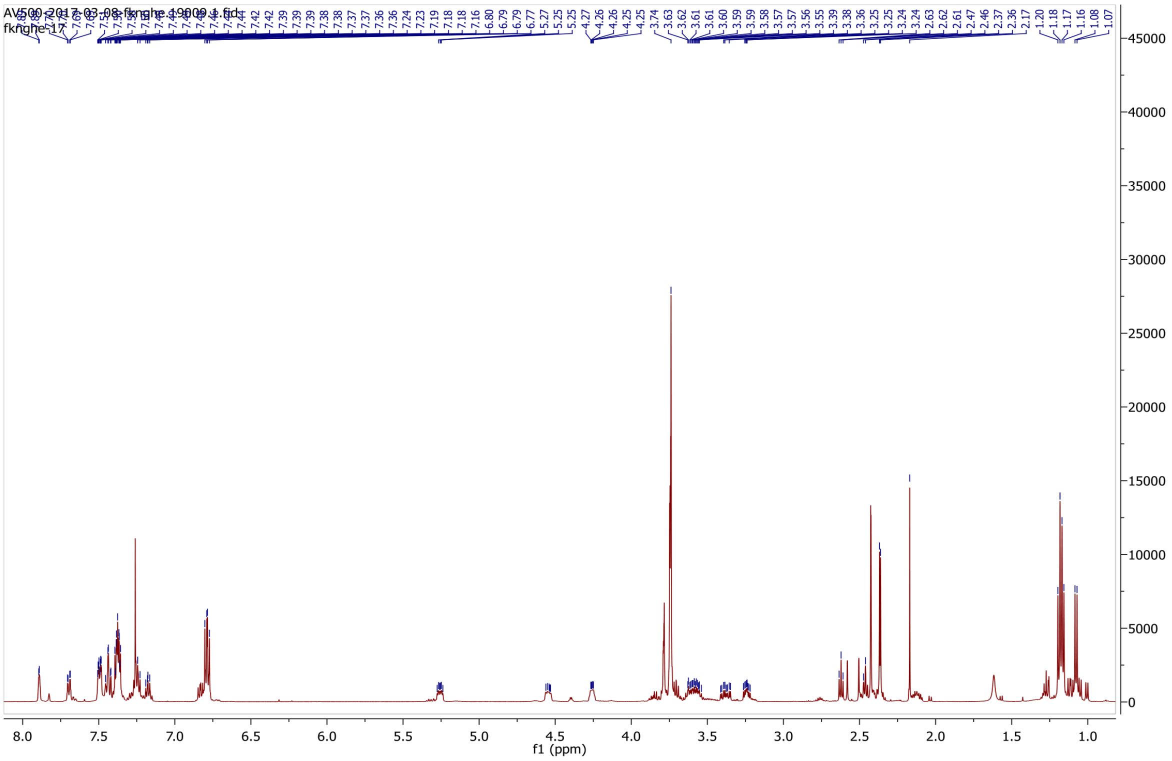

Fig. 212 ^{1}H spectrum of compound **23**.

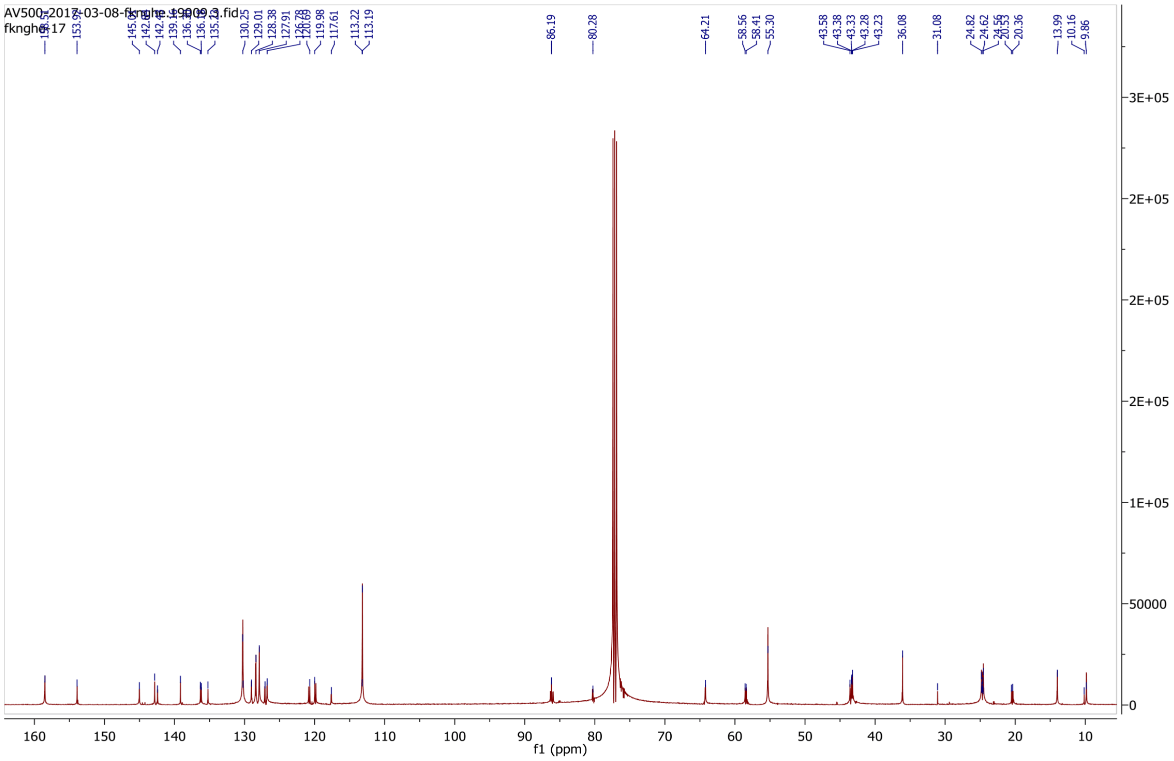

Fig. 213 ^{13}C spectrum of compound **23**.

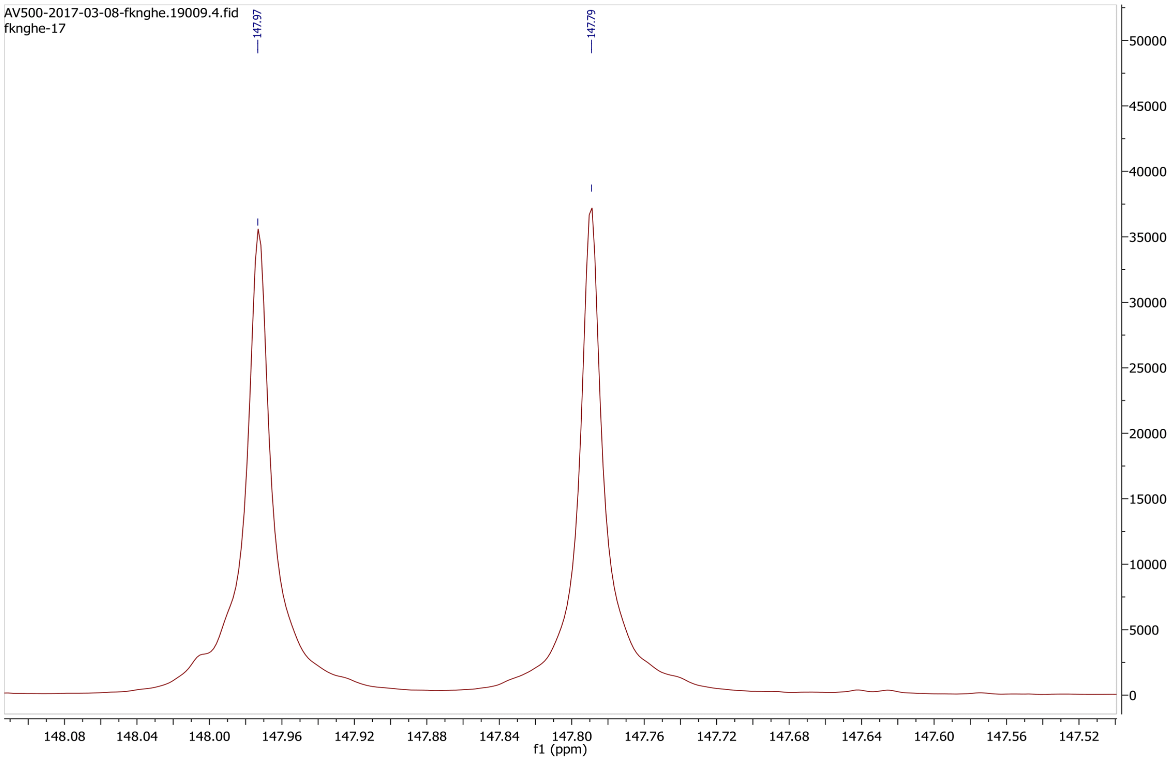

Fig. 214 ^{31}P spectrum of compound **23**.

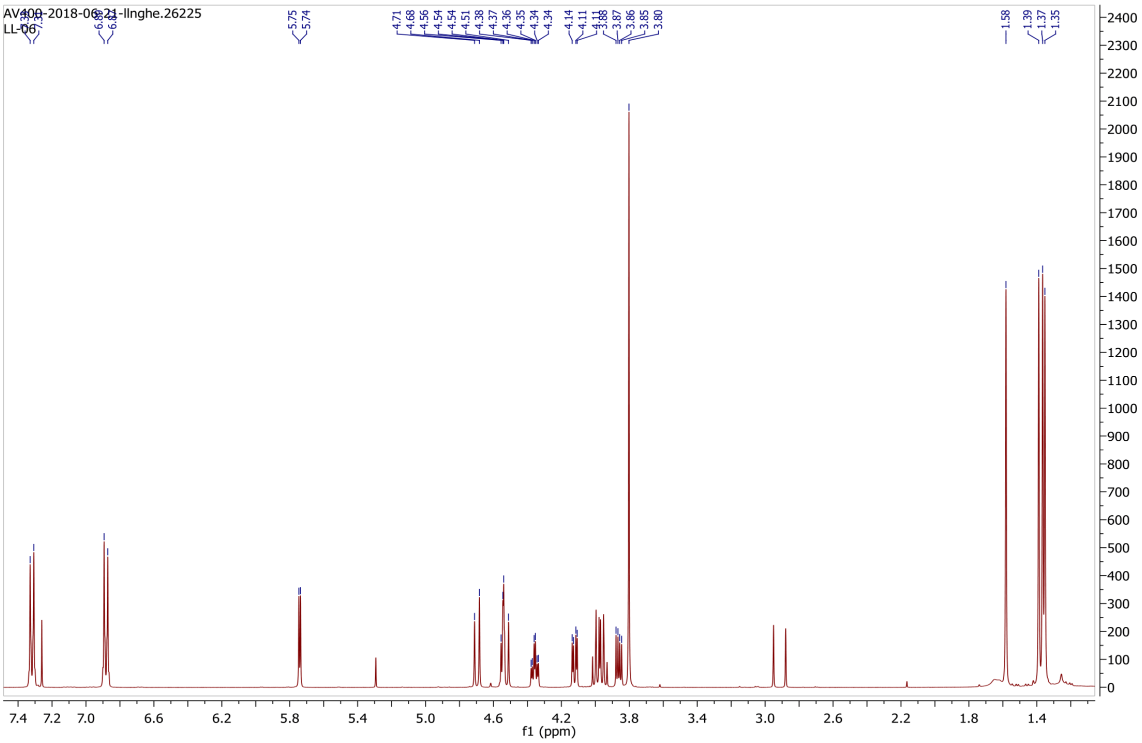

Fig. 215 ^{1}H spectrum of compound **25**.

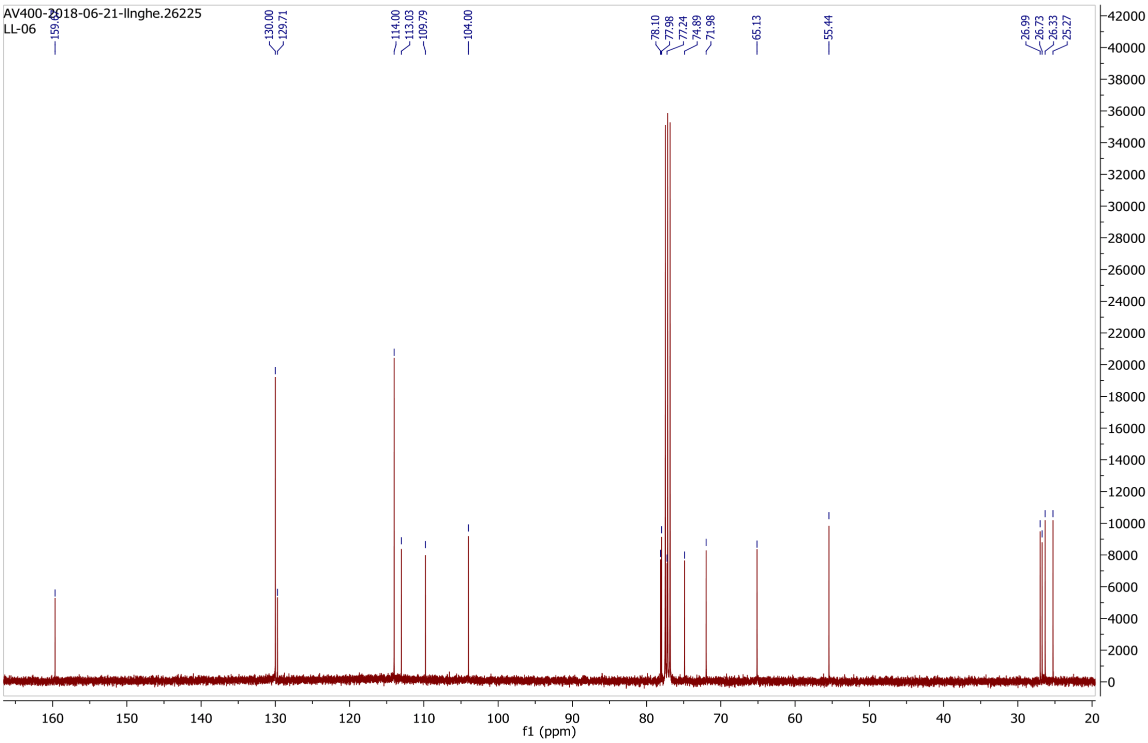

Fig. 216 ^{13}C spectrum of compound **25**.

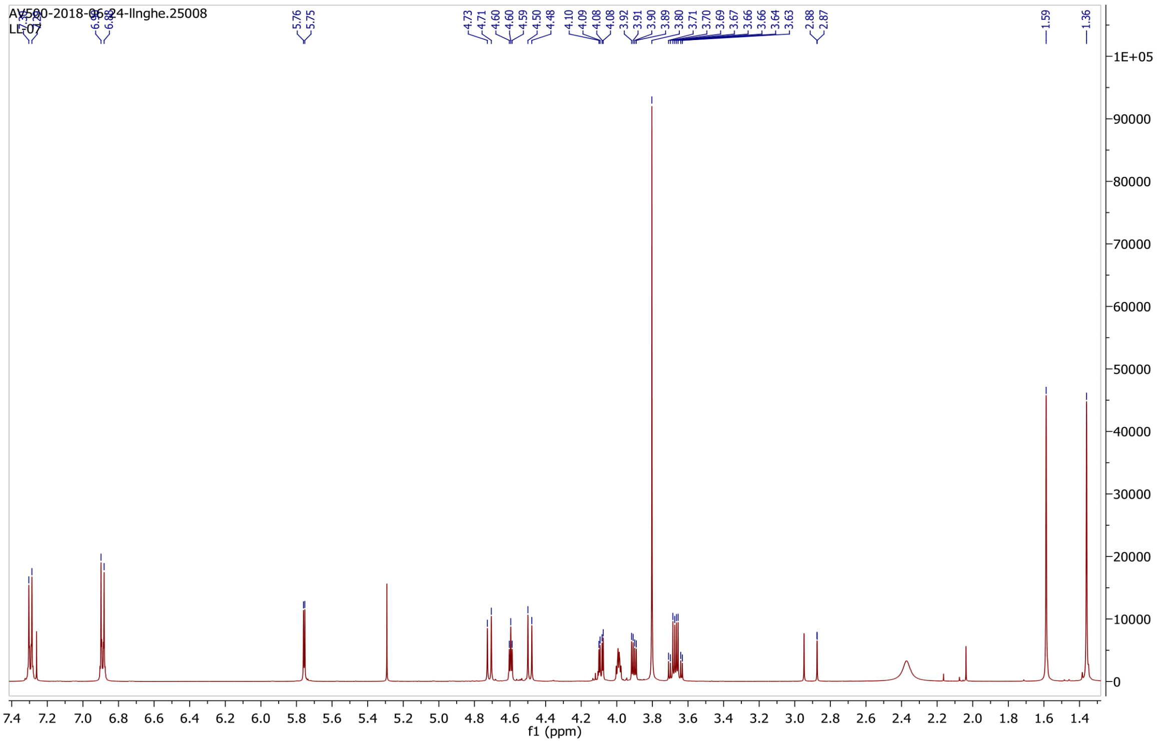

*Fig. 217 ^{1}H spectrum of compound **26**.*

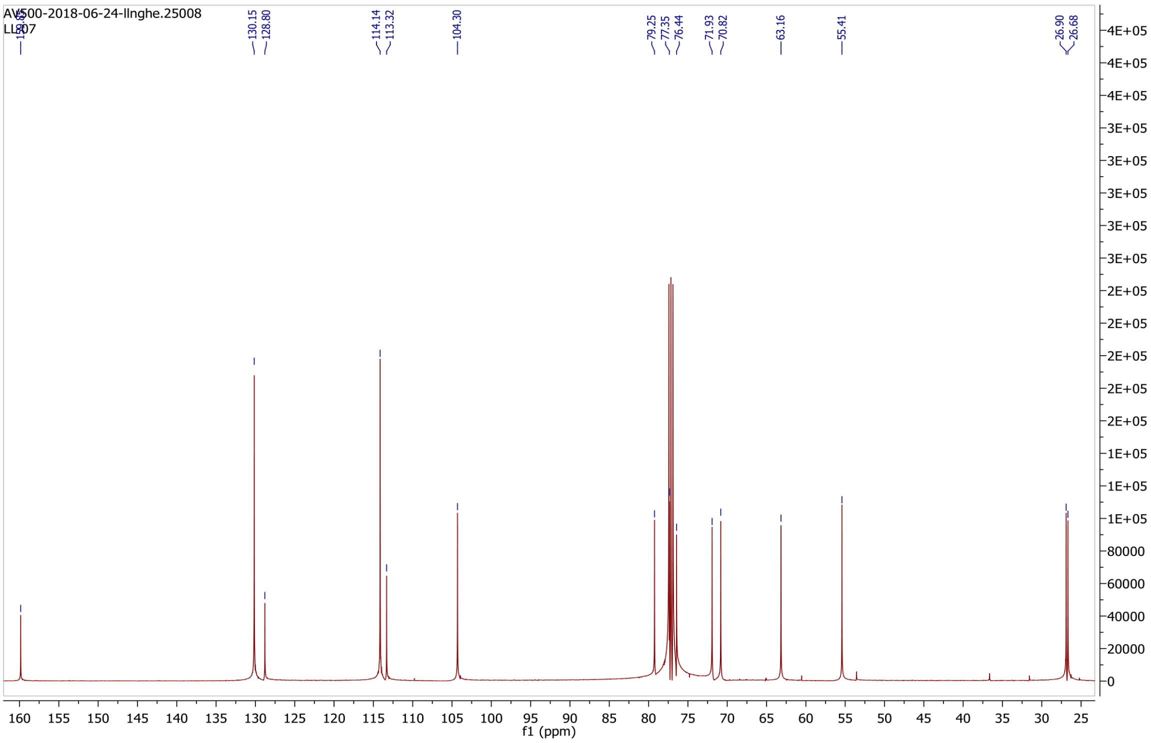

*Fig. 218 ^{13}C spectrum of compound **26**.*

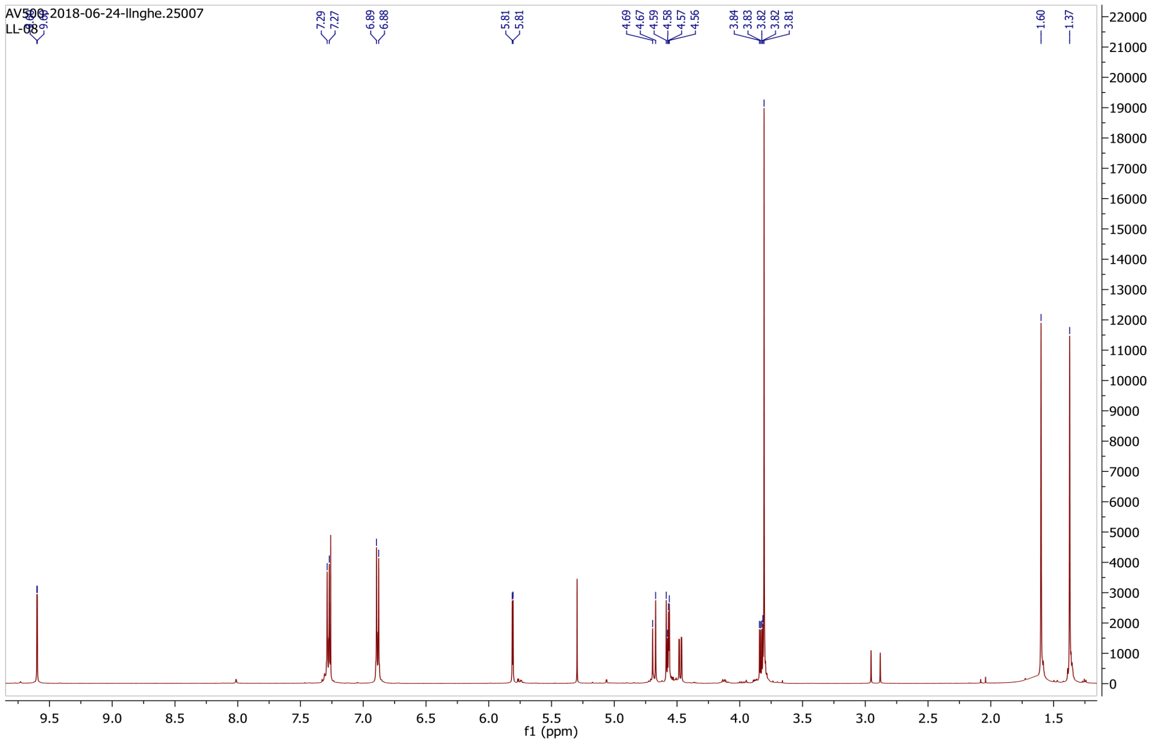

*Fig. 219 ^{1}H spectrum of compound **27**.*

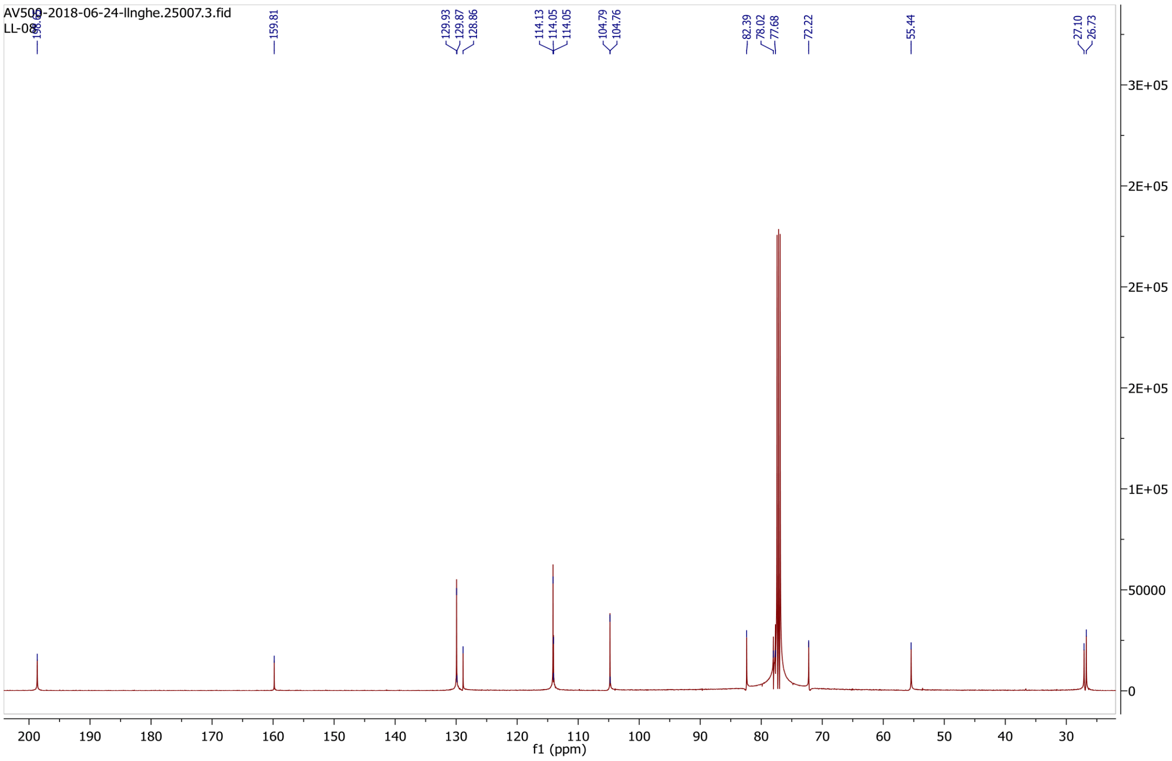

*Fig. 220 ^{13}C spectrum of compound **27**.*

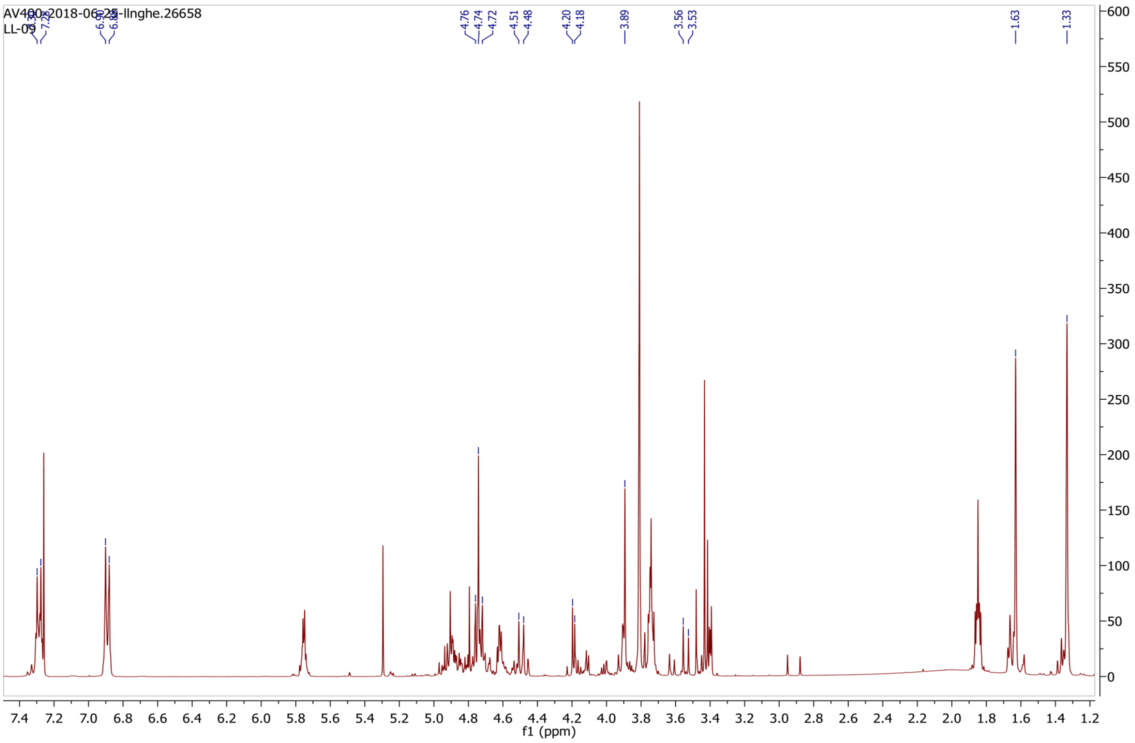

Fig. 221 ^{1}H spectrum of compound ***28****.*

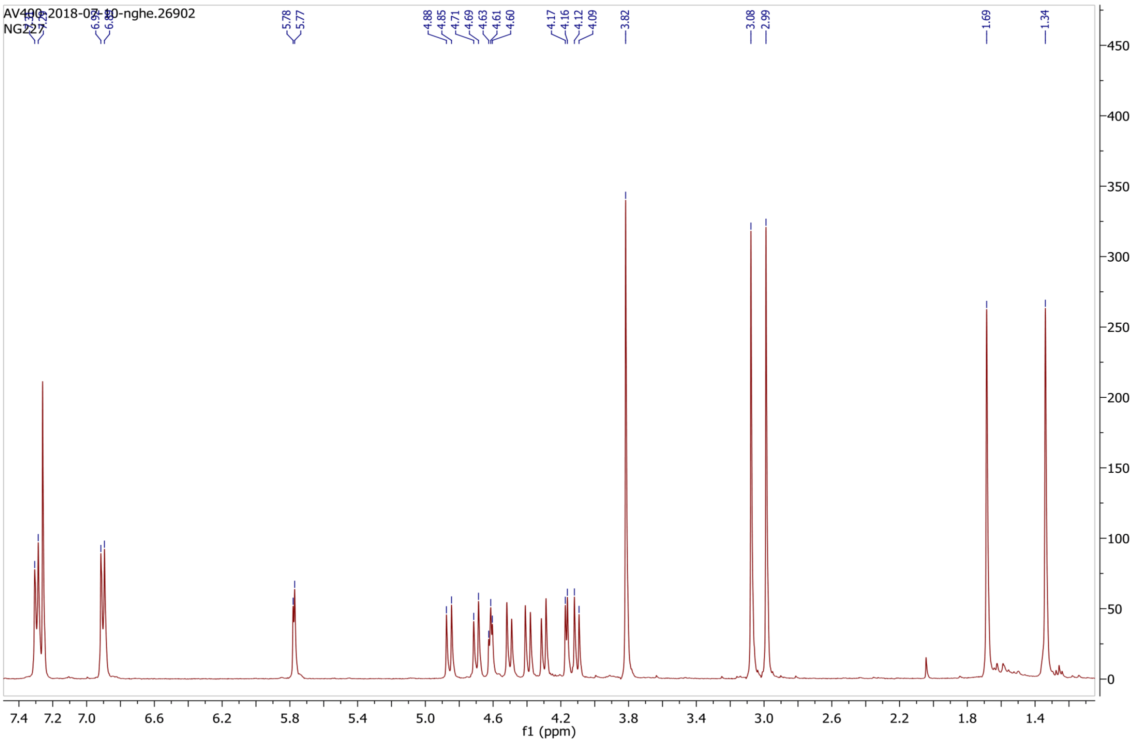

Fig. 222 ^{1}H spectrum of compound ***29****.*

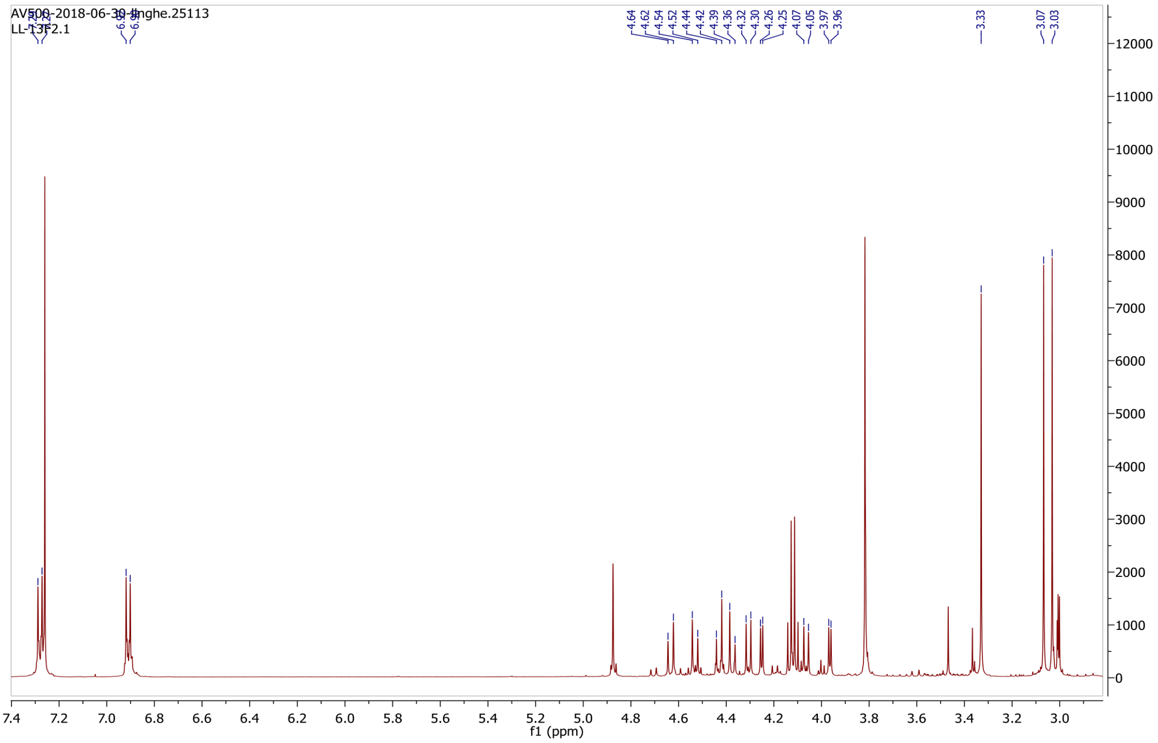

Fig. 223 ^{1}H spectrum of compound **30**.

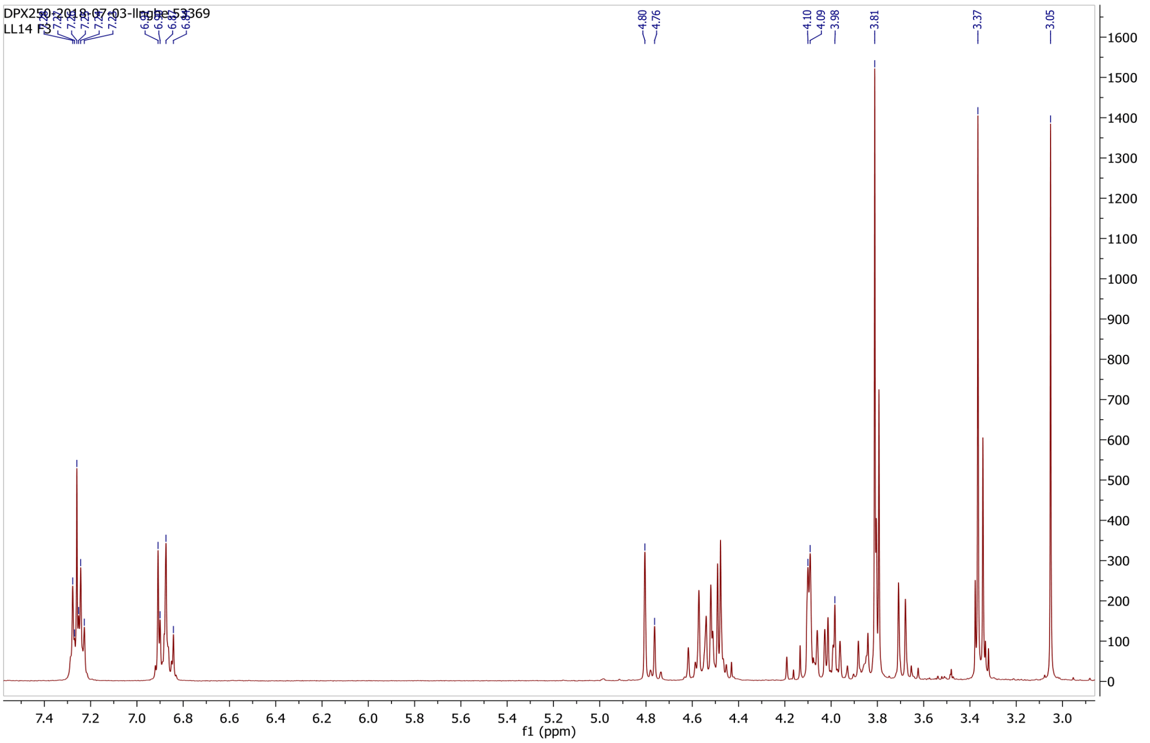

Fig. 224 ^{1}H spectrum of compound **31**.

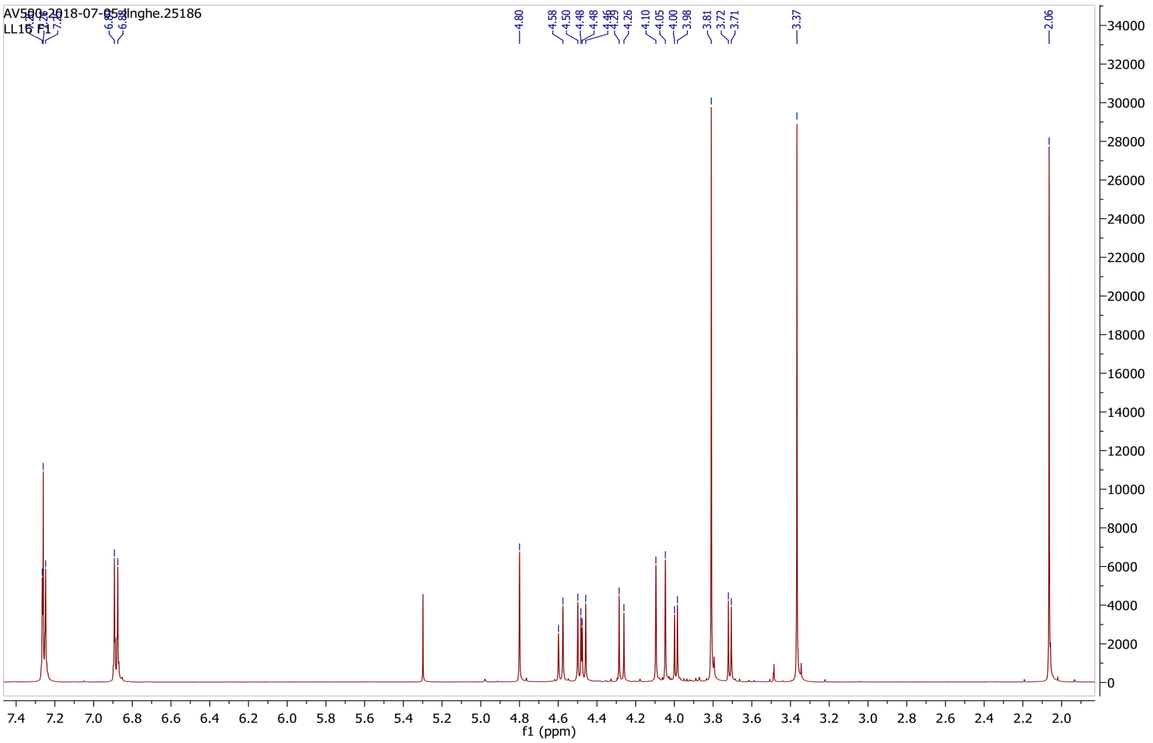

*Fig. 225 ^{1}H spectrum of compound **32**.*

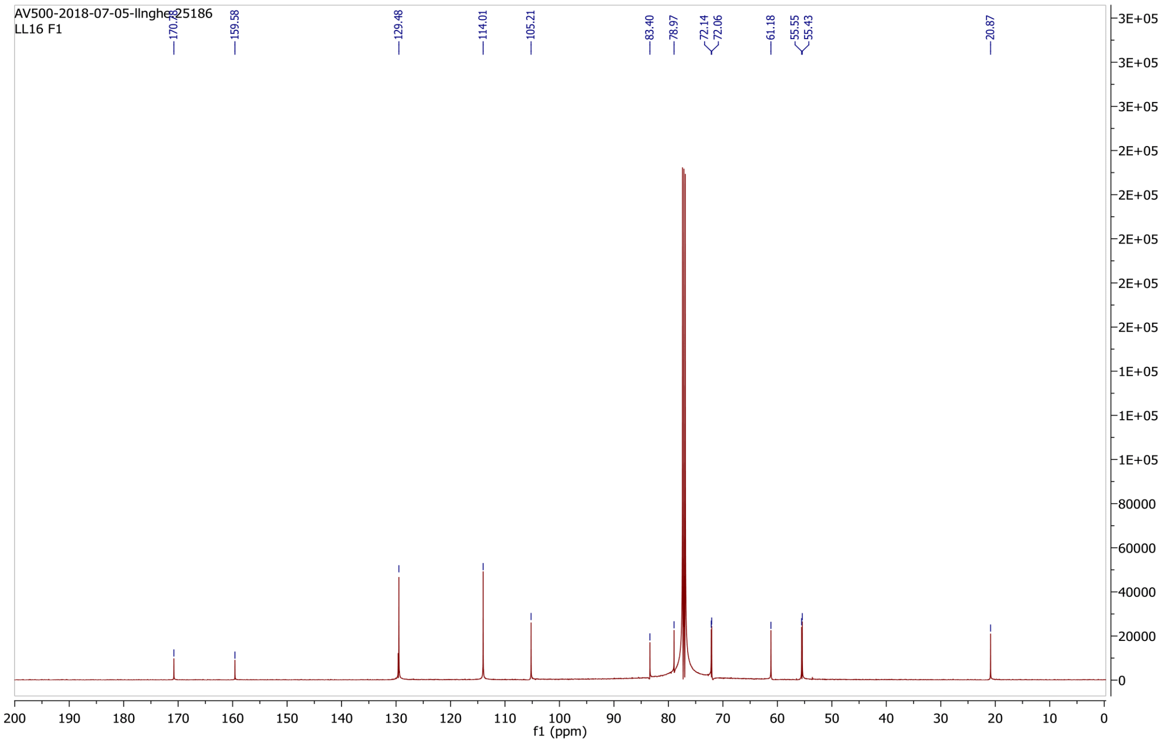

*Fig. 226 ^{13}C spectrum of compound **32**.*

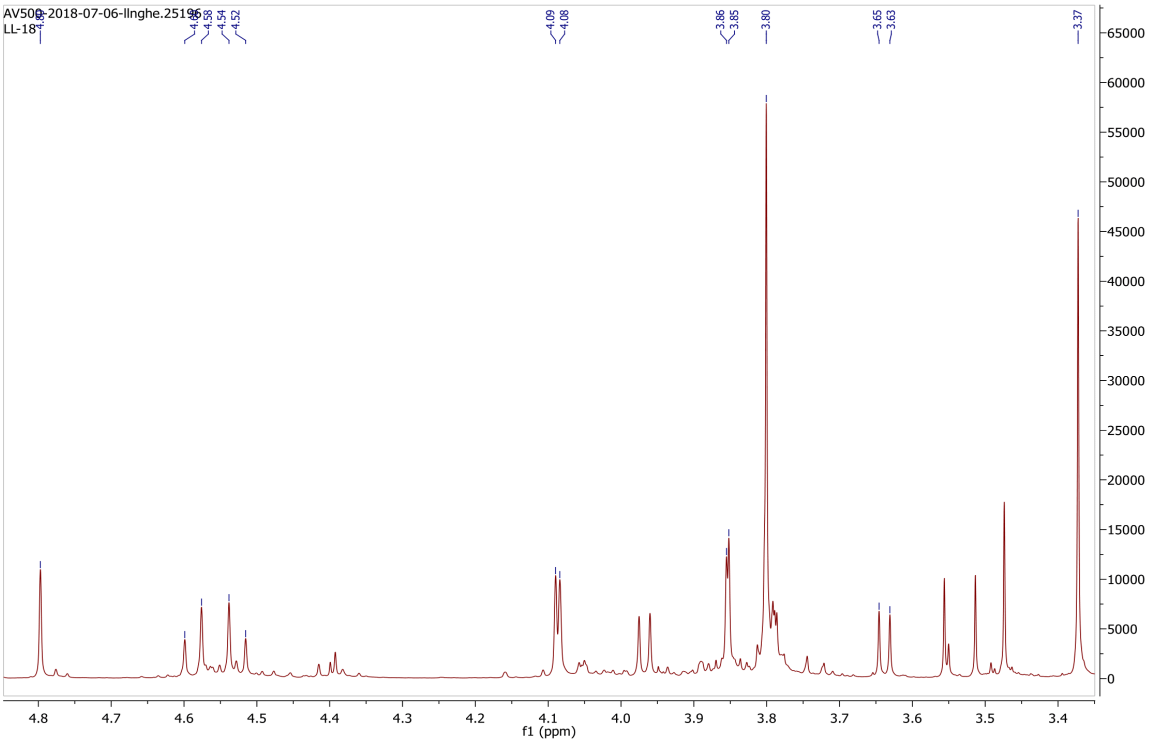

Fig. 227 ^{1}H spectrum of compound ***33****.*

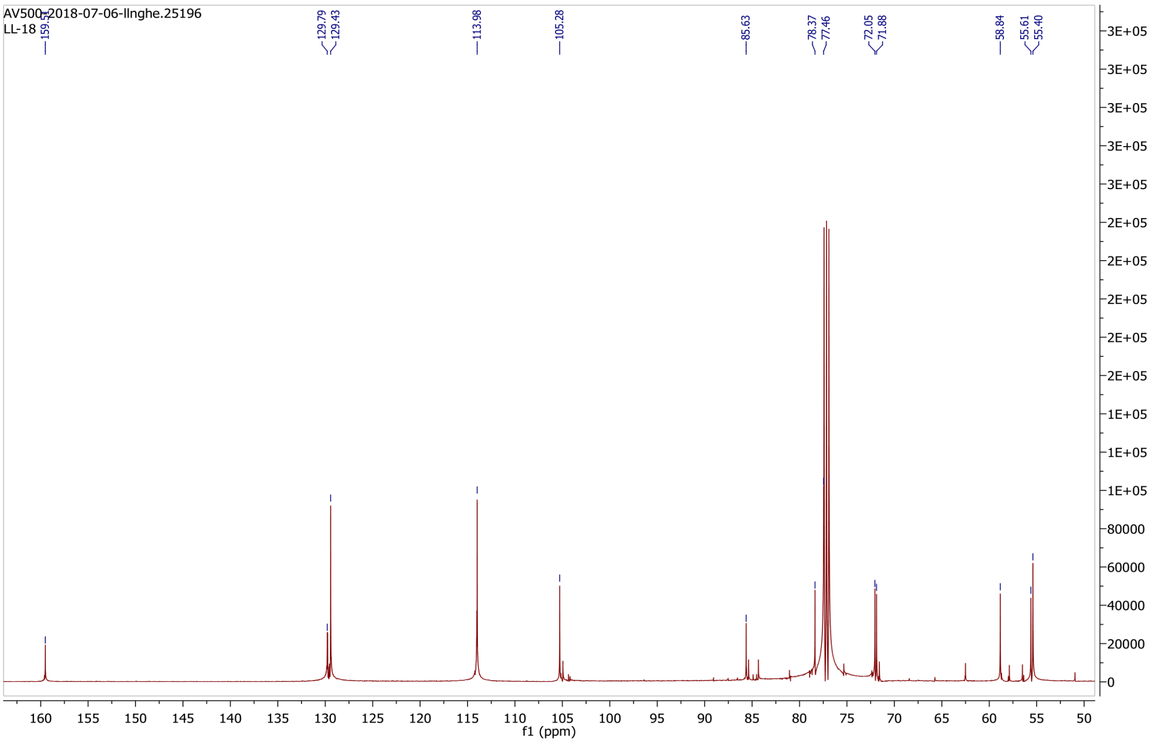

Fig. 228 ^{13}C spectrum of compound ***33****.*

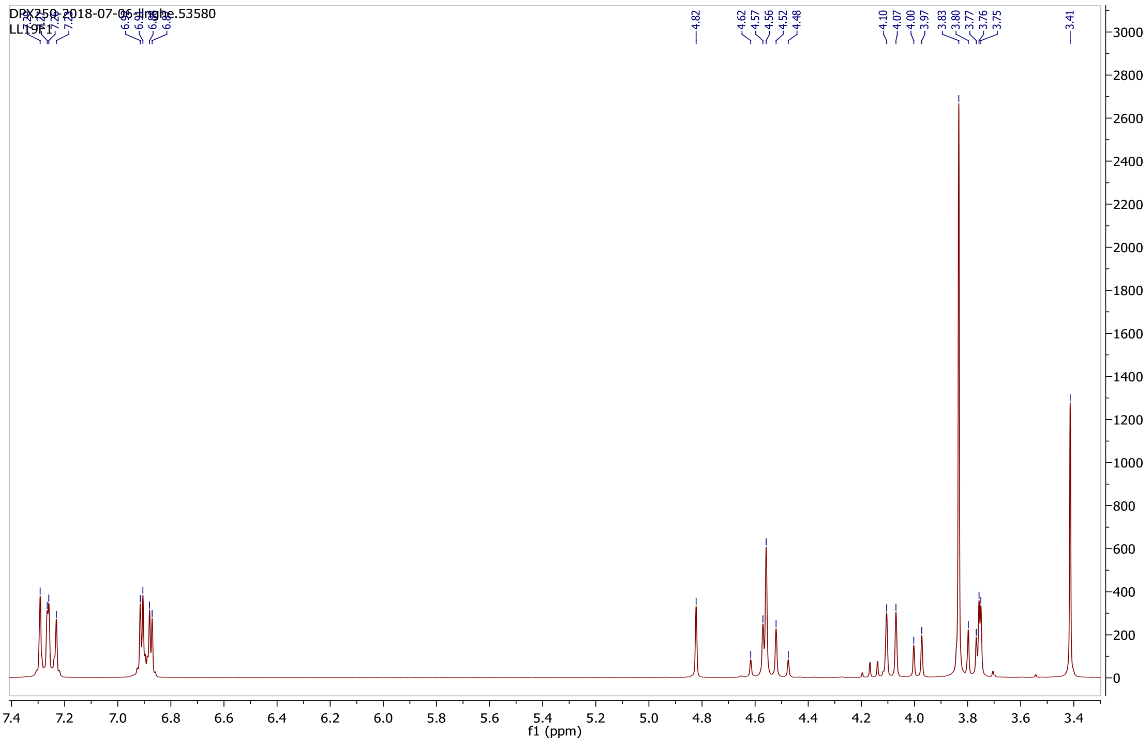

Fig. 229 ^{1}H spectrum of compound **34**.

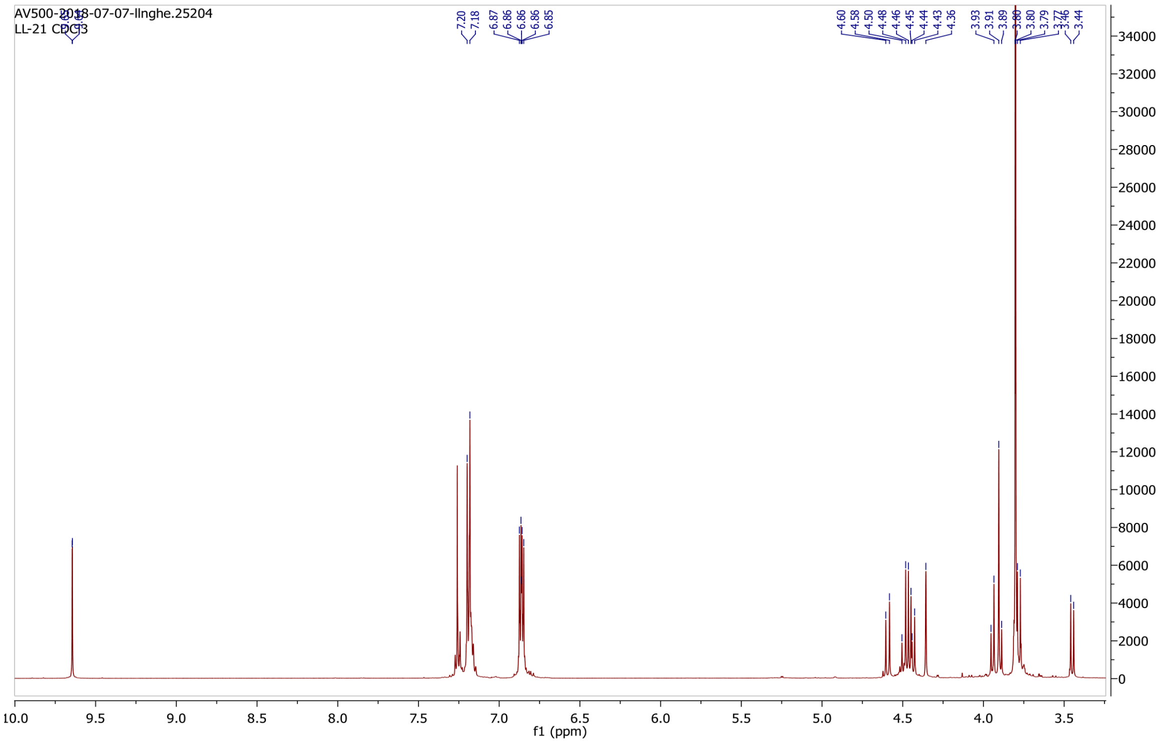

Fig. 230 ^{1}H spectrum of compound **35**.

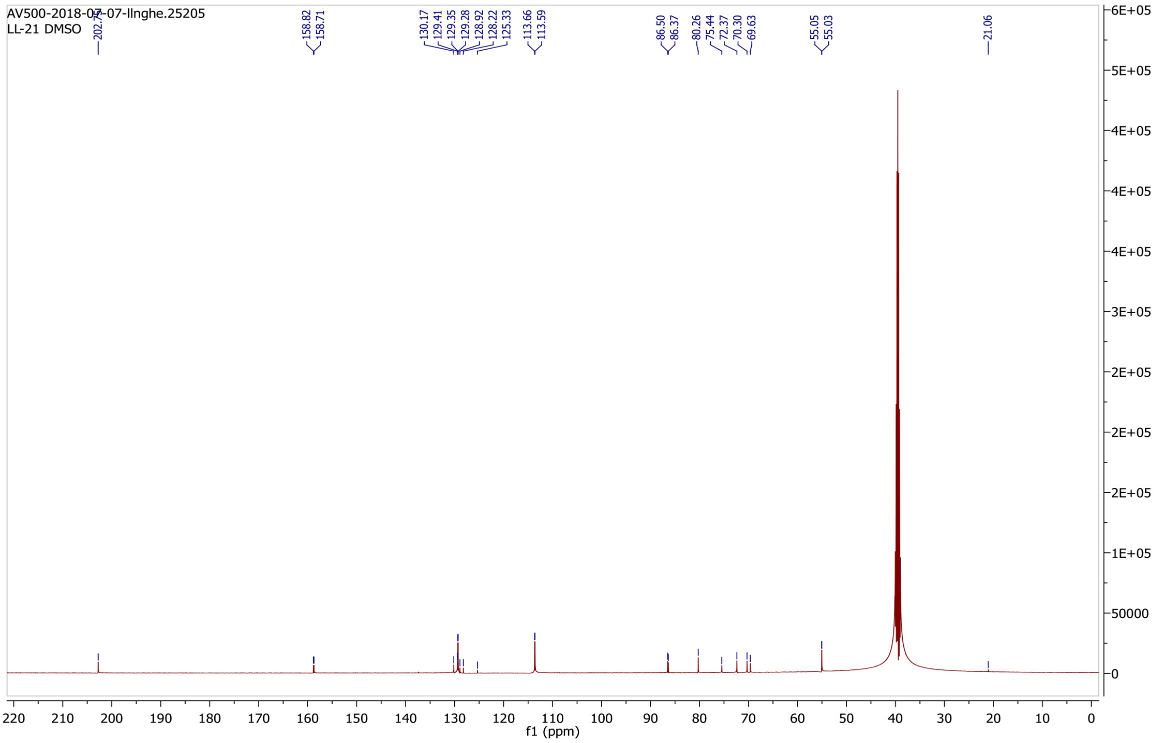

Fig. 231 ^{13}C spectrum of compound **35**.

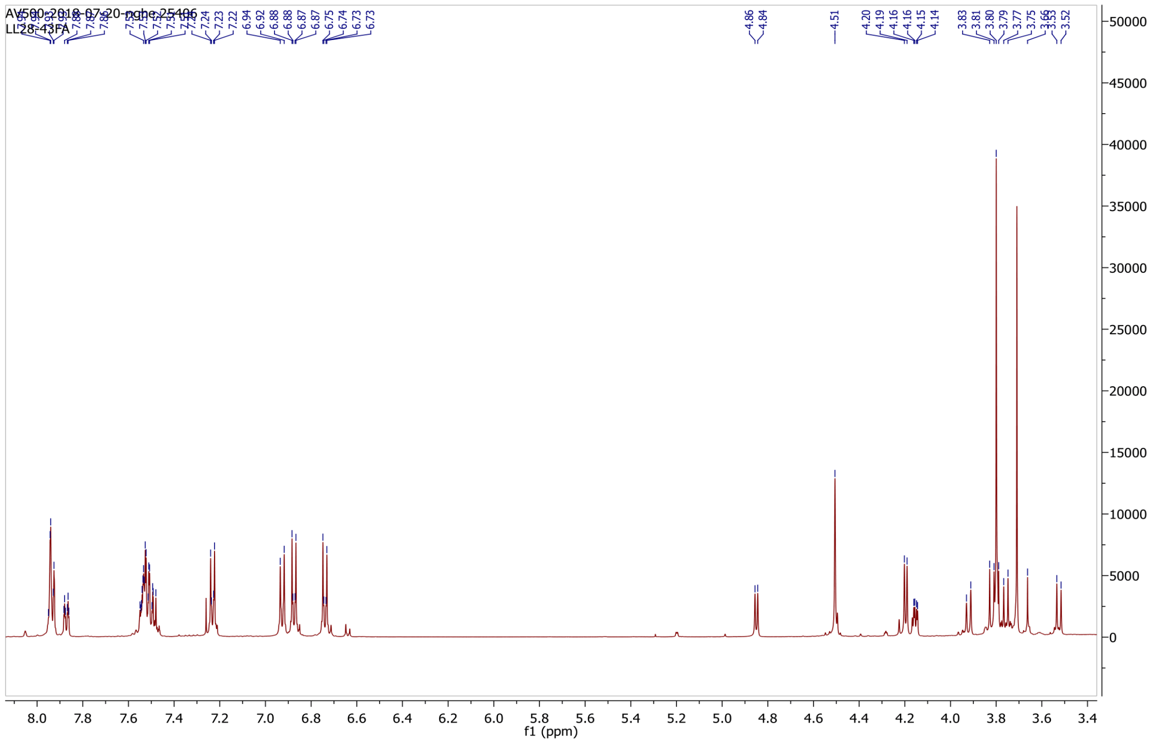

Fig. 232 ^{1}H spectrum of compound **36**.

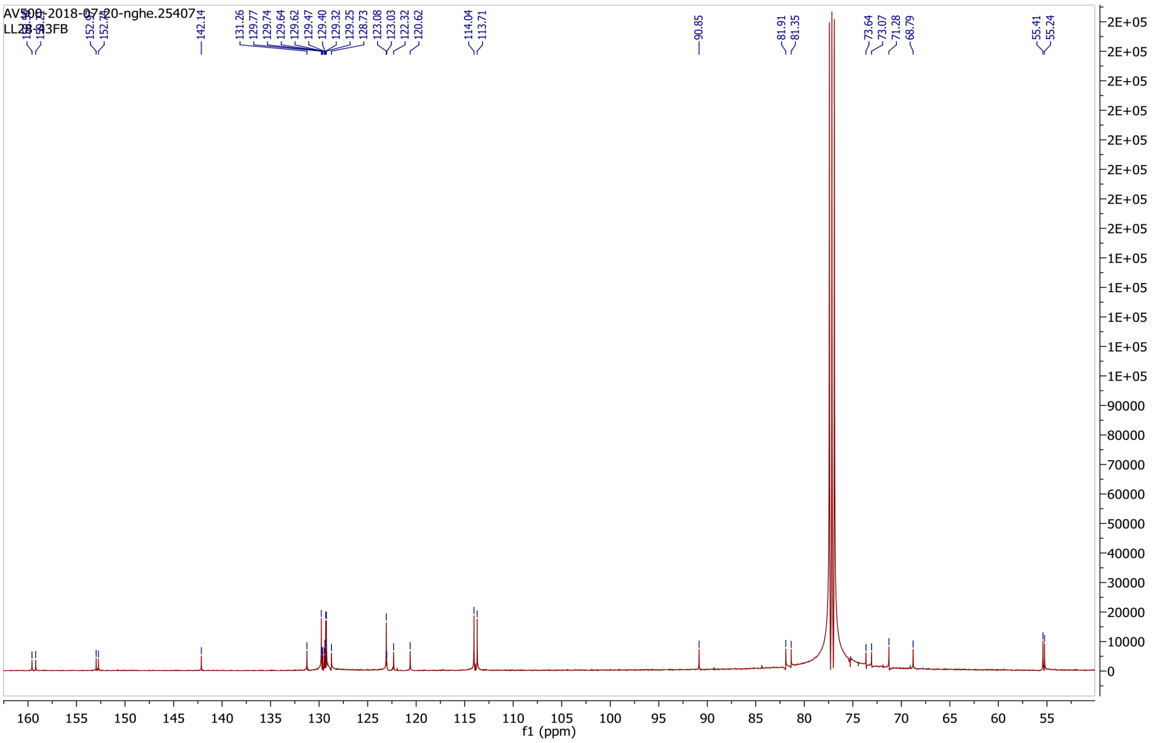

Fig. 233 ^{13}C spectrum of compound **36**.

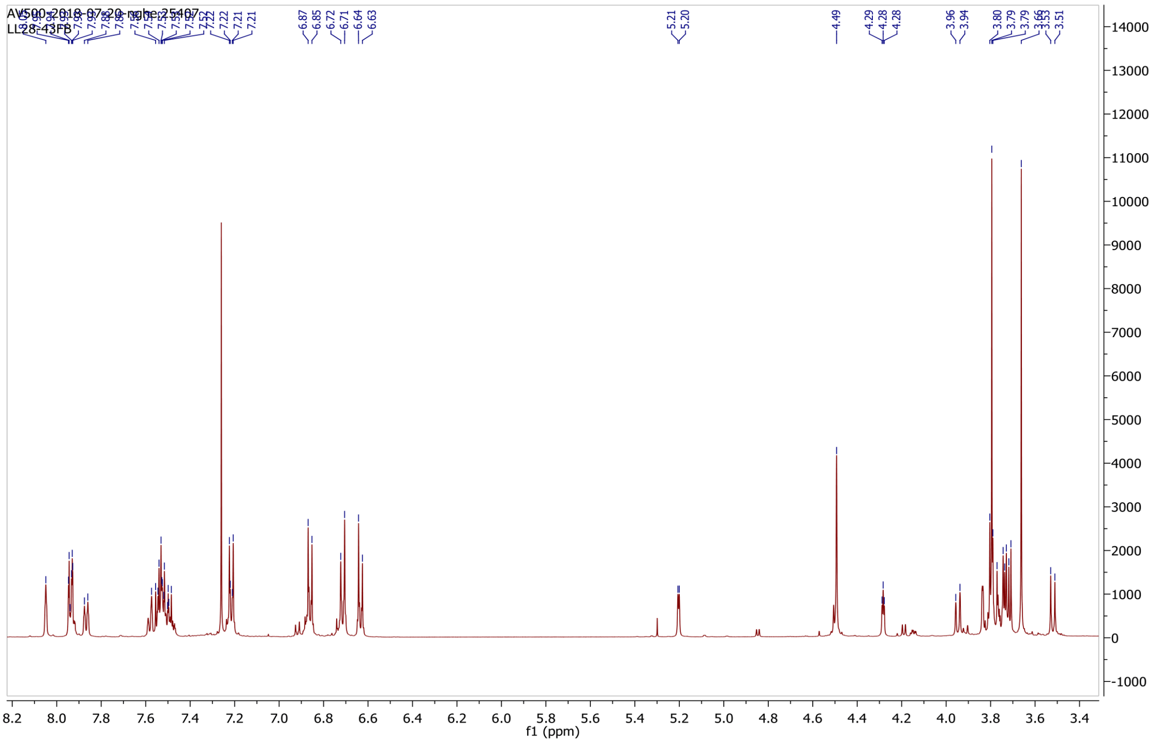

Fig. 234 ^{1}H spectrum of compound **37**.

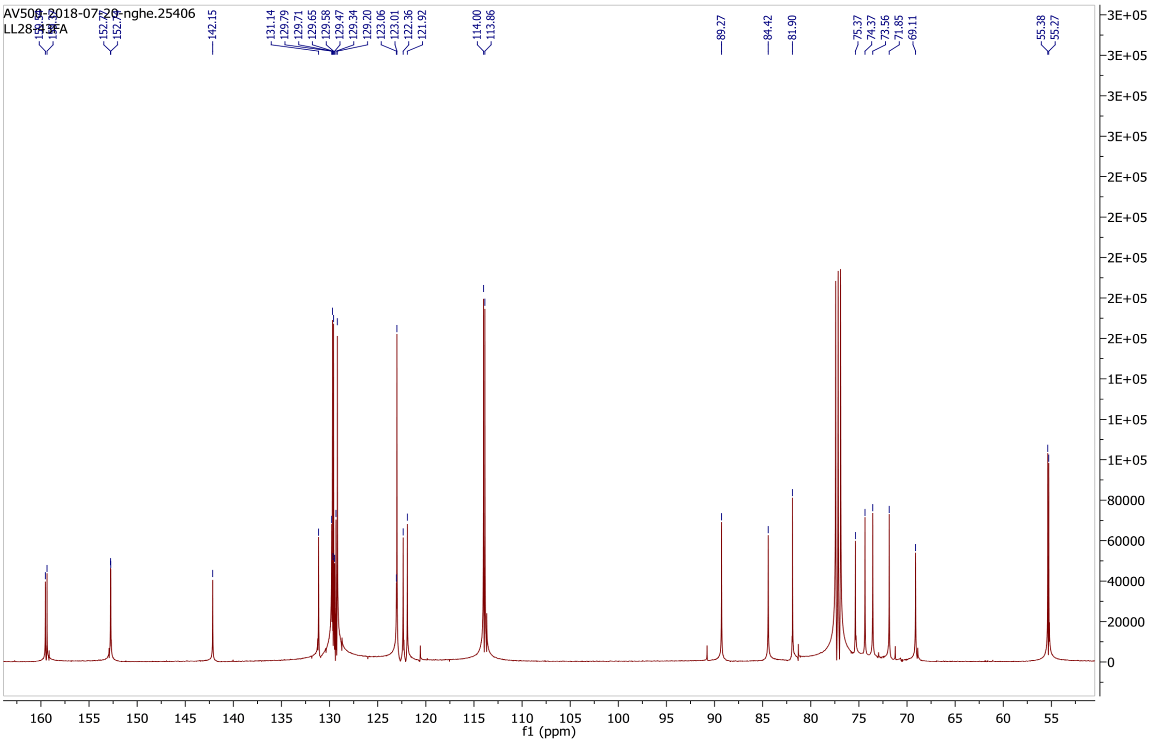

Fig. 235 ^{13}C spectrum of compound **37**.

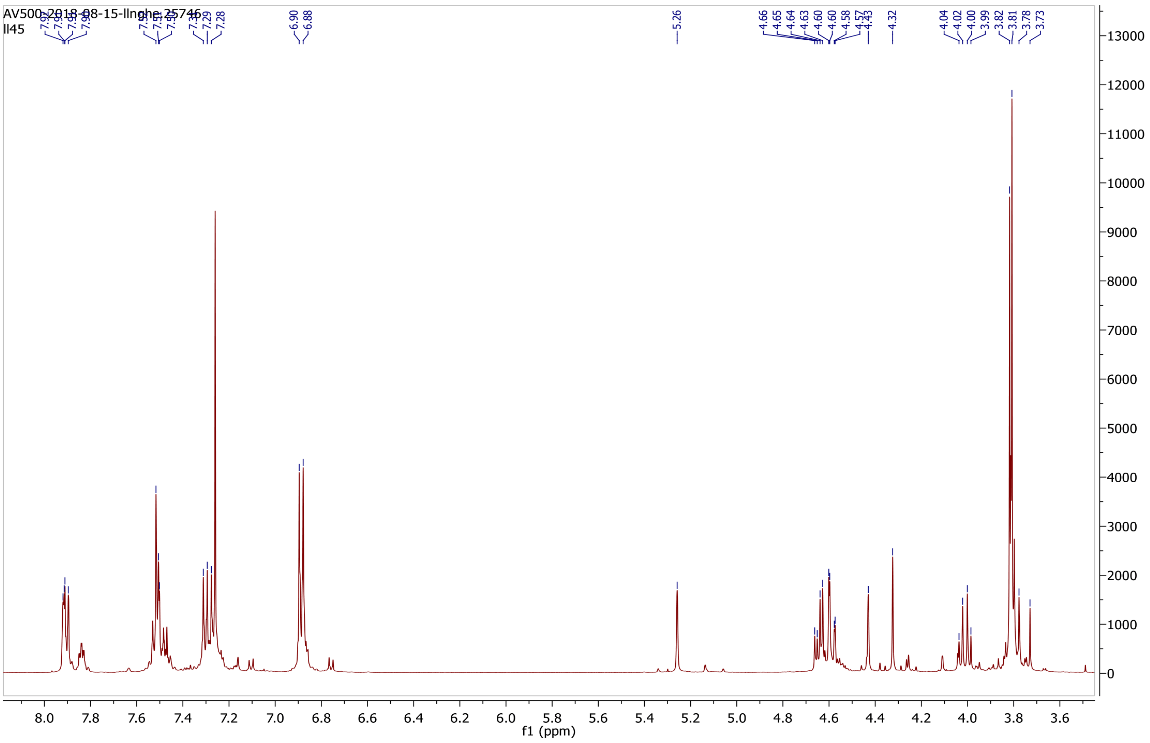

Fig. 236 ^{1}H spectrum of compound **38**.

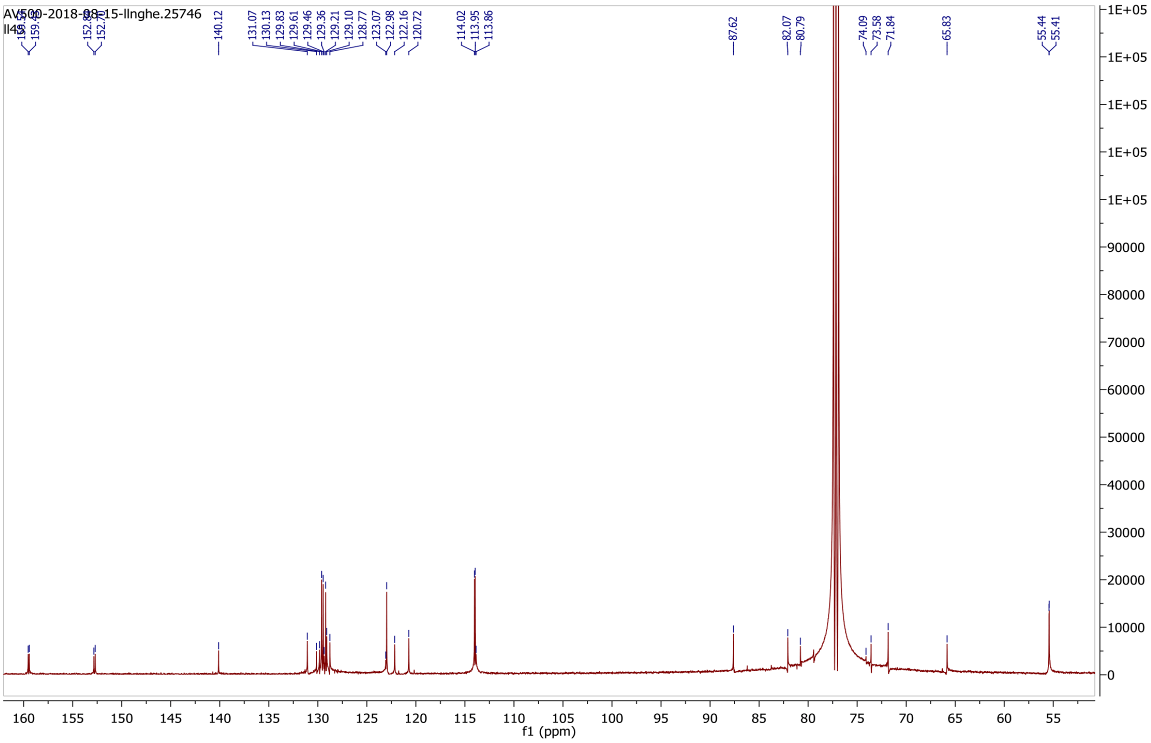

Fig. 237 ^{13}C spectrum of compound **38**.

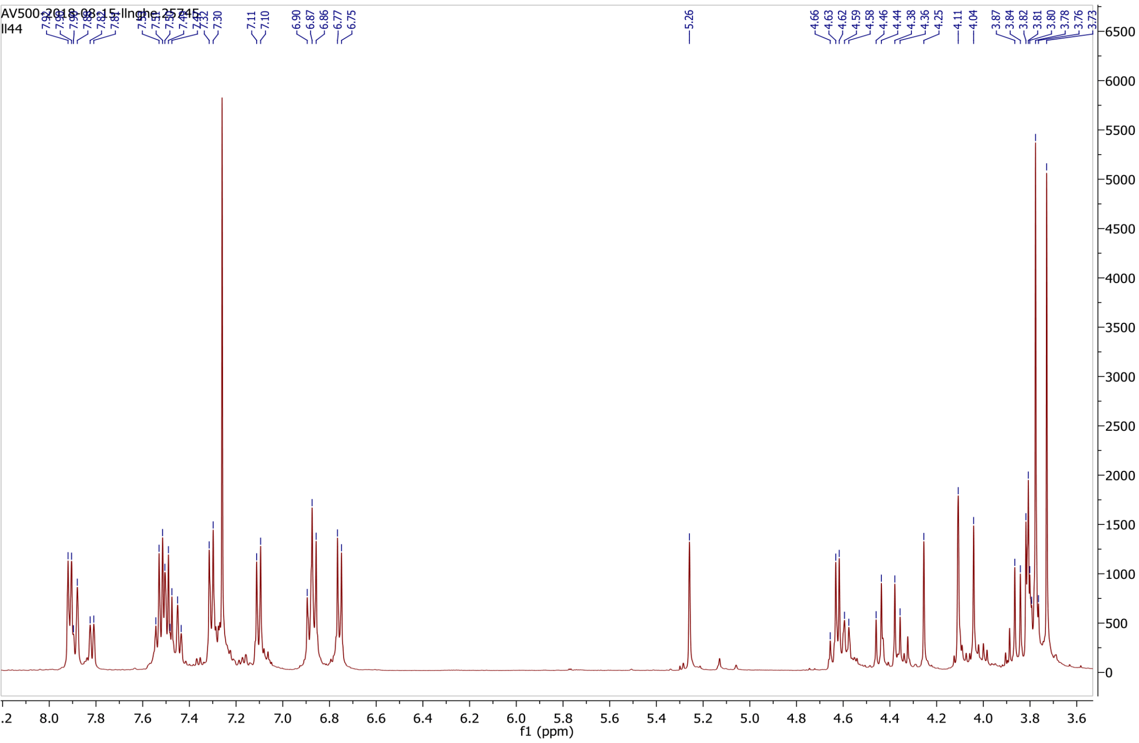

Fig. 238 ^{1}H spectrum of compound **39**.

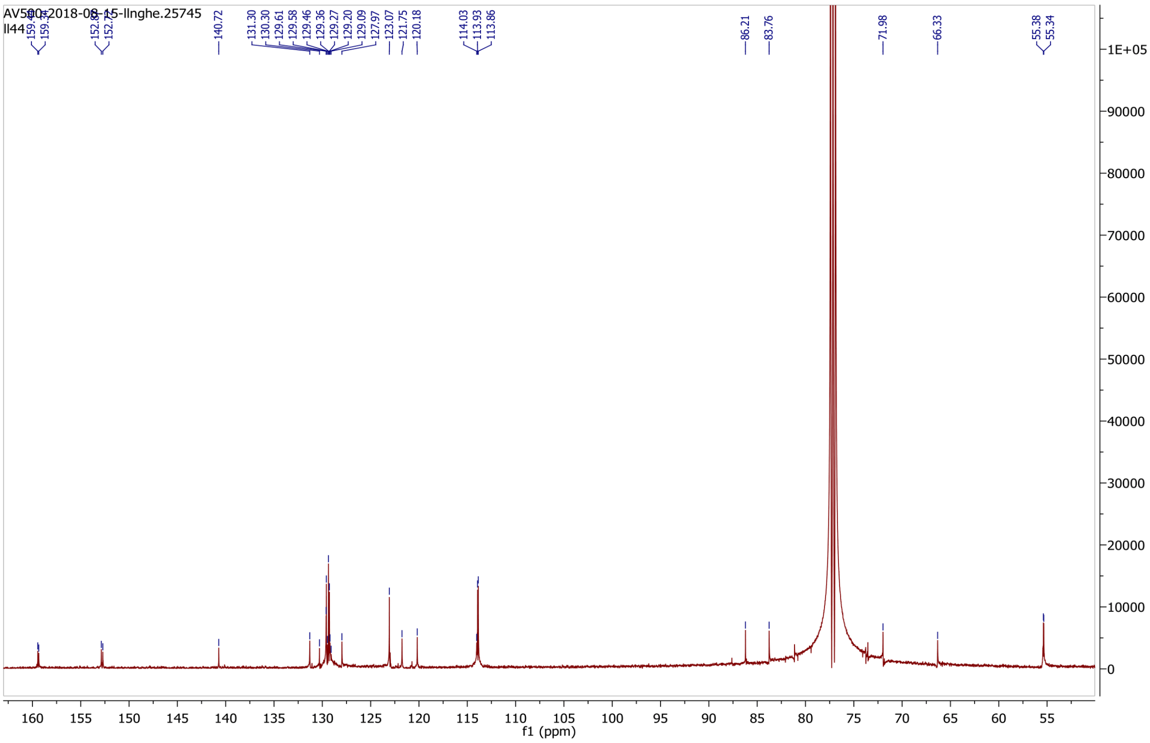

Fig. 239 ^{13}C spectrum of compound **39**.

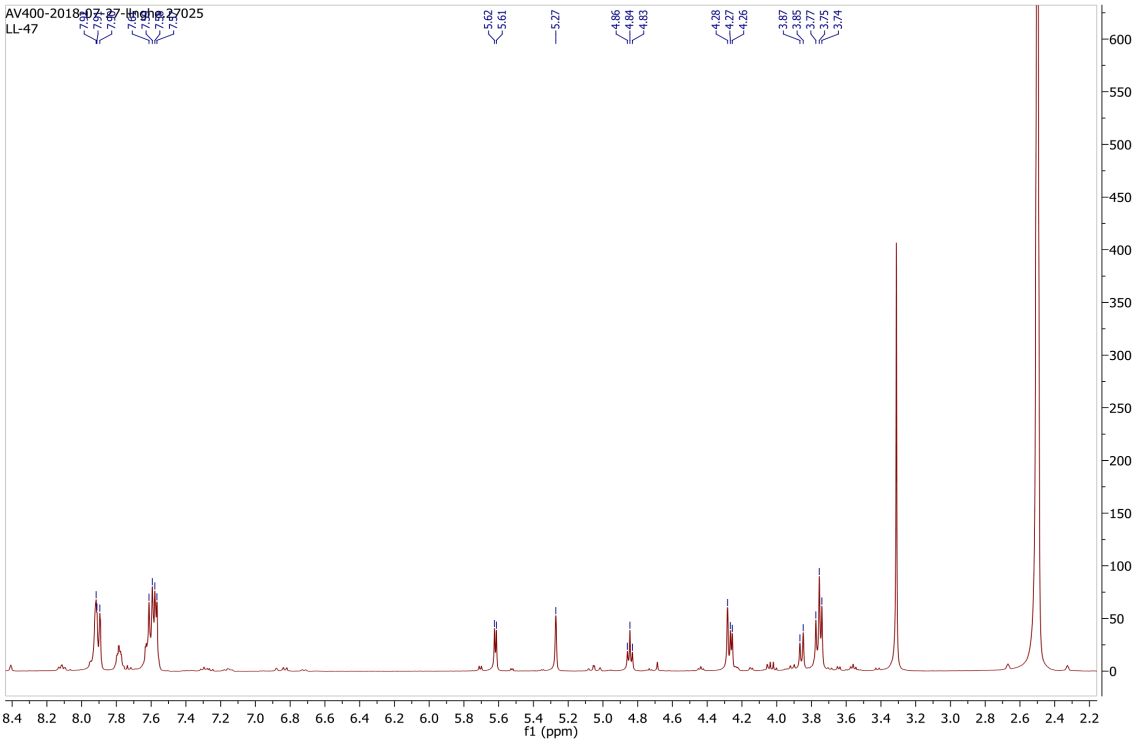

Fig. 240 ^{1}H spectrum of compound **40**.

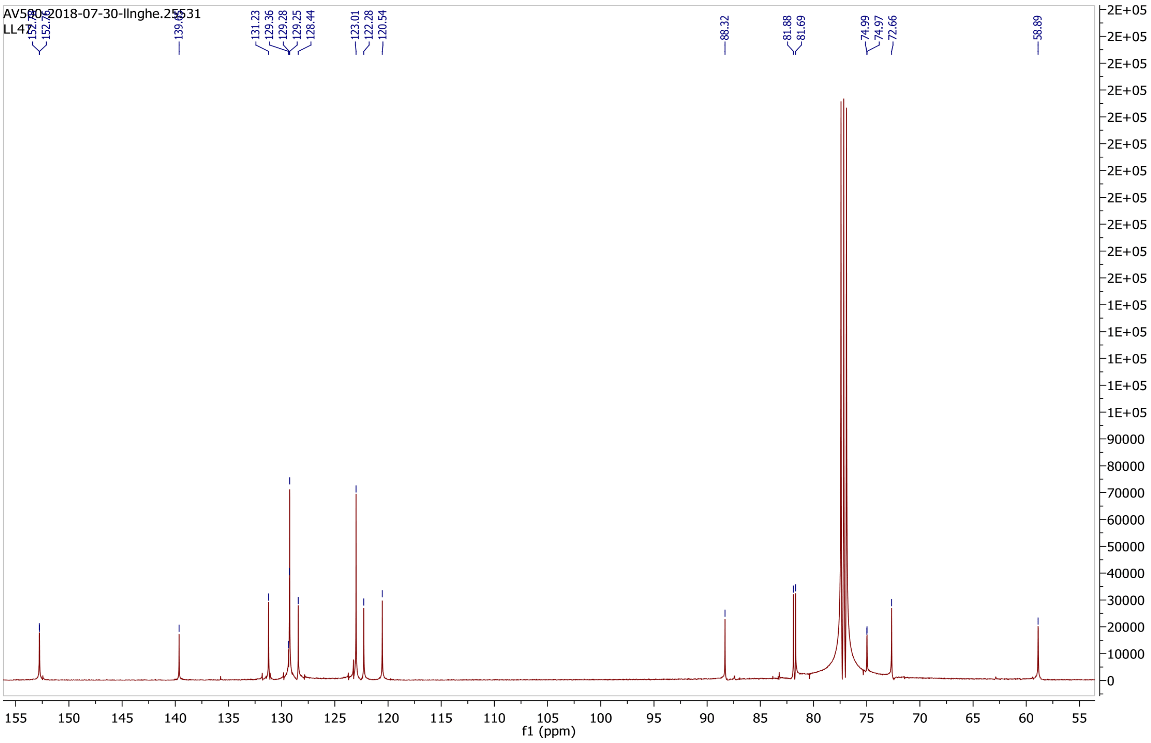

Fig. 241 ^{13}C spectrum of compound **40**.

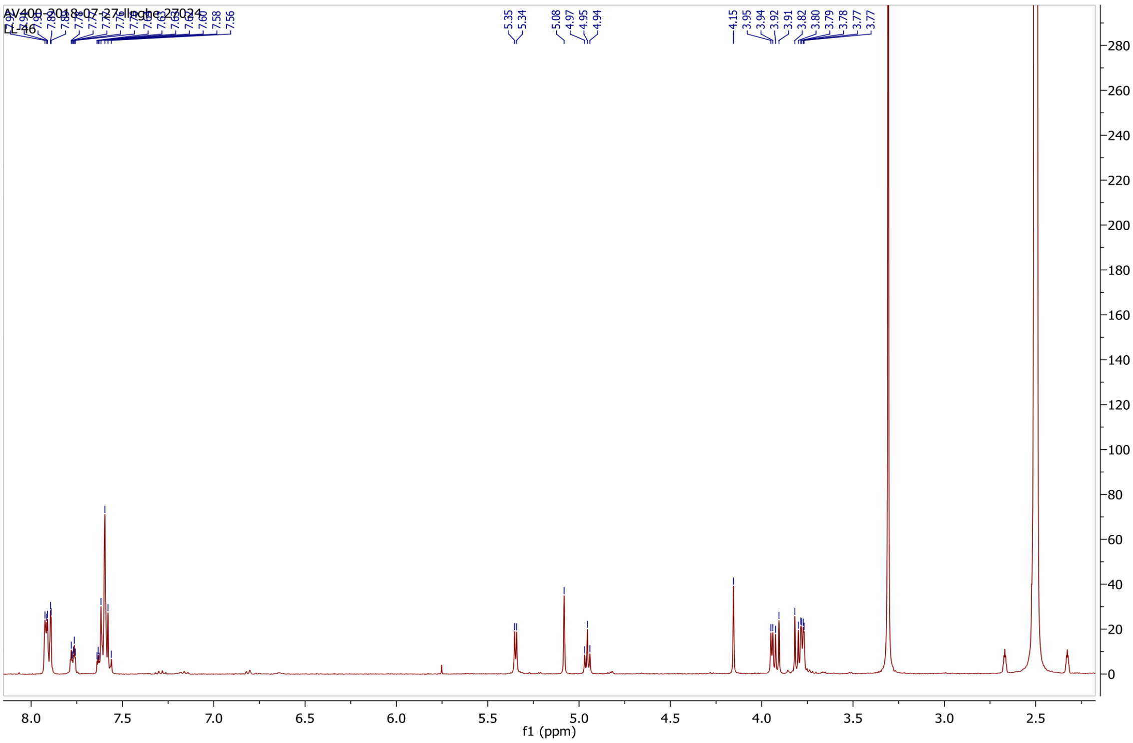

Fig. 242 ^{1}H spectrum of compound **41**.

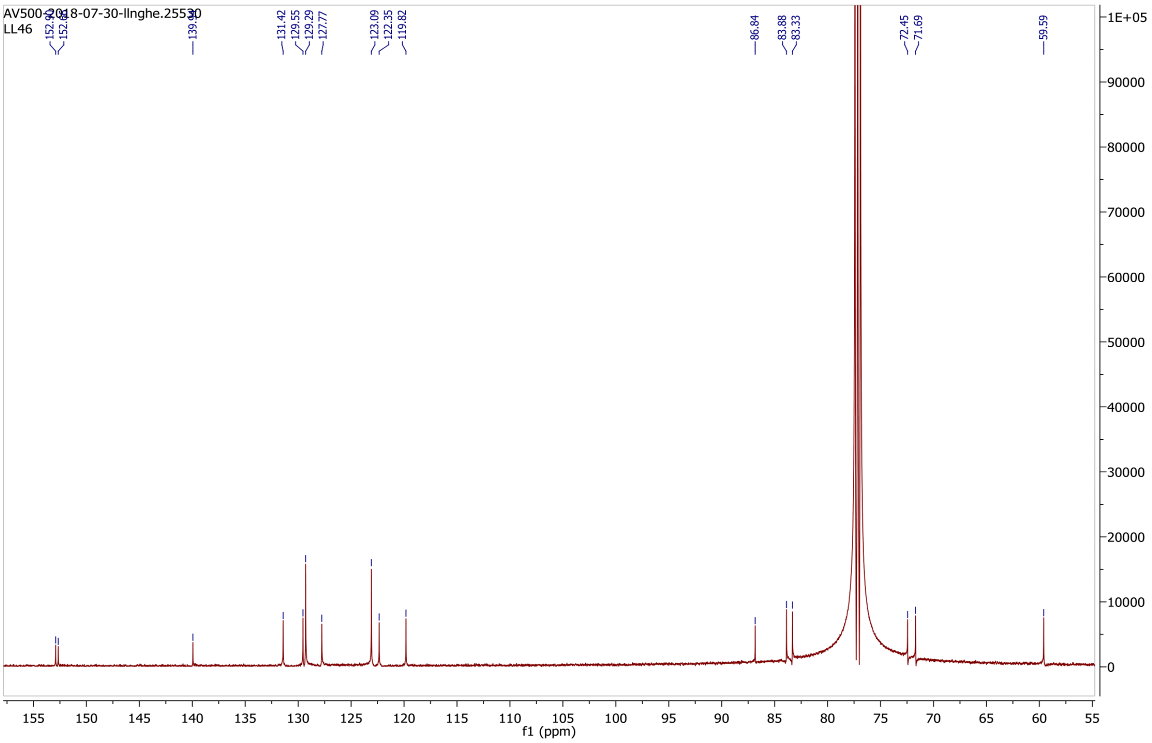

Fig. 243 ^{13}C spectrum of compound **41**.

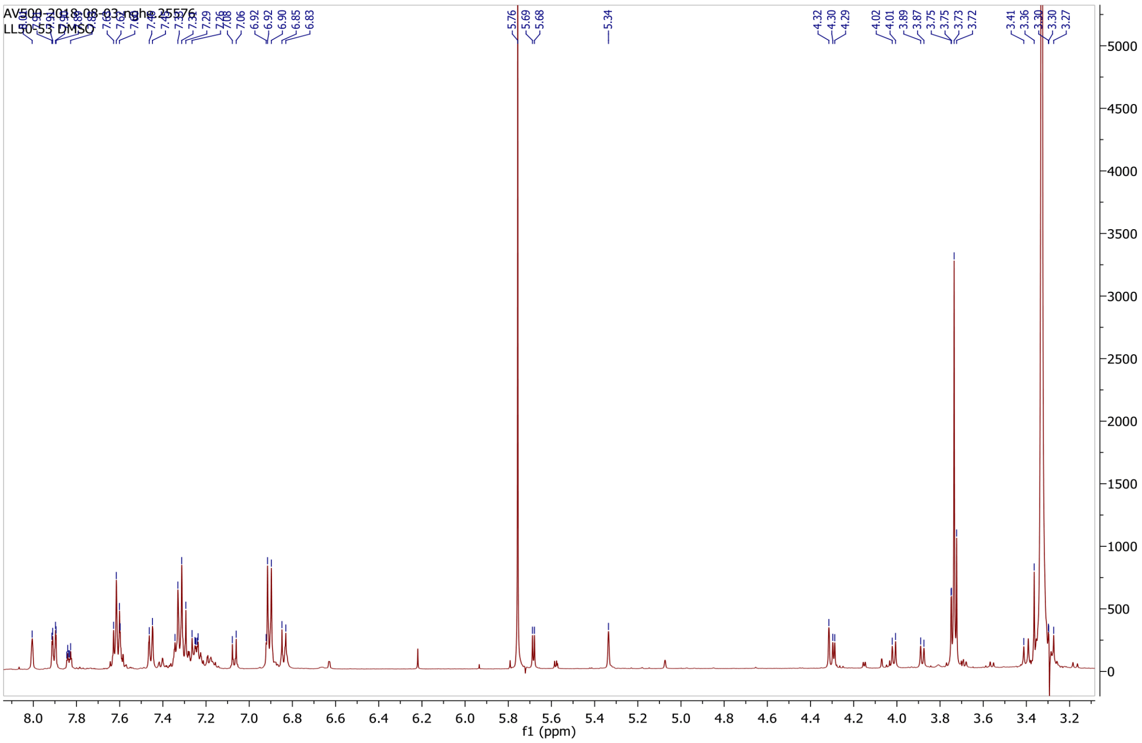

Fig. 244 ^{1}H spectrum of compound **42**.

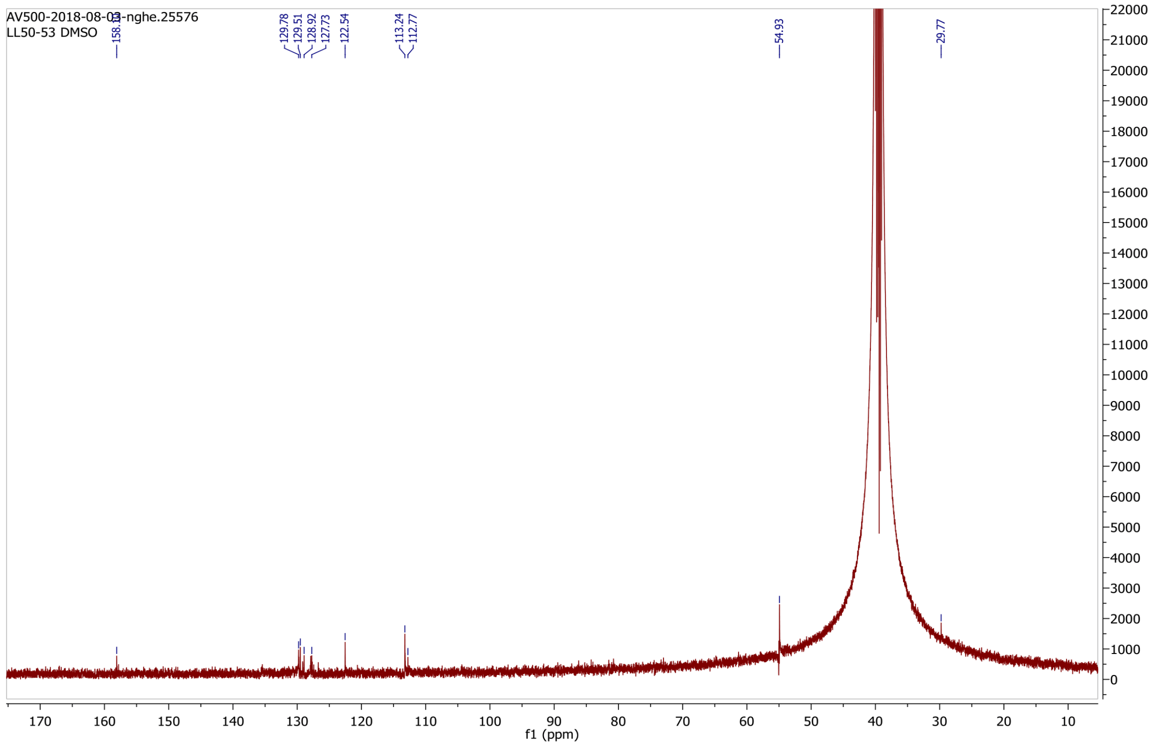

Fig. 245 ^{13}C spectrum of compound **42**.

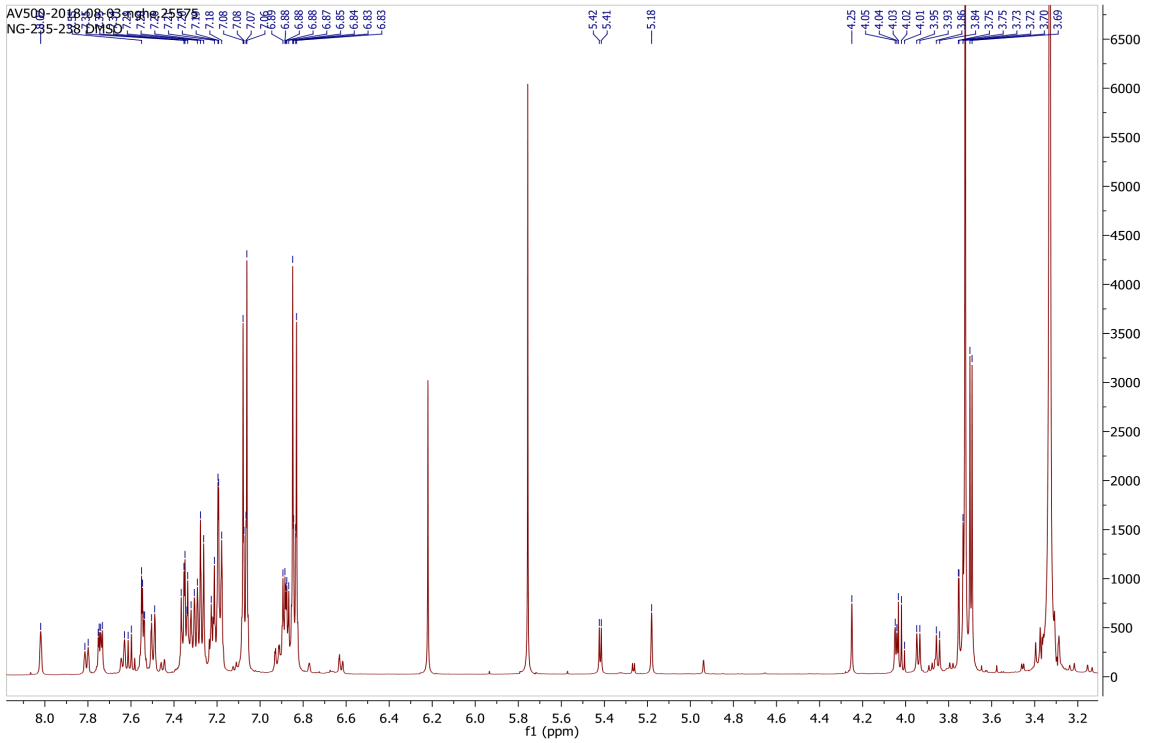

Fig. 246 ^{1}H spectrum of compound **43**.

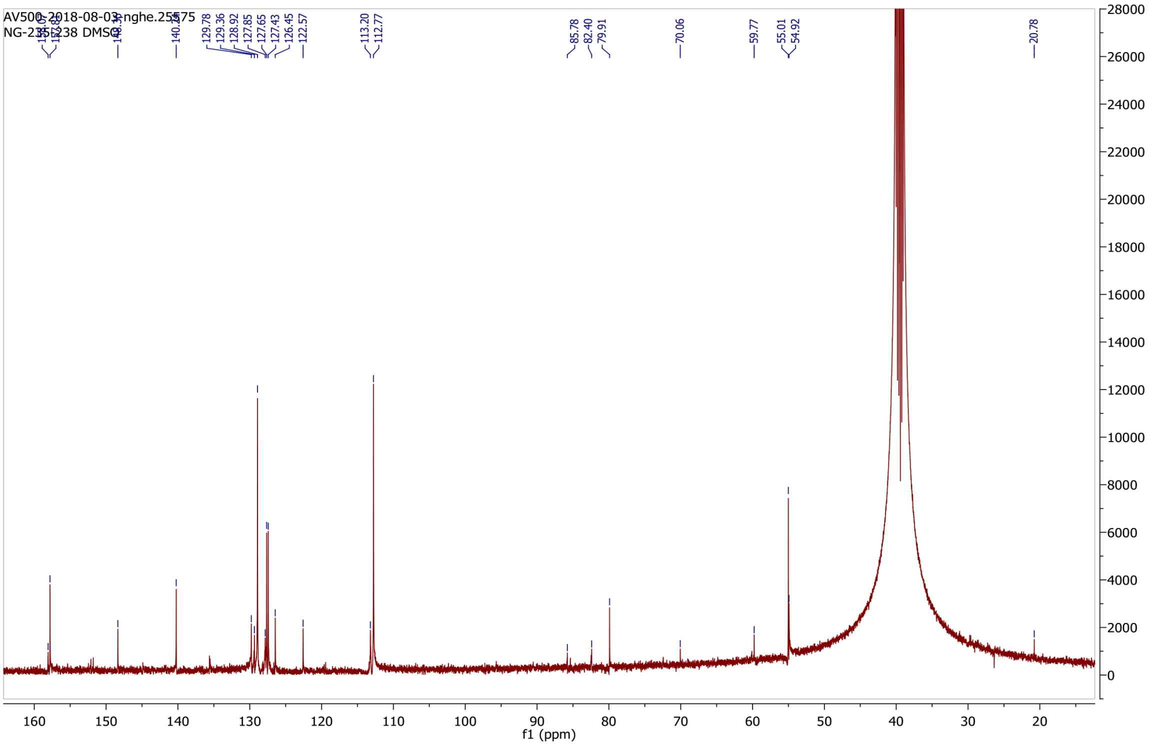

Fig. 247 ^{13}C spectrum of compound **43**.

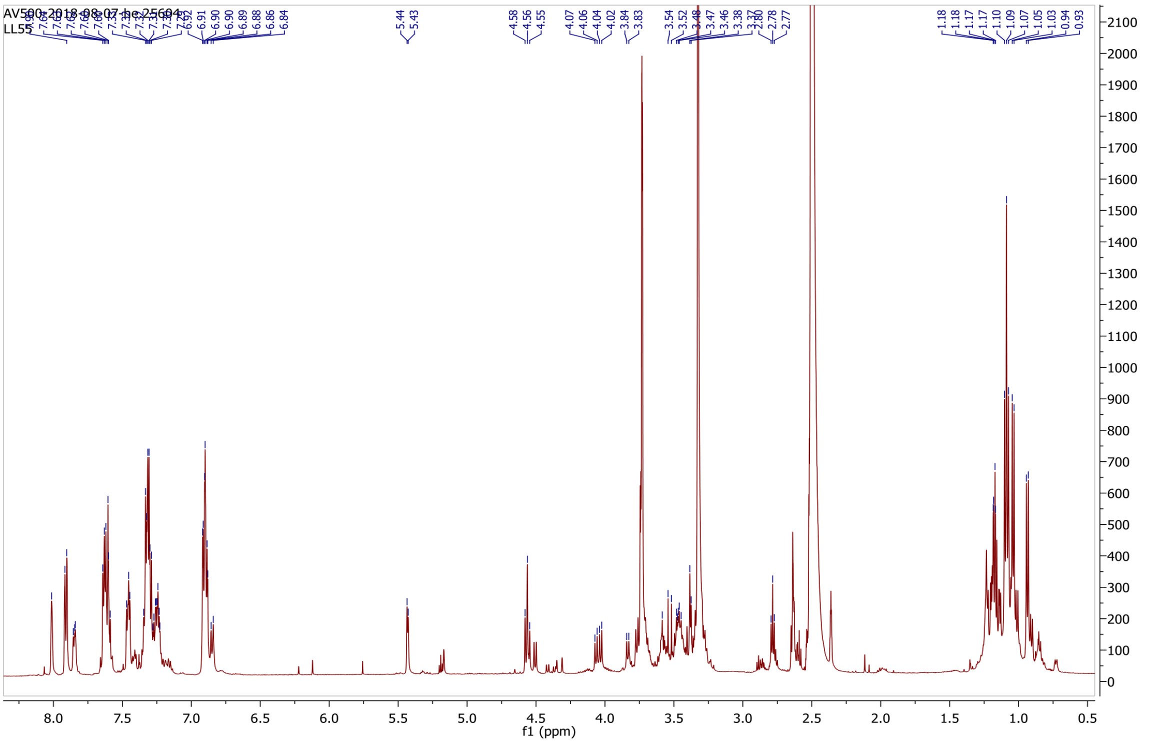

Fig. 248 ^{1}H spectrum of compound **44**.

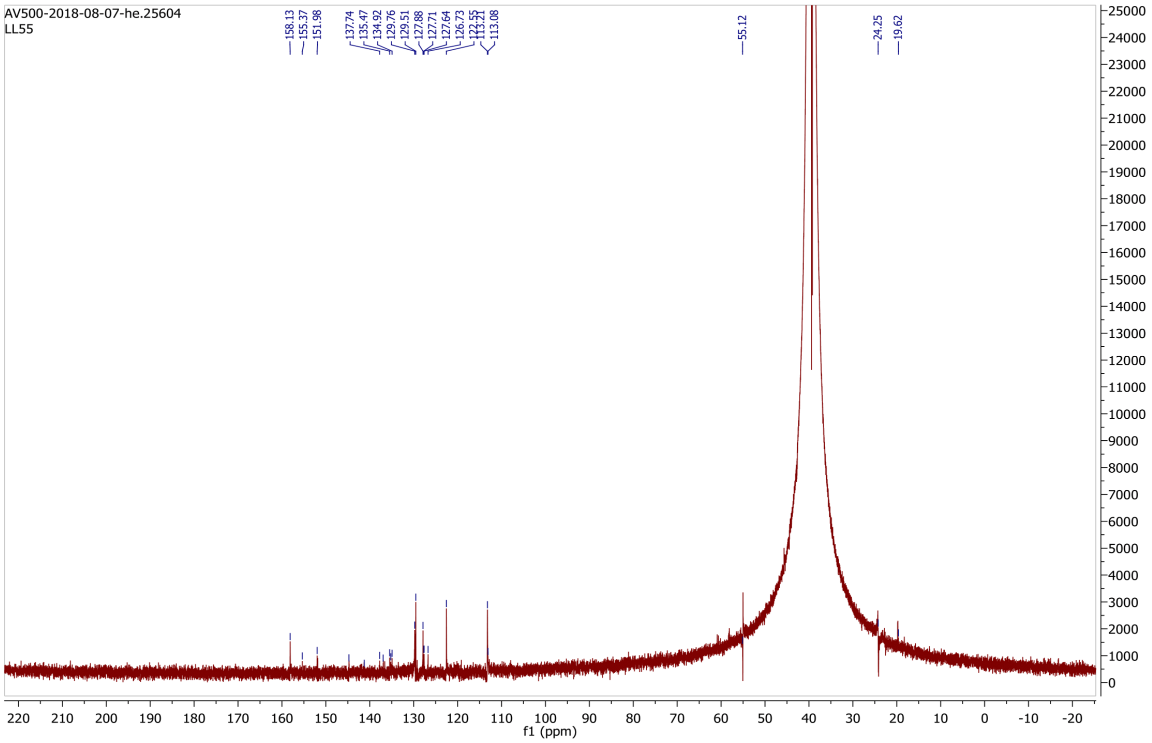

*Fig. 249 ^{13}C spectrum of compound **44**.*

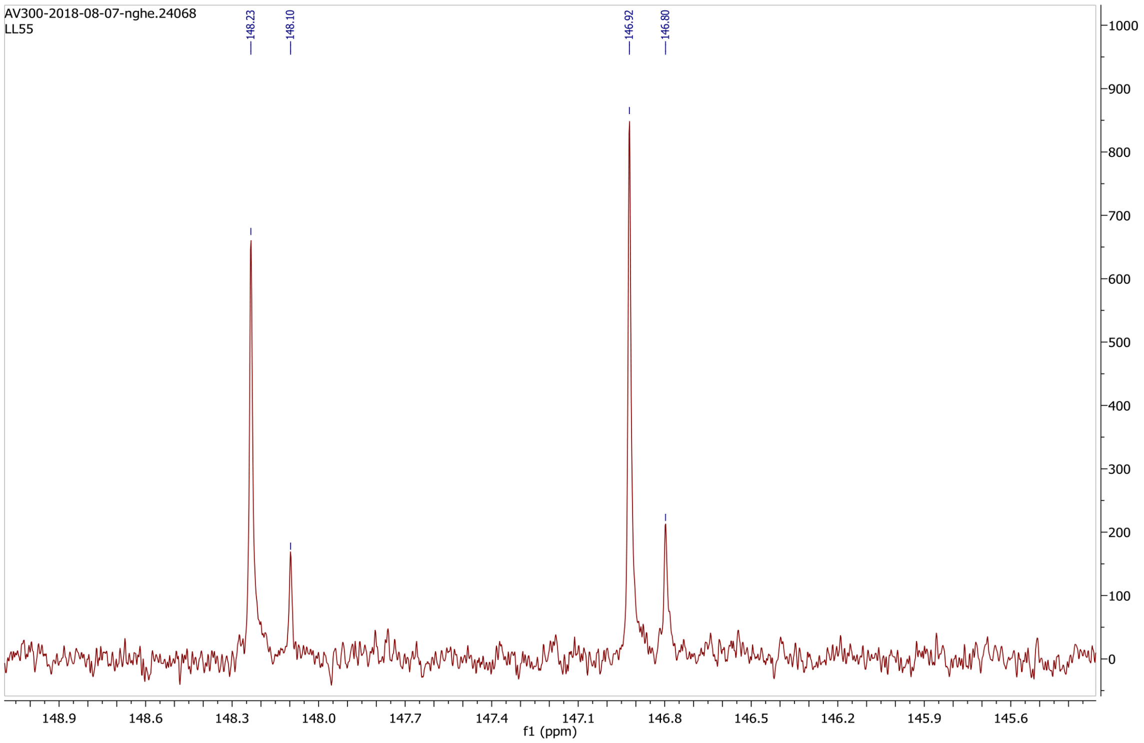

*Fig. 250 ^{31}P spectrum of compound **44**.*

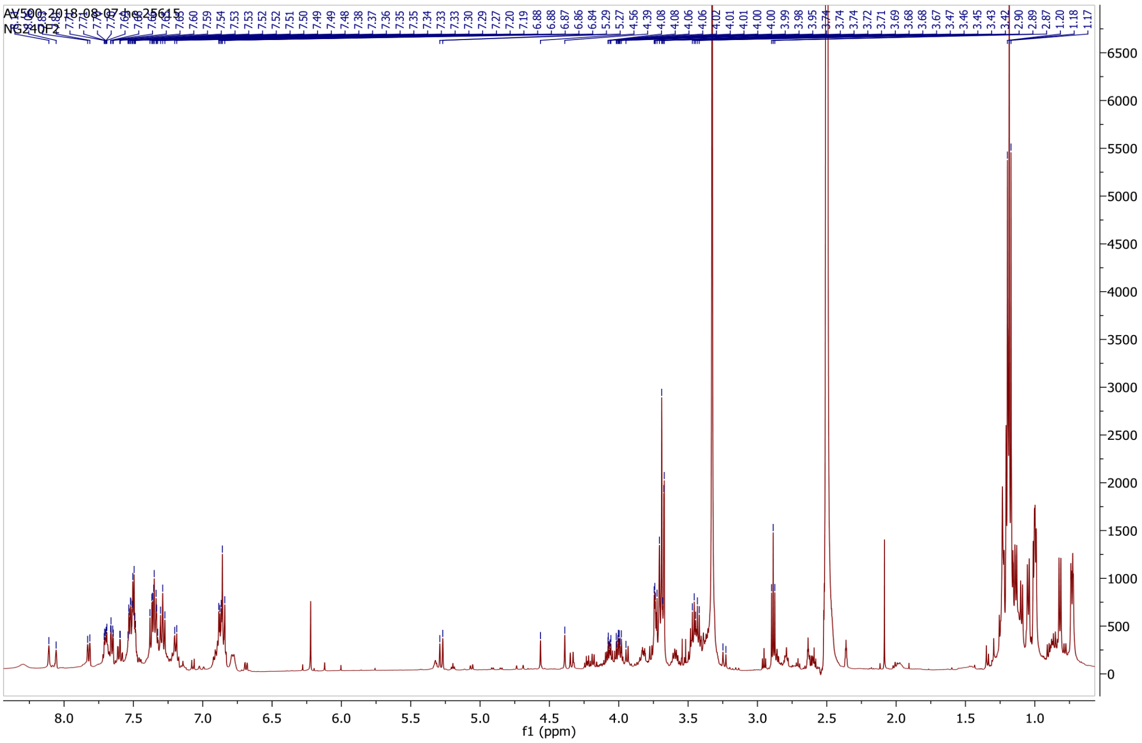

Fig. 251 ^{1}H spectrum of compound **45**.

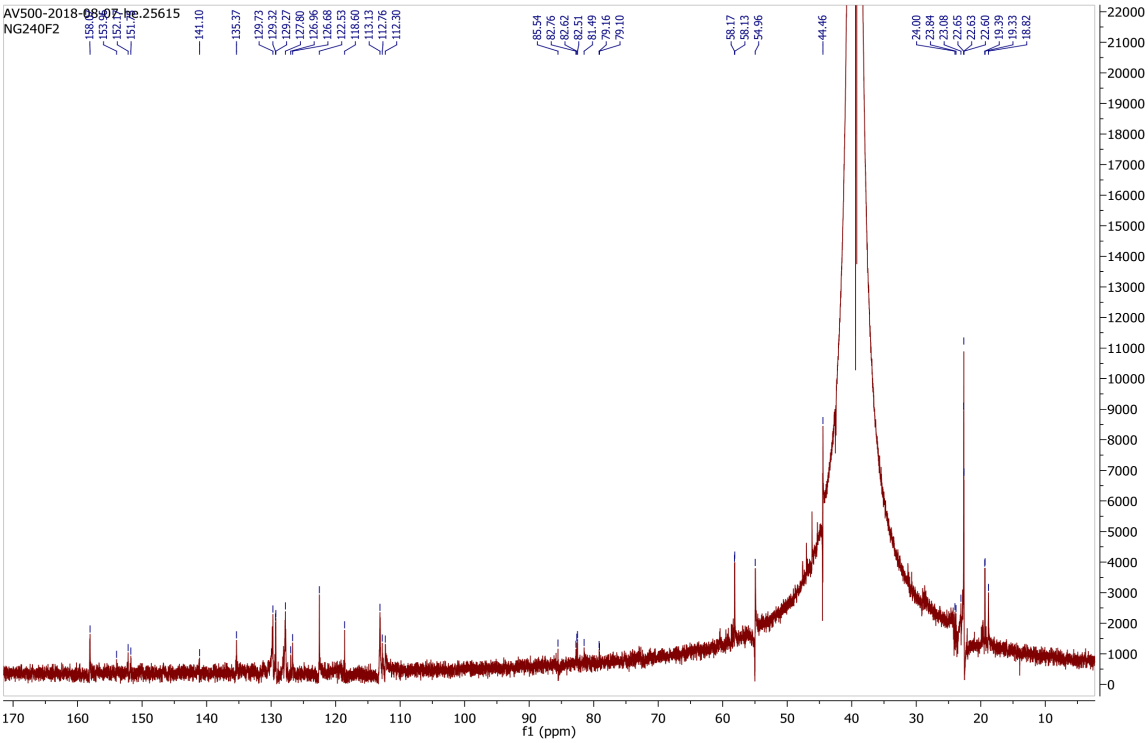

Fig. 252 ^{13}C spectrum of compound **45**.

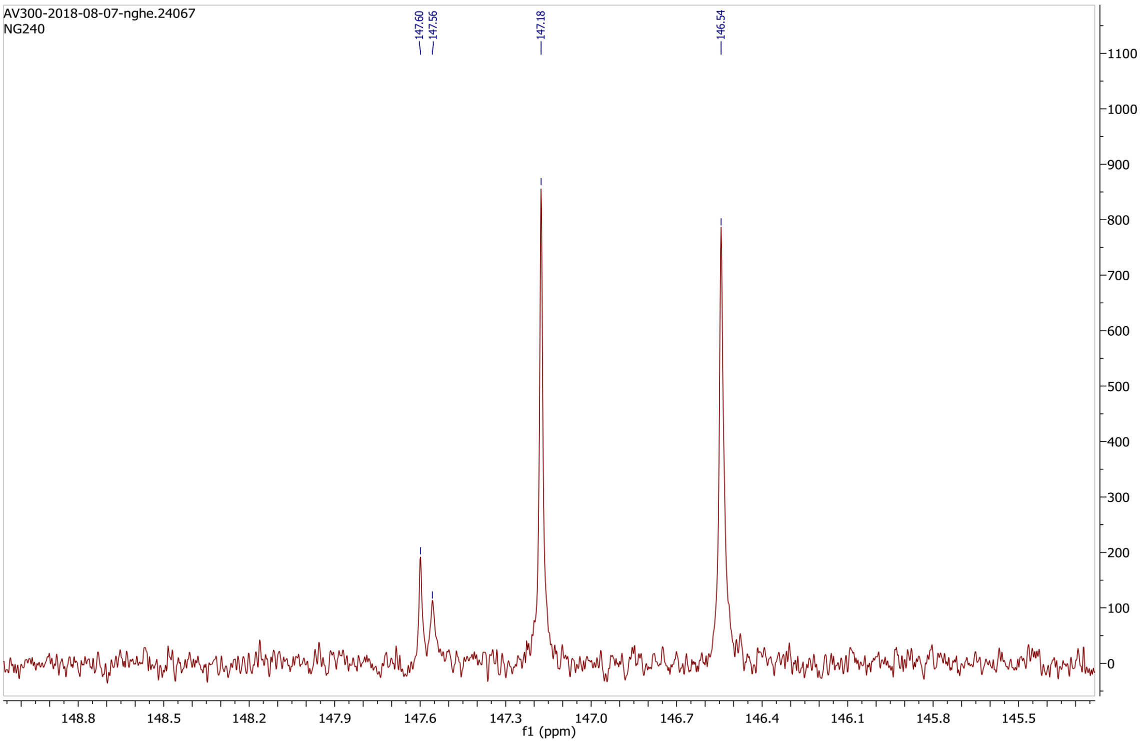

Fig. 253 ^{31}P spectrum of compound **45**.

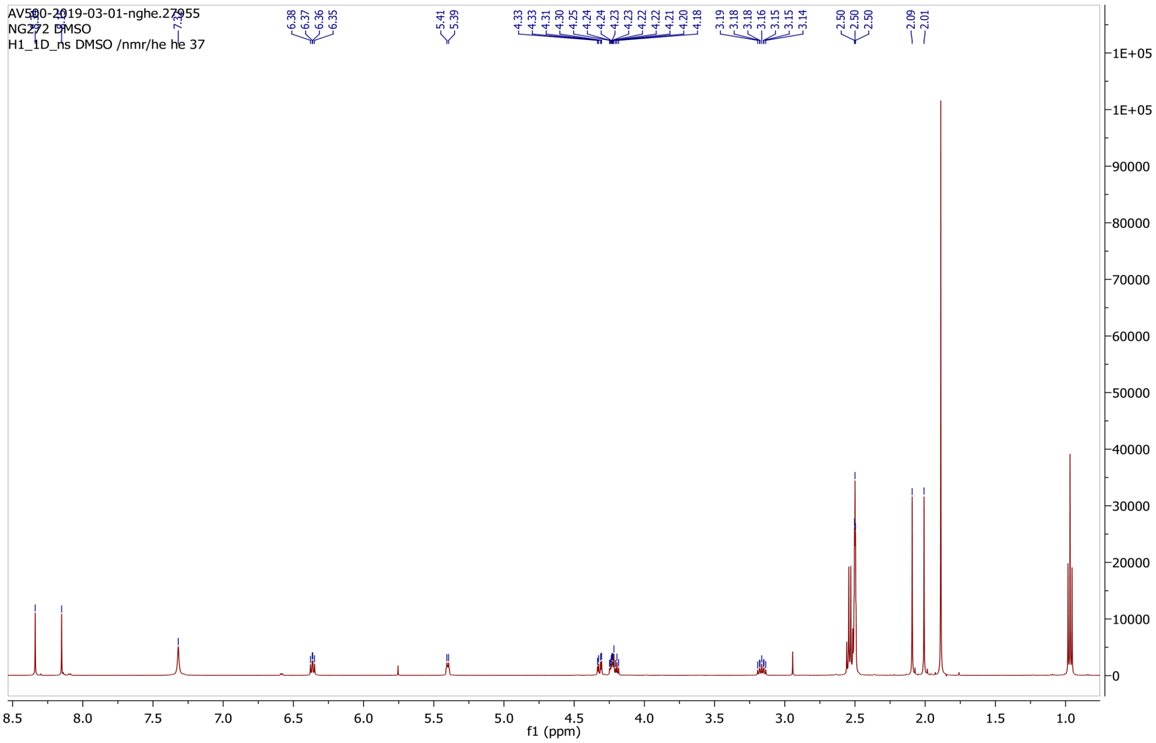

Fig. 254 ^{1}H spectrum of compound **46**.

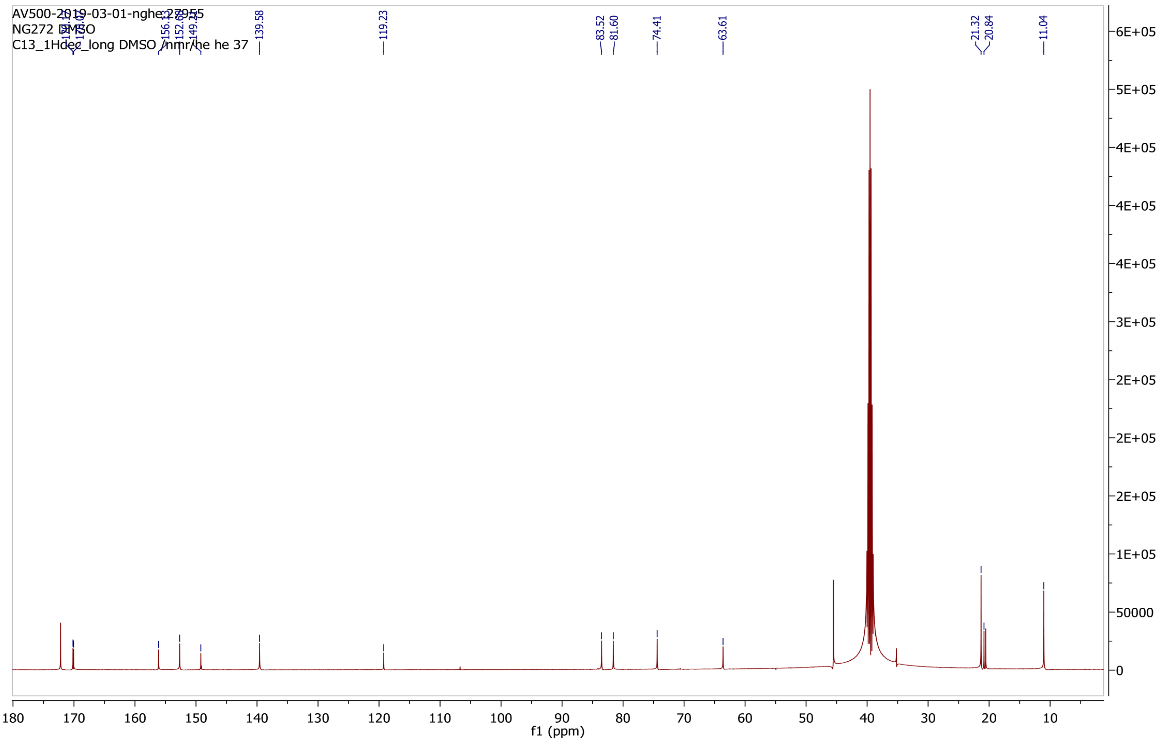

Fig. 255 ^{13}C spectrum of compound **46**.

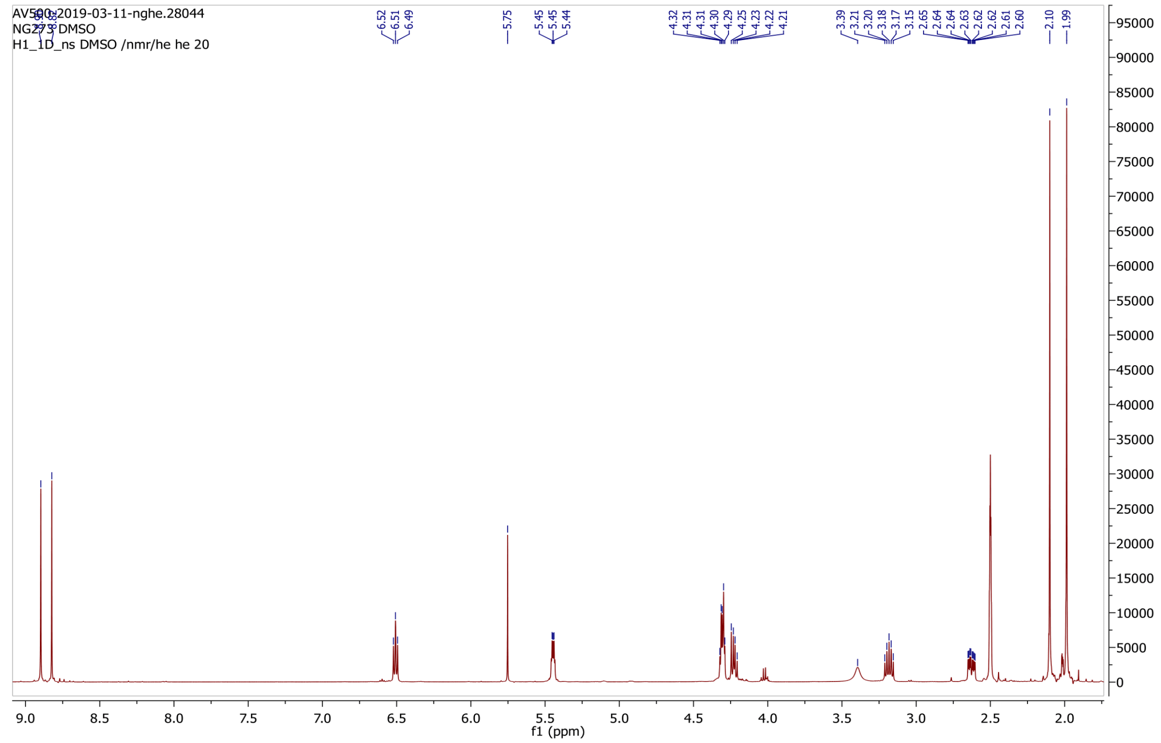

Fig. 256 ^{1}H spectrum of compound **47**.

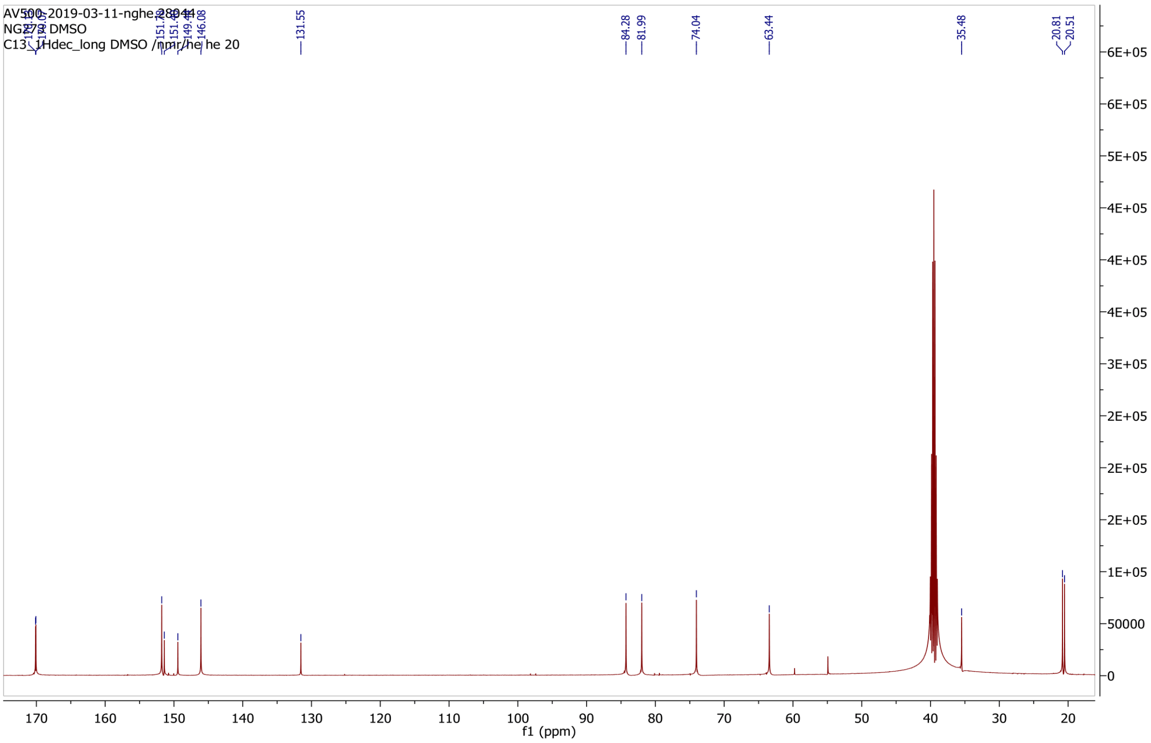

Fig. 257 ^{13}C spectrum of compound ***47****.*

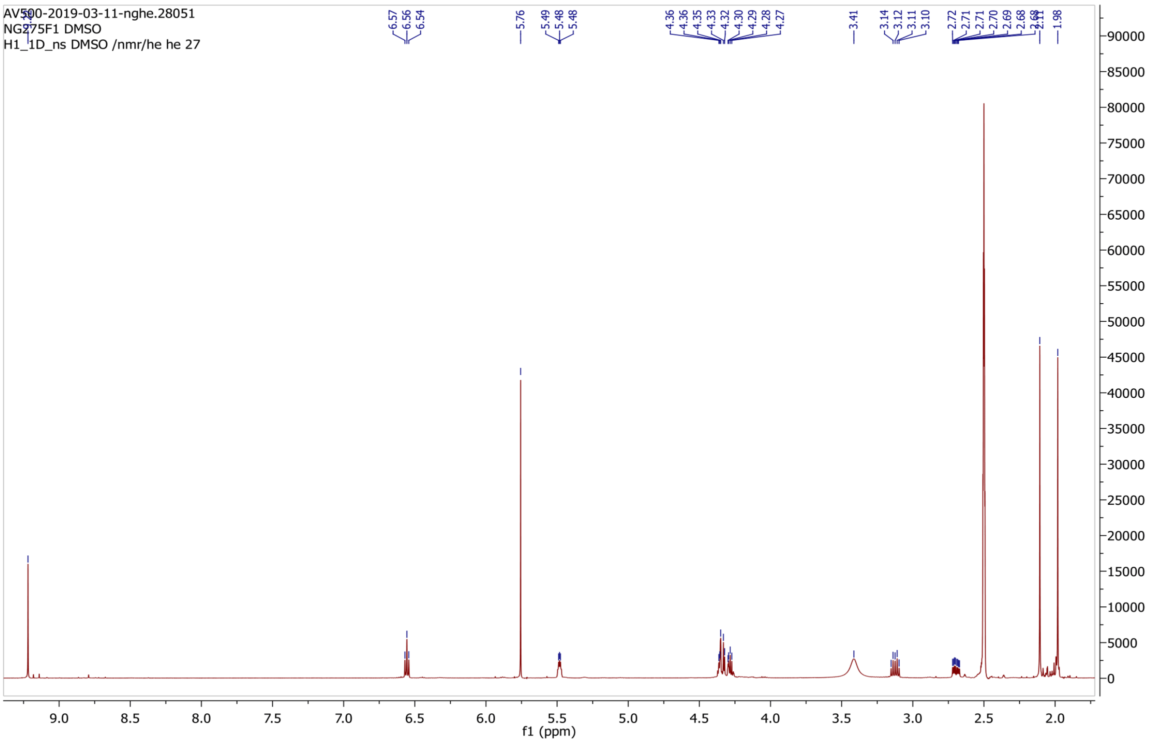

Fig. 258 ^{1}H spectrum of compound ***48****.*

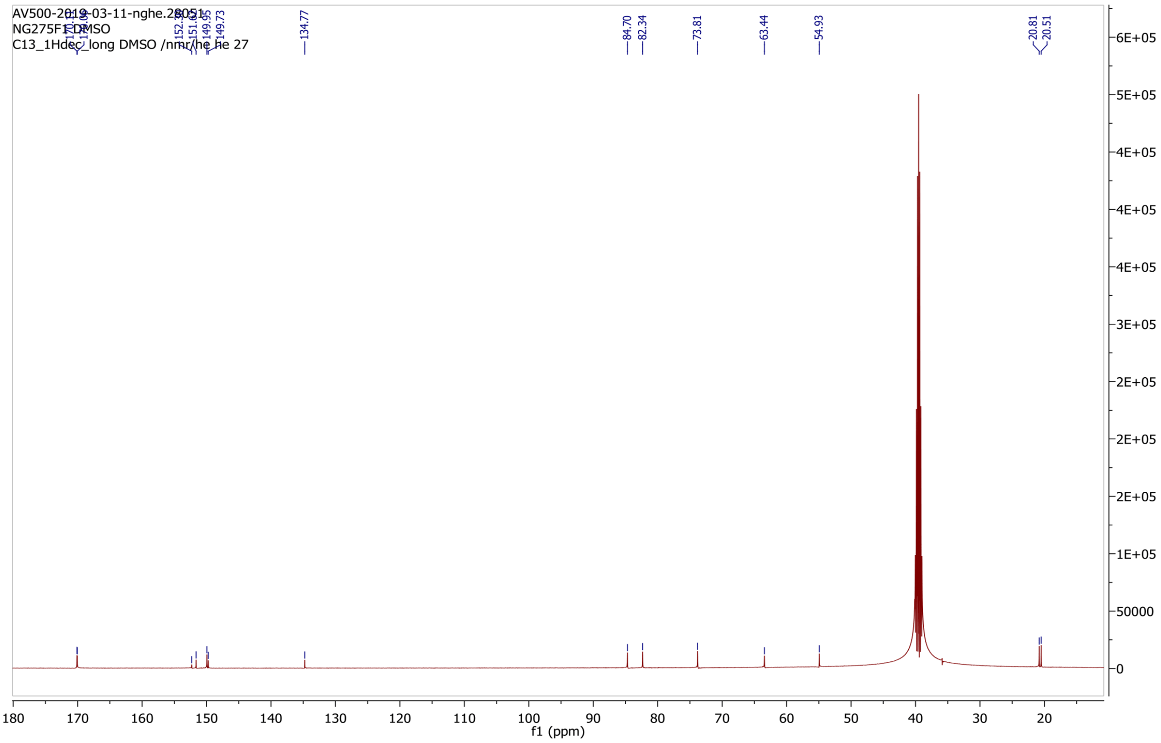

Fig. 259 ^{13}C spectrum of compound **48**.

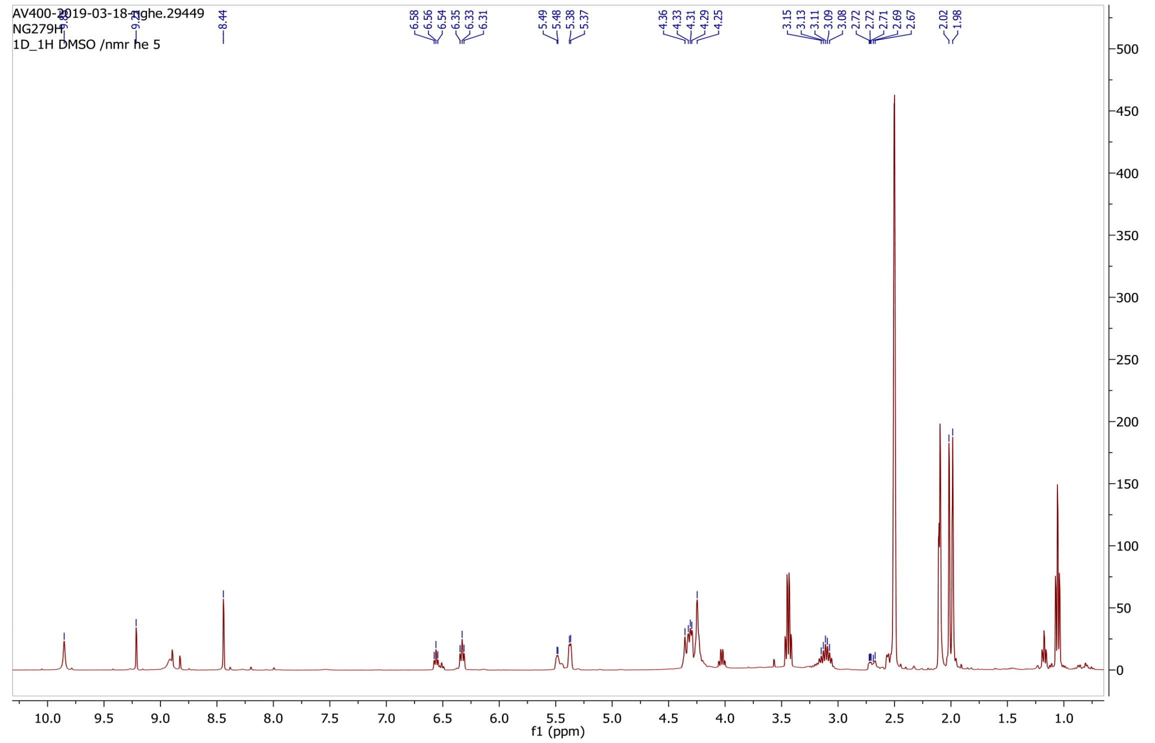

Fig. 260 ^{1}H spectrum of compound **49**.

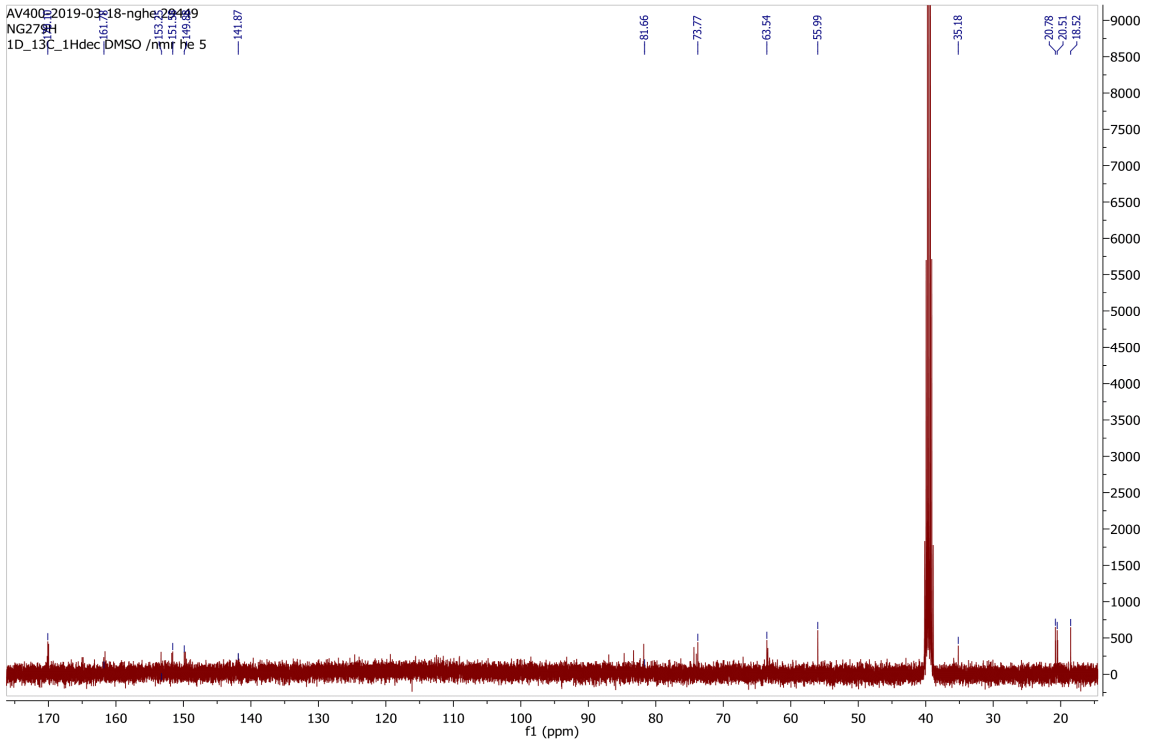

Fig. 261 ^{13}C spectrum of compound **49**.

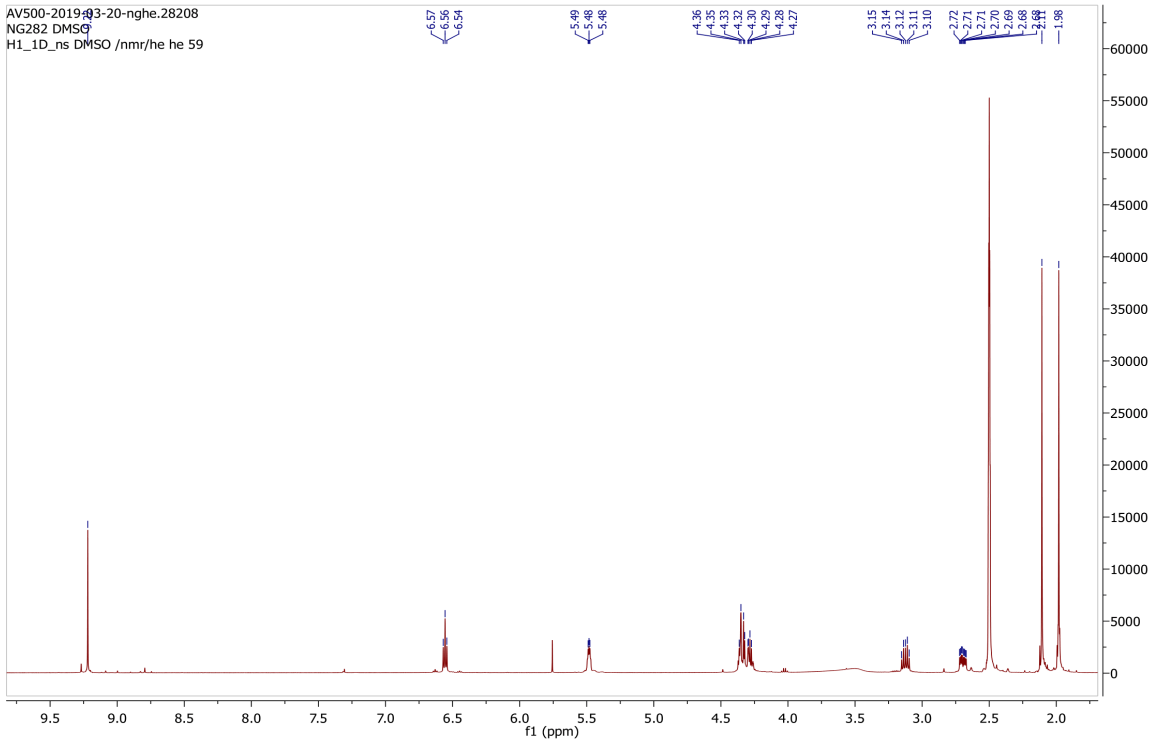

Fig. 262 ^{1}H spectrum of compound **50**.

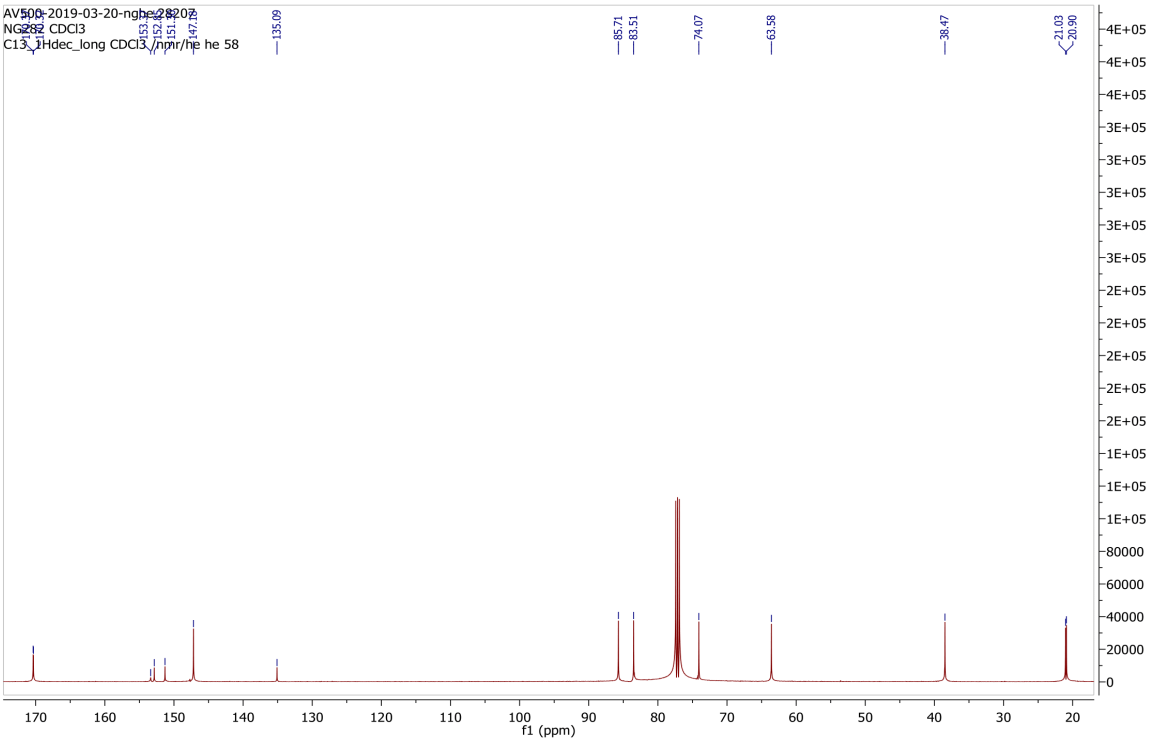

*Fig. 263 ^{13}H spectrum of compound **50**.*

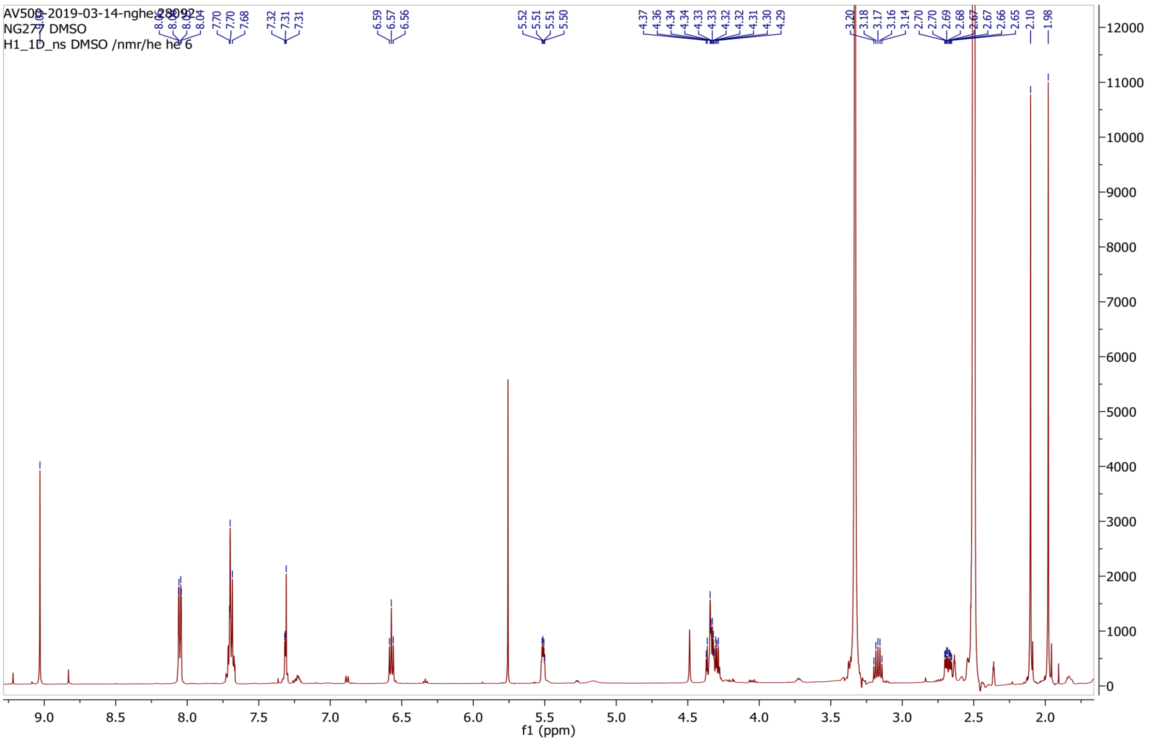

*Fig. 264 ^{1}H spectrum of compound **51**.*

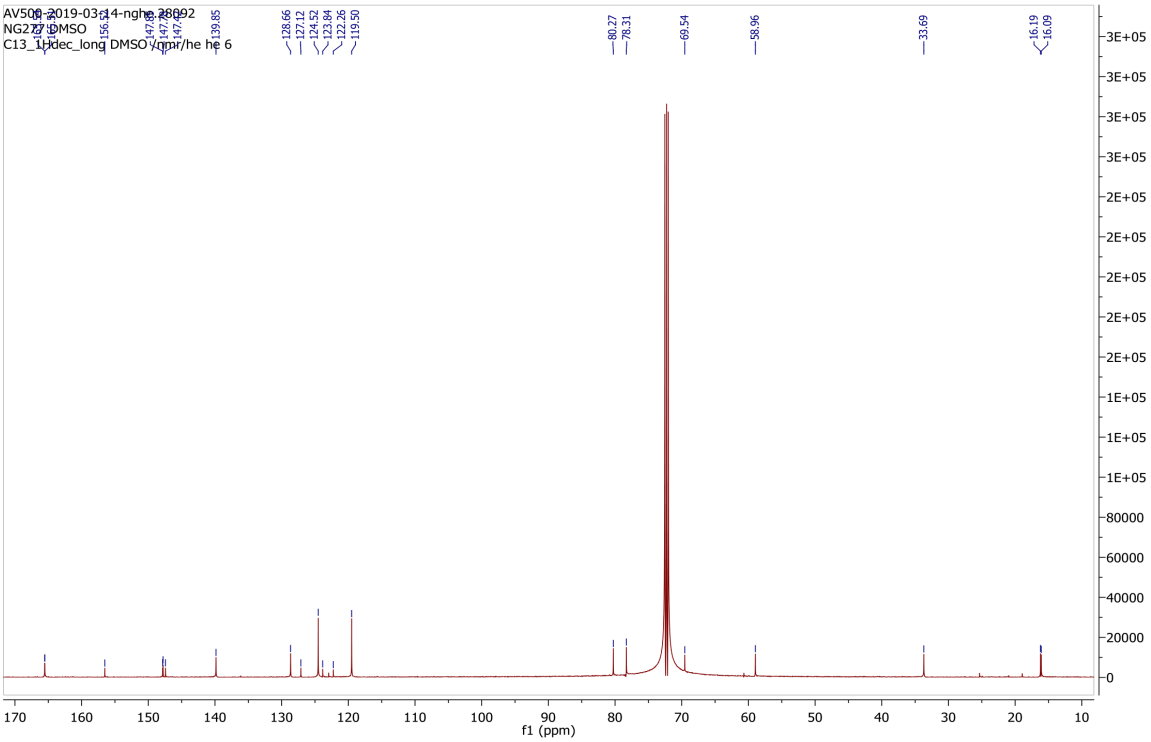

Fig. 265 ^{13}C spectrum of compound ***51****.*

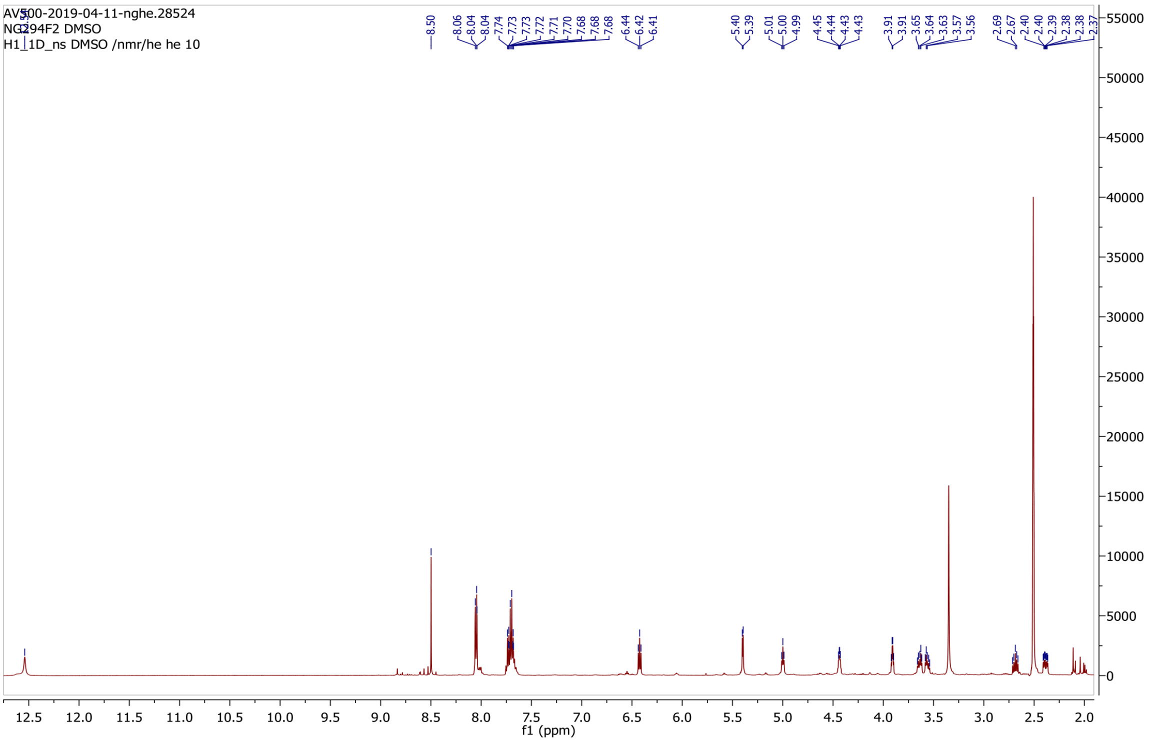

Fig. 266 ^{1}H spectrum of compound ***52****.*

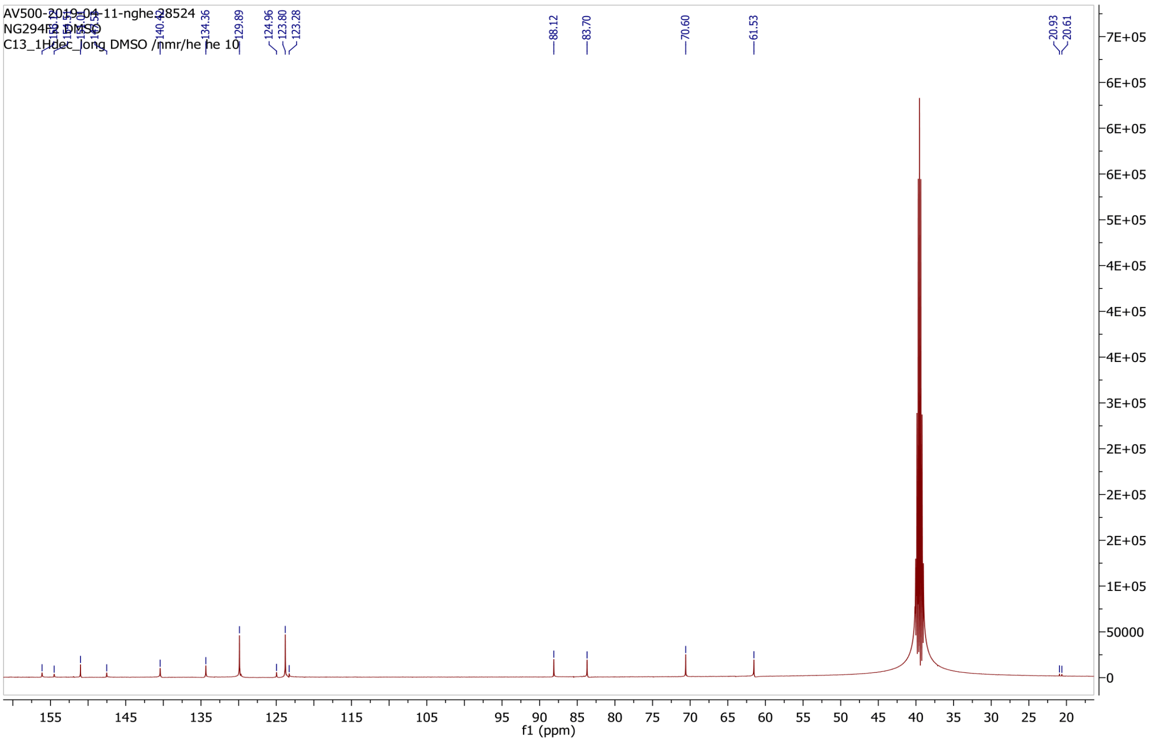

*Fig. 267 ^{13}C spectrum of compound **52**.*

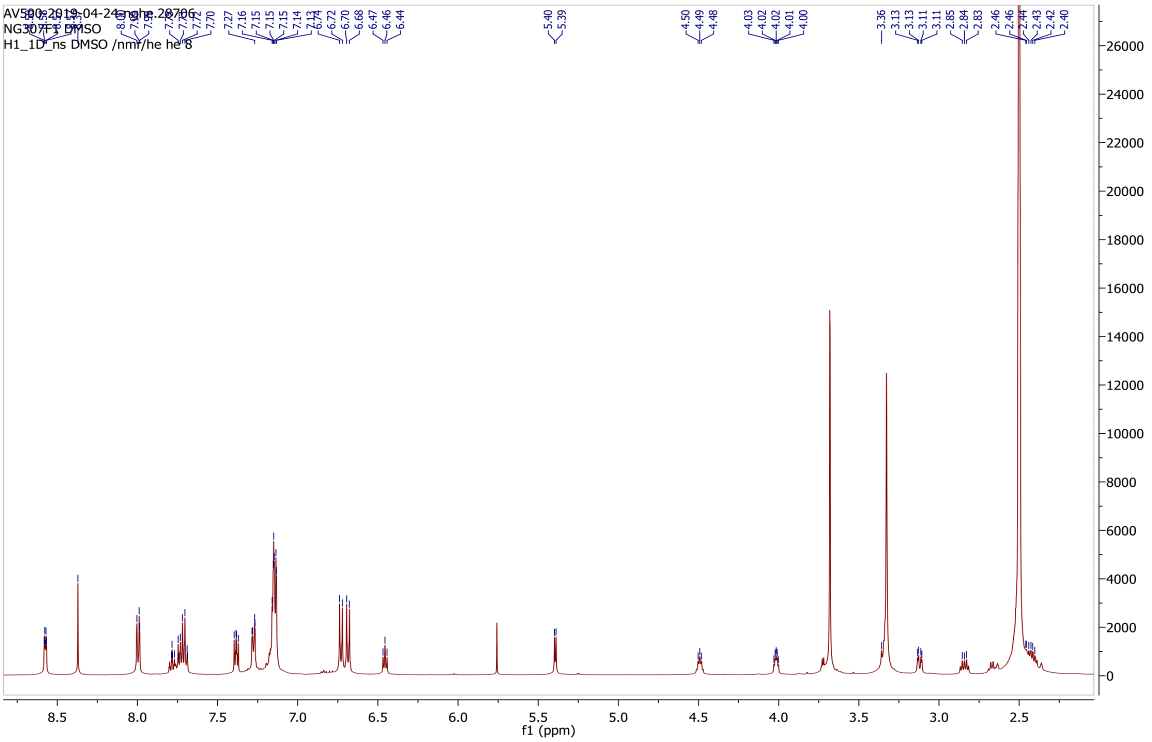

*Fig. 268 ^{1}H spectrum of compound **53**.*

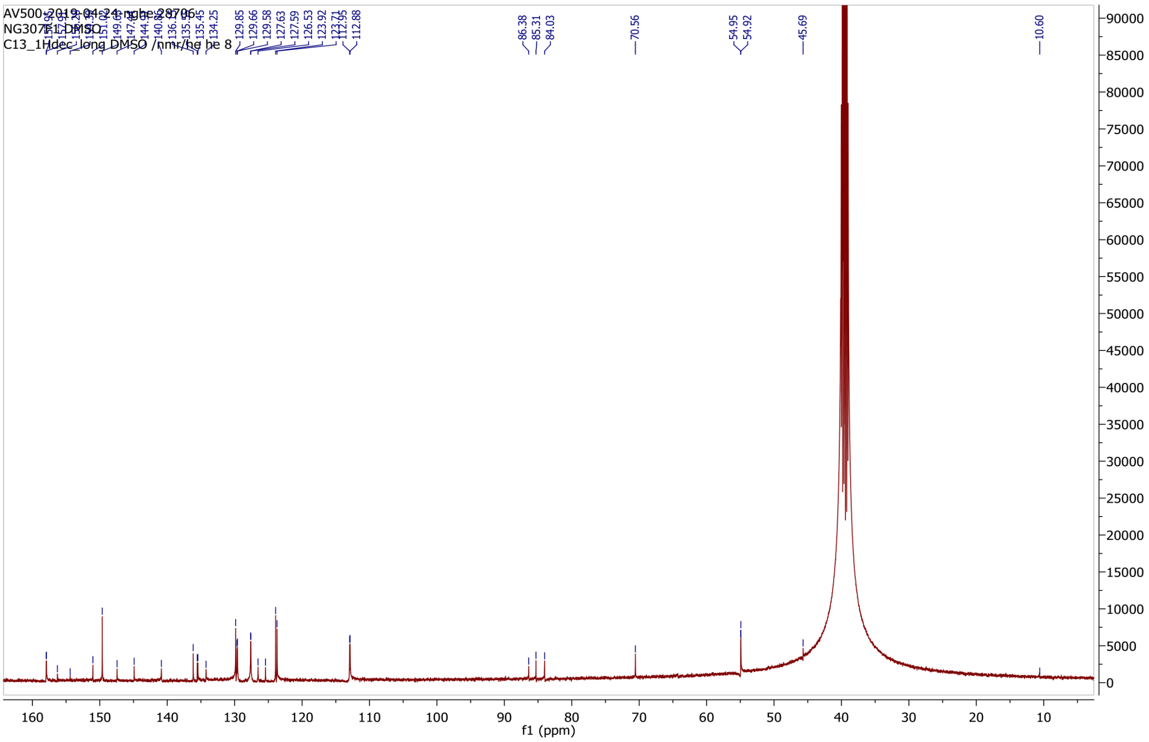

Fig. 269 ^{13}C spectrum of compound **53**.

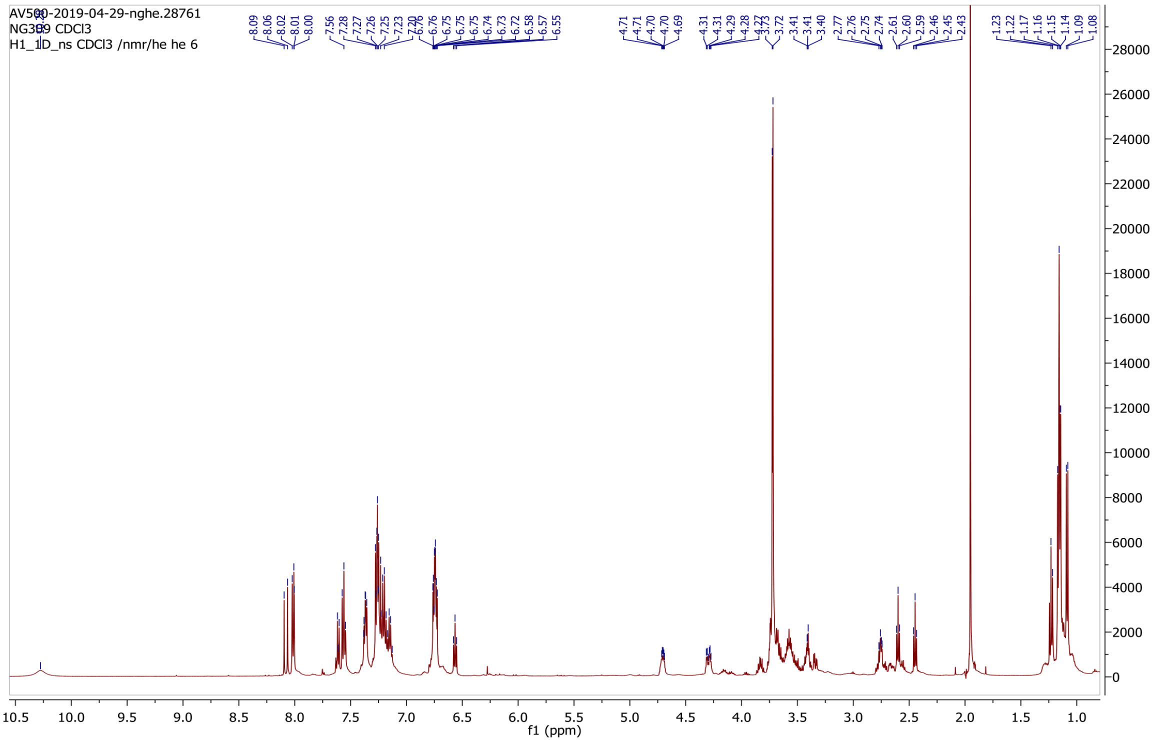

Fig. 270 ^{1}H spectrum of compound **54**.

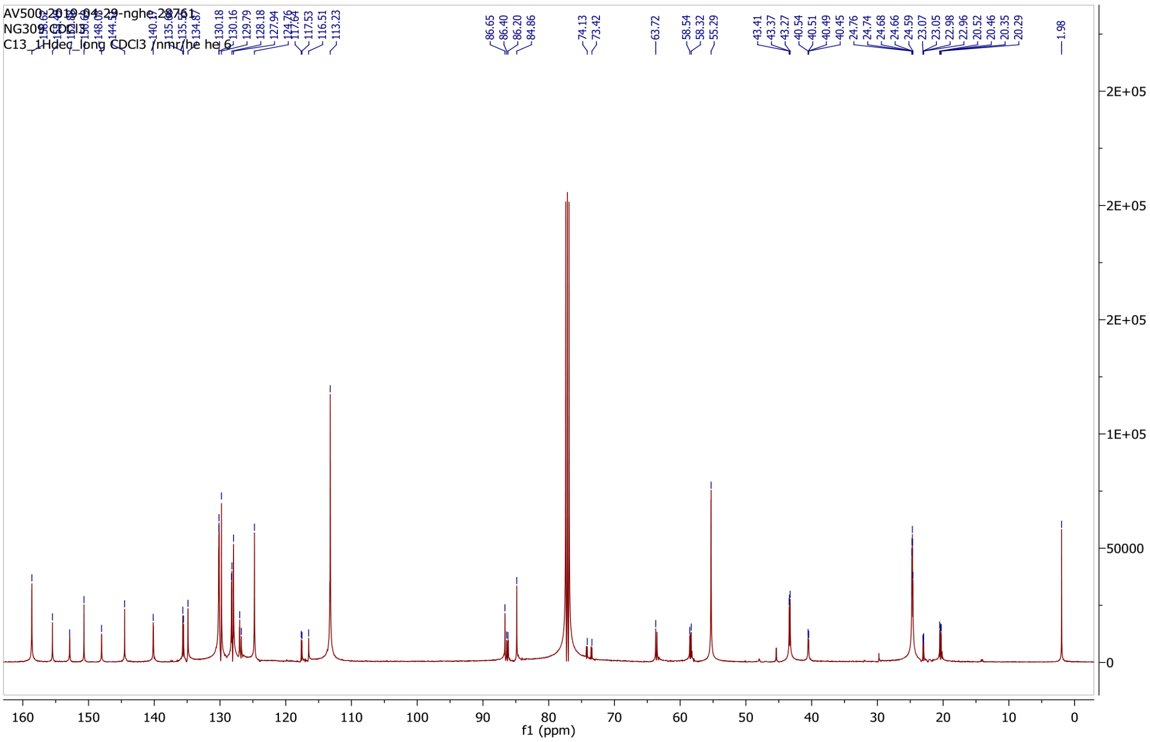

*Fig. 271 ^{13}C spectrum of compound **54**.*

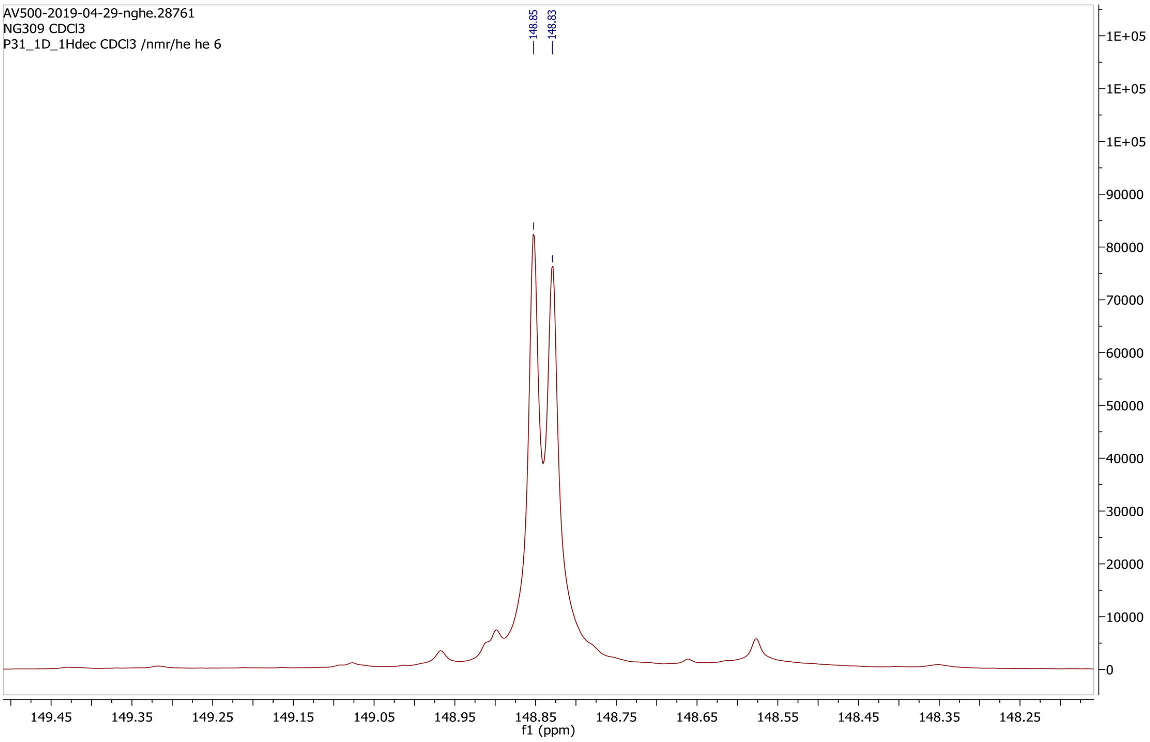

*Fig. 272 ^{31}P spectrum of compound **54**.*

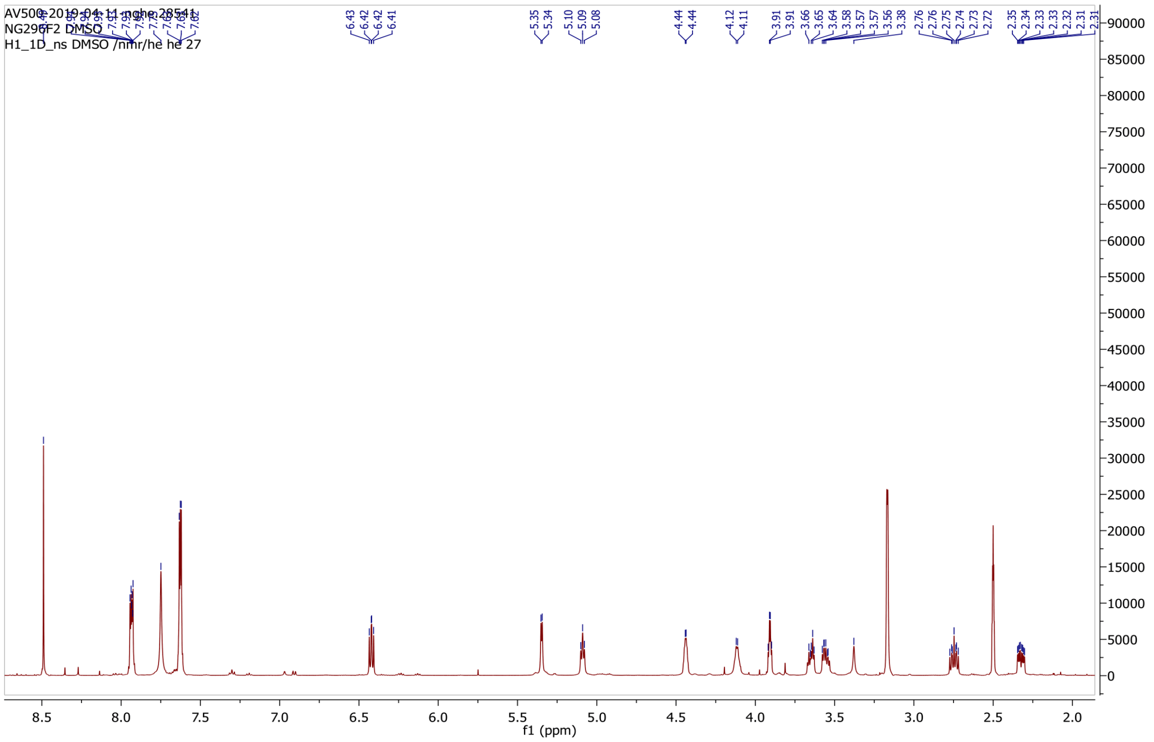

Fig. 273 ^{1}H spectrum of compound **55**.

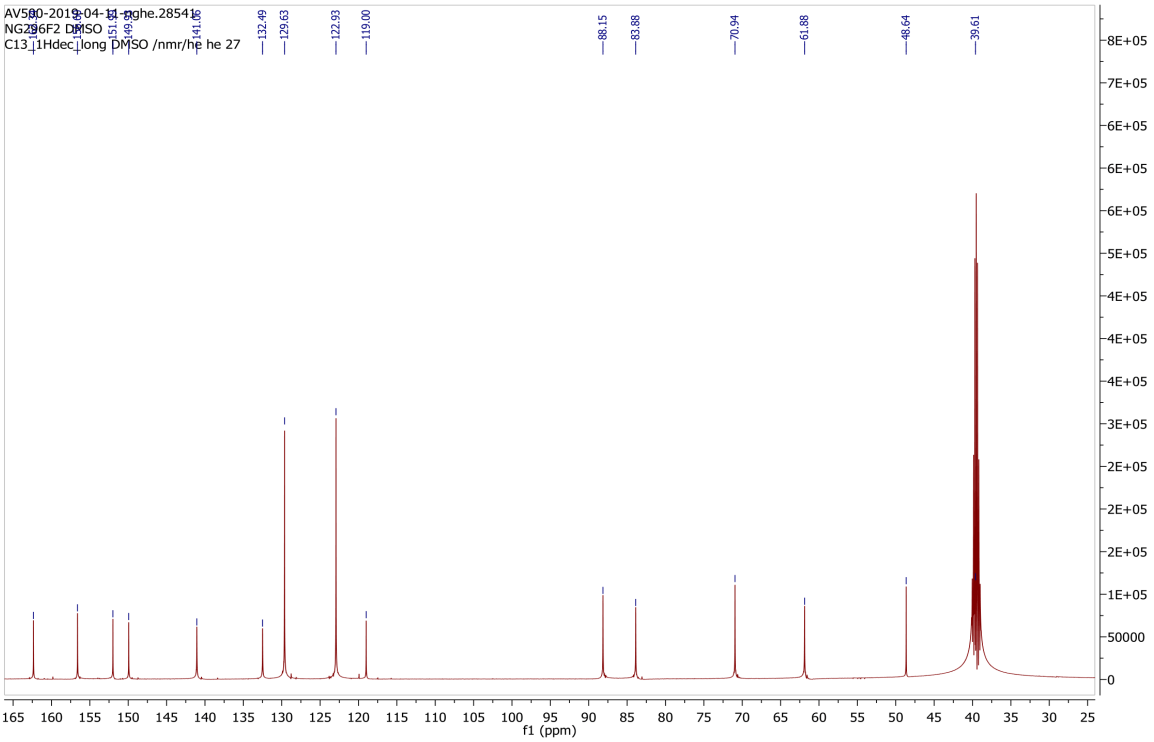

Fig. 274 ^{13}C spectrum of compound **55**.

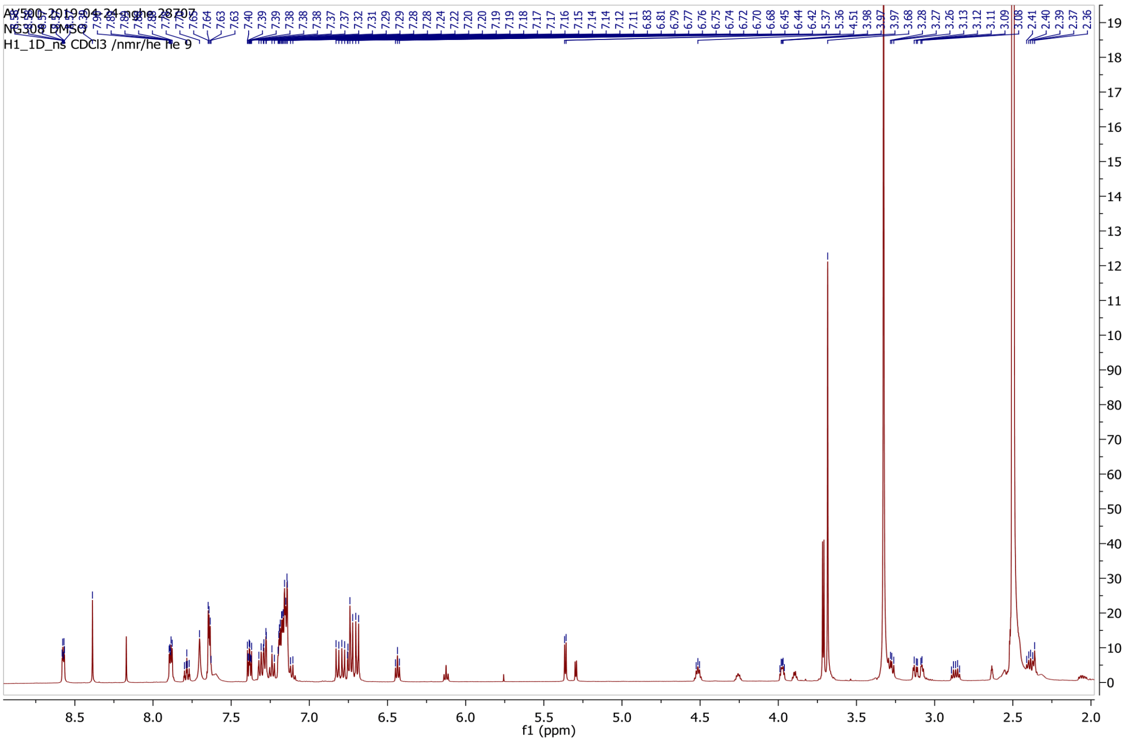

Fig. 275 ^{1}H spectrum of compound **56**.

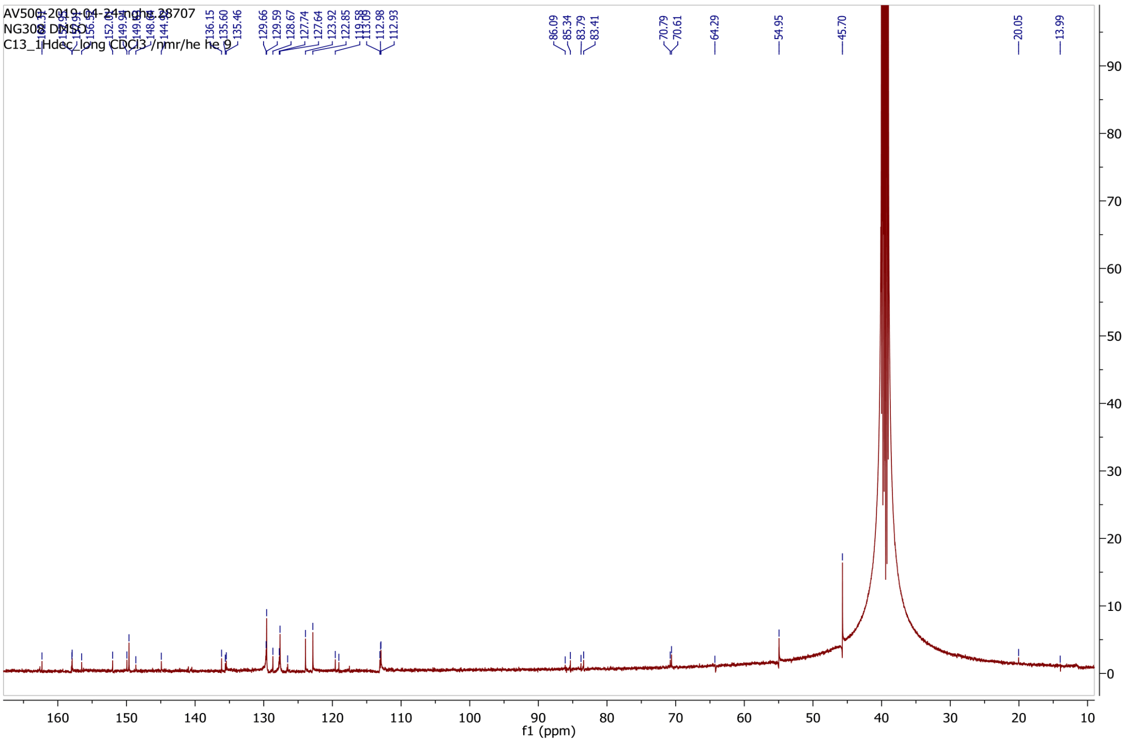

Fig. 276 ^{13}C spectrum of compound **56**.

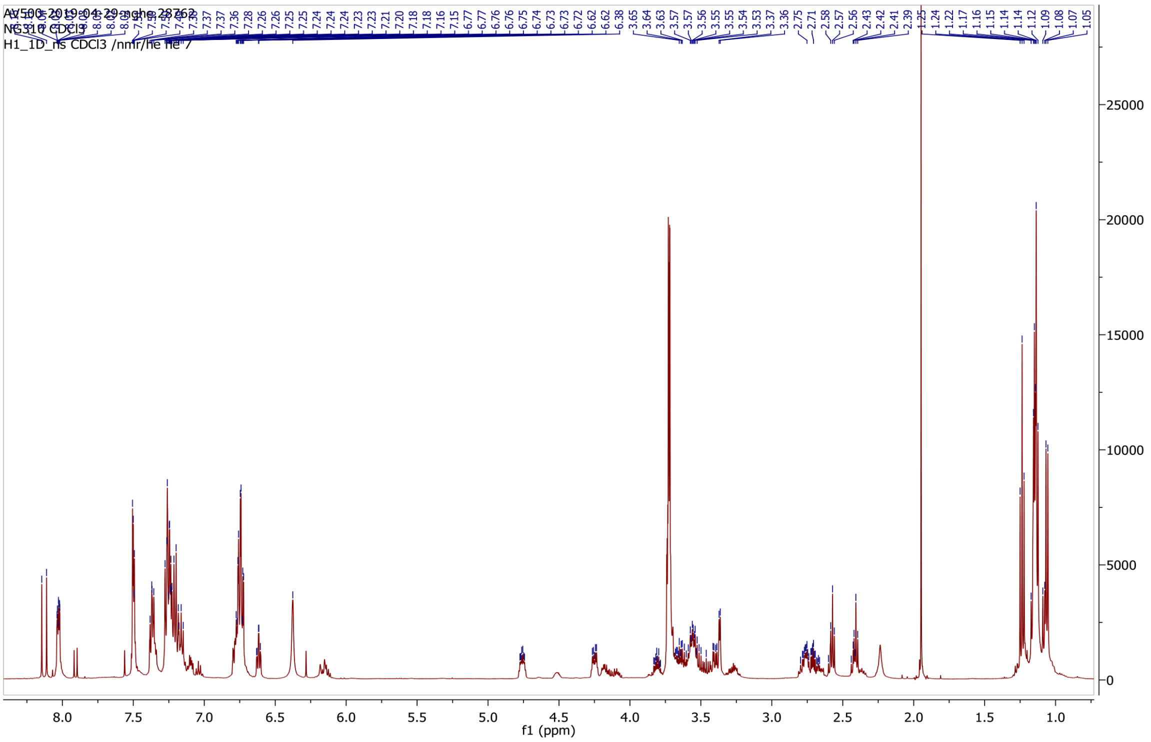

Fig. 277 ^{1}H spectrum of compound ***57****.*

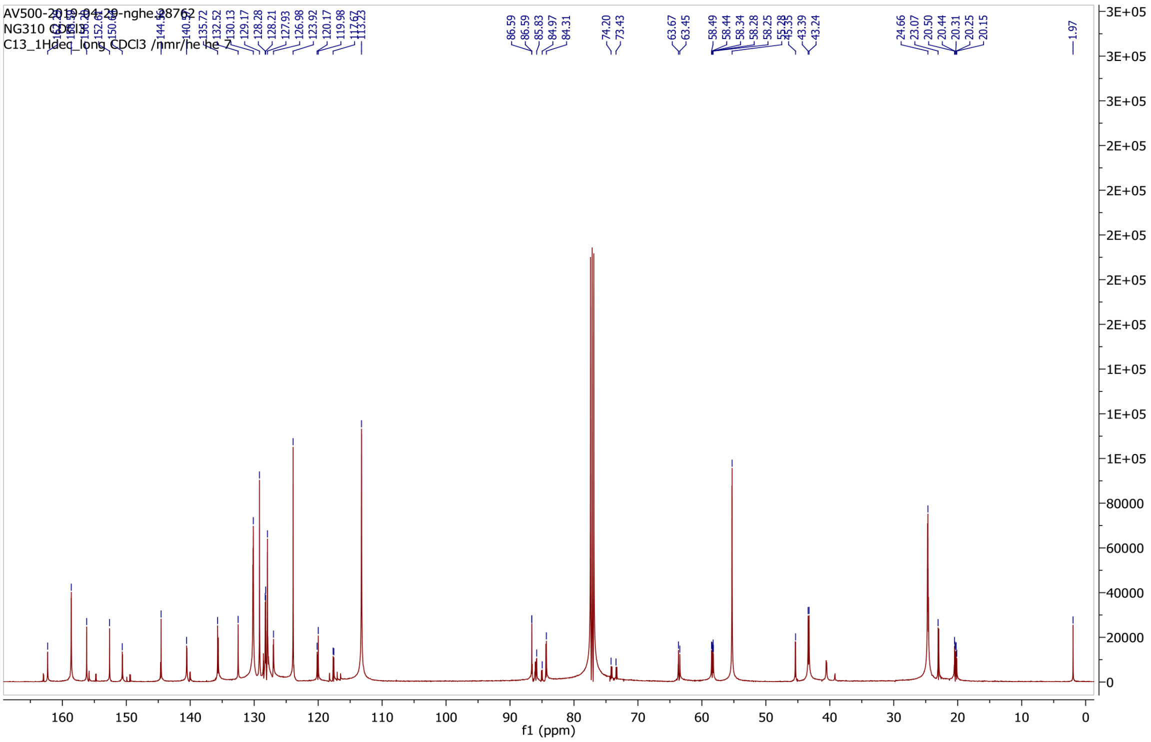

Fig. 278 ^{13}C spectrum of compound ***57****.*

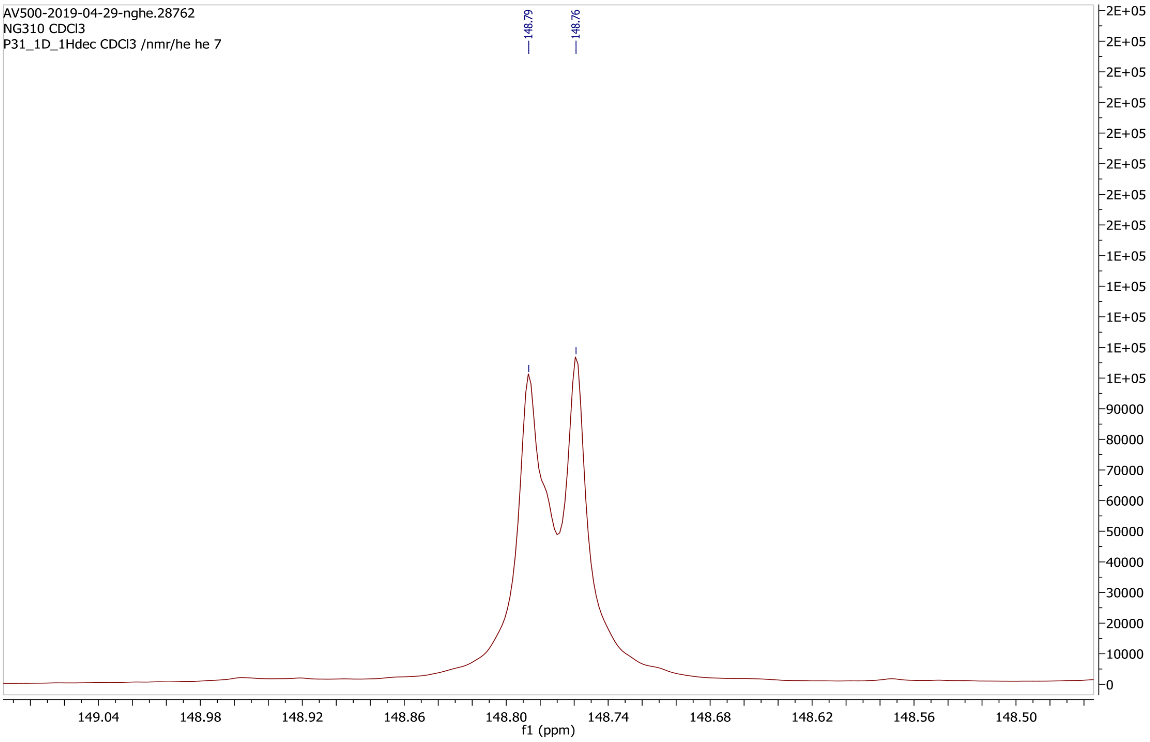

Fig. 279 ^{31}P spectrum of compound ***57****.*

6.2 List of abbreviations

AA	acrylamide
Ac	acyl
Acac	acetylacetone
a-dPAGE	analytical denaturing PAGE
a-nPAGE	analytical native PAGE
Azo	azobenzene
AFM	atomic force microscopy
APS	ammonium peroxodisulfate
aq.	aqueous
Ar	aryl
BAA	*bis*-acrylamide
Bn	benzyl
Ca.	circa (Latin) approximately
CE	cyanoethyl
Cy	cyclohexane
dA_{Azo}	2-Phenyldiazenyl-2’-deoxyadenosine
DAB	dabcyl-modification
DCM	dichloromethane
DDQ	2,3-dichloro-5,6-dicyanobenzoquinone
dG_{Azo}	2-Phenyldiazenyl-2’-deoxyguanosine
DIPEA	di-*iso*propyl ethyl amine
DMAP	4-*N*,*N*-dimethylamino-pyridine
DMT	4,4’-dimethoxytrityl
DNAzo	desoxyribonucleic acid analogue azobenzene *C*-nucleoside
EA	ethyl acetate
ECH	3-hydroxyproprionitrile
eq	equivalents
ESI	electrospray ionisation
Et	ethyl
Et al.	et alia (Latin) and others
FAM	5’,6’-fluorescein-modification
Imi	imidazole
LED	light emitting diode
LNA	locked nucleic acid
LNAzo	locked nucleic acid analogous azobenzene *C*-nucleoside
MALDI	matrix-assisted laser desorption ionization
mAzo	*meta*-(phenyldiazenyl)phenyl
Me	methyl
m-pyrAzo	3-((1,3,5-trimethyl-1H-pyrazol-4-yl)diazenyl)phenyl
*mi*RNA	*micro*-RNA
MS	mass spectra

MsCl	methanesulfonyl (mesyl) chloride
NMR	nuclear magnetic resonance
ON	oligonucleotide
p-dPAGE	preparative denaturing PAGE
^{i}Pr	*iso*propyl
^{n}Bu	*n*-Butyl
PAGE	polyacrylamide gel electrophoresis
PBS	phosphate buffered saline
Ph	phenyl
PSS	photostationary state (equilibrium state, at which no change of isomeric distribution of a photoswitch occurs anymore during irradiation with a specified wavelength)
py	pyridin
p-pyrAzo	4-((1,3,5-trimethyl-1H-pyrazol-4-yl)diazenyl)phenyl
RP-HPLC	reversed phase high performance liquid chromatography
rt	room temperature (25 °C)
*t*Azo	*D*-threoninol-azobenzene
TBAN	tetrabutyl ammonium nitrate
TBD	1,5,7-triazabicyclo(4.4.0)dec-5-ene
TEA	triethylamine
TEMED	tetramethylethylenediamine
TFA	trifluoroacetic acid
TFAA	trifluoroacetic acid anhydride
THF	tetrahydrofuran
TIPDS	tetra-*iso*propyl-disiloxyl
TLC	thin layer chromatography
T_M	melting point (temperature, were the same amount of single stranded and duplex oligonucleotide is present)
TMAD	tetramethylazodicarboxamide
TOF	time of flight
UV/vis	ultra violet/visible

6.3 References

[1] J. D. Watson, F. H. C. Crick, *Nature* **1953**, *171*, 737–738.

[2] R. E. Franklin, R. G. Gosling, *Nature* **1953**, *171*, 740–741.

[3] M. H. F. Wilkins, A. R. Stokes, H. R. Wilson, *Nature* **1953**, *171*, 738–740.

[4] B. Alberts, *Molecular Biology of the Cell*, Garland Science, Taylor And Francis Group, New York, NY, **2015**.

[5] J. B. Hays, M. E. Magar, B. H. Zimm, *Biopolymers* **1969**, *8*, 531–536.

[6] N. C. Seeman, *J. Theor. Biol.* **1982**, *99*, 237–247.

[7] J. D. Watson, F. H. Crick, *Nature* **1953**, *171*, 964–967.

[8] R. Holliday, *Genet. Res.* **1964**, *5*, 282–304.

[9] N. C. Seeman, *Sci. Am.* **2004**, *290*, 64–75.

[10] J. Chen, N. C. Seeman, *Nature* **1991**, *350*, 631–633.

[11] Y. Zhang, N. C. Seeman, *J. Am. Chem. Soc.* **1994**, *116*, 1661–1669.

[12] N. C. Seeman, *Annu. Rev. Biochem.* **2010**, *79*, 65–87.

[13] P. W. K. Rothemund, *Nature* **2006**, *440*, 297–302.

[14] S. M. Douglas, A. H. Marblestone, S. Teerapittayanon, A. Vazquez, G. M. Church, W. M. Shih, *Nucleic Acids Res.* **2009**, *37*, 5001–5006.

[15] S. M. Douglas, H. Dietz, T. Liedl, B. Högberg, F. Graf, W. M. Shih, *Nature* **2009**, *459*, 414–418.

[16] Y. Ke, S. M. Douglas, M. Liu, J. Sharma, A. Cheng, A. Leung, Y. Liu, W. M. Shih, H. Yan, *J. Am. Chem. Soc.* **2009**, *131*, 15903–15908.

[17] Y. Ke, N. V. Voigt, K. V. Gothelf, W. M. Shih, *J. Am. Chem. Soc.* **2012**, *134*, 1770–1774.

[18] N. Stephanopoulos, *ChemBioChem* **2019**, DOI 10.1002/cbic.201900075.

[19] D. Han, S. Pal, Y. Yang, S. Jiang, J. Nangreave, Y. Liu, H. Yan, *Science* **2013**, *339*, 1412–1415.

[20] F. Zhang, S. Jiang, S. Wu, Y. Li, C. Mao, Y. Liu, H. Yan, *Nat. Nanotechnol.* **2015**, *10*, 779–784.

[21] E. Benson, A. Mohammed, J. Gardell, S. Masich, E. Czeizler, P. Orponen, B. Högberg, *Nature* **2015**, *523*, 441–444.

[22] R. Veneziano, S. Ratanalert, K. Zhang, F. Zhang, H. Yan, W. Chiu, M. Bathe, *Science* **2016**, *352*, 1534–1534.

[23] Y. Ke, L. L. Ong, W. M. Shih, P. Yin, *Science* **2012**, *338*, 1177–1183.

[24] B. Wei, M. Dai, P. Yin, *Nature* **2012**, *485*, 623–626.

[25] M. Endo, S. Yamamoto, K. Tatsumi, T. Emura, K. Hidaka, H. Sugiyama, *Chem. Commun.* **2013**, *49*, 2879.

[26] P. Wang, S. Hyeon Ko, C. Tian, C. Hao, C. Mao, *Chem. Commun.* **2013**, *49*, 5462.

[27] P. Wang, C. Tian, X. Li, C. Mao, *Small* **2014**, *10*, 3923–3926.

[28] P. Wang, T. A. Meyer, V. Pan, P. K. Dutta, Y. Ke, *Chem* **2017**, *2*, 359–382.

[29] F. Hong, F. Zhang, Y. Liu, H. Yan, *Chem. Rev.* **2017**, *117*, 12584–12640.

[30] C. Brieke, F. Rohrbach, A. Gottschalk, G. Mayer, A. Heckel, *Angew. Chem. Int. Ed.* **2012**, *51*, 8446–8476.

[31] W. Szymański, J. M. Beierle, H. A. V. Kistemaker, W. A. Velema, B. L. Feringa, *Chem. Rev.* **2013**, *113*, 6114–6178.

[32] P. Klán, T. Šolomek, C. G. Bochet, A. Blanc, R. Givens, M. Rubina, V. Popik, A. Kostikov, J. Wirz, *Chem. Rev.* **2013**, *113*, 119–191.

[33] S. Wiedbrauk, H. Dube, *Tetrahedron Lett.* **2015**, *56*, 4266–4274.

[34] S. Ogasawara, I. Saito, M. Maeda, *Tetrahedron Lett.* **2008**, *49*, 2479–2482.

[35] S. Ogasawara, M. Maeda, *Angew. Chem. Int. Ed.* **2008**, *47*, 8839–8842.

[36] S. Ogasawara, Mizuo. Maeda, *Angew. Chem. Int. Ed.* **2009**, *48*, 6671–6674.

[37] S. Ogasawara, M. Maeda, *Bioorg. Med. Chem. Lett.* **2011**, *21*, 5457–5459.

[38] S. Barrois, H.-A. Wagenknecht, *Beilstein J. Org. Chem.* **2012**, *8*, 905–914.

[39] J. Andersson, S. Li, P. Lincoln, J. Andréasson, *J. Am. Chem. Soc.* **2008**, *130*, 11836–11837.

[40] M. Hammarson, J. Andersson, S. Li, P. Lincoln, J. Andréasson, *Chem. Commun.* **2010**, *46*, 7130.

[41] D. D. Young, A. Deiters, *ChemBioChem* **2008**, *9*, 1225–1228.

[42] S. Barrois, C. Beyer, H.-A. Wagenknecht, *Synlett* **2012**, *23*, 711–716.

[43] C. Beyer, H.-A. Wagenknecht, *Synlett* **2010**, *2010*, 1371–1376.

[44] L. Briquet, D. P. Vercauteren, E. A. Perpète, D. Jacquemin, *Chem. Phys. Lett.* **2006**, *417*, 190–195.

[45] F. Hamon, F. Djedaini-Pilard, F. Barbot, C. Len, *Tetrahedron* **2009**, *65*, 10105–10123.

[46] P.-O. Åstrand, P. S. Ramanujam, S. Hvilsted, K. L. Bak, S. P. A. Sauer, *J. Am. Chem. Soc.* **2000**, *122*, 3482–3487.

[47] G. R. Mitchell, N. R. King, *Macromol. Symp.* **1999**, *137*, 155–165.

[48] M. Quick, A. L. Dobryakov, M. Gerecke, C. Richter, F. Berndt, I. N. Ioffe, A. A. Granovsky, R. Mahrwald, N. P. Ernsting, S. A. Kovalenko, *J. Phys. Chem. B* **2014**, *118*, 8756–8771.

[49] S. Samai, D. J. Bradley, T. L. Y. Choi, Y. Yan, D. S. Ginger, *J. Phys. Chem. C* **2017**, *121*, 6997–7004.

[50] P. Mondal, G. Granucci, D. Rastädter, M. Persico, I. Burghardt, *Chem. Sci.* **2018**, *9*, 4671–4681.

[51] C.-W. Chang, Y.-C. Lu, T.-T. Wang, E. W.-G. Diau, *J. Am. Chem. Soc.* **2004**, *126*, 10109–10118.

[52] M. Liu, H. Jinmei, H. Abe, Y. Ito, *Bioorg. Med. Chem. Lett.* **2010**, *20*, 2964–2967.

[53] S. Mori, K. Morihiro, S. Obika, *Molecules* **2014**, *19*, 5109–5118.

[54] K. Morihiro, O. Hasegawa, S. Mori, S. Tsunoda, S. Obika, *Org. Biomol. Chem.* **2015**, *13*, 5209–5214.

[55] S. Keiper, J. S. Vyle, *Angew. Chem. Int. Ed.* **2006**, *45*, 3306–3309.

[56] H. Asanuma, T. Yoshida, T. Ito, Makoto. Komiyama, *Tetrahedron Lett.* **1999**, *40*, 7995–7998.

[57] S. Patnaik, P. Kumar, B. S. Garg, R. P. Gandhi, K. C. Gupta, *Bioorg. Med. Chem.* **2007**, *15*, 7840–7849.

[58] L. Wu, K. Koumoto, N. Sugimoto, *Chem. Commun.* **2009**, 1915.

[59] L. Wu, Y. Wu, H. Jin, L. Zhang, Y. He, X. Tang, *MedChemComm* **2015**, *6*, 461–468.

[60] L. Wu, Y. He, X. Tang, *Bioconjug. Chem.* **2015**, *26*, 1070–1079.

[61] J. Thevarpadam, I. Bessi, O. Binas, D. P. N. Gonçalves, C. Slavov, H. R. A. Jonker, C. Richter, J. Wachtveitl, H. Schwalbe, A. Heckel, *Angew. Chem. Int. Ed.* **2016**, *55*, 2738–2742.

[62] M. McCullagh, I. Franco, M. A. Ratner, G. C. Schatz, *J. Am. Chem. Soc.* **2011**, *133*, 3452–3459.

[63] H. Asanuma, T. Ito, M. Komiyama, *Tetrahedron Lett.* **1998**, *39*, 9015–9018.

[64] H. Asanuma, T. Ito, T. Yoshida, X. Liang, M. Komiyama, *Angew. Chem. Int. Ed.* **1999**, *38*, 2393–2395.

[65] H. Asanuma, T. Takarada, T. Yoshida, D. Tamaru, X. Liang, M. Komiyama, *Angew. Chem. Int. Ed.* **2001**, *40*, 2671–2673.

[66] H. Kashida, X. Liang, H. Asanuma, *Curr. Org. Chem.* **2009**, *13*, 1065–1084.

[67] X. Liang, H. Asanuma, H. Kashida, A. Takasu, T. Sakamoto, G. Kawai, M. Komiyama, *J. Am. Chem. Soc.* **2003**, *125*, 16408–16415.

[68] Y. Kim, J. A. Phillips, H. Liu, H. Kang, Weihong. Tan, *Proc. Natl. Acad. Sci. U. S. A.* **2009**, *106*, 6489–6494.

[69] Y. Liu, D. Sen, *J. Mol. Biol.* **2004**, *341*, 887–892.

[70] H. Ito, X. Liang, H. Nishioka, H. Asanuma, *Org. Biomol. Chem.* **2010**, *8*, 5519.

[71] Y. Yan, X. Wang, J. I. L. Chen, D. S. Ginger, *J. Am. Chem. Soc.* **2013**, *135*, 8382–8387.

[72] T. Goldau, K. Murayama, C. Brieke, S. Steinwand, P. Mondal, M. Biswas, I. Burghardt, J. Wachtveitl, H. Asanuma, A. Heckel, *Chem. - Eur. J.* **2015**, *21*, 2845–2854.

[73] H. Asanuma, X. Liang, H. Nishioka, D. Matsunaga, M. Liu, M. Komiyama, *Nat. Protoc.* **2007**, *2*, 203–212.

[74] X. Liang, H. Nishioka, T. Mochizuki, H. Asanuma, *J Mater Chem* **2010**, *20*, 575–581.

[75] T. Fujii, H. Kashida, H. Asanuma, *Chem. - Eur. J.* **2009**, *15*, 10092–10102.

[76] T. Fujii, M. Urushihara, H. Kashida, H. Ito, X. Liang, M. Yagi-Utsumi, K. Kato, H. Asanuma, *Chem. - Eur. J.* **2012**, *18*, 13304–13313.

[77] H. Kashida, T. Fujii, H. Asanuma, *Org. Biomol. Chem.* **2008**, *6*, 2892.

[78] K. Murayama, H. Asanuma, *ChemBioChem* **2017**, *18*, 142–149.

[79] B. Kou, J. Zhang, X. Huai, X. Liang, S.-J. Xiao, *RSC Adv.* **2015**, *5*, 5055–5058.

[80] S. Samai, T. L. Y. Choi, K. N. Guye, Y. Yan, D. S. Ginger, *J. Phys. Chem. C* **2018**, *122*, 13363–13370.

[81] M. Liu, H. Asanuma, Makoto. Komiyama, *J. Am. Chem. Soc.* **2006**, *128*, 1009–1015.

[82] X. Liang, R. Wakuda, K. Fujioka, Hiroyuki. Asanuma, *FEBS J.* **2010**, *277*, 1551–1561.

[83] D. Matsunaga, H. Asanuma, Makoto. Komiyama, *J. Am. Chem. Soc.* **2004**, *126*, 11452–11453.

[84] T. Goldau, K. Murayama, C. Brieke, H. Asanuma, A. Heckel, *Chem. - Eur. J.* **2015**, *21*, 17870–17876.

[85] S. Samai, D. J. Bradley, T. L. Y. Choi, Y. Yan, D. S. Ginger, *J. Phys. Chem. C* **2017**, *121*, 6997–7004.

[86] X. Liang, T. Mochizuki, T. Fujii, H. Kashida, H. Asanuma, *Nat. Comput.* **2012**, *11*, 231–238.

[87] J. Li, X. Wang, X. Liang, *Chem. – Asian J.* **2014**, *9*, 3344–3358.

[88] A. S. Lubbe, W. Szymanski, B. L. Feringa, *Chem. Soc. Rev.* **2017**, *46*, 1052–1079.

[89] Y. Krishnan, F. C. Simmel, *Angew. Chem. Int. Ed.* **2011**, *50*, 3124–3156.

[90] M. Endo, H. Sugiyama, *Molecules* **2018**, *23*, 1766.

[91] A. E. Marras, L. Zhou, H.-J. Su, C. E. Castro, *Proc. Natl. Acad. Sci.* **2015**, *112*, 713–718.

[92] A. Rajendran, M. Endo, H. Sugiyama, *Angew. Chem. Int. Ed.* **2012**, *51*, 874–890.

[93] B. Saccà, C. M. Niemeyer, *Chem. Soc. Rev.* **2011**, *40*, 5910.

[94] F. Praetorius, H. Dietz, *Science* **2017**, *355*, eaam5488.

[95] K. Du, S. H. Ko, G. M. Gallatin, H. P. Yoon, J. Alexander Liddle, A. J. Berglund, *Chem Commun* **2013**, *49*, 907–909.

[96] F. N. Gür, F. W. Schwarz, J. Ye, S. Diez, T. L. Schmidt, *ACS Nano* **2016**, *10*, 5374–5382.

[97] R. Schreiber, J. Do, E.-M. Roller, T. Zhang, V. J. Schüller, P. C. Nickels, J. Feldmann, T. Liedl, *Nat. Nanotechnol.* **2014**, *9*, 74–78.

[98] N. V. Voigt, T. Tørring, A. Rotaru, M. F. Jacobsen, J. B. Ravnsbæk, R. Subramani, W. Mamdouh, J. Kjems, A. Mokhir, F. Besenbacher, et al., *Nat. Nanotechnol.* **2010**, *5*, 200–203.

[99] M. Langecker, V. Arnaut, T. G. Martin, J. List, S. Renner, M. Mayer, H. Dietz, F. C. Simmel, *Science* **2012**, *338*, 932–936.

[100] K. Göpfrich, C.-Y. Li, M. Ricci, S. P. Bhamidimarri, J. Yoo, B. Gyenes, A. Ohmann, M. Winterhalter, A. Aksimentiev, U. F. Keyser, *ACS Nano* **2016**, *10*, 8207–8214.

[101] M. Langecker, V. Arnaut, J. List, F. C. Simmel, *Acc. Chem. Res.* **2014**, *47*, 1807–1815.

[102] S. Krishnan, D. Ziegler, V. Arnaut, T. G. Martin, K. Kapsner, K. Henneberg, A. R. Bausch, H. Dietz, F. C. Simmel, *Nat. Commun.* **2016**, *7*, 12787.

[103] D. Wang, Y. Zhang, D. Liu, *F1000Research* **2017**, *6*, 503.

[104] N. A. W. Bell, U. F. Keyser, *FEBS Lett.* **2014**, *588*, 3564–3570.

[105] S. Howorka, *Nat. Nanotechnol.* **2017**, *12*, 619–630.

[106] J. R. Burns, A. Seifert, N. Fertig, S. Howorka, *Nat. Nanotechnol.* **2016**, *11*, 152–156.

[107] O. I. Wilner, I. Willner, *Chem. Rev.* **2012**, *112*, 2528–2556.

[108] X. Liang, H. Nishioka, N. Takenaka, H. Asanuma, *ChemBioChem* **2008**, *9*, 702–705.

[109] M. Zhou, X. Liang, T. Mochizuki, H. Asanuma, *Angew. Chem.* **2010**, *122*, 2213–2216.

[110] X. Liang, M. Zhou, K. Kato, H. Asanuma, *ACS Synth. Biol.* **2013**, *2*, 194–202.

[111] H. Nishioka, X. Liang, T. Kato, H. Asanuma, *Angew. Chem. Int. Ed.* **2012**, *51*, 1165–1168.

[112] E. M. Willner, Y. Kamada, Y. Suzuki, T. Emura, K. Hidaka, H. Dietz, H. Sugiyama, M. Endo, *Angew. Chem.* **2017**, *129*, 15526–15530.

[113] Y. Yang, M. A. Goetzfried, K. Hidaka, M. You, W. Tan, H. Sugiyama, M. Endo, *Nano Lett.* **2015**, *15*, 6672–6676.

[114] M. Škugor, J. Valero, K. Murayama, M. Centola, H. Asanuma, M. Famulok, *Angew. Chem. Int. Ed.* **2019**, *58*, 6948–6951.

[115] Y. Yang, R. Tashiro, Y. Suzuki, T. Emura, K. Hidaka, H. Sugiyama, M. Endo, *Chem. - Eur. J.* **2017**, *23*, 3979–3985.

[116] D. K. Prusty, V. Adam, R. M. Zadegan, S. Irsen, M. Famulok, *Nat. Commun.* **2018**, *9*, DOI 10.1038/s41467-018-02929-2.

[117] G. Raghavan, K. Hidaka, H. Sugiyama, M. Endo, *Angew. Chem. Int. Ed.* **2019**, *58*, 7626–7630.

[118] E. P. Gates, J. K. Jensen, J. N. Harb, A. T. Woolley, *RSC Adv.* **2015**, *5*, 8134–8141.

[119] C. Hartl, K. Frank, H. Amenitsch, S. Fischer, T. Liedl, B. Nickel, *Nano Lett.* **2018**, *18*, 2609–2615.
[120] A. M. Hung, J. N. Cha, in *DNA Nanotechnol.* (Eds.: G. Zuccheri, B. Samorì), Humana Press, Totowa, NJ, **2011**, pp. 187–197.
[121] A. Kuzyk, Y. Yang, X. Duan, S. Stoll, A. O. Govorov, H. Sugiyama, M. Endo, N. Liu, *Nat. Commun.* **2016**, *7*, DOI 10.1038/ncomms10591.
[122] Q. Yuan, Y. Zhang, T. Chen, D. Lu, Z. Zhao, X. Zhang, Z. Li, C.-H. Yan, W. Tan, *ACS Nano* **2012**, *6*, 6337–6344.
[123] F. Tanaka, T. Mochizuki, X. Liang, H. Asanuma, S. Tanaka, K. Suzuki, S. Kitamura, A. Nishikawa, K. Ui-Tei, M. Hagiya, *Nano Lett.* **2010**, *10*, 3560–3565.
[124] Y. Kamiya, Y. Yamada, T. Muro, K. Matsuura, H. Asanuma, *ChemMedChem* **2017**, *12*, 2016–2021.
[125] T. Takenaka, M. Endo, Y. Suzuki, Y. Yang, T. Emura, K. Hidaka, T. Kato, T. Miyata, K. Namba, H. Sugiyama, *Chem. - Eur. J.* **2014**, *20*, 14951–14954.
[126] T. Tohgasaki, Y. Shitomi, Y. Feng, S. Honna, T. Emura, K. Hidaka, H. Sugiyama, M. Endo, *Bioconjug. Chem.* **2019**, DOI 10.1021/acs.bioconjchem.9b00040.
[127] C. Xu, H. Li, K. Zhang, D. W. Binzel, H. Yin, W. Chiu, P. Guo, *Nano Res.* **2019**, *12*, 41–48.
[128] D. Han, J. Huang, Z. Zhu, Q. Yuan, M. You, Y. Chen, W. Tan, *Chem. Commun.* **2011**, *47*, 4670.
[129] M. Endo, Y. Yang, Y. Suzuki, K. Hidaka, H. Sugiyama, *Angew. Chem.* **2012**, *124*, 10670–10674.
[130] Y. Yang, M. Endo, K. Hidaka, H. Sugiyama, *J. Am. Chem. Soc.* **2012**, *134*, 20645–20653.
[131] Y. Suzuki, M. Endo, Y. Yang, H. Sugiyama, *J. Am. Chem. Soc.* **2014**, *136*, 1714–1717.
[132] Y. Yan, J. I. L. Chen, D. S. Ginger, *Nano Lett.* **2012**, *12*, 2530–2536.
[133] J. J. Keya, R. Suzuki, A. Md. R. Kabir, D. Inoue, H. Asanuma, K. Sada, H. Hess, A. Kuzuya, A. Kakugo, *Nat. Commun.* **2018**, *9*, DOI 10.1038/s41467-017-02778-5.
[134] S. Ramakrishnan, H. Ijäs, V. Linko, A. Keller, *Comput. Struct. Biotechnol. J.* **2018**, *16*, 342–349.
[135] S. Woo, P. W. K. Rothemund, *Nat. Commun.* **2014**, *5*, DOI 10.1038/ncomms5889.
[136] E. Winfree, F. Liu, L. A. Wenzler, N. C. Seeman, *Nature* **1998**, *394*, 539–544.
[137] T. L. Schmidt, C. K. Nandi, G. Rasched, P. P. Parui, B. Brutschy, M. Famulok, A. Heckel, *Angew. Chem. Int. Ed.* **2007**, *46*, 4382–4384.
[138] T. L. Schmidt, A. Heckel, *Small* **2009**, *5*, 1517–1520.
[139] D. Ackermann, T. L. Schmidt, J. S. Hannam, C. S. Purohit, A. Heckel, M. Famulok, *Nat. Nanotechnol.* **2010**, *5*, 436–442.
[140] D. P. N. Gonçalves, T. L. Schmidt, M. B. Koeppel, A. Heckel, *Small* **2010**, *6*, 1347–1352.
[141] G. Rasched, D. Ackermann, T. L. Schmidt, P. Broekmann, A. Heckel, M. Famulok, *Angew. Chem. Int. Ed.* **2008**, *47*, 967–970.
[142] D. Ackermann, G. Rasched, S. Verma, T. L. Schmidt, A. Heckel, M. Famulok, *Chem. Commun.* **2010**, *46*, 4154.

[143] T. L. Schmidt, M. B. Koeppel, J. Thevarpadam, D. P. N. Gonçalves, A. Heckel, *Small* **2011**, *7*, 2163–2167.
[144] H.-S. Koo, H.-M. Wu, D. M. Crothers, *Nature* **1986**, *320*, 501–506.
[145] E. N. Trifonov, J. L. Sussman, *Proc. Natl. Acad. Sci.* **1980**, *77*, 3816–3820.
[146] Z. Wang, B. Yang, in *MicroRNA Expr. Detect. Methods*, Springer Berlin Heidelberg, Berlin, Heidelberg, **2010**, pp. 229–239.
[147] R. Owczarzy, B. G. Moreira, Y. You, M. A. Behlke, J. A. Walder, *Biochemistry* **2008**, *47*, 5336–5353.
[148] S. F. Edwards, *Proc. Phys. Soc.* **1967**, *92*, 9–16.
[149] A. Shaw, E. Benson, B. Högberg, *ACS Nano* **2015**, *9*, 4968–4975.
[150] X. Shu, J. Dawei, C. Chengjun, W. Lihua, H. Qing, *Sci. Sin. Chim.* **2015**, *45*, 1220.
[151] D. R. Latulippe, A. L. Zydney, *J. Chromatogr. A* **2009**, *1216*, 6295–6302.
[152] E. Largy, J.-L. Mergny, *Nucleic Acids Res.* **2014**, *42*, e149–e149.
[153] B. J. Benedikter, F. G. Bouwman, T. Vajen, A. C. A. Heinzmann, G. Grauls, E. C. Mariman, E. F. M. Wouters, P. H. Savelkoul, C. Lopez-Iglesias, R. R. Koenen, et al., *Sci. Rep.* **2017**, *7*, DOI 10.1038/s41598-017-15717-7.
[154] G. Binnig, C. F. Quate, Ch. Gerber, *Phys. Rev. Lett.* **1986**, *56*, 930–933.
[155] L. Gross, F. Mohn, N. Moll, P. Liljeroth, G. Meyer, *Science* **2009**, *325*, 1110–1114.
[156] K. Iwata, S. Yamazaki, P. Mutombo, P. Hapala, M. Ondráček, P. Jelínek, Y. Sugimoto, *Nat. Commun.* **2015**, *6*, DOI 10.1038/ncomms8766.
[157] D. G. de Oteyza, P. Gorman, Y.-C. Chen, S. Wickenburg, A. Riss, D. J. Mowbray, G. Etkin, Z. Pedramrazi, H.-Z. Tsai, A. Rubio, et al., *Science* **2013**, *340*, 1434–1437.
[158] L. Silva, *Curr. Protein Pept. Sci.* **2005**, *6*, 387–395.
[159] A. M. Whited, P. S.-H. Park, *Biochim. Biophys. Acta BBA - Biomembr.* **2014**, *1838*, 56–68.
[160] D. Pang, A. R. Thierry, A. Dritschilo, *Front. Mol. Biosci.* **2015**, *2*, DOI 10.3389/fmolb.2015.00001.
[161] S. Thamm, N. Slesiona, A. Dathe, A. Csáki, W. Fritzsche, *Langmuir* **2018**, *34*, 15093–15098.
[162] Y. L. Lyubchenko, L. S. Shlyakhtenko, *Crit. Rev. Eukaryot. Gene Expr.* **2016**, *26*, 63–96.
[163] N. E. Lonergan, L. D. Britt, C. J. Sullivan, *Ultramicroscopy* **2014**, *137*, 30–39.
[164] A. Mann, M. A. Khan, V. Shukla, M. Ganguli, *Biophys. Chem.* **2007**, *129*, 126–136.
[165] J. X. Zhang, J. Z. Fang, W. Duan, L. R. Wu, A. W. Zhang, N. Dalchau, B. Yordanov, R. Petersen, A. Phillips, D. Y. Zhang, *Nat. Chem.* **2018**, *10*, 91–98.
[166] T. E. Ouldridge, P. Šulc, F. Romano, J. P. K. Doye, A. A. Louis, *Nucleic Acids Res.* **2013**, *41*, 8886–8895.
[167] Y. Yin, X. S. Zhao, *Acc. Chem. Res.* **2011**, *44*, 1172–1181.
[168] J. Strueben, M. Lipfert, J.-O. Springer, C. A. Gould, P. J. Gates, F. D. Sönnichsen, A. Staubitz, *Chem. - Eur. J.* **2015**, *21*, 11165–11173.
[169] H. B. B:urgi, J. D. Dunitz, J. M. Lehn, G. Wipff, *Tetrahedron* **1974**, *30*, 1563–1572.
[170] H. B. Burgi, J. D. Dunitz, Eli. Shefter, *J. Am. Chem. Soc.* **1973**, *95*, 5065–5067.

[171] C. H. Heathcock, L. A. Flippin, *Chem. Informationsdienst* **1983**, *14*, DOI 10.1002/chin.198339103.
[172] A. M. Smith, M. C. Mancini, S. Nie, *Nat. Nanotechnol.* **2009**, *4*, 710–711.
[173] M. Dong, A. Babalhavaeji, S. Samanta, A. A. Beharry, G. A. Woolley, *Acc. Chem. Res.* **2015**, *48*, 2662–2670.
[174] S. Crespi, N. A. Simeth, B. König, *Nat. Rev. Chem.* **2019**, *3*, 133–146.
[175] J. Calbo, C. E. Weston, A. J. P. White, H. S. Rzepa, J. Contreras-García, M. J. Fuchter, *J. Am. Chem. Soc.* **2017**, *139*, 1261–1274.
[176] C. E. Weston, R. D. Richardson, P. R. Haycock, A. J. P. White, M. J. Fuchter, *J. Am. Chem. Soc.* **2014**, *136*, 11878–11881.
[177] V. Adam, D. K. Prusty, M. Centola, M. Škugor, J. S. Hannam, J. Valero, B. Klöckner, M. Famulok, *Chem. - Eur. J.* **2018**, *24*, 1062–1066.
[178] M. W. Haydell, M. Centola, V. Adam, J. Valero, M. Famulok, *J. Am. Chem. Soc.* **2018**, *140*, 16868–16872.
[179] P. Mondal, M. Biswas, T. Goldau, A. Heckel, I. Burghardt, *J. Phys. Chem. B* **2015**, 150720105134009.
[180] M. I. Mitov, M. L. Greaser, K. S. Campbell, *ELECTROPHORESIS* **2009**, *30*, 848–851.
[181] N. Grebenovsky, T. Goldau, M. Bolte, A. Heckel, *Chem. - Eur. J.* **2018**, *24*, 3425–3428.
[182] H. Asanuma, T. Ishikawa, Y. Yamano, K. Murayama, X. Liang, *ChemPhotoChem* **2019**, 3, 418.
[183] C. F. Bennett, *Annu. Rev. Med.* **2019**, *70*, 307–321.
[184] R. Rupaimoole, F. J. Slack, *Nat. Rev. Drug Discov.* **2017**, *16*, 203–222.
[185] A. A. Levin, *N. Engl. J. Med.* **2019**, *380*, 57–70.
[186] M. A. Campbell, J. Wengel, *Chem. Soc. Rev.* **2011**, *40*, 5680.
[187] A. Khvorova, J. K. Watts, *Nat. Biotechnol.* **2017**, *35*, 238–248.
[188] S. Obika, Y. Hari, K. Morio, T. Imanishi, *Tetrahedron Lett.* **2000**, *41*, 215–219.
[189] B. Ravindra Babu, A. K. Prasad, S. Trikha, N. Thorup, V. S. Parmar, J. Wengel, *J. Chem. Soc. Perkin 1* **2002**, 2509–2519.
[190] J. A. Dale, D. L. Dull, H. S. Mosher, *J. Org. Chem.* **1969**, *34*, 2543–2549.
[191] N. Grebenovsky, L. Luma, P. Müller, A. Heckel, *Chem. – Eur. J.* **2019**, 25, 12298.
[192] F. Lottspeich, J. W. Engels, Eds. , *Bioanalytik*, Spektrum, Akad. Verl, Heidelberg, **2009**.
[193] K. Remaut, B. Lucas, K. Braeckmans, N. N. Sanders, S. C. De Smedt, J. Demeester, *J. Controlled Release* **2005**, *103*, 259–271.
[194] M. Baltzinger, K. K. Sharma, Y. Mély, D. Altschuh, *Nucleic Acids Res.* **2013**, *41*, 10414–10425.
[195] S. Ogasawara, M. Maeda, *Nucleic Acids Symp. Ser.* **2008**, *52*, 369–370.
[196] S. Ogasawara, M. Maeda, *Angew. Chem. Int. Ed.* **2009**, *48*, 6671–6674.
[197] E. Merino, *Chem. Soc. Rev.* **2011**, *40*, 3835.
[198] R. Wang, C. Jin, X. Zhu, L. Zhou, W. Xuan, Y. Liu, Q. Liu, W. Tan, *J. Am. Chem. Soc.* **2017**, *139*, 9104–9107.
[199] S. Ogasawara, *ACS Chem. Biol.* **2017**, *12*, 351–356.
[200] M. J. Wanner, G.-J. Koomen, *J. Chem. Soc. Perkin 1* **2001**, 1908–1915.

[201] N. Regner, T. T. Herzog, K. Haiser, C. Hoppmann, M. Beyermann, J. Sauermann, M. Engelhard, T. Cordes, K. Rück-Braun, W. Zinth, *J. Phys. Chem. B* **2012**, *116*, 4181–4191.

[202] S. Herre, T. Schadendorf, I. Ivanov, C. Herrberger, W. Steinle, K. Rück-Braun, R. Preissner, H. Kuhn, *ChemBioChem* **2006**, *7*, 1089–1095.

[203] B. Maerz, S. Wiedbrauk, S. Oesterling, E. Samoylova, A. Nenov, P. Mayer, R. de Vivie-Riedle, W. Zinth, H. Dube, *Chem. - Eur. J.* **2014**, *20*, 13984–13992.

[204] D. Li, Y. Yang, C. Li, Y. Liu, *Spectrochim. Acta. A. Mol. Biomol. Spectrosc.* **2018**, *200*, 1–9.

[205] D. Scarpi, L. Bartali, A. Casini, E. G. Occhiato, *Eur. J. Org. Chem.* **2013**, *2013*, 1306–1317.

[206] U. Wichai, S. A. Woski, *Org. Lett.* **1999**, *1*, 1173–1175.

[207] C. E. Weston, A. Krämer, F. Colin, Ö. Yildiz, M. G. J. Baud, F.-J. Meyer-Almes, M. J. Fuchter, *ACS Infect. Dis.* **2017**, *3*, 152–161.

[208] R. Yamaguchi, T. Imanishi, S. Kohgo, H. Horie, H. Ohrui, *Biosci. Biotechnol. Biochem.* **1999**, *63*, 736–742.

[209] J. Parsch, J. W. Engels, *J. Am. Chem. Soc.* **2002**, *124*, 5664–5672.

[210] M. Reinfelds, V. Hermanns, T. Halbritter, J. Wachtveitl, M. Braun, T. Slanina, A. Heckel, *ChemPhotoChem* **2019**, 3, 441.

6.4 Acknowledgements

My biggest gratitude I have to express to my parents and my family, who have been supporting me throughout all of my life and made it possible for me to reach the pinnacle of education I am about to reach.

In Prof. Dr. Alexander Heckel I found a supervisor who, aside of providing me with a thrilling topic, was always pleasant to work with on a personal level. His input of knowledge combined with the freedom to express myself in the laboratory he gave me led to the best possible outcome my time in his group could have. Therefore, I would like to express my gratitude towards him as a mentor and as human being alike.

My special gratitude goes to my former laboratory colleague Dr. Patrick Seyfried, for supporting me with his profound knowledge, which guided me through difficult tasks in my work.

Dr. Matiss Reinfelds was more than just a colleague to me, but a true friend. The time at the fume hood went flying, when we engaged in one of our many conversations. I admire his attiude towards science and his general kindness and helpfulness. The time together in the lab will never be forgotten.

Patricia Müller and I know each other since day 1 at the Goethe university, since our joint time in the Heckel group I value her as a colleague and friend alike. I want to express my gratitude for the fruitful conversations, scientific and personal alike.

Also I would like to thank Dr. Tomaš Slaniná for sharing his wisdom with me and for always being a friend and great colleague.

I would like to thank the KST of the Heckel group, especially Lurchi Lurchinski, Ronny, 3-2-1 Anja, Rebecco Tobacco and Fulgi-Volki for the nice cooking evenings, productive subgroup meetings and the pleasant lab time. I found another family in you.

Of course I would like to thank the other helping hands of the Heckel group as well. Heike Köhler, Martin Held, Alexandra Schuck and Dr. Christian Grünewald where always eager to help.

A great deal of my work has been made possible by the helping hands of my interns. The contribution of Anton Frühauf, Bastian Jacob, Emina Seperovic, Fabian Link, Frank Kaiser, Johanna Ehrler, Naciye Keklik, Phuong Thao Trinh, Rahime Ormoz, Satsuki Ishii and Strahinja Lucic was very essential for the

progress of the research topics they were working on and I would like to express my gratitude here.

Aside of being my sole bachelor student, Larita Luma was the most eager worker and learner I came across in my academic career. Her contribution to the LNAzo project was without doubt of utmost importance and I will observe your scientific career with great pleasure. She came to me in a difficult time of my life and I value her as a person every single day ever since.

The work of a scientist at the Goethe university would not be possible without the helping hands of the service personnel in the background. Therefore I would like to thank Julia Kiedrowski, Ralf Salomon, Dana Dobbs and Daniel Engelhardt from the chemical counter (*Chemikalienausgabe*), Wilhelm Lohbeck and Keve Bitto of the waste disposal facility (*Zentrales Zwischenlager für chemische Sonderabfälle*), Andreas Münch, Dr. Uwe Hener, Simon Zenglein and Matthias Brandl for the mass spectrometric service (*Serviceeinheit Massenspektrometrie*), Gabrielle Sentis of the NMR facility (*NMR-Serviceabteilung)* and Dr. Michael Bolte of the X-ray crystallography department (Serviceeinheit Röntgenstrukturanalyse).

6.5 Declaration

The work presented in this dissertation was executed by me, Nikolai Grebenovsky, under the supervision of Prof. Dr. Alexander Heckel, if not stated otherwise. Whenever a figure or text is identical to previous publications, it is stated in the thesis that corresponding material is reprinted with the explicit copyright permission of the authors and publishers.

Following figures are reprints from the work of other authors and/or provided by others:

Fig. 4, 18, 19, 20, 21, 22, 23, 24, 25, 26, 55.

6.6 Curriculum vitae

Personal information

Name: Nikolai Michal Grebenovsky
Address: Annemarie-Goßmann-Straße 64
65207, Wiesbaden (Germany)
Date birth: 02.03.1989
Place of birth: Wiesbaden (Germany)
Citizenship: german
E-mail address: nikolai.grebenovsky@gmail.com

Education

01/2016-12/2019	Doctoral studies in chemistry Institute of Organic Chemistry and Chemical Biology, Goethe University Frankfurt am Main Title of the dissertation: “Development of New Concepts for Photoswitchable DNA-Nanostructures”, supervised by Prof. Dr. Alexander Heckel
10/2013-10/2015	Master studies in chemistry (very good; 1.5) Institute of Organic Chemistry and Chemical Biology, Goethe University Frankfurt am Main Title of the master thesis: “Development of new Azobenzene *C*-nucleosides for the light-induced control of the stability of nucleic acid duplexes” under supervision of Prof. Dr. Alexander Heckel
10/2008-03/2013	Bachelor studies in chemistry (good; 2.1) Institute of Organic Chemistry and Chemical Biology, Goethe University Frankfurt am Main Title of the bachelor thesis: “Synthesis of Novel Building Blocks for the Torgov-Reaction” under supervision of Prof. Dr. Michael Göbel
Until 06/2008	High school education (Abitur) at the Carl-von-Ossietzky-Oberstufengymnasium in Wiesbaden

6.7 List of scientific publications

[I] P. Seyfried, L. Eiden, N. Grebenovsky, G. Mayer, A. Heckel, *Angew. Chem.* **2017**, *129*, 356.

[II] N. Grebenovsky, T. Goldau, M. Bolte, A. Heckel, *Chem. – Eur. J.* **2018**, *24*, 3425.

[III] N. Grebenovsky, L. Luma, P. Müller, A. Heckel, *Chem. – Eur. J.* **2019**, 25, 12298.